EVGA 2019

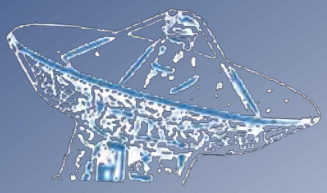

24th Meeting of the European VLBI Group for Geodesy and Astrometry

3rd IVS VLBI Training School

http://www.oan.es/evga2019/

MT MECHATRONICS

UNIVERSIDAD DE LAS PALMAS DE GRAN CANARIA

1989 30 2019

eite escuela de ingeniería de telecomunicación y electrónica

Cabildo de Gran Canaria

GranCanaria

GOBIERNO DE ESPAÑA | MINISTERIO DE FOMENTO | INSTITUTO GEOGRÁFICO NACIONAL

IDeTIC

RAEGE

Proceedings of the 24th European VLBI Group for Geodesy and Astrometry Working Meeting

17-19 March 2019
Las Palmas de Gran Canaria, Spain

edited by R. Haas, S. Garcia-Espada, and J. A. López Fernández

24th European VLBI Group for Geodesy and Astrometry Working Meeting
Las Palmas de Gran Canaria, Spain, 17-19 March 2019

Hosted by University of Las Palmas de Gran Canaria (ULPGC)

Title:
Proceedings of the 24th European VLBI Group for Geodesy and Astrometry Working Meeting

Authors:
Mentioned in each chapter

Editors:

Edited in November 2019

Administración General del Estado Publications Catalogue:
https://cpage.mpr.gob.es

Publisher:

Design and layout:
Servicio de Edición y Trazado (IGN)
(Subdirección General de Geodesia y Cartografía)

Depósito Legal: M-38563-2019
NIPO: 162-19-040-6 (paper version)
NIPO: 162-19-041-1 (electronic version)
DOI: 10.7419/162.08.2019
ISBN: 978-84-416-5634-5

Cover picture:
Poster of the 24th European VLBI Group for Geodesy and Astrometry Working Meeting

This book has been printed in recycled paper.
November 2019, Madrid, Spain

CNIG: Calle General Ibañez de Ibero, 3
28003 - Madrid (España)
www.cnig.es – consulta@cnig.es

Preface

The 24th Working Meeting of the European VLBI Group for Geodesy and Astrometry (EVGA) was held at the University of Las Palmas de Gran Canaria (ULPGC) 17–19 March 2019. The meeting was embraced by a number of other VLBI related activities at Las Palmas de Gran Canaria. Prior to the EVGA 2019, the 3rd IVS Training School on VLBI for Geodesy and Astrometry was held 14–16 March. And after the EVGA 2019, the IVS Analysis workshop, several VLBI splinter meetings and the 22nd IVS Directing Board meeting were held on 20–21 March.

There were 114 registered participants at the EVGA2019 meeting (Figure 1) which is a new record in the history of the EVGA working meeting (Figure 2). The participants came from 18 different countries, both from inside and outside Europe. Out of these 114 participants, 22 % were women. The percentage of women participating at EVGA meetings has been increasing steadily during the last years, which is a good sign that the VLBI community is moving forward towards gender balance.

The EVGA working meeting 2019 started with an ice breaker and registration on Sunday, 17 March, followed by the actual conference was held on Monday and Tuesday, 18 and 19 March.

Fig. 1: Picture of the EVGA 2019 participants at the campus of the University of Las Palmas de Gran Canaria (ULPGC).

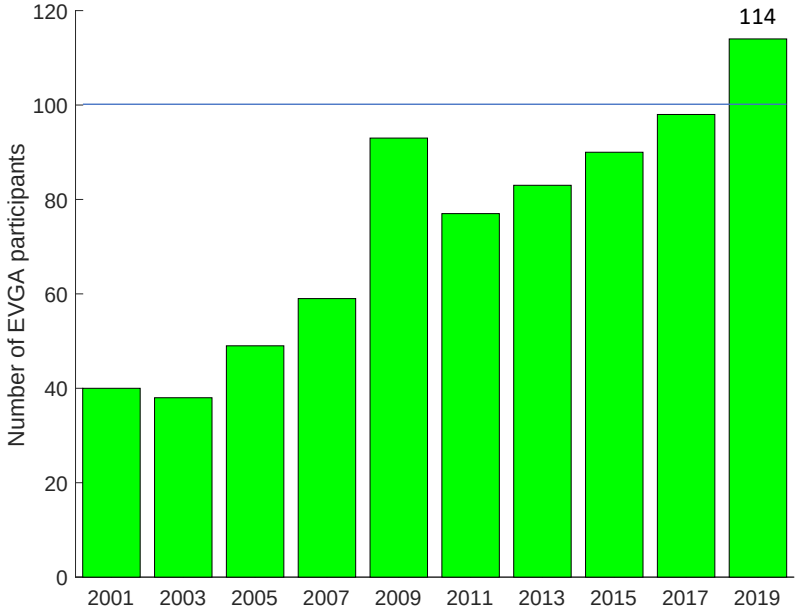

Fig. 2: Number of participants at EVGA working meetings in the last two decades.

The participants contributed with many interesting presentations on the current status of geodetic and astrometric VLBI and corresponding technical development and scientific results. In total there were 52 oral presentations and 39 poster presentations. The corresponding articles of the majority of these presentations are collected in this proceedings book. The conference dinner on Tuesday evening closed the meeting.

We want to thank all participants for sharing their findings with the audience during interesting oral and poster presentations. We want to thank the scientific organising committee for putting together a very interesting meeting program. The program and the list of participants are provided in Appendix-A. We are of course also grateful to all authors for preparing their proceedings contributions. The electronic version of these proceedings will be made available on the EVGA webpage evga.org.

The large number of participants at the EVGA 2019 Working Meeting, and the high quality and interesting oral and poster presentations are very good indications that European VLBI community is very active and on a good track. I am thus optimistic and convinced that we will see a strong contribution of the EVGA to VGOS!

November 2019
Rüdiger Haas (EVGA chair)

Message by José Antonio López Fernández

Subdirector for Astronomy, Geophysics and Space Applications at IGN Spain

Ten years ago, the embryo of the VGOS project (formerly known as VLBI2010), the Twin Telescope of Wettzell, started their early steps. In 2010, the IGN joined VGOS with RAEGE, a network with four radio telescopes to be located in the Iberian Peninsula, Canary Islands and Azores Islands. A project which means a big step forward not only for Spain, also for VGOS and an important technical and scientific collaboration between Spain and Portugal.

RAEGE means also a firm commitment from IGN to space geodesy, trying to turn Yebes Observatory into a GGOS Core Station, covering a big part of the Atlantic region and placing radio telescopes in three different tectonic plates. Ten years later, RAEGE now works with the radio telescopes in Yebes and Santa Maria, Azores, and contributes with receiver technology sharing our know-how and lessons learned with our partners at VGOS.

We are doing our best to put into operation the Artenara RAEGE radio telescope in Gran Canaria in order to be one of the VGOS partners as soon as possible. The organization of the 24th EVGA meeting in Las Palmas is one of these efforts and we can say that it has been a very definitive and important impulse for us. Now we are closer to that objective thanks to this event and to the help from the community. We are really proud to be organizers of a meeting that have offered us the chance to gather the best geodetic VLBI professionals around the world. We have been also lucky to verify how a new generation is born, as we have noticed with its successful VLBI school, knocking on VLBI's door and assuring the mid and long term space geodesy in the world.

From IGN we are grateful to the EVGA chair for trusting on us, to our sponsors MT Mechatronics, manufacturer of most of the modern VGOS radio telescopes, to the Cabildo of Gran Canaria for their support and to the impressive and excellent Las Palmas University team. Honestly we couldn't afford the organization of the meeting without their participation. Let's hold the line. All together we will achieve VGOS to be a reality soon.

November 2019
José Antonio López Fernández
Astronomy, Geophysics and Space Applications Subdirector at IGN

This page is intentionally left blank.

EVGA 2019 organising committees

Local Organising Committee (LOC)

- Susana Garcia-Espada (Chair)
- Víctor Araña Pulido
- Esther Azcue Infanzón
- Rubén Bolaño
- David Cordobés Gallo
- Itahiza Domínguez Cerdeña
- Pablo Dorta
- Abel García Castellano
- Yaiza Gómez Espada
- Víctor Puente García

Scientific Organising Committee (SOC)

- Rüdiger Haas (Chair) (Chalmers University of Technology, Sweden)
- Sabine Bachmann (Bundesamt für Kartographie und Geodäsie, Germany)
- Johannes Böhm (Vienna University of Technology, Austria)
- Susana Garcia-Espada (Instituto Geográfico Nacional, Spain)
- Laura La Porta (Reichert GmbH / Bundesamt für Kartographie und Geodäsie, Max Planck Institute for Radioastronomy, Germany)
- Evgeny Nosov (Institute of Applied Astronomy of the Russian Academy of Sciences, Russia)
- Nataliya Zubko (Finnish Geospatial Research Institute, Finland)

This page is intentionally left blank.

Contents

Technology Sessions

Observations Sessions

Analysis Sessions

Appendices

The Status of RAEGE

P. de Vicente, J. A. López Fernández, S. Garcia-Espada, R. Bolaño, L. Santos

Abstract The current document summarizes the status of the RAEGE network composed of four VGOS radio telescopes in Spain and Portugal. The radio telescope at the observatory of Yebes is fully operational and integrated in the VGOS core network. The station of Santa Maria has already seen the first light and yielded fringes with a tri-band receiver (S, X and Ka band) but it is still under commissioning, and the other two stations have not been built yet although progress is going on.

Keywords VGOS · IVS · Radio telescopes · Receivers

1 Introduction

RAEGE stands for Red Atlántica de Estaciones Geoespaciales (Atlantic Network of Geo Spatial Stations). It is composed of 4 stations in Spain and Portugal. The first operative station is located at the Observatory of Yebes in the Iberian peninsula and the second operative antenna at the island of Santa Maria, Azores Islands. The other two, not yet built, will be located in the Gran Canaria Island, Canary Islands and in Flores, Azores Islands. All four stations will be become part of the global IVS VGOS network, retaining its characteristic of being part of RAEGE network and devoting a small fractional time for local/regional studies.

Pablo de Vicente
Observatory of Yebes - Instituto Geográfico Nacional
Cerro de la Palera S/N Yebes, Spain

José Antonio López Fernández
Instituto Geográfico Nacional
C/General Ibañez de Ibero, Madrid, Spain

Susana Garcia-Espada · Rubén Bolaño
Instituto Geográfico Nacional - RAEGE Santa Maria station, Azores, Portugal

Luis Santos
Regional Government of Azores, São Miguel, Portugal

(Correspondence: p.devicente@oan.es)

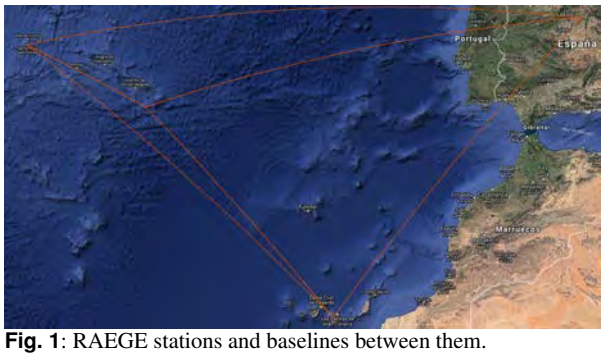

Fig. 1: RAEGE stations and baselines between them.

The baselines between the stations are basically East-West, East-South West and West-South East and their lengths span from 600 to 2400 km. Fig. 1 shows the baselines on a map.

The four stations are located on three different plates (see Fig. 2): the Eurasian, the African and the American one. The strategic distribution of the stations will allow to determine relative movements of the plates as a function of time. Observations within VGOS or dedicated ones will serve for this purpose.

2 The Yebes station

The Yebes VGOS station (Fig. 3) was built in 2013 and it is in operation as a VGOS telescope equipped with

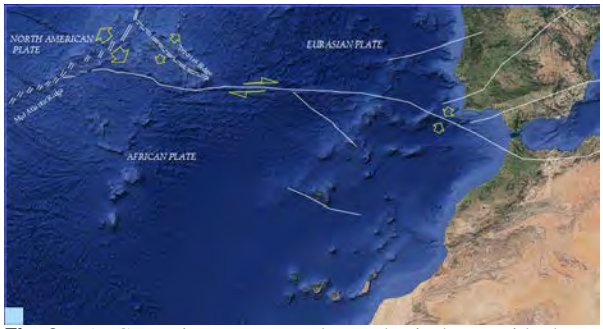

Fig. 2: RAEGE stations superposed on a physical map with plate borders.

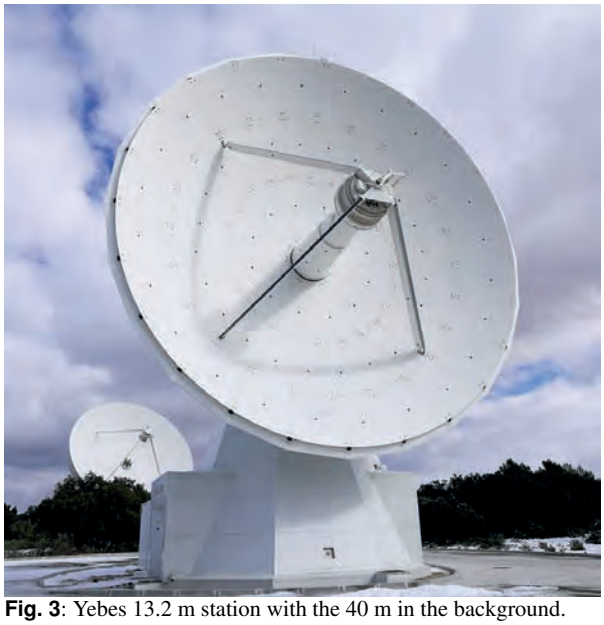

Fig. 3: Yebes 13.2 m station with the 40 m in the background.

a broad band receiver (2 – 14 GHz) since April 2016. It is one of the seven current core VGOS stations and it has taken part in tests along 2016, 2017, 2018 and 2019. The periodicity of the observations since 2017 is 14 days, lasting 24 hours for each observation. In 2017 we took part in 24 observations, whereas in 2018 we took part in less observations (19) due to a mechanical error at the antenna and in 2019, by the time of this report, we have already observed 11 times.

Yebes is also taking part in the EU-VGOS initiative, see Alef et al. (2019), as one of the three core European stations. The observations take place every 15 days and precede the VGOS sessions. These observations last a few hours and are used for testing several parts of the overall process which encompasses scheduling, observing, correlation, fringe fitting, analysis and data archiving.

The broad band receiver installed at the telescope was designed and built at the Observatory of Yebes. The system temperature is 50 K in average, being below that value at frequencies where no RFI is present. RFI is a severe problem at the site and to avoid saturation of the LNAs and of the optical fiber amplifiers a high band pass filter at 3 GHz was installed. Besides, to protect the optical fiber system a 6 dBm PIN diode power limiter is in place. The behaviour of the receiver has improved substantially after these two measures, which mitigate the RFI, were implemented.

Since 2017 the telescope has used 4 RDBEG backends and one Mark6 recorder and generates data in complex format. Four down conversion modules built at the Observatory of Yebes are in place before each RDBEG. The down conversion units with tunable local oscillators, yield two IF signals 500 MHz bandwidth, each in the selected frequency interval, across the VGOS wide band. VGOS data are transferred using disk packs to Haystack correlator except in the last epoch when they have been transferred via Internet. All EU-VGOS are transferred via Internet to Bonn correlator.

The Observatory of Yebes is a Technological Development Center for the IVS and it performs a number of works which are described in López Perez et al. (2019). The main tasks are related to the development of cryogenic active (amplifiers) and passive devices, cryogenic receivers, and the improvement of the geodetic phase cal system.

The Yebes Observatory will become soon a geodetic core station after the future installation of a SLR telescope. This telescope together with the current two GNSS antennas (one in the international network and the second in a national network), the gravimeters and the VGOS radio telescope, will provide coordinates in different reference systems. A local tie composed of 23 concrete pillars connects all the previous points and provides the local link between the different reference systems.

In the future a correlator will be deployed at the Observatory of Yebes for the RAEGE network. We are also developing an analysis group at the IGN headquarters which has started processing legacy IVS data using WHERE software from NMA and VIEVS from the University of Vienna.

3 The Santa Maria station

The Santa Maria station (see Fig. 4) is located at Santa Maria island at an altitude of 240 m. The first single dish observations at Santa Maria station took place in 2017 and the first fringes were obtained in 2018 (see Fig. 5).

The radio telescope is equipped with a tri-band receiver that covers S band (2 – 2.7 GHz), X band (7.5 – 9 GHz) and Ka band (28 – 33 GHz), with system temperatures close to 50 K in average. The receiver was built at the Observatory of Yebes and it is similar to the ones installed at Ishioka and Ny-Ålesund. It allows to perform legacy IVS VLBI observations. The data acquisition system is a DBBC2 and the recording system a Mark5B+. There is a second Mark5B+ at the station for transferring data to the correlator. The Internet connection has a low data rate, 80 Mb/s, which allows transfers but prevents high speed connections.

Some legacy IVS observations in tag-along mode have been performed in 2018 and 2019 but several problems with the antenna and the receiver have prevented a continuous operation of the station. The issues are still being worked out.

The broad band receiver for Santa Maria is already built and pending of tests at the Observatory of Yebes. The installation date at the antenna will depend on the availability of VGOS backends and the broad band donwconversion system.

Fig. 4: Santa Maria 13.2 m station from a drone.

4 The Gran Canaria station

The local government of Gran Canaria granted in 2018 the usage of a terrain for the construction of the future VGOS radio telescope and the control building. The site is at 1100 m of altitude and in a natural protected area. The strict requirements needed to protect the local environment have delayed the construction for a very long time. Meanwhile funds for all previous civil works have been secured and the administrative paperwork is being sorted out to be able to start the conditioning of the site by late 2019, since construction works are prohibited between March and September for environmental reasons.

The antenna, already built by MT Mechatronics, is stored in a warehouse at Gran Canaria island and undergoes periodic inspections until it gets installed at its definitive site.

The Observatory of Yebes has deployed two people at Gran Canaria to track the progress of the station. The agreement between the IGN and the University of Las Palmas of Gran Canaria to provide technical support to the telescope has allowed to host the IGN staff at the premises of the university. Part of the future technical works will be done together with the University.

5 The Flores station

The Flores station is the least developed one of the RAEGE network. The administrative paperwork to get the ownership of the terrains has started. This station will be fully funded by the Regional Government of the Azores.

The soil conditions are being evaluated and the RFI environment was measured some years ago. Currently the weather conditions are being analyzed since the location shows strong and frequent winds. This condition should be taken into account in the design of the radio telescope to prevent corrosion and difficulties in the operation and maintenance of the telescope.

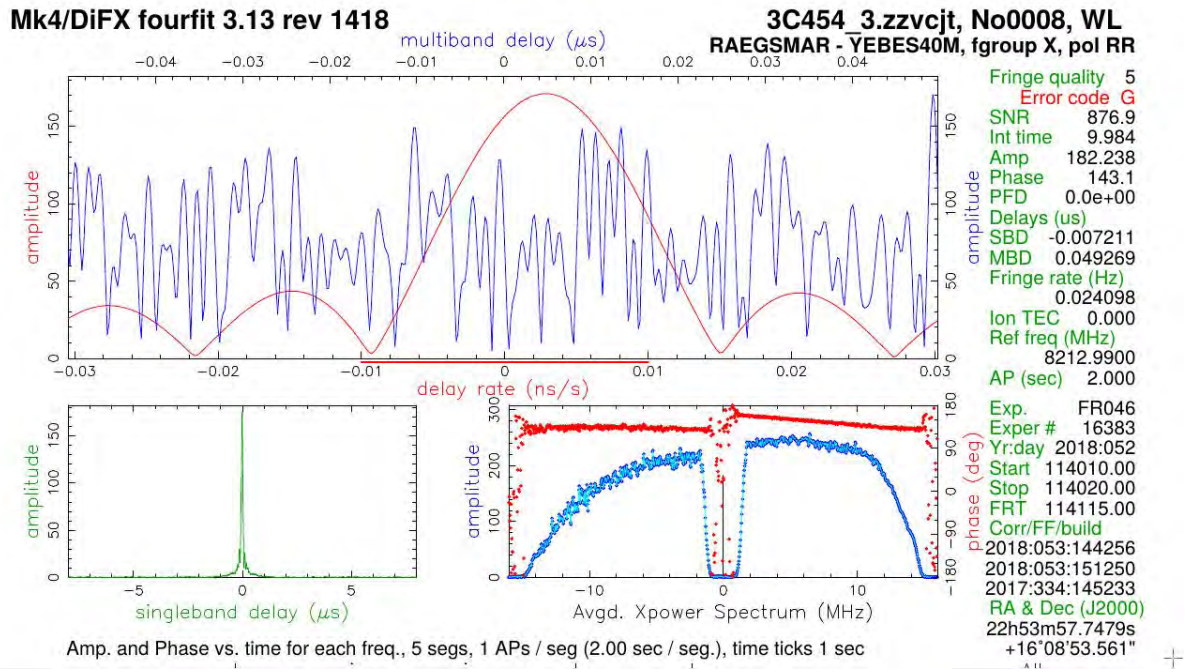

Fig. 5: A fourfit plot with X band fringes between the Santa Maria 13.2 m station and the 40 m radio telescope at Yebes.

References

Alef W, Anderson J M, Bernhart S., et al. (2019) The EUropean-VGOS Project. In: R. Haas, S. Garcia-Espada, J. A. López Fernández (eds.): *Proc. 24th EVGA Working Meeting*, 107–111

López Perez A, de Vicente P, López Fernández J A, et al. (2019) Instrumentation Developments for VGOS at IGN Yebes Observatory. In: R. Haas, S. Garcia-Espada, J. A. López Fernández (eds.): *Proc. 24th EVGA Working Meeting*, 22–26

Status of the Onsala Twin Telescopes — Two Years After the Inauguration

R. Haas, S. Casey, J. Conway, G. Elgered, R. Hammargren, L. Helldner, K.-Å. Johansson, U. Kylenfall, M. Lerner, L. Pettersson, L. Wennerbäck

Abstract We give a brief overview on the status of the Onsala twin telescopes (OTT), two years after their inauguration. The different components of the VGOS systems are briefly described, and the development towards routine operations.

Keywords VGOS · Onsala twin telescopes · DBBC3

1 Introduction

The Onsala twin telescopes (OTT) (Fig. 1) are two identical VGOS telescopes that were designed by MT Mechatronics GmbH. The OTT were installed during 2015/2016 in a distance of 75 m from each other. The ceremonial inauguration took place in May 2017 in connection to the 23rd Working Meeting of the European VLBI Group for Geodesy and Astrometry (EVGA) (Haas et al., 2019). Within the International VLBI Service for Geodesy and Astrometry (IVS) the OTT are known as ONSA13NE and ONSA13SW, with 2-character abbreviations OE and OW, respectively. The telescopes have a ring-focus design with a main reflector diameter of 13.2 m. As all VGOS telescopes they have fast slewing speeds: 12 and 6°/s in azimuth and elevation, respectively. The RMS surface accuracy of the main reflectors was determined to be 82 μm and 102 μm for OE and OW, respectively (Lösler et al., 2017), which is fulfilling the VGOS requirements.

Fig. 1: The Onsala twin telescopes at night, with OW (left) and OE (right). Photo taken by Armin Corbin in early 2019.

2 The signal chain

The OTT are equipped with cryogenic broadband receiving systems that were built at Onsala and are to a large degree identical (Pantaleev et al., 2017a). However, they have two different feed horns. OW is equipped with an Eleven-Feed of type 2017EFiC-2-14C-8P. It has hybrid couplers to reduce the needed number of low noise amplifiers from eight to two. The design is compact and wide band, with an opening angle of 65°, dual linear polarized covering a frequency range of 2 – 14 GHz. The intention when designing the system was to achieve compatibility with the legacy S/X systems. OE is equipped with a Quad-Ridged Feed Horn (QRFH) that was purchased

Rüdiger Haas · Simon Casey · John Conway · Gunnar Elgered · Roger Hammargren · Leif Helldner · Karl-Åke Johansson · Ulf Kylenfall · Mikael Lerner · Lars Pettersson · Lars Wennerbäck
Chalmers University of Technology, Department of Space, Earth and Environment, Onsala Space Observatory, SE-439 92 Sweden

(Correspondence: rudiger.haas@chalmers.se)

from Caltech. The type is QRFH-60S-6-3 which was customized for an opening angle of 60° and a frequency range of 3 – 18 GHz. The intention when designing this system was to avoid the RFI-polluted lower S-band frequencies. The two receiving systems are interchangeable so that both OTT should be able to co-observe in mixed-mode with legacy S/X systems, however, not simultaneously.

The backends are located in the observatory control room at the 20 m radome enclosed telescope, approximately 500 m straight line distance from the telescopes. The radio frequency (RF) signals are sent from the telescopes via optical fibres which are approximately 1 km long since they are burried 70 cm below the soil surface and cannot follow the straight line. The cable length variations are monitored with cable delay measurement systems (CDMS). Each of the telescopes is equipped with four RF-over-fibre (RFoF) transmitters each located on the receiver trolley, two for vertical and two for horizontal polarization. Due to a high level of radio frequency interference (RFI) in the lower end of the frequency range and potential problems with saturation, the polarizations are split into a low (2.0 – 6.0 GHz) and a high frequency part (3.8 – 18.0 GHz). The corresponding RFoF receivers are located in the control room, close to the backends.

The OTT use one DBBC3 backend (Tuccari et al., 2018) each. These DBBC3s are of type DBBC3-8L8H, i.e. equipped with 8 IF-modules with 4096 MHz bandwidth each. There are eight analogue conditioning modules, called GCoMo, each covering 4 GHz of RF-input. The RF-signals are fed into the DBBC3s according to Tab. 1. Since the highest frequency band (11.4 – 15.2 GHz) is not yet used for VGOS test observations, RF-band (3.8 – 7.6 GHz) is currently split and fed into the two middle modules. However, the systems are prepared to cover higher frequencies in the future, see the range marked in red in Tab. 1.

Table 1: RF input to the DBBC3s. For the current VGOS test experiments, Band-3 and Band-4 are fed with the same frequency range. However, all systems are prepared to be fed with a higher frequency band (red) in the future.

	OW - Eleven-Feed	OE - QRFH
RF-band	Bandwidth (GHz)	Bandwidth (GHz)
Band-1	2.0 – 3.8	3.0 – 3.8
Band-2	3.8 – 7.6	3.8 – 7.6
Band-3	3.8 – 7.6	3.8 – 7.6
Band-4	7.6 – 11.4	7.6 – 11.4
	(11.4 – 15.2)	(11.4 – 15.2)

3 Pointing and sensitivity

Soon after the official inauguration in May 2017, first light was achieved with both OTT and radio source signals could be detected. Following this, during the summer of 2017 the work continued to derive pointing models. Fig. 2 depicts the current level of pointing residuals for both telescopes. The RMS residuals for OE are 14.8 arcsec and 10.3 arcsec in elevation (E) and orthogonal to elevation (xE), and for OW 15.6 arcsec and 13.2 arcsec, respectively.

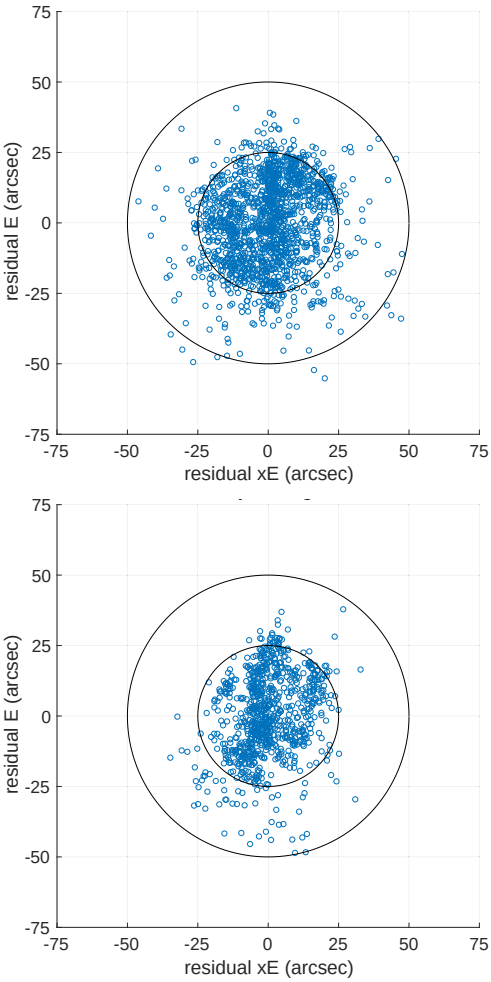

Fig. 2: Pointing residuals for OE (top) and OW (bottom).

In the autumn of 2017 first interferometric tests were done. In a test on 25 September, fringes were found for some RF bands for OE, and on 5 October also for OW. Both systems were adjusted and finally on 13 November 2017 fringes were found in all 4 RF-bands for OE. It took until 8 February 2018 before the same was achieved with OW.

Extensive measurements were performed to characterize the OTT system performance at the frequencies currently used for VGOS test sessions. Fig. 3 depicts system equivalent flux density (SEFD) measurements. In general, except for the lowest frequency range, around 3.0 – 3.5 GHz, which is affected heavily by RFI disturbances, the goal of 2000 Jy is achieved with both systems. However, there are also RFI around 5.2 GHz and 5.8 GHz for horizontal polarization.

A complete monitoring of the broadband sensitivity, i.e. not only the current VGOS frequencies, is planned for the future.

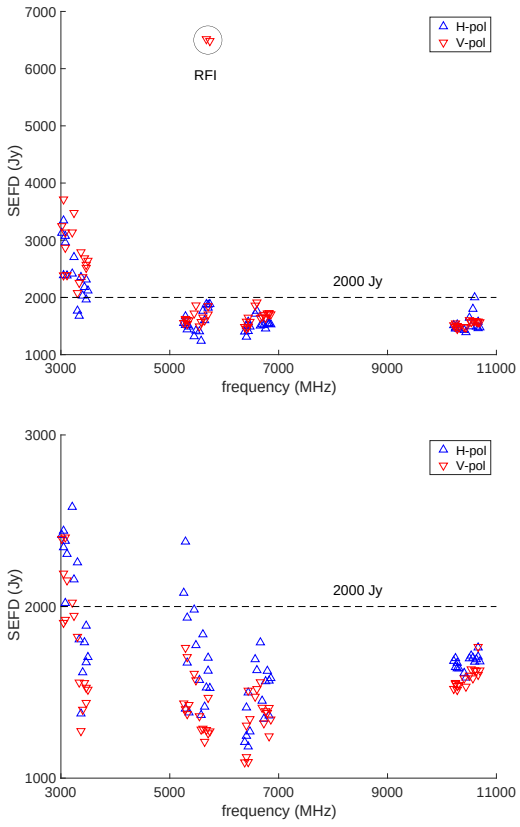

Fig. 3: SEFD measurements for OE (top) and OW (bottom).

4 Data recording and transfer

The OTT use Flexbuff computers as recorders. Currently there are two such machines, with 330 TB and 432 TB storage capacity, respectively. The backend systems can be flexibly connected to any of the recorders. Extensive tests have verified that recordings of up to 50 Gb/s are possible. Fig. 4 gives an overview of the current connectivity of the OTTs. The connectivity to the outside world is using two 10 Gb/s links, but can easily be upgraded to 100 Gb/s if necessary.

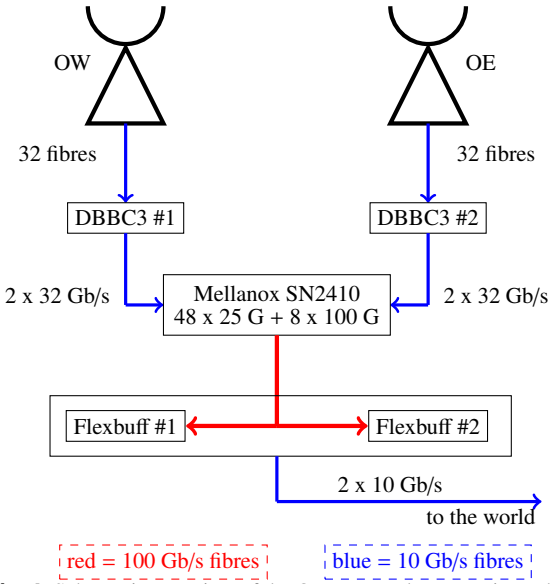

Fig. 4: Schematic overview of the OTT network connection. The two Flexbuffs have currently 330 TB and 432 TB storage capacity, respectively.

5 VGOS operations

We are very thankful to Ed Himwich for his support to integrate the DBBC3 control into the VLBI Field System (FS). The OTT operations can now be performed completely with the Field System FS 9.12.12 VGOS branch. This includes:

- configuration of the DBBC3 backends
- direct communication with the antenna control unit
- control of data recording
- control of the cable delay monitoring system (CDMS), including phase cal (PCAL)

There is one FS per OTT-system. They are interchangeable and can be accessed remotely. The telescopes themselves can be monitored via live-feed cameras, both in the control room as well from the outside. Additional monitoring of numerous telescope status parameters is possible via the in-house software "Bifrost". The data recording is monitored during observations with spectra and sampler statistics information that are displayed graphically on the FS screen.

During 2017, we participated in 6 VGOS test (VT) sessions of 24 h length, either with one or both systems. The VT-sessions are observed currently with 8 Gb/s and are correlated at Haystack observatory. There were problems with weak fringes and the level of the phasecal signals, so that no useful VGOS databases resulted. In 2018 we participated with OE in total in 18 of the 24 h VT sessions. One of these sessions was observed with both OTTs. While the PCAL situation improved during 2018, there were problems with the DBBC3s. These problems caused data loss and no VGOS databases could be produced. In 2018 a lot of work was spent on improving the stability of the DBBC3s. Finally, the last VT-session in December 2018, which was also observed with both OTTs, was problem-free. Besides the international VT-sessions, we also observed with OE in 10 shorter sessions (4–6 h) with the European VGOS partner stations Wettzell and Yebes. These European VGOS (EV) sessions are correlated in Bonn. We also observed 6 sessions of various observation length together with Kashima, the so-called OK-sessions with different frequency setup than the standard VT-sessions and 16 Gb/s recording. A list of the 2017/2018 observations is provided in Haas et al. (2019b).

After the steep learning curve in 2017/2018 with continual system improvements, the situation became stable in early 2019. We participate in both the bi-weekly VT-sessions as well the EV-sessions, and the performance is in general good and stable. The first VGOS databases that could be analysed are `19JAN07VG` and `19JAN22VG`.

6 Further aspects

During the summer of 2018 a photogrammetric survey of OE was performed with an unmanned aerial vehicle (UAV). The aim was to investigate the elevation-dependent variations of the focal length (Lösler et al., 2019a) and to derive a model for signal path variation (SPV) in the telescope optics due to gravitational deformation (Lösler et al., 2019b).

The OTT were also equipped with a temperature and humidity monitoring system. Temperatures are monitored in different levels and directions in the telescope towers, inside the telescope azimuth and elevation cabins, and at various places along the optical fibres.

Furthermore, a local geodetic survey network with 6 concrete pillars was established around the OTT and a first epoch survey was performed (Heep, 2018). This is the basis for a classical local-tie survey which is planned for 2020.

In early 2019 first short baseline interferometry measurements were performed between the OTT and ON, the Onsala 20 m telescope, using X-band observations (Marknäs, 2019), see Tab. 2.

Table 2: Baseline length (L) and standard deviation (σ) in the Onsala telescope cluster, derived from local interferometric measurements at X-band performed in early 2019 (Marknäs, 2019).

Baseline	L (m)	σ (mm)
`OE - OW`	74.9612	± 0.2
`OE - ON`	468,6819	± 0.5
`OW - ON`	540.3115	± 0.4

7 Conclusions and outlook

A little less than two years after their official inauguration the OTTs have become operational. They are used operationally on a regular basis for VGOS observations. Data observed in the IVS VT-sessions are sent to the correlator at Haystack observatory and VGOS databases for post-processing are produced. Data observed in the European EV-sessions are sent to the correlator at Bonn. The plan is to continue to contribute to VGOS observations, both on the international and the European level.

One important aspect for the upcoming months will be to start to also observe in the so-called mixed-mode, using both the OTT and the Onsala 20 m radio telescope that is used for IVS S/X legacy observations. Further steps are to do additional local interferometry observations with the Onsala telescope cluster and to

perform a classical local-tie survey and determination of the reference points.

On the system level, work will continue to fine-tune the pointing models, to derive gain curves, and to calibrate the OTT.

References

Haas R, Casey S, Elgered G, et al. (2019) Status of the Onsala Twin Telescopes – One Year After the Inauguration. In: K. L. Armstrong, K. D. Baver, D. Behrend (eds.): *IVS 2018 General Meeting Proceedings*, NASA/CP-2019-219039, 17–19

Haas R, Hobiger T, Elgered G, et al. (2019) Onsala Space Observatory – IVS Network Station Activities during 2017–2018. In: K. D. Baver, D. Behrend, K. L. Armstrong (eds.): *International VLBI Service for Geodesy and Astrometry 2017+2018 Biennial Report*, in press

Heep N (2018) Erweiterung des terrestrischen Kontrollnetzes der Twin-Teleskope an der Fundamentalstation Onsala. Bachelor thesis, Frankfurt University of Applied Sciences, 66 pp.

Lösler M, Eschelbach C, Haas R (2017) Unified model for surface fitting of radio telescope reflectors. In: R. Haas, G. Elgered (eds.): *Proc. 23rd EVGA Working Meeting*, 29–34

Lösler M, Eschelbach C, Haas R, et al. (2019a) Measuring Focal-Length Variations of VGOS-Telescopes Using Unmanned Aerial Systems. In: R. Haas, S. Garcia-Espada, J. A. López Fernández (eds.): *Proc. 24th EVGA Working Meeting*, 17–21

Lösler M, Haas R, Eschelbach C, et al. (2019b) Gravitational Deformation of Ring-Focus Antennas for VGOS – First Investigations at the Onsala Twin Telescopes Project. *J Geod*, doi:10.1007/s00190-019-01302-5

Marknäs V (2019) Connecting the Onsala Telescope Cluster Using Local Interferometry. Master's thesis, Department of Space, Earth and Environment, Chalmers University of Technology

Tuccari G, Alef W, Dornbusch S, et al. (2018) DBBC3 – the new wide-band backend for VLBI. In: *Proceedings of Science*, 344, 14th European VLBI Network Symposium & Users Meeting (EVN 2018), doi:10.22323/1.344.0140

Pantaleev M, Haas R, Billade B, et al. (2017) Onsala Space Observatory – IVS Technology Development Center Activities during 2015–2016. In: K. D. Baver, D. Behrend, K. L. Armstrong (eds.): *International VLBI Service for Geodesy and Astrometry 2015+2016 Biennial Report*, NASA/TP-2017-219021, 301–305

Pantaleev M, Helldner L, Haas R, et al. (2017) Design, Implementation and Tests of the Signal Chain for the Twin Telescopes at Onsala Space Observatory. In: R. Haas, G. Elgered (eds.): *Proc. 23rd EVGA Working Meeting*, 15–19

Establishment of a New Fundamental Site Ny-Ålesund

L. M. Tangen

Abstract We started to build the first part of the road and bridge in 2013. The rest was done in 2014. Veidekkearctic did the construction work from Oct. 2014 to Oct. 2015. Both telescopes arrived April 2016. GNSS, DORIS and Gravity is in operation. Tests with Tri-band-feed are done and the first broadband feed will arrive summer 2019.

Keywords Road · Bridge · Telescope

1 Start up

We started summer 2013 with building the road half the way and a bridge. During the summer, a ship came and put the new fiber optic cables from Longyearbyen to Ny-Ålesund on the seabed.

Next summer the rest of the road was made and the station area was prepared for construction work.

Veidekke Arctic got the contract and they started up autumn 2014 with all fundaments for the buildings and the geodetic equipment.

The most exciting part was how deep we had to dig down for the VLBI fundaments. Test drillings said 4 meters and that was correct.

The construction work had to be done during the winter. The Governor of Svalbard had this as a part of their permit to build. To do construction work outside at Svalbard, during the winter can be a challenge, but Veidekke did this very well.

In spring 2015, the VLBI towers were finished and the local tie fundaments were done. The local tie fundaments are made as a tripod. Three steel pipes are drilled down in solid rock. They are frozen with water in the permafrost. Logging of the stability is done, and all tripod fundaments are not stabile enough. We have made more fundaments with one H formed steel pole. They are better.

All buildings (station, gravity, SLR and walkways) and all geodetic fundaments were finished and delivered to Kartverket Oct 2015.

2 Technical solutions

The station has to power systems. A UPS system with generator and the standard one. The UPS is made for critical systems as maser and cooling only. It is not possible to move the telescopes when the station run on UPS/generator.

To keep all signal cables from technical room to the receiver as stable as possible, they have an own insulated and heated box in the walkways.

3 Telescopes

The telescopes arrived Ny-Ålesund in April 2016 and delivered to Kartverket in September from MT Mechatronics.

Leif Morten Tangen
Norwegian Mapping Authority, Geodetic Institute, Kartverksveien 21, Hønefoss, NO-3511 Norway

(Correspondence: Leif.Morten.Tangen@kartverket.no)

Fig. 1: The new station in winter

4 Other things

- Maser (T4 Science) in operation June 2016
- Tri-band feed from Yebes for tests in NS (Ny-Ålesund South)
- ACS from Yebes for antenna control
- Backend: DBBC3 and Flexbuff
- First broadband feed from Yebes summer 2019
- SLR 2022
- GNSS in operation Nov 2015
- Local tie
- DORIS about 400 m away, connected with local tie
- Constructor blogg http://veidekkearctic.no/

5 Other challenges

- Lack of VGOS correlation capacity
- Test of full VGOS not possible
- Lack of up to date development plan for VGOS operation/analyzing capacity
- VGOS HW/infrastructure must be built to match the development plan in item 3.
- Operational cost of the Observatory in standby without observing is about 100 k€.
- Damaging for geodetic activities not to fully utilize the Observatory due to lack of international correlation capacity

6 Opportunities

Take a closer look to this link and check if you can send an apply for support: https://ec.europa.eu/info/funding-tenders/opportunities/portal/screen/opportunities/topic-details/infradev-01-2019-2020;freeTextSearchKeyword=;typeCodes=1;statusCodes=31094501,31094502;programCode=null;programDivisionCode=null;focusAreaCode=null;crossCuttingPriorityCode=null;callCode=Default;sortQuery=deadline;orderBy=desc;onlyTenders=false;topicListKey=topicSearchTablePageState

Efforts and Attempts to Develop VGOS-like Stations in China

J. Li, C. Liu, H. Zhang, D. Zhao, Q. Fan, F. Shu, R. Zhao, J. Wang, X. Zhang, G. Wang, X. Yang, L. Yu, Y. Jiang, S. Guo, L. Wang

Abstract The development of the China VLBI network (CVN) is reviewed in this presentation, especially concerning the efforts and attempts to develop new stations of the VLBI Global Observation System (VGOS), the next generation radio telescopes for astrometry and geodesy.

Keywords VLBI · CVN · VGOS · Radio telescope · Astrometry · Geodesy

1 Introduction

In contrast to satellite-related techniques such as Satellite Laser Ranging (SLR) and Global Navigation Satellite Systems (GNSS), Very Long Baseline Interferometry (VLBI) is outstandingly characterized in several aspects. The measurement of VLBI is not detrimentally affected by the uncertainties of Earth gravity field model, nor the motion of the Earth center. VLBI precisely determines the relative position / direction of observation stations and targets. VLBI observation is in the radio frequency domain and so is available round the clock and in almost all the weathers except extremely bad ones such as typhoon, heavy rain or snow. The extragalactic radio sources (ERS) of several billions of light years are almost fixed onto the deep space background of the Universe. By taking ERS as referencing target, VLBI determines the relative uncertainty of baseline length up to 1 ppb (1E-9) or better on the global scale and with extremely high long stability. VLBI determines all the dimensions of Earth Orientation parameters (EOP) including UT1, polar motion and corrections to nutation / precession model, precisely ties the terrestrial reference frame (TRF) with the celestial reference frame (CRF).

In this presentation, it is described from the point of view of the authors about the efforts and attempts to develop stations of the VLBI Global Observation System (VGOS) in China. Section 2 presents a brief overview of the China VLBI Network for astrometry and geodesy (CVN). Section 3 presents a description of the current situation to develop VGOS-like stations in China. Section 4 describes some considerations on the development of new VGOS stations. Section 5 concludes the presentation with some discussion on future work.

Jinling Li · Cong Liu · Hui Zhang · Daxin Zhao · Qingyuan Fan · Fengchun Shu · Rongbing Zhao · Jinqing Wang · Xiuzhong Zhang · Guangli Wang · Linfeng Yu · Yongbin Jiang · Shaoguang Guo · Lingling Wang
Shanghai Astronomical Observatory, Chinese Academy of Sciences, Shanghai 200030, China

Xuhai Yang
National Time Service Center, Chinese Academy of Sciences, Lintong, Xi'an 710600, China

(Correspondence: jll@shao.ac.cn)

2 Overview of the CVN development

The key techniques sustain the high precision operation performance of VLBI mainly include the followings. The progressive improvement in data recording rate from kilo-bits per second (k bps) to mega- and to gigabits, and from single to multi channels, which significantly increases the technical sensitivity. The invention of the bandwidth synthesis technique, which achieves equivalent delay precision of wide frequency

band by synthesizing the data from multi-narrow frequency channels. If the whole wide band was sampled, quantized and recorded, the data volume would be huge and so be costing much more recording medium. And if only a narrow band was recorded, the delay uncertainty would be relatively large. The Hydrogen maser which is essentially high in frequency stability, permits those remote stations individually and synchronously collecting the interferometry data which could be centrally correlated following the observation sessions. The advanced receiving device of low equivalent noise temperature permits the high technical sensitivity. The sophisticated astrometric and geophysical models and the improved methods of observation data processing contribute the high quality and precision of VLBI products.

In China the VLBI technique development started from early 1970s. An experimental system of radio telescope was constructed at Shanghai Astronomical Observatory (SHAO), Chinese Academy of Sciences (CAS) in 1974. As shown in Fig. 1 (a), the diameter of the antenna is 6 m. With this system some international VLBI experiments were initiated by cooperation with for instance the 100-m telescope at Effelsberg in 1981 and the 26-m telescope at Kashima in 1985 (Wan et al., 1983, 1987; Heki, 1995; Li et al., 2010).

The Sheshan 25-m antenna system (Fig. 1 (b)) at Shanghai is the first modern radio telescope in China, which participated in VLBI observation from 1987 (Li and Wang, 2001). The Nanshan 25-m radio telescope at Urumqi (Fig. 1 (c)) performed observation from 1994. The two 25-m antennas are the network components of the International VLBI Service for astrometry and geodesy (IVS) and the reference stations in the International Terrestrial Reference Frame (ITRF). They also significantly improve the U-V coverage of the European VLBI network (EVN).

In 2000, a mobile VLBI station was constructed by SHAO for the Xi'an Surveying and Mapping Institute. The station is located at Yunnan Astronomical Observatory, Kunming, China. It is a 3-m antenna system and had contributed to the China Lunar Exploration Project (CLEP) in the experimental observation phase.

Directly promoted by CLEP, in 2006 the Miyun 50-m antenna at Beijing (Fig. 1 (d)) and the Phoenix Mountain 40-m antenna at Kunming (Fig. 1 (e)) were commissioned and the SHAO VLBI correlation center began routine operations (Hong, 2007). Due to the further requirements of China's subsequent lunar and deep space exploration, the Tianma 65-m radio telescope at Shanghai (Fig. 1 (f)) was essentially constructed by the end of 2012 (Li et al., 2014). The current observation bands cover L, S, C, X, Ku, K, Ka and Q.

Fig. 1: The CVN radio telescopes.

We also have several radio telescopes for deep space exploration in China, for instance the 35-m at Kashi and the 64-m at Jiamusi. Now we are developing some broadband VLBI (VGOS-like) stations for astrometry and geodesy as well as for satellite navigation.

3 VGOS-like stations in China

Since 1980s the conventional VLBI observation for astrometry and geodesy has been at S/X dual frequency bands, centered at about 2.3/8.4 GHz. With the progressively wide application of radio frequency active emission in national defense, economy development and daily life, the radio interference to the passive reception of astrometric and geodetic VLBI observation at S-band becomes more and more serious. In addition to the rapid development of electronic technology and the increasing demand of accuracy for astrometric and geodetic VLBI products, the technical specifications were recommended for the next generation radio telescopes for astrometry and geodesy (Petrachenko et al., 2009).

We have roughly three types of VGOS-like stations with different systematic designs and technical

Fig. 2: Pictures of the Tianma13 telescope.

specifications, supported by different institutions and / or through different projects. Type I, NTSC13, National Time Service Center (NTSC), CAS. Type II, Tianma13, SHAO, CAS. Type III, Sheshan13, SHAO, CAS. The antennas are all about 13 m in diameter, with high slew rate as 12 °/s in azimuth and 6 °/s in elevation.

3.1 NTSC13

The frequency band of NTSC13 is 1.2 GHz ~ 9 GHz. The efficiency is higher than 50 %. The equivalent temperature of the receiver is about 70 K. There are three stations of NTSC13 located at Kashi, Changchun and Sanya, mainly for the corrections of systematic uncertainties in the tracking / positioning of navigation satellite.

3.2 Tianma13

The frequency band of Tianma13 is 3 GHz ~ 18 GHz. The efficiency is about 50 %. The equivalent temperature of the receiver is about 20 K. As shown in Fig. 2, the left panel is a satellite map of the yard of Tianma 65-m antenna, the Tianma13 is at the right-lower corner.

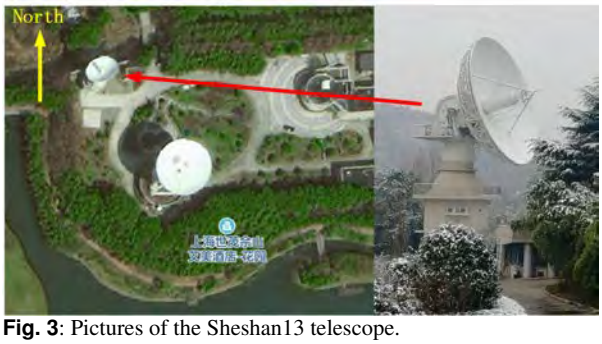

Fig. 3: Pictures of the Sheshan13 telescope.

3.3 Sheshan13

In Fig. 3, the left panel is a satellite map of the yard of Sheshan 25-m antenna, the Sheshan13 is at the left-upper corner. The broadband receiver of Sheshan13 is 2 GHz ~ 14 GHz with typical equivalent temperature as 18 K. The dual band X/Ka receiver is 7 GHz ~ 9.5 GHz / 28 GHz ~ 34 GHz and the equivalent temperature as 15 K / 25 K. The data recording is 4 channels of bandwidth 512 MHz and would be updated to 1 GHz.

Fig. 4 shows the system temperature (T_{sys}) of Sheshan13. The broadband is about 40 K but contaminated by many interference signals below 6 GHz and at about 13 GHz. The dual band frequency is down converted to 3 GHz ~ 12 GHz. The system temperature at X-band is about 30 K and at Ka-band about 60 K. Table 1 lists out the aperture efficiency and the system equivalent flux density (SEFD) at various frequencies and at elevation about 50°. For the broadband the typical aperture efficiency is above 50 % and the SEFD is about 1600 Jy. On 14 September 2018 we got the first fringe at broadband between Sheshan13 and Tianma13. Fig. 5 shows a recent fringe example. We are planning to join in VGOS trial experiment in a tagged along mode in the next step to further test and improve the station observation system.

4 Considerations of new VGOS stations

VLBI is hitherto the sole technique to determine CRF, EOP and TRF simultaneously. VLBI is applied to determine the orientation and the referencing positions / directions of the CRF as well as its densification.

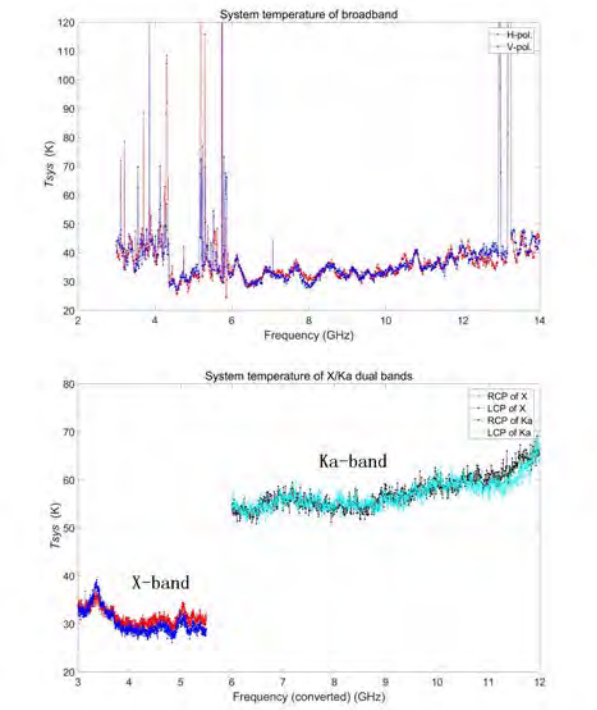

Fig. 4: The system temperature of Sheshan13.

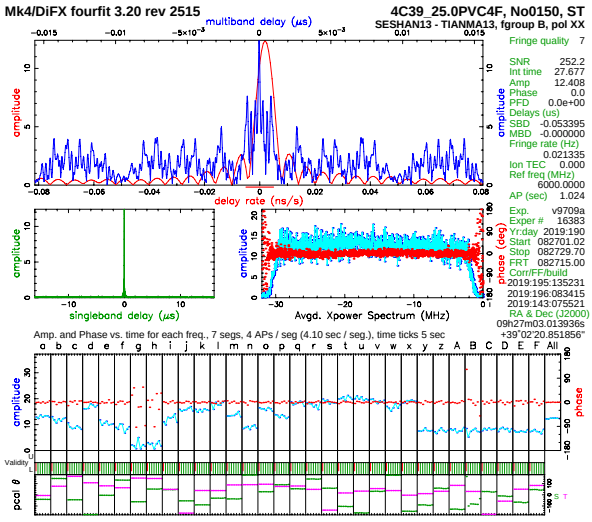

Fig. 5: The broadband fringe between Sheshan13 and Tianma13.

VLBI determines the angular positioning precisions of ERS up to milli-arcsecond (mas) or better. In TRF the VLBI technique provides the referencing stations and determines the scale factor. The positioning precision of long distance on the Earth is up to 1 ppb or better. VLBI precisely determines all the EOP, improves the studies of the EOP stimulation mechanism, Earth inner

Table 1: The aperture efficiency and SEFD of Sheshan13.

Frequency (GHz)	Elevation (°)	Efficiency (%)	SEFD (Jy)
Broadband			
4.45	56.99	52.26	2019
5.45	57.23	64.15	1522
6.45	57.48	42.74	1596
7.45	57.78	46.01	1501
8.45	58.03	53.71	1585
9.45	58.28	50.74	1669
10.45	58.53	54.71	1547
11.45	58.82	50.33	1706
Dual band X/Ka			
7.15	45.19	61.78	1268
8.65	47.27	62.26	1171
9.15	45.86	61.36	1578
30.85	51.10	49.11	2892

structure modeling (Free core nutation) and geophysical models, in particular provides crucial and reliable external constraints of geophysical models.

The selection of a new astrometric and geodetic VLBI observation site requires comprehensive considerations about the radio interference background, climate characteristics, historical archive of disastrous weather records, geographical location, as well as convenience in transportation, water and electricity supply, electronic communication and so on. Some other aspects are also meaningful to be mentioned concerning for instance the geometric shielding of the antenna, Ka-band observation and supporting to deep space exploration.

Fig. 6 shows the correlation between the station vertical coordinate and the excess zenith delay of atmosphere (Wen et al., 2017) from covariance analysis, where σ_U, σ_{Z_d} and R_{UZ_d} represent respectively the uncertainty of the vertical coordinate, that of the excess zenith delay and the correlation coefficient. It is shown that the coefficient is larger than 0.80 at elevation 20°, and is still larger than 0.55 even at elevation 7°. Therefore in the selection of a new site the significant geometric shielding should be avoided in order to get precise vertical coordinate determination of the station.

Compared to X-band, the advantages of VLBI observations at Ka-band include more compact extragalactic sources, relatively smaller effect of core shift, as well as helpful to improve the precision in the realization of radio celestial reference frame and in the linkage to the quasi-inertia optical frame of Gaia project (Li et al., 2017). Advantages in terms of deep

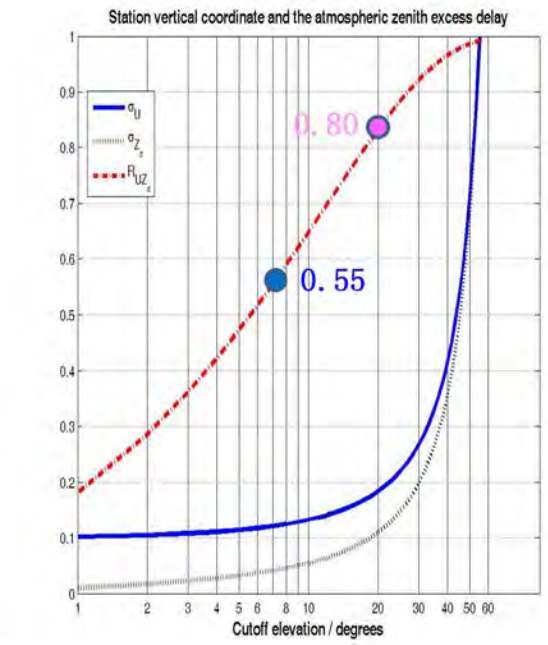

Fig. 6: Correlation between the station vertical coordinate and the excess zenith delay of atmosphere.

space exploration are high in telemetry data rate, high in VLBI tracking precision, and helpful to mitigate detrimental effects of ionosphere and solar plasma on the observed time delay. Disadvantages include relatively weak extragalactic sources, high precision requirement of reflector and antenna pointing, and susceptible to atmospheric absorption and emission effects. But the loss in system sensitivity due to these factors could be mostly compensated by the rapid development in high data rate sampling and recording techniques. Therefore the Ka-band VLBI observations are strongly recommended in the development of new VGOS stations.

5 Concluding remarks

Since the development of the experimental system of radio telescope in China in 1970s, the CVN has been greatly contributed to studies of astrophysics, astrometry and geodesy for more than forty years, and also to the CELP and other deep space exploration projects of China for more than ten years. Various institutions / institutes of China through various projects are now devoting to the development of the next generation radio telescopes for astrometry and geodesy, the VGOS-like stations. As the continuation of technical practice and the accumulation of implementation experience we will have more new VLBI stations in the near future. We are also seeking opportunities to develop some international VGOS-like stations by cooperation. Some considerations on the development of VGOS stations are presented for criticism and reference.

References

Heki K (1995) Movement of the Shanghai station: Implication for the tectonic of eastern Asia. *J Commun Res Lab*, 42(1): 65–72

Hong X (2007) VLBI techniques and application in the Chang'E lunar orbiter (in Chinese). *Chinese Journal of Nature*, 29(5): 297–299

Li J, Huang F, Sun Z (2017) Analysis of the advantages and disadvantages of astrometric and geodetic VLBI observation at Ka-band. *Geomatics and Information Science of Wuhan University*, 42(2): 257–262

Li J, Wang G (2001) The relative motion of Shanghai VLBI station to the stable part of Eurasia plate. *Annals of Shanghai Observatory Academia Sinica*, (22): 57–62

Li J, Wei E, Sun Z, et al. (2010) Discussion on future configuration design of Chinese astrometric and geodetic VLBI network. *Geomatics and Information Science of Wuhan University*, 35(6): 670–673

Li J, Xiong F, Yu C, et al. (2014) Precise determination of the reference point coordinates of Shanghai Tianma 65-m radio telescope. *Chinese Science Bulletin*, 59 (21): 2558–2567

Petrachenko B, Niell A, Behrend D, et al. (2009) Design aspects of the VLBI2010 system. In: D. Behrend, K. Baver (eds.), *IVS 2009 Annual Report*, NASA/TP-2009-214183, 13–67

Wan T, Qian Z, Wu L, et al. (1983) Summary results of the Shanghai-Effelsberg VLBI experiment. *Chinese Astronomy and Astrophysics*, 7(2): 145–150

Wan T, Wu H, Qian Z, et al. (1987) The first joint Sino-Japanese experiment of very-long-baseline interferometry (VLBI). *Science in China Ser A*, XXX(3): 307–316

Wen B, Li J, Sun Z, et al. (2017) Discussion about the shielding of topographical features surrounding the astrometric and geodetic VLBI station. *Geomatics Science and Engineering*, 37(1): 21–25

Measuring Focal Length Variations of VGOS Telescopes Using Unmanned Aerial Systems

M. Lösler, C. Eschelbach, R. Haas, A. Greiwe

Abstract VLBI radio telescopes are large technical facilities whose structures are affected by several deformation patterns. In particular, temperature- and gravity-dependent deformations bias the estimated global telescope position and, therefore, if uncorrected, deteriorate the geodetic results that can be derived from the geodetic VLBI analysis. The rigidity of a telescope structure under varying acting forces is restricted by its structural properties. Large conventional radio telescopes are more affected by deformation effects than the new compact-designed VGOS antennas. The design document for the next generation VLBI system (today called VGOS) states <300 µm as requirement for the path length stability. A traceable metrological system that can be used to check this stability level must be at least three times better than the requirements. Close range photogrammetric methods fulfil these accuracy requirements but usually need a crane during the survey of a telescope. To avoid the latter, an unmanned aerial system was used for the first time to evaluate the possible deformation of the main reflector surface of the north-eastern of the Onsala twin telescopes (ONSA13NE). The focal length of the ring-focus paraboloid was derived in several elevation angles to study the gravitational deformation effects on the main reflector of this VGOS antenna.

Keywords VGOS · Ring-focus paraboloid · Antenna deformation · Focal length · Unmanned aircraft system

Michael Lösler · Cornelia Eschelbach
Frankfurt University of Applied Sciences, Laboratory for Industrial Metrology, Nibelungenplatz 1, DE-60318 Frankfurt am Main, Germany

Rüdiger Haas
Chalmers University of Technology, Onsala Space Observatory, SE-439 92 Onsala, Sweden

Ansgar Greiwe
University of Applied Sciences Bochum, Lennershofstraße 140, DE-44801 Bochum, Germany

(Correspondence: michael.loesler@fb1.fra-uas.de)

1 Introduction

The backbone of the next generation geodetic VLBI system will be formed by a new designed type of radio telescopes. These new radio telescopes, often refereed to as VGOS[1] radio telescopes, are of a more compact design and are able to move faster than conventional radio telescopes. One of the most important advantages of the compact design is the stability of the telescope structure against acting forces. However, radio telescopes are large technical facilities and the rigidity is restricted by structural properties. Known deformation patterns of conventional radio telescopes like thermal expansions (e.g. Haas et al., 1999), seasonal variations (e.g. Mähler et al., 2018) or gravitational sags (e.g. Bergstrand et al., 2018) can be fully transferred to the VGOS generation of radio telescopes, but have partly smaller amplitudes. Moreover, most of the VGOS radio telescopes make use of an improved main reflector design, i.e., the ring-focus paraboloid. Hence, measurement methods and mathematical models, which were suitable for conventional radio telescope, are not necessarily applicable for VGOS.

Thermal and seasonal variations of VGOS antennas have been investigated and modeled (e.g. Lösler et al., 2013; Mähler et al., 2018). However, gravitational de-

[1] VLBI Global Observing System

formations of the main reflector are not studied in detail so far. In this investigation, the focal length variations of ONSA13NE, the north-eastern of the Onsala twin telescopes, is derived to analyse the deformation behavior of a VGOS antenna. Moreover, an unmanned aerial system (UAS) is used to observe the main reflector in several elevation angles, for the first time.

2 UAS-based observation strategy

Close range photogrammetry has a long history in radio telescope surveying, dating back to the early 1960s (e.g. Findlay, 1964). Usually, photogrammetric methods are used to adjust the panels of the main reflector (e.g. Süß et al., 2012). On the one hand, advantages are the achievable uncertainties of $\ll 100\,\mu m$ for discrete signaled markers and no heavy equipment has to be mounted onto the telescope which may cause further deformations. On the other hand, a large crane is needed to retrieve a block configuration with suitable camera positions in several elevation angles of the telescope.

Since recent years, unmanned aerial systems (UAS) are well-established as sensor platform for small format close range aerial photogrammetry. The unmanned aerial vehicle (drone) is equipped with several navigation sensors, e.g. GNSS and IMU, and remote controlled by a ground-station. Usually, the waypoints of the flight path as well as the trigger points for the camera are scheduled by a flight plan. Due to practical reasons, in this project the camera was controlled remotely by the pilot via video screen.

The equations of the central projection, which transforms three dimensional object coordinates $(X_P\ Y_P\ Z_P)^T$ to corresponding planar image coordinates $(x'\ y')^T$, are given by

$$x' = x'_0 - c\frac{r_{11}(X_P-X_0)+r_{21}(Y_P-Y_0)+r_{31}(Z_P-Z_0)}{r_{13}(X_P-X_0)+r_{23}(Y_P-Y_0)+r_{33}(Z_P-Z_0)} + \Delta x', \tag{1a}$$

$$y' = y'_0 - c\frac{r_{12}(X_P-X_0)+r_{22}(Y_P-Y_0)+r_{32}(Z_P-Z_0)}{r_{13}(X_P-X_0)+r_{23}(Y_P-Y_0)+r_{33}(Z_P-Z_0)} + \Delta y'. \tag{1b}$$

Here, the principal distance c, the principal point x'_0, y'_0 and the distortion effect parameters $\Delta x'$, $\Delta y'$, which compensate for the radial-symmetric lens distortion and the decentring distortion, are known as interior orientation, which are usually constant for all images of a photogrammetric bundle. The parameters of the exterior orientation refer to the image position and orientation w.r.t. the global reference frame and are given by

$$\mathbf{P}_0 = \begin{pmatrix} X_0 \\ Y_0 \\ Z_0 \end{pmatrix}, \qquad \mathbf{R} = \begin{pmatrix} r_{11} & r_{12} & r_{13} \\ r_{21} & r_{22} & r_{23} \\ r_{31} & r_{32} & r_{33} \end{pmatrix},$$

respectively (cf. Luhmann, 2018, Ch. 4.2.1).

The weight of the camera restricts the operating time of the UAS. For that reason, a lightweight 380 g consumer camera Sigma DP3 Merrill was used instead of a heavy high-precision photogrammetric camera. This yields in a flight time of about 25 min. Due to the fact that consumer cameras are not geometrically stabilized, the parameters of the interior orientation were calibrated in-situ during the bundle adjustment for each measurement campaign (e.g. Luhmann, 2018, Ch. 4.4.2).

The image sensor of the camera based on the Foveon chip and captures full color information for each pixel (e.g. Greiwe and Gehrke, 2013). For comparison, the elements of color filter arrays like Bayer pattern are only sensitive for one waveband and the full color is obtained by interpolations (e.g. Verhoeven, 2010). Figure 1 depicts the differences in acquired spectral information between a Foveon based sensor and a color filter array. Full true color information increases the micro-contrast and leads to better image measurements e.g. edge detection during the analysis process. The main reflector surface of ONSA13NE[2], the north-eastern of the Onsala twin telescopes, was equipped by 72 discrete 12-bit coded markers. Additionally, four markers were attached

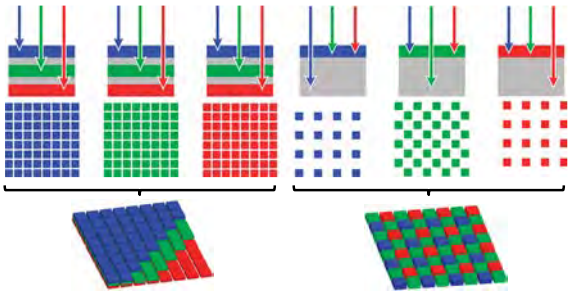

Fig. 1: Differences in spectral information acquirements between Foveon based sensorS (left) and color filter arrays like Bayer pattern (right) (Verhoeven, 2010).

[2] https://youtu.be/sNnHvBaQ3_w

Fig. 2: The VGOS radio telescope ONSA13NE equipped with several coded markers, scale-bars and coordinate cross during the UAS-based photogrammetric survey of the main reflector surface.

at the sub-reflector together with a coordinate cross, which approximately defines the datum of the resulting point clouds by six markers. To transfer the point cloud into a metric system six carbon fiber scale-bars were attached at the sub-reflector, at the strut elements and at the rim of the dish. Figure 2 depicts the prepared main reflector surface of the ONSA13NE during a UAS-based measurement campaign, using a HP-TS960 (HEXAPILOTS).

To obtain a possible deformation pattern of the main reflector, measurement campaigns were carried out redundantly from elevation 0° up to 90° using a step-size of 10° as well as one time in 34°. The flight plan for each elevation angle consists of two flight lines and two concentric spatial circles around the axis of symmetry of the main reflector, cf. Table 1. Figure 3 depicts the established flight plan for elevation angle 30°.

Table 1: Parameter of the flight plan that is used for each measurement campaign. The distances are related to the apex of the main reflector surface.

Type	Traverse (m)	Circle (m)	
Distance	14	14	19
Radius	–	6.5	11.5

Instead of using a configuration where the camera orientation is aligned to the axis of symmetry of the main reflector, the diametrical direction of the main reflector was pointed for each taken image. About 150 suitable images were taken per campaign and analysed by the bundle adjustment software package *AICON 3D Studio*. The software extracts coded markers as well as natural circular targets at the telescope e.g. screws automatically. Thus, more than 500 points are used during the adjustment process per campaign. The uncertainties of the coded markers are between 80 µm and 120 µm w.r.t. the global datum. A detailed description is given by Lösler et al. (2019).

3 Focal length variations

As most of the new VGOS radio telescopes, the main reflectors of the Onsala twin telescopes are designed as rotational symmetric ring-focus paraboloids (e.g. Pantaleev et al., 2017). A ring-focus paraboloid results by combining two quadric surfaces, i.e. a paraboloid and a cylinder. A closed mathematical model of a double-elliptic ring-focus paraboloid was recently derived by Lösler et al. (2017, 2018a,b, 2019) and reads

$$a_1^2(x_i - r_i n_{x,i})^2 + a_2^2(y_i - r_i n_{y,i})^2 = z_i. \qquad (2)$$

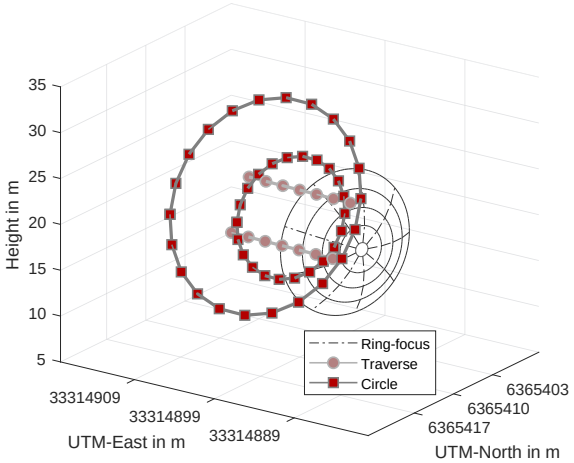

Fig. 3: Established flight plan for elevation angle 30° that consists of two traverses and two circles. The main reflector surface is plotted in the background.

Here, a_1 and a_2 are the parameters of the elliptic paraboloid and $(x_i\ y_i\ z_i)^{\mathrm{T}}$ are the coordinates of the ith point lying on the paraboloid surface. The point-dependent cylinder parameter $r_i = f(b_1, b_2, \phi)$ results from the inverse semi-major and the inverse semi-minor axes b_1 and b_2, respectively, and the cylinder orientation ϕ. The normalized normal vector perpendicular to the cylinder axis is denoted by $\mathbf{n}_i$. In case of a rotational symmetric ring-focus paraboloid, the restrictions $a_1 = a_2$ and $b_1 = b_2$ hold (cf. Lösler et al., 2018a,b). By applying a rotation sequence and a translation, the canonical form is transformed to an arbitrary position in space.

The estimated point sets of each bundle adjustment were corrected for thermal expansions. The parameters of the ring-focus paraboloid were derived by Eq. 2 using a proper errors-in-variables (EIV) solver. For rigorous uncertainties propagation, the dispersion of the estimated point sets was introduced to the EIV to define the a-priori stochastic model of the observations.

Table 2 summarizes the campaign-wise estimated overall RMS values. The panels were adjusted at elevation 34°, thus, smallest deviations can be expected for elevation angles close to 34°. This assumption is confirmed by the estimated RMS values, because larger values can be found close to 0° and 90°, whereas smallest values are given from 30° to 50°.

Table 2: Estimated RMS w.r.t. different survey elevations ϵ.

ϵ	0°	10°	20°	30°	34°	40°	50°	60°	70°	80°	90°
RMS	204	187	200	167	169	192	182	173	178	221	282
in µm	190	194	166	147	–	154	155	162	167	227	292

The paraboloid parameter a yields the focal length via $F = \frac{1}{4a^2}$.

Figure 4 depicts the estimated focal lengths of the 21 measurement campaigns by red dots. Red error-bars indicate the related uncertainties (2σ). The focal length varies in a range of ±1.1 mm and depends on the elevation angle. The maximum occurs at 90°, which confirms the assumption that the main reflector becomes flatter in higher elevation positions (cf. Lösler et al., 2019).

To predict the variations by a suitable function, a common cosine function was adapted, i.e.,

$$F(\epsilon) = 3.7017\,\mathrm{m} - 2.3\,\mathrm{mm}\cos\epsilon. \qquad (3)$$

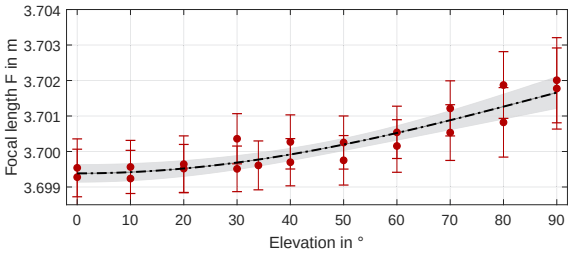

Fig. 4: The estimated focal length of the 21 measurement campaigns with uncertainties (2σ) are illustrated by red dots. The derived prediction function and the related confidence interval (2σ) are plotted in black and grey, respectively.

The resulting prediction function is plotted as black line. The grey colored band indicates the related 2σ confidence.

For comparison, the variations of the focal length are 10-times smaller than reported for conventional radio telescopes (e.g. Sarti et al., 2009; Nothnagel et al., 2013; Bergstrand et al., 2018). The compact-design as well as technological improvements result in a higher rigidity and damped deformations and correspond to the theoretical intention of the VGOS-specifications (Petrachenko et al., 2009).

4 Conclusions

For the fist time, elevation-dependent gravitational deformations of the main reflector of a VGOS-specified radio telescope were studied in detail at the Onsala Space Observatory. The focal length of the north-eastern of the Onsala twin telescopes (ONSA13NE) varies by about ±1 mm and can be predicted by a cosine function.

For this purpose, photogrammetric methods were used to observe the radio telescope in several elevation angles. Instead of using a large crane for data recording, an unmanned aircraft system (UAS) carried out the surveying campaigns. To our knowledge, this was the first time that an UAS is used in radio telescope surveying. The uncertainties of a discrete measured point was about 100 µm and fulfilled the requirements to be at least three times better than the expected variations. Summarized, for free-standing radio telescopes, the UAS provides a promising and practicable surveying method. Neither a crane is required nor additional heavy equipment has to be mounted.

Acknowledgements We thank Lars Wennerbäck and Christer Hermansson for mounting and dismounting the coded markers and the scale-bars at the radio telescope.

This research project is part of the JRP 18SIB01 "Large-scale dimensional measurements for geodesy" (GeoMetre) and has received funding from the EMPIR programme co-financed by the Participating States and from the European Union's Horizon 2020 research and innovation programme.

References

Bergstrand S, M. Herbertsson M, Rieck C, et al. (2018) A gravitational telescope deformation model for geodetic VLBI. *J Geod*, 93(5), 669–680, doi:10.1007/s00190-018-1188-1

Findlay J W (1964) Operating Experience at the National Radio Astronomy Observatory. *Annals of the New York Academy of Sciences*, 116(1), 25–40, doi:10.1111/j.1749-6632.1964.tb33937.x

Greiwe A, Gehrke R (2013) Foveon Chip oder Bayer Pattern - geeignete Sensoren zur Aerophotogrammetrie mit UAS. In: T. Luhmann, C. Schumacher (eds.): *Photogrammetrie - Laserscanning - Optische 3D-Messtechnik: Beiträge der 12. Oldenburger 3D-Tage 2013*, Wichmann, Offenbach, 334–343, ISBN: 978-3879075287

Haas R, Nothnagel A, Schuh H, et al. (1996) Explanatory supplement to the section 'Antenna Deformation' of the IERS Conventions (1996). In: H. Schuh (Eds.): *Explanatory supplement to the IERS conventions (1996)*, Deutsches Geodätisches Forschungsinstitut (DGFI), München, **71**, 26–29

Lösler M, Neidhardt A, Mähler S (2013) Impact of Different Observation Strategies on Reference Point Determination – Evaluations from a Campaign at the Geodetic Observatory Wettzell. In: N. Zubko and M. Poutanen (eds.): *Proc. 21st EVGA Working Meeting*, 255–260, ISBN: 978-951-711-296-3

Lösler M, Eschelbach C, Haas R (2017) Unified Model for Surface Fitting of Radio Telescope Reflectors. In: R. Haas, G. Elgered (eds.): *Proc. 23rd EVGA Working Meeting*, 29–34, ISBN: 978-9188041098

Lösler M, Eschelbach C, Haas R (2018a) Applying Bootstrapping in the Framework of Uncertainty Estimation exemplified by Surface Analysis. *zfv – Zeitschrift für Geodäsie, Geoinformatik und Landmanagement*, 140(4), 224–232, doi:10.12902/zfv-0214-2018

Lösler M, Eschelbach C, Haas R (2018b) Zur Modellierung eines Ring-Focus-Paraboloids. In: T. Luhmann, C. Schumacher (eds.): *Photogrammetrie – Laserscanning – Optische 3D-Messtechnik: Beiträge der 17. Oldenburger 3D-Tage 2018*, Wichmann, Offenbach, 222–234, ISBN: 978-3-87907-643-7

Lösler M, Haas R, Eschelbach C, et al. (2019) Gravitational Deformation of Ring-Focus Antennas for VGOS – First Investigations at the Onsala Twin Telescopes Project. *J Geod*, doi:10.1007/s00190-019-01302-5

Luhmann T (2018) *Nahbereichsphotogrammetrie - Grundlagen, Methoden und Anwendungen*, Wichmann, Berlin, 4th edn, ISBN: 978-3879074792

Mähler S, Klügel T, Lösler M, *et al.* (2018) Permanent Reference Point Monitoring of the TWIN Radio Telescopes at the Geodetic Observatory Wettzell. *avn – Allgemeine Vermessungsnachrichten*, 125(7), 210–219

Nothnagel A, Eichborn M, Holst C (2013) Improvment of focal length results of Effelsberg 100 m radio telescope. In: N. Zubko and M. Poutanen (eds.): *Proc. 21st EVGA Working Meeting*, 55–59, ISBN: 978-951-711-296-3

Pantaleev M, Haas R, Billade B, et al. (2017) Onsala Space Observatory – IVS Technology Development Center Activities during 2015-2016. In: K. D. Baver, D. Behrend, and K.L . Armstrong (eds.): *International VLBI Service for Geodesy and Astrometry 2015+2016 Biennial Report*, 301–305, NASA/TP-2017-219021

Petrachenko B, Niell A, Behrend D, et al. (2009) Design aspects of the VLBI2010 system. NASA/TM-2009-214180

Sarti P, Vittuari L, Abbondanza C (2009) Laser Scanner and Terrestrial Surveying Applied to Gravitational Deformation Monitoring of Large VLBI Telescopes' Primary Reflector. *J Geod*, 135(4), 136–148, doi:10.1061/(ASCE)SU.1943-5428.0000008

Süß M, Koch D, Paluszek H (2012) The Sardinia Radio Telescope (SRT) optical alignment. *Proceedings of Ground-based and Airborne Telescopes IV*, 8444, 84442G-1–84442G-16

Verhoeven G J J (2010) It's All about the Format – Unleashing the Power of RAW Aerial Photography. *Int. J. Remote Sens.*, 31(8), 2009–2042, doi:10.1080/01431160902929271

Instrumentation Developments for VGOS at IGN Yebes Observatory

J. A. López Pérez, P. de Vicente, J. A. López Fernández, F. Tercero Martínez, J. D. Gallego, J. M. Serna Puente, I. López Fernández, M. Díez González, I. Malo Gómez, C. Albo Castaño, L. Barbas Calvo, O. García Pérez, J. González García, B. Vaquero Jiménez, M. Patino Esteban, P. García Carreño, F. J. Beltrán Martínez, M. Bautista Durán, J. López Ramasco, R. Amils Samalot, G. Gómez Molina, A. Baldominos Delgado

Abstract IGN Yebes Observatory keeps on developing the required instrumentation for its RAEGE network of VGOS radio telescopes, together with broadband receivers for other institutes like NMA and FGI which are finishing their VGOS antennas. These developments include new VGOS receivers, low noise amplifiers and hybrid circuits, feed optimization, phasecal and noisecal units, cryogenic cooling control units, RFI monitorization and telescope control.

Keywords VGOS · RAEGE · Receiver · Amplifier · Feed · RFI · Geodesy

1 Introduction

The Yebes Observatory of the Spanish *Dirección General del Instituto Geográfico Nacional* (IGN) keeps on developing the required instrumentation for its RAEGE (Red Atlántica de Estaciones Geodinámicas y Espaciales) network of VGOS radio telescopes in Yebes, Santa Maria, Gran Canaria and Flores. In addition, it is developing instrumentation for other institutes, like NMA, FGI or BKG. These developments include new VGOS receivers, low-noise amplifiers and hybrid couplers, feeds, phasecal and noisecal units, vacuum and cryo-cooling control units, telescope control software and local-tie measurements. Finally, RFI monitoring is performed, too.

José Antonio López Pérez et al.
Observatory of Yebes - Instituto Geográfico Nacional
Cerro de la Palera S/N Yebes, Spain

(Correspondence: jalfernandez@fomento.es)

The observatory also operates two radio telescopes, 13.2 m and 40 m in diameter, respectively (see Fig. 1); the first one runs regularly VGOS observations and the second one, legacy IVS observations since 2008. Two GNSS receivers are managed too: one integrated in the international network and a second one in the Spanish national one. It also runs two gravimeters, an absolute and a relative superconductor one.

Funding has been approved for the installation of an SLR (Satellite Laser Ranging) station in the next 5 years which would transform Yebes Observatory into a GGOS core station.

2 RAEGE project

The Spanish-Portuguese collaboration in RAEGE project is still active and the Santa Maria station

Fig. 1: Yebes Observatory telescopes. From left to right: ESSCO 13.7 m (radome), ARIES 40 m and VGOS 13.2 m.

has resumed VLBI observations with a simultaneous tri-band (S/X/Ka) receiver.

The civil works for the VGOS telescope in Gran Canaria island have been delayed due to administrative and environmental authorizations for the selected site (Artenara). It is expected to start with these works in late 2019.

Similarly, the VGOS telescope in Flores island (Azores) is delayed too. It it expected to perform the call for tenders for the construction of this telescope in 2020.

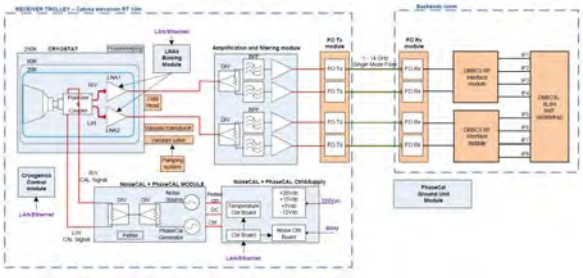

Fig. 2: Schematics of the VGOS broad band receiver for NMA and FGI.

3 Broad-band receivers

Yebes Observatory is responsible for the design and construction of three cryogenic VGOS broadband receivers: two for the Norwegian Mapping Authority (NMA) and one for the Finish Geospatial Research Institute (FGI). A fourth one is in progress for Santa Maria RAEGE/VGOS station.

These broadband receivers are cooled using a two stage cryostat (15 and 50 K) and operate between 2 and 14 GHz. They have cryogenic low noise amplifiers designed and built at Yebes laboratories and deliver a receiver temperature below 25 K along the whole band in a free RFI environment. They provide two linear orthogonal polarizations simultaneously.

Two of them will be delivered by the second half of 2019, one to NMA and one to FGI, respectively.

Fig. 2 shows the receiver block diagram in which we can see its different modules. It follows the approach shown in García Carreño et al. (2016) with some upgrades. After the cryostat, the signal is split in two sub-bands: 2.1 – 5.6 GHz and 3.6 – 11.6 GHz following Haystacks's approach to avoid the saturation of the optical fiber amplifiers from strong RFI signals in the lower part of the band. The signals once amplified, filtered and transported through optical fiber links to the backends room, are directed towards two identical DBBC3 RF interface modules designed and built at Yebes. These modules split the signals from both polarizations into four frequency sub-bands ready to be injected into the DBBC3. The filtering and conditioning module for the DBBC3 does not use tuneable LOs and in case that the observing bands change they can be adapted by replacing the pass band filters by new ones.

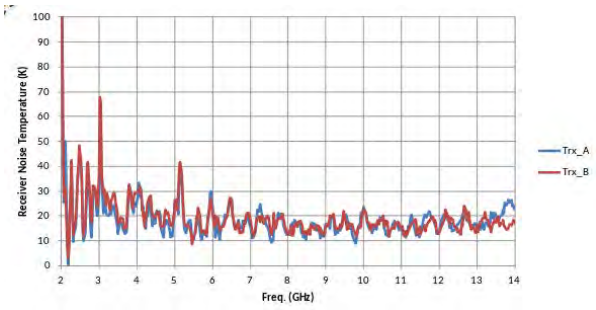

Fig. 3: Receiver temperature for the FGI broadband receiver along the band.

Fig. 3 shows the receiver temperature measured in both linear polarizations along the band. The peaks at low frequencies are mainly due to RFI associated to WiFi, UMTS, Bluetooth, WiMax and other sources of noise. They are also caused by mismatching between QRFH feed and LNAs.

The receivers use a cryogenics and vacuum control system which has been overhauled from a previous version used in the Yebes VGOS receiver. This new version has a remote ethernet connection to the Local Area Network that allows remote monitoring and control of both pumps (rotatory and turbomolecular), the cryogenic temperature, the vacuum sensors, the electrovalve, and the heat resistors and regenerators. This remote monitoring and control eases the operation of the receiver, adds stability and provides a complete time log of the cryogenics. It is integrated in the control system of the telescope and can be used by third party software.

4 Tri-band receiver for Ny-Ålesund

The NMA runs two twin VGOS radio telescopes at Ny-Ålesund station which were inaugurated during the last IVS General Meeting in June 2018. In order to test these radiotelescopes, NMA borrowed from Yebes Observatory one tri-band receiver which simultaneously works in the bands 2.2 – 2.7 GHz, 7.5 – 9 GHz and 28 – 32 GHz. The receiver was mounted first in one antenna and then in the second one to test the telescopes and determine the pointing and focusing model. The SEFD and the efficiency at X-band were estimated. Both telescopes were using the Yebes control software and the Yebes pipeline and reduction software. Receiver temperatures are below 30 K at S, X and Ka band in all cases.

Yebes staff has assisted NMA in the installation and operation of this receiver.

It has to be mentioned that the X-band LNAs were broken due to high RFI from radars emitted by ships coming in the Ny-Ålesund fjord. They were replaced and now the pointing to the fjord is avoided.

5 QFRH revisited

Yebes Observatory has worked in the optimization of the QFRH design from JPL used in the VGOS radio telescopes. The Yebes design resembles the original design but has slightly changed the profile and the connectors (coaxial ones). The antenna works between 2.3 and 14 GHz in dual linear polarization. The drawings allow to manufacture it easily. The efficiency is slightly better than the original design, above 0.55 along the whole band, but the reflection is slightly worse (see Fig. 4.

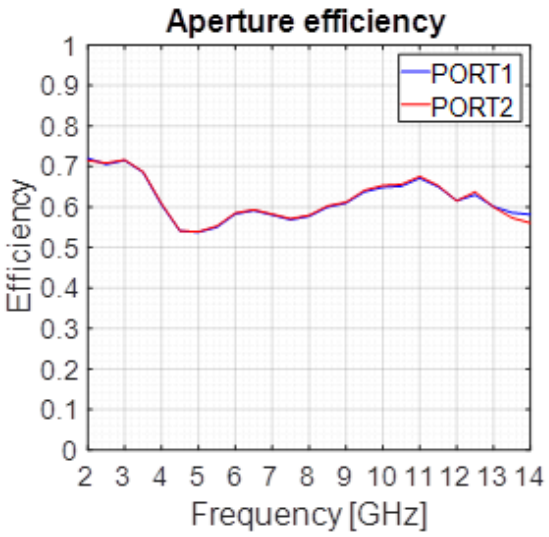

Fig. 4: Efficiency by the QFRH along the frequency band.

6 Linear to circular polarization: hybrids and software

One of the main drawbacks of broadband receivers is the need to use linear polarization. This has prevented an easy simultaneous operation with the IVS legacy observations which only use Left Circular Polarization (LCP). The usage of linear polarization generates new problems to be taken into account like variable polarization coming from the paralactic angle which differs at the different radio telescopes on the Earth. Sources may be totally or partially polarized and since their paralactic angle changes with time it is necessary to observe in both polarizations to recover the whole signal. Furthermore, instrumental effects should also be taken into account. The conversion from linear to circular polarization can be done by either software or hardware.

Yebes Observatory has developed a solution based on cryogenic 3 dB/90-deg multi-octave stripline hybrids which can be used to obtain both circular polarization signals from linear polarization ones. The usage of such devices at cryogenic temperatures (15 K) only increases 1.5 K in average the noise temperature of the LNAs. This solution guarantees cross polarization below 25 dB, an axial ratio below 1 dB, an amplitude unbalance below 0.9 dB and a phase unbalance lower than 3 degrees. To achieve such specifications the length of the lines has to be controlled with great accuracy but this is achievable using special connectors. Fig. 5 shows the hybrids performance along the frequency band. This solution has not been implemented on a geodetic VLBI receiver yet, but BRAND project from Radionet, is considering it as a first option.

The alternative approach to convert linear to circular polarization is by software using PolConvert software by Ivan Martí-Vidal. This task is part of the effort started by the EU-VGOS project which aims to create

a pipeline that performs the correlation, polarization conversion, instrumental polarization calibration and fringe fitting along the whole band to estimate the dispersive effects of the ionosphere. The goal is to obtain the final observable: the broadband delay for each scan and baseline from which the length of the baselines is estimated. EU-VGOS observes regularly with the European antennas from Onsala, Wettzell and Yebes to test this pipeline currently under development.

7 Ultra low noise wide band amplifiers

Yebes Observatory has developed two kind of low noise cryogenic ultra wide band amplifiers in the band between 2 and 14 GHz. The first option is a compact, light single-ended amplifier which is usable in a much larger band, between 0.5 and 18 GHz. The average noise temperature is 6.1 K, the gain 33.9 dB, with an input IRL of −1.5 dB and an ORL of −16.9 dB. The power consumption is 36 mW. This amplifier has a large input reflection and an alternative solution was investigated using a balanced amplifier.

The balanced amplifier uses 3 dB/90-deg hybrids and the results are excellent. The penalty for using the hybdrids is very low. The noise temperature increases only 1.5 K in average, up to 7.6 K, the gain is 33.8 dB but the IRL drops to −21 dB and the ORL to −23 dB. Two versions of balanced LNA have been developed. One for the 2 – 14 GHz band and another for the 1.5 – 15 GHz band (BRAND receiver).

The behaviour of both amplifiers is shown in Fig. 6.

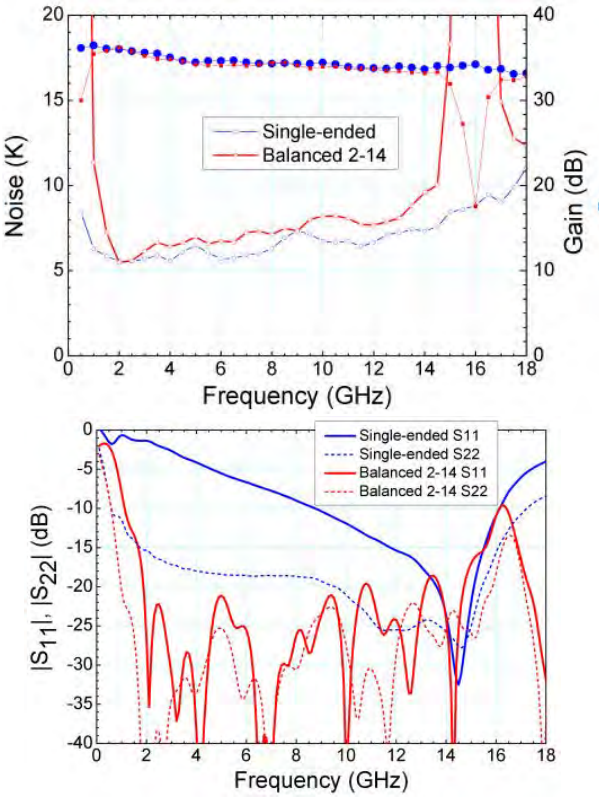

Fig. 6: Noise temperature and gain of single ended and balanced amplifiers.

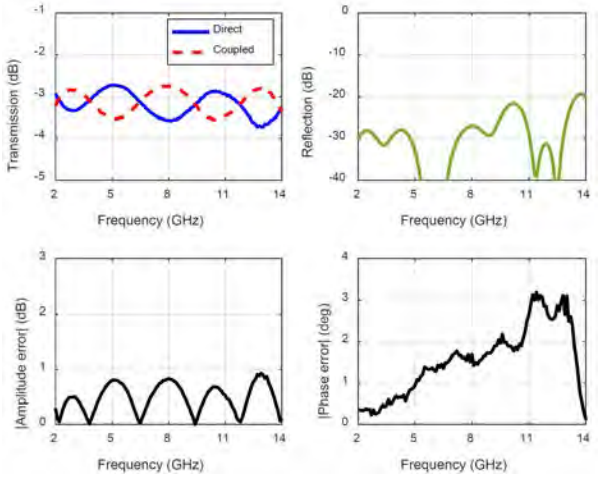

Fig. 5: Hybrid performance: transmission, reflection, amplitude error and phase error, along the frequency band.

8 Phase Cal developments

The phase cal system for VLBI is composed of two subsystems: the antenna unit and the cable delay measurement system which estimates the variable delay in the signal caused by the cables between the receiver and the VLBI backends. This system devised by A. Rogers is very powerful and it is in use at the IVS radio telescopes.

We have optimized the antenna unit system by providing extra features. The noise and phase unit at Yebes is installed at the receiver trolley, very close to the cryostat. It uses short semirigid coaxial cables to decrease the variability caused by temperature variations in the

receiver cabin. The system generates pulses 10 MHz apart and works between 2 and 14 GHz. The pulse generator is based on Hittite ultrafast logic gates, a similar approach as in Haystack. The noise cal can be switched at 80 Hz rate. The whole unit is shielded and it is temperature stabilized using a Peltier cooler and passive insulation. The control and monitoring of the unit is done with a Rapsberri Pi using Python scripts. Yebes labs have built 9 units for BKG, AGGO, NMA, FGI and Yebes and is integrating this system in the VGOS receivers in construction for NMA and FGI.

The Cable Delay Measurement System (CDMS) is based on the legacy design but it has been adapted in a single PCB to simplify its usage. A new CDMS is being developed and is still under tests; it does not require a frequency counter. The system compares the 5 MHz reference from the generator module with the 5 MHz signal coming from the antenna unit installed in the receiver trolley. Both signals are phase compared in a phase detector, whose DC output is read by a 24-bit ADC. The achieved RMS is < 5 ps, which corresponds to < 0.003 degrees in phase. This system yields higher sensitivity and lower phase noise. It is currently under tests and will be extended to other telescopes once it is validated.

9 RFI measurements

After several test to avoid a Tsys increase due to RFI, the configuration shown in Fig. 7 was adopted. A 3 GHz high-pass filter was installed at the dewar's output. In addition, a PIN diode power limiter (+6 dBm) was installed at each optic fiber link input, in order to protect them from damage due to strong RFI which is present and could enter the receiver during antenna maintenance at 0 deg elevation. With this configuration, we managed to reduce Tsys from 70 K down to 50 K.

In addition, a line of research on high temperature superconducting filters (HTS) has been started at Yebes labs (Huang et al., 2018).The initial project was a sharp HTS filter for the legacy S-band, which is the worst one in terms of RFI. The specifications for this filter were very selective in order to reject high power radiolinks close to this band.

After this, the simulation of an HTS filter for VGOS is underway with promising results. The current configuration considered for VGOS is a band-pass filter ($2-14$ GHz) with one notch at a pre-defined frequency.

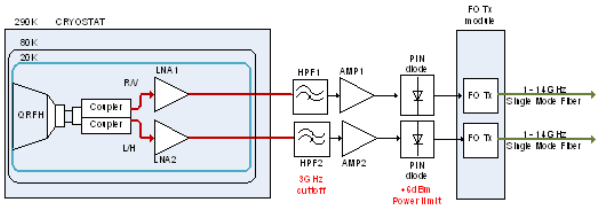

Fig. 7: Yebes VGOS receiver configuration.

Finally, it has to be mentioned that a new RFI monitoring station has started operations on the roof of the laboratory building. It allows the monitorization of RFI from 1 to 40 GHz.

10 Conclusions and outlook

Two large and ambitious goals for Yebes Observatory are planned for the next four years using European funds from regional development. The first one is the construction of a future Satellite Laser Ranging station at Yebes. In the next months we will make a study of the requirements for the telescope and ancillary equipment and the software. Once this is decided, the acquisition of the equipment will take place and later the building that hosts the telescope will be built.

The second goal consists in the extension of the current building of laboratories and workshops. The new building, whose civil works will start shortly, will host several laboratories, including a clean room and workshops to host precision milling machines and lathes as well as metrology equipment.

References

García Carreño P, Garcia Alvaro S, López Peréz J A, et al. (2016) Geodetic VLBI ultra low noise broad-band receiver for 13 meter VGOS radiotelescopes. In: *P*roc. 11th European Microwave Integrated Circuits Conference, 476–479. doi:10.1109/EuMIC.2016.7777595

Huang F., Bolli P., Cresci L., et al. (2018) Superconducting spiral bandpass filter designed by a pseudo-Fourier technique. *IET Microw. Antennas Propag.*, 12(8), 1293–1301, doi:10.1049/iet-map.2017.0940

DBBC3 Towards the BRAND EVN Receiver

G. Tuccari, W. Alef, S. Dornbusch, R. Haas, K.-Å Johansson, L. La Porta, H. Rottmann, A. L. Roy, J. Wagner, M. Wunderlich

Abstract The DBBC3 is a flexible VLBI backend and environment that supports a wide range of observational needs via a suite of FPGA firmware types. The hardware can sample up to eight 4 GHz-wide baseband signals and convert to digital streams over multiple 10GE links on fibre. The development team has an ongoing development programme that has enhanced existing modes and introduced new desired modes as user requirements evolve. Three different firmware types for observing have been implemented which will be briefly summarised: Direct Sampling Conversion (DSC), arbitrary selection of bands (OCT), Digital Down Conversion (DDC). These modes cover all the requirements of astronomical, VGOS and legacy geodetic VLBI of the present, but also of the near future. At the same time the DBBC3 is an important platform for additional new modes to be implemented for the BRAND receiver. This paper describes the use of the DBBC3 for the receiver development, pointing out which element in the current DBBC3 structure will be part of the BRAND receiver in order to simplify its introduction into the existing VLBI environment at telescopes with a DBBC3 backend.

Keywords Digital Receiver · VLBI · VLBI Backends

1 Introduction

The Digital Base-Band Converter 3 (DBBC3) is the third generation VLBI backend developed in a European collaboration under the lead of G. Tuccari (see e.g. Tuccari et al., 2019). The system is modular and, as of today, in a configuration with eight sampler/processor pairs is fully VGOS compliant. It takes as input eight 4 GHz-wide IFs in the range 0 GHz to 15 GHz. Different channel (sub-band) widths of 1-2-4-8-16-32-64-128 MHz can be selected from each 4 GHz input via Digital DownConverter (DDC) firmware for output. Alternatively OCT filters allow the selection of arbitrary parts of the band using 32-tap FIR convolutional filters acting on the time series from the sampler. Filter tap weights have been designed to produce filter widths of 512 MHz, 1024 MHz and 2048 MHz and others are possible by simply loading different weights into the tap registers. When using the 2048 MHz filter one can use two filters to cover the full 4 GHz, which makes this mode compatible with the R2DBE system used in the Event Horizon Telescope. The full 4096 MHz band can be output also without any channelisation. The resulting output data rates are 16/32/64/128 Gbps.

For the European VLBI Network (EVN) the DBBC3 shall replace the DBBC2 using its backward-compatible modes, and at the same time open the

Gino Tuccari
INAF Istituto di Radioastronomia, Sezione di Noto, Contrada Renna, IT-96017 Noto (SR), Italy

Gino Tuccari · Walter Alef · Sven Dornbusch · Laura La Porta · Helge Rottmann · Alan L. Roy · Jan Wagner · Michael Wunderlich
Max Planck Institute for Radio Astronomy, Auf dem Hügel 69, DE-53121 Bonn, Germany

Rüdiger Haas · K.-Å Johansson
Onsala Space Observatory, SE-439 92 Onsala, Sweden

Laura La Porta also at
Reichert GmbH/BKG, Hittorfstr. 26, DE-53129 Bonn, Germany

(Correspondence: tuccari@ira.inaf.it)

Fig. 1: DBBC3 VGOS model: 8 IFs with 8 groups of ADB3 samplers and CORE3 processing boards. This unit can deliver 128 Gbps with 2-bit samples (output limit is 512 Gbps).

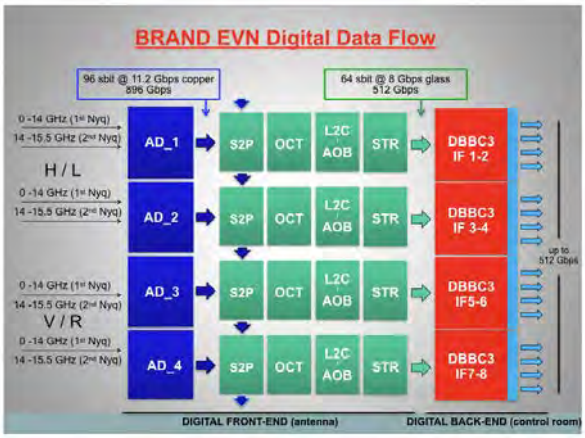

Fig. 2: Four bands (IFs) are fed to the four inputs of the sampler chip (blue). They are either one of 0 GHz to 14 GHz or 14 GHz to 15.5 GHz and one of the possible polarisations. In the FPGAs (green) the serial data streams are converted to parallel. Next step is band selection, then polarisation conversion or other pre-processing. Last the digitised data are streamed to ethernet. In the DBBC3 (red), standard VLBI channelisation and formatting are performed with output of the VLBI data to internet or recorders.

avenue to observations with data-rates up to 32 Gbps, possible with EVN's widest IFs at higher frequencies.

2 Modifying the DBBC3 for the BRAND project

The BRAND EVN project is a EU-sponsored engineering research effort to develop and build a prototype receiver with a frequency coverage from 1.5 GHz to 15.5 GHz (see Alef et al., 2019). The full band will be sampled in the receiver box without any down-conversion. All usable parts of the band will be selected on the same board as the sampler chip via four powerful FPGA processors. Pieces of up to 4 GHz width represented as 8-bit samples will be sent to the backend via optical fibres. The overall structure of the data flow can be seen in Fig 2.

The DBBC3 is used here as an ideal platform to handle 4 GHz portions of the full 14 GHz input band for creating compatible VLBI channels with the observing modes described in the introduction. The actual bandwidth of the BRAND EVN channels will be slightly different from VLBI standards due to the different sampling frequencies compatible with the sampler chip. The sampler device includes its own synthesizer which operates in a restricted range from which sampling clocks can be selected. The value selected for BRAND, 28.732 Gsps, is not a power of 2 but allows one to derive integer MHz bandwidths in the digital signal processing chain. This leads to channelised bandwidths of 7/14/28/56/112/224 MHz out from the digital frontend, from which the OCT or DDC firmware in the DBBC3 selects bands of 4/8/16/32/64/128 MHz (plus optional resampling), ensuring compatibility with the bandwidths currently used in VLBI.

The BRAND EVN data flow involving sampling and digital processing can be functionally divided into two blocks, one placed in the receiver frontend in the antenna and one in the control room where traditionally the backends are located. For this reason we can define the first part a digital frontend and the second a digital backend. The distinction is useful because different functions are performed in the two separated locations.

The main process in the digital frontend part will, in the first implementation, be the formation of 4 GHz slices as input to the digital backend. The process in the digital backend will be the normal VLBI process of further channelisation to select sub-bands from the 4 GHz slice, truncating to 2 bits, and producing VDIF streams for recording.

In more detail, the digital frontend is now the locus directly following the analogue signal path which consists of antenna, feed, filters, low-noise amplifiers and other components, all of which bring the signal to a level suitable for the sampler to sample with a nomi-

nal 8-bit depth. The digitised data from the sampler are then converted from serial to parallel streams, filtered with a 4 GHz OCT filter, decimated, time-stamped, formatted as VDIF with 8-bit depth, and prepared in IP packets for transmission on 16 10 GE links per analogue input to the digital backend. Four such analogue inputs are sampled by one sampler chip, coming from the four channels carrying the ranges 0-14 GHz/14-15.5 GHz in both polarisations from the analogue section of the receiver. (Fig 2).

The resulting data rate from the sampler is huge – more than 900 Gbps. It is transferred from the digital frontend to digital backend on a large number of optical fibers (64) carrying VLBI standard VDIF packets, which contain also the sampling time information along with the data packed as the DBBC3 receiving section requires.

The timestamps inserted by the digital frontend are the time reference used for later correlation of VLBI data, therefore the UTC 1 PPS and frequency reference must be available at the frontend digital receiver, which includes for instance connecting a GPS receiver to the digital frontend.

The digital backend DBBC3 will receive the data into the CORE3H boards via the ethernet connectors using a dedicated firmware/software to be loaded for this mode. Subsequent processing proceeds as usual for the DBBC3 when doing VLBI.

The digital frontend can in principle perform other more complex operations which will be implemented in the future, like dynamic OCT filtering for RFI mitigation, broadband polarisation conversion, and other desired tasks compatible with the DBBC3 system.

As mentioned above the first version of the firmware for the digital frontend will be to send 4 GHz bands to the DBBC3, which requires the so-called CORE3H2 configuration of the CORE3 boards. The CORE3H2 makes use of all eight transceivers on-board in receiving mode. This architecture allows one to receive 4 GHz bands with 8-bit representation, which is similar to feeding a CORE3H using the standard ADB3L sampler boards as in standard DBBC3s.

It is worth noting that if required, there could be full compatibility with a standard DBBC3 equipped with ADB3L sampler boards to be compatible with traditional receivers whose analogue signal is sampled in the backend. Indeed switching between input data to the CORE3H boards coming from the local ADB3L or via the digital frontend could be implemented by using different firmware.

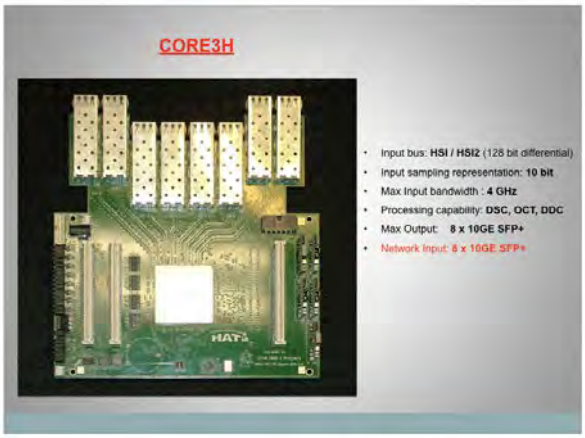

Fig. 3: The FPGA processing board CORE3H can be populated with up to eight optical transceivers. They can work as output (standard DBBC3 VDIF streams for recording) and as input to the FPGA (application for "digital" receivers.

Another architecture could also be chosen when additional functionality is required. This is for example the case for the digital linear to circular polarisation in FPGA. The conversion is required for the BRAND receiver, which is linearly polarised, to work with circularly-polarised VLBI networks. The conversion can be performed in analogue with a hybrid junction after the feed, or in the digital domain with a Hilbert transform in FPGA to give accurate 90 degree phase shift over a wide fractional bandwidth. The additional FPGA resources for performing this process in the CORE3H are not available due to the great demands of the main function of down conversion and packet forming. A clean solution can be provided by replacing a number (or all) the ADB3L with additional standard CORE3H processing boards, if required. Indeed CORE3H boards can be connected in functional sequence through their optical transceivers. The flexibility of the DBBC3 allows one to configure the system blocks in diverse ways to satisfy the changing and highly demanding requirements.

3 Conclusions and outlook

We have shown in this article that the DBBC3 is a very versatile backend. The development to adapt it to the

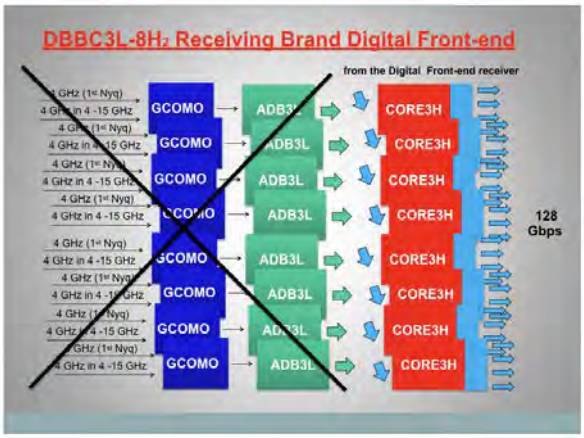

Fig. 4: The block diagram shows a DBBC3 whose analogue and sampling parts are by-passed by digital signals from the BRAND (or other) digital frontend.

BRAND digital receiver opens a cost-effective path to handle the data flood which the BRAND receiver will produce.

At the same time the BRAND digitiser/processor unit in or close to the receiver box together with the modified DBBC3 backend can be adapted efficiently to other receivers with large bandwidths. One immediate application will be the triple-band receiver for the high frequencies 22 GHz, 43 GHz, and 86 GHz. Rather than renewing the limited IF cabling of, for instance, the Effelsberg antenna we are planning to sample as much bandwidth as possible close to the triple-band receiver with the BRAND sampler/processing unit and transport the IF as digital on fibre, which is much easier. We use one or two DBBC3s to form channels (sub-bands) suitable for VLBI correlation. Assuming 8 GHz bandwidth per polarisation and receiver, we could see data rates of up to 192 Gbps on output.

It should also be noted that the control of the DBBC3 in this new mode via the Field System[1] will be an extension of the existing implementation, which should be cost effective to realise.

References

Tuccari G, Alef W, Dornbusch S, et al. (2019) DBBC3 the new wide-band backend for VLBI. In: Proceedings of the "14th European VLBI Network Symposium & Users Meeting", PoS(EVN2018)140

Alef W, Tuccari G, Dornbusch S, et al. (2019) BRAND - A wideband receiver for astronomy and geodesy. In: R. Haas, S. Garcia-Espada, J. A. López Fernández (eds.): *Proc. 24th EVGA Working Meeting*, 31–36

[1] See for instance http://www.metsahovi.fi/pub/evn-om/4fs-4.html

BRAND – A Wideband Receiver for Astronomy and Geodesy

W. Alef, G. Tuccari, S. Dornbusch, A. L. Roy, M. Wunderlich, C. Kasemann, M. Nalbach, M. Pantaleev, J. Flygare, J. D. Gallego, J. A. López Pérez, F. Tercero Martínez, G. W. Schoonderbeek, J. Hargreaves, R. de Wild, V. Bezrukovs

Abstract The BRAND wideband receiver is being developed with support from the European Union's Horizon 2020 research and innovation programme as a part of RadioNet. Its continuous frequency range from 1.5 GHz to 15.5 GHz makes it a scientifically extremely interesting development for radio astronomy. But it also covers the VGOS frequencies and even extends them to lower and higher frequencies. Used for geodesy, this could yield results superior to those that will be achieved with the traditional four VGOS bands. If we succeed in modelling an adequate feed for secondary focus, BRAND receivers could become the next generation VGOS receiver. It will also allow to retrofit traditional prime focus antennas to become compatible with VGOS antennas. The first half of the 3 1/2-year-term of the project is over, and we give an overview of the achievements so far and of what has been planned for the near future.

Keywords VLBI · EVN · Radio astronomy receiver · Digital backends · Digital receiver

Walter Alef · Gino Tuccari · Sven Dornbusch · A. Roy · Michael Wunderlich · C. Kasemann · M. Nalbach
Max Planck Institute for Radio Astronomy, Auf dem Hügel 69, DE-53121 Bonn, Germany

Gino Tuccari
also at INAF Istituto di Radioastronomia, Sezione di Noto, Contrada Renna, IT-96017 Noto (SR), Italy

Miroslav Pantaleev · Jonas Flygare
Onsala Space Observatory, SE-439 92 Onsala, Sweden

Juan D. Gallego · José Antonio López Pérez · Felix Tercero Martínez
Instituto Geográfico Nacional
C/General Ibañez de Ibero, Madrid, Spain

Gijs Schoonderbeek · Jonathan Hargreaves · Ronald de Wild
ASTRON, Netherlands Institute for Radio Astronomy, Dwingeloo, The Netherlands

Vladislavs Bezrukovs
Ventspils International Radio Astronomy Center, Ventpils, Latvia

(Correspondence: alef@mpifr-bonn.mpg.de)

1 Introduction

Under the RadioNet 'Joint Research Activity' BRAND EVN we are developing and building a prototype "digital" VLBI-receiver for the EVN (and other) telescopes. It will cover a frequency range of more than 1:10 from 1.5 GHz to 15.5 GHz (18 cm to 2 cm wavelength). It was decided in the proposal phase already to not include the 1.4 GHz band due to strong RFI below 1.5 GHz, to limit the size of the expected feed, and by including instead 15.5 GHz to make the 2 cm band of the VLBA accessible for the EVN (see Fig. 1). It should also be mentioned that frequencies below 1.5 GHz are in low demand on the EVN. Our proposal was awarded about 1.5 M€ by the EU under contract 730562, but we expect a total cost of close to 2 M€, which implies additional contributions by the partners MPIfR, INAF/Noto, OSO, UAH/IGN, ASTRON, and VUC. The project started in January 2017 and will end in August 2020. The final report with first fringes from a VLBI observation are due no later than December 2020.

The BRAND prototype will be a digital receiver, which means that the radio frequency signal will not be down-converted for further processing, but the sampling and initial digital processing will happen in the receiver box. The only analogue parts remaining are the

feed horn, high temperature superconductor (HTSC) filters and couplers, low noise amplifiers (LNA) and and additional amplification with filtering to prepare the signal for the sampler.

The sampler will convert the whole band to the digital domain, and the initial processing will select parts of the band that are (mostly) free of interference. The resulting data will be transported to the VLBI digital backend via optical fibres bypassing the legacy IF systems with their narrow bandwidths, thus providing a cheap means to achieve higher bandwidths without the need for upgrading IF systems which is expensive.

The prototype should be a prime focus receiver as those feeds are most advanced. As a number of EVN antennas can only be equipped with secondary focus receivers one task of BRAND is research in secondary focus feeds. It was decided by the project team to select Effelsberg for the prototype so as to achieve maximum visibility for the project.

The big difference to other receivers is that the whole band will be digitized without down-conversion using a single chip, so that the signals will pass through a single receiver which should keep the phase relations between all parts of the band intact. This again will allow real multi-wavelength VLBI for astronomy with software that will perform the fringe-fitting over the whole band in a coherent way. Such a fringe-fitter is also being developed under RadioNet in the 'Joint Research Activity' RINGS. Interesting for geodesy is that BRAND will extend the VGOS band to lower and higher frequencies with a high degree of flexibility with respect to the parts of the band that can be observed.

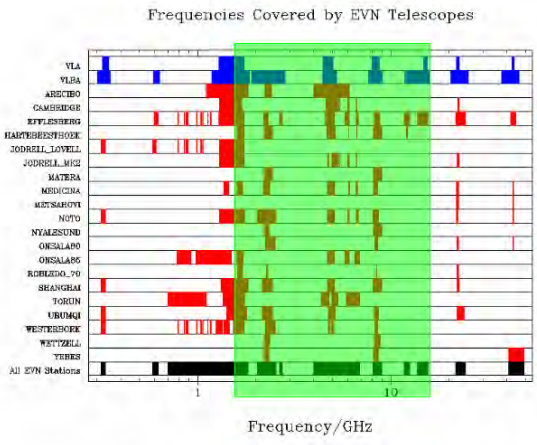

Fig. 1: In this logarithmic plot the green rectangle shows the frequency bands of EVN telescopes that the BRAND receiver will cover. Frequencies below the BRAND range are rarely observed with the EVN, and for frequencies above the EVN will probably adopt "triple-band receivers".

2 Status of the BRAND project

The work packages of BRAND are organised in a logical way according to the major parts of the receiver: frontend (analogue, incl. dewar), backend (digital, incl. firmware), software (receiver control, recording, correlation), final integration (incl. lab and telescope tests with VLBI observation) (see Fig. 2).

The BRAND EVN project is progressing more smoothly than expected: feed, HTSC filters and coupler, LNA, major digital components, and a large fraction of the firmware are available already. The design of the dewar and the analogue signal path are finished.

The first work package "Feasibility survey of EVN antennas" was finished in June 2017. Its deliverable was a report with tables of the characteristics of EVN telescopes as well as RFI measurements. The motivation of this report is to prepare the ground for the BRAND receivers at all EVN telescopes. The study on "Solutions for secondary focus" antennas is based on the same motivation.

2.1 Frontend

The Effelsberg 100 m telescope has a difficult geometry for prime focus feeds. Its opening angle is $2 \times 79°$ with an f/D ratio of 0.3. The Onsala team achieved a final best result with a Quad-Ridge Flared Horn (QRFH) feed with a dielectric inset which improves the response at the high frequencies (Flygare et al., 2018). The average aperture efficiency is about 50 % over the whole band (Fig. 3) with an input reflection of better than -10 dB. The simulated SEFD for the feed is comparable to that of the best Effelsberg feeds which reach 20 Jy. The BRAND feed has an SEFD between about 20 Jy and 40 Jy (Fig. 4).

The feed has been manufactured (see Fig. 5) and has been measured at Onsala. It was found to agree well with the simulations.

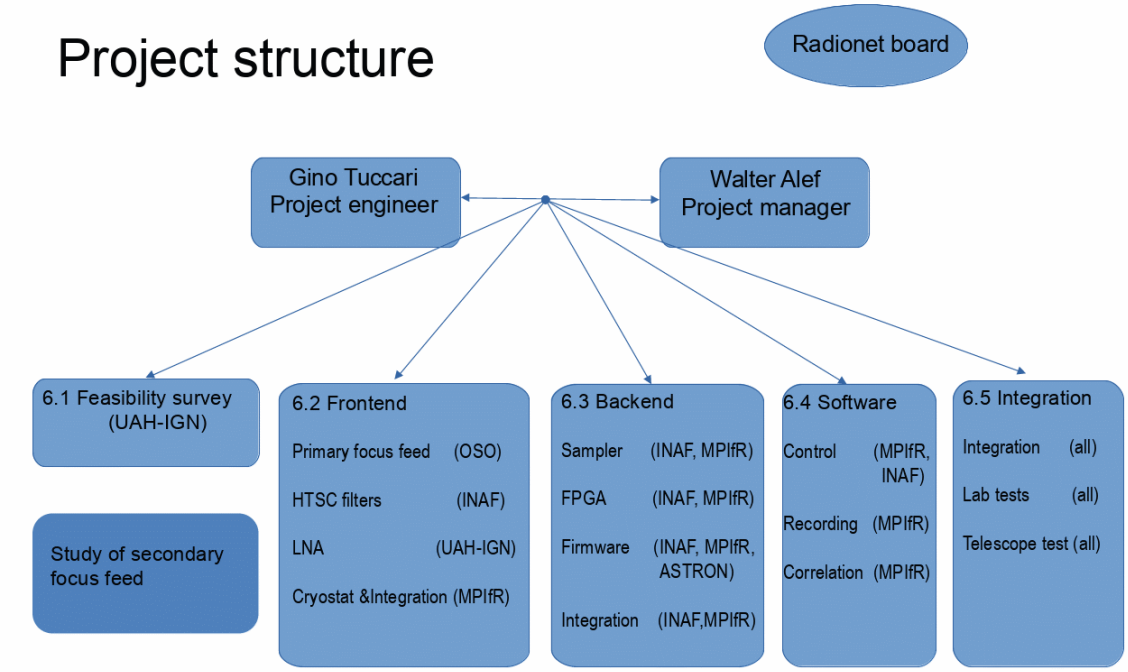

Fig. 2: Organigram of the BRAND project. The work packages are organised in a logical way according to the major parts of the receiver. The feasibility survey and the study of a secondary focus feed are not directly related to the receiver, but support later EVN-wide installation.

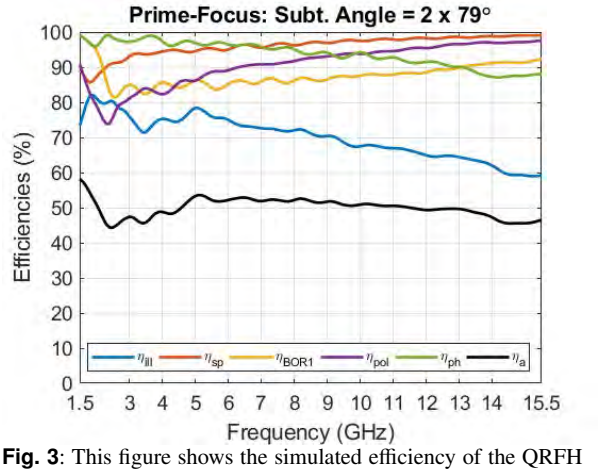

Fig. 3: This figure shows the simulated efficiency of the QRFH feed for Effelsberg (black line).

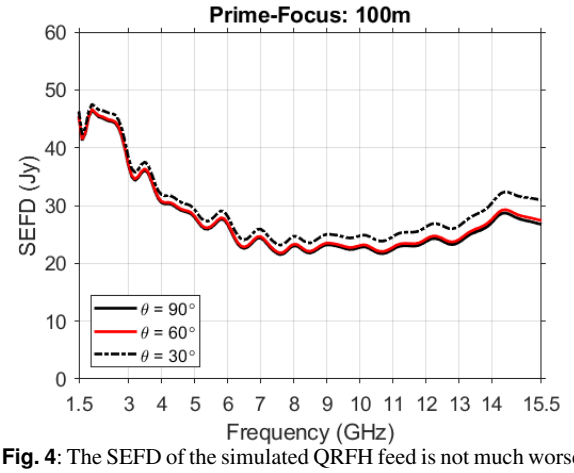

Fig. 4: The SEFD of the simulated QRFH feed is not much worse than that of the best Effelsberg receivers which reach 20 Jy.

2.2 High temperature superconductor filters

In the feasibility survey it was found that at Effelsberg the RFI is very strong below 1.5 GHz and at about 1.8 GHz and 2.2 GHz. These frequencies have to be suppressed with a HTSC filter to protect the LNA and the sampler from being driven into the non-linear regime by this RFI.

Our initial attempt to combine these two filters and the high-pass together with a direction coupler for phase-cal and calibration into one crystal was not successful. In this attempt the notch filters were not deep

Fig. 5: The manufactured QRFH feed without the dielectric inset. The flatness of the feed is due to the very large opening angle of the Effelsberg telescope of $2 \times 79°$.

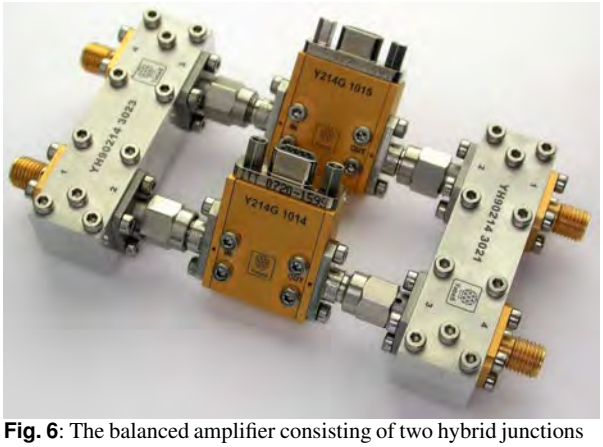

Fig. 6: The balanced amplifier consisting of two hybrid junctions at input and output and two LNAs in the middle.

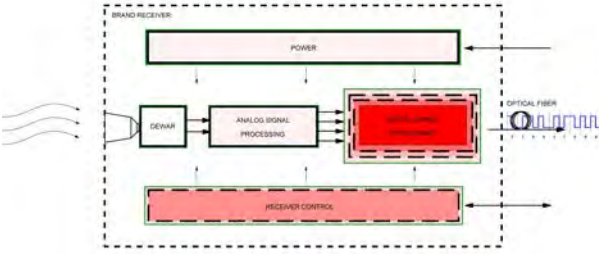

Fig. 7: Block diagram of the receiver box. The digital electronics in the box on the right needs more than 120 dB of shielding. In addition a few 100 Watts of heat have to be transported out.

enough for the existing RFI at Effelsberg. Also the drop-off below 1.5 GHz was too shallow.

The solution we could realise together with the manufacturer uses three separate devices to be connected in series: high-pass, notch filters, coupler. This will result in a slight increase in system temperature. The two times three devices were delivered in April 2019.

2.3 Low Noise Amplifier

Our partner Yebes/OAN found a solution for amplifying the whole BRAND frequency band with low noise and low input return loss (IRL). A single-ended LNA has the lowest noise, but an unacceptably high IRL, while a balanced amplifier is only a few kelvin noisier with an acceptable IRL. The disadvantage of a balanced amplifier (Fig. 6) is that for two polarisations four hybrids and four LNAs are needed.

On the other hand having an additional hybrid at the input of the balanced amplifiers opens the opportunity to use it to convert the linear polarisation to circular, which had initially not been planned. This could be done with a wideband hybrid junction at the antenna terminals before the balanced amplifier. The hybrid junction approach was demonstrated in Yebes and found to work well (phase unbalance of $\leq 2.5°$ and amplitude unbalance of ≤ 1.2 dB over the whole band) but it is critically sensitive to cable length mismatches (a 1 mm length difference contributes a phase unbalance of 27° at 15.5 GHz). This development can be used for BRAND and VGOS.

2.4 Receiver box with cryostat and analogue signal path

The design of the cryostat and receiver layout has been finished. It was determined that the feed requires a window with a diameter of 80 cm, which is just doable. A simulation of the feed with this dewar and window indicate that there will be only little effects on the beam pattern. Due to the large window the cryostat will be quite heavy (150 kg).

The analogue signal path after the first amplifier stage is standard except for splitting the signal of each polarisation into two parts 1.5 GHz to 14 GHz and 14 GHz to 15.5 GHz. This is the preferred scheme to feed the input signals to the sampler.

As the sampling and first stage of FPGA processing should be installed in the receiver box (see Fig. 7) very high shielding of RFI produced by the digital components of more than 120 dB is required. This can be achieved by a triple box. The heat of up to about 500 W produced by the sampler and FPGAs has to be transported out, which makes the whole setup very challenging.

2.5 Sampler and FPGA processing

We were able to procure 16 GHz samplers and an evaluation board under a NDA. The samplers were tested successfully and even surpassed our expectations. The sampler chip has four inputs, each for the full bandwidth and thus can handle both polarisations. If two signals of 16 GHz bandwidth are input to the sampler the output data rate is two times 56 Gsps with 8-bit samples. For an input bandwidth of 14 GHz the output data rate is only 28 Gsps with 8-bit samples. As our total usable bandwidth is only two times 14 GHz this second possibility is the preferred option.

To simplify the analogue signal chain and avoid down-conversion the input signal is split as described in the previous section (2.4), and the 14 GHz to 15.5 GHz are sampled in the second Nyquist zone. Thus all four input ports of the sampler chip will be used.

We have chosen a two-step approach for mastering the enormous data rates coming from the sampler to the FPGA chips. In a first design the evaluation board will be used for sampling, together with a first version of the FPGA processing board. Thus we can fairly early on in the project develop and test the firmware, that should receive the multiple linear data streams of sampled data output by the sampler and should reconstruct the parallel data streams which the FPGA has to process. This is a requirement for processing the data in the directly connected FPGAs.

The final design of our own sampling/processing board has started. It will handle both polarisations and the full bandwidth. One sampler chip with four inputs sampling 14 GHz will be placed in the centre of the board. The sampler will be surrounded by four Xilinx Kintec Ultrascale FPGAs. The processed data will be output via 64 fibres. The PCB will work in the microwave regime and the input data rate out from the sampler is nearly 900 Gbps. This board will have an enormous number of connections and more than 20 layers of which some have to be of high-class microwave material.

2.6 Firmware

The first big block of firmware has to interface the sampler chip with the four FPGA chips. Tests of this firmware should start in a few weeks after this conference. A second block will allow the selection of the desired and usable parts of the band. This process will also be executed on the board in the receiver box. Under development are two different kinds of firmware: 1) OCT filters, which are FIR convolutional filters acting on the time series from the sampler, which will allow the selection of arbitrary parts of the band and 2) digital down-converter firmware. These two firmware blocks have still to be tested.

The data will then have to be output via the 64 fibres and sent to the DBBC3 CORE3H backend processing boards. The required eight CORE3H boards will have all eight optical fibre connections populated with SFP+ ports. Four of these will also be used for data output from the CORE3H to the VLBI recoders, or Internet, or the telescope backend system. The latter will be required for using the BRAND receiver in single dish mode. The DBBC3 can generate narrow VLBI subbands to be compatible with existing observing modes. This firmware will enter test mode soon.

The polarization conversion firmware will be written by ASTRON in a modular fashion so that it can either be loaded to the first processing stage up in the receiver or to the DBBC CORE3H boards. A block design is ready and work is proceeding.

3 Conclusions and outlook

So far the development and the engineering of the prototype BRAND receiver has been surprisingly smooth without any major stumbling blocks.

Integration has to be done still at MPIfR together with all partners. The receiver will be tested in the lab as much as possible. Unfortunately none of the partners has an anechoic chamber where such a heavy dewar

can be handled. So we will have to wait for the testing on the telescope to measure the beam of the receiver, its noise and polarisation characteristics. We are planning to perform wide-band VLBI observation preferably with one or more VGOS antennas.

The extremely high output data-rate from the BRAND receiver of more than 64 Gbps (2-bit samples for VLBI) will require also modifications to recording and correlation software. This work package will be started late in 2019, while efforts to interface the BRAND data to the Effelsberg backend system are in the definition phase.

We expect the BRAND prototype to be ready before the end of 2020.

Acknowledgements This work has received funding from the European Union's Horizon 2020 research and innovation programme under grant agreement No 730562 [RadioNet].

References

Flygare J, Pantaleev M, Olvhammar S (2018) BRAND: Ultra-Wideband Feed Development for the European VLBI Network – A Dielectrically Loaded Decade Bandwidth Quad-Ridge Flared Horn, In: *12th European Conference on Antennas and Propagation (EuCAP2018)*, London, UK, 9–13

The Stability of Delay in VLBI Digital Backends

E. Nosov

Abstract In order to meet the VGOS requirements, the influence of instrumental delay variations from scan to scan needs to be limited to 1 ps level. Achieving this requires a certain stability of the equipment in the signal chain and implementation of a phase calibration system to measure the remaining delay variations. As the delay instability in electronic devices is strongly related to temperature fluctuations, both temperature fluctuations and temperature sensitivity of equipment have to be minimized. The paper focuses on the stability of VLBI digital backends. It describes the main sources of delay variations and provides an estimation of the respective temperature coefficients for backends developed at IAA RAS. Also the paper discusses a convenient way for in-system measurement of the inner delay variations in Multifunctional Digital Backend.

Keywords VGOS · DBE · BRAS · MDBE · Delay stability · Temperature coefficient

1 Introduction

One of the important requirements to the signal chain of VLBI radio telescopes is the stability of instrumental delay. To achieve the goal of 1-mm position accuracy specified in the VGOS project, the instrumental delay variations should be kept or at least measured with an error less than 1 ps (Petrachenko et al., 2009). This requirement, in particular, applies to the digital backend (DBE), as it is a part of the radio telescope signal chain. Although DBEs are mostly digital devices and, therefore, can not introduce unwanted delay variations to the signal after it was digitized, they still have some analog front-end before ADC, as well as circuits for generating and distributing ADC clock signal. Both of them can influence the delay, and this influence should be minimized by appropriate DBE design.

The delay instability in electronic devices is strongly associated with temperature fluctuations. Maintaining a stable temperature is an obvious way to improve the stability of the delay, but it can be complicated when DBE is located in the confined space of the antenna focal cabin, like Broadband Acquisition System (BRAS) in RT13 radio telescopes (Nosov et al., 2016). In this case, low sensitivity to temperature fluctuations is essential for DBE. To achieve this, the DBE designer needs to know the values of delay temperature coefficients (TC) for the components of the signal and clock paths in DBE in order to find the sections that contribute to the error most and improve them.

The following section provides estimations of the temperature coefficients of DBE components, obtained either from measurements performed at IAA RAS or from s-parameters and datasheets provided by component manufacturers. This data was used to design Multifunctional Digital Backend (MDBE) – the new back end developed for ”Quasar” VLBI-network (Nosov et al., 2019). It helped to significantly reduce the temperature coefficient of MDBE compared to BRAS.

Evgeny Nosov
Institute of Applied Astronomy of Russian Academy of Sciences, IAA RAS, Kutuzova emb. 10, Saint-Petersburg, Russia

(Correspondence: nosov@iaaras.ru)

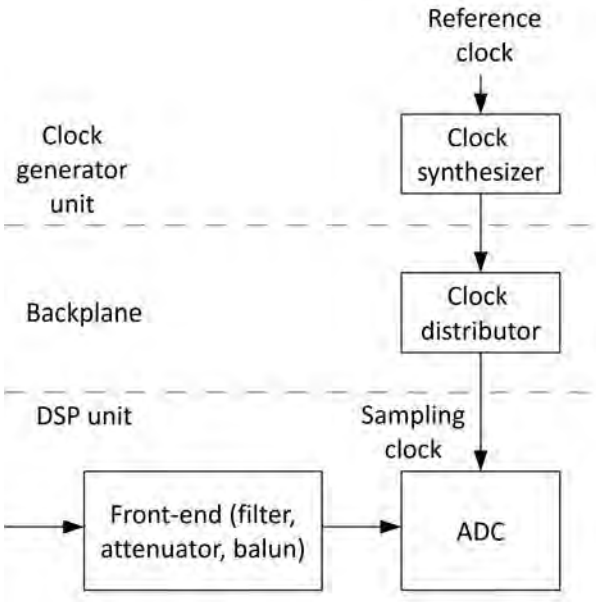

Fig. 1: Main sources of delay variations in typical DBE.

2 Temperature coefficient of DBE signal path

Both the signal path and the clock path of DBE can influence the delay stability of observed signal. Typically the input signal passes to ADC through some front-end, that prepares the signal for digitization (Fig. 1). The front-end may contain different components depending on particular DBE, but probably it has an anti-aliasing filter to limit the spectrum of the signal to one Nyquist zone, attenuator to control the input level, and a balun to convert the signal to differential form required by ADC inputs.

Attenuators have a very low group delay (tens picoseconds) and could hardly have significant TC. For example, the digital attenuator used in MDBE has TC of about 10 fs/K. This value was calculated from the plot of relative phase versus temperature, provided by the manufacturer.

Baluns for the required frequency range (up to 2 GHz) also have a low group delay (tens to few hundreds of picoseconds) and therefore will not contribute much to the total TC.

Wideband filters for required frequency range usually have TC less than 1 ps/K. For instance, the filter used in BRAS has TC less than 100 fs/K in the most of bandpass, and about 200 fs/K at cutoff frequency. These values were calculated by using s-parameters of the filter, measured at +25°C and +100°C.

In total, *TC of ADC front-end* should be significantly less than 1 ps/K, that is in agreement with the real measurements of available front-ends. For instance, the temperature coefficient of BRAS front-end is in a range of 0.1–0.2 ps/K depending on frequency. The values for MDBE front-end are even smaller (±0.1 ps/K), and are limited by the accuracy of the measurement technique. In summary, TC of DBE signal path should not significantly influence the instrumental delay variations in case of reasonably stable temperature.

3 Temperature coefficient of DBE clock path

Besides the delay fluctuations in the signal path, the observed delay of the digitized signal depends on fluctuations of the ADC sampling clock. The variations in the clock signal shift the sampling time, that is considered as the shift of the signal delay in opposite direction. That is adding 1 ps to delay in clock path reduces the instrumental delay by 1 ps.

Clock path of DBE is based on clock synthesizer, that generates ADC sampling clock from reference clock. In multichannel systems the sampling clock has to be distributed over all ADCs in the system by the clock distributor. Both the synthesizer and the distributor have some TC of delay, as well as the transmission lines in printed circuit boards (PCB), and coaxial cables.

The clock synthesizer for DBE is typically based on phase-locked loop (PLL) integrated circuit (IC). The manufacturers of PLL ICs do not provide information about their phase/delay temperature coefficients. The TC of a particular synthesizer depends on the properties of the IC, and slew rate of the reference and feedback signals. Based on the experience of IAA engineers, the TC of PLL-based synthesizers usually lay in the range of a few ps/K. ADC clock synthesizer built for BRAS has quite good TC about 1.2 ps/K. The synthesizer of MDBE was significantly improved and has TC about 0.2 ps/K.

Specialized *clock distributor* ICs give the most convenient way to feed the clock signal to all ADCs in DBE. There are many of them on the market, but only

for some the manufacturers give the temperature coefficient values. Table 1 presents several examples demonstrating the range of values, spreading from a very noticeable 2800 fs/K to negligible 35 fs/K. T hus, carefully choosing the clock distributor during DBE design can make its influence on the delay stability barely noticeable.

Table 1: Clock distributors with specified TC and maximum frequency more than 1 GHz

Part number	Temperature coefficient, fs/K
AD9508	2800
ADCLK854	2000
MAX9312	500
LTC6953	350
SY89112U	150
SY58034U	65
ADCLK954	50
NB7L1008M	35

The delay in *PCB transmission lines* also varies with temperature. The propagation delay in stripline can be estimated as (Johnson and Graham, 2003).

$$T_{pd} = \frac{\sqrt{\varepsilon_r}}{c}, \tag{1}$$

where ε_r is a relative permittivity and c is the speed of light. One of the most popular material for PCBs is FR4, that have ε_r about 4.5 and its temperature coefficient about 400 ppm/K (Coonrod, 2011). From (1) it is easy to find that with total length of lines from the reference clock input to ADC clock input being 40 cm the delay temperature coefficient of the lines is about 0.6 ps/K.

Luckily, there are more advanced PCB materials on the market. For example, RO4350B material has ε_r = 3.66 and TC of just 50 ppm/K. This material is often used for high-frequency applications where a relatively small increase in the total cost of the system is justified by a significantly better performance. The PCBs of MDBE are manufactured as a mixture of RO4350B (for clock and high-speed lines) and FR4 (for all others lines) layers. The 40 cm line implemented at RO4350B has TC of just 0.06 ps/K, that is ten times less than for FR4. Therefore, with an appropriate PCB material the TC of PCB lines is negligible. It should be noted that for microstrip lines the PCB material does less contribution to the propagation delay, and the appropriate TC will be even less than for stripline.

Besides PCB lines, DBE can also contain *coaxial cable* assemblies. Long coaxial cables in antenna cable loop can cause significant instability of delay, but not in the case of DBE. Usually the length of the cable assemblies in DBE, if any, is much less than 1 meter. Even PTFE-based cable, that has so called temperature knee at room temperature (Czuba and Sikora, 2011), is not able to cause noticeable delay instability. For instance, 15 cm of SM141FEP cable has TC of about 30 fs/K at room temperature, which is negligible in comparison to the other sources of instability.

The ADC itself can also cause some instability of delay, but at the moment I have no data about the temperature coefficient of any high-speed ADC. It will be measured for MDBE in 2020.

4 Temperature coefficients of BRAS and MDBE

Based on the information above, we can estimate the total TC of BRAS and MDBE clock paths (Table 2). As the influence of signal path is negligible, the total TC of the systems will be almost the same as in the table, but with the opposite sign. There is no information about TC of the clock distributors used in BRAS, but we know the values for similar distributors and can use it for an approximate estimation. As was mentioned, at the moment we also don't know the TC for the ADCs.

Table 2: Estimation of temperature coefficients for BRAS and MDBE

Part	BRAS	MDBE
Clock synthesizer	1.2 ps/K	0.2 ps/K
Clock distributor	2 ps/K	0.05 ps/K
PCB	0.6 ps/K	0.06 ps/K
ADC	-	-
Total	> 3.8 ps/K	> 0.31 ps/K

Table 2 shows that BRAS would have TC of more than 3.8 ps/K while really measured value for BRAS is about 4.5 ps/K, i.e. close to the estimation. As you can see in the Table 2, from the stability point of view each part of MDBE was significantly improved in comparison with BRAS. The real measurements will be performed in the beginning of 2020, and MDBE has specialized calibration circuits to simplify this measurements.

5 Internal delay measurement in MDBE

The ADC used in MDBE needs some calibration signal, preferably a tone, to calibrate gains, voltage offsets and clock phases of its internal cores. One of the possible options to generate such signal is to use a divided copy of the sampling clock (e.g. 256 MHz) available in the clock synthesizer. This signal, properly prepared, is distributed over ADCs in MDBE and measured by PCAL extractor unit in FPGA. The received information about phase and amplitude of the signal is used to calibrate the ADC, but it also can be used to monitor the stability of internal delay.

Figure 2 explains the calibration circuits. The calibration signal comes from either the input clock distributor (100 MHz) or the clock synthesizer (256 MHz) and goes to the ADCs through additional clock distributor IC. This IC is placed close to the ADC clock distributor (2048 MHz), and thus has almost the same temperature. The length of all lines is aligned. For the case of 256 MHz signal it means that instabilities influencing the calibration and ADC clock signals are almost the same. The observed variations of the phase (initial phase is insignificant and not shown), expressed in units of time (Δt_1), are actually the difference between variations of the calibration signal and the ADC clock signal:

$$\Delta t_1 = \Delta t_{in} + \Delta t_{synt} + \Delta t_{dist} + \Delta t_{PCB} - \Delta t_{clk},$$

where Δt_{in}, Δt_{synt}, Δt_{dist} and Δt_{PCB} are delay variations in input clock distributor, clock synthesizer, sampling clock distributor, and clock lines in PCB correspondingly. The variations of ADC clock Δt_{clk} consist of almost the same parts:

$$\Delta t_{clk} = \Delta t_{in} + \Delta t_{synt} + \Delta t_{dist} + \Delta t_{PCB} + \Delta t_{ADC}.$$

Consequently, the measured value Δt_1 directly shows the variations in ADC:

$$\Delta t_1 = -\Delta t_{ADC}.$$

In case of 100 MHz signal used for measurements, it will contain the same components as 256 MHz signal except variations of the clock synthesizer Δt_{synt}:

$$\Delta t_2 = \Delta t_{in} + \Delta t_{dist} + \Delta t_{PCB} - \Delta t_{clk}$$

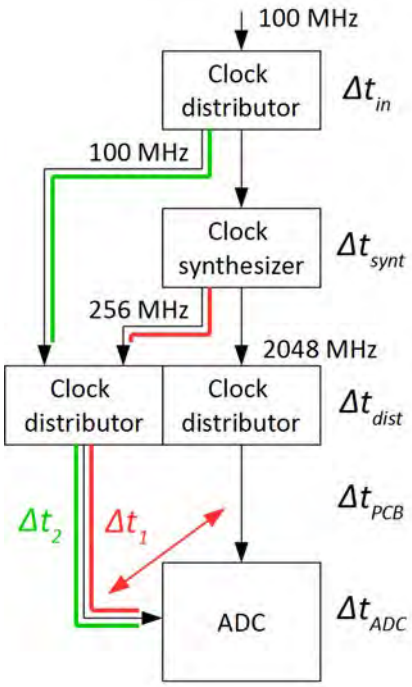

Fig. 2: Embedded delay measurement circuits in MDBE.

As a result, the measured value Δt_2 shows the delay variations in both synthesizer and ADC:

$$\Delta t_2 = -\Delta t_{synt} - \Delta t_{ADC}.$$

Periodic measurements of Δt_1 and Δt_2 allow to control the delay variations in the clock synthesizer Δt_{synt} and in the ADCs Δt_{ADC}. Adding one more clock distributor allows measuring also Δt_{dist} and Δt_{PCB}, though these variations are expected to be insignificant (less than 100 fs/K). As signal to noise ratio is high, the expected accuracy of the measurements is much better than 1 ps. This was approved by modeling with digitization effects taken into account.

6 Conclusions

VLBI digital backends can have temperature coefficient of delay as high as several ps/K, what is noticeable for VGOS applications and can influence overall instrumental delay. The variations in a DBE are included in overall instrumental delay, that normally is to be measured with phase calibration system. Nevertheless, it is always preferable to keep the variations

small. An analysis of instability sources in DBEs has allowed to make the temperature coefficient of MDBE several times better than for BRAS. The remaining instability of MDBE is measured by embedded calibration circuits that help to separate internal instabilities from the variations of the input signal. It gives the stations a convenient tool to control the signal chain performance.

References

Petrachenko B, Niell A, Behrend D, et al. (2009) Design Aspects of the VLBI2010 System. Progress Report of the VLBI2010 Committee. NASA Technical Memorandum, NASA/TM-2009-214180, 58 pp.

Nosov E, Melnikov A, Marshalov D (2016) Operating Experience of Broadband Acquisition System on RT-13 Radio Telescopes. In: D. Behrend, K. D. Baver, K. L. Armstrong (eds.): *IVS 2016 General Meeting Proceedings*, NASA/CP-2016-219016, 53–57

Nosov E, Ivanov D, Ipatov A, et al. (2019) Extending of "Quasar" VLBI-network: VGOS-compatible radio telescope in Svetloe. In: K. L. Armstrong, K. D. Baver, D. Behrend (eds.): *IVS 2018 General Meeting Proceedings*, NASA/CP-2019-219039, 12–16

Johnson H, Graham M (2003) High-speed Signal Propagation: Advanced Black Magic. Prentice Hall Professional

Coonrod J (2011) Understanding When To Use FR-4 Or High Frequency Laminates. Onboard Technology, 25–30

Czuba K, Dominik Sikora D (2011) Temperature Stability of Coaxial Cables. *Acta Physica Polonica A*, 119(4), 553–557

A Simulator to Generate VLBI Baseband Data in Matlab

J. Gruber, J. Böhm, A. Nothnagel, M. Schartner

Abstract VLBI radio telescopes represent a sophisticated interconnection of electronic devices. The final product of each observation by a radio telescope is the baseband data. In this presentation, we show a software tool as part of the Vienna VLBI and Satellite Software (VieVS) which generates simulated VLBI baseband data. This simulator is written in Matlab and contains a telescope model which is based on the parametrization of real antenna key characteristics. Moreover, source characteristics such as the signal structure from satellites as well as spatial velocities of sources and receivers are taken into account in the model. Advanced Digital Signal Processing (DSP) algorithms of Matlab are applied to model the antenna system. We will present the various model components of the simulator and discuss potential applications of such a tool. Finally, we show the first results of simulation experiments with the processing in a real VLBI processing chain.

Keywords Baseband data simulation · Correlation

Jakob Gruber, Johannes Böhm, Matthias Schartner
Technische Universität Wien, Department of Geodesy and Geoinformation, Gußhausstraße 27-29/E120, AT-1040 Vienna, Austria

Axel Nothnagel
Universität Bonn, Institut für Geodäsie und Geoinformation, Nußallee 17, DE-53115 Bonn, Germany

(Correspondence: jakob.franz.gruber@geo.tuwien.ac.at)

1 Introduction and motivation

In Very Long Baseline Interferometry (VLBI), baseband data are referred to as the filtered, down-converted, sampled, and quantized electric field strength measurements at each telescope. They represent the final output of each station and act as input data for the correlator to initialize raw data processing. The digital baseband data file contains the time-tagged stream of samples recorded at each station. They are cross-correlated to determine the fundamental VLBI observable. In this work, we present a software tool written in Matlab, which generates such data streams based on the simulation of the VLBI observation process.

The simulator contains a telescope model which is based on the parametrization of real antenna key characteristics and a source model that allows the generation of a specific signal structure. The model parameters are described in Chapter 3 and the systematic, theoretical analysis of the methods are presented in Chapter 2. Baseband data are usually stored in a specific format with a few commonly used format descriptions available. In Chapter 4 the implementation of such a format converter (formatter) is shown.

Existing baseband data simulators have already been successfully used for various studies. The program called 'enoise' (Nishioka, 2015) developed by the VLBI group of Academia Sinica Institute of Astronomy and Astrophysics (ASIAA) has used their simulator to test the zoom band mode of the Distributed FX (DiFX) correlator (Deller et al., 2007). The simulator 'Datasim' (Meyer-Zhao, 2018), which is part of the current DiFX software package, was used for the simulation of higher sampling rates for the Atacama Large Millimeter/submillimeter Array

(ALMA). Both simulators use functions implemented in DiFX and apply them in a reverse engineering way. In contrast, the presented baseband data simulator is developed from scratch and can serve as an independent data source to test correlation algorithms and new observing modes.

The software design of this simulator is intended to be flexible in terms of the source and the antenna model. With this, various types of input signals can be modeled and simulations to artificial satellites with specific signal structures can be carried out. In general, due to the flexible model design and the toolboxes offered by the built-in advanced signal processing routines of Matlab, it is possible to be variable with respect to the simulation of new VLBI observation scenarios (e.g., signal structures, new observing modes). Using the formatter to link the simulated baseband data sets to established correlators, it is possible to pipe simulated data through the real VLBI processing chain. This enables proofs of concepts and evaluating the technical feasibility of simulated observation scenarios.

The development of algorithms for a baseband data simulator implies the inverse mathematical formulation as they are required for certain operations within the correlation process. That applies in particular for the alignment of the telescope data streams due to the difference in signal arrival times and the fringe-rotation due to the Doppler shift. This kind of knowledge gain helps our group to get a better understanding of the operations within the correlator and might be helpful for a more significant interpretation of the correlator feedback. Debugging the observation process to infer a certain antenna behavior from the correlator response might also be another potential field of study.

In this paper, we focus on the description of the computational concept. It provides a general overview of the realization of an independent and flexible baseband data simulator written in Matlab. In analogy to the first fringe detection, the Chapter 5 'First Light' describes the fringe detection of a first basic observation simulation with the presented baseband data simulator.

2 Methodology and realization with Matlab

The baseband data simulator is implemented with Matlab and makes use of the built-in digital signal processing toolbox. The digital signal creation for any sky-frequency is carried out at baseband. The down-conversion from sky-frequency to baseband is not simulated because two times the sky-frequency would be required for the sampling rate. This means at least a sampling rate of 16 GHz would be needed for a signal composed of frequencies in the low X-band at around 8 GHz. A signal simulation of a rather short simulation time of one second would already require 16×10^9 samples, which would exceed the internal memory capabilities of currently used computers. Due to the linearity of the down-conversion it is also possible to carry out any kind of signal manipulation at baseband without degrading the simulation process. To apply and simulate signal manipulation arising from any kind of electronic device within the real antenna signal chain, so-called transfer functions are used. A transfer function is a mathematical representation of the signal manipulation in the frequency domain and describes the relation between the output from the device for possible inputs. The main computational concept of the presented simulator is contained in the formulation of a transfer functions for the antenna system with its individual electronic devices. The transfer functions are applied on the input signal to account for any signal delay, amplitude modification, and phase distortion. The various simulation and modeling possibilities which are currently implemented are described in Chapter 3.

Currently, the Matlab function *randn* is used to generate normally distributed random numbers which are used to simulate source noise and receiver noise. A transfer function with a linear phase term is used to delay the source signals by the difference of signal arrival times between two telescopes. The Doppler shift is modulated in the time domain using the Hilbert transform. The a priori values for the difference in signal arrival times and the telescope velocities are calculated with the Vienna VLBI and Satellite Software (VieVS) (Böhm et al., 2018). The amplitude scale for source and receiver noise is defined by the fundamental relation of signal power with the variance of Gaussian noise. The built-in Matlab Fast Fourier Transformation *fft* is used to switch between the time and the frequency domain. All operations in the simulator are performed using double precision. In the last step the signal with 64-bit amplitude precision is quantized by the number of bits defined in the model parametrization (see Chapter 3).

3 Model parameters

A variety of model parameters is used to characterize the VLBI observation process within this baseband data simulator. There are variables to parametrize the source and the antenna model. Further specifications with respect to other noise components, the observing mode, and the observing geometry can also be made. The source model can be specified by the signal type of the source, either Gaussian noise or signals with a certain structure (e.g. Differential One-way Ranging tones). The normalized amplitude of the selected signal is then scaled proportionally by the specified received signal strength. It is characterized by flux density or antenna temperature values. Besides the source model, the simulator also consists of an antenna model to account for signal filtering and manipulation. Sensitivity parameters in terms of the noise level within the receiver can also be simulated choosing real antenna key parameters like the System Equivalent Flux Density (SEFD) or system temperature (Tsys). A passband filter can be designed with a built-in Matlab toolbox to account for the amplitude and phase response of the total antenna system and for the individual electronic components. Phase distortion can be modeled by specifying a variance for phase noise. Other noise components which affect the antenna system temperature can be modeled by setting individual noise temperatures for the cosmic microwave background, ionosphere and radio-frequency interference (RFI). To define the observing mode, the sampling frequency or observed bandwidth, the number of bits for the digital signal quantization and the number of channels with respect to the sky frequency can be selected. The observation duration can also be defined for each station independently. To consider the observing geometry, a delay accounting for the difference in signal arrival times can be simulated and the Doppler shift due to the relative velocity between the source and antenna platforms can be modeled. Finally, the date of observation needs to be specified to link the observation to a point in time. A more comprehensive list of the model parameters within the presented baseband data simulator can be found in Table 1.

Table 1: Parameter names and their parametrization to configure the presented baseband data simulator

Name	Parameterization
Signal type	Gaussian noise
	User defined signal structure
Received signal strength	Flux density (Jy)
	Antenna temperature (K)
Sensitivity	SEFD (Jy)
	Tsys + effective telescope area (K+m^2)
Sky frequency	(Hz)
Passband filter design*	Ideal
	User defined
Phase calibration signal	Tone frequency spacing (Hz)
Phase distortion	Variance (rad)
System delay	(s)
Polarization	Circular, linear**
Further noise components	(K)
Observation duration	(s)
Sampling	Sampling frequency (Hz)
	Bandwidth (Hz)
Number of bits	(Integer value)
Number of channels	(Integer value)
Group delay	(s)
Velocity station 1	(s/m)
Velocity station 2	(s/m)
Velocity source	(s/m)
Date	YYYY/MM/DDDD/hh/mm/ss
Source name	String
Station name 1	2-letter ASCII code
Station name 2	2-letter ASCII code

* filter for each electronic device
** future implementation

4 Storage format and simulation pipeline

In a final step, the filtered, down-converted, sampled and the quantized data stream is converted to a data format which can be used for further processing at the correlators. Such a format converter is referred to as formatter and represents one of the key components for the presented simulator. It is capable to provide the simulation output in a convenient format which can be used for correlation in the same way as for real baseband data. The same VLBI processing chain consisting of correlation, fringe-fitting, post-correlation processing, and analysis can be fed with either real or simulated baseband data, which allows for profound comparisons and enables various correlation studies. Such a formatter is implemented in Matlab as part of the presented baseband data simulator. The used format is the VLBI Data Interchange Format (VDIF), which can be read by commonly used correlators such as the Distributed FX (DiFX) correlator. The basic VDIF struc-

ture consists of data frames, each containing a short self-identifying data frame header, followed by a data array (containing the actual samples). The Matlab formatter is capable to play back the VDIF format and also supports multi-channel recording and recording of several bits per sample. Once the simulated baseband data is stored in the VDIF format, it can be used for further processing. In this work we use DiFX and the Haystack Observatory Postprocessing System (HOPS) to correlate and carry out a delay estimation of the simulated baseband data sets. Besides the VDIF database, also a simple but sufficient VLBI Experiment (VEX) file is generated automatically. It matches the simulated observation parametrization and can be easily used for the DiFX correlation and further processing. Table 2 shows the software packages and databases used in the realization of our simulation pipeline.

Table 2: Software packages and databases involved in the simulation pipeline.

Model parametrization	ASCII file
Baseband data simulator	Matlab program
Baseband data sets	VDIF format
Correlation	DiFX correlator
Fringe-fitting	fourfit

5 First Light

The presented baseband data simulator is the first software solution written in a higher level programming language which is independent of computation algorithms of existing correlators. Figure 1 shows the result of a simple observation simulation and serves as a test object for a basic evaluation of the algorithms within the simulator.

The simulation is based on a scenario with a radio source radiating Gaussian noise observed by two telescopes with realistic SEFD values of 3000 Jy at both telescopes. The telescopes are placed at the same location to isolate the results from Earth rotation effects and large baselines delays. This concept is referred to as zero-baseline observation. Results from non-zero-baseline observations are not described within this work and will be subject to other studies. The rather short observation duration for the presented test simulation is set to two seconds to work around memory issues. One bit is used for quantization and a sampling rate of 32 MHz is applied. The sky frequency is set to 8212.99 MHz. In order to compensate for the short observation time but to secure a fringe-detection the source flux is increased up to 150 Jy. The fourfit SNR estimation after the correlation with DiFX yields a value of 201 while the apriori SNR calculation using the model parameters yields a value of 221. Taking into account the sophisticated SNR calculation with an uncertain determination of the efficiency factors, the values are in a good agreement, which indicates a proper amplitude scaling for the simulated receiver and source noise. A delay of -123 ns is applied for Stat1 to evaluate the implemented delay application method. The estimated delay yields a value of -121 ns. This comparison indicates a proper application of the linear phase term in the simulation process. The difference of 2 ns might be due to a different fringe-reference time which shifts the delay to another point in time, whereas the delay rate absorbs the remaining difference. An ideal passband filter design is applied for this simulation to model the antenna frequency response. The amplitude and phase spectrum of the correlation function also shows a flat behavior which indicates that all applied algorithms do not manipulate the resulting amplitude and phase spectrum. The drop in amplitude for the last sample might be due to the sampling of the frequency spectrum and cannot be seen for finer spectral resolution within the correlation process.

The comparison between expected and real processed values shows a good agreement in general. The remaining discrepancies can arise from various error sources, which might not specifically be dedicated to the simulator algorithms. The used concept of very short observation time and the zero-baseline observation might have some impact and might cause an unusual behavior within the correlation and fringe-fitting process. With the increased source flux value to compensate for the short observation time, the ratio of the source noise amplitude and receiver noise amplitude gets larger than usual. Some further investigations are required to verify the application of short observation intervals.

6 Conclusions and outlook

The presented basic evaluation of amplitude scaling, delay application, and passband filtering serves as the first proof of concept for the baseband data simulator written in Matlab. It shows that it is possible to realize such an implementation with a higher level program-

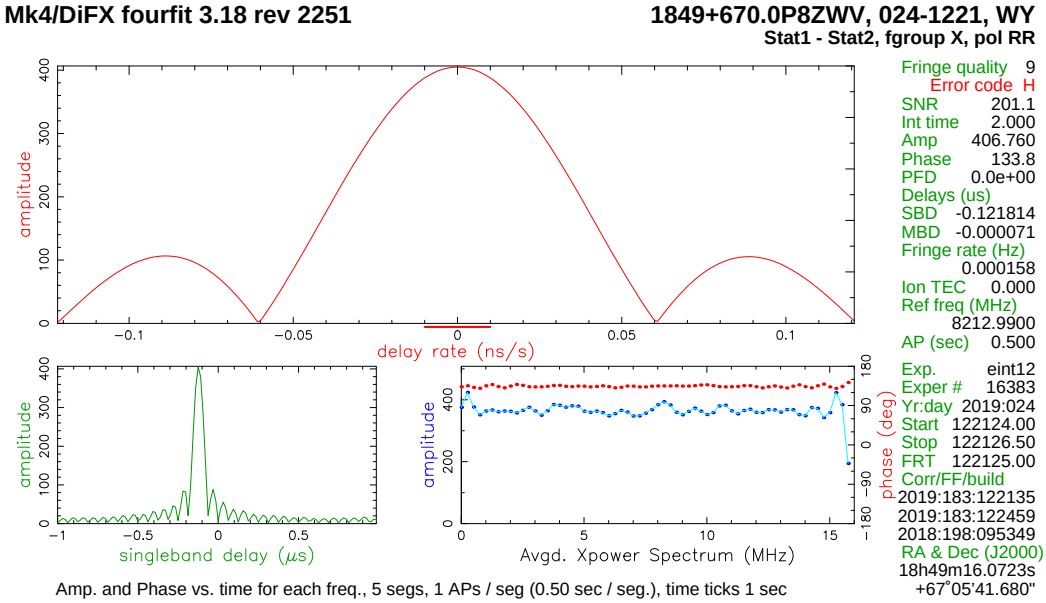

Fig. 1: Fourfit output of simulated baseband data after correlation with the DiFX software. The plot shows the correlation function in the time domain with a distinct peak in green color, the delay rate function in red and a flat amplitude and phase spectrum in blue and red. The simulation setup is configured as follows: two seconds observation time, one-bit quantization, 32 MHz sampling rate, 150 Jy source flux, 3000 Jy SEFD for both telescopes, ideal bandpass filtering, 123 ns delay application.

ming language from scratch without dependencies on existing correlators. The built-in routines *randn*, *fft* and the filter design toolbox prove to be a handy foundation for such a digital signal processing software realization. With VLBI baseband data being characterized by very high data rates, memory issues for any kind of software realization are unavoidable and not related to Matlab. It is a problem for other (proprietary) programming languages as well. Of course, with respect to the run time of the program, other languages will have advantages in contrast to higher level programming languages. However, some effort has been made to apply parallel computing strategies to keep the simulation run time short.

We see a lot of potential application for the simulation of new observing modes and in particular for satellite observations. The simulation pipeline can be used to test correlators with special observation setup and source characteristics. The evaluation of correlation results with short duration and large source amplitude in comparison to commonly used longer observation time seems to be an important field of study for efficient and memory inexpensive simulations. There is still the possibility to use the supercomputing infrastructure at TU Wien, but it would be much more efficient to obtain reliable correlation results with short observation intervals as well.

Future work regarding software development will address the implementation of non-zero-baseline observations and the possibility to simulate linear polarized observations. This could be of great interest in testing the multi-band delay estimation for VGOS observations.

References

Böhm J, Böhm S, Boisits J, et al. (2018) Vienna VLBI and Satellite Software (VieVS) for Geodesy and Astrometry. *PASP*, 130, 044503, doi:10.1088/1538-3873/aaa22b.

Meyer-Zhao Z (2018) Datasim – A VLBI baseband data simulator. *DiFX User and Developer Workshop 2018, Wettzell*

Nishioka H (2015) DiFX activities at ASIAA. *DiFX User and Developer Workshop 2015, Hobart*

Deller A T, Tingay S J, Bailes M, et al. (2007) DiFX: A Software Correlator for Very Long Baseline Interferometry Using Multiprocessor Computing Environments. *PASP*, 119, 318–336, doi:10.1086/513572

Optical Fiber Links Used in VLBI Networks and Remote Clock Comparisons: the LIFT/MetGesp Project

R. Ricci, M. Negusini, F. Perini, C. Bortolotti, M. Roma, R. Ambrosini, G. Maccaferri, M. Stagni, M. Nanni, E. Kravchenko, M. Siciliani de Cumis, L. Santamaria, G. Bianco, C. Clivati, A. Mura, F. Levi, D. Calonico

Abstract The synchronization between atomic clocks plays an important part in both radio astronomical and geodetic Very Long Baseline Interferometry, as the clocks are responsible for providing time and frequency reference at radio stations. The availability of highly stable optical fiber links from a few radio observatories and their national metrological institutes has recently allowed the streaming of frequencies from optical clocks based on the Sr/Yb lattice technology (even two order of magnitudes more stable than H-maser clocks). We will present the current status of the Italian Link for Frequency and Time (LIFT) and the ongoing efforts to realize a geodetic experiment utilizing the radio stations in Medicina and Matera connected in common clock via the optical fiber link. We will then show the results from the latest VLBI clock timing experiments also making use of the LIFT link to compare atomic clocks of the three italian radio VLBI antennas (Mc, Sr and Nt) using the rms noise in the interferometric phase. VLBI clock timing proves more effective than Global Navigation Satellite System and less expensive than Two-Way Satellite Frequency and Time Transfer in synchronizing remote clocks.

Roberto Ricci · Monia Negusini · Federico Perini · Claudio Bortolotti · Mauro Roma · Roberto Ambrosini · Matteo Stagni · Mauro Nanni · Evgeniya Kravchenko
INAF-Istituto di Radioastronomia, Via Gobetti 101, Bologna, IT-40129 Italy

Cecilia Clivati · Alberto Mura · Filippo Levi · Davide Calonico
Istituto Nazionale di Ricerca Metrologica (INRiM), Via delle Cacce 91, Torino, IT-10135 Italy

Giuseppe Bianco · Mario Siciliani de Cumis · Luigi Santamaria
ASI-Centro di Geodesia Spaziale "Giuseppe Colombo" Località Terlecchia snc, Matera, IT-75100 Italy

(Correspondence: ricci@ira.inaf.it)

Keywords Instrumentation VLBI · Optical fiber · Frequency reference dissemination · Atomic clock timing

1 Introduction

Three are the main research areas in which frequency reference dissemination is important: (i) radioastronomy, (ii) relativistic geodesy and (iii) clock metrology. In radioastronomy time and frequency optical fiber links can offer faster operations, they will provide more stable clocks for mm-VLBI operating above 80 GHz (where the H-maser clocks are an important limit to phase stability together with atmospheric turbulence and a limit to the resolution, see (Rioja et al., 2012; Nikolic et al., 2013) for a reference. Existing mm-VLBI telescopes in Europe that could benefit from high stability in optical fiber links are in Germany (Effelsberg), Spain (IRAM and Yebes), Sweden (Onsala) and Finland (Metsahövi): better (angular) resolution from mm-VLBI runs including these observatories will positively affect the study of radio jets in compact radio sources. Moreover, in geodetic VLBI, in order to achieve 1-mm positioning accuracy clock uncertaninty at 10^{-16} are required (Neill et al., 2005). The study of radio pulsar will also gain through absolutely accurate time provided by fiber-optic streamed frequency references (Lyne et al., 2016).

The most performing clocks at the moment are optical clocks which utilize a transition in the optical band interrogated by a highly stable laser in a ultra cooled (μK) lattice of Strontium or Ytterium (Ushijima et al., 2015). The frequency stability and accuracy of the best optical lattice clock is nowadays about two order of magnitudes better (a few parts in 10^{-18} after a few

1000 s of operation). This huge accuracy and stability can be put to the use also in the field of relativistic geodesy, an example of which is chronometric levelling where the gravitationally shifted frequency difference of two portable optical clocks can determine their altitude difference with an accuracy of ~ 10 cm (Grotti et al., 2018). Optical fiber links are used to remotely compare the clocks.

The third reason to operate long-haul highly stable optical fiber links is clock metrology (Lisdat et al., 2016). Apart from the italian case, France, Germany, the UK and Poland are equipping themselves with optical fiber links to connect each other's national metrological institutes. This will make possible the comparison of highly performing optical lattice clocks across Europe. At the same integration time the optical links are orders of magnitude more stable than satellite-based frequency reference dissemination techniques such as Global Navigation Satellite Systems and Two-way Satellite Frequency Transfer. This international optical fiber network for clock metrology will bring to the redefinition of the SI second in the near future (Riehle, 2017).

2 Method

The MetGeSp (Metrology for Geodesy and Space) project is an offshoot of the LIFT (Italian Link for Frequency and Time) infrastructure. MetGeSp aims at disseminating a highly stable and accurate frequency reference signal via an optical fiber link to a series of Italian facilities. The Italian National Institute of Metrology (INRiM) in Turin generates the frequency reference which is streamed via the LIFT link to Modane (under the Frejus tunnel) to study relativistic geodesy, to the Milan Financial District, to the INAF-Istituto di Radioastronomia radio station for radio and geodetic VLBI experiments, to Florence's Italian Lab for Non-linear Spectroscopy (LENS) for tests on optical clock frequency accuracy, to the Fucino Plain (Telespazio Facility) for global satellite navigation (Galileo network) and finally to Matera (Centre for Space Geodesy). The creation of a common clock between the Medicina and Matera radio stations is the main radio-VLBI related goal of the MetGeSp project (see Section 5).

A detailed description of the optical fiber link would be beyond the scope of this paper. Briefly the RF signal generated by the INRiM clock is up-converted to the frequency of a 1.5 μm laser via an opto-electronic device (an optical frequency comb) and the phase is kept synchronized via a phase-locked loop. The laser signal is beamed along a dedicated (dark) fiber. In order to prevent signal attenuation Erbium-doped Field Amplifiers (EDFAs) are set along the link. A remote control in Turin is used to minimize gain instabilities over time in the EDFAs. Excellent noise cancellation is achieved via a round-trip servo mechanism which allows to reach a frequency stability of the order of 10^{-19} in terms of Allan deviation over 1000 seconds. On Nov 7th 2018 the LIFT link saw its first light in Matera CSG (Fig. 1). With a span of 1800 km LIFT is now one of the longest frequency reference dissemination link in the world. The total span between Turin and Matera is covered in 4 legs and the laser signal is regenerated in Medicina, Florence (LENS), Pozzuoli (Institute of Optics) and Matera (ASI-CSG). In Matera and Medicina the signal is down-converted via another optical frequency comb to the RF domain. The resulting RF (5 MHz, 10 MHz and 1 PPS) are used directly in the VLBI receiver chain and for remote clock comparison. More details are found in Calonico et al. (2014) and Clivati et al. (2015).

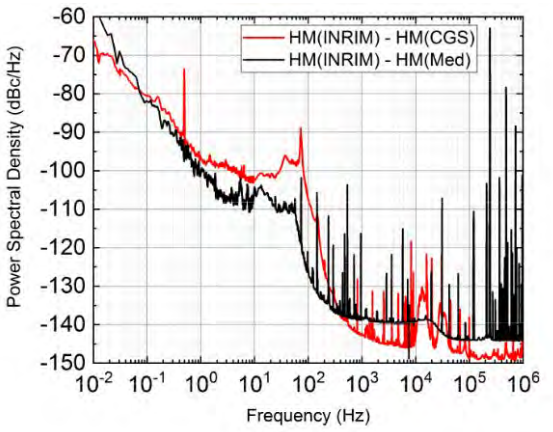

Fig. 1: First light of the LIFT link in Matera: Ma-Mc H-maser comparison via the power spectral density

3 Results

The first VLBI test making use of the LIFT optical fiber link between the Medicina radio station and Turin was the geodetic experiment EUR137 in September 2015 (published in Clivati et al. (2017)): the local and remote H-maser frequency signals were alternately injected into the VLBI data acquisition chain and the data from the two clocks were analyzed as two separate experiments.

In order to further test the VLBI and link set-up in view of a common-clock experiment between Medicina and Matera stations two 24 hour-long S/X-band geodetic experiments were carried out on in July 2017 and April 2018 utilizing the Medicina, Noto and Matera stations. Medicina received the frequency signal from Turin for the all duration of the runs. The data were correlated in Bologna with the local DiFX correlator (Deller et al., 2007) and fringe fitted using the Haystack Observatory Post-processing Software *fourfit* (Cappallo, 2017). The geodetic tools CALC/SOLVE and nuSolve (Bolotin et al., 2014) were used to analyze the correlated data. In the former of two test sessions a few unlocks were found and fixed at the geodetic analysis stage. The latter geodetic session ran smoothly without any link unlocks, but problems with correlating Noto scans resulted in the usage of only the Medicina-Matera observation pairs in the geodetic analysis. The group delay weighted rms residuals after station, clock and atmosphere model subtraction are 56 ps on the Mc-Nt baseline and 46 ps on the full July 2017 experiment.

An alternative way to study remote clock synchronization using VLBI antennas makes use of the statistics of the interferometric phase (Krehlik et al., 2017).

Table 1: Summary of the VLBI clock timing observations: project codes, the observing dates, the stations involved, the bands used and whether the Medicina station was receiving or not the remote frequency standard from INRiM. Baselines with Metsahövi could not be correlated because of a data format problem.

Project code	Date	stations	Band	Mc rem clock?
VT001	20180118	Mc,Nt,Ma,Ys,Mh	S/X	No
VT003	20180124	Mc,Nt,Tr	C	No
VT005	20180219	Mc,Nt,Tr	C	No
VT006	20180220	Mc,Nt,Tr,Ys	C	Yes
VT007	20181123	Ma, Eb, On	S/X	No
VT008	20190205	Mc, Sr	C-hi	Yes
VT009	20190204	Mc, Sr	C-hi	No

To this purpose a series of VLBI clock timing experiments were performed with a network comprising the stations of Medicina, Noto, Matera, Yebes and Metsähovi in January/February 2018 (Effelsberg station accepted to take part in one run but it was wind stowed for the full time). Many factors contribute to the deterioration of the interferometric phase stability, the most important being atmospheric instabilities, gain elevation effects and antenna thermal deformations. In order to minimize these performance degrading effects the VLBI runs were carried out at night during the winter months on a point-like radio source (15-min scans in 3-hour runs at medium/high antenna elevation to minimize air mass absorption). In Table 1 we report a summary of the VLBI clock timing observations. The VT007-9 experiments were 6 hours long on two calibrator arcs and were carried out in February 2019.

The S/X-band observations (VT001 and VT007) were performed with the stardard geodetic frequency set-up and bit rate. The C-band observations were performed with a radio astronomical VLBI frequency set-up: the observing band was split into 4 contiguous 8-MHz wide sub-bands (IFs) of 32 frequency channels each just below the sky frequency of 5 GHz. The C-hi observations set-up has 8 4-MHz wide contiguous sub-bands in dual polarization mode at a centre frequency of 6.7 GHz. The Bologna DiFX correlator was used to correlate the station data which were then read into FITS files. The fringe fitting and frequency averaging were done in AIPS (Greisen, 2003). The data were read out from AIPS into ASCII tables and the statistics on the phase stability were computed scan-by-scan according to Krehlik et al. (2017): the scan samples were separated into couples (*even statistics*) and triplets (*odd statistics*) and then first differences and interpolated-value differences were computed together with their root mean square. The C/C-hi band experiments had 2-bit sampling and 1-sec time integration. The central 80 % of the bandpass was used in the analysis, thus removing the less sensitive sloping wings. The time synchronization was computed using the formula:

$$\Delta t_{\mathrm{rms}} = \frac{\Delta\phi_{\mathrm{rms}}}{2\pi\nu_0},$$

where Δt_{rms} is the rms time synchronization between clocks, $\Delta\phi_{\mathrm{rms}}$ is the phase rms noise and ν_0 is the sky centre frequency in each sub-band. The results of the VT008/9 experiments are shown in Table 2. The results are in good agreement with Krehlik et al. (2017)

Table 2: Results of the VLBI timing experiments in C-hi band: the tag rem(loc) means that Medicina was using remote(local) H-maser frequency reference. Only *even* statistics is shown.

Project code	pol	HM	$\Delta t_{\rm rms}$	error bar
VT008	RR	rem	3.08	0.03
VT009	RR	loc	2.31	0.03
VT008	LL	rem	3.79	0.04
VT009	LL	loc	2.79	0.03

on the same timescale. We also found similar statistical values for $\Delta t_{\rm rms}$ for remote and local clocks for the Medicina station.

4 Conclusions and outlook

The LIFT infrastructure is able to deliver a frequency reference signal from the Italian Metrological Institute (INRiM) to remote locations via an optical fiber link with unprecedented stability (of the order of a few parts in 10^{-19} in 1000 s integration time based on Allan standard deviation).

Geodetic VLBI experiments are performed with the remote frequency reference provided to the Medicina radio station. The wrms residuals in the group delays are in agreement with the statistics found in experiments using local clocks.

The ASI-Centre for Space Geodesy (ASI-CSG) in Matera was reached by the LIFT link and the first light was achieved in Matera on Nov 7th 2018. The link now spans 1800 km of optical fiber in four legs: Turin-Medicina, Medicina-Florence, Florence-Pozzuoli and Pozzuoli-Matera. At the end of each leg the laser signal is regenerated and kept in phase synch.

RMS stastistics on the interferometric phase noise was successfully used in remote and local clock timing experiments utilizing the radio/geodetic VLBI technique. The level of synchronization between clocks is estimated to be better than a few pico-seconds over 900-second observing scans in good to excellent observing conditions.

In the near future the following developments are planned:

- a VLBI vs GPS frequency stability analysis in the CONT14 and CONT17 campaigns focusing in particular on the co-located stations of Matera and Onsala compared to Wettzell;
- a series of *common-clock* geodetic experiments in which both Medicina and Matera stations are going to receive remote frequency reference from Turin;
- a comparison of Japan's NICT and Italy's INRiM optical clocks via VLBI utilizing the portable Japanese MARBLE 2.4-metre antennas, one of which is at the moment installed at the Medicina radio station (see Sekido et al., 2019, for details on this project);
- the usage of interplanetary space probe tones and the ΔDOR (Differential One-way Ranging) technique to compare clocks at two receiving radio stations;
- the usage of the LIFT link for possible future VLBI timing experiments between the Medicine/Turin and Polish Torun/KM-FAMO optical clocks;
- the testing of the White Rabbit/Precise Time protocol technology for digital dissemination of frequency reference signals and for clock synchronization.

Acknowledgements We thank the VLBI partners from Yebes Observatory (B. Tercero Martínez, J. González García, P. de Vicente), Torun Observatory (A. Marecki, P. Wolak, M. Gavroǹski), Metsahövi Observatory (J. Kallunki, J. Tammi), Effelberg Observatory (A. Kraus, U. Bach), Matera CSG (G. Colucci, M. Paradiso, F. Schiavone), Noto radio station (P. Cassaro, S. Buttaccio), Onsala Observatory (R. Haas, J. Yang, M. Lindqvist), Sardinia Radio Telescope (S. Poppi, G. Surcis) and the staff of the Medicina radio station for their support during the VLBI runs.

References

Bolotin S, Baver K, Gipson J, et al. (2014) The VLBI Data Analysis Software *v*Solve: Development Progress and Plans for the Future. In: D. Behrend, K. D. Baver, K. L. Armstrong (eds.): *IVS 2014 General Meeting Proceedings*, Science Press (Beijing), 253–257, doi:ISBN 978-7-03-042974-2

Calonico D, Bertacco E K, Calosso C E, et al. (2014) High-accuracy coherent optical frequency transfer over a doubled 642-km fibre link. *Appl. Phys. B*, 117, 979–986, doi:10.1007/s00340-014-5917-8

Cappallo R (2017) HOPS fourfit user's manual Version 1.0. *HOPS web page:* www.haystack.mit.edu/tech/vlbi/hops.html

Clivati C, Costanzo G A, Frittelli M, et al. (2015) A coherent fibre-optic link for Very Long Baseline Interferometry. *IEEE*

Trans. on Ultrason. Ferroel. Freq. Contr., 62, 1907–1912, doi:10.1109/TUFFC.2015.007221

Clivati C, Ambrosini A, Artz T, et al. (2017) A VLBI experiment using a remote atomic clock via a coherent fibre link. *Nature Scientific Reports*, 7:40992, doi:10.1038/srep40992

Deller AT, Tingay SJ, Bailes M, et al. (2007) DiFX: A Software Correlator for VLBI Using Multiprocessor Computing Environments. *PASP*, 119, 318–336, doi:10.1086/513572

Greisen E (2003) AIPS, the VLA, and the VLBA. In: A Heck (ed.): *Information Handling in Astronomy - Historical Vistas*, Astrophysics and Space Science Library, 285, Springer, doi:10.1007/0-306-48080-8_7

Grotti J, Koller S, Vogt S, et al. (2018) Geodesy and metrology with a transportable optical clock. *Nature Physics*, 14, 437–441, doi:10.1038/s41567-017-0042-3

Krehlik P, Buczek L, Kolodziej J, et al. (2017) Fibre-optic delivery of time and frequency to VLBI station. *A&A*, 603, 48, doi:10.1051/0004-6361/201730615

Lisdat C, Grosche G, Quintin Q, et al. (2016) A clock network for geodesy and fundamental science. *Nature Communications*, 7, 1–7, doi:10.1038/ncomms12443

Lyne A et al. (2016) The formation, life and uses of pulsars – nature's finest cosmic clocks. *Proceedings of 2016 European Frequency and Time Forum*, doi:ISBN: 9781509007219

Neill A, Whitney A, Petrachenko B, et al. (2005) VLBI2010: Current and Future Requirements for Geodetic VLBI Systems. Report of the Working Group 3 to the IVS Director Board, https://ivscc.gsfc.nasa.gov/about/wg/wg3/IVS_WG3_report_050916.pdf

Nikolic B, Bolton R C, Graves S F, et al. (2013) Phase correction for ALMA with 183 GHz water vapour radiometers. *A&A*, 552, A104, doi:10.1051/0004-6361/201220987

Riehle F (2017) Optical clock networks. *Nature Photonics*, 11, 25–31, doi:10.1038/nphoton.2016.235

Rioja M, Dodson R, Asaki Y, et al. (2012) The impact of Frequency Standards on Coherence in VLBI at the Highest Frequencies. *AJ*, 144, 121, doi:10.1088/0004-6256/144/121

Sekido M, Takefuji K, Ujihara H, et al. (2019) ITA-JPN Broadband VLBI Experiment for Optical Clock Comparison. In: R. Haas, S. Garcia-Espada, J. A. López Fernández (erds.): *Proc. 24th EVGA Working Meeting*, 52–56

Ushijima I, Takamoto M, Das M, et al. (2015) Cryogenic optical lattice clocks. *Nature Photonics*, 9, 185–189, doi:10.1038/nphoton.2015.5

ITA-JPN Broadband VLBI Experiment for Optical Clock Comparison

M. Sekido, K. Takefuji, H. Ujihara, H. Hachisu, N. Nemitz, M. Pizzocaro, C. Clivati, D. Calonico, T. Ido, M. Tsutsumi, E. Kawai, K. Namba, Y. Okamoto, R. Takahashi, J. Komuro, R. Ichikawa, H. Ishijima, F. Bregolin, F. Levi, A. Mura, E. Cantoni, G. Cerretto, F. Perini, G. Maccaferri, M. Negusini, R. Ricci

Abstract NICT has developed a broadband VLBI (very-long-baseline interferometry) system for intercontinental frequency transfer. After domestic tests in Japan, a 2.4 m diameter VLBI station was exported and installed at Medicina astronomy observatory of INAF in Italy in 2018. We have started VLBI experiments for optical clock comparison on an Italy-Japan intercontinental baseline. Reference signals generated by an ytterbium (Yb) optical lattice clock at INRiM in Torino and by a strontium (Sr) lattice clock at NICT headquarters in Koganei are compared by a series of links, which include a coherent optical fiber link between INRiM and Medicina and intercontinental VLBI observation between Medicina and Koganei. A series of VLBI experiments was performed from Oct. 2018 to Feb. 2019. Yb and Sr lattice clocks were repeatedly operated throughout the same period for frequency comparison.

Keywords Broadband VLBI · Frequency comparison

Mamuro Sekido · Kazuhiro Takefuji · Hideki Ujihara · Masanori Tsutsumi · Ejii Kawai
NICT Kashima Space Technology Center, 893-1 Hirai, Kashima 314-8501, Japan

H. Hachisu · N. Nemitz · T. Ido · K. Namba · R. Ichikawa · H. Ishijima
NICT Headquaters, 4-2-1 Nukui-Kita-Machi, Koganei, Tokyo 184-8795, Japan

M. Pizzocaro · C. Clivati · D. Calonico · F. Bregolin · F. Levi · A. Mura · E. Cantoni · G. Cerretto
Istituto Nazionale di Ricerca Metrologica, IT-10135 Turin, Italy

F. Perini · G. Maccaferri · M. Negusini · R. Ricci
Institute of Radioastronomy, National Institute of Astrophysics, IT-40129 Bologna, Italy

(Correspondence: sekido@nict.go.jp)

1 Introduction

Driven by fast development of high accuracy optical frequency standards reaching 10^{-18} accuracy (Riehle et al., 2018), re-definition of the "second" as the unit of time is being discussed in the metrological community (Riehle, 2015). For this, accurate frequency comparison between atomic clocks at distant locations is an important technology. Frequency transfer by optical fiber-link reaches uncertainties below 10^{-18} (Lopez et al., 2012; Predehl et al., 2012; Calonico et al., 2014), but it requires an infrastructure of suitable fibers and bi-directional optical amplifiers. Two-way Satellite Time & Frequency Transfer (TWSTFT) is another technique used for international time and frequency links over distances of thousands of km. Advanced TWSTFT using carrier phase has a potential to reach instabilities in the order of 10^{-17} (Fujieda et al., 2016). This relies on the availability of suitable communication satellites. Limited available bandwidth and high operating costs are additional drawbacks. Observation of GPS satellites is routinely used to maintain time links between national time standards agencies. The lowest uncertainty of frequency links by GPS signals is in the order of 10^{-16}, achieved by a technique of precise point positioning processing with integer ambiguity solution(IPPP) (Petit et al., 2015). VLBI is another space geodetic technology with potential for precise frequency comparison over intercontinental distance. In contrast to TWSTFT, VLBI is not restricted by the availability of communication satellites or the requirement of licensed radio transmission. The VLBI technique relies on observing extragalactic radio sources of the international celestial reference frame (ICRF). These form fiducial points in the sky, whereas GPS observations rely on estimated satellite orbits, that vary

with time. High precision GPS processing observes phase signals that require careful processing to avoid errors from cycle ambiguities. Broadband VLBI provides an absolute group delay observable that is free from ambiguity, and precision in the order of pico seconds. These properties are the foundation for long-term stable VLBI frequency links. Based on this perspective, we have developed a broadband VLBI system for an intercontinental frequency link. We expect to achieve uncertainties in the order of 10^{-17} with comparing stable hydrogen maser (HM) standards over several days of time span.

The concept of broadband VLBI observation proposed as VLBI Global Observing System (VGOS) (Petrachenko et al., 2009; Niell et al., 2018) is an innovative system to improve the delay measurement precision by one order of magnitude over conventional S/X-band VLBI. This is achieved by ten times wider bandwidth of observing radio frequency. A higher data acquisition rate contributes to improvement of observing sensitivity as well. Based on these advanced properties, we implemented a broadband VLBI system using small diameter transportable VLBI station for frequency comparison.

2 Broadband VLBI system and observation scheme

2.1 Broadband VLBI system

Our broadband VLBI system named GALA-V (Sekido et al., 2017) implements the broadband VLBI concept of the VGOS. Radio telescopes capable of observing the frequency range of 3 – 14 GHz are used for observation. The employed observation mode differs slightly from the prototype VGOS 'Proof of Concept(PoC)' implementation (Niell et al., 2018) developed by MIT Haystack observatory and NASA/GSFC. In contrast to the PoC VGOS terminal, which acquires data on more than one hundred channels with 32 MHz frequency width, we adopted a simpler data acquisition using four channels of 1 GHz bandwidth. A unique technique in our data acquisition system (DAS) is the use of RF-Direct sampling (RFDS) (Takefuji et al., 2012). The observed radio signal of one polarization is amplified by low noise amplifier and divided into two upper and lower frequency band, limited to 8192 MHz width by anti-aliasing filters. Each signal is then digitized at radio frequency with 16,384 MHz sampling rate. Frequency selection and band shaping are performed by digital signal processing implemented in the sampler. Four streams of 2048 Msps 1 bit quantization data comes out via optical fiber cables as Ethernet packet stream in VDIF format (Whitney et al., 2014) per single polarization. Compared to 16 MHz width conventional S/X-band VLBI, 1024 MHz bandwidth provides a sensitivity advantage by a factor of $\sqrt{1024/16} = 8$ for single channel fringe detection.

The advanced delay precision and sensitivity of the broadband VLBI open the possibility to utilize small diameter stations for geodesy and frequency transfer over intercontinental distances. Besides wideband data acquistion, we employ joint observation with a large diameter antenna (R) to compensate the low sensitivity of small diameter antennas (A,B). By using the closure delay relation, the delay observable of the A-B baseline is composed of a linear combination of$R$-A and R-B baselines. This scheme is not only useful for using small VLBI stations, but also for eliminating the delay variation due to large diameter antennas; such as gravitational distortion and electric cable length variation due to temperature and stress change. We name this type of observation "Node-Hub" style (NHS) (Sekido, 2017), and have confirmed it by domestic evaluation in Japan and intercontinental experiments between Italy and Japan.

2.2 Frequency link with transportable broadband VLBI station

Prior to the experiments over intercontinental baseline, we evaluated the system in a collaboration between National Metrology Institute of Japan (NMIJ) and NICT, two national metrological agencies in Japan, that generate the local time scales UTC(NMIJ) and UTC(NICT). These time scales are regularly compared with UTC and reported to BIPM. This provides an excellent basis to evaluate the NHS VLBI frequency link with respect to the other techniques, and we confirmed that eliminating the delay variation caused by large diameter antenna indeed results in an improved post-fit

delay residual: The experiments show a weighted RMS of about 10 picoseconds.

The difference of UTC(NMIJ)-UTC(NICT) obtained by precise point positioning (PPP) analysis of GPS data is routinely published by BIPM (BIPM, 2017). Integer-ambiguity PPP (IPPP) processing (Petit et al., 2015) provides further improvements. G. Petit and J. Leute of BIPM have courteously provided IPPP data for the UTC(NMIJ)-UTC(NICT) time difference. Comparison of double difference data between VLBI-GPS(IPPP) and GPS(PPP)-GPS(IPPP) over a 10 days span indicates that the VLBI frequency link has better performance than GPS(PPP), at least for long time spans.

Table 1: VLBI sessions performed from Oct.2018 to Feb. 2019. VLBI observation between MARBLE1(Medicina) and MARBLE2(Koganei) is formed by the NHS scheme in joint observation with the Kashima 34 m antenna.

ExpCode	Start Time(UT)	Length[h]	No. Scans
GV8278	05 Oct.2018 07:39	31	593
GV8287	14 Oct.2018 15:35	30	460
GV8297	24 Oct.2018 21:00	29	436
GV8308	04 Nov.2018 02:30	29	464
GV8318	14 Nov.2018 08:00	29	464
GV8328	24 Nov.2018 13:30	29	415
GV8338	04 Dec.2018 19:00	29	471
GV8349	14 Dec.2018 00:30	29	457
GV8359	25 Dec.2018 06:00	29	476
GV9015	15 Jan.2019 06:00	29	479
GV9025	25 Jan.2019 03:00	36	573
GV9035	04 Feb.2019 03:00	31	706
GV9045	14 Feb.2019 03:00	36	786

3 Intercontinental broadband VLBI between Italy and Japan

After the domestic experiments in Japan, a 2.4 m diameter broadband VLBI station (MARBLE1) was transported to the Medicina astronomy observatory of INAF/IRA for experiments on an intercontinental baseline. INRiM and NICT are both operating optical lattice clocks as secondary frequency standards. The reference frequency generated by the Yb optical lattice clock at INRiM (Torino) is transferred to Medicina observatory by a coherent fiber link (Clivati et al., 2015), and is used to evaluate a local hydrogen maser (HM). The HM signal is used as the reference of broadband VLBI observation with the 2.4 m antenna. In the same way, a HM at NICT headquarters (Koganei) is evaluated using Sr lattice clock NICT-Sr1. The HM provides the reference signal for the counterpart 2.4 m VLBI station (MARBLE2) at Koganei. The Kashima 34m antenna contributes to this broadband VLBI in order to improve signal to noise ratio. Observations between the two small VLBI stations are realized by the NHS processing scheme. Fig. 1 shows an overview of the project to link the Yb clock at INRiM and the Sr clock at NICT.

The 2.4 m dish and components of VLBI station were delivered to Medicina in July 2018 and assembled over the course of few days (Fig.2).

Local infrastructure was prepared by INAF and INRiM, such as optical fiber for signal transmission to the observation room and access to the high speed research networks GARR and GEANT. Thanks to the antenna control software FS9 developed by NASA/GSFC, pointing observations to establish the antenna model were easily realized, along with remote antenna operation from Japan. An initial fringe test was conducted with the support of Ishioka VGOS station of the Geospatial Information Authority of Japan (GSI). Except for the antenna control of Ishioka station, all operation (antenna & DAS control, data transfer, correlation processing) for the fringe test was performed remotely from Medicina during the installation visit, and interferometer fringes were successfully detected. The main series of broadband VLBI experiments via the NHS scheme were then conducted from Oct. 2018 to Feb. 2019 with session length about 30 h, repeated at a 10 days interval (Table 1).

Fig. 3 shows an example of the delay residuals of the VLBI analysis over the Medicina-Koganei baseline. The weighted RMS of the delay residual was 24 ps in this case. A peculiar splitting of the delay residual for radio sources 3C418 and 2022+542 is clearly visible in the plot. Xu et al. (2019) have reported that 3C418 shows strong signatures of radio source structure in group delay measurement. Investigation on calibration techniques for the radio source structure effects has been continued (Bolotin et al., 2019; Xu et al., 2019). Thus we need to minimize the influence of radio source structure by careful selection of radio sources in scheduling the VLBI session until the calibration method will become widely available.

A detailed discussion of geodetic results and frequency comparisons obtained in these experiments will be reported in separate publications.

4 Summary

A transportable 2.4 m broadband VLBI station was installed at Medicina astronomy observatory of INAF for an intercontinental frequency link experiment. Precise frequency comparison between the Yb lattice clock at INRiM and the Sr lattice clock at NICT has been performed by using intercontinental broadband VLBI, with local hydrogen masers acting as flywheels. VLBI sessions were conducted from Oct. 2018 to Feb. 2019 with both Yb and Sr clocks operating throughout the same period. The experiments make use of newly developed signal processing for polarization synthesis and broadband bandwidth synthesis, and confirmed that the 2.4 m diameter size radio telescopes achieve a precision of few tens of pico seconds in NHS measurements over an intercontinental baseline. In addition, radio source structure effects were clearly detected in our data. Until a calibration technique for this effect will become available, we are going to minimize this influence by source selection in scheduling the VLBI session.

Acknowledgements We thank T. Suzuyama and K. Watabe of NMIJ for supporting development of broadband VLBI to compare UTC(NMIJ)-UTC(NICT). G. Petit and J. Leute of BIPM for providing GPS IPPP solution for comparison of UTC(NMIJ)-UTC(NICT). Quick data transfer of VLBI data is supported by high speed research network GARR, GEANT, Internet2, TransPAC, APAN, and JGN.

References

BIPM (2017) Local representation of UTC. *BIPM Annual Report on Time Activities*, 12, 41, ISBN 978-92-822-2268-3, ISSN 1994-9405

Bolotin S, Baver K, Bolotina O, et al. (2019) The source structure effect in broadband observations. In: R. Haas, S. Garcia-Espada, J. A. López Fernández (eds.): *Proc. 24th EVGA Working Meeting*, 224–228

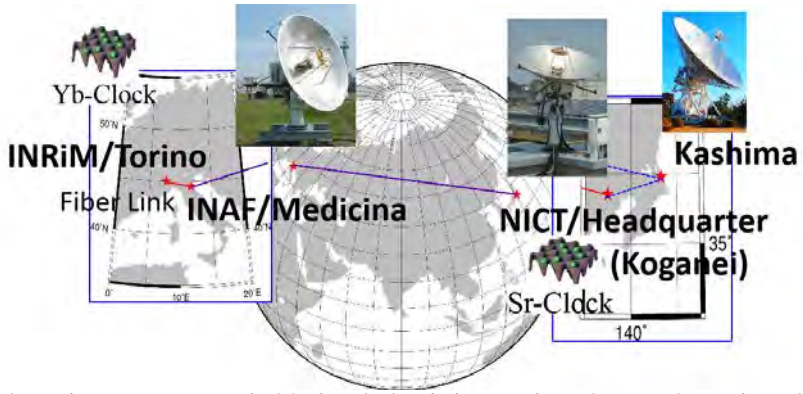

Fig. 1: Overview of the project to compare optical lattice clocks via intercontinental VLBI observation. The Yb lattice clock at INRiM and the Sr clock at NICT are compared by a series of links including optical fiber link between INRiM and Medicina, and intercontinental VLBI observation between Medicina and Koganei.

Fig. 2: Installation of transportable VLBI station at Medicina. The transportable 2.4 m antenna consists of separate assemblies for the dish and Az/El drive system. Three persons are sufficient to assemble the system in two days of work (Left and Center). A small air-conditioned box, located 30 m from the antenna, contains antenna control system(right).

Calonico D, Bertacco E K, Calosso C E, et al. (2014) High-accuracy coherent optical frequency transfer over a doubled 642-km fiber link. *Appl. Phys. B*, 117, 3, 979–986, doi:10.1007/s00340-014-5917-8

Clivati C, Costanzo G A, Frittelli M, et al. (2015) A Coherent Fiber Link for Very Long BaselineInterferometry. *IEEE Trans on Ultrason. Ferroel. Freq. Contr.*, 62, 1907–1912, doi:10.1109/TUFFC.2015.007221

Fujieda M, Gotoh T, Amagai J (2016) Advanced two-way satellite frequency transfer by carrier-phase and carrier-frequency measurements. *J. Phys. Conf. Ser.* 723, doi:10.1088/1742-6596/723/1/012036

Lopez O, Haboucha A, Chanteau B, et al. (2012) Ultra-stable long distance optical frequency distribution using the Internet fiber network. *Opt. Express*, 20, 21, 23518–23526, doi:10.1364/OE.20.023518

Niell A, Barrett J, Burns A, et al. (2018) Demonstration of a Broadband Very Long Baseline Interferometer System: A New Instrument for High-Precision Space Geodesy. *Radio Sci.*, 53, doi:10.1029/2018RS006617

Petit G, Kanj A, Loyer S, et al. (2015) 1×10^{-16} frequency transfer by GPS PPP with integer ambiguity resolution. *Metrologia*, 52, 301–309

Petrachenko B, Niell A, Behrend D, et al. (2009) Design Aspects of the VLBI2010 System. *Progress Report of the VLBI2010 Committee*, NASA/TM-2009-2014180

Predehl K, Grosche G, Raupach S M F, et al. (2012) A 920-kilometer optical fiber link for frequency metrology at the 19th decimal place, *Science*, 336, 6080, 441–444, doi:10.1126/science.1218442.

Riehle F (2015) Towards a Re-definition of the Second Based on Optical Atomic Clocks, *Comptes Rendus Physique*, 16, 5, 506–515, doi:10.1016/j.crhy.2015.03.012

Riehle F, Gill P, Arias F, et al. (2018) The CIPM list of recommended frequency standard values: guidelines and procedures. *Metrologia*, 55, 188–200

Sekido M (2017) Node - HUB Style VLBI with Broadband System. *IVS NICT-TDC News* 37, 22–25, www2.nict.go.jp/sts/stmg/ivstdc/news_37/pctdc_news37.pdf

Sekido M, Takefuji K, Ujihara H, et al. (2017) Broadband VLBI System GALA-V and Its Application for Geodesy and Frequency Transfer. In: R. Haas, G. Elgered (eds.): *Proc. 23rd EVGA Working Meeting*, 5–9

Takefuji K, Kondo T, Sekido M et al. (2012) High-order Sampling Techniques of Aliased Signals for Very Long Baseline Interferometry. *PASP* 124, 1105–1112, doi:10.1086/668232.

Whitney A, Kettenis M, Phillips C et al. (2014) VLBI Data Interchange Format (VDIF) Specification. https://vlbi.org/vlbi-standards/vdif/

Xu M H, Anderson J M, Gong S, et al. (2019) Structure effects in broadband VGOS data. Presentation at the 24th EVGA Working Meeting, Gran Canaria www.oan.es/evga2019/EVGA2019_PDF/O322_EVGA2019_Xu.pdf

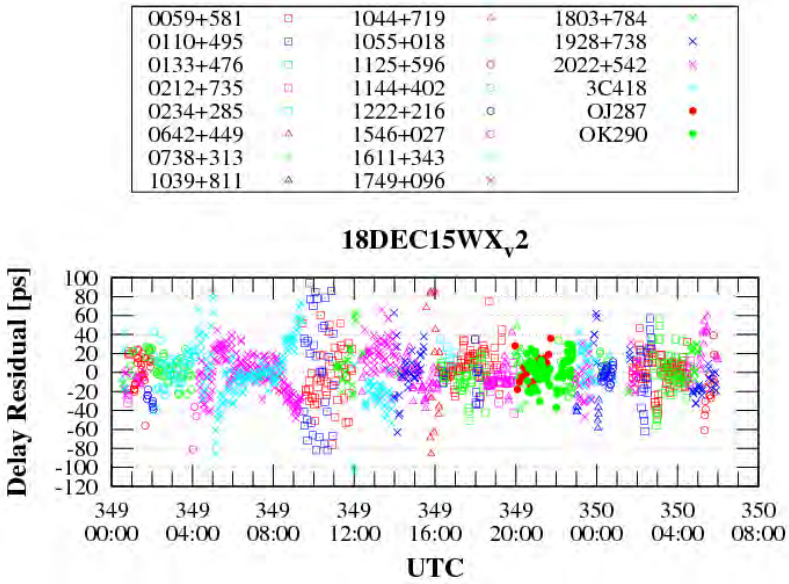

Fig. 3: Post-fit delay residual plotted for each source measured by 2.4 m diameter antenna pair over the Medicina-Koganei baseline. We attribute the split of residual for 3C418 to radio source structure.

Research and Application of VLBI Differential Phase Delays in Lunar Exploration

X. Zheng, Q. Liu, F. Shu, Y. Huang, P. Li, Z. Xu, Z. Chu

Abstract During the mission of Tracking and Data Relay Satellite of Chang'e-4 mission (TDRSS-C4) in May 2018, same-beam VLBI observations between TDRSS-C4 and Longjiang-2 (Microsatellite B) were successfully carried out by the Chinese VLBI network (CVN) during the Earth-to-Moon transfer section. After data processing and analysis, differential phase delay (DPD) of same-beam VLBI was calculated successfully. Combining ranging, range rate and bandwidth synthesis group delay data, the orbit determination of two satellites were successfully accomplished by using DPD which continued more than one hour on May 22. After orbit determination, the residuals of DPD were 4.97 ps (BJ-KM), 5.37 ps (BJ-UR), 4.40 ps (BJ-TM), 4.87 ps (KM-UR), 2.97 ps (KM-TM) and 3.64 ps (UR-TM), respectively.

Keywords TDRSS-C4 Microsatellite B · Differential Phase Delay

1 Introduction

The same-beam VLBI technology uses the main-beam of a radio telescope to receive the signals emitted from two satellites simultaneously. After the correlation processing, the phase delays of the two satellites are differentiated in order to calculate the Differential Phase Delay (DPD). During the data processing, the first difference between two stations and the second difference between the phases delay of two satellites are calculated. Because the angular distance between the two satellites are very close, the DPD eliminates the influence of the atmosphere and ionosphere on the propagation paths of the two satellites' signals, and the effect of the internal delay of the observation equipment, and it achieves the accuracy of picosecond (ps) order.

Historically, the Apollo Program carried out by NASA used the same-beam technology. In Japan, same-beam VLBI observations of the Rstar and Vstar satellites were carried out in the SELENE mission in 2008. The calculated DPD was applied to orbit determination and lunar gravity field model calculation. The orbit determination accuracy of Rstar and Vstar reached 10 m and better (Hanada et al., 2010). In the Chinese Chang'e-3 mission in 2013, DPD of same-beam VLBI between Lander and Rover were successfully calculated and used for monitoring the position of the Rover on the lunar surface, and also used for relative positioning between Lander and Rover (Liu et al., 2014).

During the mission of TDRSS-C4 in May 2018, TDRSS-C4 and Microsatellite B, which was designed by Harbin Institute of Technology, separated from the rocket and entered the Earth-Moon transfer orbit in turn. In the Earth-Moon transfer section, the two satellites were close enough to meet the requirements of same-beam VLBI observations. So while CVN (including BJ, KM, UR, TM) observed TDRSS-C4, at the same time, the signal of Microsatellite B was also successfully observed. In this paper, DPD between Microsatellite B and TDRSS-C4 was investigated.

Xin Zheng · Qinghui Liu · Fengchun Shu · Yong Huang · Peijia Li · Zhijun Xu · Zhanghu Chu
Shanghai Astronomical Observatory, Chinese Academy of Sciences, Nandan Road 80, Shanghai, China

(Correspondence: zhengxin@shao.ac.cn)

2 Schedule

The VLBI Center for Deep Space Exploration at the Shanghai Astronomical Observatory, Chinese Academy of Sciences (SHAO), received the precise ephemeris of TDRSS-C4 and Microsatellite B, and the predicted orbits of these two satellites were calculated for the observation schedule. Because TDRSS-C4 was the main task of CVN, the accuracy of the precise ephemeris of TDRSS-C4 was on the order of several hundred meters. The accuracy of the precise ephemeris of Microsatellite B was far lower than that of TDRSS-C4.

The schedule which was in the same-beam VLBI mode used the predicted orbits of the two satellites to calculate both geometric delay models, and output a job file for the VLBI correlator. The job file recorded both geometric delay models of the two satellites and wrote these models in the same format in turn, while the difference was just the satellite identification.

3 Correlator

The VLBI hardware correlator at SHAO processed the observation data of the stations according to the job file, and output data files and tab files with a known format. Because there were two satellite models in the job file, correlator outputted two data files and two tab files with satellite identifications while the same time tags of both two data files and two tab files. These four files were what the correlator output in the same-beam VLBI observation mode.

4 Differential phase delay

The software that calculated differential phase delay reads the data files and tab files, at the same time reads the time configuration file which the schedule output and the correction files which contain the atmospheric and ionospheric delays in the observation direction of the telescopes. Finally, it outputs the bandwidth synthesis group delay data of these two satellites and DPD data during the same-beam VLBI observation model is used.

4.1 DOR signals

CVN aimed at TDRSS-C4 and received S-band DOR signals from the two satellites. The DOR signals from TDRSS-C4 included one main carrier and two side tones. The main carrier frequency was 2234 MHz and the signal-to-noise ratio (SNR) was about 40 dB. The DOR signal transmitted by Microsatellite B also contained one main carrier and two side tones. The main carrier frequency was 2275 MHz, SNR was about 45 dB, −DOR and +DOR SNR were about 30 dB. The frequency difference between the two main carriers was 41 MHz.

4.2 Correlation phase

One data file and tab file contained cross-correlation data of which integral time was 0.98304 sec and totaling 5 cycles. Each integral period could extract six correlation phases of the main carrier of two satellites. In this paper, correlation phase of the observed data on May 22, 2018 was analyzed. Fig. 1(a) shows six-minutes of the correlation phase of TDRSS-C4 on the BJ-TM baseline. Fig. 1(b) shows the residual phase after eighth-order polynomial fitting of the correlation phase of TDRSS-C4. Fig. 2(a) depicts a six-minutes correlation phase of Microsatellite B on the BJ-TM baseline. Fig. 2(b) shows the residual phase after eighth-order polynomial fitting of the correlation phase of Microsatellite B. Comparing figs. 1(a) and 2(a), 1(b) and 2(b), the correlation phase change rate of TDRSS-C4 was estimated to be −0.5 ps/s, and that of microsatellite B was about 12 ps/s. The correlation coefficient of correlation phase between the two satellites was high, which means that the correlation phases of two satellites which was extracted from the data file were correct and the correlation phases for the period of 6 minutes had no integer ambiguity.

4.3 Bandwidth synthesis group delay

The bandwidth synthesis group delay includes the geometric delay model of the satellite and the difference between the geometric delay model of the satellite and the actual value. Error contributions such as at-

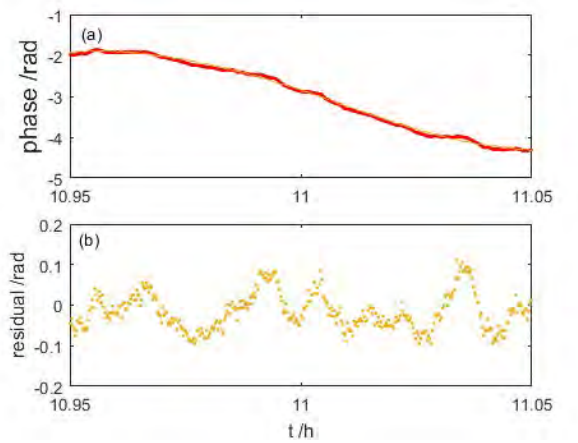

Fig. 1: (a) Correlation phases of TDRSS-C4 on BJ-TM baseline for 6 minutes; (b) Residual phases after an 8th-order polynomial fitting.

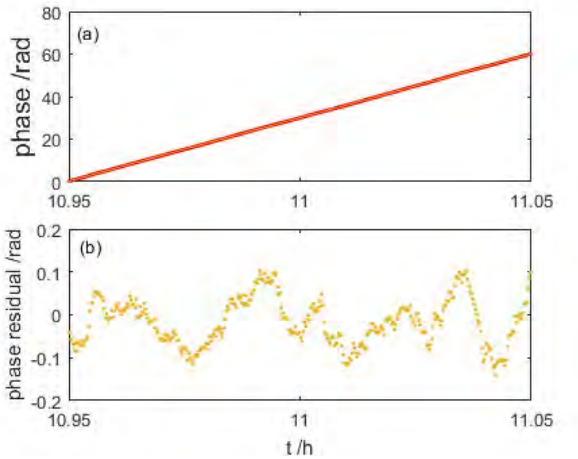

Fig. 2: (a) Correlation phases of Microsatellite B on BJ-TM baseline for 6 minutes; (b) Residual phases after an 8th-order polynomial fitting.

mospheric delay, ionospheric delay, equipment internal delay and clock differences need to be corrected. Figure 3 shows the residual of bandwidth synthesis group delay against the geometric delay model of Microsatellite B. Judging from Fig. 3, combined with station coordinates, parameters such as predicted orbit and baseline length, the accuracy of Microsatellite B prediction was thought to be on a level of 20 km.

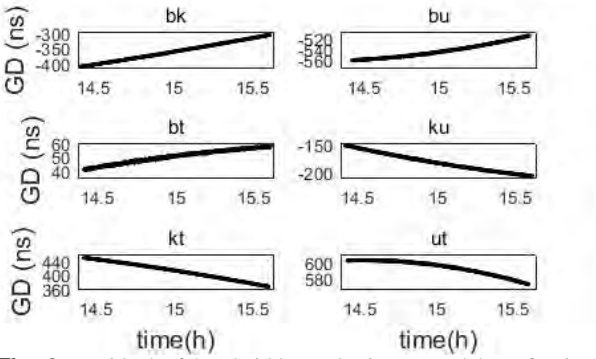

Fig. 3: Residual of bandwidth synthesis group delay of Microsatellite B.

4.4 DPD

Differential group delay (DGD) was obtained by differentiating the group delay of two satellites.

However, the calculation of DPD was relatively complicated. The main error factors affecting the DPD were almost cancelled through the subtraction of two satellites' phase delay. However, the ionospheric delay was inversely proportional to the square of the frequency. If the signal frequencies of the two satellites were different, the ionospheric delay must be considered on calculation of the DPD, and an equation to compute the ionospheric delay is shown in Equation 1.

$$(\tau^2_{ion} - \tau^1_{ion}) = \frac{k \times \Delta TEC}{c}\left[(\frac{1}{f_2})^2 - (\frac{1}{f_1})^2\right] \qquad (1)$$

Here, $(\tau^2_{ion} - \tau^1_{ion})$ is the difference of two satellites' ionospheric delays. The factor is $k = 40.28 m^3/s^2$. The expression ΔTEC means the difference of Total Electron Content in the line-of-sight direction of radio telescope which could be calculated according to the model or GNSS (Global Navigation Satellite System) observation data, and c is the speed of light. Furthermore, f_1, f_2 indicate the frequencies of the two satellites signals.

By subtracting the two geometrical delay models and subtracting the two residual phase delays, and then adding the two terms, DPD with bias was obtained, as shown in Equation 2. Because, the offset was a constant bias in a continuous arc, it could be calibrated during the orbit determination for DPD data spanning for more than 1 hour.

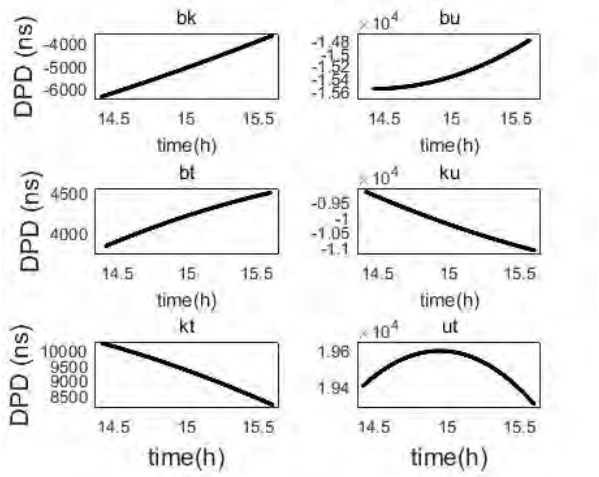

Fig. 4: DPD which continued more than one hours and could be used for orbit determination and relative positioning.

$$\tau_{dpd} = (\tau^2_{geo} - \tau^1_{geo}) + (\frac{\varphi_2}{2\pi f_2} - \frac{\varphi_1}{2\pi f_1}) + (m_2 - m_1) + (\tau^2_{ion} - \tau^1_{ion}) \quad (2)$$

Here τ_{dpd} was DPD. The terms τ^1_{geo} and τ^2_{geo} indicate the geometric delay model of the two satellites. The terms φ_1 , φ_2 show the correlation phases of two satellites, and $(m_2 - m_1)$ indicated the constant bias of DPD

According to the calculation algorithm of DPD, the software calculated DPD between two satellites during TDRSS-C4 and Microsatellite B both in the Earth-Moon transfer orbit which in the same-beam VLBI observation model. After analyzing all of DPD data, it was found that there were more than one hour continuous observations from 14.5 (UTC) to 16 (UTC) on May 22, 2018. In the whole arc, TDRSS-C4 and Microsatellite B were flying to the Moon in their scheduled orbits. Fig. 4 shows the DPD which observed continuously more than one hour, 6 baselines. Fig. 5 shows the residual of DPD after fitting by 8th order polynomial, UR-TM baseline. In the next step, these DPD were used for orbit determination and relative positioning between TDRSS-C4 and Microsatellite B.

5 Orbit determination

Range, range rate and bandwidth synthesis group delay of Microsatellite B on May 22 were used for a first orbit determination. Since the accuracy of the precise ephemeris of Microsatellite B was far less than that of TDRSS-C4, the orbit accuracy of Microsatellite B was improved to hundreds of meters. Fig. 6 shows the residuals of the bandwidth synthesis group delay of Microsatellite B after orbit determination. Finally, the orbit accuracy of both TDRSS-C4 and Microsatellite B both reached hundred of meters, and the success rate was increased by using the same-beam VLBI DPD orbit determination.

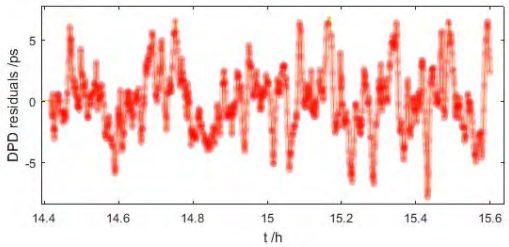

Fig. 5: Residuals of DPD after 8-power polynomial fitting.

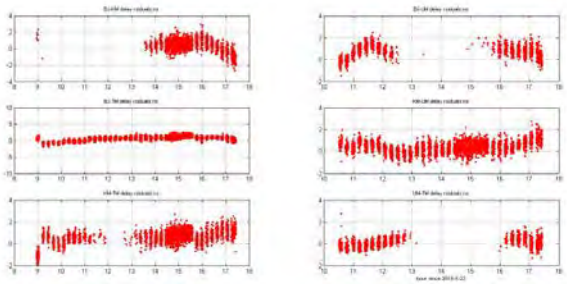

Fig. 6: Residuals of the bandwidth synthesis group delay of Microsatellite B after orbit determination. Shown are 6 baselines.

After a first orbit determination, the accuracy of both satellite orbits reached hundreds of meters. Then, DPD was applied for the second orbit determination. Using ranging, range rate and bandwidth synthesis group delay of both satellites, and DPD that was calculated by both satellites' data, the orbits of these two satellites (TDRSS-c4 and Microsatellite B) were improved. As shown in Fig. 7, the residual of six baselines of DPD after orbit determination can be calculated to be 4.97, 5.37, 4.40, 4.87, 2.97, 3.64 ps, respectively. The systematic deviation of the six baselines is −0.6, −0.675, 0.118, 0.016, 0.43, 0.416 ns.

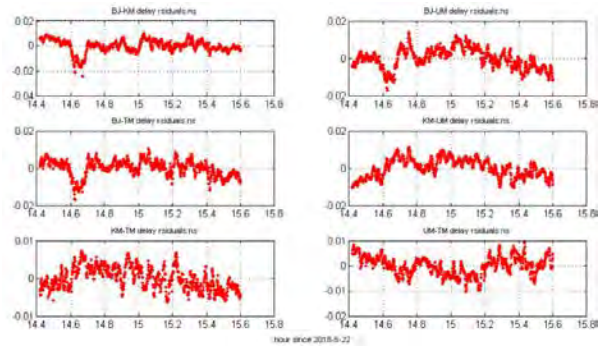

Fig. 7: The residuals of DPD after orbit determination. Shown are 6 baselines.

6 Conclusions

Same-beam VLBI observations between TDRSS-C4 and Microsatellite B were successfully carried out by CVN during the Earth-to-Moon transfer section in May 2018. We correctly calculated the DPD data and successfully used the DPD data for orbit determination for these two satellites. The residuals of six baselines can be calculated to be 4.97 5.37 4.40 4.87 2.97 3.64 ps, respectively.

Acknowledgements This paper is sponsored by the Natural Science Foundation of China General Program (11803069, 11803070, 11773060), the Key Laboratory of Planetary Sciences, the Opening Project of Shanghai Key Laboratory of Space Navigation and Positioning Techniques, and the Chinese Lunar Exploration Project. The authors appreciate the support from the CVN and VLBI center in SHAO.

References

Hanada H, Iwata T, Liu Q, et al. (2010) Overview of Differential VLBI Observations of Lunar Orbiters in SELENE for Precise Orbit Determination and Lunar Gravity Field Study. *Space Science Reviews*, 154, 123–144, doi:10.1007/s11214-010-9656-9

Liu Q, Zheng X, Huang Y, et al. (2014) Monitoring motion and measuring relative position of the Chang'E-3 rover. *Radio Sci.*, 49, 1080–1086, doi:10.1002/2014RS005449

Comparison of Results Between CVN and K5 Software Correlators

T. Kondo, W. Zheng, L. Liu, J. Zhang, F. Shu, L. Tong, F. Tong

Abstract CVN (China VLBI Network) software correlator has been developed by SHAO for the lunar mission. Recently it has been upgraded to a general correlator to handle the geodetic VLBI observations data. Observed values, such as delay, delay rate, and fringe amplitude, obtained by CVN software correlator and fringe fitting software “fourfit”have been compared with those obtained by K5 processing system consisting of software correlatorand fringe fitting software independent from CVN system. As a result, it has been confirmed that CVN and K5 results show a good coincidence.

Keywords CVN correlator · K5 correlator

1 Introduction

CVN (China VLBI Network) software correlator developed by SHAO for the lunar mission has been upgraded to a general correlator to handle the geodetic VLBI observations data. K5 software correlator has been developed by NICT (National Institute of Information and Communications Technology, Japan) VLBI group (Kondo et al., 1999) for processing geodetic VLBI data. We have conducted the comparison between CVN and K5 software correlators. Observed values, such as delay, delay rate, and fringe amplitude, obtained by CVN software correlator and fringe fitting software ”fourfit” (Cappallo, 2014) have been compared with those obtained by K5 software correlator. K5 and CVN comparison results show a good coincidence with each other on fine (multi-band) delay, delay rate, and fringe amplitude. The average of the standard deviation of the differences between X band fine delays is 7.6 psec. As for the delay rate, the average of differences at X band is 0.00±0.09 ps/s. As for the fringe amplitude at X band, the average of ratio (CVN/K5) is 0.98±0.11. K5 correlator is used by GSI (Geospatial Information Authority of Japan) VLBI group for a routine IVS VLBI data processing, so that CVN correlator has enough performance to process geodetic VLBI data.

Tetsuro Kondo · Weimin Zheng · Lei Liu · Juan Zhang · Fengxian Tong
Shanghai Astronomical Observatory, 80 Nandan Doad, Shanghai, 200030, China

Tetsuro Kondo also
National Institute of Information and Communications Technology, Japan

(Correspondence: kondo@shao.ac.cn)

2 Definition of delay

2.1 Baseline-based processing system

K5 processing system is a baseline-based processing system. Observed delay is defined as the time required for the wavefront passing through the reference station (X) at the epoch (PRT: Processing Reference Time) to pass through the other station (Y). On the other hand, as for the earth-centered epoch system like the CVN system, observed delay is defined as the difference between the time a certain wavefront, that passes through the earth center at the epoch, passed through the X station and the time the same wavefront passed through the Y station.

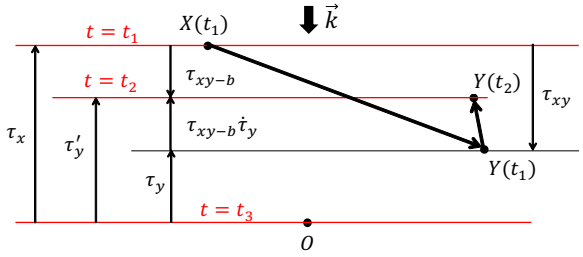

Fig. 1: Observed delay in case of baseline-based processing system. Let t_2 be the time when a certain wavefront, that passed through the X station at t_1 (epoch), passes through the Y station. Observed delay is given as $t_2 - t_1$ ($= \tau_{xy-b}$). O is the center of the earth and **k** is the wave propagation direction.

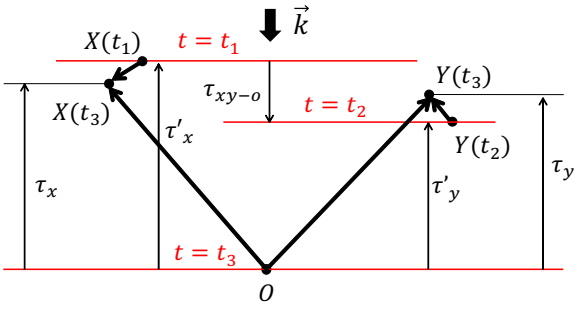

Fig. 2: Observed delay on a earth-centered epoch system. Observed delay is $t_3 - t_2 = \tau'_x - \tau'_y$ where t_2 and t_3 are the time a certain wavefront, that passes the earth center at t_1 (epoch), passed through the X station and the time the same wavefront passed through the Y station.

In Fig. 1, t_2 is the time when a certain wavefront, that passed through the X station at t_1 (epoch), passes through the Y station. Let geometrical delays against the earth center at t_1 be τ_x and τ_y for X and Y stations, and a geometrical delay against the earth center of Y station at t_2 be τ'_y. Observed delay is expressed as $\tau_{xy-b} = t_2 - t_1 = \tau_x - \tau'_y$. From the figure, τ'_y can be given as

$$\tau'_y = \tau_y + \tau_{xy-b}\dot{\tau}_y \tag{1}$$

where $\dot{\tau}_y$ is the changing rate of τ_y at t_1, i.e., delay rate. Therefore τ_{xy-b} can be written as

$$\begin{aligned}\tau_{xy-b} &= \tau_x - (\tau_y + \tau_{xy-b}\dot{\tau}_y) \\ &= \tau_{xy} - \tau_{xy-b}\dot{\tau}_y \end{aligned} \tag{2}$$

where $\tau_{xy} = \tau_x - \tau_y$. Solving Eq.(2) for τ_{xy-b}, we get

$$\tau_{xy-b} = \frac{\tau_{xy}}{1+\dot{\tau}_y}$$

Moreover considering $|\dot{\tau}_y| \ll 1$, we finally get

$$\tau_{xy-b} = \tau_{xy}(1-\dot{\tau}_y) \tag{3}$$

2.2 Earth-centered epoch processing system

In case of earth-centered epoch system, observed delay is defined as the difference between the time a certain wavefront, that passes through the earth center at the epoch, passed through the reference station (X) and the time the same wavefront passed through the remote station (Y). In Fig. 2, t_1 and t_2 correspond to these two times, and t_3 is the epoch. Let geometrical delays against the earth center at t_3 be τ_x and τ_y for X and Y stations, a geometrical delay against the earth center for X station at t_1 be τ'_x, and a geometrical delay against the earth center for Y station at t_2 be τ'_y. Observed delay is expressed as $\tau_{xy-o} = t_2 - t_1 = \tau'_x - \tau'_y$. From the figure, τ'_x can be expressed as

$$\tau'_x = \tau_x - \tau'_x\dot{\tau}_x$$

where $\dot{\tau}_x$ is the changing rate of τ_x at t_3 ($\dot{\tau}_x < 0$ under the condition illustrated in the figure). Solving for τ'_x, we obtain

$$\begin{aligned}\tau'_x &= \frac{\tau_x}{1+\dot{\tau}_x} \\ &\fallingdotseq \tau_x(1-\dot{\tau}_x) \\ &\quad (\because |\dot{\tau}_x| \ll 1).\end{aligned} \tag{4}$$

Similarly for τ'_y, we get

$$\tau'_y = \tau_y(1-\dot{\tau}_y). \tag{5}$$

Hence observed delay is given as follows.

$$\begin{aligned}\tau_{xy-o} &= \tau'_x - \tau'_y \\ &= \tau_x(1-\dot{\tau}_x) - \tau_y(1-\dot{\tau}_y) \\ &= \tau_x - \tau_y - \tau_x\dot{\tau}_x + \tau_y\dot{\tau}_y.\end{aligned}$$

Using relations $\tau_{xy} = \tau_x - \tau_y$ and $\dot{\tau}_{xy} = \dot{\tau}_x - \dot{\tau}_y$, we get

$$\tau_{xy-o} = \tau_{xy}(1-\dot{\tau}_y) - \tau_x\dot{\tau}_{xy}. \tag{6}$$

Since τ_{xy-b} is expressed by Eq. (3), τ_{xy-o} can be rewritten as

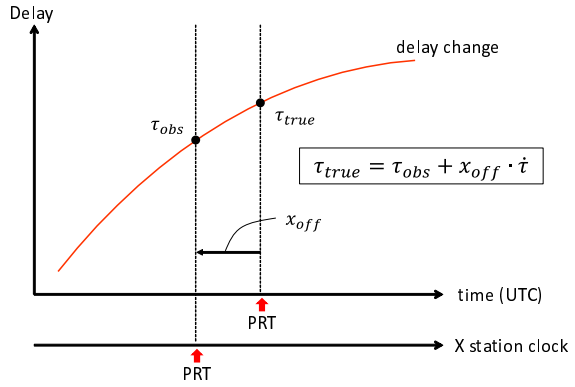

Fig. 3: Relation between X-station clock offset and observed delay. In case that correlation processing is carried out without correction of clock offset, the epoch (PRT: Processing Reference Time) of observed value shifts by the amount of clock offset. Therefore observed delay at the true PRT can be obtained by compensating the delay change during the period of the clock offset.

$$\tau_{xy-o} = \tau_{xy-b} - \tau_x \dot{\tau}_{xy}. \quad (7)$$

Namely the correction based on the term "$-\tau_x \dot{\tau}_{xy}$" is necessary for a comparison between τ_{xy-b} and τ_{xy-o}.

We can get the same correction term, as described later, by treating as the shift of the epoch when comparison is made.

3 Observed delay correction

3.1 X-station clock offset

Fig. 3 shows the relation between X-station clock offset and observed delay. In case that correlation processing is carried out without correction of clock offset, the epoch (PRT: Processing Reference Time) of observed delay shifts by the amount of clock offset. Therefore observed delay at the true PRT, τ_{true}, can be obtained by compensating the delay change during the period of clock offset. Assuming the clock offset is a very short time, we can neglect the higher order terms such as 2nd and higher of the Taylor's formula. So that τ_{true} is given as

$$\tau_{true} = \tau_{obs} + x_{off} \cdot \dot{\tau}_{xy} \quad (8)$$

where x_{off} is the X-station clock offset and $\dot{\tau}_{xy}$ is the delay rate.

3.2 Earth centered epoch correction

The definition of the epoch is different between the baseline-based processing system and the earth-centered epoch processing system. It is therefore necessary to compensate for the difference of the epoch to carry out the comparison of the both observed delays. In order to match the epoch of the baseline-based processing system to that of the earth-centered epoch processing system, at first the time of the wavefront, that reaches the center of the Earth at the epoch, passing the X station is computed. Thendelay observed by the baseline-based processing is corrected so as to compensate this time difference. This compensation is given by shifting the epoch of the baseline-based delay by τ'_x shown in Fig. 2. Therefore the correction is given as

$$\tau_{obs-o} = \tau_{obs-b} - \tau'_x \cdot \dot{\tau}_{xy} \quad (9)$$

where τ_{obs-b} is the observed delay obtained by the baseline-based system and τ_{obs-o} is that by the earth-centered epoch system. Moreover

$$\tau'_x = \tau_x - \tau'_x \cdot \dot{\tau}_x$$

then solving for τ'_x, we get

$$\tau'_x = \tau_x(1 - \dot{\tau}_x) \quad (10)$$

Substituting this to Eq.(9), we get

$$\tau_{obs-o} = \tau_{obs-b} - \tau_x \cdot \dot{\tau}_{xy} + \tau_x \dot{\tau}_x \dot{\tau}_{xy} \quad (11)$$

Absolute values of τ_x, $\dot{\tau}_x$, and $\dot{\tau}_{xy}$ on the earth are at most 0.02sec, 1.5×10^{-6}s/s, and 3×10^{-6}s/s, respectively. Hence maximum value of $|\tau_x \dot{\tau}_x \dot{\tau}_{xy}|$ does not exceed 1×10^{-13}sec(=0.1psec), and the value is small enough compared with the measurement accuracy of the current system. So that this term can be neglected, then we get

$$\tau_{obs-o} = \tau_{obs-b} - \tau_x \cdot \dot{\tau}_{xy}. \quad (12)$$

This is the same as Eq. (7).

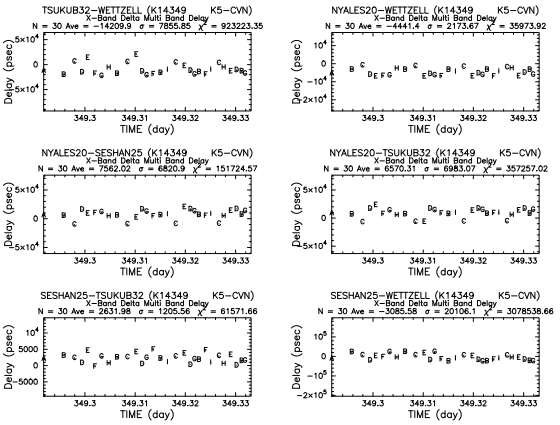

Fig. 4: Result of the comparison of fine delay (multi-band delay) at X band. An alphabetical symbol means a radio source. No correction is applied to K5 results. Standard deviation of differences reaches a large value of 20 nsec at the SESHAN25-WETTZELL baseline.

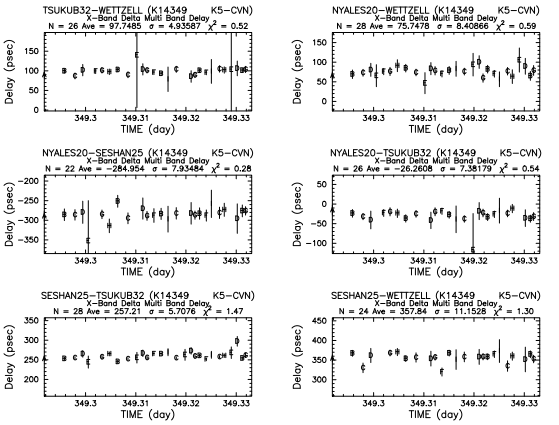

Fig. 5: Result of the comparison of fine delay (multi-band delay) at X band. The latest version is used for K5 processing, i.e., X-station clock offset is compensated during a correlation processing. Earth-centered epoch correction is applied to these K5 results. χ^2 is less than 1 for most of the baselines. This means the difference is less than the theoretical error caused by thermal noises, i.e., K5 and CVN results show a good coincidence.

3.3 Summary of corrections

Corrections for observed delays obtained by K5 system can be summarized as follows.

$$\tau_{obs-o} = \tau_{obs-b} + (x_{off} - \tau_x)\dot{\tau}_{xy} \tag{13}$$

By differentiating Eq. (13) with respect to time, we get the relation regarding observed delay rates as follows.

$$\dot{\tau}_{obs-o} = \dot{\tau}_{obs-b} - \dot{\tau}_x\dot{\tau}_{xy} + (x_{off} - \tau_x)\ddot{\tau}_{xy} \tag{14}$$

where theoretical values of τ_x, $\dot{\tau}_x$, $\dot{\tau}_{xy}$, and $\ddot{\tau}_{xy}$ are used for an actual calculation.

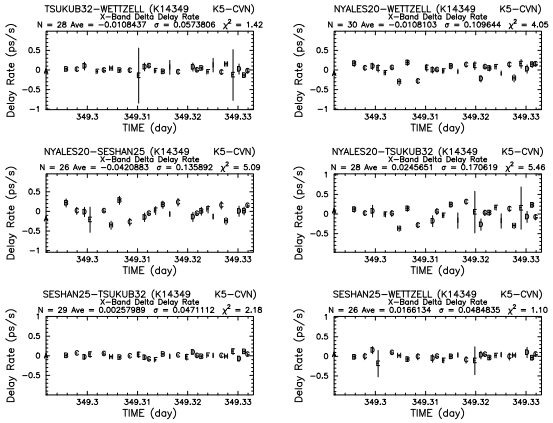

Fig. 6: Result of the comparison of delay rate at X band. The latest version is used for K5 processing, i.e., X-station clock offset is compensated during a correlation processing. Earth-centered epoch correction is applied to K5 results. K5 and CVN results well coincide with each other, and the average of difference is 0.00 ± 0.09 ps/s.

4 Results of comparison

As for comparison studies, we use the VLBI experiment data conducted on 2014/349 07h-08h UT. Four stations, such as NYALES20, SESHAN25, TSUKUB32, and WETTZELL, were participated in the experiment.

As for K5 processing system, the latest version that compensates X clock offset during a correlation processing is used, therefore the correction of X clock offset is unnecessary in the comparisons.

Fig. 4 shows the result of the comparison of fine delay (multi-band delay) at X band. No correction is applied to K5 results. Standard deviation of differences is about 1.2 nsec at the SESHAN25-TSUKUB32 baseline, but it reaches a large value of 20 nsec at the SESHAN25-WETTZELL baseline.

Fig. 5 shows the same as Fig. 4, but the earth-centered epoch correction is applied to K5 results. Standard deviation of differences ranges from 4.9 psec to 11.1 psec. χ^2 is less than 1 for most of the baselines. This means the difference is less than the theoretical error based on thermal noises, i.e., K5 and CVN results show a good coincidence.

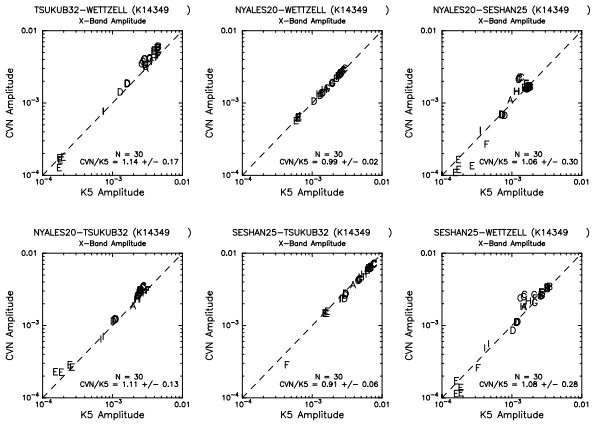

Fig. 7: Result of the comparison of fringe amplitude at X band. Both amplitudes well coincide with each other. The average of CVN/K5 is 1.05 ± 0.16.

Fig. 6 shows the result of the comparison of delay rate at X band. K5 and CVN results well coincide with each other, and the average of difference is 0.00 ± 0.09 ps/s.

Fig. 7 shows the result of the comparison of fringe amplitude at X band. Both amplitudes well coincide with each other. The average of CVN/K5 is 1.05 ± 0.16. All results for X band are summarized in Table 1.

Table 1: Summary of comparison between K5 and CVN

Fine Delay (K5-CVN) (psec)

	Ts-Wz	Ny-Wz	Ny-Sh	Ny-Ts	Sh-Ts	Sh-Wz	mean
mean	97.7	75.7	-285.0	-26.3	257.2	357.8	79.5
σ	4.9	8.4	7.9	7.4	5.7	11.1	7.6

Delay Rate (K5-CVN) (ps/s)

	Ts-Wz	Ny-Wz	Ny-Sh	Ny-Ts	Sh-Ts	Sh-Wz	mean
mean	-0.010	-0.011	-0.042	0.025	0.003	0.017	-0.003
σ	0.050	0.110	0.136	0.171	0.047	0.048	0.094

Amplitude Ratio (CVN/K5)

	Ts-Wz	Ny-Wz	Ny-Sh	Ny-Ts	Sh-Ts	Sh-Wz	mean
CVN/K5	1.03	0.97	0.97	1.04	0.90	0.98	0.98
σ	0.12	0.01	0.16	0.08	0.10	0.16	0.11

Station ID: Ts(TSUKUB32), Wz(WETTZELL), Ny(NYALES20), Sh(SESHAN25)

5 Conclusion

Results obtained by CVN software correlator have been compared with those obtained by K5 software correlator. Earth-centered epoch correction and X clock offset correction are applied to K5 results. As a result, K5 and CVN results shows a good coincidence with each other on observed values, such as, fine (multi-band) delay, delay rate, and fringe amplitude. The average of the standard deviation of the differences between X band fine delays is 7.6 psec. As for the delay rate, the average of differences at X band is 0.00 ± 0.09 ps/s. As for the fringe amplitude at X band, the average of ratio (CVN/K5) is 0.98 ± 0.11. Offsets seen in delay is thought to be due to the difference of fringe fit algorithm that can be influenced by an instrumental delay (phase structure in a channel and band). However, they do not affect geodetic results, because these offsets can be treated as a clock offset at a baseline analysis.

Acknowledgements A part of this work has been funded by Chinese Academy of Sciences (CAS) President's International Fellowship Initiative, Grant No. 2018VEA00017.

References

Cappallo R (2014) Correlating and fringe-fitting broadband VGOS data. In: D. Behrend, K. D. Baver, K. L. Armstrong: *IVS 2014 General Meeting Proceedings*, Science Press (Beijing), 91–96

Kondo T, Sekido M, Kiuchi H (1999) KSP bandwidth synthesizing software. *J. Commun. Res. Lab, 66*(1), 67–76

Status of the Future RAEGE Radio Telescope at Gran Canaria

D. Cordobés, V. Araña, J. A. López Pérez, A. García, I. Domínguez Cerdeña, J. Ticay, P. Dorta, I. Pérez, J. A. López Fernández, J. Gómez González

Abstract The IGN in cooperation with the Azores Regional Government, is developing since 2012 the RAEGE network, which consists of four VGOS antennas for space geodetic observation. Currently, two of the four antennas are operative at Santa Maria (Azores) and Yebes (Guadalajara, Spain). The third antenna will be operational by 2021 at Gran Canaria (Spain) with the cooperation of the University of Las Palmas de Gran Canaria (IDeTIC-ULPGC). We present here the progress made on the site selection, construction and a snapshot of the future projects for the VLBI antenna of Gran Canaria.

The site was selected after a longterm noise measurement all along the island. The chosen final site is close to Artenara village at an altitude of 1100 m and presents the lowest measured electromagnetic noise. At the present time, we have finished the bureaucratic procedures with local administrations and almost finished the architecture projects for the different buildings of the site.

The Artenara station will have a fully compliant VGOS radio telescope, equipped with a broadband receiver in the 2 – 14 GHz band. In addition to these, the facilities at Artenara will also include an absolute gravimeter, a GNSS receiver and a seismic station, with the goal of turning Artenara RAEGE site into a Geodetic Fundamental Station.

Keywords VGOS · RAEGE · Gran Canaria

1 Introduction

The RAEGE (Red Atlántica de Estaciones Geodinámicas Espaciales) project results from a Memorandum of Understanding between the Spanish National Geographic Institute (IGN, Ministerio de Fomento, Gobierno de España) and the Government of the Portuguese Autonomous Region of Azores (Secretaria Regional da Ciência, Tecnologia e Equipamentos, Governo dos Açores), signed in 2011, to meet the international developments needed to set up a VLBI (Very Long Baseline Interferometry) Geodetic Observing System - VGOS.

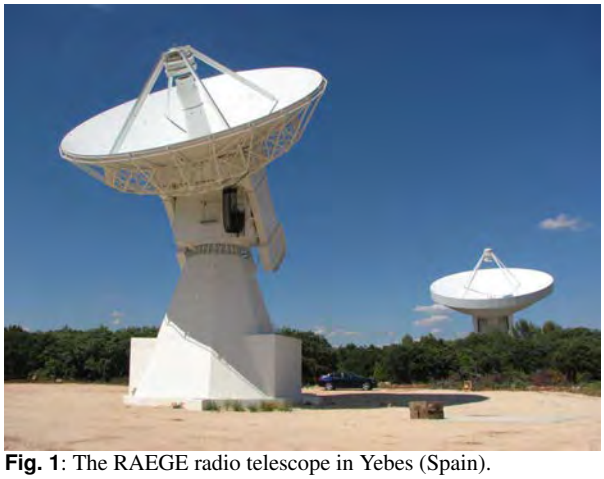

Fig. 1: The RAEGE radio telescope in Yebes (Spain).

David Cordobés · José Antonio López Pérez · Abel García · Itahiza Domínguez Cerdeña · José Antonio López Fernández · Jesus Gómez González
Instituto Geográfico Nacional
C/General Ibañez de Ibero, Madrid, Spain

Víctor Araña · Jaime Ticay · Pablo Dorta · Iván Pérez
Instituto para el Desarrollo Tecnológico y la Innovación en Comunicaciones (IDeTIC), Universidad de Las Palmas de Gran Canaria (ULPGC), Spain

(Correspondence: d.cordobes@oan.es)

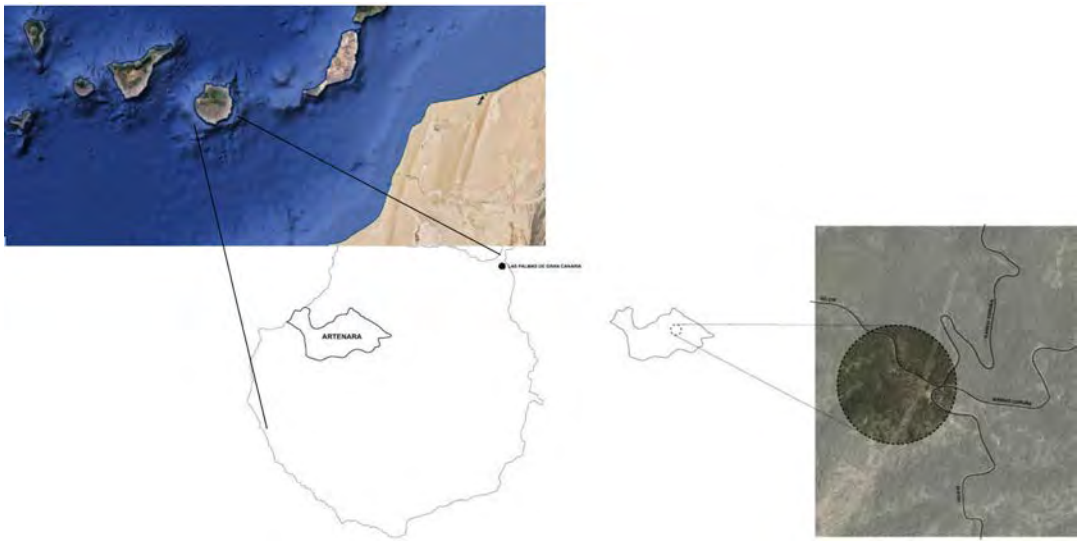

Fig. 2: Site location at Gran Canaria and zoom to the Artenara municipality.

The project consists of a network of four fully equipped Geodetic Fundamental Stations in Spain (Yebes, Guadalajara and Gran Canaria, Canary Islands), and Azores, Portugal (Santa Maria and Flores islands) and two Base Centres (Yebes/Spain and Lagoa-São Miguel/Azores), dedicated to astronomy, geodesy and geophysics studies.
The basic equipment of all RAEGE's Geodetic Fundamental Stations is:

- VGOS radio telescope (13.2 m diameter; operation up to 90 GHz; Fast slewing speed)
- Gravimeter
- Permanent GNSS station
- Maser clock
- Seismic station

2 The radio telescope

The construction of the radio telescope started at the end of 2010 when the contract for the design, construction, and commissioning of the first three radio telescopes was awarded to MT Mechatronics (Germany). The design of the radio telescopes was completed in the summer of 2011. During 2011 and 2012 the backstructures of the three radio telescopes were built by Asturfeito in Asturias, Spain. Other parts, such as the reflector panels, were fabricated by COSPAL Composites in Italy. The RAEGE radio telescopes are Azimuth/Elevation turning head telescopes, reaching azimuth and elevation slew speeds of $12^o/s$ and $6^o/s$, respectively. The optical design is based on a 13.2 m ring focus reflector. In its basic configuration, the observation frequency is in the range of $2-40$ GHz. It can be enhanced up to 100 GHz by using additional options. For geodetic telescopes it is essential to be able to accurately measure the position of the intersection of the azimuth and elevation axes. Therefore a concrete pillar is installed at the center of the telescope tower, allowing the installation of a measurement system to be located at the intersection of axes and visible from the outside through openings. Another important requirement in geodetic VLBI is path length stability. In order to handle path length errors, an active deformation measurement and "flexible body compensation" (FBC) method is foreseen, similar to established methods used for surface and focus/pointing error corrections.
The specifications of the radio telescope are:

- Max. azimuth, elevation speed: $12^o/s$, $6^o/s$
- Acceleration: $3^o/s^2$
- Frequency operation range: up to 40 GHz
- Path length error < 0.26 mm
- Elevation, azimuth movement range: $0-100^o$, $0-540^o$
- Pointing accuracy < 16 arcsec
- Power consumption < 170 kW
- Aperture efficiency > 60 % at 8 GHz (using VGOS receiver).

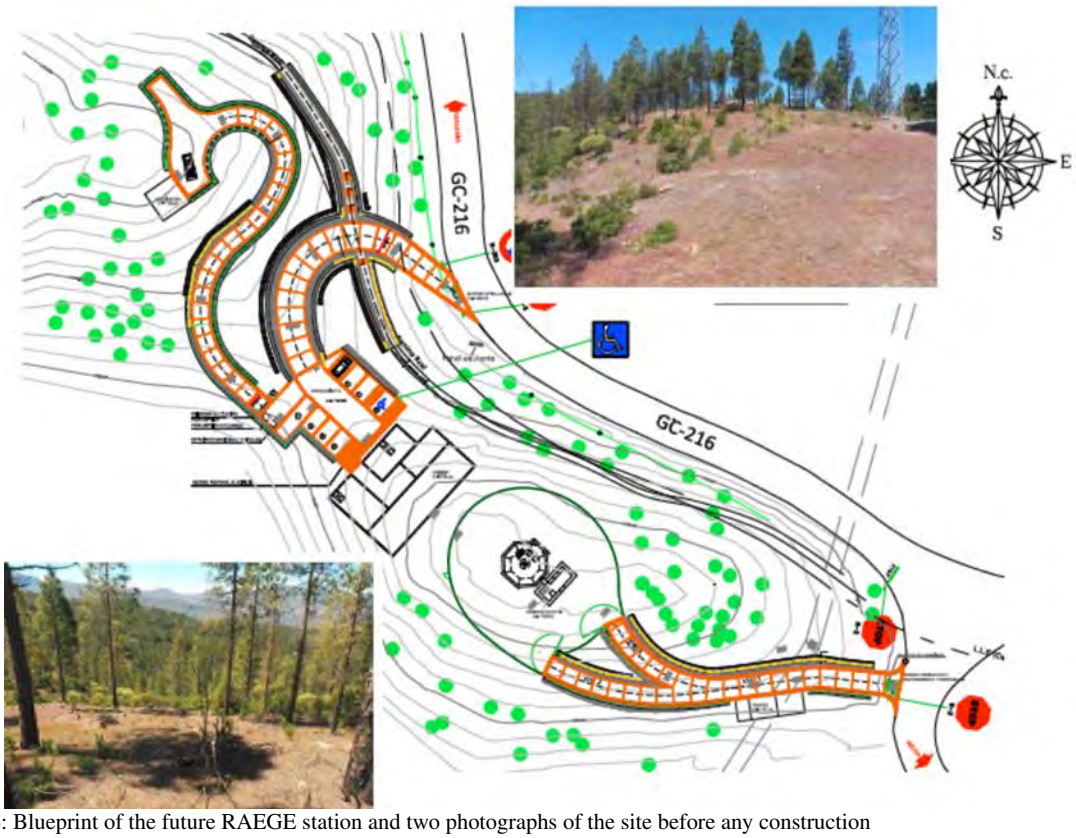

Fig. 3: Blueprint of the future RAEGE station and two photographs of the site before any construction

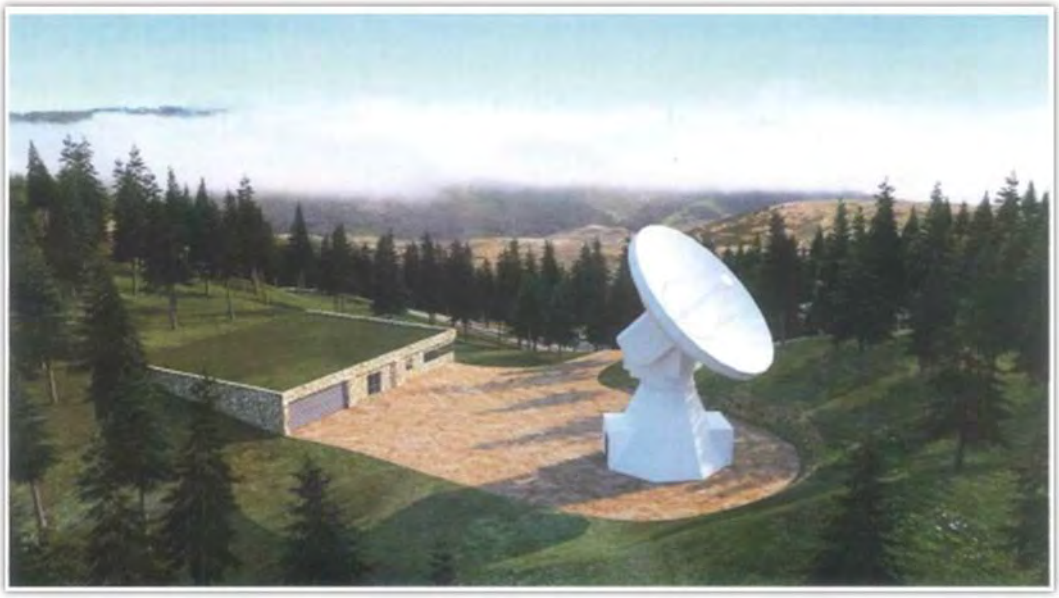

Fig. 4: Artistic reproduction of the future radio telescope.

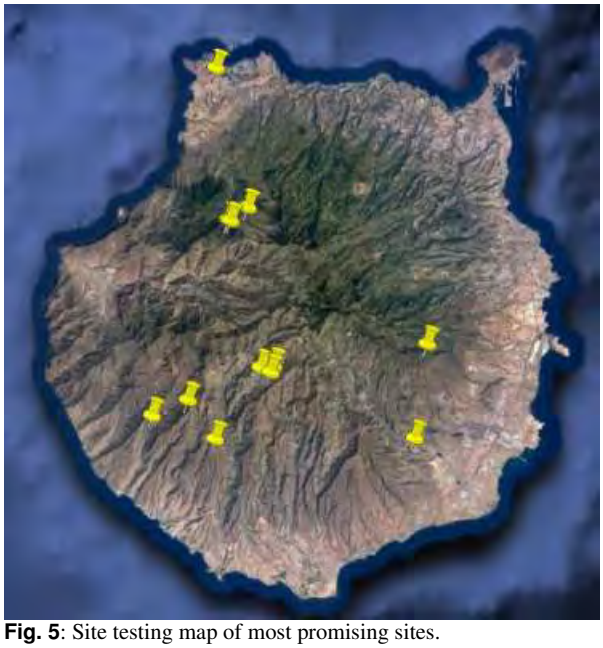

Fig. 5: Site testing map of most promising sites.

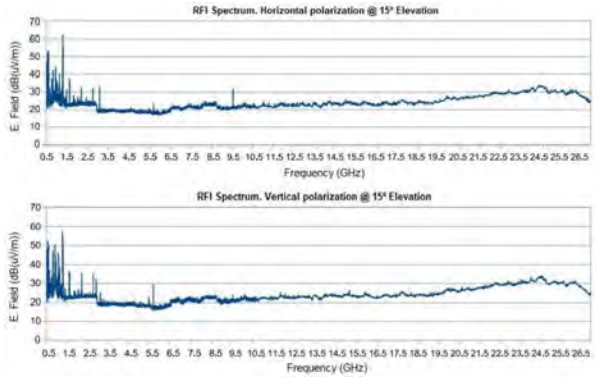

Fig. 6: RFI measurement for the selected site.

3 Site selection

Several factors were considered for the selection of the RAEGE Gran Canaria site:

- Low RFI in order to maximize the observing frequency band of the radio telescope
- High altitude (1100 m a.s.l) to avoid clouds during longest periods of the year
- Low humidity
- Public owned terrain that can be transferred to the IGN
- Electrical infrastructure available
- Geological stability. The site is located close to Artenara village on old ignimbrite rocks with various million years. Most recent volcanic activity is far from the site and the probability of a future volcanic eruption on the island is of lower than 1 % for the next 100 years.

The RAEGE Gran Canaria site was chosen after an intensive RFI measurement campaign around the island. At the center of Gran Canaria there are some militar and meteorological radars whose electromagnetic radiation covers most of the island so it was hard to find a suitable place with low RFI levels. Eventually Artenara was chosen as it is shadowed by a nearby mountain from the radar, and as it is in the border of a natural park, the electromagnetic pollution is guaranteed to remain the lowest possible for the future years.

4 Status and future work

Currently, the radio telescope is kept inside containers in a warehouse of Gran Canaria island and we are waiting for the bureaucratic permissions to start the civil works at the site. If everything goes well, we expect to begin the works by the end of 2019. The first stage will be the conditioning of the terrain and the construction of the interior roads. In a second stage, the radio telescope will be built. In the final stage, which will be by 2021, the control building will be made, and the station will be operative. We hope to achieve the first fringes during 2022.

First Steps in Gravitational Deformation Modelling of the VLBI Yebes Radio Telescopes

A. Prudencio, E. Azcue, J. López Ramasco, S. Garcia-Espada, Y. Gómez Espada, V. Puente, M. Valdés

Abstract In this work, the first steps in the gravitational deformation modelling of the VLBI antennas of Yebes by using terrestrial laser scanner are presented. A preliminary simulation of the measurements and its processing in Matlab and the future work and campaigns are shown.

Keywords Gravitational deformation · Terrestrial Laser Scanner · VLBI

1 Introduction

Geodetic VLBI is one of the most accurate geodetic techniques for the study of the size and shape of the Earth, its rotation and time variations. This accuracy is achieved taking into account all the error sources involved in the process.

Andrea Prudencio
Department Section of Astronomy and Geodesy, Faculty of Mathematics, University Complutense of Madrid, ES-28040 Madrid, Spain

Esther Azcue · Yaiza Gómez Espada · Víctor Puente · Marcelino Valdés
Instituto Geográfico Nacional
C/General Ibañez de Ibero, Madrid, Spain

J. López Ramasco
Observatory of Yebes - Instituto Geográfico Nacional
Cerro de la Palera S/N Yebes, Spain

Susana Garcia-Espada
Instituto Geográfico Nacional - RAEGE Santa Maria station, Azores, Portugal

(Correspondence: anpruden@ucm.es)

The effect of gravity in VLBI antennas is one of these errors that should be taken into account in the analysis of VLBI data. This effect can reach several millimeters and it has to be determined specifically for each radio telescope (Sarti et al., 2009).

The National Geographic Institute of Spain (IGN) works to achieve the optimal operation in their stations. This includes the determination of this effect. In this work the first steps to the antenna gravitational deformation modelling and the tools developed for the data processing are shown.

2 Goal

The aim of this work is to present the first steps in gravitational deformation modelling of the Yebes radio telescopes. At the end of 2018, the IGN acquired a Terrestrial Laser Scanner (LS) that will be used to measure the gravitational deformation at different elevations of the IGN telescopes. Before the campaign planning, a preliminary study of this effect has been made. The objective was to start developing some tools that could be useful to plan the campaign and to model the LS cloud in the future. Four Matlab routines were developed with the next objectives:

- To study and analyse the gravitational influences on large VLBI telescopes. Simulation of a LS measurements affected by structure's self weight and white noise.
- To determine the best fit paraboloid to the point cloud simulated and to estimate the deformation parameters (3 translations, 2 rotations and focal length variation).

- To compare the best fit paraboloid obtained with the original data.
- To contrast the gravitational deformations at different telescope elevations and to plot these differences.

3 Routines

3.1 Gravitational deformation simulation

A simulation of deformations in a generic antenna was made by using the Finite Element Method (FEM). It was considered in the model that the deformation caused by the structure's self weight is proportional to the square of the height (Cheng, 2009) and some boundary conditions were taking into account. This deformed dish together with white noise added simulate the measurements of a LS and it will be used in the next routines as a test point cloud. Several point cloud densities and sigma for the white noise can be selected, see Fig. 1.

3.2 Best-fit paraboloid estimation

In order to associate the model to a best-fit paraboloid, a Matlab function was written. A least-squares adjustment is computed to estimate six parameters: three translations to transform the origin of the model in the vertex of the paraboloid, two rotations to solve any misalignment between them and the focal length variation, see Fig. 2.

3.3 Best-fit paraboloid comparison

A Matlab function was programmed for doing a comparison between the point cloud and the best fit paraboloid. This function generates a plot output and some statistics of the adjustment, see Fig. 3.

3.4 Best-fit paraboloid estimation

A Matlab function for studying the relative deformations of the dish at different elevation angles was programmed. An interpolation between clouds to a common grid is done for evaluating the differences in that points. Also a summary of the best-fit paraboloid parameters in each angle is done, see Fig. 4.

4 Conclusions and future plans

Comparing the model to different bibliography (Sarti et al., 2009; Artz et al., 2014) these programs seem to work correctly. In the light of these results, it is expected to use these routines with the real data measurements of the scanner that will be used to determine gravitational influences on Yebes antennas. Future plans:

1. To improve the simulation function incorporating more information of the antenna's structure. Currently a very simple and generic model was used because its primary aim was only to simulate the measurements of the laser for developing the rest of the programs.
2. To plan and carry out the survey in the Yebes antennas with the laser scanner over the next months.
3. To contrast these results with the model obtained with the laser scanner data.

References

Artz T, Springer A, Nothnagel A (2014) A complete VLBI delay model for deforming radio telescopes: the Effelsberg case. *J Geod*, 88, 1145–1161, doi:10.1007/s00190-014-0749-1

Cheng J (2009) The Principles of Astronomical Telescope Design. Springer, 634 p.

Clark T A, Thomsen P (1988) Deformations in VLBI Antennas NASA TM-100696, 96 p.

Sarti P, Vittuari L, Abbondanza C (2009) Laser Scanner and Terrestrial Surveying Applied to Gravitational Deformation Monitoring of Large VLBI Telescopes' Primary Reflector. *J Surv Eng*, 135(4):136–148, doi::10.1061/(ASCE)SU.1943-5428.0000008

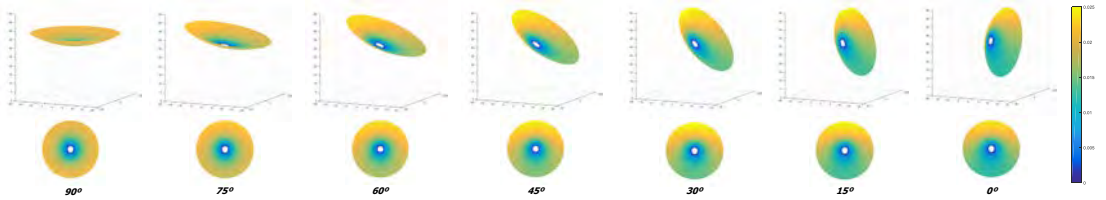

Fig. 1: Simulation of the deformations of the dish at different elevations in 3 and 2 dimensions (along the elevation axis). A 40 m antenna and 15 m focal length was considered, similar to the Yebes antenna. Deformations in meters.

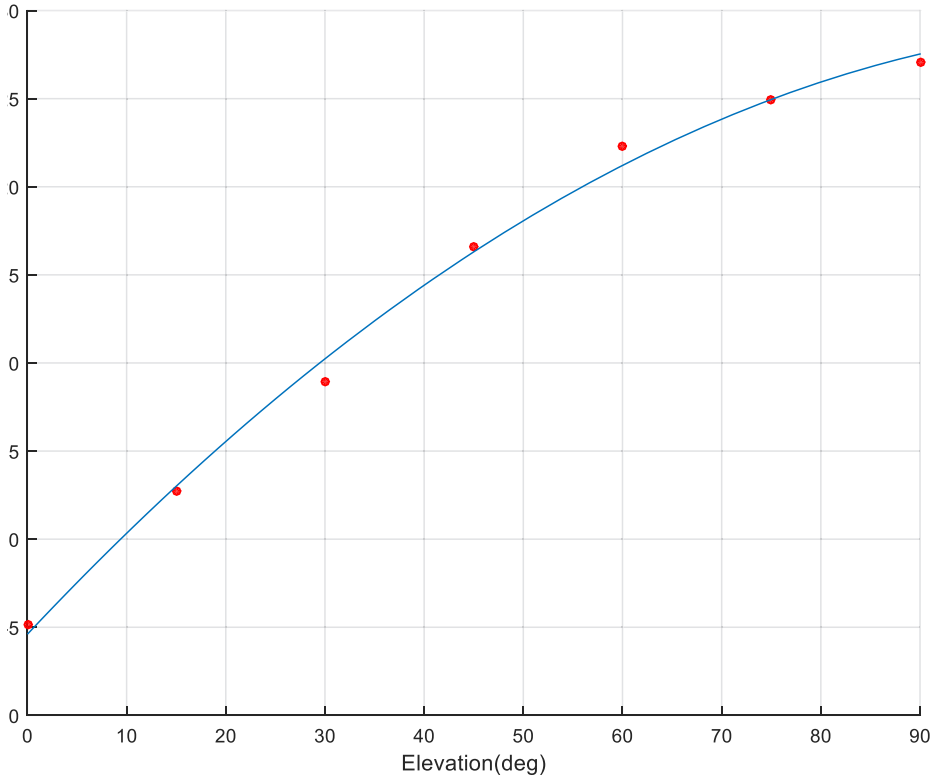

Fig. 2: Focal length variations estimated for the 40 m antenna simulated in different elevations. In red the estimated values, in blue the 2nd order polynomial adjusted.

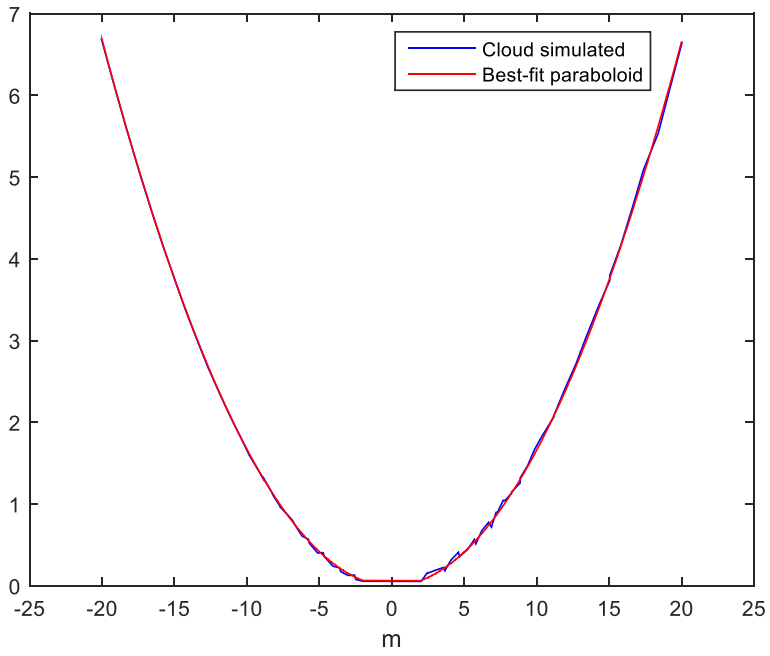

Fig. 3: Transcect of the deformed model and the best-fit paraboloid along the elevation axis at 30 degrees elevation.

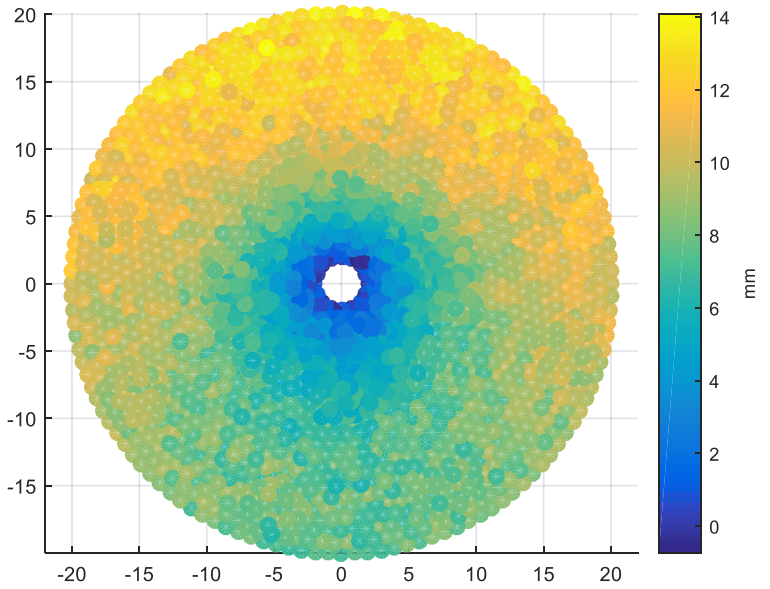

Fig. 4: Relative deformations of the dish between the model at 30º and the one at 90º. Units: X and Y axis in meters, deformations in millimeters.

The Onsala Tide Gauge Station: Experiences From the First Four Years of Operation

G. Elgered, J. Wahlbom, L. Wennerbäck, L. Pettersson, R. Haas

Abstract A tide gauge station was installed at the Onsala Space Observatory in 2015. The official tide gauge station includes several independent senors: one radar and three pneumatic sensors (also referred to as bubblers). The radar and two bubblers are mounted in a well and one bubbler outside the well. Additional sensors such as one laser sensor and three radar sensors have been used during different time periods in order to further assess the quality of the acquired sea level data. Here we compare the four official sensors and the laser sensor which was installed in April 2016. The expected accuracy (one standard deviation) for all of these sensors is approximately 3 mm, according to the datasheet specifications. Results from the first four years of operations are used to assess and estimate the actual accuracies by means of comparisons between the sensors. We observe typical biases over time scales of months of up to 10 mm. Biases are caused by uncertainties of the reference level of the sensor, the density of the water for the bubblers, multipath effects for the radar, and nonlinearities with temperature for the laser. The observed monthly standard deviation between the sensors in the well vary between 2 mm and 6 mm, which is roughly consistent with the data sheet specifications.

Keywords Sea level · Tide gauge station

Gunnar Elgered · Lars Wennerbäck · Lars Pettersson · Rüdiger Haas
Chalmers University of Technology, Onsala Space Observatory, SE-439 92 Onsala, Sweden

Jonas Wahlbom
App-pharm Sweden AB, Skalkarike, Hästängen 2, SE-541 96 Väring, Sweden

(Correspondence: gunnar.elgered@chalmers.se)

Fig. 1: The tide gauge station at the Onsala Space Observatory.

1 Introduction

The location of the Onsala geodetic VLBI telescopes close to the coast line motivates continuous and accurate sea level observations, especially given the recent finding of an accelerating global sea level rise (Nerem et al., 2018). A tide gauge station (Fig. 1) was developed and constructed in house, with advise from the Swedish Meteorological and Hydrological Institute (SMHI). Since the end of June 2015 it is an official site in SMHI's national monitoring network of the sea level.

In Section 2 we describe the individual sensors. In Section 4 we present the sea level observations acquired so far, and in Section 4 we summarise the levelling carried out in order to connect the sea level data to the reference markers at the observatory. Finally, the conclusions are given in Section 5.

2 Sea level sensors

The official tide gauge station has several independent sensors: one radar (Fig. 2) and three pneumatic sensors

Fig. 2: The down-looking radar sensor, Campbell CS476, operating at 26 GHz, mounted at the top in the centre of the well.

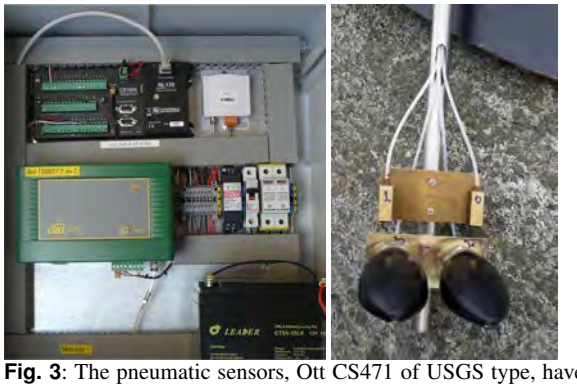

Fig. 3: The pneumatic sensors, Ott CS471 of USGS type, have a compressor (green unit, left) located in the measurement hut. Each compressor is connected to a nozzle (right) via a plastic pipe. Two nozzles are used at the bottom of the well, and one nozzle is located close to the bottom outside of the well. The original black nozzles corroded rapidly in the salty water and were replaced by the ones located just above (manufactured in copper) in October 2016 (see also Fig. 5).

(Fig. 3, also called bubblers). Now in July 2019 there are also one laser (Fig. 4) and two more radar sensors installed in the well for quality assessment of the official data (Fig. 5).

The Campbell CS476 radar is our main sensor and is in the following referred to as CS476. The pneumatic sensors (bubblers) are offered with different accuracy. The type used are by the manufacturer Ott referred to be of USGS type (possibly because they fulfil requests from the United States Geological Survey). The three pneumatic sensors are in the following referred to as USGS1, USGS2, and USGS3. The bubbler USGS3, originally mounted outside the well, was taken out of operation on 17 April, 2019. This sensor is discussed further in the next section.

The laser sensor was installed 29 April 2016 (Börjesson et al., 2016). A reflector is floating in a pipe and its surface is above the actual sea level. The reflector used up to 13 September 2017 was 9 mm above the sea level. Thereafter, a new improved reflector was installed. Its reflecting surface is 11 mm above the sea level. These corrections have been taken into account when presenting the results. For more details about the laser, see Micro-Epsilon (2016).

The VEGA61 radar is similar to the sensors used in the Swedish observational network operated by SMHI.

Fig. 4: The laser sensor is mounted on the inside wall of the well. A reflecting target is floating on the sea surface inside the pipe.

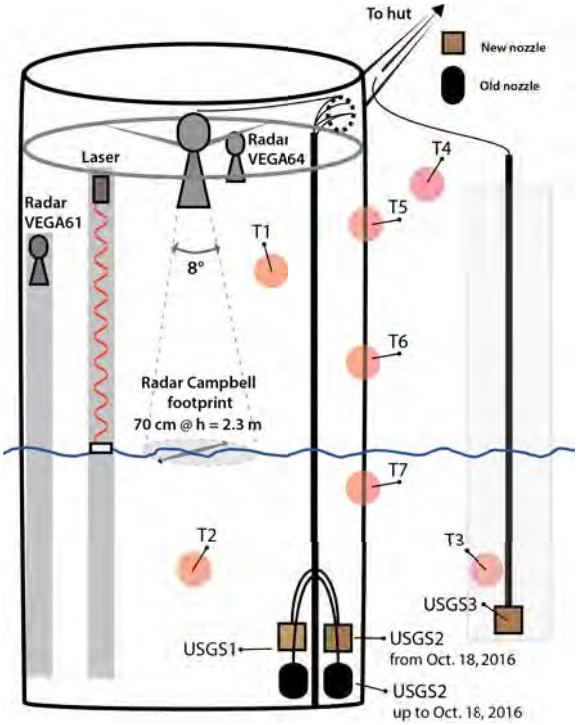

Fig. 5: Design of the tide gauge well. The official sensors are the Campbell radar CS476, mounted at the top in the centre and the three USGS bubblers. The pink circles denote temperature sensors, for the air and the water inside the well (T1 and T2) and outside of the well (T3 ad T4), and in the insulation layer of the well (T5–T7). The inner diameter of the well is 1.4 m. The insulation in the walls is 30 cm and the thickness of the outer concrete rings is 15 cm, resulting in an outer diameter of the well of 2.3 m.

The radar signal is propagating in a vertically mounted circular waveguide. It has been acquiring data since 1 December 2016.

The VEGA64 radar was installed more recently in order to investigate any possible differences due to multipath effects compared to the main sensor, the CS476 radar. The VEGA64 radar is operating in a higher frequency range, 76–80 GHz. It has a lens horn antenna which implies a more narrow beam angle. The full width half power beam width is 3.0° compared to the CS476 that has an 8° beam angle. It has acquired data from 14 September 2018.

The sketch shown in Fig. 5 gives an overall impression of the design and the approximate locations of the sensors and Fig. 6 depicts the present setup of sensors in the well. In the next section we compare the four official sensors and the laser sensor.

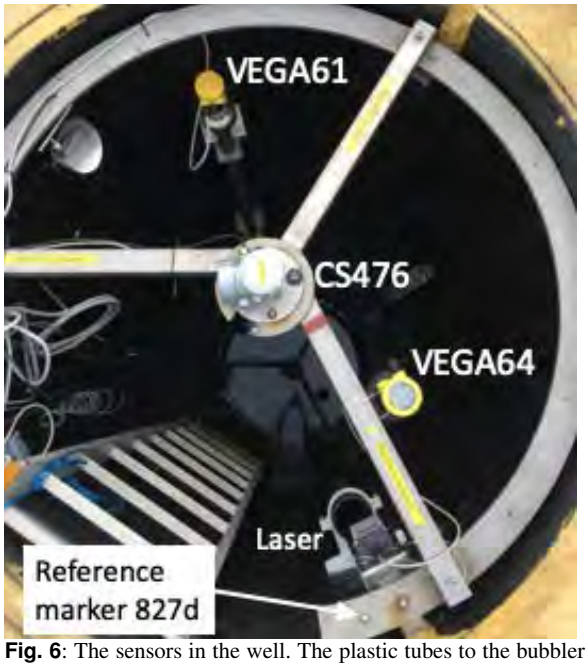

Fig. 6: The sensors in the well. The plastic tubes to the bubbler sensors goes into the water to the left just outside of the photo. The photo is taken on 23 August 2018.

Finally, it shall be mentioned that an additional tide gauge station is operated at the observatory using GNSS technology. It has been acquiring data since 2011. This station is primarily used to investigate different analysis methods in the processing of GNSS data and the results are for example compared to the official station presented in this paper. For more details on the GNSS tide gauge station and its results, see Löfgren et al. (2014); Löfgren and Haas (2014); Hobiger et al. (2014); Strandberg et al. (2016, 2017, 2019).

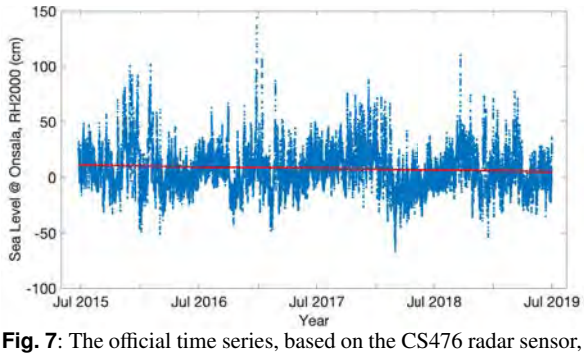

Fig. 7: The official time series, based on the CS476 radar sensor, is available from the SMHI web page. The sea level variations at Onsala are mainly caused by weather, and not by tides. The highest sea level measured so far, approximately +1.5 m, was during the storm Urd in December 2016.

3 Observational results

The official time series, based on the CS476 radar sensor, from the start in June 2015 until the end of June 2019 is shown in Fig. 7. Using these four years of data we estimate a linear trend of −1.4 cm/year (the red line in Fig. 7). The expected long term trend should be close to zero, because both the land uplift as well as the global sea level have been estimated to be slightly above 3 mm/year (BKG, 2018; Nerem et al., 2018). The negative value obtained for this time series is mainly due to the low sea levels observed during the first half of 2018. This illustrates the need for stable long time series of observations in order to assess any changes in climate related parameters. The international standard averaging period to calculate a single data point when monitoring a climate parameter is 30 years. This was decided at a meeting in Warsaw in 1935, at which the directors of most national meteorological institutes took part (Førland et al., 1992).

An example of sea level observations with the radar CS476 and the laser showing the short term variations during the month of December 2018 is presented in Fig. 8. The corresponding differences are shown in Fig. 9. For this month the bias (radar − laser) is 3.8 mm and the standard deviation of the differences is 4.3 mm.

Monthly biases and SDs between the radar and four other sensors have been calculated from samples with the temporal resolution of 1 min and are summarised in Table 1.

Table 1: Monthly biases and standard deviations between the radar sensor and the other sensors

Radar CS476 vs.	Monthly bias (mm)	Monthly standard deviation (mm)
Laser	3 – 4	2 – 5
USGS1	1 – 10	2 – 5
USGS2	1 – 9	2 – 6
USGS3	6 – 14	2 – 14

Biases are caused by uncertainties of the reference level of the sensors, plus the salinity and temperature determining the density of the water for the USGS bubblers, multipath effects for the radar, and an uncertainty of the reference level of the floating reflector for the laser. In terms of their monthly biases it is clear that the laser and radar show superior stability compared to the bubblers.

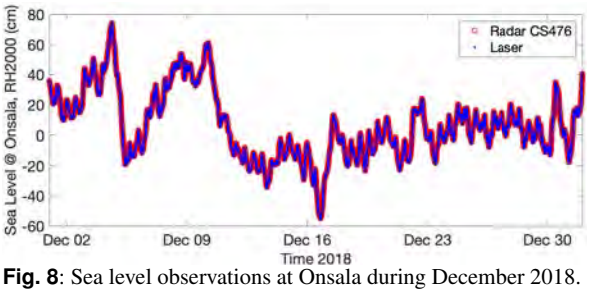

Fig. 8: Sea level observations at Onsala during December 2018.

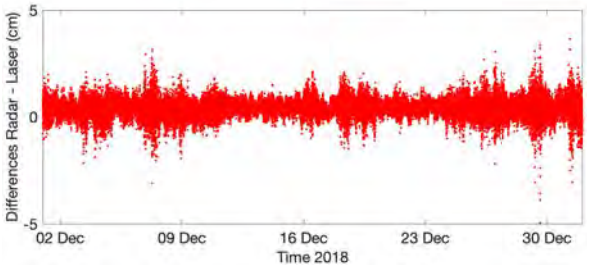

Fig. 9: Time series of the difference between the CS476 radar and the laser sensor.

The USGS3 bubbler, mounted outside the well is expected to show a larger variability given that the well acts as a low-pass filter. However, we have noted, apart from just looking at the SDs, that a systematic negative bias sporadically occurs, compared to the other sensors. We have no obvious explanation for this behaviour and as mentioned above the sensor has been taken out of operation on 17 April, 2019.

4 Vertical control

Given the importance of monitoring the sea level with the highest possible accuracy, levelling of reference markers has been carried out (at least) annually. Fig. 10 depicts the area close to the tide gauge station including the reference markers. In order to illustrate the stability of the tide gauge station the levelling results of the reference marker 827d are summarised in Table 2. This marker is the one most easily accessible, and is therefore the most frequently measured, of the markers located inside the well. We note that the standard deviation of these levelling results is 0.3 mm. The most recent levelling results were documented by Heep (2018).

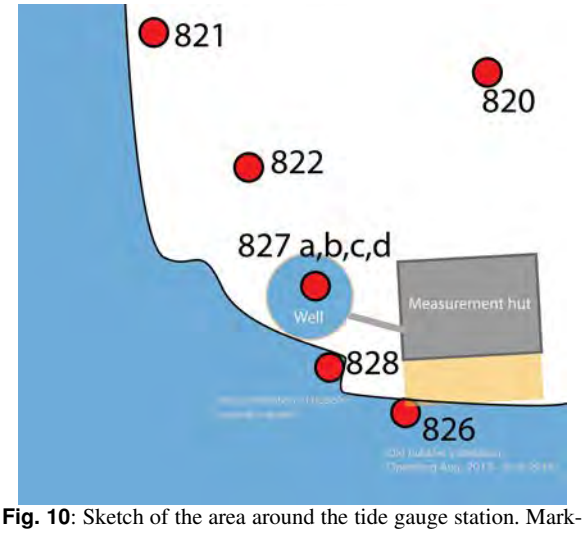

Fig. 10: Sketch of the area around the tide gauge station. Markers 820, 821, and 822 are steel markers mounted in the bedrock. Marker 826 is on the pipe protecting the plastic tube to the nozzle of an old bubbler, taken out of operation in June 2015, markers 827a, b, c, and d are on the upper side of the mount for sensors in the well, and marker 828 is on the bubbler outside the well.

Table 2: The levelling results of reference marker 827d

Date	RH2000 vertical coordinate of 827d (m)
2015-08-13	2.4875
2016-08-05	2.4868
2017-06-01	2.4871
2017-07-26	2.4874
2017-08-11	2.4872
2018-08-23	2.4875

5 Conclusions and outlook

We find that the different sensors roughly perform according to their specifications. The radar and the laser sensors appear to be more stable in terms of long term systematic errors. Therefore, future work will focus on these two sensors, plus the additional two radar sensors installed in the well. A possible development may be that the present primary sensor, the CS476 radar, is replaced by the high frequency VEGA64 radar. However, in order to take such a decision, extensive comparisons between the laser and the different radar sensors must first be carried out.

References

Bundesamt für Kartographie und Geodäsie (BKG) (2018) "VTRF Station Positions & Velocities", http://www.ccivs.bkg.bund.de/EN/Quarterly/VTRF-Results/VTRF-Stations/vtrf-stations_node.html, last access: 15 Nov. 2018.

Börjesson E, Jansson J, von Rosen Johansson C (2016) Test och implementering av en laserbaserad havsnivåmätare (in Swedish), Bachelor Thesis, Dep. of Earth and Space Sciences, Chalmers Univ. of Tech.

Førland E J, Hanssen-Bauer I, Nordli P Ø (1992) New Norwegian climate normals—but has the climate changed? *Norwegian J. Geography*, 46, 83–94, doi::10.1080/00291959208552287

Heep N (2018) Erweiterung des terrestrischen Kontrollnetzes der Twin-Teleskope an der Fundamentalstation Onsala. *Bachelor-Thesis*, Frankfurt Univ, of Applied Sci., Matrikelnummer 1138382.

Hobiger T, Haas R, Löfgren J (2014) GLONASS-R: GNSS reflectometry with a Frequency Division Multiple Access-based satellite navigation system. *Radio Sci.*, 49(4), 271–282, doi:10.1002/2013RS005359

Löfgren J, Haas R, Scherneck H-G (2014) Sea level time series and ocean tide analysis from multipath signals at five GPS sites in different parts of the world. *J Geodyn*, 80, 66–80, doi:10.1016/j.jog.2014.02.012

Löfgren J, Haas R (2014) Sea level measurements using multi-frequency GPS and GLONASS observations. *EURASIP J. Adv. in Signal Proc.*, 2014:50, doi:10.1186/1687-6180-2014-50

Micro-Epsilon, Instruction Manual optoNCDT ILR 1181 / 1182, Micro-Epsilon Messtechnik GmbH & Co. KG, Königbacher Str. 15, 94496 Ortenburg, Germany, http://www.micro-epsilon.se, last access: 21 Sep. 2016.

Nerem R S, Beckley B D, Fasullo J T, et al. (2018) Climate-change—driven accelerated sea-level rise detected in the altimeter era. *PNAS*, 115(9), 122–125, doi:10.1073/pnas.1717312115.

Strandberg J, Hobiger T, Haas R (2016) Improving GNSS-R sea level determination through inverse modeling of SNR data. *Radio Sci.*, 51, 1286–1296, doi:10.1002/2016RS006057

Strandberg J, Hobiger T, Haas R (2017) Sea Ice Detection Using Ground-Based GNSS-R. *IEEE GRSL*, 14(9), 1552–1556, doi:10.1109/LGRS.2017.2722041

Strandberg J, Hobiger T, Haas R (2019) Real-time sea-level monitoring using Kalman filtering of GNSS-R data. *GPS Solutions*, 23:61, doi:10.1007/s10291-019-0851-1

VLBI-GNSS Collocation Survey at the Ishioka VLBI Station

H. Munekane, M. Umei, H. Ueshiba, S. Matsumoto, T. Wakasugi, S. Kurihara

Abstract We conducted a collocation survey campaign in November 2018 to determine a local tie vector between the Ishioka VLBI station and the IGS station ISHI. In order to estimate the VLBI antenna invariant point (IVP), the azimuth and elevation axes were estimated from trajectories of targets installed inside the antenna cabin. The offset between the azimuth and elevation axes was ~ 0.2 mm and the error in the orthogonality of the axes was sufficiently small. Finally, we determined the coordinate of the IVP as the intersection of the axes, and precisely estimated the local tie vector between the Ishioka VLBI station and the IGS station ISHI.

Keywords Local tie vector · VLBI · GNSS

1 Introduction

The International Terrestrial Reference Frame (ITRF) is constructed by a combination of different sets of station coordinates provided by the four space geodetic techniques; Doppler Orbitography by Radiopositioning Integrated by Satellite (DORIS), Global Navigation Satellite System (GNSS), Satellite Laser Ranging (SLR), and Very Long Baseline Interferometry (VLBI). In order to achieve this combination, it is necessary to have relative positions, or local tie vectors, between instruments at a collocation site which has multiple space geodetic techniques.

The Geospatial Information Authority of Japan (GSI) started the construction of the Ishioka geodetic station in 2011. The Ishioka geodetic station has two space geodetic instruments; VLBI and GNSS. The VLBI observation system at the Ishioka geodetic station (Ishimoto et al., 2016) is designed for the next-generation VLBI system called VGOS, which is promoted by the International VLBI service for Geodesy and Astrometry (IVS) . The construction of the VLBI antenna was completed in March 2014, and the station has participated in the international observations since 2015. The GNSS station ISHI has been in operation since 2014, and added to the International GNSS Service (IGS) network in 2018.

The GSI has so far performed VLBI-GNSS collocation surveys at Tsukuba, Shintotsukawa, Aira, and Chichijima station in Japan (Matsuzaka et al., 2002) and contributed to the construction of ITRF. We conducted the collocation survey at the Ishioka geodetic station in November 2018 in order to provide the local tie vector for forthcoming ITRF 2020.

2 Observations

Fig. 1 shows a panoramic view of the Ishioka geodetic station. Four pillars and a VLBI ground marker are installed in the station. The collocation survey was performed using these pillars and the VLBI ground marker for determining the local tie vector between the VLBI antenna invariant point (IVP) and the reference point of the IGS station ISHI. The survey was performed from

Hiroshi Munekane · Michiko Umei · Haruka Ueshiba · Takahiro Wakasugi · Shinobu Kurihara
Geospatial Information Authority of Japan, 1 Kitasato, Tsukuba city, 305-0811 Japan

(Correspondence: munekane-h96nu@mlit.go.jp)

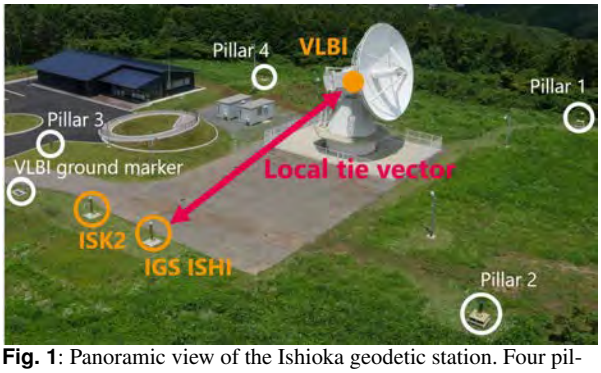

Fig. 1: Panoramic view of the Ishioka geodetic station. Four pillars and a VLBI ground marker are arranged around the VLBI telescope. The IGS station ISHI is installed about 40 m away from the VLBI telescope. ISK2 is also installed as an auxiliary for ISHI.

8th to 22nd November 2018. The details of the survey will be described in the following sections.

2.1 Surveys among pillars/VLBI ground marker

We measured the horizontal angles, vertical angles and spatial distances among the pillars and the VLBI ground marker by a Total Station (TS). Then we carried out leveling surveys between pillars or the VLBI ground maker to determine relative heights. In addition, we conducted GNSS surveys at the pillars 2 and 3, and at a nearby mountain, Mt. Tsukuba in order to measure the orientation angle of the local frame so that one may express the survey results in a geocentric reference frame.

2.2 Surveys between pillars and IGS station

We measured the horizontal angles and spatial distances between pillars and the IGS station. Since the antenna reference point (ARP) of the IGS station is not directly observable, we averaged the horizontal angles to the left and the right side end of the choke ring antenna, and used their mean value in the following calculation. Regarding the distance from the pillars to the IGS station, we first measured a spatial distance from each pillar to the point closest to it on the bottom of the choke ring antenna, and then calculated the distance from the pillars to the ARP using the design value of the antenna. In addition, regarding the height of ARP, we measured the height of a point on the bottom of the antenna with respect to pillars by the leveling surveys, which may be considered as the height of the ARP.

2.3 Determination of the VLBI antenna invariant point (IVP)

The IVP of the VLBI antenna is defined as the intersection of the azimuth and elevation axes. Its position should be determined indirectly since it is not directly observable. For that purpose, we first installed the targets on the cabin wall. Then we observed the targets from a TS installed on cabin base, which does not follow the antenna movement (Fig. 2).

We first carried out measurements for determining the azimuth axis. We set the antenna elevation to zero, and observed four targets while changing the antenna azimuth by 30 degree from 0 to 330 degree (left in Fig. 3). Then we carried out measurements for determining the elevation axes. In order to investigate the dependency of the estimated elevation axes on azimuthal direction, we tentatively estimated the elevation axes at the azimuth of 125 degree and 215 degree. For each antenna azimuth, we observed two targets while changing the antenna elevation by 10 degree from 0 to 90 degree (right in Fig. 3). In total, we obtained 48 target positions for the determination of the azimuth axis and 40 target positions for the determination of the elevation axes. Finally, we carried out TS observations from the TS on the cabin base to the surrounding pillars to determine the positions of the TS.

3 Results

We first calculated coordinates of pillars, the VLBI ground marker, ARP of IGS, and the targets inside the cabin in the local frame with least squares adjustment. Then we fit circles or arcs to the coordinates of the targets to estimate the azimuth and elevation axes. The azimuth axis was estimated as a straight line connecting the center of four circles which correspond to the

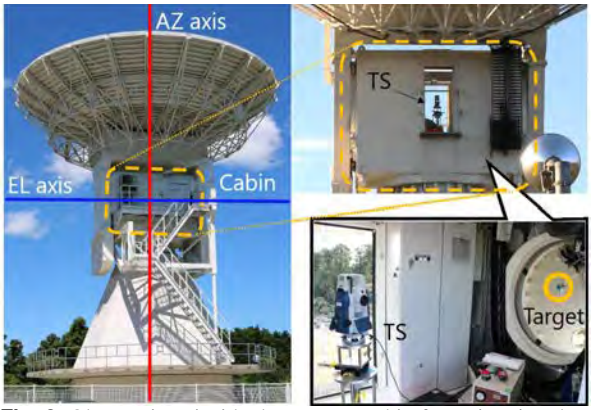

Fig. 2: Observations inside the antenna cabin for estimating the azimuth and elevation axes. The TS was put on the cabin base, which does not follow the antenna movement.

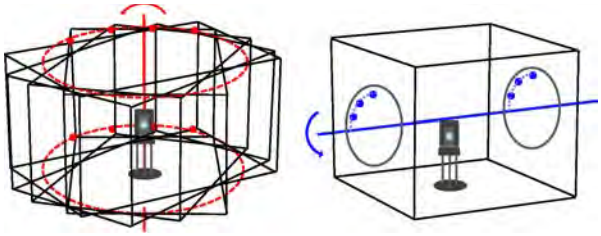

Fig. 3: Observations of the targets on the cabin wall. We observed the targets from the TS while rotating the antenna azimuth (left) and elevation (right).

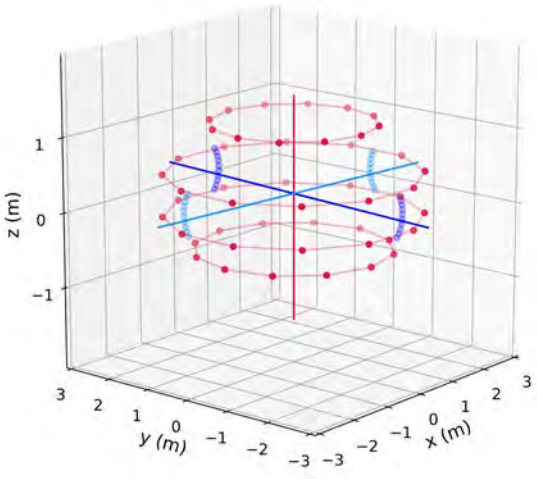

Fig. 4: Red, blue, and light blue dots show the estimated positions of targets with the telescope rotated around the azimuth axis, elevation axis at azimuth of 125 degree, and elevation axis at azimuth of 215 degree, respectively. Red, blue, and light blue lines represent the corresponding axes.

trajectories of four targets. Likewise, the elevation axis was estimated as a straight line connecting the center of two arcs which correspond to the trajectories of two targets. The elevation axes were estimated for azimuth of 125 degree and 215 degree. The estimated azimuth axis and two elevation axes are shown in Fig. 4.

We calculated offsets and angles between the azimuth axis and two elevation axes (Fig. 5). Offsets between the azimuth axis and elevation axes for azimuth of 125 degree and 215 degree were 0.2 mm and 0.1 mm, respectively. The angles between the azimuth axis and two elevation axes were 90.0006 degree and 89.9954 degree, respectively.

Finally, we calculated the local tie vector between the IVP of VLBI antenna and the IGS reference point in the geocentric frame (Table 1). To confirm our calculation, we independently calculated the local tie vector with the adjustment software pyaxis (LINZ, 2015). We found that the differences of the local tie vectors between those by our calculations and those by pyaxis were negligibly small in practical use though they slightly exceed the standard deviations of 0.6 mm, 0.6 mm, and 0.5 mm for x, y, and z component, respectively.

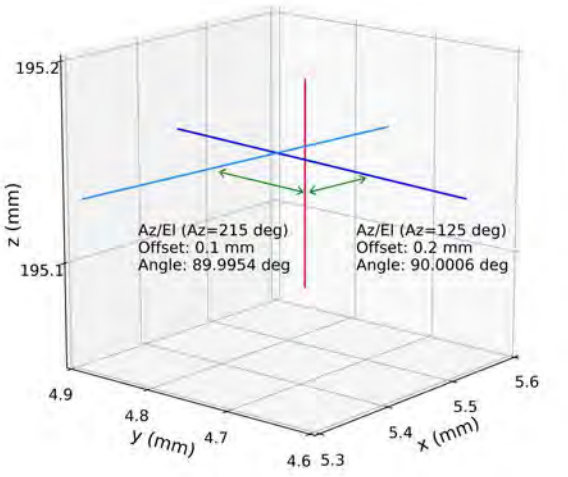

Fig. 5: Offsets and the orthogonality of the axes. Line colors are the same as shown in Fig. 4.

Table 1: The estimated local tie vector between the IVP of the VLBI antenna and the IGS reference point in the geocentric reference frame.

	X (m)	Y (m)	Z (m)	Baseline (m)
IVP → ISHI	−12.7427	10.8578	−37.0948	40.6976
IVP → ISHI (pyaxis)	−12.7408	10.8612	−37.0957	40.6987
Δ	−0.0019	−0.0034	0.0009	−0.0011

4 Summary

We carried out the collocation survey at the Ishioka geodetic station in November 2018. The IVP of the VLBI antenna was determined as the intersection of azimuth and elevation axes, which were estimated by the TS observations of the targets inside the cabin from the cabin base. We found that the Offsets between the azimuth axis and elevation axes are sufficiently small, and the orthogonality of the axes hold to a high precision. Then, we successfully estimated the local tie vector between VLBI and GNSS reference points with sufficient accuracy. In order to investigate the seasonal variation of the local tie vector, we will conduct the same survey in a different season in 2019.

Acknowledgements We would like to thank Land Information New Zealand (LINZ) for making the pyaxis software publicly available (https://github.com/linz/python-linz-pyaxis). We acknowledge Dr. Chris Crook at LINZ for his assistance for the use of the software.

References

Ishimoto M, Umei M, Wakasugi T, et al. (2016) Status on the Ishioka Geodetic Observing Station. *IVS NICT-TDC News*, 36, 9–12

Land Information New Zealand 2015 - Warkworth Observatory Local Tie Survey *Land Information New Zealand Record*, A1387321

Matsuzaka S, Hatanaka Y, Nemoto K, et al. (2002) VLBI-GPS Collocation Method at Geographical Survey Institute. In: N. R. Vandenberg, K. D. Baver (eds.): *IVS 2002 General Meeting Proceedings*, NASA/CP-2002-210002, 96–100

Progress and Current Status of the VGOS Project at the Metsähovi Geodetic Research Station

N. Zubko, J. Näränen, N. Kareinen, J. Eskelinen, M. Poutanen

Abstract A new VGOS radio telescope has been installed during the summer 2018 at Metsähovi Geodetic Research Station, Finland. The manufacturer has commissioned the telescope in 2018–2019. Work on the antenna control software and communication with the VLBI Field System is underway. Integration of the signal chain components is moving forward. A broadband receiver with a quad-ridge feed horn (QRFH) operating at frequency range of 2.4 – 14.1 GHz and filtering and pre-amplifier modules have been manufactured by IGN-Yebes technology development center. They are expected to be delivered to Metsähovi during the fall of 2019. The DBBC3 and Flexbuff recording system has been installed and partly tested. Integration of the signal chain components has been planned for 2019–2020. Test observations of the complete VGOS telescope system are expected by the end of 2020.

Keywords VGOS · Telescope · Hardware

1 Introduction

The new radio telescope dedicated for the VLBI Global Observing System (VGOS) has been installed at the Metsähovi Geodetic Research Station (Fig. 1). Metsähovi station is a key infrastructure of the Finnish Geospatial Research Institute (FGI) and one of the core sites of the Global Geodetic Observing System (GGOS). It is located in Southern Finland (60.2^{o} N, 24.4^{o} E).

Metsähovi is one of the few geodetic stations that has all major geodetic observing instruments co-located. These include satellite laser ranging (SLR), very long baseline interferometry (VLBI), global navigation satellite systems (GNSS), superconducting and absolute gravimeters, and a DORIS beacon. The

Fig. 1: The VGOS telescope at Metsähovi Geodetic Research Station.

Natalyia Zubko · Juri Näränen · Niko Kareinen · J. Eskelinen · Markku Poutanen
Finnish Geospatial Research Institute (FGI), National Land Survey of Finland, Geodeetinrinne 2, FI-02430, Masala, Finland

(Correspondence: nataliya.zubko@nls.fi)

Ministry of Agriculture and Forestry has allocated a special funding for the renewal of Metsähovi instruments and infrastructure during 2012–2018.

The VGOS project in Finland has been started in the beginning of 2016. It is funded by the National Land Survey of Finland together with the Finnish Ministry of Forestry and Agriculture.

2 Telescope

The 13.2 m parabolic dish antenna has been designed by MT Mechatronics GmbH. The main technical characteristics of the telescope are described in the Table 1.

The telescope arrived to the site in the middle of June 2018 and the work on telescope assembling continued until end of the August 2018. Fig. 2 shows some phases of assembling the telescope. The manufacturer has commissioned and evaluated telescope performances during 2018–2019. A site acceptance has been performed in June 2019. We plan to start our own telescope tests together with receiver after its arrival and installation in autumn 2019.

The design of the telescope also includes a steel pedestal, making it different from other telescopes produced by the same manufacturer (e.g. telescopes installed at Onsala or Yebes observatories). Special measures were taken to provide temperature stability and its monitoring in the pedestal to ensure the reference point stability. A system for constant temperature and humidity control along the pedestal has been installed. The pedestal's temperature is monitored with 12 temperature sensors. In the future we plan to use sensor's data for the characterisation of the system.

Table 1: Telescope technical characteristics

Title	Description
Antenna mount	Standard azimuth-elevation type
Reflector optics	Cassegrain, ring focus
Diameter of the main reflector	13.2 m
Surf. accuracy of the main refl.	< 0.3 mm rms
Surf. accuracy of the subrefl.	< 0.1 mm rms
Antenna motion	
Velocity in Az axis	12 deg/s
Velocity in El axis	6 deg/s
Acceleration in Az axis	2.5 deg/s^2
Acceleration in El axis	2.5 deg/s^2

Cable wrap is placed on the ground level of the pedestal. The Antenna Control Unit together with the power cabinet are located on the first level (Fig. 3).

3 Signal chain

The telescope will be equipped with a broadband receiver manufactured by IGN-Yebes technology development center. Estimated site installation time is October 2019. The receiver has quad-ridge feed horn (QRFH), designed to measure both linear polarisations at frequency range of 2.1 – 14.1 GHz. The signal from the receiver will pass trough the filtering and pre-amplifier modules, each polarisation component is divided to low (2.1 – 5.6 GHz) and high (3.6 – 14.1 GHz) frequency bands. Then the signal is transferred over fiber link to the backend located in the instrumentation room of the station main building. Before signal digitization it will pass through the filter bank module, where the signal will be divided to 5 channels (both vertical and horizontal polarisation components) according to the Table 2.

Table 2: The selected frequencies for the filtering module

IF1 GHz	IF2 GHz	IF3 GHz	IF4 GHz	IF5 GHz
2.1 – 4.0	3.6 – 7.6	4.6 – 8.6	7.6 – 11.6	10.6 – 14.1

The digital backend is DBBC3, produced by HatLab Tuccari et al. (2017). It has been installed in instrumentation room and its testing is planned after the receiver installation. A Flexbuff system will be used for signal recording.

An upgrade to internet fiber connection is planned, so data can be e-transferred with high speed to the correlator.

4 Future plans

The integration and testing of the complete signal chain together with telescope is planned for the 2020. After successful test of our complete system we expect to join VGOS network observations in test mode.

Fig. 2: Telescope construction.

Fig. 3: First level of the pedestal with ACU and other equipment.

References

Tuccari G, Alef W, Wunderlich M, et al. (2017) DBBC3: The new Flexible, Wide-band VLBI Backend. In: R. Haas, G. Elgered (eds.): *Proc. 23rd EVGA Working Meeting*, 78–80

Centralized Monitoring of VLBI Antennas for Seamless Auxiliary Data

A. Neidhardt, E. Barbieri, J. Bachem, M. Schönberger, M. S. Hameed, L. Carlin, R. Aktas, S. Jingyao, A. Szomoru

Abstract Twelve institutes from eight different countries have teamed up in the JUMPING JIVE project, currently financed by the Horizon 2020 Framework Program of the EU for four years. The project is led by JIVE, the Joint Institute for VLBI ERIC, located in Dwingeloo (the Netherlands). The Technical University of Munich with the Geodetic Observatory Wettzell participates in this project integrating monitoring systems for global VLBI interfaces. Existing techniques were analyzed and compared. A test setup was implemented selecting the best-rated solution. It was installed at the Wettzell observatory. The current status of the monitoring task with a focus on gathering seamless auxiliary data is described here, which is also a benefit for the IVS Task Force of Seamless Auxiliary Data.

Keywords Monitoring · Seamless auxiliary data

Alexander Neidhardt
FESG Wettzell, TU of Munich, Geodetic Observatory Wettzell, Sackenrieder Str. 25, DE-93444 Bad Kötzting, Germany

E. Barbieri · M. S. Hameed · L. Carlin · R. Aktas · S. Jingyao
FESG, TU of Munich, Arcisstr. 21, DE-80333 Munich, Germany

J. Bachem · M. Schönberger
BKG, Geodetic Observatory Wettzell, Sackenrieder Str. 25, DE-93444 Bad Kötzting, Germany

Arpad Szomoru
Joint Institute for VLBI ERIC, Oude Hoogeveensedijk 4, NL-7991 PD Dwingeloo, The Netherlands

(Correspondence: neidhardt@fs.wettzell.de)

1 Introduction

In 2014, the IVS task force for seamless auxiliary data was founded during the IVS General Meeting in Shanghai. Goal of this group is to define data which are currently available only in session log files but would be permanently required for analysis. But before the selection of data could be done, a framework had to be created to communicate, store and archive such data on a centralized monitoring system. As task 8 of project "Jumping JIVE" (see JIVE, 2019) about centralized real-time monitoring of the EVN supported by the Technical University of Munich ideally fed also for seamless auxiliary data, the infrastructure was extended. A well tested version is now available and under test with the O'Higgins antenna (Antarctica), the antennas of the Wettzell observatory (Germany), and partly with AGGO in La Plata (Argentinia).

2 Technical implementation of the monitoring system

The monitoring system consists of two data streams: one uses dynamical web pages from a web server on the NASA Field System PC (see other paper), the other is based on mechanisms of the professional monitoring system ZABBIX. Sites can individually decide which streams they want to support.

If the general data set from the NASA Field System is supported (offering 110 parameters from the NASA Field System shared memory in real-time), the station staff must install and configure the e-RemoteCtrl server using predefined HTML templates dynamically filled by the server. No additional program, like a web

server, is required. It only supports the passive monitoring without any commanding interface. The configuration (e.g., port or update rates) can be made individually at each site. All template files can be adapted by station staff to prepare them for individual requirements, as long as the standardized tags are used which identify the value items. The dynamical updating of the web pages is then done by the server. It is suggested that all antennas at least support this stream.

If additional system parameters should be monitored, the use of ZABBIX agents and a proxy server is suggested. Zabbix is a monitoring platform supporting the collecting and presentation of monitoring data (Zabbix, 2018). A ZABBIX agent runs on different platforms and collects data such as CPU, memory, disk and network access (Zabbix, 2019). Agents can even run on platforms with limited resources. Agents can be active, getting a list of value items to be monitored and sending the values actively to a central server. They can also be configured to be passively waiting for value requests and replying with current data.

ZABBIX agents already include a set of items, like network status with number of transmitted bytes or errors, CPU load, memory use, disk volumes, process status, file information, text logs, or operating system details.

A ZABBIX proxy acts like a central monitoring server collecting data from different ZABBIX agents. Data are buffered locally to be requested by a ZABBIX server at the monitoring center. ZABBIX proxies are the key technology to distribute data from an antenna site to a central monitoring archive.

Additionally, proxies can use SNMP calls to request data from specific devices, like UPS, rack coolers, and so on. Therefore, ZABBIX offers a huge set of possibilities already include.

3 Connection to a seamless auxiliary data archive

Currently, the first productive system for a seamless auxiliary data archive is installed at the Wettzell observatory. Due to security restrictions of the different sites, only direct one-to-one Secure Shell (SSH) connections between a site-specific PC and the central monitoring server e.g. at Wettzell observatory are allowed. Stations get an SSH key file and an individual user account.

Additionally, a Linux script ”autossh_run.sh” is offered, which establishes a secure SSH connection between the site-specific PC (e.g. the NASA Field System PC or a separate monitoring PC) and the ZABBIX server at Wettzell using the SSH key (see Fig. 3). The script also keeps the connection alive or reestablishes it after a blackout or failure situation. The SSH communication is used for the creation of reverse tunnels from the ZABBIX server to a site-specific PC which are used for the transfer of monitoring data. Each site is allocated with an individual HTTP port and an individual ZABBIX port as end-point of the tunnel on the ZABBIX server.

On the central monitoring server itself, scripts fetch a copy of the web pages from the NASA Field System PC via the HTTP-tunnel (usually each second) and extract all related values from the pages using the predefined, standardized tags. If individual, site-specific tags are used, specific scripts can be used. The programs send the extracted values dynamically to the ZABBIX server and into the database. The ZABBIX server also uses the site-specific proxy via the ZABBIX port to request additional monitoring data. To simplify the monitoring of additional data, station staff must create

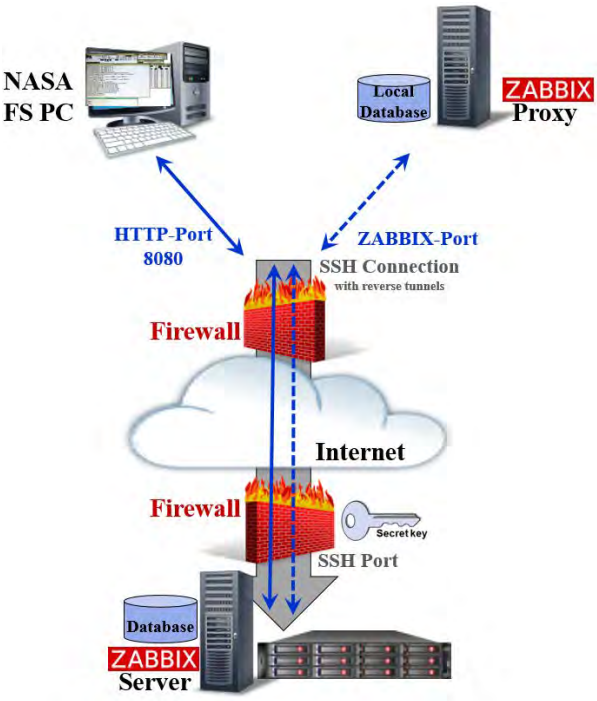

Fig. 1: Connecting site monitoring to a centralized monitoring archive.

own templates for ZABBIX hosts (monitoring control points), so that hosts and corresponding presentations can directly be uploaded to the central ZABBIX server. The timing of these requests is defined via the ZABBIX server web page.

An additional script "ZabbixAPI.py" on the server machine reads required seamless auxiliary data from the ZABBIX database and copies them into daily files (one per item). These files are organized with directories based on year, month, antenna name, and sensor name. Current tests extract temperature, humidity, and pressure. The internal structure of each file is very simple. It contains the ZABBIX item identifier which should never change, UTC clock in Unix time, UTC clock in regular UTC, and the value for that time stamp (see Fig. 2).

ITEM	CLOCK	DATETIME (UTC)	VALUE
26733	1551996101	2019-03-07 22:01:41	5.8000
26733	1551995801	2019-03-07 21:56:41	6.1000
26733	1551995501	2019-03-07 21:51:41	5.9000
26733	1551995201	2019-03-07 21:46:41	5.7000
26733	1551994902	2019-03-07 21:41:42	5.7000
26733	1551994602	2019-03-07 21:36:42	5.8000
26733	1551994301	2019-03-07 21:31:41	5.6000
26733	1551994002	2019-03-07 21:26:42	5.6000
26733	1551993700	2019-03-07 21:21:40	5.5000
26733	1551993401	2019-03-07 21:16:41	5.5000

Fig. 2: Extracted seamless, auxiliary data of one sensor.

4 Using the seamless auxiliary data archive

To use data from the archive, a user account and a web page account is necessary. It can be requested from the administrator of the archive. The web page account can be used to access the ZABBIX web pages (see Fig. 3). They offer plots, charts and screens with historic data for the last three month. The idea is to offer a fast way for plotting and diagnosing specific system situations and behavior.

The user account can be used to download files archived on the file system. The idea behind is to offer a simple way to get a whole collection of data for a longer time period for analysis.

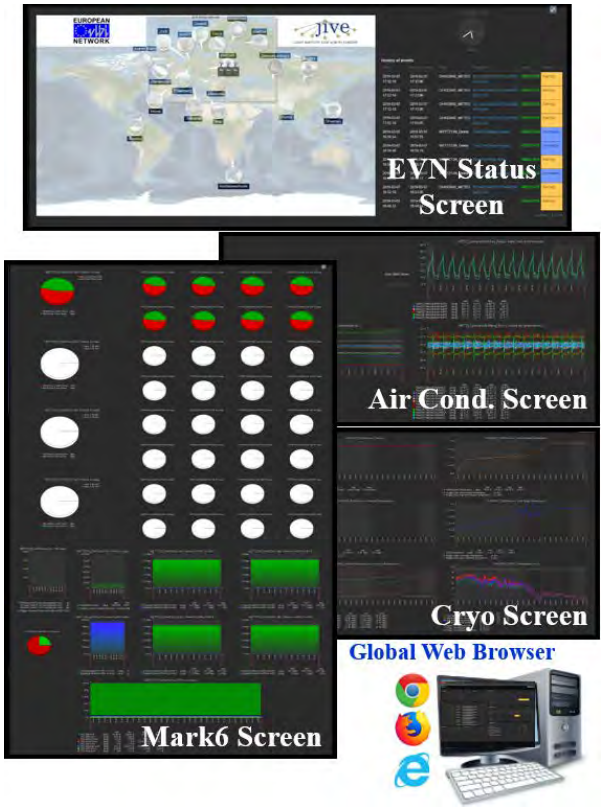

Fig. 3: ZABBIX web interface to seamless auxiliary data archive.

5 Joining and supporting the seamless auxiliary data archive

A first technical solution for continuous data acquisition is now available with the system described. Therefore, both antennas and analysts should now start to join and support the archive.

On the one hand, stations should install at least the e-RemoteCtrl software and the SSH-communication to send in data in real-time. If additional sites will participate, developers and administrators can test the system and communication under different circumstances over world area networks. On the other hand, analysis centers should discuss requirements to define specifications especially about:

- which parameters are required for analysis
- which time intervals are required
- which format is required in best case
- which stations can and will participate
- which station log books with meta-data are useful
- ...

Any support is welcome!

6 Conclusion and outlook

The system is under test with the Wettzell antennas on a final productive server. There is a continuous improvement because different computer network situations lead to different issues. The idea is now to motivate antenna sites and analysts to participate.

Acknowledgements This project has received funding from the European Union's Horizon 2020 research and innovation programme under grant agreement No 730884 - JUMPING JIVE.

References

JIVE (2019) JUMPING JIVE https://jive.eu/jumping-jive, Download 2019-07-15

Zabbix LLC (2018) The Ultimate Enterprise - class Monitoring Platform https://www.zabbix.com/, Download 2018-09-13

Zabbix LLC (2019) Zabbix Agent https://www.zabbix.com/zabbix_agent, Download 2019-07-15

Remote Access to the NASA Field System via Web Browser

A. Neidhardt

Abstract Remote control offers advantages for operation of VLBI radio telescopes. Night shifts and weekend shifts can be operated remotely. Engineers win the ability to support student operators or fix failure situations from home. Operation centers can monitor important health states. Using the remote control software "e-RemoteCtrl" for the NASA Field System, remote control and attendance have been possible for years. During the past years, "e-RemoteCtrl" was extended with a rudimentary, integrated web server. Therefore, operators are now able to access the Field System parameters via web browser. 110 parameters are accessible and can be extended with individual station-specific values.

Keywords Remote access · Operation · Web server

1 Introduction

A new browser-based access to the NASA Field System was shown at the IVS General Meeting in Longyearbyen, Spitsbergen, Norway. Since then, the software has been continuously updated and bugs were fixed. Currently, tests are ongoing to use it for O'Higgins, Antarctica and AGGO in La Plata, Argentinia.

Alexander Neidhardt
FESG Wettzell, TU of Munich, Geodetic Observatory Wettzell, Sackenrieder Str. 25, DE-93444 Bad Kötzting, Germany

(Correspondence: neidhardt@fs.wettzell.de)

2 Current version of web front-end

The browser-based monitoring uses the e-RemoteCtrl environment developed during the NEXPReS project funded by the European Union (see Ettl et al., 2012; Neidhardt, 2017). The original remote access is extended with an elementary web server thread which is part of e-RemoteCtrl. It just supports the needs of remote monitoring of Field System data. It reads template files and dynamically replaces specific tags with corresponding data. The server behavior can be adapted by changing the configuration file.

The web pages can be used with a standard web browser (tested are Chrome, Firefox, and Internet Explorer) all over the local network when connecting to the HTTP port of the e-RemoteCtrl server on the NASA Field System PC. All pages are automatically updated according to a predefined timing.

The following web pages are currently supported:

- System Status Monitor
- Mark5 Remaining Capacity
- System Temperatures
- Log
- Webcam (requires correct settings in the configuration file)
- Antenna (requires adaption of the e-RemoteCtrl-specific station code)
- Station Monitoring (requires regular updates of station-specific HTML file)
- Phase Cal Monitoring (for Mark4 systems)

Standard settings offer a web monitoring port 8080. A controlling port 8081 is under development. One can get the latest release of the software from Wettzell observatory. It also supports the IVS task force for seamless auxiliary data (see separate paper). Secured Inter-

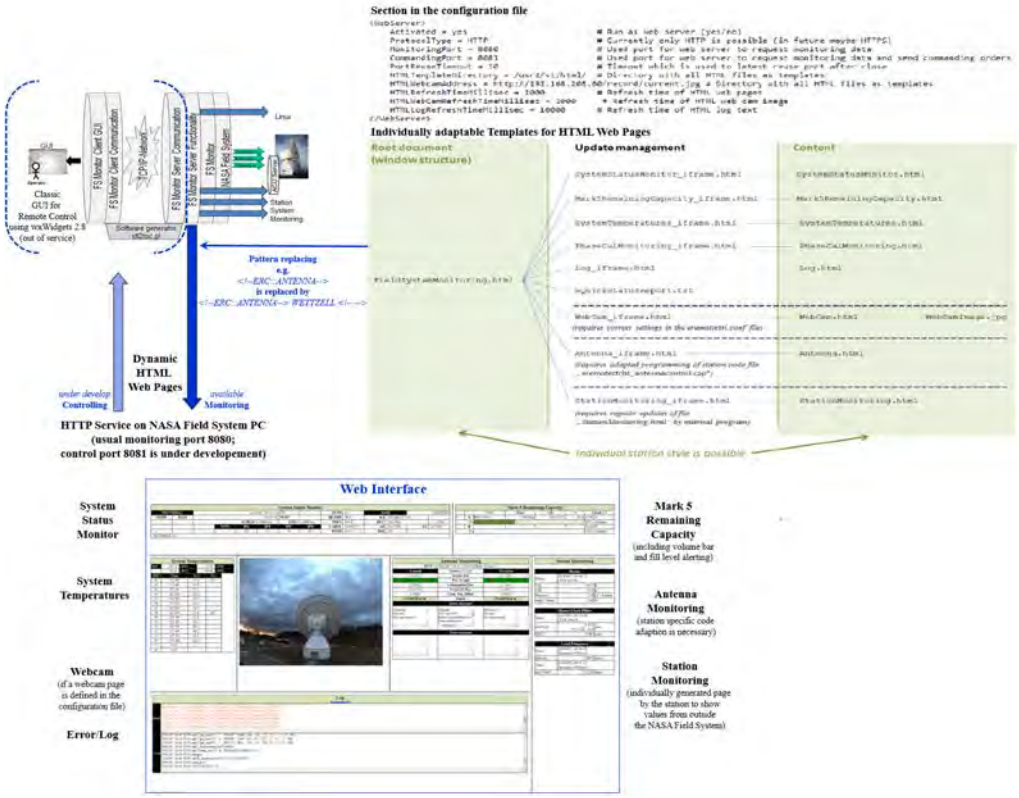

Fig. 1: Web-based extension of e-RemoteCtrl software and corresponding web front-end.

net access via HTTPS from all over the world is additionally supported using a centralized monitoring infrastructure currently located at Wettzell observatory (see separate paper).

Fig. 1 shows an overview of the new web-based access.

3 New elements of the front-end

Keeping the general structure and also the pure, elementary HTML with only some Javascript sections, some extensions were made. The Mark5 Remaining Capacity frame now shows a volume bar graphically presents the fill state of the modules. It changes from green to red if a fill state of more then 97 percent is reached and directly works as a notification. The Phase Cal Monitoring frame is not anymore part of the shown elements in the standard installation because it is just available for older Mark4 systems or systems supporting that feature in the NASA Field System.

Additionally, a demonstration of the Station Monitoring frame was created at the 20m antenna of the Wettzell observatory. A shell script fetches station-specific monitoring data, like dewar information, frequency offsets between maser or local time and frequency distributors and some master clocks, and counter values for GPS minus fmout and Mark5 frequency delays. The shell script is activated as a cronjob each minute, reads all data and echos corresponding HTML structures to the Station Monitoring web page. The shell script also interprets values against trigger levels and colorizes such values with color codes if they are out of defined limits. Each antenna must create and update its own Station Monitoring page. It can also be used for antenna monitoring data if the station code of e-RemoteCtrl should not be programmed.

For further processing on centralized system monitoring servers, individual values in the station-specific section should be tagged with characterizing identifiers in the same style as the official values.

Very useful is the already existing classification of NASA Field System errors with different color codes to

separate between warnings and real errors in the Log section. Warnings in this case classify situations with reduced data quality. Errors are issues with no or broken data recordings. The severity level can be defined in the configuration file of e-RemoteCtrl.

4 Conclusion and outlook

The current web interface is permanently used by operators of the VLBI telescopes of the Wettzell observatory. Web pages are also accessible from the Internet as copies on a centralized monitoring server offering a regular web browser without direct access to the individual NASA Field System PC. Current student project at the Technical University of Munich implement a more sophisticated version of the web pages especially for mobile devices.

References

Ettl M, Neidhardt A, Schönberger M, et al. (2012) e-RemoteCtrl: Concepts for VLBI Station Control as Part of NEXPReS; In: D. Behrend, K. D. Baver (eds.): *IVS 2012 General Meeting Proceedings*, NASA/CP-2012-217504, 128–132

Neidhardt A (2017) Applied Computer Science for GGOS Observatories. Communication, Coordination and Automation of Future Geodetic Infrastructures. *Springer International Publishing Switzerland*, ISBN 978-3-319-40137-9.

Space Low-Frequency Radio Observatory and the Earth-Moon VLBI Experiment

W. Zheng, T. An, J. Zhang, L. Liu

Abstract A Space Low-Frequency Radio Observatory project is proposed. It aims at high resolution observations of the compact radio sources, e.g. black hole, pulsar, exoplanets, etc. The project plans to send two 30 meter-diameter radio telescopes to the earth elliptical orbit. The space telescopes could work together with the earth-based VLBI (Very Long Baseline Interferometry) network, Square Kilometre Array (SKA) and Five-hundred-meter Aperture Spherical radio Telescope (FAST) to achieve high resolution and sensitivity. This paper describes the general mission concept, the technique parameters and the operational modes. The major scientific objectives cover broad astronomical fields. It offers astronomers unique opportunities to make revolutionary discoveries in the field of exoplanets, pulsars, gravitational wave electromagnetic counterparts, as well as probing the evolutionary history of the Universe. The unprecedented high resolution enables the accurate astrometry, allowing for supplying precise localization of pulsars, FRBs (Fast Radio Bursts), GRBs (Gamma Ray Bursts) at milliarcsecond (mas) level. In the subsequent China's Lunar Exploration Project, there will be a chance of the Earth-moon VLBI experiment. It is possible to place the space telescope in the lunar orbit or on the moon surface in the future.

Keywords Space low-frequency radio observatory · Space VLBI · Earth-Moon VLBI experiment

Weimin Zheng · Tao An · Juan Zhang · Lei Liu
Shanghai Astronomical Observatory, Chinese Academy of Sciences, Shanghai 200030, China

(Correspondence: zhwm@shao.ac.cn)

1 Introduction

The limitation of the ground VLBI angular resolution is restricted by the Earth diameter. Given the same frequency, to get the higher angular resolution, Space VLBI (SVLBI) is unique choice. SVLBI is a technique in which an array of space radio telescopes or an array of ground radio telescopes observes a source in conjunction with one or more orbiting radio telescopes (Ulvestad, 1999). It can employ Space-Earth baselines or Space-Space ones to get the better *uv* coverage and higher angular resolution. After the first generation SVLBI projects of VLBI Space Observatory Program (VSOP) and RadioAstron, there are considerations of the next generation SVLBI with more space telescopes, more big space antennas to get the better *uv* coverage and sensitivity. The observation frequency is more focused on millimeter band and cm-dm band or even lower (Gurvits, 2019).

The earth-based Chinese VLBI Network (CVN) plan to extend to the space in the future and there are several proposals. One proposal is the Space Low-Frequency Radio Observatory, which is proposed to image the fine structure of compact celestial objects such as black hole, pulsar and so on. It offers astronomers unique opportunities to make revolutionary discoveries in exoplanets, pulsars, gravitational wave electromagnetic counterparts, and to probe the evolutionary history of the Universe. The unprecedented high resolution enables the accurate astrometry, allowing for supplying precise localization of pulsars, FRBs, GRBs at mas level. The mission plans to launch two 30 meter-diameter radio telescopes into an earth elliptical orbit, and works together with the earth-based VLBI network, Square Kilometre Array (SKA) and Five-hundred-meter Aperture Spherical

radio Telescope (FAST) to get very high resolution and very high sensitivity. The low frequency observatory will carry out observation in radio band from 30 MHz to 1.7 GHz. In the subsequent China's Lunar Exploration Project (CLEP), there will be a chance of the Earth-moon VLBI experiment, using the antenna of the lunar orbit Tracking and Data Relay Satellite (TDRS) to construct the first Earth moon space VLBI experimental system. Because the Earth-moon VLBI baseline is over 300 km, the experiments of astrometry, astrophysics and the deep-space tracking will be carried out. After this, a 10 m level radio telescope is planned to be constructed on the moon surface in the future by the astronaut.

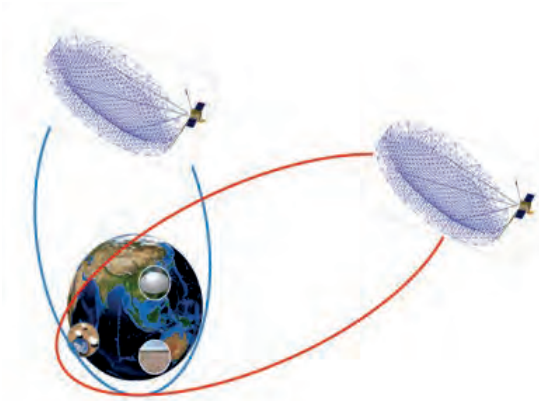

Fig. 1: Space Low-Frequency Radio Observatory with two 30 meter parabolic antennas.

2 Space Low-Frequency Radio Observatory

Over the past half a century, SVLBI has unique applications in high-resolution imaging of fine structure of astronomical objects and high-precision astrometry, owing to the key long space-Earth or space-space baselines beyond the Earth's diameter. China has been actively involved in the development of space VLBI in recent years.

Supported by the Strategic Priority Program on Space Science, CAS, the researches of the space mm-wavelength VLBI array (SMVA) has been carried out since 2012. SMVA, the long mm-wavelength space VLBI including two 10 m space telescopes working at frequencies up to 43 GHz. These two telescopes will obtain observations together with ground telescopes to achieve a highest resolution of 20 micro-arcseconds (μas). The main motivation is to obtain a better understanding of AGN (Active Galactic Nuclei) jet physics and the emission structure around the supermassive black holes (SMBHs) (Hong et al., 2019). Despite important progress, some technical challenges in the area of space millimeter waves remain difficult to overcome in the short term.

Because many unique scientific studies can be done in the low frequency, including studies of the early Universe and cosmological structure formation, directly resolving the SMBH binaries, precise positioning and distance measurements of pulsars and other transients, etc. The suitable space environment is beneficial to low-frequency space radio research and technologies, low frequencies are easier to achieve than high frequencies.

With the completion of Five hundred meter Aperture Spherical Telescope (FAST) and the imminent start of the Square Kilometre Array phase1 (SKA1), we have entered a new era. The establishment of a generalized space low-frequency space radio observatory can achieve high sensitivity and high resolution in both low-frequency bands with the help of large ground-based low-frequency telescopes such as FAST, SKA, GBT (Green Bank Telescope) and space VLBI technology.

The Space Low-Frequency Radio Observatory (SLRO) involves launching dual space telescopes with diameters of 30 m into large elliptical orbits with heights between 2,000 km and 90,000 km, working with FAST, SKA, GBT, it will allow imaging of the ultra-low frequency radio sky at unprecedented high resolutions (0.4 mas at 1.67 GHz and 20 mas at 30 MHz) and with high sensitivity at the sub-mJy level (An et al., 2019).

2.1 Major scientific goals

Compared with previous space VLBI program, the baseline sensitivity of the present Space VLBI mission increases by a factor of 10 or higher owing to adding the newly constructed giant ground telescopes, (e.g., FAST, SKA1), and the resolution is 10 times higher than ground-only VLBI network below L band. The combination of two space telescopes significantly im-

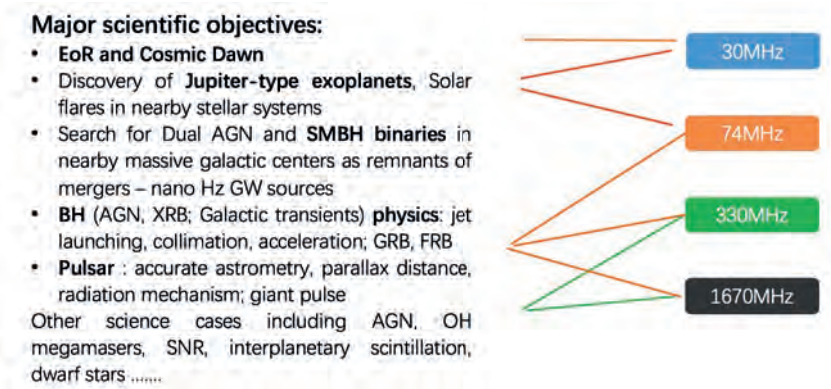

Fig. 2: Major scientific goals and their corresponding observation frequencies.

proves the *uv* coverage on space-ground baselines, and thus increases the image performance. We expect to detect weak and compact population of Galactic (e.g., radio stars, pulsars) and extragalactic radio sources (e.g., radio quiet AGN) which are not well known yet. The space VLBI at the 30-300MHz frequency range will open a new window to observe the radio emission from Jovian-type exoplanets, marking an important step in exoplanet studies, and also offers an opportunity to observe the total power spectrum of EoR and Cosmic Dawn. The Major scientific goals and their corresponding observation frequencies are listed in Fig. 2.

2.2 Mission concept

The space low frequency radio observatory consists of two space radio telescopes each equipped with a 30 meter antennas. The main parameters of the mission are listed in Tab. 1. The observatory will carry out space-ground, space-space VLBI and single dish space based observations. Besides the space radio telescope, a Space VLBI scientific data center will be built in the Sheshan campus of Shanghai Astronomical Observatory. The planned construction period is 7 years and is divided into 2 stages. In the first stage (5 year), the first satellite will be delivered in orbit to carry out single dish and space-ground VLBI observations. Also the ground facility will also finish construction in this stage. In the second stage (2 year), the second satellite will be in operation.

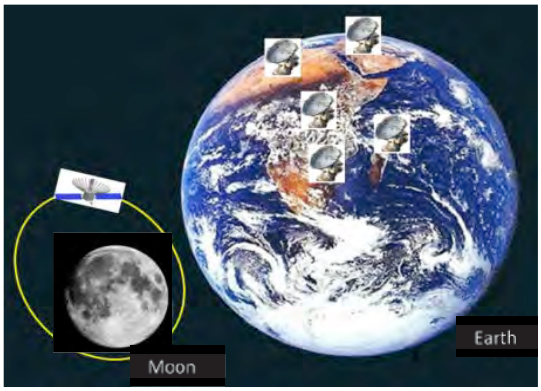

Fig. 3: Earth-moon VLBI experiment.

2.3 Operational modes

Three operational modes are summarized as follows:

- **Space-ground VLBI**. Unprecedented super VLBI network: two space-based VLBI Stations plus large ground telescopes (SKA1, FAST, QTT, etc.). New window (30 – 300 MHz) for space VLBI.
- **Space-space VLBI (single baseline)**. Space-based VLBI, long integration time, fast response of super-burst of OH masers, auroral radiation from extrasolar systems.
- **Space-based single dish**. EoR power spectrum, pulsar timing array, etc.

2.4 Key technologies

The construction and operation of large space radio telescopes are of huge challenge for Chinese

Table 1: Main parameters of the mission.

Parameter	Setting
Antenna size	30 meter
Orbit height	2,000 km - 90,000 km
Inclination angle	28.5°
Frequency configuration	30 MHz, 74 MHz, 330 MHz, 1.7 GHz
Weight	1.5 ton per satellite
Resolution	20 mas (30 MHz), 8 mas (74 MHz), 2 mas (300 MHz), 0.4 mas (1.7 GHz)
Sensitivity	sub-mJy (baseline, 10 min integration), 1 mJy/beam (image, 1 hour, 1.6 GHz)
Ground Station	FAST + SKA + other large VLBI antennas

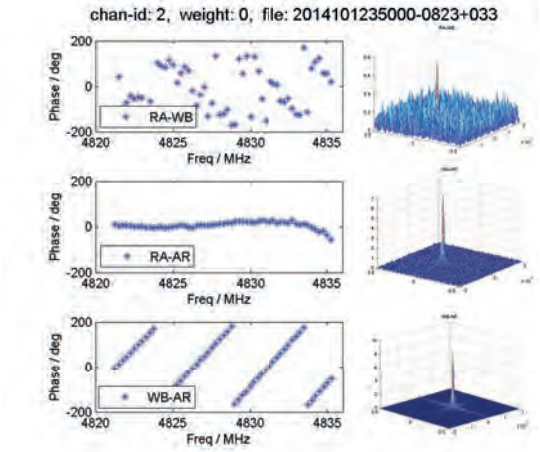

Fig. 4: Fringes of rk01yv, RA-Spekr-R antenna on board; WB-WSTRBORK, AR-ARECIBO. C-band VLBI observation.

astronomers and engineers. As a result, experts in different fields must work together to overcome various kinds of difficulties. In particular, we summarize the key technologies involved in current low frequency radio observatory.

- Large diameter space antenna production and in orbit calibration.
- Large inertia space telescope fast maneuver and stabilization.
- Low frequency space telescope electromagnetic shielding.
- Low frequency VLBI coordinated observation.

3 Earth-moon VLBI experiment

In the subsequent China's Lunar Exploration Project, there will be an Earth-moon VLBI experiment, using the relay antenna of the lunar orbit Tracking and Data Relay Satellite (TDRS) and CVN ground antennas to construct the first Earth moon space VLBI experimental system. We hope using the earth-moon VLBI system to verify the key space VLBI technology. Because the Earth-moon VLBI baseline is over 300 km, the experiments of astrometry, astrophysics and the deep-space tracking will be carried out. After this, a radio telescope is planned to be constructed on the moon surface in the future by the astronaut. The main parameters of the experimental SVLBI are:

- Antenna diameter: 4.2 m
- Band: X
- Orbit: 200 km × 8,500 km
- Length of baseline: 400,000 km

With the support of Astro Space Center (ASC) of Lebedev Physical Institute of Russian Academy of Sciences (RAS), we have obtained the space VLBI fringe of RadioAstron observation data using CVN correlator. To process the RadioAstron space-ground baseline data, CVN correlator updates the delay model and the data format of RDF (RadioAstron Data Format).

We have processed the data observed on 2014 (code: rk01yv) and obtained fringes (Fig. 4).

4 Conclusions

In the era of FAST and SKA, the low frequency radio astronomy will be the new frontier. Space VLBI is the future direction of CVN. A proposal of a Space Low-Frequency Radio Observatory with two 30 m space antennas has been put forward.

Space VLBI is the future direction of CVN. The low-frequency radio observatory will achieve both high sensitivity and high resolution, and are expected to make innovative achievements in early cosmology, supermassive black holes, and more. To advance this

project, we hope to conduct technical verification in the subsequent lunar VLBI project.

Acknowledgements This work is sponsored by the Natural Science Foundation of China (11573057), the Key Laboratory of Radio Astronomy of CAS, Shanghai Key Laboratory of Space Navigation and Positioning Technology, Shanghai the CAS Key Technology Talent Program, the Program of Shanghai Subject Chief Scientist, Advanced Research Project of Strategic Priority Program on Space Science, CAS (XDA15016100), CAS Key Technology Talent Program and Ten-thousand Talents Program, Shanghai Leading Talents program, and Fundamental Science Data Sharing Platform (DKA2017-12-02-09).

We would like to express our gratitude to the researchers (Alexey Rudnitskiy, Andrey Andrianov, Sergey Likhachev and so on) from Astro Space Center (ASC) of Lebedev Physical Institute of Russian Academy of Sciences (RAS) who not only provided the raw data and helped us to understand RadioAstron system and the observation mode.

References

Hong X, Shen Z, An T, et al. (2019) The Chinese Space Millimeter-Wavelength VLBI Array – a Step toward Imaging the Most Compact Astronomical Objects. *Acta Astronaut.*, 102, 217–225, doi:10.1016/j.actaastro.2014.05.026

Gurvits L I (2019) Space VLBI: from first ideas to operational missions. *ASR*, doi:10.1016/j.asr.2019.05.042

An T, Hong X, Zheng W, et al. (2019) Space very long baseline interferometry in China. *ASR*, doi:10.1016/j.asr.2019.03.030

Ulvestad J S (1999) Space Very Long Baseline Interferometry, Synthesis Imaging in Radio Astronomy II. In: G. B. Taylor, C. L. Carilli, R. A. Perley (eds.) *ASP Conference Series*, 180

An Artificial Radio Signal for VLBI Satellite Tracking

A. Jaradat, F. Jaron, A. Nothnagel

Abstract It has been shown that VLBI observations of satellites orbiting the Earth bear the potential of improving the frame-ties between terrestrial and celestial reference frames. A dedicated satellite mission, however, is currently not in orbit yet nor is there any satellite emitting a radio signal which is optimal for the observation with VLBI. Here we review the technical feasibility of the generation of a broad-band noise signal, its amplification, and emission. We find that a satellite could be equipped with the necessary instrumentation with relatively low power consumption. This could make it an interesting option, e.g., for GNSS satellites, thus enabling co-location in space.

Keywords VLBI transmitter · Satellite · GNSS

1 Introduction

Observing Earth satellites with ground based VLBI is of increasing interest for geodetic applications. The reason for this is that it has been shown that including satellite observations into geodetic VLBI sessions can improve the frame ties between celestial and terrestial reference frames, see Fig. 1 (Anderson, 2015) and Fig. 2 (Plank, 2013).

Ahmad Jaradat · Frédéric Jaron[1] · Axel Nothnagel
Institute of Geodesy and Geoinformation, University of Bonn, Nußallee 17, DE-53115 Bonn, Germany
(1) now at Max Planck Institute for Radio Astronomy, Auf dem Hügel 69, DE-53121 Bonn, Germany

(Correspondence: s7ahjara@uni-bonn.de, nothnagel@uni-bonn.de)

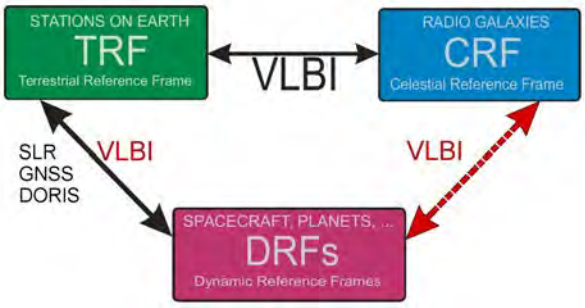

Fig. 1: VLBI observations of Earth satellites fill the missing direct link between the celestial reference frame and the dynamic reference frames of satellites. Figure taken from Anderson (2015).

Several experiments have been made to observe GNSS satellites with VLBI radio telescopes by Haas et al. (2014); Tornatore et al. (2014); McCallum et al. (2016), but neither the frequency setup nor the signal power was adequate to the usual VLBI observing mode and caused a number of problems. Furthermore, Hellerschmied et al. (2016) observed Cubesat which was too fast so that the tracking caused problems and it only had DOR tone emission which is problematic for VLBI post-processing and analysis.

In the time of writing there is not any satellite mission in orbit which has been designed for the purpose of being observed with VLBI.

2 Link budget

In order to be suitable to be observed by geodetic VLBI, the transmitted signal should be similar to the radiation of a quasar in terms of spectrum and intensity.

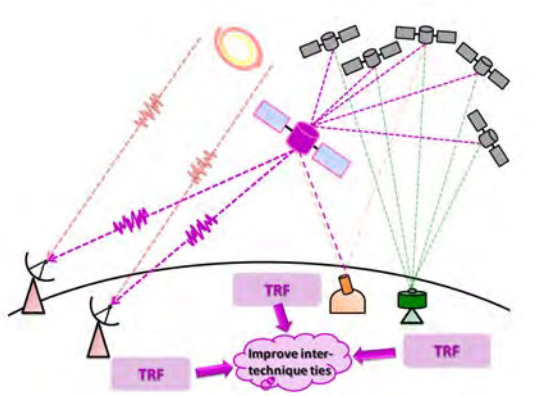

Fig. 2: Principle of a space tie. A satellite is tracked simultaneously by different space-geodetic techniques, realizing a platform for co-location in space. Figure taken from Plank (2013).

In other words, the spectrum has to be as flat as possible and it should cover a frequency range from 2 to 14 GHz to be suitable for both legacy S/X observations and the upcoming VGOS. Furthermore, a trade off has to be done for the received intensity. On the one hand, the received intensity has be similar to a typical quasar, in order to avoid any change in the attenuation level at the telescopes. On the other hand, since the satellite is moving, the integration time has to as short as possible, thus, the received intensity has to be relative large. The initial assumption could be $\sim 1-10$ Jy.

In order to compute the intensity of the transmitted signal, the link budget has to be calculated, which is the total gains and losses of the signal intensity from the transmitter to the receiver, which consist mainly of the the antenna gain and path losses (free path loss and atmospheric attenuation) as shown in Fig. 3:

$$\text{Transmitted signal} = \text{Received signal} - \text{Antenna gain} + \text{Path losses}. \quad (1)$$

Signal consideration: The received signal which will be studied here has 10 Jy intensity, emitted by a GNSS satellite (20 000 km altitude), and received by a 13 m antenna (VGOS standard) at 5° elevation angle.

Antenna gain: The parabolic antenna gain is given by (Stutzman and Thiele, 2012)

$$\text{Antenna Gain} = 10\log_{10} k\left(\frac{\pi d}{\lambda}\right)^2, \quad (2)$$

where λ is the signal wavelength, d is the diameter of the antenna, and k is the efficiency factor, which we assume to be $k = 0.5$ here. The antenna gain of Eq. (2) is plotted in Fig. 4 for different wavelengths ($\lambda = 15, 3.8, 2.1$ cm, i.e., frequencies $\nu = 2, 8, 14$ GHz).

Path losses: While the signal travels from the satellite to the antenna, it suffers from intensity attenuation due to free path loss (FPL) and atmospheric attenuation.

The FPL can be thought of as the signal spreading out as an increasing sphere. As the signal has to cover a wider area, conservation of energy tells that the energy in any given area will reduce as the area covered becomes larger. It could be calculated using the following expression (Anderson, 2003):

$$\text{FPL} = 32.44 + 20\log_{10}(F_{MHz}) + 20\log_{10}(D_{km}). \quad (3)$$

Here F is the frequency in MHz and D is the distance between the satellite and the antenna in km. In the worst case, while the elevation angle ϵ is 5° the distance will be 25040.4 km.

Atmospheric attenuations are estimated according to the ITU recommendations (ITU, 2016). With assuming that the total path length between antenna and clouds as source of rain is 5 km in the zenith direction, which will be 57 km at elevation down to $\epsilon = 5°$, and with standard atmospheric conditions, surface pressure at sea level of 1013 hPa and humidity of 7.5 g/m^3. Figure 5 shows the attenuation due to the dry and the wet parts of the atmosphere.

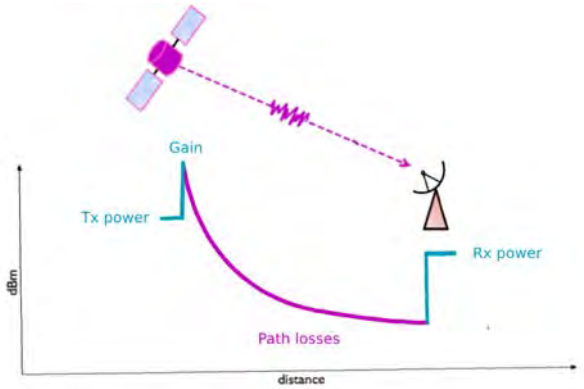

Fig. 3: The change of the signal intensity with distance and antenna gain during propagation a signal from a satellite to a telescope (Link budget).

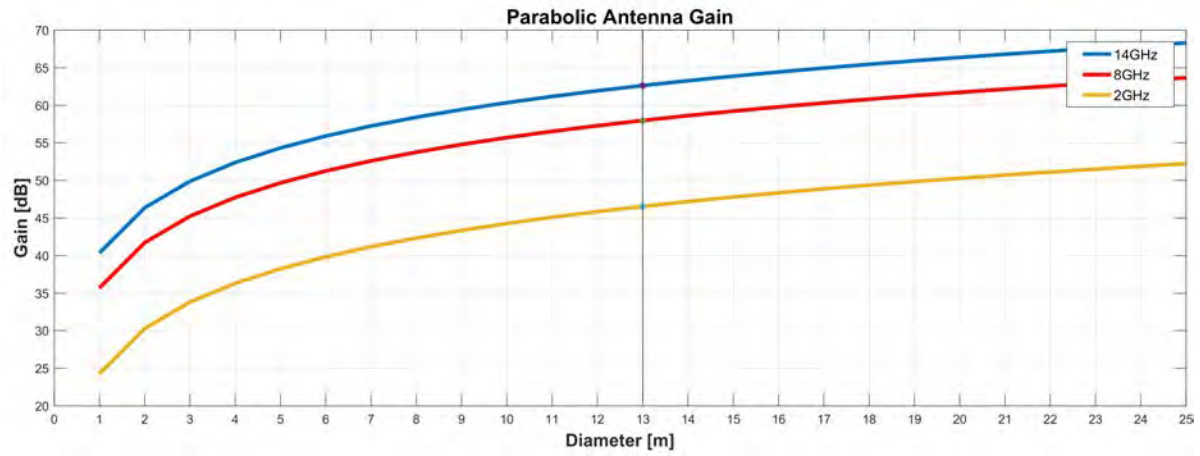

Fig. 4: Parabolic dish antenna gain at different frequencies and antenna diameter.

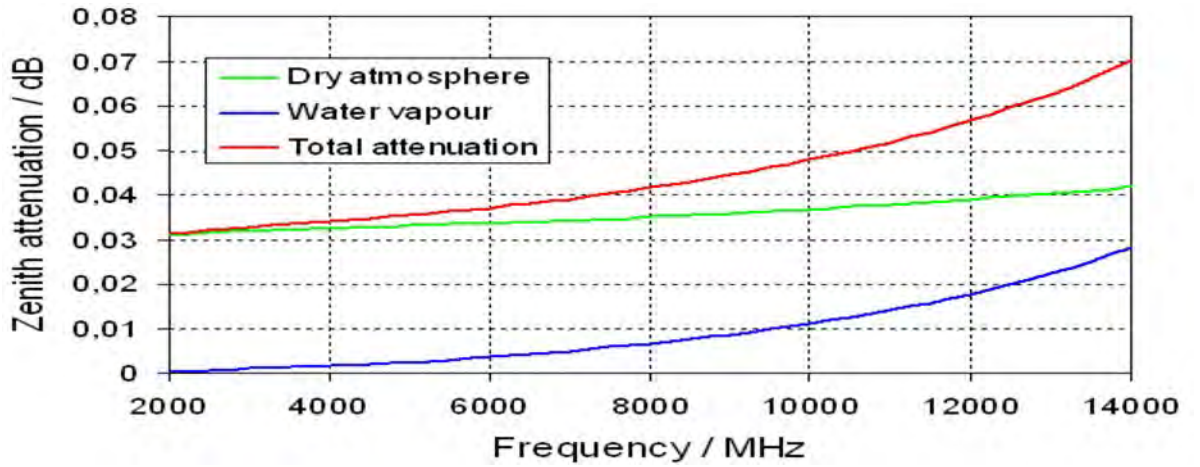

Fig. 5: Atmospheric attenuation per kilometer.

3 Instruments

To generate such a signal, a noise generator could be used, i.e., a noise diode. The intensity of the noise diode signal is defined by ENR (Excess Noise Ratio), which shows how much the noise source is above thermal noise in its power. Thus, the intensity can be approximated by adding the ENR to a typical thermal noise level of $-204\,\mathrm{dBW/Hz}$. The typical ENR of a noise diode is between 10 and 20. Thus, an amplifier is needed in order to generate a signal with the required intensity (see Table 1). Since the bandwidth of the generated signal is wide, i.e., $\sim 12\,\mathrm{GHz}$, a special kind of antenna should be used in order to avoid any changes in the gain, phase center, polarization, and radiation pattern across the band. A log-spiral antenna can serve these requirements (see Fig. 6).

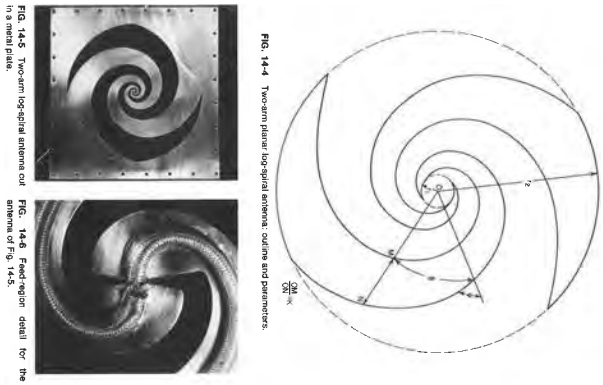

Fig. 6: Log-spiral antenna. Figure taken from Johnson and Jasik (1984).

4 Signal strength

Table 1 shows the link budget results and the minimum required transmitted intensity considering the properties of the signal as mentioned in Sect. 2.

Table 1: Results of the link budget, which shows the total attenuation of the signal intensity. Attenuation + received intensity = transmitted intensity.

	Frequency		
Gain-Loss	2 GHz	8 GHz	14 GHz
Received intensity dBW Hz^{-1} m^{-2}	−260 dBW		
Free path loss at $\epsilon = 5°$ dBW	188	200	204
Atmospheric attenuation at $\epsilon = 5°$, dBW	0.5	0.5	1.5
Antenna gain dBW	−46.5	−58	−63
Total transmitted intensity dBW Hz^{-1} m^{-2}	−118	−117.5	−117.5

5 Conclusions and outlook

We have investigated a possible signal to be emitted from a satellite and observed by geodetic VLBI. The goal of this is to improve the frame ties between ITRF and IRCF. We define the main characteristics of this signal to be close to the radio emission from a quasar in order to be suitable for the observation with geodetic VLBI. We computed the intensity of the signal, which could be emitted from a GNSS satellite by computing the link budget of the signal.

Furthermore, we looked into the instruments which could be used to generate and transmit this signal. Noise diode and amplifier could be used to generate and amplify the signal. A spiral antenna could be a proper antenna to emit this signal, because it belongs to the class of frequency independent antennas, which operate over a wide range of frequencies. Further investigations should be done on these instruments in terms of environmental circumstances and power consumption.

The calculations presented here show that an artificial noise signal can be generated at the required intensity. This makes it an interesting option to add to, e.g., a GNSS satellite, thus implementing co-location in space. Further investigation of the possible emitted spectrum of the generated signal is needed in order to find the optimal solution for the entire analysis chain from correlation to final parameter estimation.

Acknowledgements This research is supported by the Deutsche Forschungsgemeinschaft, DFG, project number NO 318/14-1. AJ thanks the Nachlass-Zetsche-Stiftungsfonds for financial support.

References

Anderson H R (2003) Fixed broadband wireless system design. John Wiley and Sons

Anderson J (2015) Ties between kinematic and dynamic reference frames (D-VLBI). http://www.iap.fr/gagnes/talks/Anderson_GAGNES.pdf

Haas R, Neidhardt A, Kodet J, et al. (2014) The Wettzell-Onsala G130128 experiment – VLBI-observations of a GLONASS satellite. In: D. Behrend, K. D. Baver, K. L. Armstrong (eds.): *IVS 2014 General Meeting Proceedings*, Science Press (Beijing), 451–455

Hellerschmied A, Plank L, McCallum J, et al. (2016) Scheduling of VLBI satellite observations with VieVS. In: A. Nothnagel, F. Jaron (eds.): *Proc. First International Workshop on VLBI Observations of Near-field Targets*, 1–5

ITU 2016 Recommendation ITU-R P.676-11 (09/2016)

Johnson R C, Jasik H (1984) Antenna engineering handbook, 2nd edition, New York, McGraw-Hill Book Company

McCallum J, Plank L, Hellerschmied A, et al. (2016) Technical challenges in VLBI observations of GNSS sources. In: A. Nothnagel, F. Jaron (eds.): *Proc. First International Workshop on VLBI Observations of Near-field Targets*, 7–10

Plank L (2013) VLBI satellite tracking for the realization of frame ties. PhD thesis, TU Wien

Stutzman W L, Thiele G A (2012) Antenna theory and design. John Wiley and Sons.

Tornatore V, Haas R, Casey S, et al. (2014) Direct VLBI observations of global navigation satellite system signals. In: C. Rizos, P. Willis (eds.): "Earth on the Edge: Science for a Sustainable Planet", *IAG Symposia*, 139, 247–252, Springer, Berlin, Heidelberg, doi:10.1007/978-3-642-37222-3_32

The Bonn Correlator and VGOS Sessions

L. La Porta, W. Alef, S. Bernhart, A. Müskens, H. Rottmann, T. Schüler, J. Wagner

Abstract The MPIfR/BKG correlator in Bonn has a long experience in processing IVS sessions and it has been preparing for handling broadband experiments for years. We would like to give an estimate of our current capabilities for a sustainable VGOS duty cycle.

Keywords VGOS · Correlation

1 Introduction

The Bonn correlator is operated jointly by the Max Planck Institute for Radio Astronomy (MPIfR) in Bonn and by the Federal Agency for Cartography and Geodesy (Bundesamt für Kartographie und Geodäsie, BKG), with the support of the Institute of Geodesy and Geoinformation (IGG) of the Bonn University. The MPIfR hosts the correlator facility and shares with the BKG the costs of the cluster, of most of the staff and of the Internet connectivity. The IGG contributes to the connectivity of the cluster and pays one member of the geodetic staff. Since January 2017 the personnel responsible for the correlation of geodetic sessions is employed by the BKG via a private contractor, the Reichert GmbH.

An extensive description of the Bonn correlator personell and activities, as well as technical details for example concerning the software tools exploited for post-processing may be found in the IVS Biennial Report (La Porta et al., 2019). Here we will focus on the information relevant for our considerations.

The Bonn correlator is a Distributed FX software correlator (Deller et al., 2011). It is installed on a High Performance Computing (HPC) cluster (see Fig. 1), which consists of:

- 68 nodes with 20 compute cores each,
- three head nodes for executing more correlations in parallel,
- 56 Gbps Infiniband interconnect between all nodes,
- 1.5 PB of disk space organized in RAID units and combined in a BeeGFS parallel cluster file system,
- 15 Mark 5 playback units, and 9 Mark 6 playback units each with four bays (see Fig. 2).

Fig. 1: New HPC cluster at MPIfR seen through a glass wall.

Laura La Porta · Simone Bernhart
Reichert GmbH, Hittofstraße 26, DE-53129 Bonn

Walter Alef · Helge Rottmann · Jan Wagner
Max-Planck-Institut für Radioastronomie, Auf dem Hügel 69, DE-53121 Bonn

Arno Müskens
Institut für Geodäsie und Geoinformation der Rheinischen Friedrich-Wilhelms Universität Bonn, Nußallee 17, DE-53115 Bonn

Torben Schüler · Laura La Porta · Simone Bernhart
Geodätisches Observatorium Wettzell, Bundesamt für Kartographie und Geodäsie, Sackenrieder Str. 25, DE-93444 Bad Kötzing

(Correspondence: laporta@mpifr-bonn.mpg.de)

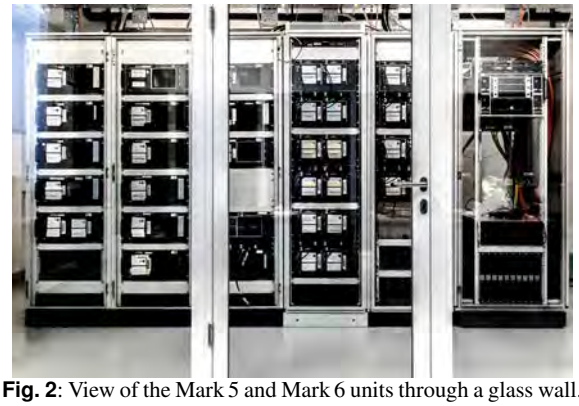

Fig. 2: View of the Mark 5 and Mark 6 units through a glass wall.

The HPC cluster is connected to the Internet through two 1-Gbit lines.

2 Our experience with EU-VGOS test sessions

In March 2018 - upon an initiative of W. Alef - the Bonn Correlator Center started a collaboration with the three European stations of Wettzell, Onsala and Yebes, equipped with both standard S/X- and broadband systems, to carry out a European VGOS Proof-of-Concept study (EU-VGOS). We refer you to the Proceeding of W. Alef for an exhaustive report about the project and the results achieved so far. Here we will restrict our discussion mainly to the aspects related to data transfer and storage.

The aim of the project is to verify the processing chain for VGOS experiments end-to-end, from the scheduling to the geodetic analysis of the derived observables. All parties are learning about and investigating the various aspects of the project, from the more technical ones, as system settings and data recording at the station, to data decoding and correlation, and finally to the post-processing of the data, i.e. to the fringe-fitting. This is necessary in light of the forthcoming IVS-VGOS era. In particular, most of the European stations have different back-end systems w.r.t. the American sites, and they must rely mostly on their own resources to debug their systems with the support of the correlator and of the DBBC team in Bonn. As an example, these first test sessions revealed that the VDIF multithreaded files generated via VGOS broadband systems sometimes show anomalies. Namely, the threads are not correctly interleaved in time: for each time tag there should be all threads present in the file, whereas some threads appear with a certain delay w.r.t. the others. As a result DiFX's decoding buffers can overflow, thus leading to data loss. The percentage of correlated data decreased by 70 % in the worst cases we experienced. The problem can be circumvented by reordering the threads in the raw data file and merging them into a single-thread, but that extra-step costs time and storage space. As this work-around is time-consuming and requires additional storage space, it is unsuitable for routine operations. J. Wagner is currently implementing a fix for the issue.

Test observations were performed shortly before the IVS VGOS-Test (VT) sessions by adopting the same frequency set-up, thus minimizing both the effort for the participating stations and the risk to jeopardize the official IVS sessions. Dual polarization observations were carried out in four 512 MHz wide bands at about 3 GHz, 5 GHz, 6 GHz and 10 GHz. In each band 8 channels of 32 MHz were sampled with 2-bits, thus providing an acquisition rate of 8 Gbps. The test sessions lasted 4 hours and included about 150 scans with a typical duration of 30 seconds, but also targeted 3-4 strong calibrators for which longer scans of about 120 seconds were performed. The amount of data recorded at each station was of about 6 TB. Assuming to use the maximal data transfer rate currently available between each stations and the correlator, i.e. 600 Mbps, it would take between 1.5 to 4.5 days to complete the transfers of the raw data to Bonn. In practise, VGOS is not yet in the production phase in Bonn and we could not dedicate our internet connection entirely to the project, so that it took on average $2-4$ weeks to fetch all data.

Due to the above mentioned issues with multi-thread vdif data, we first have to convert the files into single-thread data. For 6 TB of data that process takes about half a day on our cluster. The correlating time of one test session amounts to $2-3$ hours: the correlator needs on average $1-1.5$ minutes to complete one job (or equivalently one scan). We currently assume one day for fringe-fitting and DB-creation, but it could become shorter as we collect experience in handling the post-processing procedures. In the best case scenario (i.e. bandwidth reserved for running transfers in parallel) we may generate a database within 3.5 days after the observations. In a more

realistic scenario - geodesy is not the only nor the main activity at the Bonn correlator - we would transfer the data of the stations one after the other, but we would start converting as soon as we get the data and we could complete post-processing within 6 days after the observations.

3 Future IVS-VGOS intensive sessions

For 2019 the IVS plans to start VGOS intensive sessions on a regular basis. One option would be to schedule two stations equipped with VGOS systems, for example Wettzell and Kokee, for weekly one hour sessions. If we stick to the frequency set-up currently used in VT sessions and adopt a typical geodetic schedule, then we would have 15 second on source followed by 30 seconds slewing time, thus leading to about 80 scans per session for a total of 1.2 TB of data per station. If we reserved the bandwidth to the transfers of the raw data, as we usually do for the INT3 sessions on Mondays, and performed the transfers with a rate of 800 Mbps for both stations, then it would take about 200 minutes to fetch all data. On the Bonn HPC cluster it would take 1 hour to correlate the experiment and a few hours for post-processing and for generating the database. In conclusion, if observations were carried out at 7:00 UT we may deliver the dabatase within one working day.

4 Future IVS-VGOS 24-hour sessions

As an exercise we would like to extrapolate these latency times to 24-hour sessions with a larger number of participating stations, as in the case of the VT sessions. It is straightforward to estimate how long it will take to fetch the raw data with a 2 Gbps line and how much storage space will be needed. The storage capacity in Bonn would be sufficient for the time being. There are various factors, which may affect the correlator performance. For example, the playback rate, but that is not going to be an issue in Bonn, given that we have a 56 Gbps interconnection between the nodes. Among the various factors which may affect the correlator performance, the only limiting one could be the computing capability. On a HPC with the same characteristics as in Bonn the computing time increases linearly with the amount of data to be correlated (H. Rottmann, private communication).

Let us consider a 24-hour geodetic session (30 seconds on source, for a total of about 580 scans) with 6 stations and an acquisition rate of 8 Gbps. Under these conditions $16-17$ TB of data would be recorded at each antenna. With the present internet connections we could carry out at most 3 transfers at 600 Mbps in parallel (one has to note that a few stations have larger bandwidth at disposal) therefore it would take approximately 4 days per station to fetch the raw data and a minimum of 10.5 days to fetch all data for correlation. If stations opted for sending Mark6 modules instead, it would take $1-2$ weeks for the data to reach the correlator, based on Haystack's experience. Moreover, it would imply having a budget for shipping cost, which is currently not the case for the Bonn correlator, at least for geodesy. If we completed the post-processing within 2 days, then in the best case scenario we would submit the database within $10-11$ days after observations, although based on Haystack's experience with the IVS-VT sessions a month would seem a more realistic estimate.
Nowdays the bottle neck in the pipeline is without any doubts the transfer of raw data to the correlation center.

5 Conclusions and outlook

According to the IVS Strategic Plan for the Period 2016–2025 (Nothnagel et al. 2016), geodetic VLBI should transition from S/X systems to VGOS systems during this decade. The progress is slower than foreseen, for example only 6 instead of 16 VGOS stations are operational at present. Moreover, the difficulties related to data transfers and storage are such that so far only bi-weekly sessions with a low acquisition rate have been conducted on a regular basis within the IVS activities. In recent years new correlation centers have been founded and started cooperating with the IVS, however the Bonn correlator is still a main actor on the IVS scene and matches VGOS requirements at least in terms of computing capabilities. It can therefore serve as test bed to understand the pace at which VGOS production may begin.

We considered the initial VGOS observing schedule with daily 1-hour sessions. Based on our experience

with the EU-VGOS test sessions, our correlator center can deliver the database of a VGOS intensive session with the current set-up within 24-hour from observations, thus matching the timeliness achieved for INT3. We underline that this is far from the IVS final goal as laid out by the Board of Directors in 2016, which is to produce such a database every 3-hour and with both a much larger network and a higher acquisition rate.
In the case of 24-hour sessions the latency time increases to $10-11$ days already under these initial conditions, i.e. 6 stations and a 8 Gbps acquisition rate. A feasable production cycle would be of roughly a couple of weeks for a correlator with similar characteristics as in Bonn. One would therefore need at least 15 correlators to share the work load to carry out observations 24/7.

The main issues for VGOS regular observations are the transfer and the storage of the data both at the stations and at the correlator end. The costs for internet connections are still rather expensive, although the situation may vary significantly from one country to another. Stations would need at least a 2 Gbps line, whilst correlators should have at least 10 Gbps to allow e-transfer of the data. Stations should be equipped with local buffering systems (i.e. using flexbuff for recording) or they should purchase twice as many modules as those needed for the sessions in one week. Correlators would also need quite some extra storage space and new agreements should be stipulated between stations and correlators to cover those costs. Countries that build an antenna to participate in geodetic sessions should also include in the budget some funding for the logistics to make the correlation of the collected data at all possible. Ideally, they should also contribute to the costs of the correlation centers as well.

References

Deller A T, Brisken W F, Phillips C J, et al. (2011) DiFX-2: A More Flexible, Efficient, Robust, and Powerful Software Correlator, *PASP*, 123, 275–287

Nothnagel A, Behrend D, Bertarini A, et al. (2016) Strategic Plan of the IVS for the Period 2016-2025. In: D. Behrend, K. D. Baver, K. L. Armstrong (eds.): *IVS 2016 General Meeting Proceedings*, NASA/CP-2016-219016, 3–12

La Porta L, Alef W, Bernhart S, et al. (2019) The Bonn Correlation Center, *IVS 2017+2018 Biennial Report*, in press

The EUropean-VGOS Project

W. Alef, J. M. Anderson, S. Bernhart, P. de Vicente, J. González García, R. Haas, L. La Porta, I. Martí Vidal, A. Müskens, A. Nothnagel, C. Plötz, H. Rottmann, T. Savolainen, T. Schüler, D. Small, J. Wagner

Abstract In Spring 2018 the Bonn correlation centre started a collaboration with the three European stations of Wettzell, Onsala and Yebes, equipped with both S/X- and broadband systems, to perform VGOS-like test sessions. The aim is to verify and develop further the processing chain for VGOS experiments end-to-end, from the scheduling to the analysis of the derived observables. We will present the current status of the project.

Keywords VGOS · VLBI broadband observations

Walter Alef · Helge Rottmann · Jan Wagner · Tuomas Savolainen
Max Planck Institute for Radio Astronomy, Auf dem Hügel 69, DE-53121 Bonn, Germany

Simone Bernhardt · Laura La Porta
Reichert GmbH/BKG, Hittorfstr. 26, DE-53129 Bonn, Germany

Arno Müskens · Axel Nothnagel
Institute of Geodesy and Geoinformation, University of Bonn, Nußallee 17, DE-53115 Bonn, Germany

Pablo de Vicente · Javier Gonzaléz García · I. Martí Vidal
Observatorio de Yebes (IGN), Cerro de la Palera S/N, Yebes, Guadalajara, Spain

Christian Plötz · Torben Schüler
Geodätisches Observatorium Wettzell, Bundesamt für Kartographie und Geodäsie (BKG), Sackenrieder Str. 25, DE-93444 Bad Kötzting, Germany

Rüdiger Haas
Chlamers University of Technology Onsala Space Observatory, SE-439 92 Onsala, Sweden

James M. Anderson
Technical University of Berlin, Institut für Geodäsie und Geoinformationstechnik, Straße des 17. Juni 135, DE-10623 Berlin, Germany, also at: GFZ German Research Centre for Geosciences, Department 1, Geodesy, Telegrafenberg, DE-14473 Potsdam, Germany

Tuomas Savolainen
Aalto University Department of Electronics and Nanoengineering, PL 15500, 00076 Aalto, Finland, also at: Aalto University Metsähovi Radio Observatory, Metsähovintie 114, FI-02540 Kylmälä, Finland

Des Small
Joint Institute for VLBI ERIC, Oude Hoogeveensedijk 4, NL-7991 PD Dwingeloo, The Netherlands

(Correspondence: alef@mpifr-bonn.mpg.de)

1 Motivation and aims

The main motivation for starting a scientific investigation on VGOS is the will to speed up the transition from classical geodetic VLBI to broadband observations. According to the initial IVS strategic plan, VGOS production should have started already by the end of 2017, but the complexity of the project and the lack of manpower led to a long delay in implementing production VGOS observations. VGOS telescopes, some of which were inaugurated as early as 2013, are standing idle most of the time much to the chagrin of their funding agencies. So VGOS antennas are available and are ageing, while telescope crews still lack practice in VGOS observing.

In 2015 the Bonn cluster was upgraded following the IVS-VGOS correlation plans of Petrachenko et al. (2014), which foresaw an increasing demand that has not yet become real as of 2019. The cluster will be old in 2020 and should be renewed in 2020 to 2022. Only recently IVS-VGOS data have been made available, which is necessary not only for training correlator personnel, but also for studying the steps in data reduction after correlation.

Since 2015 bi-weekly test sessions have been carried out by the IVS under the lead of the MIT Haystack

group, which developed a path for observing, correlating and fringe-fitting of VGOS data (see e.g. Cappallo 2014). Their approach exploits the "pseudo-Stokes-I" (Intensity), which ignores instrumental and source polarisation, as well as changes and differences between the position of the peak in total and in polarised intensity. From astronomical observations it is known that the angle of the source polarisation can vary more rapidly than total intensity. It is also known that instrumental polarisation leakage leads to delay errors.

Investigations of Anderson and Xu (2018) have shown that the effects of source structure on the delays have been underestimated and will affect VGOS to a larger extent due to the expected reduced noise in such data. The whole problem is aggravated by variation of the source structures and the position of the centroid which can change with time. The position of the centroid as a function of frequency is another relevant source of systematic errors in VLBI broadband data.

Unfortunately no scientific investigation exists up to date, which studies the various effects and their contributions to the geodetic residuals of VGOS data.

Wideband astronomical VLBI data as recorded for the Event Horizon Telescope (EHT) have triggered new software efforts for polarisation conversion and for fringe-fitting. While VLBI observations have been performed with circular polarisation, ALMA, a key element of the EHT, can only deliver linear polarisation. It is therefore necessary to convert ALMA data from linear to circular polarisation basis (Martí-Vidal et al., 2016), which is done after correlation. Similarly, VGOS receivers produce linear polarisation, whereas geodetic legacy S/X systems measure circular polarisation.

The standard fringe-fitters (FF) cannot handle wideband data, because they do not take properly into account the effects of ionosphere, source structure and polarisation. A new fringe fitting task for broad and non-contiguous frequency bands, as well as correction for dispersive delays is being developed for the astronomical CASA package (van Bemmel et al., 2019). So there are new options for fringe-fitting geodetic data which should be explored. Some of the astronomical (global) FFs can take the source structure as a natural input, which makes them good candidates also for geodesy involving source structure corrections.

To the authors it is clear that in order to reach 1 mm positional accuracy, all steps of VGOS observing and data reduction have to be optimised. That will require a broad range of expertise and sufficient manpower. The whole geodetic/astronomical community should ideally join forces, given that astronomy is also moving to an era of broadband observations and shares common open issues with geodetic VLBI. The DiFX software correlator community is an example of how successful such an open collaboration can be.

2 Observations and correlation

The first test sessions were dedicated to test the performance of the instruments. Having a minimum of 3 stations allows any problems identified to be isolated at a specific station. The three participating stations are equipped as follows:

- ONSA13NE (ONSA13SW became operational only recently): 13.2 m antenna, QRFH receiver, VLBI back-end DBBC3 with flexbuff recording
- WETTZ13S (WETTZ13N not equipped with broadband receiver yet): 11-feed receiver, VLBI back-end 2 DBBC2 with Mark6 recording
- RAEGYEB: 13.2 m antenna, QRFH receiver, VLBI back-ends are 4 RDBEG with Mark6 recording

The EU-VGOS sessions have been scheduled by using both SKED and SCHED and include standard geodetic sources (time on source $\sim$ 30 sec) and at regular intervals strong calibrators (integration time $\sim$ 120 sec) that cover a wide range of parallactic angles during the observation. Good parallactic angle coverage of a calibrator is necessary for accurate polarisation conversion. The observations last 4 hours and include sources with high and low fractional polarisation in order to test the polarisation leakage calibration method.

So far we have adopted the same frequency setup as used in the IVS-VT sessions — four bands with dual linear polarisation:

- 3000.40 MHz – 3480.40 MHz
- 5240.40 MHz – 5720.40 MHz
- 6360.40 MHz – 6840.40 MHz
- 10200.40 MHz – 10680.40 MHz

In each band we sample 8 channels of 32 MHz bandwidth at a sample rate of 64 MS/s using two bits, thus resulting in a data rate of 8 Gbit/s. Data are recorded either using Flexbuff (JIVE) or on Mark6 modules

in VDIF[1] format. The stations generate multi-thread VDIF data in slightly different flavours:

- Onsala (real data) – 1 VDIF file per scan with 8 threads, 8 channels per thread
- Wettzell (real data) – 1 VDIF file per scan with 4 threads (1 for each band), 16 channels (8 channels x 2 linear polarisations) per thread
- Yebes (complex data) – 1 VDIF file per scan with 4 threads, 16 channels per thread

The recorded data are later "e-transferred" to the Bonn correlator via the Internet.

The file-based correlation and the backend setup have hit a few corner case issues in DiFX correlation. The main issue is thread-clumpiness inside recordings. The specifications of the recorded data format and its multi-threaded multi-channel capability allow great flexibility in the time sequencing of data frames inside one file. In EU-VGOS test experiments, station backends and recorder setups have produced VDIF files that adhere to the specifications, but that contain frames of individual threads in long data bursts rather than in a clean round-robin order. This "clumpiness" conspires against DiFX and its buffer-based VDIF decoding approach. High data loss (low visibility data weights) are seen when the burst length exceeds the preset DiFX VDIF decode buffer size. Curiously, the problem persists even when threads of a multi-threaded VDIF file are extracted into single-thread VDIF files that are then correlated simultaneously in DiFX via its "multi-datastream" support.

Conversely, the low data weight issue does not occur when the original Mark6 scatter(-gather) fragment file sets (usually not available via e-transfer) are used as input for correlating a scan. The difference is likely due to the different VDIF reading path that DiFX uses for "scattered" Mark6 versus "gathered" file based correlation.

The above problem has also been reported by MIT Haystack. At Bonn the issue is worked around by a preprocessing step prior to correlation. The multi-threaded multi-channel VDIF files of all stations are converted into single-threaded multi-channel files using DiFX utility "vmux" configured for a very large buffer size (≥ 800 MB). This recovers visibility data weights from a previous worst of ≤20 % to generally ≥99 %. However, due to the overhead at the correlator such a preprocessing step is not ideal. To omit the VDIF preprocessing step, development of improved support for general multi-threaded VDIF was also welcomed by the NRAO and is in progress at Bonn MPIfR. An initial implementation is being tested.

[1] VDIF specifications, cf. https://vlbi.org/vlbi-standards/vdif/

3 Data analysis

The conversion of linear polarization into circular is performed using the PolConvert algorithm (Martí-Vidal et al., 2016). The conversion process needs to be fed with the phase-gain difference and the amplitude-gain ratio between the two linear polarizers (X and Y) of each antenna. These quantities can be estimated using the Global Cross-Polarization Fringe Fitting (GCPFF) algorithm, as implemented in PolConvert, using a scan of a calibrator source (ideally, a source with either a low fractional linear polarization and/or a wide parallactic-angle coverage in the observations).

Before running the GCPFF, we applied an initial estimate of the phase-gain difference between polarizers, based on the values of the phasecal tones found for X and Y at each integration time. The relative gain amplitudes were also estimated from the autocorrelations at each polarizer (after filtering the peaks due to the phasecal tones).

Then, we selected a strong calibrator (3C 84) and solved for any additional X/Y relative phases that could remain (after the phasecal corrections), as well as for additional X/Y amplitude ratios. These additional relative gains (both in phase and amplitude) could be caused, for instance, by different phasecal cabling to the two polarization components, or to the particulars of the signal path of each polarization channel.

These additional X/Y relative phases (which are added to the phasecal differences between X and Y) and X/Y relative amplitudes (which are applied on top of the autocorrelation ratios) are shown in Fig. 1. On the one hand, the X/Y phase difference computed by the GCPFF can be roughly modeled as one single multiband delay across the whole EU-VGOS frequency coverage. On the other hand, the amplitude ratios show different values for each band and can depart substantially from unity (hence introducing a large instrumental ellipticity, if they were not taken into account in the conversion).

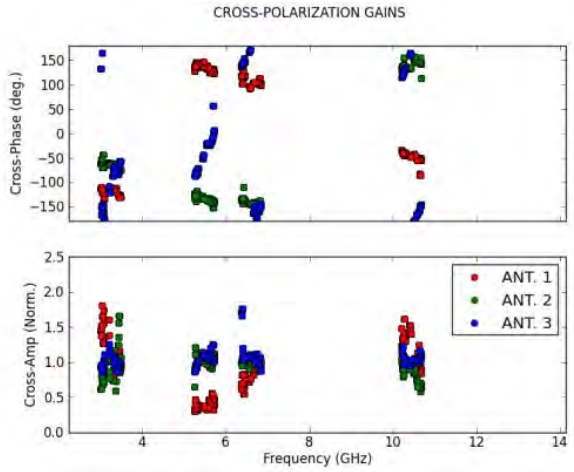

Fig. 1: X/Y relative phases (top) and amplitudes (bottom) for Oe (ANT. 1), Ws (ANT. 2) and Yj (ANT. 3).

3.1 First results

Fig. 2 and Fig. 3, respectively, show the amplitudes of all correlation products, for a scan of a strong calibrator source, before (i.e., XX, XY, YX and YY) and after (i.e., RR, RL, LR, LL) conversion from linear to circular, as a function of frequency channel (each increasing with frequency). It can clearly be seen how most of the power is coherently injected into RR and LL.

In Fig. 4, we show the antenna gains derived for the same calibrator scan using the standard Global Fringe Fitting (GFF) algorithm. The GFF has been applied to the Stokes I fringes in each independent IF. The phase-cal tones (which are now the same for the R and L channels) have been applied before the GFF. As it can be seen in the figure, all gain quantities (phase, delay and rate) can be properly connected among the different EU-VGOS bands, hence showing the possibility of

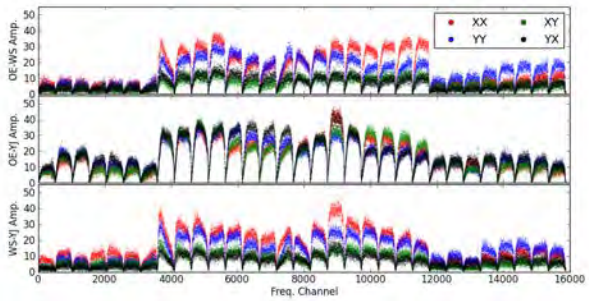

Fig. 2: Linear polarisations (XX, YY, XY, YX) amplitudes of all sampled channels for a scans on 3C84.

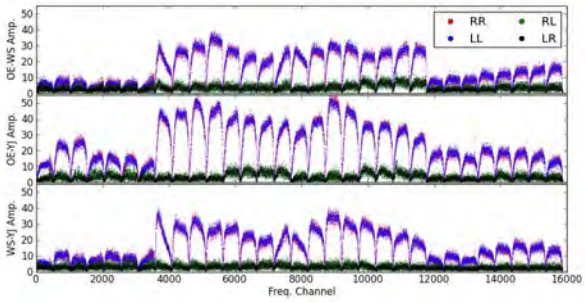

Fig. 3: Circular polarisations (RR, LL, RL, LR) amplitudes of all sampled channels for a scans on 3C84.

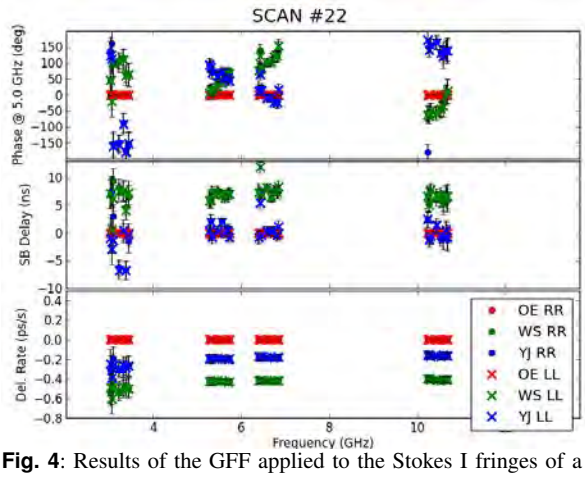

Fig. 4: Results of the GFF applied to the Stokes I fringes of a scan on 3C 84, obtained after polarisation conversion.

performing a consistent multi-band analysis over all the VGOS frequency coverage.

The GFF gains can be applied to all four polconverted correlation products, in order to perform an image deconvolution in full polarization. We have performed a multi-frequency synthesis (MFS) image deconvolution (Sault and Wieringa, 1994) using all scans of source 3C 279. The preliminary imaging results are astonishingly good, as can be seen in Fig. 5. White contours show the brightness distribution of Stokes I, while the red contours show the I residuals after subtracting a centered point source. The red contours are well aligned into the same direction as the known jet of 3C 279, hence indicating that EU-VGOS is resolving the source. The orange raster plot shows the brightness distribution in linear polarization, which is shifted from the I peak just in the same direction of the jet. The polarized brightness, polarization angle, and its peak shift roughly agree with published results from dedicated

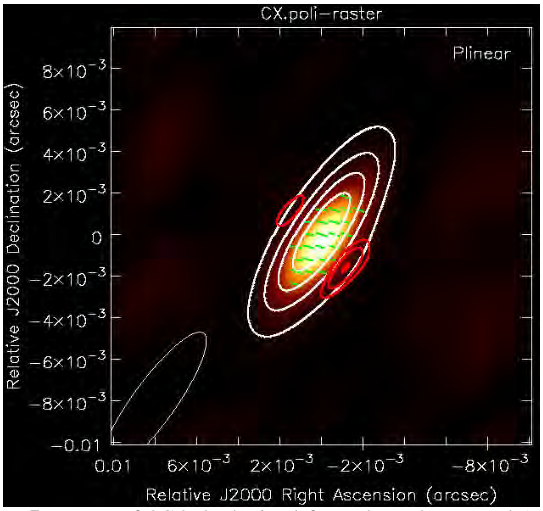

Fig. 5: Image of 3C 279 obtained from the polconverted (and fringe-fitted) EU-VGOS data.

VLBI observations of this source at other frequencies (e.g., Rani et al., 2018).

4 Conclusions and outlook

Both astronomy and geodesy are transitioning to a new era of broadband VLBI observations. That opens new frontiers for both fields of research, as well as new challenges on the way to the results. The EU-VGOS project answers the urgent need to further investigate some aspects related to the new technology and to the methodology in processing and analyzing the data.

Note that the European stations have different backend systems w.r.t. the American sites, therefore they must rely on their own resources to debug them. The correlation constitutes an expensive but powerful diagnostic tool, thus allowing to verify the station performance. We adopt different observational strategies for our sessions, thus allowing us to focus on the various aspects to be tested. We need to characterize the bandpass response of the instruments and how it changes with time, and to verify the performance of the pulse calibration system. We will monitor over many months the stability of the gain (amplitude and phase) in time, as well as its frequency dependency.

The wideband receivers use linearly polarized feeds, so that the baseline correlations are highly mixed among the parallel and cross-hand polarization terms due to the earth geometry. We will determine the instrumental delays between the X- and Y-polarisation components and their leakages. Moreover, we will investigate how the polarisation leakage changes with frequency and with the targeted source. Last but not least, we will check the RFI situation for each station.

All collaborating parties, stations, correlator and analysts, are gaining insights in the various aspects of the project, from the more technical ones, as system settings and data recording at the stations, to the elaboration phases, including data decoding and correlation, and finally to the post-processing of the data. As mentioned in the previous section, we also plan to develop and test against each other alternative FF approaches for processing VGOS data.

Our preliminary results show the potential of VLBI broadband data. We are aware of the huge amount of work necessary to accomplish all our goals and we welcome experts in the VLBI community and other VGOS telescopes who wish to cooperate with us to make VGOS production a reality as fast as possible.

References

Anderson J M, Xu M H (2018) Source Structure and Measurement Noise Are as Important as All Other Residual Sources in Geodetic VLBI Combined. *J Geophys Res (Solid Earth)*, 123 https://ui.adsabs.harvard.edu/#abs/2018JGRB..12310162A

Cappallo R J (2014) Correlating and Fringe-fitting Broadband VGOS Data. In: D. Behrend, K. D. Baver, K. L. Armstrong (eds.): *IVS 2014 General Meeting Proceedings*, Science Press (Beijing), ISBN 978-7-03-042974-2 https://ivscc.gsfc.nasa.gov/publications/gm2014/019_Cappallo.pdf

Martí-Vidal I, Roy A, Conway J, et al. (2016) Calibration of mixed-polarization interferometric observations. Tools for the reduction of interferometric data from elements with linear and circular polarization receivers *A&A*, 587, 143

Petrachenko B, Bertarini A, Alef W, *et al.* (2014) VGOS Data Transmission and Correlation Plan, Internal Report, VGOS Project Executive Group (VPEG), Version: November 18, 2014, https://ivscc.gsfc.nasa.gov/technology/vgos-docs/VGOS_DataTransmissionCorrelation_Plan_141118.pdf

Rani B, Jorstad S G, Marscher A P (2018) High-resolution polarization imaging of the Fermi blazar 3C 279. *7th Fermi symposium proceedings (Fermi 2018)*, PoS(IFS2017)020

Sault R J, Wieringa M H (1994) Multi-frequency synthesis techniques in radio interferometric imaging. *Astronomy and Astrophysics Suppl.*, 108, 585

van Bemmel I, Small D, Kettenis M, et al. (2019) CASA on the fringe: VLBI data processing in the CASA software package. *Proc. 14th European VLBI Network Symposium & User Meeting (EVN 2018)*, PoS(EVN2018)079

Implementation of a Geodetic Path at the JIVE Correlator

M. E. Gómez, M. Kettenis, P. Charlot, R. M. Campbell, A. Keimpema

Abstract This paper reports on the progress towards the implementation of a complete geodetic path for the EVN Software Correlator at JIVE (SFXC). It is conducted as part of the JUMPING JIVE project funded by the Horizon 2020 Framework Programme of the EU. JUMPING JIVE is dedicated to enhance the position of JIVE and the European VLBI Network (EVN) within the future of radio astronomy. This includes implementation of new capabilities, among which is the possibility to correlate geodetic-type experiments and export them in a standard fashion so that they can be further processed by the usual geodetic software packages. The implementation of this new capability requires (i) to make SFXC able to handle complex geodetic-like schedules with sub-netting, and (ii) to incorporate total quantities and measured phase-cal values in the data provided to the users. To facilitate post-processing, it was also decided to convert the correlator output to the standard geodetic Mark4 format. All such developments are now complete. To test the implementation, we have reprocessed IVS session R1872 and compared the output from SFXC with that obtained at the DIFX correlator in Bonn, where the session was originally processed. The methodology is explained here and partial results of the comparison are given. These indicate a 5.5 ps wrms for the Total Multiband Delay difference between the two correlators.

Keywords JUMPING JIVE · EVN · VLBI

Maria Eugenia Gómez · Patrick Charlot
Laboratoire d'Astrophysique de Bordeaux, Pessac, France

Mark Kettenis · Robert M. Campbell · Aard Keimpema
Joint institute for VLBI-ERIC, Dwingeloo, The Netherlands

(Correspondence: maria.gomez@u-bordeaux.fr)

1 Introduction

JUMPING JIVE is the acronym for Joining up Users for Maximizing the Profile, the Innovation and Necessary Globalization of JIVE, a project funded by the European Union's Horizon 2020 programme. The project[1] is divided into ten work packages (WP) that cover various aspects from dissemination to technical developments and future science with the European VLBI Network (EVN). In this paper we are concerned with WP6 activities which have to do with the implementation of full geodetic capabilities at the EVN software correlator at JIVE (SFXC). This means that the correlator should be able to:

1. Correlate data with proper handling of geodetic sessions which are scheduled with sub-netting;
2. Attach the correlator model to the correlator output;
3. Attach phase-calibration information to the correlator output;
4. Provide correlator output in the appropriate format for further geodetic post-processing.

From the correlator output, an analysis center shoud then be able to:

5. Post-process and export the data.

The items listed above constitute also the steps of the procedure followed to validate the whole implementation at JIVE. The first step was accomplished at the end of 2017: one hour of an IVS-R1 session (which included sub-netting) was successfully correlated (Colomer et al., 2019). Steps 2 to 4 were also accomplished and are described in Keimpema and Kettenis (2019).

[1] https://jive.eu/jumping-jive

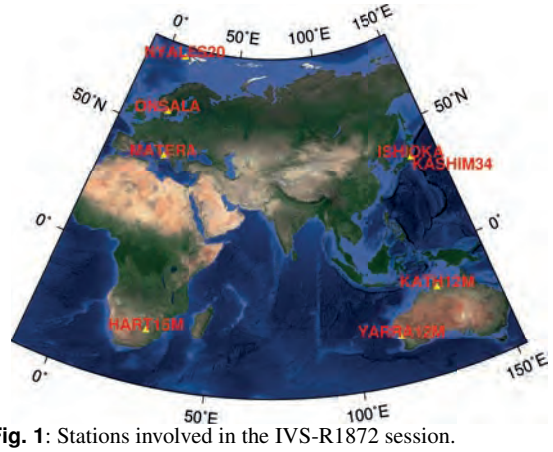

Fig. 1: Stations involved in the IVS-R1872 session.

In the following, we will focus on step 5. For that purpose, a whole 24-hour IVS session, IVS-R1872 (held on December 10, 2018) was selected. This experiment involved eight IVS stations (Fig. 1) and observed a total of 1069 scans.

2 Methodology

2.1 Correlation

IVS-R1872 was originally correlated with the DIFX correlator in Bonn. For the purpose of the project, it was also subsequently correlated at JIVE with SFXC. Both correlator outputs were exported into the standard geodetic Mark4 format. Additionally, the Bonn correlator center further exported the data into vgosDB format (version 1), which is the newest and current format for geodetic datasets, after post-processing. A difference in the processing is that SFXC used a delay model based on CALC 10 whereas the delay model used with DIFX was CALC 11.

2.2 Post-processing and data export

In order to check the Mark4 implementation and post-processing, we devised a validation procedure in two stages. The first stage comprised checking our ability to find fringes and to produce vgosDB file version 1. This was done using the correlated Mark4 files provided by the Bonn Correlator Center for IVS-R1872. They also provided us with post-processed data and the vgosDB file version 1 so that we could check our results against theirs. The comparison was done at the level of vgosDB files. The second stage of the validation comprised post-processing JIVE-correlated data for that session and compare our results with respect to those obtained in Bonn.

In the post-processing, we applied exactly the same control file as that used at the Bonn Correlation Center because there was no reason to introduce changes when processing the data correlated at JIVE. We used Fourfit (HOPS 3.18 rev 2251) for that purpose and vgosDbMake-0.4.3 to transform the data into vgosDB format. The selected version of each software was not arbitrary: it was the same as that employed in Bonn in order to avoid potential differences due to software version or other issues. Netcdf library and Octave tools were used to extract and plot the data.

According to Corey and Titus (2012), differences at the ps level between results from the two correlators should be expected. Because of differences in the correlation process and correlator architecture, the comparison was not straightforward. The time of each observation is tagged according to what is called the Fourfit Reference Time (FRT) which may differ from one correlator to the other, due to differences in how the correlators search for the first valid input data for each scan. This situation causes natural discrepancies in the Total Multiband Delay (TOTMBD) just because we are evaluating this quantity at different FRTs. For this reason, in the section below, we just show results concerning those observations that end up with the same FRT in Bonn and JIVE.

3 Results

Figure 2 shows results after comparing the vgosDB file sent by Bonn and our own vgosDB file obtained from Bonn correlated data (stage 1). The plots are for the TOTMBD and Signal to Noise Ratio (SNR) quantities in X-band. There are no appreciable differences between the two datasets at the 15-digit significancy level for any observation. This is replicated for S-band and for all the other observables like e.g. single-band delays. This initial check guarantees that no bias will

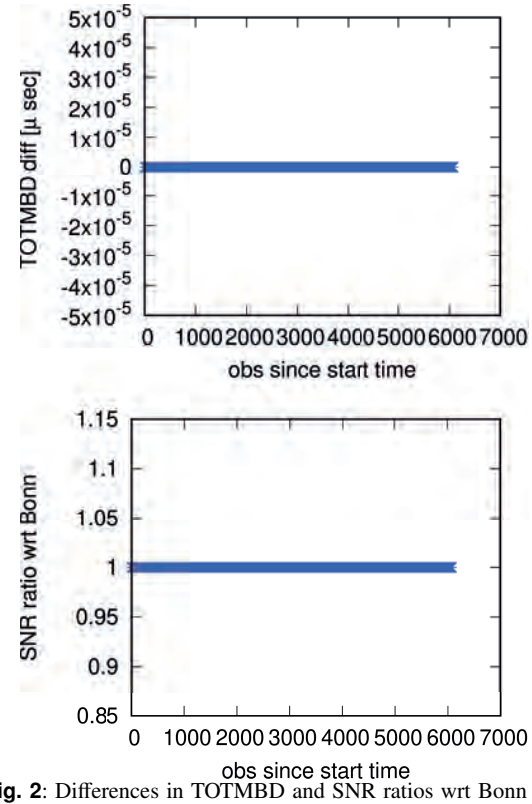

Fig. 2: Differences in TOTMBD and SNR ratios wrt Bonn obtained after comparing the original and reproduced vgosDB files from Bonn for IVS-R1872 session.

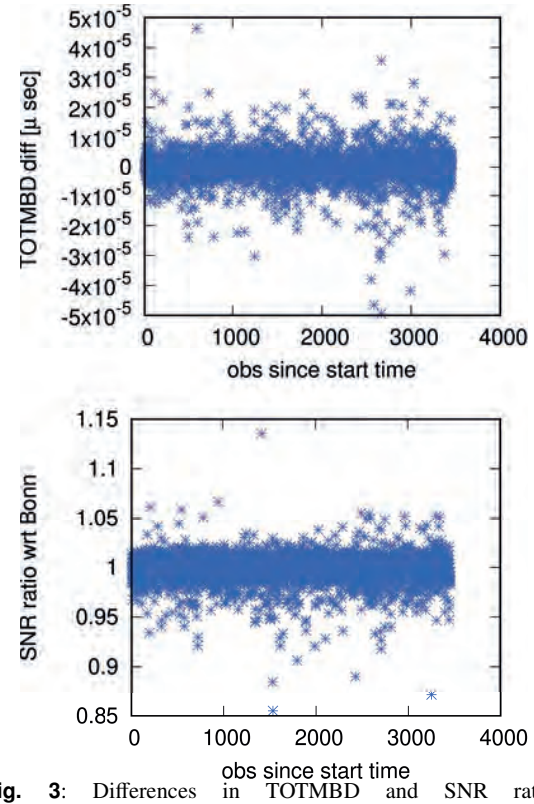

Fig. 3: Differences in TOTMBD and SNR ratios (SNR_{JIVE}/SNR_{Bonn}) obtained after comparing the vgosDB files produced by SFXC and the Bonn DiFX correlator for IVS session R1872. The comparison is limited to those observations that have the same FRTs.

come from local implementation or software version differences.

In order to reproduce the previous analysis, but now comparing the output of both correlators, we took all those observations that have the same FRT and a quality code greater than zero and we plotted the TOTMBD differences and SNR ratios for this subset of data (Fig. 3). There are 3462 of such observations within a total of 5826 observations in the session. Statistics of the TOTMBD differences indicate a 5.5 ps wRMS (weighted RMS) with all values below 50 ps and 80 % of them below 5 ps. In the case of the SNR ratio, the average value is 0.998, which means that there is no bias between SFXC and the Bonn DiFX correlator. The magnitudes of the differences between the two correlators, for the TOTMBD and SNR quantities, are according to what is expected (see Corey and Titus, 2012) and confirm that the geodetic path is correctly implemented on SFXC. The corresponding vgosDB file for IVS session R1872 is the first dataset produced in standard geodetic format after correlation with SFXC. Further study is being done on the remaining observations (i.e. those that do not have the same FRTs) in order to complete comparisons for the entire session.

4 Conclusions

We have shown that the EVN Software Correlator at JIVE (SFXC) has the capability to correlate data from a standard geodetic session and its output can be fully analysed with the most common geodetic tools. Using data correlated through SFXC we were able to produce the first dataset in the vgosDB standard geodetic format. SNR ratios and TOTMBD differences between SFXC and the Bonn DiFX correlator were analysed for those observations that have the same FRTs and are at the anticipated level. The comparison for the rest of the observations (those that do not have the

same FRTs) will also be accomplished after devising a proper scheme in order to fully complete the work.

Acknowledgements The authors would like to thank Laura La Porta and the Bonn Correlator Center for providing us with the correlated and post-processed data of the IVS-R1872 session as well as all the auxiliary files. We are also grateful to Laura La Porta for useful discussions. This research received funding from the European Union's Horizon 2020 Research and Innovation Programme, under grant agreement No. 730884.

References

Colomer F, Campbell R, Kettenis M, et al.(2018) Geodetic capabilities of the JIVE SFXC correlator. In: K. L. Armstrong, K. D. Baver, D. Behrend (eds.): *IVS 2018 General Meeting Proceedings*, NASA/CP-2019-219039, 117–120

Corey B, Titus M (2012) Multiband delay differences between Mk4 hardware and DiFX software correlations. *MIT Haystack Observatory memorandum, 2012 September 18.*

Keimpema A, Kettenis M (2019) Recent technical developments at JIVE. Presentation at 24th EVGA Working Meeting, Gran Canaria, www.oan.es/evga2019/EVGA2019_PDF/O115_EVGA2019_Keimpema.pdf

Activity Report on the Asia-Oceania VLBI Group (AOV)

T. Wakasugi

Abstract The Asia-Oceania VLBI Group for Geodesy and Astrometry (AOV) was established in 2014 as a subgroup of the International VLBI Service for Geodesy and Astrometry (IVS) in order to foster regional collaboration of VLBI. The AOV has been coordinating regular VLBI observing sessions since 2015. The total number of sessions amounts to 30 at the end of 2018, and 19 stations in five countries have participated in these sessions. The Geospatial Information Authority of Japan (GSI) has actively involved in the AOV as not only an observing station but also a scheduler and correlator. This talk will summarize activities of the AOV since its launch.

Keywords AOV

Fig. 1: The AOV logo.

1 Introduction

As you already know, the Asia-Oceania (AO) region is highly dynamic in geophysics and climate, with a large number of destructive earthquakes, tsunamis, typhoons, and cyclones. To enhance disaste resilience for the region, determination of the geodetic reference frame is essential through precise Earth observations and better understanding of tectonic plate motion, atmospheric variations etc. VLBI components in the AO region are rapidly glowing compared to IVS launch. More international collaboration is important to take full advantage of components in the region. In addition, momentum for rise of the position in the VLBI community is glowing.

To realise those ambition, some asian researchers discussed the idea of regional collaboration on geodetic and astrometric VLBI in Asia during the 21st EVGA Meeting in Finland in 2013. After that, the idea was extended to oceanian region for more effective cooperation. The foundation of a regional VLBI community for Asia-Oceania region was agreed at the 30th IVS Directing Board Meeting in September, 2013. The group was named as Asia-Oceania VLBI Group for Geodesy and Astrometry and its acronym was called AOV (Figure 1) (Kurihara et al., 2015).

Takahiro Wakasugi
Geospatial Information Authority of Japan 1 Kitasato, Tsukuba, Ibaraki 305-0811 Japan

(Correspondence: wakasugi-t96kg@mlit.go.jp)

2 Status of the AOV

The kick-off meeting was held at Shanghai in conjunction with the 8th IVS General Meeting and Terms of Reference was discussed and finalized. Jim Lovell from University of Tasmania (UTAS) was elected to the first AOV Chair and he pointed out Ryoji Kawabata (GSI) as the Secretary. AOV observations in the framework of the IVS master schedule started at March 2015. Takahiro Wakasugi (GSI) and Lucia McCallum (UTAS) assumed as the second Chair and Secretary since 2017.

AOV is composed of 12 organizations in five countries (Figure 2). A total of 19 stations has been involved in AOV sessions as of the end of 2018. Observed data are transferred and correlated at the Tsukuba VLBI Correlator operated by GSI or Shanghai Correlator operated by Shanghai Astronomical Observatory (SHAO). Scheduling tasks are shared with GSI, SHAO, and UTAS (Figure 3). AOV sessions were carried out six times per year until 2017, and are performed 12 times per year since 2018. Figure 4 shows the summary of AOV sessions planned in 2019. There are six geodetic sessions and six astrometric sessions this year. All sessions are performed at the data rate of 1 Gbps. Upgrade of the system at Syowa station in Antarctica (128 Mbps so far) enalbed us to carry out such high-rate sampling observations.

AOV face-to-face meetings have been held three times so far to exchange information and disucss various things concerning the AOV. Following the previous meetings (Hobart, Australia in 2015 and Kobe, Japan in 2017), the 3rd AOV meeting took place from November 9 – 10, 2018 in Canberra hosted by Geoscience Australia (GA) in conjunction with the 21st International Laser Ranging Workshop. A total of 20 people joined the meeting from Australia, China, Japan, New Zealand, Thailand, Russia, and USA (Figure 5). The conference is composed of the group discussion among AOV members, and a presentation-style workshop including two speekers (Michael Pearlman and Toshimichi Otsubo) from SLR expert as well as speakers from local host organization (Wakasugi and Titov, 2018). The minutes of the group discussion and all presentation slides are available on the meeting website (http://auscope.phys.utas.edu.au/aov/meetings/aov2018/3rdaovgm.html).

Organizations	Country	Organizations	Country
Commonwealth Scientific and Industrial Research Organization (CSIRO)	AUS	Korea Astronomical and Space Science Institute (KASI)	KOR
Geoscience Australia (GA)	AUS	National Geographic Information Institute (NGII)	KOR
University of Tasmania (UTAS)	AUS	Geospatial Information Authority of Japan (GSI)	JPN
Shanghai Astronomical Observatory (SHAO)	CHN	National Astronomical Observatory of Japan (NAOJ)	JPN
Xinjiang Astronomical Observatory (XAO)	CHN	National Institute of Information and Communications Technology (NICT)	JPN
Auckland University of Technology (AUT)	NZL	National Institute of Polar Research	JPN

Fig. 2: Member organisations of the AOV.

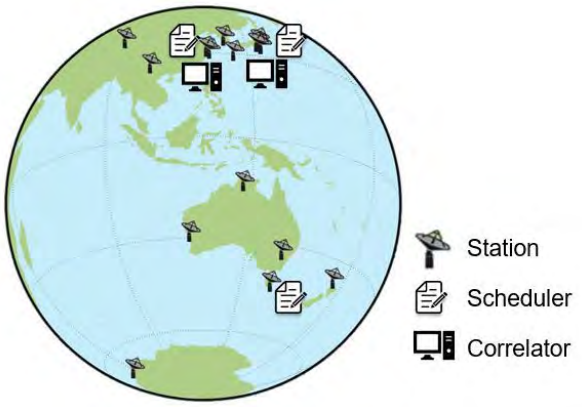

Fig. 3: AOV components.

Session	Date	Num. of stations	Scheduler	Correlator	Data rate	Bandwidth	Purpose
AOV031	JAN21	8	SHAO	SHAO	1 Gbps	1 GHz	Astro.
AOV032	FEB12	9	GSI	GSI	1 Gbps	512 MHz	Geodesy
AOV033	MAR20	8	SHAO	SHAO	1 Gbps	1 GHz	Astro.
AOV034	APR03	10	SHAO	SHAO	1 Gbps	1 GHz	Astro.
AOV035	MAY14	9	GSI	GSI	1 Gbps	512 MHz	Geodesy
AOV036	JUN18	9	SHAO	SHAO	1 Gbps	1 GHz	Astro.
AOV037	JUL17	8	SHAO	SHAO	1 Gbps	1 GHz	Astro.
AOV038	AUG07	10	UTAS	GSI	1 Gbps	512 MHz	Geodesy
AOV039	SEP17	10	GSI	GSI	1 Gbps	512 MHz	Geodesy
AOV040	OCT15	10	SHAO	SHAO	1 Gbps	1 GHz	Astro.
AOV041	NOV12	9	UTAS	GSI	1 Gbps	512 MHz	Geodesy
AOV042	DEC03	9	GSI	GSI	1 Gbps	512 MHz	Geodesy

Fig. 4: AOV sessions in 2019.

3 Conclusions and outlook

The Asia-Oceania VLBI Group for Geodesy and Astrometry (AOV) is an international collaboration in order to foster regional collaboration of VLBI established in 2014 as a subgroup of the IVS. AOV has performed international geodetic and astrometric VLBI observations regularly. AOV meetings have been held three times so far.

Some AOV components have begun their own research towards VGOS. Several intercontinental broad-

Fig. 5: Group photo at the 3rd AOV meeting in Canberra.

band experiments have already been performed between Kashima (NICT), Ishioka (GSI), and Hobart (UTAS) stations. In addition, VGOS stations in China and Thailand will be available in near future. We will work in close collaboration towards a realization of VGOS.

References

Kurihara S, Lovell J, Cho J, *et al.* (2015) Foundation of the Asia-Oceania VLBI Group for Geodesy and Astrometry. In: K. D. Baver, D. Behrend, K. L. Armstrong (eds.): *IVS 2014 Annual Report*, NASA/TP-2015-217532, 20–25

Wakasugi T, Titov O (2018) Geoscience Australia Hosts 3rd AOV Meeting in Canberra. *IVS Newsletter*, Issue 52, 6,

Results With the Scheduling Software VieSched++

M. Schartner, J. Böhm

Abstract The Department of Geodesy and Geoinformation at Technische Universität Wien has recently developed a new scheduling software called VieSched++ as part of the Vienna VLBI and Satellite Software (VieVS). VieSched++ is written in C++, it features an elaborate backward fill-in mode for minimizing station idle time and runs multiple versions of the same schedule in a fast batch mode using different optimization criteria and parameters. Large scale Monte-Carlo simulations with VieVS can then be used for selecting the best schedule for the purpose of the session within this sample. In particular, the schedules can be optimized for the given network, source list, observing mode and scientific goal. VieSched++ has already been successfully used for scheduling multiple official IVS sessions.

Keywords Scheduling · VieVS · VieSched++ software

1 Introduction

The first step of every VLBI experiment is the creation of an observing plan, the so-called schedule, which is then distributed to the participating stations. The schedule makes sure that the observations are synchronized between the stations and at least two stations observe the same source simultaneously. Therefore, the schedule determines which sources are observed in which sequence and also which and how many observations are later available for the analysis.

While several software packages exist for analyzing geodetic or astrometric VLBI sessions, like Calc/Solve (Bolotin et al., 2014), the Vienna VLBI and Satellite Software (VieVS) (Böhm et al., 2018), OCCAM (Titov et al., 2004), c5++ (Hobiger et al., 2010), Where (Hjelle et al., 2017) or GINS (Bourda et al., 2007), this is not the case for scheduling. In the past, almost all geodetic sessions were scheduled with a software called sked (Vandenberg, 1999) while astronomic sessions are scheduled using Sched (Walker, 2018). For geodesy and astrometry, the only notable exception were AUSTRAL sessions (Plank et al., 2017) which were, in the past, scheduled using a Matlab based scheduler (Sun, 2013) which is part of VieVS. However, starting in 2018 several observing programs are now scheduled using a new modern scheduling software called VieSched++ (Schartner and Böhm, 2019) which is also part of VieVS. The following lists shows some of the official International VLBI Service for Geodesy and Astrometry (IVS) (Nothnagel et al., 2017) schedules, generated with VieSched++:

- AUA (035, 037, 040, 041, 044, 047)
- AUM (001 - 010)
- T2 (129, 130, 131, 132)
- EURR&D (09, 10)
- EUR (149)
- OHG (171, 118, 119)
- CRF (110)
- CRDS (102, 103)
- INT3 (021, 028, 035, 042, 049, 056, 063... 182)

Matthias Schartner · Johannes Böhm
TU Wien, Department of Geodesy and Geoinformation, Gußhausstraße 27–29, AT-1040 Vienna, Austria

(Correspondence: matthias.schartner@geo.tuwien.ac.at)

2 Method

VieSched++ is written in C++ and uses a brute force approach to generate schedules, similar to sked (Gipson, 2010). However, all algorithms are newly developed to be able to generate high-quality schedules. For example, VieSched++ uses a recursive scan selection to minimize station idle time (Schartner and Böhm, 2019a,b). It provides an automated iterative source selection and great care was taken to fine-tune the optimization parameters to implement a good scan selection. Since the complexity of optimizing a schedule is very high, VieSched++ comes along with a multi-scheduling feature which is able to not only generate one single schedule but multiple ones simultaneously. These schedules can then be used in the VieVS VLBI software directly for simulations and based on those simulations the best schedule can be selected.

More information about the features and algorithms used in VieSched++ can be found in Schartner and Böhm (2019a).

The schedules further discussed in section 4 are created using the multi-scheduling feature. On average, 500 schedules are generated per session varying the weight factors, as they have the biggest impact on the scan selection logic, see Schartner et al. (2017) or Schartner and Böhm (2019a,b). Each of these schedules is simulated 500 times using the VieVS VLBI software. The simulation includes tropospheric turbulences, clock drifts, and white noise (Pany et al., 2011). The same simulation parameters are used for all sessions and all stations. The troposphere is simulated using a turbulence simulator with C_n values of $1.8 \cdot 10^{-7}$ $m^{-1/3}$ and a scale height of 2 km (Nilsson et al., 2007). The clock is simulated using random walk and integrated random walk corresponding to 10^{-14} at 50 minutes (Herring et al., 1990). Additionally, 30 ps white noise is added to the observations.

3 Results

In the following subsections, results gained for the T2, EURR&D and INT3 observing programs are further discussed and compared with previously submitted schedules generated with sked. The schedules generated with VieSched++ are highlighted in blue in Table 1 and Table 2. The fact that the sked schedules are performing that poorly compared to the VieSched++ schedules is not necessarily due to limitations in the sked scheduling software but also due to the fact that these schedules were created using bad scheduling parameters. By using different scheduling parameters, the sked solution could be improved as well (John Gipson, personal communication 2019). However, optimizing scheduling parameters is not that easy in sked and these schedules were submitted and observed with this unoptimized schedules.

3.1 T2

The aim of the T2 schedules is to provide accurate station coordinates for estimating terrestrial reference frames. These sessions consist of the biggest station networks of all official IVS sessions with 15 to 22 participating stations. However, the network geometry is far from optimal. Since most of the stations are in the northern hemisphere (Plank et al., 2015) this situation is also reflected in the T2 network geometry. For example, 15 stations are participating in session T2129 but only two of those are in the southern hemisphere, namely HartRAO and O'Higgins.

The observations are recorded using a low sampling rate of 128 Mbit/s which is problematic since some of the stations have very low sensitivity with a system equivalent flux density (SEFD) of more than 10.000. The suboptimal geometry of the network, together with the low recording rate makes it especially hard to include O'Higgins into the schedule. O'Higgins has very high SEFD values of 10.000 in X-Band and 18.000 in S-Band and is located in Antarctica.

Table 1 compares statistics of schedules generated with sked and VieSched++.

In the previously submitted schedules generated with sked, the number of observations with O'Higgins is always below 100 after 24 hours. One of the goals of the new schedules is to include O'Higgins better into the session. By using VieSched++ it is possible to increase the number of observations with O'Higgins by a factor of four as can be seen in Table 1.

In general, the number of observations with VieSched++ is about twice the number of observations with sked, sometimes even three times, while the number of scans roughly stays the same or is even lower.

Table 1: comparison of statistics between schedules created with sked (top) and VieSched++ (bottom, blue) for T2 sessions

	#sta	#scans	#obs	%idle	%obs	#obs Oh
T2123	19	617	6773	30.98	50.46	79
T2124	17	733	7175	28.10	44.54	22
T2125	17	1064	5528	22.94	53.70	48
T2126	17	1075	6081	24.55	49.66	98
T2127	19	627	6304	34.30	45.22	73
T2128	18	803	5983	26.24	44.90	97
T2129	15	526	12713	8.20	66.90	400
T2130	22	626	16730	10.45	69.24	451
T2131	19	771	15714	4.33	73.68	267
T2132	18	631	10219	6.04	73.37	406

This means that on average scans with more participating stations are scheduled. Additionally, it is possible to reduce the idle time of the stations by a factor of two to three and increase the observing time by almost 50 %.

3.2 EURR&D

Similar to the T2 session, the aim of the EURR&D sessions is to provide high accuracy station coordinates for terrestrial reference frames. The network consists of mostly European stations and the observing rate is 512 Mbit/s, which makes it easier to generate a good schedule.

Table 2 compares statistics of schedules generated with sked and VieSched++.

Table 2: Comparison of statistics between schedules created with sked (top) and VieSched++ (bottom, blue) for EURR&D sessions

	#sta	#scans	#obs	%idle	%obs
EURD05	8	374	10134	25.00	39.97
EURD06	6	538	8061	21.63	30.87
EURD07	8	344	9437	36.42	29.40
EURD08	7	361	7215	25.78	33.08
EURD09	8	665	11565	5.78	39.03
EURD10	8	669	13480	3.08	42.70

Compared to the results from T2 listed in Table 1 the improvement regarding scheduling statistics seems lower based on the statistical values. However, VieSched++ is able to generate schedules with a higher number of observations but this time the number of scans also increases. The main difference between the sked schedules and the VieSched++ schedules is the

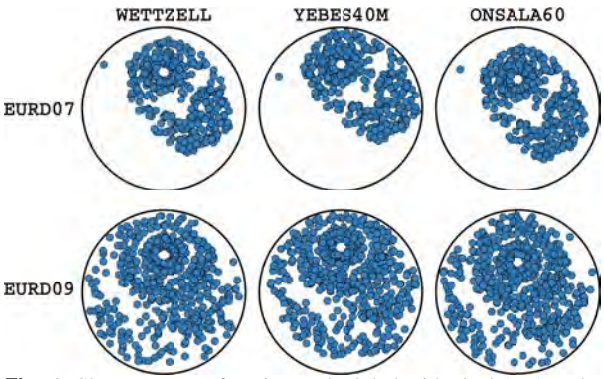

Fig. 1: Sky coverage of stations scheduled with sked (top) and VieSched++ (bottom).

sky coverage of the stations as shown in Figure 1. Since sked only schedules scans with the full network it focuses mainly on one small part of the sky. This results in low slew times and thus many observations but also in a very poor sky coverage as shown in Figure 1 for EURD07. In contrast VieSched++ decides to split the network more often resulting in a way better sky coverage as shown in Figure 1 for EURD09. A good sky coverage helps to estimate tropospheric time delays which are one of the major error sources in geodetic VLBI (Schuh and Böhm, 2013). Especially observations at different elevations are necessary to distinguish tropospheric delays, clocks and station heights which are highly correlated (Nothnagel et al., 2002).

Compared to the sked solutions it is possible to reduce the idle time by a factor of four to five as shown in Table 1. The time gained is used mostly for slewing purposes to achieve better sky coverage.

3.3 INT3

The purpose of the INT3 sessions is to provide dUT1 values. The network consist of four to five stations, the observing rate is 1024 Mbit/s and the session duration is only one hour. Since the complexity of intensive schedules is relatively simple due to the low number of stations and short session duration, scheduling of intensive sessions is rather easy compared to global 24-hour sessions. Therefore, it was not expected to gain significant improvement when changing from sked to VieSched++. However, Figure 2 shows that even for

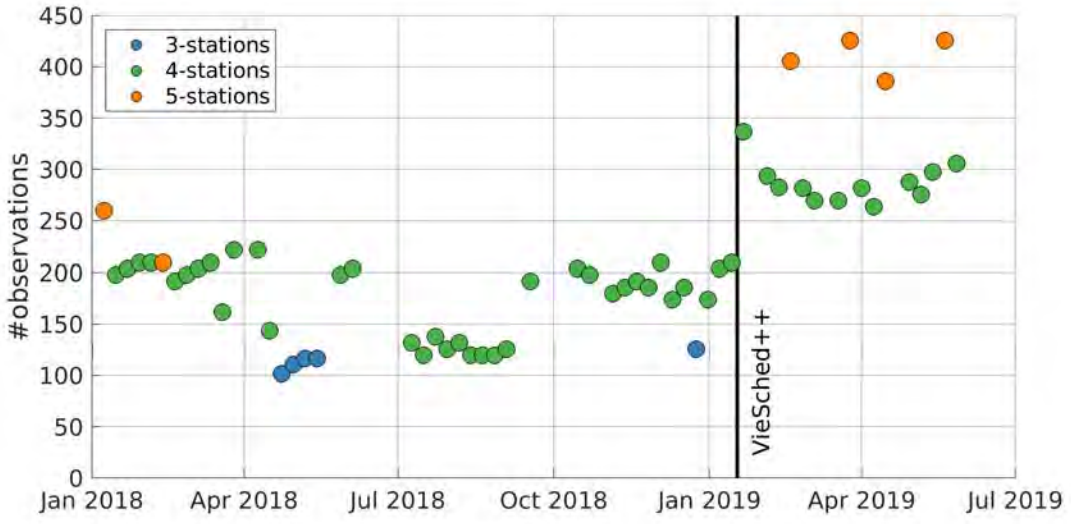

Fig. 2: Number of observations in INT3 sessions color-coded by number of participating stations.

intensive sessions the number of observations can be improved.

Figure 3 shows the dUT1 formal error gained from intensive sessions as they are listed in the analysis reports. The values are color-coded by the number of participating stations, the analysis center which delivered the analysis report and by the observing rate. Figure 4 shows the same values, but this time only the INT3 sessions are colored. Starting with 21st of January 2019, VieSched++ is used to generate these schedules.

It can be seen that the INT3 sessions provide the most accurate dUT1 estimates, due to the higher number of stations and the higher observing rate. While Figure 2 shows the number of scheduled stations, Figure 3 and Figure 4 show the number of stations which were actually observing the session, since it can happen that one station drops out.

Figure 4 shows, that by changing the scheduling software to VieSched++ the formal errors of the dUT1 values is improved to solutions from the previous half year. At the beginning of 2018, the accuracy was roughly at the same level, while after April 2018 the results got significantly worse. It is unclear why this happened, however, it corresponds with a time period where the number of observations was also very low as seen in Figure 2.

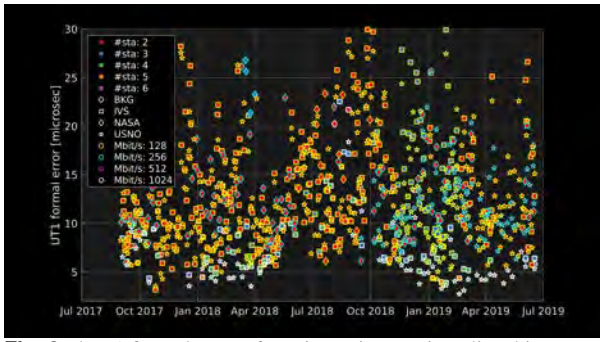

Fig. 3: dUT1 formal errors from intensive sessions listed in analysis reports, color-coded by number of stations, analysis center and sampling rate.

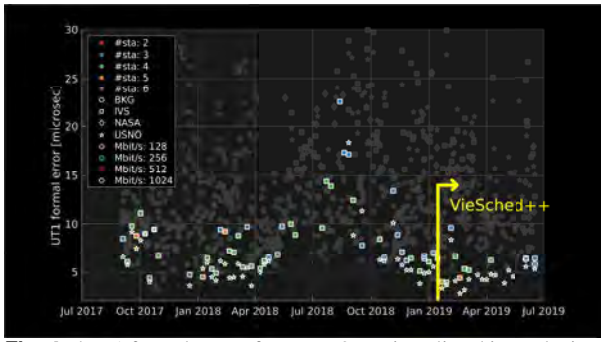

Fig. 4: dUT1 formal errors from INT3 sessions listed in analysis reports, color-coded by number of stations, analysis center and sampling rate.

4 Conclusions and outlook

VieSched++ is a new, modern VLBI scheduling software written in C++. It uses many new features and algorithms to generate high-quality schedules. While generating optimized schedules for VLBI experiments should be the norm, unfortunately, this is not the case. This work shows, that it is possible to achieve twice the number of observations compared to previously uploaded results. Based on the newly created optimized schedules, improvements can also be expected during analysis for these sessions. Unfortunately, so far this could only be verified for INT3 sessions since most other sessions are not yet correlated and no VgosDB database are available for analysis at the moment.

While VieSched++ is already stable and freely available through our GitHub page https://github.com/TUW-VieVS, development continues to improve the quality of the generated schedules even further. Additionally, a YouTube channel called *"VieVS"* is available, where the usage of VieSched++ is explained.

References

Böhm J, Böhm S, Boisits J, et al. (2018) Vienna VLBI and Satellite Software (VieVS) for Geodesy and Astrometry. *PASP*, 130, 044503, doi:10.1088/1538-3873/aaa22b

Bolotin S, Baver K, Gipson J, et al. (2014) The VLBI Data Analysis Software *v*Solve: Development Progress and Plans for the Future. In: D. Behrend, K. D. Baver, K. L. Armstrong (eds.): *IVS 2014 General Meeting Proceedings*, Science Press (Beijing), 253–257

Bourda G, Charlot P, Biancale R (2007) VLBI analyses with the GINS software for multi-technique combination at the observation level. *Proceedings of the Annual meeting of the French Society of Astronomy and Astrophysics*, 82

Gipson J (2010) An Introduction to Sked. In: D. Behrend, K. D. Baver (eds.): *IVS 2010 General Meeting Proceedings*, NASA/CP-2010-215864, 77–84

Herring T, Davis J, Shapiro I (1990) Geodesy by radio interferometry: The application of Kalman Filtering to the analysis of very long baseline interferometry data. *J Geophys Res*, 95, 12561–12581, doi:10.1029/JB095iB08p12561

Hjelle G A, Dähnn M, Fausk I, et al. (2017) Introducing a New Software for Geodetic Analysis. *EGU General Assembly Conference Abstracts*, 19, 8486

Hobiger T, Otsubo T, Sekido M, et al. (2010) Fully automated VLBI analysis with c5++ for ultra-rapid determination of UT1. *Earth, Planets and Space*, 62, 933–937 doi:10.5047/eps.2010.11.008

Nilsson T, Haas R, Elgered G (2007) Simulations of atmospheric path delays using turbulence models. *Proc. 18th EVGA Working Meeting*, 175–180

Nothnagel A, Vennebusch M, Campbell J (2002) On correlations between parameters in geodetic VLBI data analysis. In: Na. R. Vandenberg, K. D. Baver (eds.): *IVS 2002 General Meeting Proceedings*, NASA/CP-2002-210002, 260–264

Nothnagel A, Artz T, Behrend D, et al. (2017) International VLBI Service for Geodesy and Astrometry. *J Geod*, 91, 711–721 doi:10.1007/s00190-016-0950-5

Pany A, Böhm J, MacMillan D, et al. (2011) Monte Carlo simulations of the impact of troposphere, clock and measurement errors on the repeatability of VLBI positions. *J Geod*, 85, 39–50, doi:10.1007/s00190-010-0415-1

Plank L, Lovell E J, Shabala S, et al. (2015) Challenges for geodetic VLBI in the southern hemisphere. *ASR*, 85, doi:10.1016/j.asr.2015.04.022

Plank L, Lovell E J, McCallum J N, et al. (2017) The AUSTRAL VLBI observing program. *J Geod*, 85, doi:10.1007/s00190-016-0949-y

Schartner M, Böhm J, Mayer D, et al. (2017) Recent Developments in Scheduling with VieVS. In: R. Haas, G. Elgered (eds.): *Proc. 23rd EVGA Working Meeting*, 113–116

Schartner M, Böehm J (2019a) VieSched++: A New VLBI Scheduling Software for Geodesy and Astrometry. *PASP*, 131, 084501, doi:10.1088/1538-3873/ab1820.

Schartner M, Böehm J (2019b) VieSched++: A new Scheduling Tool in VieVS. In: K. L. Armstrong, K. D. Baver, D. Behrend (eds.): *IVS 2018 General Meeting Proceedings*, NASA/CP-2019-219039, 71–75

Schuh H, Böehm J (2013) Very Long Baseline Interferometry for Geodesy and Astrometry. *Berlin, Heidelberg: Springer*, 339–376, doi:10.1007/978-3-642-28000-9_7.

Sun L (2013) VLBI scheduling strategies with respect to VLBI2010. *Geowissenschaftliche Mitteilungen*, 92.

Titov O, Tesmer V, Böhm J (2004) OCCAM v.6.0 Software for VLBI Data Analysis. In: N. Vandenberg, K. D. Baver (eds.): *IVS 2004 General Meeting Proceedings*, NASA/CP-2004-212255, 267–271

Vandenberg N R (1999) sked: Interactive/Automatic Scheduling Program. *Greenbelt, MD: Goddard Space Flight Center*.

Walker R C (2018) The SCHED user manual.

INT9 - ΔUT1 Determination Between the Geodetic Observatories AGGO and Wettzell

C. Plötz, T. Schüler, H. Hase, L. La Porta, M. Schartner, J. Böhm, S. Bernhart, C. Brunini, F. Salguero, J. Vera, A. Müskens, G. Kronschnabl, W. Schwarz, A. Phogat, A. Neidhardt, M. Brandl

Abstract The AGGO radio telescope, located at La Plata in Argentina, comprises together with the radio telescopes in Wettzell, Germany a baseline configuration spanning a longitude difference of 71°. Therefore, starting in the middle of 2018, tests were initiated to prove the usability for ΔUT1 determination between the traditional S/X VLBI systems at AGGO and Wettzell. The 6 m AGGO radio telescope was scheduled in combination with the 20 m radio telescope Wettzell (RTW) and the 13.2 m Wettzell North (WETTZ13N) in weekly VLBI tests for ΔUT1 determination, named INT9. The scheduling of INT9 sessions was done with *sked* and the time duration was set to be two hours each. The sessions were conducted mostly on Thursdays, just before the normal INT-1 Intensive session takes place. The recording mode needed to be evaluated step by step to increase gradually from a standard 256 Mbit/s recording mode to 1 Gbit/s. The latter mode yields a higher amount of scans in a given time period. The goal is to exploit the highest ΔUT1 determination accuracy between AGGO and Wettzell as possible. We will report our initial experiences with the VLBI operation at both observatories and compare first results between official ΔUT1 measurements and the INT9 derived values as well as a potential future outlook of this INT9 VLBI application.

Keywords Intensive · ΔUT1 · Geodetic Observatory Wettzell · AGGO

Christian Plötz · Torben Schüler · Gerhard Kronschnabl · Walter Schwarz · A. Phogat
Geodätisches Observatorium Wettzell, Bundesamt für Kartographie und Geodäsie (BKG), Sackenrieder Str. 25, DE-93444 Bad Kötzting, Germany

Hayo Hase
Argentinean German Geodetic Observatory, Bundesamt für Kartographie und Geodäsie (BKG), Sackenrieder Str. 25, DE-93444 Bad Kötzting, Germany

Claudio Brunini · F. Salguero · J. Vera
Argentinean German Geodetic Observatory, Conicet, Camino Gral. Belgrano Km 40 - Berazategui, Provincia de Buenos Aires, Argentina

Alexander Neidhardt · M. Brandl
Forschungseinrichtung Satellitengeodäsie (FESG), Technische Universität München, Sackenrieder Str. 25, DE-93444 Bad Kötzting, Germany

Matthias Schartner · Johannes Böhm
TU Wien, Department of Geodesy and Geoinformation, Gußhausstraße 27–29, AT-1040 Vienna, Austria

Arno Müskens
Institute of Geodesy and Geoinformation, University of Bonn, Nußallee 17, DE-53115 Bonn, Germany

Laura La Porta · Simone Bernhart
Reichert GmbH/BKG, Hittorfstr. 26, DE-53129 Bonn, Germany

(Correspondence: ploetz@fs.wettzell.de)

1 Introduction

The Argentinean German Geodetic Observatory (AGGO) was successfully re-initiated after the transport from Chile to Argentina. Due to the extended idle period, several components of the VLBI system were defect or showed malfunctions.

In particular, the analog baseband converters and the up-converter of the analog backend had failures and needed to be repaired. After this maintenance, the VLBI system at AGGO became operational in spring 2018. The VLBI system needed to be tested carefully

and its stability had to be evaluated, before taking part again in the normally scheduled VLBI sessions within the International VLBI Service (IVS) (Nothnagel et al., 2017). This was done first with test sessions coordinated between the Bundesamt für Kartographie und Geodäsie (BKG) radio telescopes of the Geodetic Observatory Wettzell and AGGO. When the first fringes were successfully found, the demand came up to evaluate geodetic VLBI applications. A ⊿UT1 determination is a favorable geodetic application, due to the longitude difference of 71° between AGGO and Wettzell. Therefore, a demonstration program including a series, consisting of test sessions was initiated to prove that this baseline configuration is sufficient for the ⊿UT1 determination.

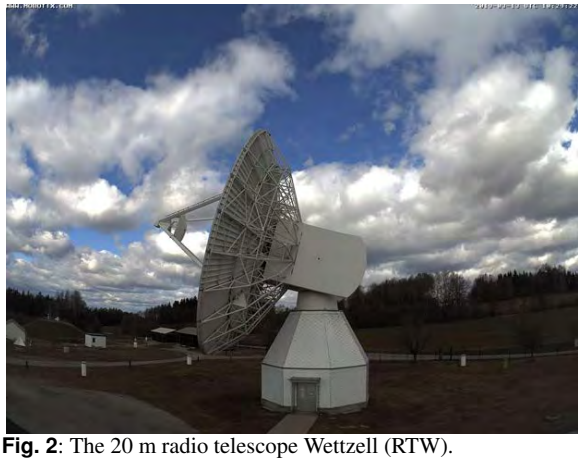

Fig. 2: The 20 m radio telescope Wettzell (RTW).

The 20 meter radio telescope Wettzell (RTW or Wz) of the geodetic observatory Wettzell constitutes a stable reference station within the VLBI community since 1983. Especially, the ⊿UT1 Intensive measurement INT-1 with a one hour session between the RTW and the 20 meter radio telescope of Kokee Park is normally observed every week from Monday until Friday. Thus, a comparison of the ⊿UT1 performance of the Wettzell to AGGO baseline in relation to the frequently observed baseline Wettzell to Kokee Park would be of high interest. Another aspect is that the most VLBI stations are located on the northern hemisphere, including VLBI stations that are involved in frequent Intensive ⊿UT1 VLBI measurements, whereas AGGO is located on the southern hemisphere. Additionally, the difference in latitude of 84° might provide information about an estimate of the polar motion. Though, the pole position was held fixed in those initial investigations.

The challenges to overcome were to establish the complete processing chain, i.e. scheduling the Intensive session, correlating with the *DiFX* software correlator (Deller et al., 2007) and obtaining results from analysis. The main limitation is the rather high system equivalent flux density (SEFD) of the AGGO radio telescope. Therefore, with the same observing mode (256 Mbit/s) as for an INT-1 Intensive observation, a rather long observation time on a radio source is necessary to reach a minimum signal to noise ratio (SNR) goal of 20 in X-band and 15 in S-band. The tests were then focused to test the 1 Gbit/s mode, which is also feasible with the old analog backend of AGGO. This 1 Gbit/s mode is used successfully with the weekly INT-3 Intensive observations.

Fig. 1: The 6 m radio telescope AGGO.

Fig. 3: The 13.2 m twin radio telescopes Wettzell.

2 Method

Several issues needed to be solved in order to reach Intensive observation capability. The scheduling was done initially with the scheduling program *sked* (Gipson, 2010) and later on with *VieSched++* (Schartner and Böhm, 2019). As a first approach, the formerly proven VLBI mode with 256 Mbit/s and one-bit sampling was chosen. This is a standard mode in R1 sessions and was frequently used before with IVS-R1 sessions at AGGO. Hence, the first test observation resulted in immediate fringes and analysis results. The SEFD of the 20 meter RTW is 750 Jy in X-band and 1000 Jy in S-band. In contrast, the values of AGGO are 10000 Jy in X-band and 15000 Jy in S-band. The only way to achieve more scans per observation time is to increase the total data rate to yield a reasonable number of scans within two hours of Intensive observation time, with the given antenna characteristics. Thus, the use of the 1 Gbit/s mode was clearly the preferred observation mode, because this one enables more scans and leads to better analysis results as the 256 Mbit/s total data rate mode. However, it was quite tricky to set up the backend properly with the VLBA4 analog backend of AGGO during these tests. In particular the trackform layout for the DiFX software correlator, which has to be set up in the session vex file, turned out to be more complicated than expected. The raw data was correlated at the VLBI correlator in Bonn first and then some sessions were correlated at Wettzell. The analysis of the INT9 sessions was done with *VieVS* (Böhm et al., 2018) at the TU Vienna.

Fig. 4: Baseline configuration of AGGO and Wettzell. The distance between Wz and Ag appears as surface distance.

Table 1: Characteristic antenna parameters.

	RTW (Wz)	TTW1 (Wn)	AGGO (Ag)
antenna diameter (m)	20	13.2	6
S-SEFD (Jy)	1150	1050	15000
X-SEFD (Jy)	750	1400	20000
Az-speed ($^\circ s^{-1}$)	4	12	6
El-speed ($^\circ s^{-1}$)	1.5	6	2

The twin radio telescope TTW1 (WETTZ13N or Wn) is equipped with a S/X/Ka-band receiving system and scheduled regularly in the IVS observation program. Depending on the availability of the respective telescopes, this Wettzell radio telescope was also scheduled alone or even together with the 20 m radio telescope in conjunction with AGGO. This leads to three different baseline configurations.

- Ag – Wz
- Ag – Wn
- Ag – Wn – Wz

In general, the session scheduled with all three radio telescopes is expected to give the best accuracy of the UT1 formal error. Most of the observations were scheduled on Thursdays between 16 and 18 UT before the regular INT-1 session between Wettzell to Kokee Park takes place.

3 Results

The first analysis results of the session wb207q, observed with the 256 Mbit/s mode, showed an UT1 formal error of 105 µs. The number of scans is very low, only 25 scans in two hours and no further improvements like consolidated coordinates of AGGO were applied.

The next milestone could be achieved when the 1 Gbit/s observation mode worked correctly. The session wb213q consisted of 35 scans within two hours of observation. This caused the UT1 formal error to decrease by almost 50 % to 56 µs. Consequently, the

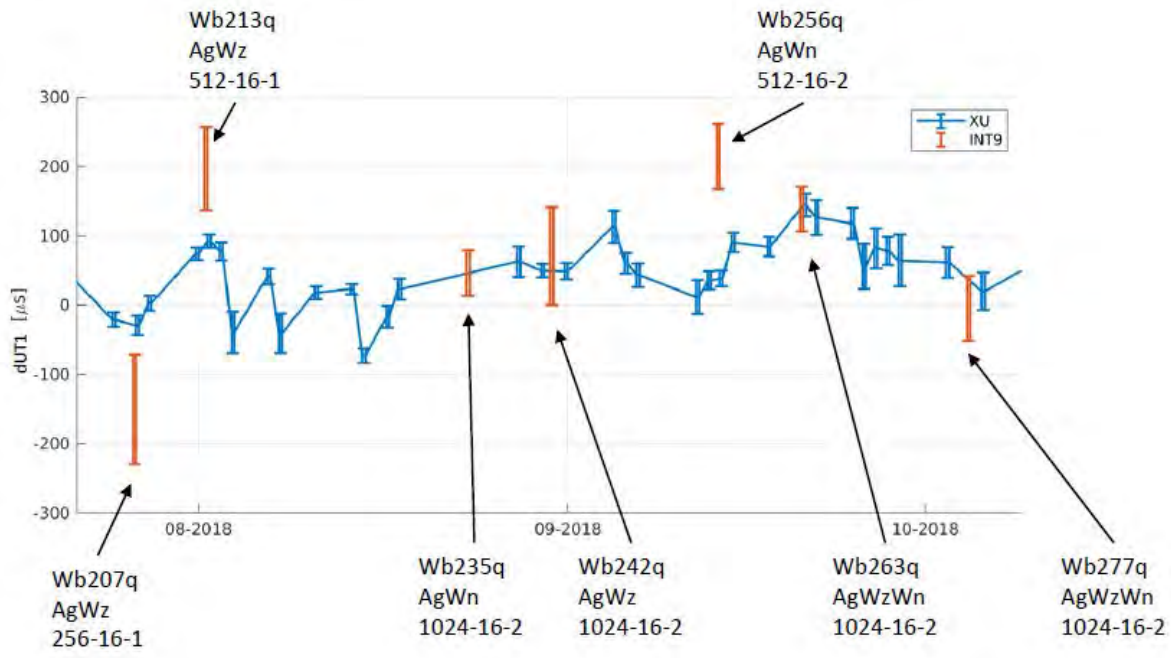

Fig. 5: ⊿UT1 with respect to C04.

triple configuration with both radio telescopes involved at Wettzell and AGGO lowered the formal error of UT1 to 48 µs again.

Figure 5 depicts the UT1 estimates as well as their formal uncertainties in contrast to the IERS-C04 time series. For comparison, the INT-1 estimates (XU) and their formal uncertainties are displayed as well. It can be seen that the estimates of the 1 Gbit/s agree quite well with the INT-1 results. The formal uncertainties tend to be a bit higher than their INT-1 counterparts. It is expected that the accuracy increases as soon as the station coordinates of the relatively new AGGO station are known more precisely. Additionally, further improvement is expected as soon as the scheduling is fine-tuned.

Simulations of this triple configuration yield a UT1 formal error of about 30 µs. The simulations were made using VieVS according to Pany et al. (2011) and include tropospheric time delays, clock drifts and white noise. The troposphere was simulated with C_n values of $1.8 \cdot 10^{-7}$ $m^{-1/3}$, a scale height of 2 km and a constant wind velocity of 8 m/s towards east (Nilsson et al., 2007). The clock was simulated as the sum of a random walk and an integrated random walk with an Allan standard deviation (ASD) of 1×10^{-14} seconds after 50 minutes (Herring et al., 1990). Finally, 30 ps of white noise was added to the observations.

Unfortunately, it turned out that the schedules of the observed sessions were not fully optimized for the sessions. Figure 6 compares the simulated formal errors between different scheduling approaches. By using VieSched++, optimized schedules are generated and compared with the observed schedules based on simulations. It can be seen that it is possible to increase both, the number of observations per session as well as the expected formal uncertainties of the UT1 estimate.

4 Conclusions and outlook

The initial performance of the INT9 test sessions between AGGO and both Wettzell radio telescopes is encouraging. If everything is settled a formal UT1 error of about 30 µs appears to be feasible. The upgrade of the analog VLBA4 backend system with a DBBC2 is planned by the end of 2019 or the beginning of 2020. This might improve the system performance and stability of AGGO. Further improvements can be expected by optimizing the scheduling and selecting the sources more carefully as done in Gipson and Baver

Sessions	Optimized schedule for simulation		Observed schedule for initial phase of INT9			
	Number of Observations	UT1 formal error [µs]	Number of Observations	UT1 error [µs]	Stations	Mode / Mbps
wb207q	28	79.2	25	104.7	AgWz	256
wb213q	52	44.7	35	55.7	AgWz	1024
wb256q	36	55.4	29	53.5	AgWn	512
wb263q	129	30.8	123	47.9	AgWnWz	1024
wb277q	129	34.3	102	70.1	AgWnWz	1024

Fig. 6: INT9 comparison between simulation and measurement. The indicated *UT1 formal error* was determined by simulation. The *UT1 error* shows the results gained by the observations.

(2015). Then a test of even 2 Gbit/s total data rate might be an option to get more scans per observation. Further careful evaluation of important parameters like source selection, correct application of the radio telescope specific peculiar time offsets, radio frequency interference (RFI) avoidance zones, consolidated coordinates of AGGO could improve the results of ΔUT1. A routine setup of a triple radio telescope configuration, consisting of RTW, TTW1 and AGGO might yield the best formal errors. Regularisation of the INT9 campaign including a rapid correlation and subsequent data analysis is foreseen in 2019 and 2020. Finally, AGGO demonstrated its potential to a self-contained estimation of ΔUT1.

References

Böhm J, Böhm S, Boisits J, et al. (2018) Vienna VLBI and Satellite Software (VieVS) for Geodesy and Astrometry, *PASP*, 130(986), 044503, doi:10.1088/1538-3873/aaa22b

Deller A, Tingay S, Bailes M, et al. (2007) DiFX: A software correlator for very long baseline interferometry using multi-processor computing environments. (Swinburne U., Ctr. Astrophys. Supercomput.). Feb 2007. 41 pp. *PASP* 119, 318, doi:10.1086/513572

Gipson J (2010) An Introduction to Sked. In: D. Behrend, K. D. Baver (eds.): *IVS 2010 General Meeting Proceedings*, NASA/CP-2010-215864, 77–84

Gipson J, Baver K (2015) Improvement of the IVS-INT01 sessions by source selection: development and evaluation of the maximal source strategy. *J Geod*, 90(3), 287–303, doi:10.1007/s00190-015-0873-6

Herring T, Davis J, Shapiro I (1990) Geodesy by radio interferometry: The application of Kalman Filtering to the analysis of very long baseline interferometry data. *J Geophys Res*, 95, 12561–12581, doi:10.1029/JB095iB08p12561

Nilsson T, Haas R, Elgered G (2007) Simulations of atmospheric path delays using turbulence models. *Proc. 18th EVGA Working Meeting*, 175–180

Nothnagel A, Artz T, Behrend D, et al. (2017) International VLBI Service for Geodesy and Astrometry. *J Geod*, 91, 711–721, doi:10.1007/s00190-016-0950-5

Pany A, Böhm J, MacMillan D, et al. (2011) Monte Carlo simulations of the impact of troposphere, clock and measurement errors on the repeatability of VLBI positions. *J Geod*, 85, 39–50, doi:10.1007/s00190-010-0415-1

Schartner M, Böhm J (2019) VieSched++: A New VLBI Scheduling Software for Geodesy and Astrometry. *PASP*, 131, 1002, doi:10.1088/1538-3873/ab1820

LCONT18 - The Local Continuous Measurement Campaign at the Geodetic Observatory Wettzell of 2018

T. Schüler, C. Plötz, G. Kronschnabl, W. Schwarz, A. Neidhardt, M. Brandl, L. La Porta, S. Bernhart

Abstract LCONT18 was the local continuous measurement campaign of the year 2018 to derive local ties, i.e. relative radio telescope positions, at the Observatory. The baseline adjustment was performed using X-band group delay data at the traditional center frequency of 8.6 GHz. Ionospheric delays cancel out due to high spatial correlation over these baselines as short as 123 m and less. Data were collected over two weeks. Preliminary analysis results of an initial subset of data are presented in this paper. Compared to other local experiments conducted between 2015 and 2017, the LCONT18 data set suffers from X-band radio interference. Though S-band interference is common, problems in X-band have not yet registered so far. However, millimetre repeatability can still be reached.

Keywords Local radio telescope positioning · Local ties · Short baseline interferometry · Geodetic Observatory Wettzell · LCONT

Torben Schüler · Christian Plötz · Gerhard Kronschnabl · Walter Schwarz
Geodetic Observatory Wettzell, Federal Agency for Cartography and Geodesy, Sackenrieder Str. 25, DE-93444 Bad Kötzting

Torben Schüler also
University of the Federal Armed Forces Munich, Faculty of Aerospace Engineering, DE-85577 Neubiberg

Alexander Neidhardt · Martin Brandl
Geodetic Observatory Wettzell, Technical University Munich, Sackenrieder Str. 25, DE-93444 Bad Kötzting

Laura La Porta · Simone Bernhart
Bonn Correlator, Reichert GmbH

(Correspondence: schueler@fs.wettzell.de)

1 Introduction

The Wettzell radio telescope triple is a local network of VLBI telescopes comprising two VGOS-capable systems with an antenna aperture of 13.2 m and one traditional system with a diameter of 20 m. Each of these telescopes has its individual receiving system at the moment: Whilst *Wz* (RTW, the 20 m telescope) features a legacy S/X-receiver, *Wn* ("Wettzell North" - TWIN1) can be equipped with either a tri-band receiver (S/X/Ka) or a broadband feed (not used in this campaign), and *Ws* ("Wettzell South" - TWIN2) is equipped with a broadband receiver ("Elevenfeed").

LCONT18 was a local intensive measurement campaign between Dec, 3rd and Dec, 14th 2018. For the first time, the complete network observed both synchronously and continuously for a duration of two weeks (twice 5 working days in sequence). It is named in analogy to the well-known international CONT-campaigns organized by the IVS. Data were collected in a standard 256 Mbit/s recording mode with a duration of up to 24 hours from Monday till Friday. The individual baselines *WzWn* as well as *WnWs* had been tested before minimizing the risk of failure.

LCONT18 is the most exhaustive local campaign planned so far at Wettzell. This is important, because the individual baselines observed up to now are not sufficient to assess all essential/substantial questions related to the relative radio telescope positioning over local baselines. In summary, the purpose of this measurement campaign is as follows:

1. We want to investigate the day-to-day repeatability of the local telescope coordinates (local baselines) in detail. The period at the beginning of December

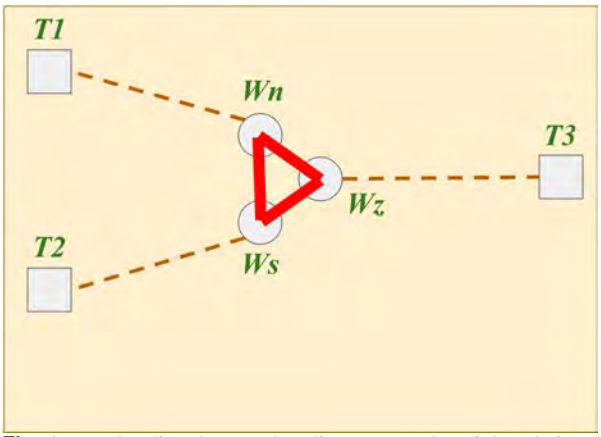

Fig. 1: Local radio telescope baselines are used as tight relative coordinate constraints to obtain rigid relative telescope positions when serving as an array to network observations requiring high coordinate precision.

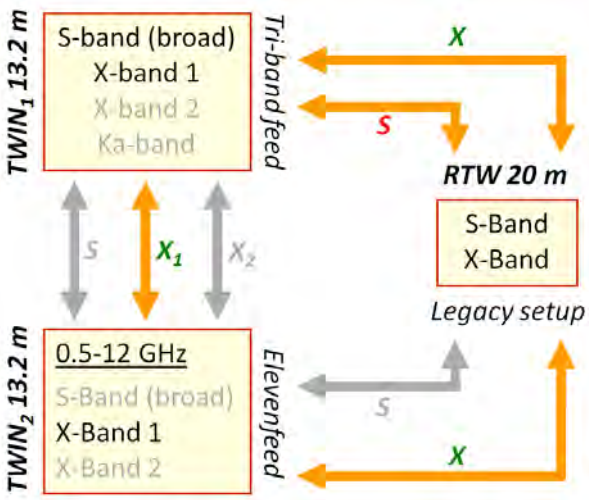

Fig. 2: Receiver setup at the three local telescopes: The traditional S-/X-setup of *Wz* (20 m, RTW) is raised as a standard for the network observations. X-band data at the identical center frequency of 8.6 GHz are recorded at both *Wn* and *Ws*.

2018 is a suitable time slot for this, because a local terrestrial survey was conducted right in advance. Automatic local GPS positioning is operational since 2014 at Wettzell yielding sub-millimetre repeatability between (weekly) solutions. The accuracy potential of VLBI will be compared to that of GNSS.

2. The best compromise between observation duration and baseline accuracy will be investigated having full data sets of up to 24 hours each day.
3. Observing with three telescopes allows us assessing possible loop closure errors. Such errors can stem from residual source structure uncertainties, but more likely from remaining clock and other system-related errors. Hence, LCONT18 will provide a better insight into the systems compared to all local activities carried out so far.

Apart from the experimentation purposes outlined before, it should be mentioned that precise local ties are of high importance. The precise relative positions will be used as tight constraints in global adjustments. This is particularly important for short Intensive-like (INT) sessions where the three Wettzell telescopes can serve three individual partner telescopes - see Fig. 1. Coordinates are usually held fixed in Intensive sessions.

We will report about our operational experiences gained during this campaign, and will portray first results for the network adjustment.

2 Method

Data were sampled using a rate of 256 Mbit/s, similarly to previous local experiments and current IVS Rapid sessions.

The three telescopes at Wettzell feature different receiving systems as indicated in Fig. 2. We preferred to run the network in a conventional mode during LCONT18 mainly focusing on group delay observations at the traditional 8.6 GHz X-band center frequency. A future LCONT campaign may exploit the additional capabilities of the two TWIN telescopes, e.g. it is possible to sample two X-band windows with *Wn* (TWIN1) and *Ws* (TWIN2).

The signals measured by *Wz* (RTW 20 m) as well as *Wn* (TWIN1) are received in circular polarisation (RHCP), whereas *Ws* (TWIN2) received the signals in dual linear polarisation. As a consequence, the correlation process involving *Ws* will provide two geodetic input files with group delays derived from vertical as well as horizontal polarisation raw data.

The session planning was supported by the coordination software LEVIKA IVS SU (Schüler et al., 2018), scheduling was done using sked.

The group delay observations were adjusted using in-house software LEVIKA SBA (Short Baseline Analysis). We performed data pre-screening and derived the number of clock error estimation intervals

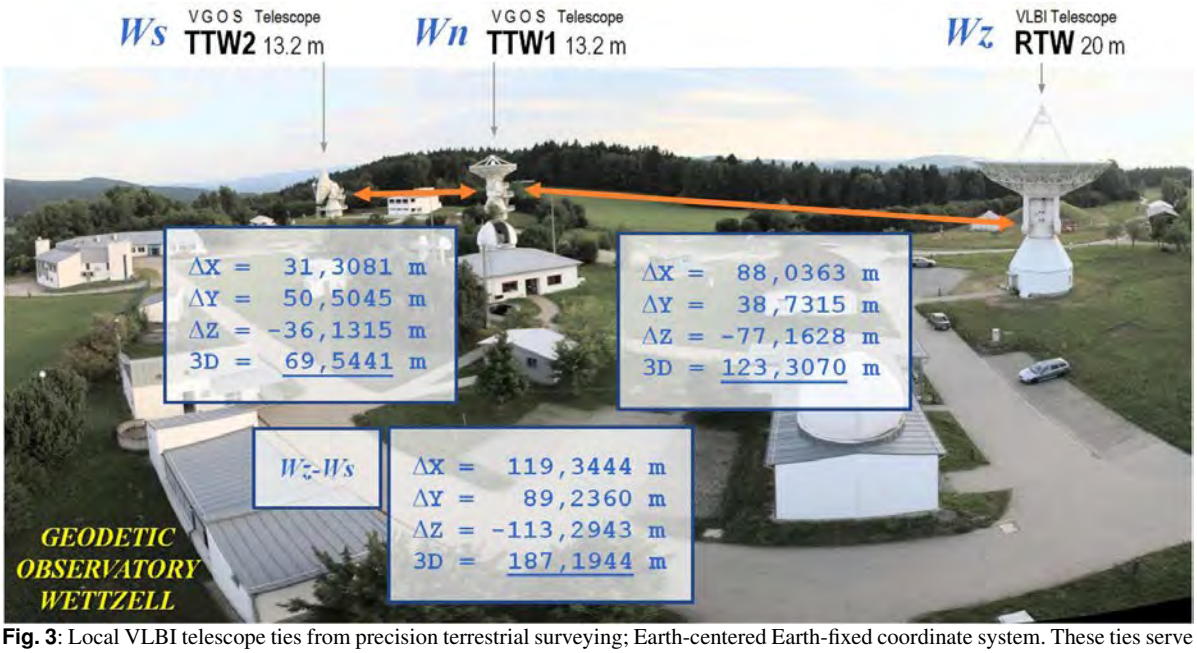

Fig. 3: Local VLBI telescope ties from precision terrestrial surveying; Earth-centered Earth-fixed coordinate system. These ties serve as reference values for LCONT18.

with help of a linear filter. This means that a flexible number of estimation intervals is defined individually rather than setting the estimation interval to a fixed value (e.g. one hour).

The local relative positions of the telescopes are by far more precise than long baseline coordinate results due to the virtual identity of the atmospheric delays within the distances of less than 200 m at Wettzell. However, the height difference between the old and the two new telescopes has to be taken into consideration in tropospheric delay modelling since it means a change in pressure and thus a millimetre-range change in zenith hydrostatic delay. In contrast, the two TWIN-telescopes are exactly located at the same height level. Tropospheric delay compensation was enabled by default (Schüler, 2014). However, we did not estimate any additional tropospheric delay nuisance parameter, because these parameters turned out to be statistically insignificant.

3 Results

Fig. 4 shows the observation statistics of the selected LCONT18 sessions presented in this contribution. Column n is depicting the number of group delay observations (scans) actually used in the adjustment process. Though the two TWIN-telescopes exhibit VGOS slew speeds (12°/s in azimuth and 4°/s in elevation direction), the maximum number of observations achievable in this network is limited by *Wz* (RTW, 20 m). That telescope is slewing at a speed of max. 4°/s (azimuth) and 1.5°/s (elevation) limiting the number of scans to approximately 1,000 within 24 hours. Interruptions of LCONT18 by INT-sessions (Intensives, UT1-determination) were permitted. Consequently, the total number of observations is expected to be a bit smaller here.

However, the actually achieved observation statistics are considerably smaller, and particularly low on Dec, 12th. A large amount of X-band data was rejected resulting in a major loss of geodetic observations. Fig. 6 portrays this situation graphically for the selected day: Red vertical lines indicate group delay observations that had been deleted as a result of the data pre-screening procedure. A major loss of data occurs between 9 h and 13 h UT. The source of radio-frequency interference, either internal or external, is still unclear. Normally, X-band data are less affected by contaminating RFI compared to S-band data (usually omitted in local analysis). This phenomenon was not observed during previous local sessions (Schüler et al., 2015; Halsig et al., 2018).

Date	Pol	Baseline	$n_{\Delta T}$	n	s_0 mm
2018-12-03	H	WETTZ13N -> WETTZ13S	0	733	3.1
2018-12-03	V	WETTZ13N -> WETTZ13S	0	741	2.6
2018-12-11	H	WETTZ13N -> WETTZ13S	0	800	2.8
2018-12-11	V	WETTZ13N -> WETTZ13S	0	848	2.4
2018-12-12	H	WETTZ13N -> WETTZ13S	0	738	2.1
2018-12-03		WETTZ13N -> WETTZELL	10	810	3.0
2018-12-03		WETTZ13N -> WETTZELL	12	803	3.1
2018-12-11		WETTZ13N -> WETTZELL	12	873	3.2
2018-12-12		WETTZ13N -> WETTZELL	11	785	3.6
2018-12-03	H	WETTZ13S -> WETTZELL	5	741	4.5
2018-12-03	V	WETTZ13S -> WETTZELL	5	786	4.5
2018-12-11	H	WETTZ13S -> WETTZELL	17	798	3.7
2018-12-11	V	WETTZ13S -> WETTZELL	12	853	3.7
2018-12-12	H	WETTZ13S -> WETTZELL	10	631	4.4

Fig. 4: Preliminary LCONT18 session analysis: Both horizontally and vertically polarised signals received by *Ws* can be correlated with the data of the other telescopes. "WETTZ13N" is *Wn* (TWIN1), "WETTZ13S" is *Ws* (TWIN2) and WETTZELL is *Ws* (RTW). $n_{\Delta T}$ indicates the number of clock error compensation intervals in the parameter estimation process. It is zero for the TWIN telescope baseline since these telescopes have a common clock. n is the number of observations (scan, group delays) after data pre-screening and outlier rejection. s_0 is the standard deviation of unit weight à posteriori representing the precision of a single group delay in X-band.

Date	Pol	Baseline	$n_{\Delta T}$	ΔS [mm]
2018-12-03	H	WETTZ13N -> WETTZ13S	0	-1.9
2018-12-03	V	WETTZ13N -> WETTZ13S	0	-1.6
2018-12-11	H	WETTZ13N -> WETTZ13S	0	-1.8
2018-12-11	V	WETTZ13N -> WETTZ13S	0	-1.7
2018-12-12	H	WETTZ13N -> WETTZ13S	0	-2.4
2018-12-03		WETTZ13N -> WETTZELL	10	2.6
2018-12-03		WETTZ13N -> WETTZELL	12	1.4
2018-12-11		WETTZ13N -> WETTZELL	12	-0.7
2018-12-12		WETTZ13N -> WETTZELL	11	0.1
2018-12-03	H	WETTZ13S -> WETTZELL	5	2.4
2018-12-03	V	WETTZ13S -> WETTZELL	5	3.3
2018-12-11	H	WETTZ13S -> WETTZELL	17	-1.2
2018-12-11	V	WETTZ13S -> WETTZELL	12	0.6
2018-12-12	H	WETTZ13S -> WETTZELL	10	-0.7

Fig. 5: Preliminary LCONT18 session analysis: ΔS indicates the 3D spatial deviation of the LCONT18 baseline adjustment from the local terrestrial surveying results

The clock error estimation intervals vary considerably between 5 and 17. A small number indicates a clock drift behaviour that appears to be close to a linear drift. Surprisingly, the baseline *Wn-Wz* features 10 and 12 clock intervals on Dec, 3rd, whereas the number is just 5 for the baseline *Ws-Wz*, although both *Wn* and *Ws* are connected to the same hydrogen maser. This suggests that other impacting error sources are dominant rather than the maser itself. One possible source of instability can be the cable delay unit (not yet activated at the TWIN telescopes during LCONT18) or, theoretically, the digital back-ends.

The standard deviation of unit weight à posteriori is in the range of less than 5 mm, i.e. usually around 10 ps or less. This is slightly higher than previous sessions, but can be explained by the higher level of radio interference.

The spatial deviations from the precision surveying results are randomly distributed for the baselines *WnWz* as well as *WsWz* and in the range of a couple of millimetres. Once again, this exceeds previous experiences a bit (i.e. around one millimetre with a tendency to the sub-millimetre domain), see Phogat et al. (2018). Note that baseline *WnWs* between the two TWIN-telescopes seems to be systematically biased, though the magnitude equals the results obtained for the other baseline. This requires further attention.

4 Conclusions and outlook

LCONT18 was carried out at the end of year 2018 over two working weeks. A limited first set of data and results is presented in this paper. The results reveal that there is still plenty of work to do.

Both data quality and results are slightly inferior compared to previous local experiments (that had usually been limited to baseline *WnWz*), though the data are still usable. A considerably high level of radio-frequency interference was observed during some of the LCONT18 days yielding a data loss of 10 % to 30 %. The baseline accuracy is degraded by a factor of two or even three compared to previous experiments and is in the range of one to three millimetres.

Regarding our future work, we firstly will analyse the complete data set and try to tackle down the problems revealed. One important aspect is also to determine the best compromise between session duration and baseline accuracy, since we assume that less than 24 hours of observation are sufficient under real local conditions. Moreover, the investigation of the usage of phase rather than group delays can be of value for the future, though it will currently not be much effective in case RFI limits the accuracy. That, however, is a new phenomenon observed for the first time at Wettzell, and has to be traced back and mitigated accordingly.

Subsequently, the local sessions will be distributed equally over the year to continuously obtain local relative positions of the telescopes in order to provide tight baseline constraints for all experiments carried

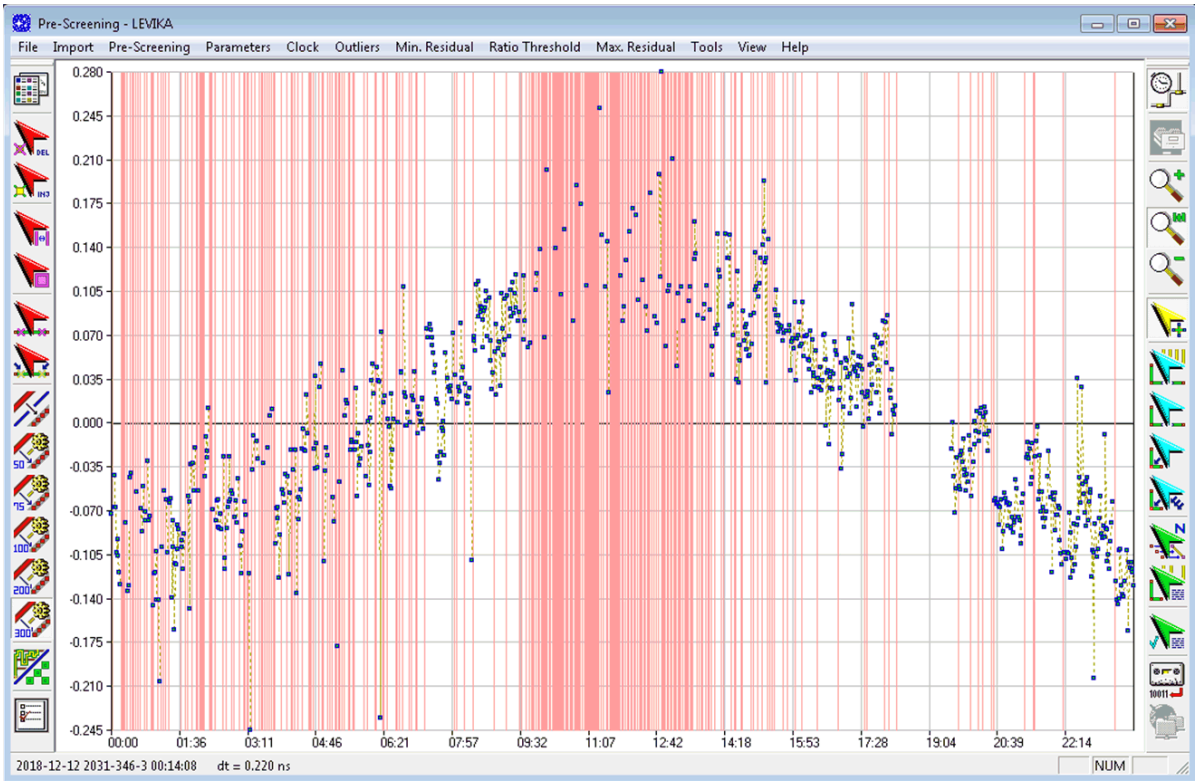

Fig. 6: Fails.

out at Wettzell including more than one local telescope. These local routine sessions are foreseen to take place each two months in order to capture possible annual deviations (”annual wave”).

Acknowledgements We gratefully acknowledge the support of the Bonn Correlator. This work was carried out in the framework of the project ”GeoMetre” as part of the EMPIR initiative. 18SIB01 GeoMetre is receiving funding from the EMPIR programme co-financed by the Participating States and from the European Union’s Horizon 2020 research and innovation programme.

References

Halsig S, Bertarini A, Haas R, et al. (2018) Atmospheric refraction and system stability investigations in short-baseline VLBI observations. *J Geod*, doi:10.1007/s00190-018-1184-5

Phogat A, Kronschnabl G, Plötz C, et al. (2018) Short Baseline Observations at Geodetic Observatory Wettzell. *Data*, 3, 64, doi:10.3390/data3040064

Schüler T (2014) The TropGrid2 standard tropospheric correction model. *GPS Solut*, 18:123, doi:10.1007/s10291-013-0316-x

Schüler T, Kronschnabl G, Plötz C, et al. (2015) Initial Results Obtained with the First TWIN VLBI Radio Telescope at the Geodetic Observatory Wettzell. *Sensors* , 15, 18767-18800, doi:10.3390/s150818767

Schüler T, Plötz C, Phogat A (2018) BKG CVC - The Central VLBI Observation Coordination Office of the Federal Agency for Cartography and Geodesy at the Geodetic Observatory Wettzell. In: K. L. Armstrong, K. D. Baver, D. Behrend (eds.): *IVS 2018 General Meeting Proceedings*, NASA/CP-2019-219039, 135–139

Preliminary Work on Promoting Radar Astronomical Study

J. Sun, J. Ping, S. Han, F. Shu, L. Ma, W Chen, L. Cui

Abstract Radar astronomical observations provide information on surface characteristics, orbits, and rotations for a wide variety of solar system objects. Based on a complex of radio telescopes of the Chinese VLBI network (CVN), in cooperation with the domestic radar transmitters, we present the current radar astronomical observations to the Moon. The spectrum of the reflected radio signals was obtained and the Doppler frequency shift in bistatic radar mode was measured. And the powers ratio of the reflected signals with left- and right-hand circular polarizations was determined, which allowed to stuy the near-surface wavelength-scale roughness of the Moon. The future radar astronomical developments, taking into consideration the possible international joint observations, are also introduced in the paper.

Jing Sun · Jinsong Ping
National Astronomical Observatory, 20A Datun Road, Beijing 100101, China

Songtao Han
Beijing Aerospace Control Center, 26 Beiqing Road, Beijing 100094, China

Fengchun Shu
Shanghai Astronomical Observatory, 80 Nandan Road, Shanghai 200030, China

Langming Ma
National Time Service Center, 3 Shuyuandong Road, Xian 710600, China

Wen Chen
Yunnan Observatory, P.0.Box110, Kunming 650011, China

Lang Cui
Xinjiang Astronomical Observatory, 150 Science 1-Street, Urumqi 830011, China

(Correspondence: sunjing@bao.ac.cn)

Keywords Radar VLBI · Moon

1 Introduction

Radar astronomy is one of the most effective techniques for determining the physical properties and orbital elements of the planets and small bodies in the solar system. The size, shape, spin period, and surface properties can be obtained using radar observations. Progressive updates of the NASA Goldstone and NSF Arecibo systems, primarily by moving to higher frequencies and more powerful transmitters, have made these two radar systems the dominant instruments for current radar studies of the solar system (Ostro et al., 2007).

Based on the project of the Low Frequency VLBI Network (LFVN), the VLBI radar (VLBR) for the investigations of the solar system bodies have been developed. LFVN arranges VLBR experiments since 1999 with the help of the C-band transmitter of Evpatoria RT-70 and X-band transmitter of Goldstone RT-70. The VLBR combines the radar sounding of space objects with a powerful transmitter and the receiving of radar echoes by an array of radio telescopes in VLBI mode. The VLBR supplements the traditional radar methods with the interferometric reception of a ground-based transmitter's signal reflected from the object (Nechaeva et al., 2015, 2013). VLBR allows to measure the variations of proper rotation of the Earth group planets and determine the trajectories of planets and asteroids in the Radio Reference Frame (Ipatov et al., 2016). VLBR has successfully been tested in a large series of international experiments: study of short-periodic variation of proper rotation for the Earth

group planets, improving the orbits of asteroids crossing the Earth orbit, measuring the space debris population at geo-stationary and high-elliptic orbits (Molotov et al., 2008; Tuccari et al., 2006).

There are several fully steerable dishes equipped with powerful X band transmitter in China, that are used for the deep spacecraft communications. The close collaboration of radar transmitters with the Chinese VLBI network (CVN) gives the opportunity to apply the VLBI technique for receiving and analysis of echo signals. The first successful radar detection of the Moon was carried out on Jul. 2, 2017. Since 2017 radar observations are regularly organized at the National Astronomical Observatory of the Chinese Academy of Sciences (NAOC) in cooperation with the domestic radar instruments to transmit and the radio telescopes of the CVN to receive the echoes. Primary goal is developing and validation of the radar astronomical method to obtain the information on trajectory parameters, attitude motion, and shape for known objects. The efforts of six sessions during 2017-2019 were concentrated on the observations to the Moon.

2 Experiments

A collaboration program is in development with the domestic radar team was initiated in 2017, and six experiments have been carried out for radar astronomical research of the Moon. The radar transmitter and a complex of radio telescopes spaced by hundreds and thousands of kilometers were the basis of the experimental facilities. Preparing for pointing of all antennas was done by the ChangE-3 lander coordinates. The domestic radar antenna illuminated the Moon with continuous wave (CW) signal at a frequency of X band in left-hand circular polarization. The carrier frequency was not changed over time and the transmitter power reached 8 kW. The signal reflected from the Moon was received in the VLBI mode with the radio telescopes of the CVN simultaneously in left- and right-hand circular polarizations, i.e. in the same (SC) and opposite (OC) circular polarizations as that of the transmitted wave. Data recording was carried out in the frequency band of 2 MHz. The echo signal was quantized and written in digital form on the Mark5B modules.

The echo signals reflected from the Moon were confidently detected by each antenna in all the sessions, which provided reliable data at all stages of processing. After the radar sessions, the echo rawdata from each receiving antenna were transmitted to NAOC for further data processing.

3 Preliminary results

A spectral analysis of the received signal at each receiving point was done for further calculation of frequencies. The spectral analysis of the obtained information was to measure the frequency difference between the emitted and the received signals. The difference, namely Doppler frequency shift, is conditional on the radial velocity of the object on the track ”transmitter-Moon-receiver”. The Doppler shift was determined using the peaks of the frequency spectra. Using the fast Fourier transform, the frequency of Doppler shift is measured in one-second intervals with a frequency resolution of 1 Hz from our measurements.

The spectra of the signals reflected from the Moon were received with the Kunming RT-40 and Sanya RT-13 simultaneously over the entire interval of our observations, as presented in Fig. 1 and Fig. 2, respectively. Solid and dashed lines denote echo power in the OC and SC polarizations. The vertical axis shows the amplitude of the received signal in relative units, horizontal axes display frequency in Hertz. Echo power is plotted in standard deviations versus Doppler frequency relative to the estimated frequency of echoes from the Moon’s center of mass. The pattern of the spectrum shape is seen to be repeated at two independent stations, suggesting a high accuracy of the measurements.

By calculating radial velocity of the Moon relative to the transmitting antenna and the receiving antennas, the computed Doppler frequency shift for each of the reception points was obtained. The experimental Doppler frequency shifts were determined by the spectrum maximum frequency in bistatic mode. According to the results of spectral processing of data, recorded at Kunming RT-40, the series of Doppler frequency shifts were measured for the Moon. As a whole, the measured Doppler shifts are in good an agreement with the calculated values from the lunar ephemeris. Fig. 3 displays the difference of calculated and experimental

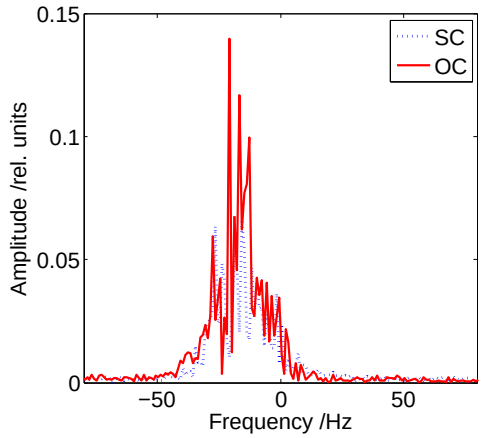

Fig. 1: Opposite- and same-circularization continuous wave echo power spectra of the Moon obtained with the Kunming RT-40 at 02:50:00 UT on Apr. 26, 2019. The frequency resolution is 1.0 Hz.

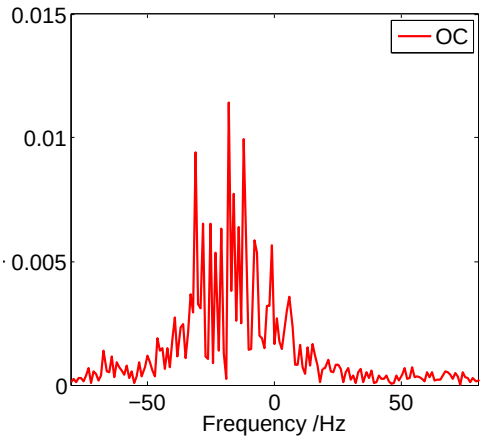

Fig. 2: Opposite-circularization continuous wave echo power spectra of the Moon obtained with the Sanya RT-13 at 02:50:00 UT on Apr. 26, 2019. The frequency resolution is 1.0 Hz.

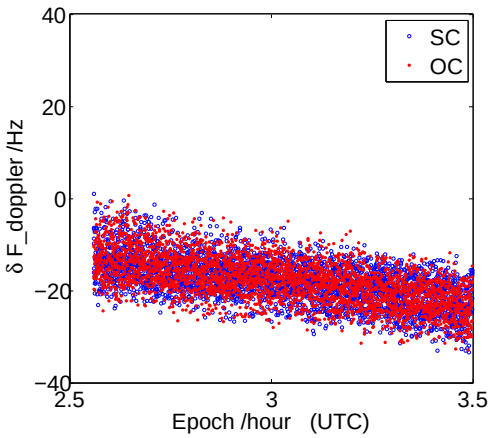

Fig. 3: The difference of measured and calculated Doppler frequency shifts at Kunming RT-40 between 02:30:00 to 03:00:00 UT on April 26, 2019.

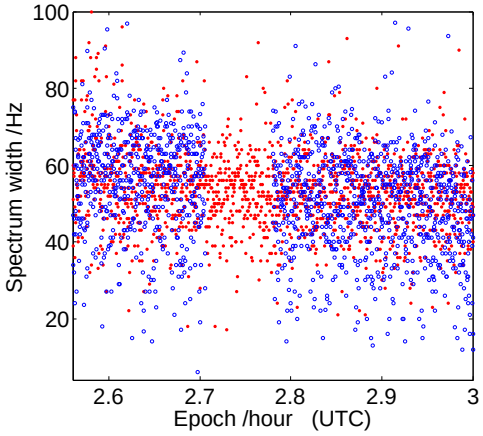

Fig. 4: Variation in the width of the reflected signal power spectra with time. The filled and open circles mark the spectrum widths for the Kunming RT-40 and Sanya RT-13 at the corresponding times, respectively.

Doppler frequency shifts at Kunming RT-40. The observations of the Doppler shift of the reflected signal frequency were obtained, and the mean-root-square error is around 5 Hz in this experiment.

The power spectrum bandwidth as function of time can be used for obtain the spin period in case of long observation series. For all the received stations, the spectrum broadening of the echo signal reflected from the Moon was less than 100 Hz. In Fig. 4, the filled and open circles mark, respectively, the spectrum widths for the Kunming RT-40 and Sanya RT-13 at the corresponding times. The measurement starts from 02:30:00 UT on April 26, 2019 and lasts for 30 minutes. The profile line width is determined by the rotation of the Moon's reflecting surface, while its change is indicative of the shape asymmetry.

Circular polarization of the signal is reversed after reflection from the plane surface and the maximum power of the reflected signal is expected in the OC polarization, though some of the signal, due to sec-

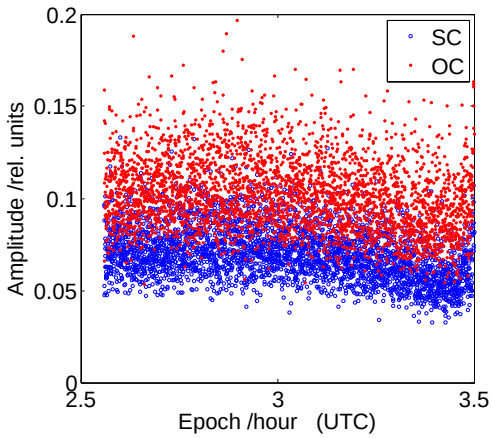

Fig. 5: The spectrum amplitude obtained at Kunming RT-40 with SC and OC, respectively.

ondary reflections, is received with the same polarization. The ratio of SC to OC is a measure of near-surface wavelength-scale roughness (Bondarenko et al., 2017; Ipatov et al., 2016). In our case, this quantity μC (circular polarization coefficient) is μC = 0.688 for Kunming RT-40 and μC = 0.655 for Jilin RT-13. Fig. 5 shows the spectrum amplitude obtained at Kunming RT-40 with SC and OC, respectively.

4 Conclusions and discussions

The signal transmitted at X band with the domestic radar and reflected from the Moon was successfully received with the radio telescops of the Chinese VLBI Network. Obtained results confirm the possibility and effectiveness of the bistatic radar observations of the Moon using radio telescopes of the CVN as receiving part of a bistatic configuration. It was shown that receiving and processing of the continuous wave echo allows to estimate the value of the Doppler frequency with sufficient accuracy. Following this positive experience we plan to continue the interference frequency in VLBI mode. The multiplication of signals, recorded in two VLBI-stations, will be carried out to measure the frequency of the interference (fringe rate), which depends on the angular velocity of the investigated object.

If the object is illuminated with a noise or the LFM-signal for a given mode, the spatial delay is measured. This delay represents the time difference of the signal propagation from the object to the two receiving telescopes and it is determined from the angular coordinates of the object. We also consider the processing of noise or LFM-signal with significantly lower signal-to-noise ratio than in the case of monochromatic signal.

In future, the bistatic radar observations of the potentially dangerous asteroid during its close approach to the Earth will be carried out. And the precise measurement of ephemeris of space debris fragments are important for the prognosis of the dangerous approaches with operational satellites.

Acknowledgements This study made use of data collected through the CVN (Chinese VLBI Network). The authors wish to thank the staff of radio telescopes and radar team for participating in the experiments. The authors thank the National Natural Science Foundation of China (NSFC) for funding projects 11833001 and 11603001.

References

Bondarenko Yu, Medvedev Yu, Vavilov D, et al. (2017) Radar observations of near-Earth Asteroids using the Quasar VLBI Network Telescopes. *European Planetary Science Congress 2017*, 11

Ipatov A, Bondarenko Yu, Medvedev Yu, et al. (2016) Radar Observations of the Asteroid 2011 UW158. *Astronomy Letters*, 42, 12, 850–855, doi:10.1134/S1063773716120021

Molotov I, Nechaeva M, Falkovich I, et al. (2008) Astrometry of the Solar System Bodies with VLBI Radar. In: A. Finkelstein, D. Behrend (eds.): *IVS 2008 General Meeting Proceedings*, 30–34

Nechaeva M, Antipenko A, Bezrukov V, et al.(2013) An Experiment on Radio Location of Objects in the Near-Earth Space with VLBI in 2012. *Baltic Astronomy*, 22, 35–41

Nechaeva M, Dugin N, Antipenko A, et al. (2015) VLBI Radar of the 2012 DA14 Asteroid. *Radiophysics and Quantum Electronics*, 57, 10, 691–699, doi:10.1007/s11141-015-9555-8

Ostro S (2007) Planetary radar. *Encyclopedia of the Solar System*, 735–764.

Tuccari G, Molotov I, Volvach A, et al. (2006) e-NRTV - Radar VLBI Network LFVN. In: D. Behrend, K. D. Baver (eds.): *IVS 2006 General Meeting Proceedings*, NASA/CP-2006-214140, 236–240

Observations of Radio Sources Near the Sun

O. Titov, S. Lambert, B. Soja, F. Shu, A. Melnikov, J. McCallum, L. McCallum, M. Schartner, A. de Witt, D. Ivanov, A. Mikhailov, S. O. Yi, W. Chen, B. Xia, M. Ishigaki, S. Gulyaev, T. Natusch, S. Weston

Abstract Geodetic Very Long Baseline Interferometry (VLBI) data are capable of measuring the light deflection caused by the gravitational field of the Sun and large planets with high accuracy. The parameter γ of the parametrized Post-Newtonian (PPN) formalism estimated using observations of reference radio sources near the Sun should be equal to unity in the general relativity. We have run several VLBI experiments tracking reference radio sources from 1 to 3 degrees from the Sun. The best formal accuracy of the parameter γ achieved in the single-session mode is less than 0.01 percent, or better than the formal accuracy obtained with a global solution included all available observations at arbitrary elongation from the Sun. We are planning more experiments starting from 2020 using better observing conditions near the minimum of the Solar activity cycle.

Keywords VLBI · General relativity · Ionosphere

Oleg Titov
Geoscience Australia, PO Box 378 Canberra, AU-2601 Australia

Sébastien Lambert
SYRTE, Observatoire de Paris, Université PSL, CNRS, Sorbonne Université, LNE, Paris, France

Benedikt Soja
Jet Propulsion Laboratory, California Institute of Technology, 4800 Oak Grove Drive, Pasadena, CA 91109, USA

Fengchun Shu · Wen Chen · Bo Xia
Shanghai Astronomical Observatory, 80 Nandan Road, Shanghai, 200030, China

Alexei Melnikov · Dmitrii Ivanov · Andrei Mikhailov
Institute of Applied Astronomy, Kutuzov Embankment, 10, Saint-Petersburg, RU-191187, Russia

Jamie McCallum · Lucia McCallum
University of Tasmania, Private Bag 37, Hobart, Tasmania, 7001, Australia

Aletha de Witt
Hartebeesthoek Radio Astronomy Observatory, PO Box 443, Krugersdorp, 1740, South Africa

Matthias Schartner
Department of Geodesy and Geoinformation, Research Group Advanced Geodesy, TU Wien, Gußhausstraße 27–29/E120.4, Wien, AT-1040, Austria

Sang Oh Yi
National Geographic Information Institute, Space Geodetic Observatory, Sejong, PO Box 30060, South Korea

Masafumi Ishigaki
Geospatial Information Authority of Japan 1, Kitasato, Tsukuba 305-0811, Japan

Sergei Gulyaev · Tim Natusch · Stuart Weston
Institute for Radio Astronomy and Space Research, Auckand University of Technology, Auckland, 1010, New Zealand

(Correspondence: oleg.titov@ga.gov.au)

1 Introduction

In accordance with General Relativity the radio waves slow down due to the gravitational potential of the Sun (the so-called Shapiro effect; see Shapiro, 1964, 1967), making very long baseline interferometry (VLBI) a useful tool for testing General Relativity by means of the parameterized post-Newtonian (PPN) formalism (Will, 1993). Nevertheless, the accuracy of the PPN parameter γ obtained from absolute or differential VLBI observations (Fomalont et al, 2009; Lambert and Le Poncin-Lafitte, 2009, 2011) remains worse than the current best limit of $(2.1 \pm 2.3) \times 10^{-5}$ based on Cassini radio science experiment (Bertotti et al, 2003) by an order of magnitude. The upper limits on the parameter

γ have been improved substantially in the past 30 years (Robertson and Carter, 1984; Robertson et al, 1991; Lebach et al, 1995; Fomalont and Kopeikin, 2003), but some authors (Shapiro et al, 2004; Lambert and Le Poncin-Lafitte, 2009) found degradation in the estimates of γ with elongation, and suggested that this systematic effect may limit the improvement in the VLBI-derived γ upper limits, despite the dramatic growth in the number of observations in recent decades.

The current paper focuses on radio source approaches at angular distances less than three degrees from the centre of the Sun in order to measure the light deflection effect at the highest magnitude and, thus, to avoid a possible bias caused by observations at larger elongations. We report on two special VLBI sessions, AUA020 (May 2017) and AOV022 (May 2018), on the single-session estimates of γ.

2 Data

A dedicated geodetic VLBI experiment (AUA020, 01-02 May, 2017, part of AUSTRAL program) was scheduled to probe the gravitational delay effect using a network of seven radio telescopes (Svetloe, Zelenchukskaya, Badary, HartRAO, Seshan25, Sejong, and Hobart26). Two radio sources 0229+131 and 0235+164 were observed at range of angular distances from 1.15° to 2.6° from the Sun. The position of both radio sources with respect to the Sun at the start of the experiment is shown on Fig. 1. A serious issue in such a configuration is the solar thermal noise that penetrates to the signal through the side lobes, and could cause loss of data due to striking the signal-to-noise ratio. To overcome the problem, one has to

1) select strong radio sources with larger correlated flux density in both frequency bands,

2) use large radio telescopes with narrow side lobes and better sensitivity, and

3) use the highest possible data rate recording (e.g., 1 Gbps) to gain a better signal-to-noise ratio during the same integration time.

More details about the schedule design are published in (Titov et al, 2018).

The target radio source 0229+131 is a defining source of the ICRF2 whose position is given with an accuracy close to the ICRF2 noise floor of 40 μas. The position of the second target 0235+164 is less accurate

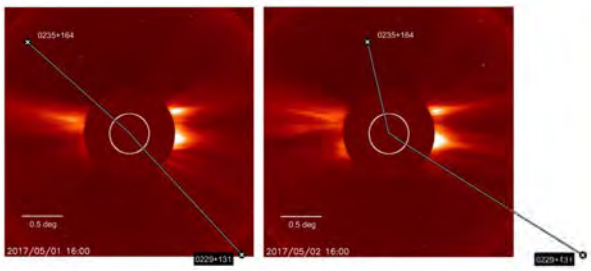

Fig. 1: Geometry of the radio sources close to the sun at the start (Left) and at the end (Right) of VLBI session AUA020 with respect to a LASCO C2 image of the solar corona. The Sun is hidden behind the occultation disc of the coronagraph, with the white inner circle representing the limb of the Sun. The field-of-view is 1.5 degrees elongation.

by a factor of five but still at the level of the ICRF2 median error and largely below the millisecond of arc. Both sources are compact and their structure indices measured at the time of the ICRF2 work were of 2.4 and 1.3, respectively, ensuring a structure delay lower than 2 ps (Fey and Charlot, 1997).

3 Analysis and Results

For purpose of cross-checking the results and testing their robustness, we processed the VLBI session AUA020 within two independent teams with two independent geodetic VLBI analysis software packages. The duplication of the analyses with two software packages also allows to use some specific options that are available on only one of them. The first analysis package is OCCAM (Titov et al., 2004) that implements the least-squares collocation method (Titov, 2000) for calibrating the wet troposphere fluctuations, and to account for the mutual correlations between observables. The second one is Calc/Solve (Ma et al., 1986), developed and maintained by the geodetic VLBI group at NASA GSFC, that uses classical least-squares. More details about the data analysis design are discussed in (Titov et al, 2018)

Table 1 shows the results of the AUA020 experiment data analysis. Uncertainties on γ lie between 0.9×10^{-4} and 4×10^{-4}. Our estimates appear therefore as precise as that obtained from global solutions using thousands of VLBI experiments (Lambert and Le Poncin-Lafitte, 2009, 2011). The formal error is about two times lower when γ is fitted to the observations of

the radio source that is two times closer to the centre of the Sun (0235+164) than to that of its counterpart (0229+131). Using all scans returns a result similar to using only scans relevant to 0229+131 and 0235+164, confirm that only sources a low elongation can efficiently constrain the PPN parameter. Solutions from both software packages are consistent within the standard errors. The difference of postfit rms between OCCAM and Calc/Solve might find its origin in the different modeling of the nuisance parameters (stochastic versus CPWL function). No large systematics are detected except a 2.7σ deviation in the Calc/Solve solution when only 0229+131 is used and whose origin is unclear: as both solutions started from the same a priori, the issue could rather be in the estimation method or in the handling of troposphere/clock parameters.

It appears that during session AUA020, data in three channels at Sejong station were lost due to technical reasons. Therefore, we reprocessed the previous analyses after downweighting (but not suppressing) Sejong data. (We could test this option with OCCAM only since Calc/Solve does not handle downweighting.) The postfit rms of the solution is significantly lowered. The formal error on γ is marginally lowered down to 9×10^{-5}.

For purpose of comparison of the AUA020 session with other standard geodetic VLBI sessions, we estimated γ with Calc/Solve using the parameterization described above for each of sessions of the full geodetic VLBI data base made available by the International VLBI Service for geodesy and astrometry (IVS) since 1979 (at the exclusion of intensive sessions). The median postfit rms is 27 ps that is close to the postfit rms of the AUA020 session. The distribution of the obtained values of $\gamma-1$ is shown in Fig. 2 along with distributions of errors and normalized estimates. The distribution of errors in log-scale is slightly asymmetric, exhibiting a 'tail' on its right side that might traduce results from sessions not designed for precise astrometry. Nevertheless, assuming a Gaussian shape, the log-scaled distribution peaks at 10^{-2} with a σ of ~ 0.5. This makes the error estimate from AUA020, that is two orders of magnitude less, somewhat 'outstanding'. The bottom-right panel of Fig. 2 shows that the major part of the sessions does not bring severe systematics, the estimates of γ being unity within the error bars; session AUA020 is part of the session group that presents the lowest systematics.

Table 1: Estimates of $\gamma-1$ for the session AUA020, in unit of 10^{-4}, along with the session χ^2 and the postfit rms delay r in ps.

		$\gamma-1$ 10^{-4}	σ_γ 10^{-4}	χ^2	r
OCCAM	All stations				
	All scans	0.56	1.15	0.34	28
	0235+164	1.34	1.58	0.34	28
	0229+131	−1.54	3.41	0.34	28
	Both	0.53	1.14	0.34	28
	With Sejong downweighted				
	All scans	0.91	0.94	0.27	21
	0235+164	1.64	1.29	0.27	21
	0229+131	0.32	2.83	0.27	21
	Both	0.89	0.94	0.27	21
Calc/Solve	All sources	−0.22	1.10	0.84	26
	0235+164	1.85	1.48	0.84	26
	0229+131	−6.84	2.53	0.84	26
	Both	−0.26	1.09	0.84	26

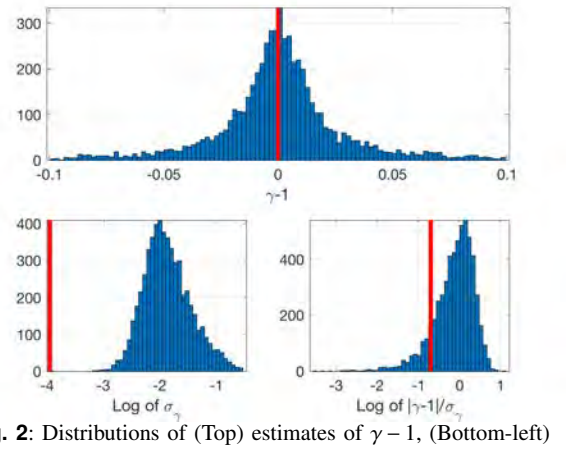

Fig. 2: Distributions of (Top) estimates of $\gamma-1$, (Bottom-left) their formal errors, and (Bottom-right) normalized estimates of $\gamma-1$ for all of the geodetic VLBI sessions. The vertical, red bar stands for the results of the AUA020 session.

Another experiment (AOV022) was undertaken on 01-02 May, 2018 with ten radio telescopes (Svetloe, Zelenchukskaya, Badary, Hobart26, Seshan25, Kunming, Ishioka, Yarragadee, Katherine, Warkworth). The same radio sources (0229+131 and 0235+164) were scheduled with the same strategy. The statistics of the result was found to be 2-3 times worse than from AUA020, presumably, due to severe source structure delay effect. Fig. 3 shows the post-fit residuals of for radio source 0229+131 for two baselines, Ishioka-Seshan25 and Badary-Zelenchk. The variations of the residuals are consistent to the variations induced by

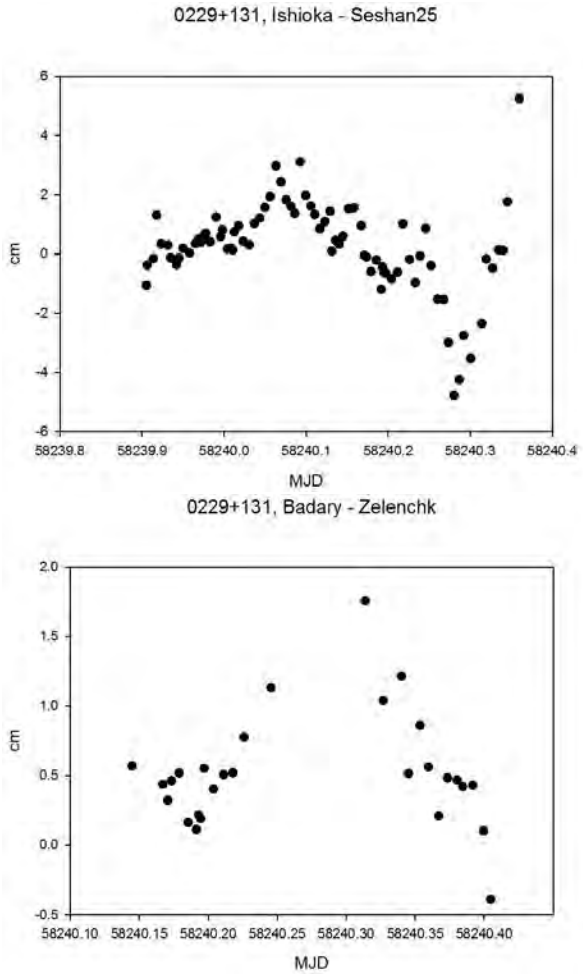

Fig. 3: Post-fit residuals of 0229+131 with baselines Ishioka-Seshan25 and Badary-Zelenchk.

the source structure (Titov and Lopez, 2018) therefore, we believe, that more detailed analysis is required to obtain a better statistic for this experiment.

4 Conclusions and outlook

In this paper we discuss our results on testing of general relativity with geodetic VLBI using the close approach of the Sun to the reference radio sources. It was a general misconception in the past that the effect of the plasma of the solar corona completely disturbs the interferometric responce for light rays passing within several degrees from the Sun. We proved that these perturbations are at an acceptable level unless the signals pass active streamers in the solar corona. Therefore, the standard dual frequency calibration facilitates the stochastic noise induced by charged particles the solar corona by the same way as for the ionosphere around the Earth.

While the systematic effects based on radial or dipole models of the corona appear to be negligible, individual group delay observations are affected by random scatter caused by small-scale coronal structure and temporal variations thereof. Since these perturbations do not systematically affect the observations, we assume that they cancel out over the period of observations (17 hours with observations angularly close to the Sun). Since the ray paths to the radio sources 0235+164 and 0229+131 within small solar elongation happened to be in quiet regions (cf. Fig. 1), the scatter was small enough that precise group delays could be successfully determined at such small elongations.

The major source of stochastic noise in VLBI measurements resides in the unknown wet troposphere delay. The difference between VLBI estimates of the wet troposphere delay and independent radiometer data appears to stay within 3 mm, or 10 ps (Titov and Stanford, 2013) suggesting that the impact of the wet troposphere delay on the astrometric light deflection angle estimation near the Sun is negligible.

Overall, a total improvement of the uncertainty on γ by a factor of ten is expected, enabling to challenge the current limit imposed by the Cassini radio science experiment of Bertotti et al (2003), although the Gaia astrometry on Solar system objects is expected to deliver an accuracy of 10^{-6} (Mignard and Klioner, 2009).

Acknowledgements This paper is published with the permission of the CEO, Geoscience Australia. B. Soja's research was supported by an appointment to the NASA Postdoctoral Program, administered by Universities Space Research Association, at the Jet Propulsion Laboratory, California Institute of Technology, under a contract with National Aeronautics and Space Administration. We are grateful to D. Gordon (GSFC) for post-processing reduction of the AUA020 data.

References

Bertotti B, Iess L, Tortora P (2003) A test of general relativity using radio links with the Cassini spacecraft. *Nature*, 425:374–376

Charlot P, Jacobs C S, Gordon D, et al. (2019) The third realization of the International Celestial Reference Frame by very long baseline interferometry. *A&A* (in preparation)

Fey A L, Charlot P (1997) VLBA Observations of Radio Reference Frame Sources. II. Astrometric Suitability Based on Observed Structure. *ApJ*, 111:95–142

Fey A L, Gordon D, Jacobs C S, et al. (2015) The Second Realization of the International Celestial Reference Frame by Very Long Baseline Interferometry. *AJ*, 150:58

Fomalont E, Kopeikin S, Lanyi G, et al. (2009) Progress in Measurements of the Gravitational Bending of Radio Waves Using the VLBA. *ApJ*, 699:1395–1402

Fomalont E B, Kopeikin S M (2003) The measurement of the light deflection from jupiter: Experimental results. *ApJ*, 598(1):704

Lambert S B, Le Poncin-Lafitte C (2009) Determining the relativistic parameter γ using very long baseline interferometry. *A&A*, 499:331–335

Lambert S B, Le Poncin-Lafitte C (2011) Improved determination of γ by VLBI. *A&A*, 529:A70

Lebach D E, Corey B E, Shapiro I I, et al. (1995) Measurement of the solar gravitational deflection of radio waves using very-long-baseline interferometry. *Phys Rev Lett*, 75:1439–1442.

Ma C, Clark T A, Ryan J W, et al. (1986) Radio-source positions from VLBI. *AJ*, 92, 1020–1029, doi:10.1086/114232

Mignard F, Klioner S (2009) Gaia: Relativistic modelling and testing. In: S. Klioner, P. K. Seidelman (eds.) *Relativity in Fundamental Astronomy – Proceedings IAU Symposium No. 261*, Cambridge University Press, 5, 306–314.

Robertson D S, Carter W E (1984) Relativistic deflection of radio signals in the solar gravitational field measured with vlbi. *Nature*, 310:572.

Robertson D S, Carter W E, Dillinger W H (1991) New measurement of solar gravitational deflection of radio signals using vlbi. *Nature*, 349:768.

Shapiro I I (1964) Fourth Test of General Relativity. *Phys Rev Lett*, 13(26):789–791.

Shapiro I I (1967) New method for the detection of light deflection by solar gravity. *Science*, 157(3790):806.

Shapiro S S, Davis J L, Lebach D E, et al. (2004) Measurement of the Solar Gravitational Deflection of Radio Waves using Geodetic Very-Long-Baseline Interferometry Data, 1979–1999. *Phys Rev Lett*, 92(12):121101, doi:10.1103/PhysRevLett.92.121101.

Titov O (2000) Estimation of subdiurnal tidal terms in UT1-UTC from VLBI data analysis. *IERS Technical Note*, 28, 11

Titov O, Tesmer V, Boehm J (2004) Occam v. 6.0 software for VLBI data analysis. In: N. R. Vandenberg, K. D. Baver (eds.): *IVS 2004 General Meeting Proceedings*, 267–271

Titov O, Stanford L (2013) Comparison of wet troposphere variations estimated from VLBI and WVR. In: N. Zubko, M. Poutanen (eds.): *Proc. 21st EVGA Working Meeting*, 151–154

Titov O, Girdiuk A, Lambert S, et al. (2018) Testing general relativity with geodetic VLBI. What a single, specially designed experiment can teach us. *A&A*, 618:A8

Titov O, Lopez Yu (2018) Two-component structure of the radio source 0014+813 from VLBI observations within the CONT14 program. *Astronomy Letters*, 44, 139.

Will C M (1993) Theory and Experiment in Gravitational Physics, Cambridge University Press

Autonomous Observations of VLBI Radio Telescopes

A. Neidhardt, E. Barbieri, J. Bachem, M. Schönberger, M. S. Hameed, L. Carlin, R. Aktas, S. Jingyao, A. Szomoru

Abstract Current techniques in software and hardware allow, to increase the automation of systems. An autonomous, state-driven processing of VLBI schedules from autonomous fetching and preparation of schedules, the operation of observations and the finalization and transfer of data is possible. Industrial monitoring suites allow a centralized overview, so that a reduced number of operators can quickly get the status of several instruments. Historic values allow the analysis of failure situations and their causes. To increase the automation and to even support autonomous observations, updates and tests are ongoing at the Wettzell observatory.

Keywords Automation · Monitoring · Centralized Network Overview

1 Introduction

Several years ago, implementations started to convert manual tasks of VLBI observation to more automated workflows. Improvements were identified amongst others in optimized networks (re-arrange VLBI networks in failure situations with dynamic observing modes, Lovell, 2016), better data quality because of defined processes instead of operator-individual behavior, and reduced requirements of manpower for operator shifts (Neidhardt, 2017, page 505 f). While it is easy to automate some specific tasks, like downloading a new schedule or starting a new schedule as invocation of the according file in the NASA Field System, other steps were challenges, like detecting and reacting on failure situations, generating automated meteorological descriptions, or recording data without changing VLBI modules. Meanwhile, technique and hardware improved. For example, Digital Baseband Converters are able to use formatters streaming data directly via 10 GBit/sec networks to storage servers (like Flexbuff systems). Industrial monitoring systems improve the collection of innumerable parameters about system health directly evaluating critical situations. A wide field of meteorological devices (like Nubiscopes for cloud coverage, rain sensors, snow sensors, etc.) extend information from elementary meteorological stations to produce quantitative, textual descriptions of the prevailing weather situation. Therefore, even complete autonomous observation are close enough to touch.

Ideas at the Wettzell observatory started early to implement such autonomous observations. The final goal is, to automatize all steps of a VLBI observation, so that at least no operator is required anymore. The operations include:

1. Autonomous checking for sessions on the different repositories
2. Prioritization and planning of local observations of sessions
3. Autonomous fetching of session schedules

Alexander Neidhardt
FESG Wettzell, TU of Munich, Geodetic Observatory Wettzell, Sackenrieder Str. 25, DE-93444 Bad Kötzting, Germany

E. Barbieri · M. S. Hameed · L. Carlin · R. Aktas · S. Jingyao
FESG, TU of Munich, Arcisstr. 21, DE-80333 Munich, Germany

J. Bachem · M. Schönberger
BKG, Geodetic Observatory Wettzell, Sackenrieder Str. 25, DE-93444 Bad Kötzting, Germany

Arpad Szomoru
Joint Institute for VLBI ERIC, Oude Hoogeveensedijk 4, NL-7991 PD Dwingeloo, The Netherlands

(Correspondence: neidhardt@fs.wettzell.de)

4. Local preparation (drudg) without human interaction
5. Local adaption and recorder selection according predefined specifications
6. Automatic start-up of local observations
7. Frequent notification and monitoring of observation status
8. Continuous quality control and alarm management
9. Individual post-processing and archiving data and meta-data

In a final development state, external partners might interact with the local control system to adapt session parameters and continuously get information about internal processes while the system makes its own decisions to control devices according to individual feedback from sensors. This state can be seen as an implementation of a ”smart observatory”

Programs and scripts at the Wettzell observatory are tested to support these automated tasks. A special setup even enables monitoring and controlling of the NASA Field System and station-specific parts. Centralized displays permanently show health states, so that even staff of the observatory guard can check and interpret system situations.

2 ”Automating” the NASA Field System

Most antennas of IVS network use the NASA Field System to control individual equipment. The system originally was written in FORTRAN but greatly extended with C code. The system is a more or less loose coupled arrangement of programs running parallel to interpret commands, control hardware, monitor system status, interact with the user, and report errors, supervised by a central program, called ”boss”. The whole observation is controlled with a predefined batch file, activating tasks when time reaches predefined time-tags. This simple sequential flow is already an automated processing, but has the disadvantage that checks and error reports are only created when time-tags define them (Neidhardt, 2017, page 409 f), and that local programs are responsible for keeping healthy states for the antenna and equipment.

Completely autonomous systems require continuous monitoring of health states to make decisions immediately in case of alerts or critical situations during observations (critical situations for humans are protected by the system hardware itself, which is certified by companies). As so many antennas use the Field System, programs for autonomous operations must include the existing version of the Field System. This requires a mechanism to manage user interaction with the Field System to interpret and quantify them. Additionally, sensors and actors which are usually directly connected to the Field System must be permanently monitored and partly controlled in parallel to the Field System commanding.

Mechanisms to do this are known from software testing of legacy programs (see Fig. 1), where existing code should be treated with error situations to measure the reactions. To do this, hardware or equipment is represented with software stubs, which communicate to both, the system under test on the one hand and the hardware on the other hand. User interactions are forced with mock objects playing the role of a user and feeding commands to the system while listening to responses. Exactly this setup can be used to increase the automation of the VLBI control using the existing NASA Filed system without touching it. The user interactions are managed with the already existing e-RemoteCtrl server originally developed to control telescopes remotely. Therefore, e-RemoteCtrl can already be seen as mock object. Interfacing the hardware is implemented with software-generated stubs offering high safety and reliability.

e-RemoteCtrl is a client-server system connecting the NASA Field System shared memory to monitor internal parameters, Ettl et al. (see 2012). Additionally, log files are read and interpreted to get current status information. Commands can also be sent using the NASA Field System mechanism to inject specific Field System commands to ”boss”. For the Wettzell monitoring system, IVS seamless auxiliary data archive, and a central monitoring system located at JIVE and part of Jumping JIVE project funded by the EU Horizon 2020 framework, e-RemoteCtrl was extended with an elementary web server. It simplifies interaction with the Field System using predefined template HTML pages where current system values are dynamically set. The values are tagged with HTML comments to find them again in the web pages later on by automated, external processes.

Software generated stubs use a mechanism described in Neidhardt (2017, page 148 f). The complete framework is defined and generated during a domain engineering process where all parts generally relevant for all stubs are programmed. Application specific

parts are described with a meta-program in a specific domain specification language, so that a software generator produces the final program taking general parts and adapting them to specific applications. Advantages are the well-tested domain part, the flexible adaption, and especially the always existing and stable safety mechanisms from the domain software.

Each stub program runs an application process and a watchdog process. The watchdog permanently controls, if the application is still running and available. The application process is split in one control and communication flow and several parallel processing lines communicating with the hardware and organized as POSIX threads. This architecture avoids time delay propagation from hardware to the Field System, keeps processes accessible, and allows a separate data extraction for additional monitoring features. It builds a monitoring bypass to the NASA Field System line, so that system health states can be controlled continuously.

3 Using the data from the monitored (NASA Field) System

While the dynamic web pages from e-RemoteCtrl can be used locally by operators with each type of Internet browser, and monitoring data from the bypass can be used with local scripts and programs to make decisions, such data can also be collected from centralized services. Therefore, a central monitoring server for VLBI health data was installed using the monitoring suite ZABBIX (Zabbix, 2018). The server is a HPE ProLiant DL380 Gen10 8SFF with 6.5 TB effective RAID volume. It runs the ZABBIX suite, a PostgreSQL database, an Apache2 web server, and several scripts and programs to fetch, extract and process data from the NASA Field Systems of the Wettzell antennas (Wz, Wn, Ws, Oh, and AGGO). Antennas individually connect to the server using SSH reverse tunnels, so that the server is able to access the NASA Field System monitoring web pages on the site-specific Field System PC. Additionally, SNMP and ZABBIX agents are used to monitor server components, UPS power supplies, rack cooling, temperature sensors, and so on. All data are stored in the database for three month. If data should be archived, they can be extracted to text files using Python scripts. Some ZABBIX mechanisms are under test to extract information also from log files.

ZABBIX offers dynamic web pages to show the history of data in line plots, pie charts, and other graphs, which can be defined by the system administrator. Additionally, ZABBIX maps and screens can be

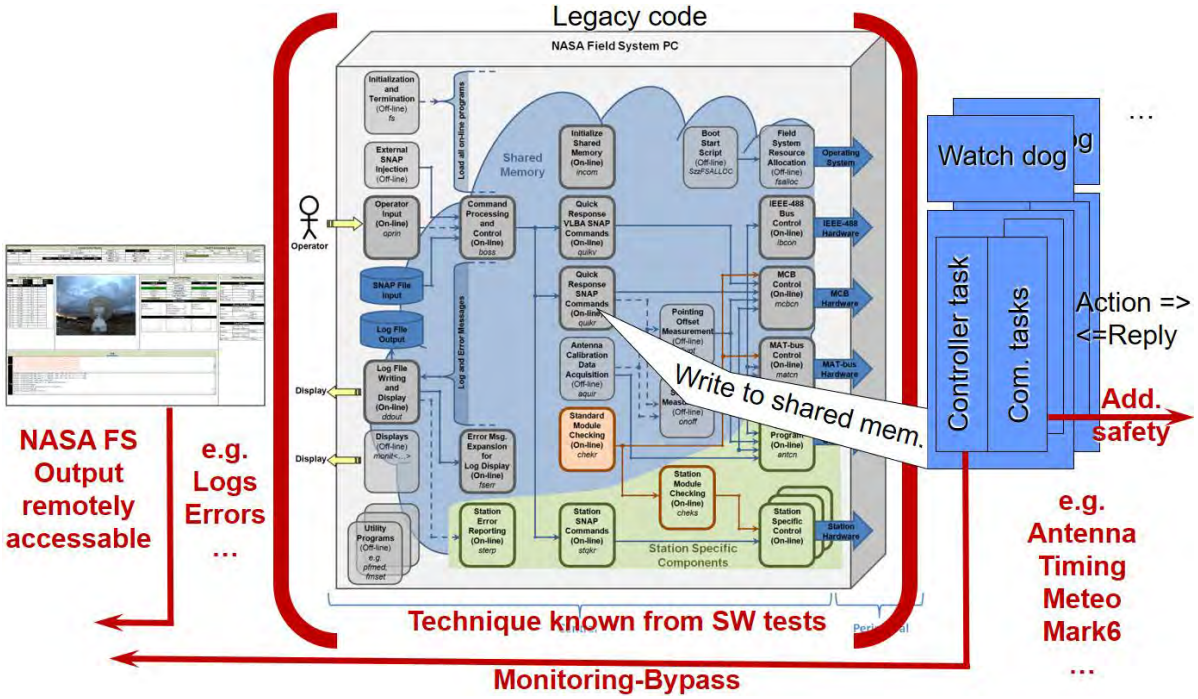

Fig. 1: A method to get system health states parallel to the NASA Field System.

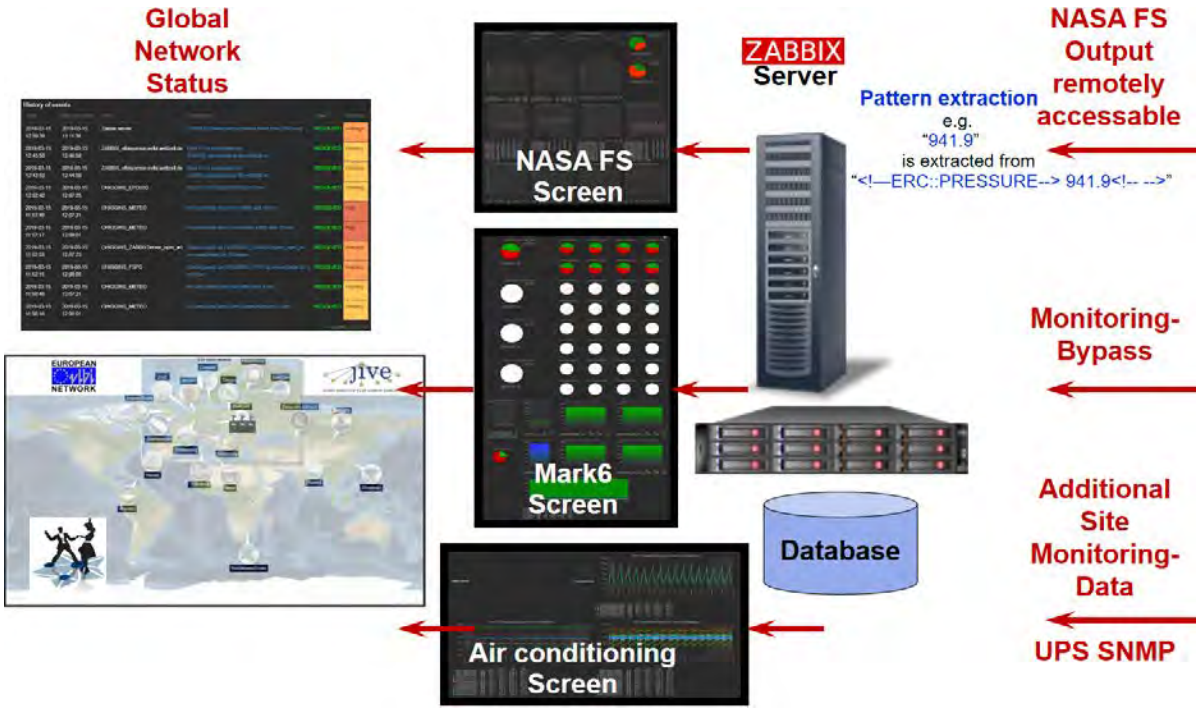

Fig. 2: The data flows from local monitoring sources to central data servers offering a complete VLBI network status.

used to show interactions and logic structures of the systems which are monitored combined with diagrams or single information. Operators are able to select specific time intervals of interest just by selecting the individual part in the diagrams with the mouse. Different user environments allow individual views of the data, so that operators get specific, detailed data sets, while for example a guard at the gate of the observatory just gets an overview of health states on a station map presented with an Android XORO MegaPAD.

Important is the include mechanism of triggers. Administrators set trigger levels or logical combination of trigger levels which are use to fire alerts. The Wettzell system uses three different levels of severity: warnings about reduced data quality (blue color code), errors about reduced or lost data (yellow color code), and alerts about situations when hardware or humans are in danger (while ZABBIX is a pure monitoring system showing health states, so that the hardware itself and local regulations must protect humans from danger).

Besides Wettzell specific presentations for an observatory monitoring and risk management, status information is also combined to global network maps for European VLBI Network (EVN) and IVS, while currently only test sites are included. A world map shows all sites and their status information, so that a centralized operator can see if one of the participating telescopes has problems. Currently dynamically adapted maps are under test to present maps just showing stations participating at the current session.

Combined with standardized data senders at the antenna sites using e-RemoteCtrl, a standardized data flow is realized, which offers a global overview of network situations and its history (see Fig. 2).

4 Towards a data achive for seamless auxiliary data

Having an existing central VLBI network monitoring, data of interest for analysts can also be extracted into text files to create an archive for seamless auxiliary data. Using a Python script written during the project Jumping JIVE, several sensor data can be extracted. Currently of interest are especially meteorological values, to keep them continuously and not just session related for the time of an active session. The result of such an extraction is shown in Fig. 3

ITEM	CLOCK	DATETIME (UTC)	VALUE
26733	1551996101	2019-03-07 22:01:41	5.8000
26733	1551995801	2019-03-07 21:56:41	6.1000
26733	1551995501	2019-03-07 21:51:41	5.9000
26733	1551995201	2019-03-07 21:46:41	5.7000
26733	1551994902	2019-03-07 21:41:42	5.7000
26733	1551994602	2019-03-07 21:36:42	5.8000
26733	1551994301	2019-03-07 21:31:41	5.6000
26733	1551994002	2019-03-07 21:26:42	5.6000
26733	1551993700	2019-03-07 21:21:40	5.5000
26733	1551993401	2019-03-07 21:16:41	5.5000

Fig. 3: Extracted seamless, auxiliary data of one sensor.

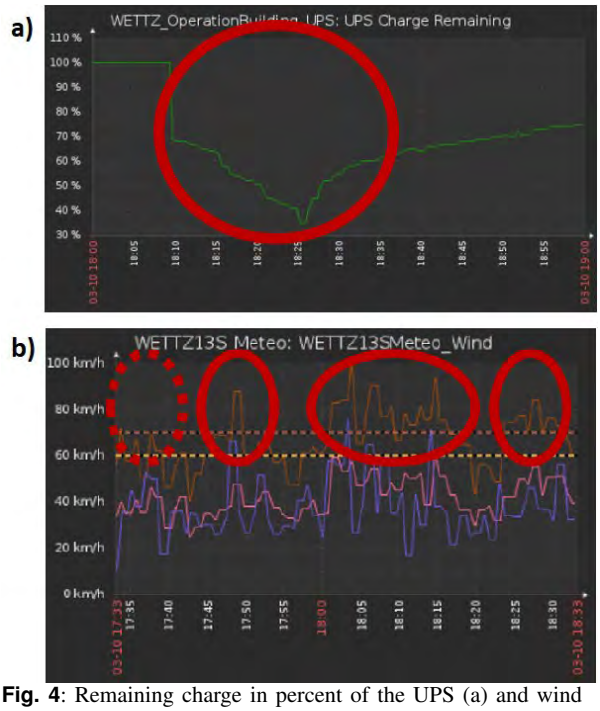

Fig. 4: Remaining charge in percent of the UPS (a) and wind stow alerts (b) during storm ”Eberhard”.

5 Conclusions and outlook

The monitoring system of the VLBI antennas at the Wettzell observatory changed from the test hardware to the final productive database server. It has been successfully active for several month. Found bugs are repaired. The data stock allows support of maintenance work, like during cold-head replacements at the cryogenic dewar. It is a support for remote diagnostics for the experts. Additionally, the tablet at the guard of Wettzell is used to identify and present critical system states.

This was successfully shown in case of a power failure during storm ”Eberhard” on March 10th, 2019 from 18:09 till 18:30 UTC (see Fig. 4). The storm caused a short power outage for the region which resulted in a chain of problems, keeping the UPS in battery mode. Without detection, the whole data center for the Wettzell telescopes would run out of power after finishing the power from the batteries. Additionally, water cooling of the racks failed. Because of the notification service of the monitoring system, the guard was informed and was able to reactivate everything guided by an expert on the phone. Besides this power failure several wind stow alerts also demonstrated that the automatic stow alert works well enough to use it for automatic antenna shutdowns in case of storm situations. The current limit is 70 km/h even if all antennas would be able to work until max. gusts of 130 km/h.

This local monitoring is going to be extended and a first autonomous operation during night shifts is planned for September 2019. It would be necessary to motivate other antennas also to provide auxiliary data for the archive to establish a global data monitoring and seamless, auxiliary data archive.

Acknowledgements This project has received funding from the European Union’s Horizon 2020 research and innovation programme under grant agreement No 730884 - JUMPING JIVE.

References

Ettl M, Neidhardt A, Schönberger M, et al. (2012) e-RemoteCtrl: Concepts for VLBI Station Control as Part of NEXPReS; In: D. Behrend, K. D. Baver (eds.): *IVS 2012 General Meeting Proceedings*, NASA/CP 132, National Aeronautics and Space Administration

Lovell J, Plank L, McCallum J, et al. (2016) Dynamic Observing with the AuScope VLBI array *5th International VLBI Technology Workshop - MIT Haystack Observatory*, https://www.haystack.mit.edu/workshop/ivtw2016/presentations/jlovell_ivtw2016.pdf, Download 2018-09-17

Neidhardt A (2017) Applied Computer Science for GGOS Observatories. Communication, Coordination and Automation of Future Geodetic Infrastructures. *Springer International Publishing Switzerland*, doi:ISBN 978-3-319-40137-9

Zabbix LLC The Ultimate Enterprise - class Monitoring Platform https://www.zabbix.com/, Download 2018-09-13

Mixed-mode VLBI Experiment with Chinese Stations in APSG40

X. He, F. Shu, W. Jiang, L. Ma, X. Yang, L. Chen

Abstract Asian Pacific Space Geodynamics (APSG) geodetic VLBI sessions are being regularly performed within the IVS to improve the accuracy of the geocentric coordinates of the participating stations in the Asia-Pacific region. In the experiment APSG40, we conducted mixed-mode observations with participation of 4 Chinese stations which have no standard geodetic recording mode available. Among them, the Chinese deep space stations located at Jiamusi and Kashi have only 100 MHz bandwidth at X and S-band respectively, and the two small antennas located at Jilin and Sanya have a wide frequency coverage of 1.2 – 9.0 GHz. The observational data have been correlated and analyzed. For the first time we derived the coordinates of Jilin and Sanya at 1 cm level by geodetic VLBI. Here we present the experiment setup, data processing method and initial results.

Keywords VLBI · Mixed-mode observations · Station coordinates

Xuan He · Fengchun Shu · Wu Jiang
Shanghai Astronomical Observatory, Chinese Academy of Science

Langming Ma · Xuhai Yang
National Time Service Center, Chinese Academy of Sciences

Lue Chen
Beijing Aerospace Control Center

(Correspondence: hexuan@shao.ac.cn)

1 Introduction

One goal of VLBI technique is to determine stations' coordinates which can be served as fiducial points of global geodetic reference frame. Accurate positions of VLBI stations are also essential for phase referencing astrometry and deep space navigation.

In 2013, two Chinese Deep Space Network (CDSN) stations, Jiamusi 66-m antenna and Kashi 35-m antenna, have been built. Each of them is equipped with a narrow-band S/X receiver covering the frequency range 2200 – 2300 MHz and 8400 – 8500 MHz. More recently, two small antennas with 13-m aperture have been deployed in Jilin and Sanya by the National Time Service Center (NTSC). They are equipped with a broadband receiver with a frequency coverage between 1.2 and 9 GHz. The received signals are combined and converted into right circular polarization. Currently only 2 bands can be acquired using digital backends in PFB mode.

Asian Pacific Space Geodynamics (APSG) geodetic VLBI sessions are being regularly performed in order to improve the accuracy of the geocentric coordinates of the participating stations in the Asia-Pacific region. In the APSG40 session, the 4 stations mentioned above have been tagged along. In addition to standard geodetic mode used by the APSG stations, another two different modes were used by CDSN and NTSC stations. We report on the mixed mode experiment, data processing method and initial results.

2 Experiment

APSG40 is the 40th APSG session conducted on July 25, 2017. A total of fourteen stations participated in the 24-h S/X dual-band geodetic experiment. Those stations are located on the four plates: Australian Plate, Eurasian Plate, Pacific Plate and North America Plate. Figure 1 shows the geographical distribution of APSG40, CDSN (Jiamusi and Kashi) and NTSC (Jilin and Sanya) stations. The primary purpose of this Asian Pacific Space Geodynamics (APSG) session is to continue monitoring the relative motions of the plates in the Asia-Pacific region. In addition, we planned to determine the precise positions of four Chinese stations which have no standard geodetic recording mode available.

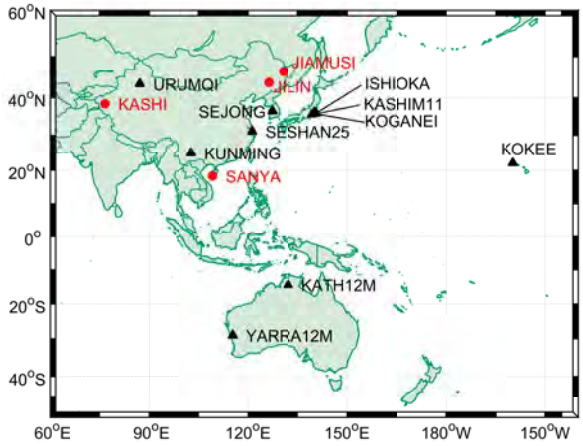

Fig. 1: Geographical distribution of participating stations, where CDSN and NTSC stations are shown in red circles.

The experiment was performed with mixed observing mode. SKED software was used for scheduling. We selected 76 geodetic good sources distributed over the whole sky. Except for Kashi and Jiamusi, the other stations have more than 200 scans. The sub-array option was used to assure that the target sources have a better coverage over the local sky of each station.

Ten APSG40 stations have 10 IF channels at the frequency range of [8.2, 8.6] GHz, and 6 IFs at the range of [2.2, 2.3] GHz. The corresponding data rate is 512 Mbps. But two CDSN stations have only 4 IFs at the range of [8.4, 8.5] GHz and 4 IFs at [2.2, 2.3] GHz. The corresponding data rate is 256 Mbps. Moreover, two NTSC stations have 16 IFs at the X band spread in the range of [8.1, 8.6] GHz, and 4 IFs at the frequency range of [2.2, 2.3] GHz. Two terminals were used to record X-band data with a 2 Gbps rate and S-band data with a 512 Mbps rate respectively.

To make it clear, Figure 2 shows APSG40, CDSN and NTSC stations X band frequency sequences with respect to 8181 MHz. The bandwidth for each IF channel is 8 MHz for APSG and CDSN stations, and 32 MHz for NTSC stations.

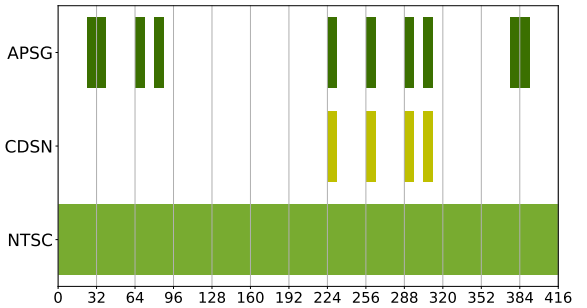

Fig. 2: X-band Frequency sequence with respect to 8181 MHz.

Considering the CDSN has only 4 IF channels and the APSG/NTSC has 10 channels in common at X-band, we optimized the frequency sequence for both cases to get better delay resolution function which showed in Figure 3. The delay ambiguity is 62.5 μs, while the sidelobes of the DRF are less than 0.6.

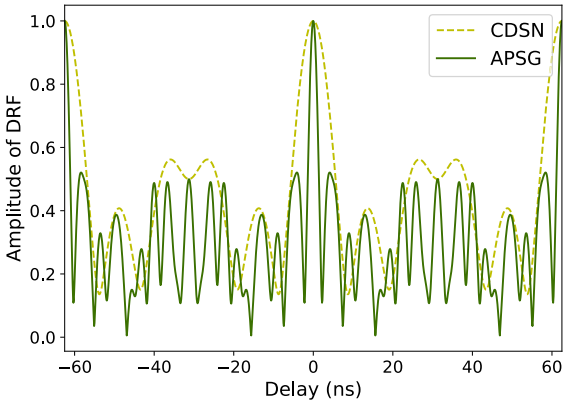

Fig. 3: X-band Delay Resolution Function for two frequency sequences.

3 Data processing

3.1 Data correlation

Data correlation of the experiment was performed at the Shanghai VLBI Correlator. Since the recording bandwidth and the frequency coverage were different among APSG, CDSN and NTSC stations, the zoom mode in the DiFX correlator was used to extract the frequency channels in common with APSG stations. We correlated the data in three different passes: APSG station only, APSG+CDSN stations, APSG+NTSC stations. The DiFX correlator outputs in each pass were converted into FITS-IDI format for further post-processing separately.

3.2 Post-correlation processing

The FITS-IDI files were loaded into PIMA (Petrov et al., 2011), a post-processing software. Phase calibration was not applied to the four Chinese stations because they have no good phase calibration signals available. After running coarse fringe fitting, we performed bandpass calibration. We checked the fringes before computation of a complex bandpass, and masked out cross-spectrum data whose amplitude is less than 0.4 at the edges of each channel.

Finally we ran fine fringe fitting and export database in GVF format for data analysis.

3.3 Data analysis

We used Psolve which supports databases in the GVF to analyze this session. At this stage, we removed Kunming, Kashim11 and Koganei related baselines because those delay observables are very noisy. The S/X combination solution after removing ionospheric effects can be applied to APSG and CDSN stations.

Unfortunately, Jilin and Sanya stations have very low sensitivities at the S-band. Therefore only X-band delay observables can be used. We had to apply GPS ionosphere model to correct X-band delays. The apriori station coordinates and velocities for APSG stations are based on ITRF2014. Those for Jiamusi and Kashi are from Xu et al. (2016). Jilin and Sanya stations did not participated in geodetic VLBI observations before. We got their approximate positions with an error less than 10 cm derived from local survey. Their velocities are considered to be 0. We chose Sheshan25 as clock reference. The estimated parameters include clock, atmosphere, UT1-TAI, nutation, and coordinates of CDSN/NTSC stations.

4 Results

The Weighted RMS (WRMS) delay residuals for the baselines to CDSN stations is 85.0 ps and for the NTSC stations is 50.7 ps. Figure 4 shows the post-fit delay residuals on the baseline Ishioka-Jilin and the WRMS is 41.7 ps.

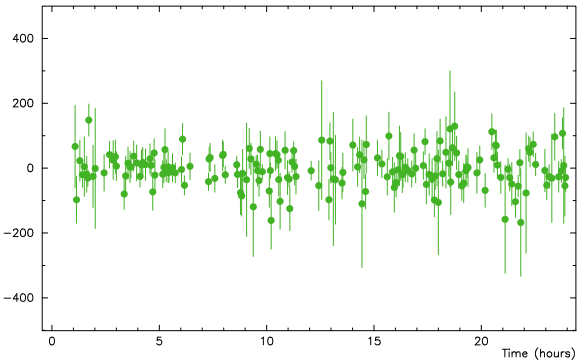

Fig. 4: Post-fit delay residuals on the baseline ISHIOKA – JILIN.

Table 1 shows the adjustments and precisions of NTSC and CDSN stations on July 25, 2017. It can be seen that the precisions in UEN components for each station vary between 0.44 and 26.70 mm. The precisions of the vertical component is much worse than that of the other two components. The positions of Jilin and Sanya have been determined with an error at 1 cm level. Jiamusi and Kashi stations have narrower frequency coverage. Thus it produces less accurate delay observables, which in turn causes larger uncertainties of station coordinates.

As shown in Figure 5, we have derived observed station SEFDs from fringe SNR information, except for Kunming, Kashim11 and Koganei which had bad performance. For APSG stations, only Urumqi had a

Table 1: The adjustments and precisions of NTSC and CDSN stations.

Coordinates	Jilin		Sanya		Jiamusi		Kashi	
	adjustment	σ	adjustment	σ	adjustment	σ	adjustment	σ
U /mm	−49.76	8.91	−58.10	12.58	−53.59	26.56	17.23	26.70
E /mm	24.64	1.87	101.36	2.53	52.94	8.87	35.70	0.44
N /mm	24.98	1.57	−20.60	2.11	−0.73	6.05	106.65	5.93

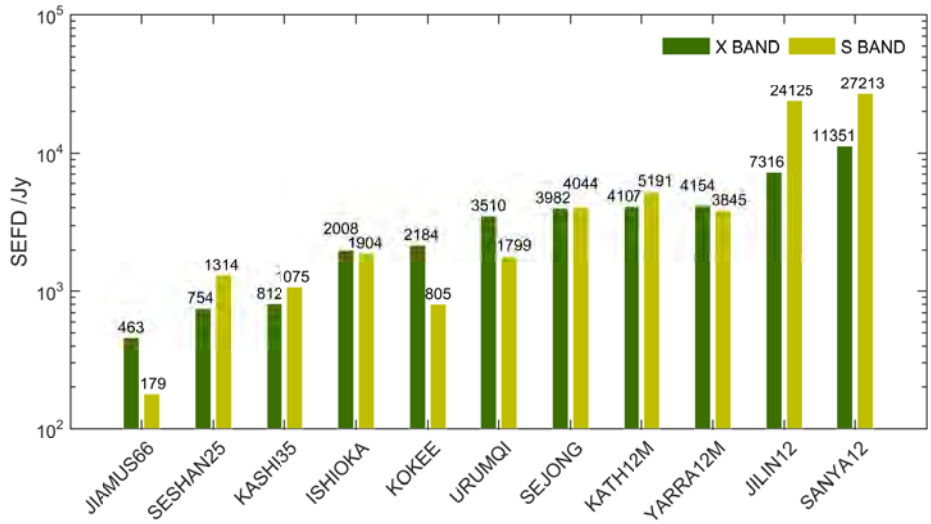

Fig. 5: Estimated station SEFDs at S/X bands in APSG40.

worse X-band SEFD value than expected. The CDSN stations had a similar performance as previous experiments. The NTSC stations had very high S-band SEFDs, probably caused by the RFI. Because we correlated the lower edge of 32 MHz bandpass against with 8 MHz bandwidth of APSG stations, Jilin had a higher SEFD at X-band. However, Sanya is still a bit noisy at X-band.

5 Summary

The mixed-mode observations with participation of four Chinese stations in APSG40 has been performed. We determined the positions of the two NTSC stations at 1 cm level in geodetic VLBI experiment for the first time. We demonstrate that those stations with non-standard geodetic observing mode can be used in geodetic experiments and their precise positions can be determined, even though there is only X-band available.

Acknowledgements This work is supported by the National Natural Science Foundation of China (Grant No. 11573056).

References

Petrov L, Kovalev Y Y, Fomalont E B, *et al.* (2011) The Very Long Baseline Array Galactic Plane Survey — VGaPS. *AJ*, 142, 35–35 doi:10.1088/0004-6256/142/2/35.

Xu D, Dong G, Wang G, et al. (2016) First geodetic VLBI sessions with the Chinese Deep Space Stations Jiamusi and Kashi. *ASR*, 58(9), 1638–1647 doi:10.1016/j.asr.2016.07.022.

Intensive Sessions with the Mauna Kea VLBA Station

C. Dieck, M. Davis, M. Johnson, J. Gipson, S. Byram, D. MacMillan

Abstract Due to its location on the Hawaiian Islands in the middle of the Pacific Ocean, the Mauna Kea station (MK-VLBA) of the Very Long Baseline Array (VLBA) is well positioned for Intensive sessions with stations in the continental United States, Western Europe, and East Asia, similar to the Kōke'e Park Geophysical Observatory (KPGO). Recently, the International VLBI Service for Geodesy and Astrometry (IVS) and the United States Naval Observatory (USNO) initiated observing sessions to characterize the MK-VLBA:WETTZELL and MK-VLBA:WETTZ13N baselines to explore their potential as operational backup baselines for IVS Intensives. The USNO has also been using MK-VLBA in similar sessions with other VLBA stations, particularly PIETOWN, in its efforts to develop a VLBA-based, consistent, high quality UT1−UTC series for use in EOP combinations. We present the status and performance of these sessions, including the detection of the MK-VLBA station displacement resulting from the Kīlauea eruption and associated earthquake, and our plan to account for this displacement in the measurement of UT1−UTC.

Keywords UT1−UTC · Intensives

Christopher Dieck · Maria Davis · Megan Johnson · Sharyl Byram
United States Naval Observatory 3450 Massachusetts Avenue NW, Washington, DC 20392 USA

John Gipson · Dan MacMillan
NVI, Inc. / NASA Goddard Space Flight Center, 8800 Greenbelt Road, Greenbelt, MD 20771 USA

(Correspondence: christopher.dieck@navy.mil)

1 The W-Series: characterizing the baselines from Mauna Kea to Wettzell

The IVS supports the International Earth Rotation and Reference Systems Service (IERS) Rapid Service / Prediction Center (RS/PC) by observing daily Intensive sessions. Only three stations are currently regularly used to make these observations (KOKEE, WETTZELL, and ISHIOKA). If more than one station is unavailable at a given time no Intensive will be observed, resulting in a degradation in the value of UT1−UTC reported by the RS/PC. Such a situation could occur in 2019 as both KOKEE and ISHIOKA will be unavailable for extended periods of time due to upgrades and maintenance, and these outages may overlap. To ensure a high-quality UT1−UTC product from the RS/PC, additional stations need to be prepared to be alternates.

Before a station can be considered part of the Intensive network, it must first make at least 60 test observations with another station in the network over the course of at least four months to characterize that baseline for use by the RS/PC (Davis et al., 2019). The VLBA station on Hawai'i at Mauna Kea (MK-VLBA) is at the eastern end of the Hawaiian Islands, ~500 km south-east of KOKEE, and would therefore be a good substitute for KOKEE when it is unavailable. Similarly, Wettzell North (WETTZ13N) is very close to WETTZELL and could act as an alternate to WETTZELL. With the goal of adding MK-VLBA and WETTZ13N to the network of Intensive-ready stations, the RS/PC, USNO Analysis Center, and IVS Coordinating Center developed a series of test Intensives in coordination with the Geodetic Observatory Wettzell

to characterize the MK-VLBA:WETTZELL (MkWz) and MK-VLBA:WETTZ13N (MkWn) baselines.

The IVS Coordinating Center determined that these sessions would be named wYYDOY with the data base code of XW (hence the name "W-series"). The backends of the VLBA and IVS S/X system are different, preventing the standard IVS Intensive observing setup from being used. The proven setup of the IVS RDV sessions, which use both VLBA and IVS stations, was thus employed. Though ideally each of the two baselines would have their own independent one hour Intensive session, the amount of time for such sessions was not available on the VLBA. By merging with the 90-minute Intensives that the USNO observes daily with the MK-VLBA and PIETOWN stations, the MkWz, MkWn, and MK-VLBA:PIETOWN (MkPt) baselines could all be observed simultaneously. This resulted in a four station network of MK-VLBA, PIETOWN, WETTZ13N, and WETTZELL being used for the W-series.

Simulations showed that a 90-minute session with the four stations would likely be sufficient to continue to meet the USNO's standards for the MkPt baseline while also meeting the requirements for characterizing the MkWz and MkWn baselines. Extending the sessions to 120 minutes *ensured* the required data quality while not exceeding the time allotted. Though IVS Intensives are typically one hour long, two hour sessions do not interfere with the characterization of baselines designed to be used for one hour sessions. Any reduction in the uncertainty due to the longer session length provides a more precise characterization which will be utilized with any one hour Intensive observed after the characterization is complete. Furthermore, the UT1−UTC rate over that time period does not have an appreciable effect on the parameter estimates or their uncertainties, as was verified in subsequent session analysis. Sessions are scheduled for the MK-VLBA:WETTZELL baseline and then PIETOWN and WETTZ13N are tagged along. The Geodetic Observatory Wettzell is able to support the sessions three times per week (only twice per week on WETTZ13N), observed at fixed times. Specifics of the schedule can be found in the IVS Intensive Master File.

As of June 30, 2019 there have been 54 successful sessions. The first few sessions had issues with the WETTZ13N station setup in the schedules, and as a result fringes were not found on baselines including WETTZ13N. The observations will continue through 2019 to accumulate the 60 observations required for baseline characterization.

Table 1 shows the expected number of scans and UT1−UTC formal error from the simulation and the results from the W-series sessions. Residuals of the USNO Analysis Center's UT1−UTC measurements from the W-series with respect to the reported values from the RS/PC's `finals.all` are shown in Figure 1 along with residuals from the KOKEE:WETTZELL Intensives for reference. All indications to date are that the baselines from the Wettzell stations to MK-VLBA will be viable backups to current operational baselines.

2 Mauna Kea displacement: detection through Mauna Kea – Pie Town Intensives

The USNO has been using the MK-VLBA station to monitor the earth's rotation for several years, primarily in conjunction with the PIETOWN station (Geiger et al., 2019). The UT1−UTC measurements resulting from these sessions have proven difficult to incorporate into the products produced by the RS/PC. As a result, the USNO Analysis Center has been evaluating the VLBA Intensive baselines to optimize a product that can be utilized by the RS/PC. In addition to exploring

Table 1: The comparison of the number of scans and the formal errors from the simulation of a single 90-minute schedule of MkPtWz to medians of those metrics from the 54 120-minute MkPtWnWz W-series sessions observed through June 30, 2019.

	90-minute Simulation		120-minute Sessions		
		UT1−UTC		Median # Scans	Median UT1−UTC
Baseline	# Scans	Formal Error (μs)	# Sessions	per Session	Formal Error (μs)
MkPt	48	21.0	49	49	35.2
MkWn	–	–	22	18	15.5
MkWz	41	5.5	50	45	7.0
PtWn	–	–	19	20	17.7
PtWz	71	4.8	47	49	12.0

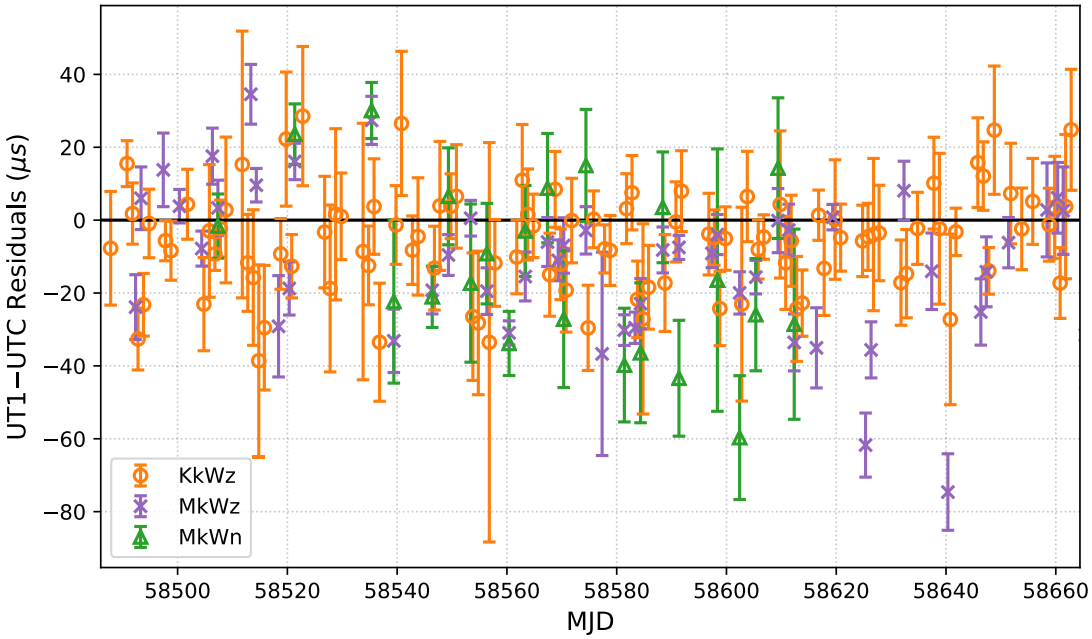

Fig. 1: The residuals of the UT1−UTC measurements from the USNO Intensive series with respect to the `finals.all` series produced by the IERS Rapid Service / Prediction Center. The W-series baselines are shown with KkWz as a reference. No systematic correction has been applied to the data in this diagram.

alternative frequency setups in different bands (Dieck et al., 2019), the USNO Analysis Center is actively developing a collection of Python scripts and functions called the General Repository of EOP Analysis Tools (GREAT).

The existing tools in GREAT revealed statistically significant impacts on the UT1−UTC time series due to motion of the MK-VLBA station. To see these impacts, the software first calculates the residuals of the time series with respect to one of three model series: `eopc04.62-now` from the Paris Observatory, `latest_midnight.eop` from the NASA Jet Propulsion Lab, or, as is used in these analyses, `finals.all` from the USNO. Then an offset and a rate is calculated by doing a least squares minimization fit. The resulting first order polynomial is subtracted from the residuals, resulting in a time series with a mean residual of zero. This process is similar to the RS/PC characterization of a baseline.

Examination of the UT1−UTC residuals at this stage suggested there is a jump in early May 2018. This event is coincident with the Kīlauea volcano eruption on Hawai‘i and the associated 6.9 magnitude earthquake, the epicenter of which is located ∼80 km south east of MK-VLBA. The topographic deflation around the island and up to ∼5 m of fault slip in the southeasterly direction (Neal et al., 2019), which occurred over the course of the eruption, could easily cause a displacement in the position of the MK-VLBA station.

To confirm that the jump is statistically significant, a tool was added to GREAT that performs a weighted moving average over a time series by employing a gaussian kernel density estimator with the kernel bandwidth determined by leave-one-out cross validation (see Feigelson & Babu, 2019). An initial pass of this smoother over the UT1−UTC residual time series from November 14, 2015 (the resumption of MkPt sessions after major maintenance at MK-VLBA) to the present revealed that the residuals not only jumped at the time of the earthquake, but exhibit an unmodeled oscillation (with a primary period of ∼193 days) throughout the baseline's history. Further smoothing was performed in two separate segments, divided at the time of the earthquake (May 4, 2018, MJD 58242.940), which demonstrates that the discontinuity in the MkPt UT1−UTC residuals is indeed statistically significant (Figure 2).

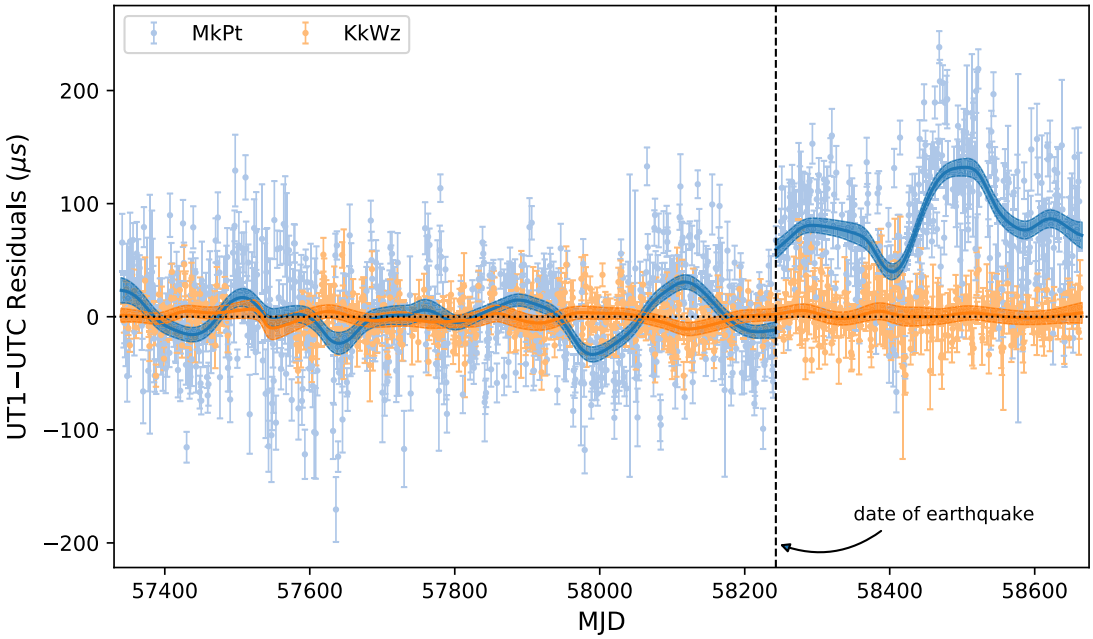

Fig. 2: The residuals of the UT1−UTC measurements from the USNO intensive series with respect to the `finals.all` series from the IERS Rapid Service / Prediction Center. These series have systematic corrections applied so that the mean residual is zero prior to the time of the earthquake, marked by the vertical dashed line. The MkPt VLBA Intensive series is in blue and the KkWz series is in orange. The light points are the residuals with errorbars for each session and the solid line is the gaussian kernel smoothed estimate with the shaded region around the line denoting the 3-sigma confidence interval of the calculation of the estimate. The discontinuity in the MkPt residual estimate demonstrates that the position of the MK-VLBA station did move, likely due to the Kīlauea eruption.

3 Future work: modeling an updated a priori position for Mauna Kea with GPS

The 'MKEA' GPS station is co-located with the MK-VLBA station at a separation of 87.8 m. We produced position solutions for the station which confirm, independently of VLBI, that there was a displacement of the Mauna Kea geodetic observation site down and to the south east with a total magnitude of ~15 mm (Figure 3).

The magnitude of the shift is consistent with the VLBI measurement; at the earth rotation speed at Mauna Kea (438 m/s), 15 mm ≈ 34 μs, within a factor of 2 of the magnitude of the jump in the UT1−UTC VLBI residuals.

UT1−UTC estimates assume a fixed position; therefore, the position displacement must be corrected to utilize any Intensive observations made with MK-VLBA, including both the W-series and the USNO VLBA Intensives. To generate a new position history, we will use the MKEA GPS position information to extrapolate a position for each epoch of observation as was done for the TSUKUB32 station by MacMillan et al. (2013) following the 2011 earthquake in Japan. Additionally, from the resulting position history of the MK-VLBA station, we will develop parametric models of the station motion such as one of the post-seismic deformation models now used in the ITRF 2014 (Altamimi et al., 2016). These would then be used to predict the station's motion and generate a priori positions for use with Intensives. Rather than doing this once, the position history and model would be regularly updated by including new GPS position information.

We expect the corrections to eliminate the jump in the residuals. Additionally, it appears upon visual inspection that oscillations in the north component of the MKEA GPS station are correlated with the oscillations seen in the MkPt baseline UT1−UTC residuals. The updated positions may then also be able correct for the unexplained oscillations, if the connection is real.

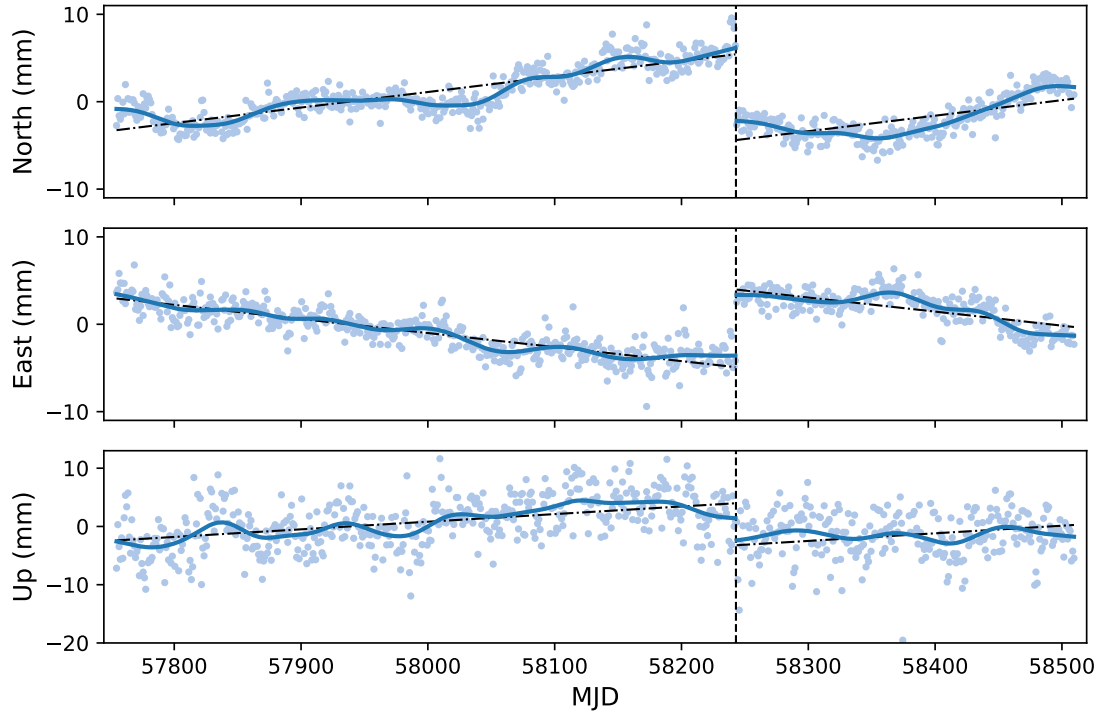

Fig. 3: Relative GPS positions of the MKEA station in the North, East, and Up local tangent coordinates. These data start January 1, 2017 and are plotted with an arbitrary zero point. The individual measurements are showing in light blue circles with the solid blue line denoting the gaussian kernel weighted moving average. The dot-dashed black line is a linear fit model to the positions both before and after the earthquake, marked by the vertical dashed line.

Acknowledgements This work would not have been possible without the work of Merri Sue Carter and Andrew Sargent of the USNO for scheduling and correlating the W-series, respectively. Thanks also to Julien Frouard of the USNO for his assistance with the application of the kernel density estimator. The authors acknowledge use of the Very Long Baseline Array under the US Naval Observatory's time allocation. This work supports USNO's ongoing research into the celestial reference frame and geodesy. The VLBA is an instrument of the National Radio Astronomy Observatory which is a facility of the National Science Foundation operated under cooperative agreement by Associated Universities, Inc.

References

Altamimi Z, Rebischung P, Métivier L, et al. (2016) ITRF2014. *JGR Solid Earth*, 121, 6109–6131, doi:10.1002/2016JB013098

Davis M, Carter M S, Dieck C (2019) The IERS Rapid Service / Prediction Centre UT1−UTC Combined Solution: Present and Future Contributions. In: R. Haas, S. Garcia-Espada, J. A. López Fernández (eds.): *Proc. 24th EVGA Working Meeting*, 184–188

Dieck C, Johnson M, Fey A, et al. (2019) Navigating Across the C-band –Experimental C-band Intensives with the VLBA. In: K. L. Armstrong, K. D. Baver, D. Behrend (eds.): *IVS 2018 General Meeting Proceedings*, NASA/CP-2019-219039, 223–227

Feigelson E, Babu G (2012) *Modern Statistical Methods for Astronomy*.

Geiger N, Fey A, Dieck C, et al. (2019) Intensifying the Intensives with the VLBA. In: K. L. Armstrong, K. D. Baver, D. Behrend (eds.): *IVS 2018 General Meeting Proceedings*, NASA/CP-2019-219039, 219–222

MacMillan D, Behrend D, Kurihara S (2013) Effects of the 2011 Tohoku Earthquake on VLBI Geodetic Measurements. In: D. Behrend, K. D. Baver (eds.): *IVS 2012 General Meeting Proceedings*, NASA/CP-2012-217504, 440–444

Neal C A, Brantley S R, Antolik L, et al. (2019) The 2018 rift eruption and summit collapse of Kīlauea Volcano. *Science* 363, 6425, 367–374, doi:10.1126/science.aav7046

Initial Analysis of IVS-INT01 Schedule Degradation due to Added Source Flux Catalog Latency

K. D. Baver, D. MacMillan, J. Gipson

Abstract Source flux catalogs provide source strength information based on observations in IVS 24-hour sessions. It is important to have up-to-date fluxes because if a source weakens without the catalog being updated to reflect that, the source will be scheduled for too little time, and its observations may fail. This is especially harmful for INT01 sessions, which have few observations. It currently takes at least two weeks to obtain and process a 24-hour session's data, so each new source flux catalog has an unavoidable minimum latency of two weeks. But, because source flux catalogs are manually generated and manually retrieved by schedulers, additional latency can be added by the time the catalogs are used for scheduling. This often occurs in practice, with added latencies, at times, of a month or longer. We look at the effect of added source flux catalog latency on IVS-INT01 schedule degradation due to unrecognized source weakening.

Keywords Source flux · Latency · Intensive · UT1

1 Introduction

Source flux catalogs provide information about source strength based on observations of the sources in IVS 24-hour sessions. It is important to have up-to-date fluxes because if a source weakens without the catalog being updated to recognize that, the source will be scheduled for too little time, and its observations may fail to achieve a viable SNR. This is a serious problem for INT01 schedules given their small number of observations. Some latency is currently unavoidable; it takes at least two weeks to obtain and process the data from 24-hour sessions. But added latency due to a delay in generating a catalog and/or using it for scheduling can be controlled. We studied the effect of this added latency on IVS-INT01 scheduling and observing, focusing on degradation (observation failure and resulting source failure and UT1 formal error increase) due to unrecognized source weakening.

We created artificial source flux catalogs spaced a week apart using IVS 24-hour session data from mid-2015 through early 2017. We then created 11 sets of 52 INT01-style base schedules spaced a week apart within 2016, where the schedules in each set were all created with a flux catalog of one of 11 added latencies: 1, 2, 3, 4, 5, 6, 8, 12, 16, 20, or 24 weeks. This allowed each latency to be tested with 52 one-hour schedules that used sources from different slices of the sky that INT01 sessions observe throughout the year.

Table 1 shows the catalogs used for combinations of schedule (session) dates and catalog latencies. We chose the 52 Mondays in 2016 as the schedule dates, and we assumed that each base schedule was made the previous Friday with a catalog that added one to 24

Table 1: The out-of-date flux catalogs of 11 added latencies used for schedules made for 52 days of the year (DOYs) in 2016.

schedule	added catalog latencies			
(session) dates	one week	two weeks	...	24 weeks
DOY 003	2015dec24	2015dec17	...	2015jul16
DOY 010	2015dec31	2015dec24	...	2015jul23
...	...	...	...	...
DOY 360	2016dec15	2016dec08	...	2016jul07

Karen D. Baver · Daniel MacMillan · John Gipson
NVI, Inc., 7257D Hanover Parkway, Greenbelt Maryland, 20770, USA

(Correspondence: karen.d.baver@nasa.gov)

weeks of latency beyond the unavoidable two week latency due to data processing. So, in line 1, the 11 Monday January 3 (day of year (DOY) 003) 2016 schedules were "created" on Friday December 31, 2015 with catalogs that had at best one week of added latency (the 2015dec24 catalog, with data through the Thursday December 9, 2015 R4 session) and at worst 24 weeks of added latency (the 2015jul16 catalog, with data through the Thursday July 1, 2015 R4 session).

We then ran two tests on the schedules. Test 1 (Section 2) evaluated the amount of theoretical schedule degradation attributable to added source flux catalog latency during scheduling. This test compared the base schedules to schedules made from flux catalogs that contained the best available (most up-to-date) information at the time of scheduling, as shown in Table 2, column 2. Test 2 (Section 3) evaluated how much degradation should actually occur if the base schedules were observed. This test used catalogs that modeled the real time fluxes at the time of observing, as shown in Table 2, column 3. Because USNO currently alternates between scheduling INT01s with an 88-source source list (the "MSS" list) and a 50-source list (the "BA 50" list), we tested both schedule types.

Source flux catalog latency depends on how fast the sources' fluxes are changing. Section 4 evaluates the MSS sources' behavior, focusing on source weakening.

We planned to work with catalogs that simulated realistic catalogs. But, while operational catalogs use averaged data from one to two months of 24-hour sessions, we accidentally only used data from a week of sessions for each catalog. Using only one week of data failed to smooth out isolated large flux changes that can occur due to errors or anomalies such as using an atypical station network. We hope to redo the study later. Meanwhile the current study provides initial insights.

Table 2: Catalogs used in testing. Column 1: 2016 "session dates". Column 2: corresponding test 1 catalogs (best available (most up-to-date) for scheduling). Column 3: corresponding test 2 catalogs ("real time" to model observing). The data in each catalog are two weeks old, so the 2016jan14 catalog, for example, has data through December 30, 2015.

schedule (session) dates	dates of best available catalogs	dates of real time catalogs
DOY 003	2015dec31	2016jan14
DOY 010	2016jan07	2016jan21
...	...	...
DOY 360	2016dec22	2017jan05

2 Scheduling degradation due to latency

The first test evaluated scheduling degradation due to added latency (how many observations would not have been scheduled if up-to-date source flux catalogs with no added latency had been used). This test is of theoretical interest only, because if up-to-date catalogs had been used, the rejected observations would have been replaced by other observations. Using old fluxes fails to recognize the weakening of some sources, and with these sources being scheduled at the shorter durations appropriate to their original, higher strengths, the sources will achieve a lower, perhaps non-viable, SNR.

We ran the GSFC *Sked* scheduling program on each base schedule to reselect fluxes under its up-to-date catalog, and we calculated the new SNR that resulted for each observation from scheduling the observation's source for the observation's original duration under the source's new flux values. We then discarded observations that failed to meet the minimum SNRs of 8 (X-band) and 10 (S-band) used in scheduling, because these observations would not have been scheduled under the up-to-date fluxes. We also determined whether the observation loss eliminated any sources from the schedule. Finally, the unweighted UT1 formal error predicted from a schedule increases as the number of scheduled observations decreases. So we compared the original and reduced schedules to determine the increase in the UT1 formal error attributable to added catalog latency. Table 2, column 2, shows the catalogs used for this test. The 24-hour data on which each catalog was based were still two weeks out-of-date, but this was the best available data at the time of scheduling.

Figure 1 shows the average number of observations for each added latency that would not have been scheduled under up-to-date flux catalogs. Averages are calculated over each latency's 52 schedules. In the MSS case, the number of unscheduled observations strictly increases with increasing latency, from 0.3 observations at one week of latency to 1.5 observations at 24 weeks of latency, and in the BA 50 case, it increases from 0.1 observations at one week of latency to a maximum of 1.4 observations at 16 weeks of latency. We used the Microsoft Excel "ttest" function to perform a two-tailed t-test on pairs of sets of 52 schedules made with catalogs of two different latencies, to see whether

the differences between their counts of unscheduled observations were statistically significant (which we defined as having a t-test confidence level of at least 85 %). The decrease in the BA 50 counts after 16 weeks of latency is statistically insignificant, as are the MSS differences starting at 16 weeks of latency.

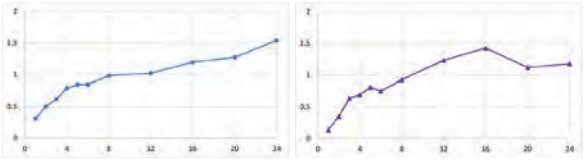

Fig. 1: The average number of observations that would not have been scheduled under up-to-date fluxes vs. added source flux catalog latency in weeks: MSS (left) and BA 50 (right).

Figure 2 shows the average number of sources that would not have been scheduled under up-to-date flux catalogs. The MSS count increases almost strictly with increasing added latency, from 0.3 to 1.3 sources at 24 weeks of latency, although its differences become statistically insignificant at 16 weeks (1.0 sources). The BA 50 count increases from 0.1 to a maximum of 0.8 at 16 weeks, although its differences become statistically insignificant at eight weeks (0.7 sources).

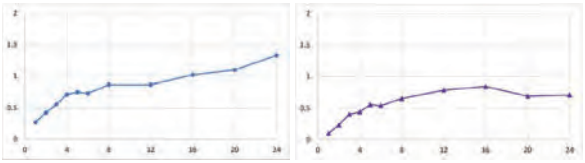

Fig. 2: The average number of sources that would not have been scheduled under up-to-date fluxes vs. added source flux catalog latency in weeks: MSS (left) and BA 50 (right).

Figure 3 shows the increase in the average unweighted UT1 formal errors due to added latency. The MSS UT1 formal error increase generally grows from 0.2 µs to 0.5 µs, although its differences become almost totally statistically insignificant at four weeks of added latency. The BA 50 UT1 formal error increase grows from 0.05 µs at one week of latency to a maximum of 0.5 µs at 12 weeks, although its differences become statistically insignificant at three weeks.

Figure 4 shows the effect of added latency on the UT1 formal error increases of individual schedules. As latency (shown by 11 groups of five bars) increases, the number of schedules with no change in the UT1 formal error (the left bar in each group) generally decreases, and the number of schedules with a formal error increase gets larger. The "> 2.5 µs" category is of concern because each week of operational INT01 schedules comes from a single template, so each base schedule represents five days of INT01 observing. The largest values (> 3.5 µs) come from flux spikes, but some individual DOYs' schedules are vulnerable to latency. For example, starting at three weeks of latency, the MSS DOY 122 schedule experiences an average increase of 2.6 µs. But in general, there is not a strict growth in the UT1 formal error increase with added latency for individual DOYs.

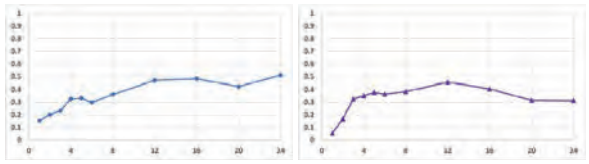

Fig. 3: The average increase in the UT1 formal error due to latency during scheduling vs. added source flux catalog latency in weeks: MSS (left) and BA 50 (right).

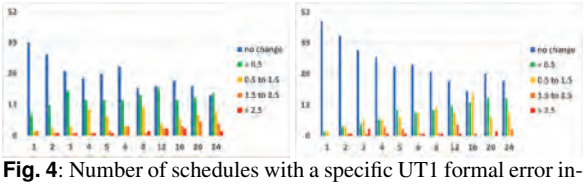

Fig. 4: Number of schedules with a specific UT1 formal error increase range (µs) at different added source flux catalog latencies for the MSS (left plot) and BA 50 (right plot) during scheduling. Groups of five bars along the X-axis represent latencies that increase from left to right. In each group, individual bars represent ranges of growing increase in the UT1 formal errors of individual schedules as the bars progress from left (no change) to right (change of > 2.5 µs) within the group.

On average, added source flux catalog latency does not greatly affect scheduling. Within latencies ranging from one to 24 weeks, the maximum average loss is only 1.5 observations and 1.3 sources, and the maximum average UT1 formal error increase is only 0.5 µs. Also, differences between average UT1 formal error increases are not statistically significant after three or four weeks of latency. The biggest danger is that some individual DOYs' schedules can experience large increases in their UT1 formal errors.

3 Observing degradation due to latency

The actual effect of added source flux catalog latency comes from the failure of scheduled observations during observing because they were scheduled for too little time to achieve a viable SNR when unrecognized source weakening occurred. This is of practical interest, because these failures are not detected until correlation, when it is too late to replace the failed observations. To evaluate this case, we used *Sked* to evaluate the base schedules under the flux catalogs that modeled the fluxes at the time of observing. Better modeling would have involved the creation of new source flux catalogs with a data span centered on the day the schedule would be "observed". But for this first effort, we re-used the schedules from test 1, and for each (Monday) test schedule, we used data through the R4 on the preceding Thursday, which are contained in the catalog dated two weeks later (e.g., for the January 3, 2016 schedules, the catalog dated 2016jan14). We used *Sked* on each base schedule to reselect fluxes under the "real time" catalogs, calculated each observation's new SNR, and discarded observations that failed to meet the minimum SNR of 7 (X- and S-band) used in correlation. We compared the remaining observations to the base schedules to evaluate the three metrics. Table 2, column 3, shows the flux catalogs used in this test.

Figure 5 (left) shows the average number of scheduled observations that would fail to be observed due to added latency. There is little effect, and the number fluctuates, presumably without statistical significance, rather than growing with increasing latency. For each schedule type, observation loss fluctuates between ~ 0.08 and 0.19 observations, much less than the maximum of ~ 1.5 in test 1. The average number of scheduled sources that would fail has an almost identical pattern, and its plot is not shown. Source loss fluctuates between ~ 0.07 and 0.15 sources, much less than the MSS and BA 50 test 1 respective maxima of 1.3 and 0.8 sources.

Figure 5 (right) shows the increase in the average UT1 formal error that would occur due to added latency. Again, latency has only a small effect, and the increase fluctuates between 0.02 μs and ~ 0.12 μs instead of growing with increasing flux catalog latency. This is again less than the 0.5 μs maximum in test 1.

Figure 6 shows the expected increase in the UT1 formal error of individual schedules due to added latency. For both the MSS and the BA 50 cases, the number of schedules with a given UT1 formal error increase (e.g., no change, change < 0.5 μs etc.) fluctuates instead of changing with increasing latency. Also ~ 45 of the 52 schedules for each latency show no change to the UT1 formal error, in contrast to test 1, where a lack of change was only seen in fewer than half of the schedules of approximately half of the latencies. So again added latency has a smaller effect on degradation during observing than on degradation during scheduling. If schedules are broken down by DOY, many DOYs' schedules show no change in the UT1 formal error for any latency, and increasing latency does not generally raise the UT1 formal error increase.

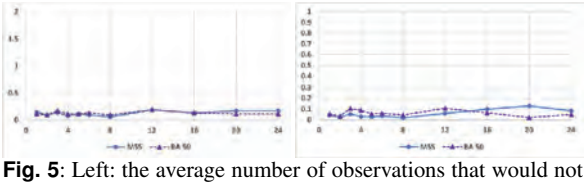

Fig. 5: Left: the average number of observations that would not have been successfully observed vs. added source flux catalog latency in weeks. Right: the average increase in the UT1 formal error during observing vs. added latency in weeks.

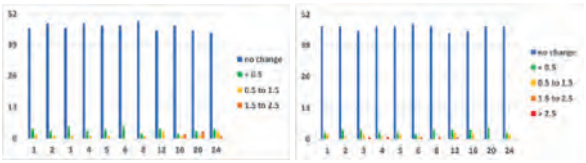

Fig. 6: Number of schedules with a particular range of UT1 formal error increase (μs) at different added source flux catalog latencies for the MSS (left) and BA 50 (right) during observing.

This test shows that added latency has little effect on observing degradation, and the effect does not increase as latency increases. We think that latency causes less observing than scheduling degradation because the correlation SNR limits are lower than the scheduling limits and exclude fewer observations.

4 Source behavior

Source flux catalog latency depends on how fast the sources' fluxes are changing. Observation durations indirectly measure fluxes because a weaker source needs more time to achieve a target SNR. So, to assess flux

change rates, we used *Sked* to calculate the scheduled durations for the 88 MSS sources at 26 DOYs, spaced 14 days apart, every five minutes for an hour starting at 18:30 UT, then averaged the durations over each hour. We performed this evaluation using the 52 2016 artificial flux catalogs to assess the sources' behavior over time. We used an INT01-style schedule but allowed durations up to 600 seconds, to look at weaker sources.

The data included 41,560 duration differences (positive, negative or zero) over a week. 15.2 % were increases, showing that the source was weakening and could be scheduled for too little time and fail to achieve a viable SNR. The average duration increase over a week was 40.6 seconds, with a standard deviation of 48.6 seconds and a maximum of 353.7 seconds (due to the unsmoothed catalog fluxes). Table 3 columns 1 and 2 show the distribution of the duration increases.

We evaluated how often unrecognized flux weakening should cause a scheduled source to become too weak to be scheduled over the next week. INT01 sources are scheduled for 40 to 200 seconds, and Table 3 column 3 shows the durations of observations that should become impossible to schedule given the duration increase in column 1. Column 4 identifies how many actual INT01 observations should be affected. To determine this, we identified the durations of 4,112 Kokee-Wettzell observations from the 2017 INT01 schedules, which all used the MSS source list. Column 4 gives the distribution of these observations within the column 3 ranges. So, using Table 3 line 1 as an example, 67.4 % of the increases should be up to 40 seconds and should cause 45.8 % of INT01 observations (the ones with a duration of 161 to 200 seconds) to exceed the 200 second maximum duration and become impossible to schedule. Because only 15.2 % of the duration differences over a week are increases, column 2 should be multiplied by 15.2 % to see how often a case should occur overall. For example, the line 1 case only occurs 67.4 x 15.2 %, or 7 %, of the time, and the line 4 case only occurs 0.6 % of the time. So the effect of latency is again small.

Table 3: Duration increases over a week under test catalogs. Column 1 shows ranges of duration increases in seconds, and column 2 shows the percentage of the increases that fell into these ranges in test schedules. Column 3 shows the duration ranges in seconds of observations that should become impossible to schedule given the duration increase in column 1. Column 4 shows the percentage of 2017 INT01 Kokee-Wettzell observations that fall into the ranges in column 3.

duration d increase over a week (secs)	percentage of increases in test schedules	durations (secs) of observations that would fail to be scheduled	percentage of occurrences in INT01 schedules
d <= 40	67.4 %	161 to 200	45.8 %
40 < d <= 80	18.4 %	121 to 200	55.1 %
80 < d <= 120	6.3 %	81 to 200	69.5 %
120 < d <= 160	4.0 %	41 to 200	90.0 %
160 < d	3.9 %	all observations	100.0 %

5 Conclusions and next steps

We generated artificial source flux catalogs to study the effect of added source flux catalog latency on the degradation of MSS and BA50 schedules in scheduling and observing. We accidentally included only a week, instead of a month or two, of data in each catalog, resulting in catalogs with unsmoothed flux spikes; however, this study offers initial insights.

Added latency degrades scheduling, and degradation generally increases with increasing latency. But the average effect is small, and its impact on UT1 formal error increase is statistically insignificant after three or four weeks. Latency causes even less degradation during observing, presumably because the correlation SNR limits are lower than the scheduling limits and exclude fewer observations. Degradation during observing fluctuates with presumed statistical insignificance instead of increasing with increasing latency.

Latency depends on how fast the sources' fluxes are changing. The average increase over a week in the length of time needed to observe a source was only 40.6 seconds. Changes of up to 40 seconds would make 45.8 % of INT01 observations too weak to be scheduled due to unrecognized source weakening, but these changes should only occur 7 % of the time.

This initial work says that added source flux catalog latency causes little degradation, but this should be confirmed using smoothed catalogs. Also, unrecognized weakening of sources is only one half of the effect of added latency. The other half is unrecognized strengthening, which counteracts degradation but can cause overly long observation durations which should be reduced to avoid wasting time that could be used for other observations. We hope to perform a more comprehensive study of source flux catalog latency later.

HartRAO Site Tie Measurements: VLBI and Ground Survey

M. Nickola, A. de Witt, M. Schartner, R. C. Botha, C. S. Jacobs, J. Gruber, H. Krásná, W. L. Combrinck, J. Böhm

Abstract A first short baseline VLBI experiment between the Hartebeesthoek Radio Astronomy Observatory's (HartRAO) 26 m legacy and co-located 15 m radio telescopes has been conducted. The local automated site tie system at HartRAO is currently being implemented and tested. The methodology of the two approaches to local tie measurement, VLBI and ground survey, as well as results from the first short baseline experiment are presented here.

Keywords VLBI · ITRF · Local tie · Short baseline

Marisa Nickola · Aletha de Witt · Roelof C. Botha
Hartebeesthoek Radio Astronomy Observatory (HartRAO), PO Box 443, Krugersdorp 1740, South Africa

Marisa Nickola · W. Ludwig Combrinck
University of Pretoria (UP), Private Bag X20, Hatfield 0028, South Africa

Matthias Schartner · Jakob Gruber · Hana Krásná · Johannes Böhm
Technische Universität Wien (TUW), Department of Geodesy and Geoinformation, Gußhausstraße 27-29/E120, AT-1040 Vienna, Austria

Hana Krásná
Astronomical Institute of Czech Academy of Sciences (ASU), Astronomical Institute ASCR, Fričova 298, 251 65 Ondřejov, Czech Republic

Christopher S. Jacobs
California Institute of Technology, Jet Propulsion Laboratory/NASA, 4800 Oak Grove Drive, Pasadena, CA 91109, United States of America

(Correspondence: marisa@hartrao.ac.za)

1 Introduction

If the Global Geodetic Observing System (GGOS) requirement of ± 1 mm accuracy (Beutler et al., 2009) is to be met for global baselines, it must be possible to at least reach this goal for the short baseline of ~113 m between the HartRAO 26 m legacy antenna and the 15 m co-located antenna (see Figure 1). Short baseline experiments allow for discovering and investigating instrumental effects and antenna structure as the antennas share a common location position, atmosphere, local geophysics and clock. Short baseline experiments also allow for determining the local tie between the telescopes. A first such short baseline experiment between the HartRAO 26 m and 15 m antennas has been conducted.

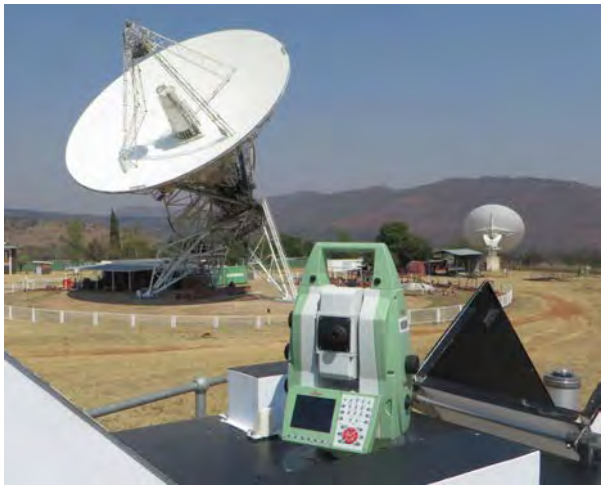

Fig. 1: Short baseline of ~113 m between the HartRAO 26 m antenna (left) and the HartRAO 15 m antenna (right), with the Leica MS50 Multistation in the foreground.

The local automated site tie system at HartRAO is currently under test. Measurements to various on-site GNSS reference stations, the NASA and Roscosmos SLRs as well as to various reference piers will be performed on a regular basis towards fully automating the system. The HartRAO 26 m, 15 m and VGOS radio telescopes will form part of these local tie measurements in due course. Measurements of VLBI reference points, antenna axis offsets (AO) and station coordinates obtained by conventional survey with the total station, will be used to complement the VLBI determined values.

2 Short baseline experiment

A first short baseline session, SBL500, was observed on the 11th of May 2018 with the HartRAO 26 m and 15 m antennas. It consisted of a 4-hour session conducted from 22:00 UT on the 11th of May until 02:00 UT on the 12th of May, well away from sunset and sunrise hours to ensure temperature stability. It was not possible to run the antennas off the same clock for this first short baseline experiment, yet. The SBL500 session was scheduled with the Vienna VLBI and Satellite software (VieVS Böhm et al., 2018) to observe ICRF-2 defining sources at X-band at 2 Gbps, covering the full range of azimuth (for east and north baseline components), elevation (separating the vertical from the troposphere) and cable wrap.

The SBL500 session was subsequently correlated at the Vienna correlator with the Distributed FX-architecture (DiFX) software VLBI correlation package, using a spectral resolution of 0.2 MHz and applying local oscillator (LO) frequency offsets of 9999.9 Hz to HARTRAO. Fringe-fitting and post-processing were also performed at the Vienna correlator making use of the Haystack Observatory Postprocessing System (HOPS) software package. The SBL500 correlator output was made available as vgosDB files. The SBL500 session was analysed with VieVS. Earth Orientation Parameters (EOPs) and coordinates of sources with the no-net-rotation (NNR) condition were not estimated. Thirty-eight other parameters were estimated as follows:

- troposphere zenith wet delay as piecewise linear offsets (PLO) every 60 minutes with loose constraints (6 parameters per station, 12 parameters in total)
- tropospheric gradients as PLO every 360 minutes with loose constraints (3 parameters per station per gradient, 12 parameters in total)
- clock PLO every 60 minutes with loose constraints, one rate and one quadratic term per clock (6 parameters for PLO and 2 for rate and quadratic term, 8 parameters in total)
- station coordinates as one offset, datum definition via no-net-rotation/no-net-translation (NNR/NNT) condition (1 parameter per station per coordinate, 6 parameters in total)

Table 1: Comparison of VieVS estimated values for baseline components and length in SBL500 and corresponding values measured during the 2014 local tie survey (Phogat et al., 2018).

Baseline component	2014 Local tie survey measurement (m)	VieVS estimation for SBL500 (m)
X	-48.0326 ± 0.0029	-48.0353 ± 0.0017
Y	102.2991 ± 0.0032	102.2991 ± 0.0021
Z	-4.1238 ± 0.0073	-4.1286 ± 0.0014
Length	113.0895 ± 0.0187	113.0908 ± 0.0020

Results for baseline components and baseline length from the VieVS VLBI analysis of SBL500 and corresponding results from IGN measurements as determined during the February 2014 local co-location survey (Muller and Poyard, 2015) are compared in Table 1. The results obtained from VLBI analysis differ at the millimetre-level from the local tie survey results.

3 Local tie ground survey

A local automated site tie system for continuous monitoring of vector ties is being implemented. The planned measurement system is to consist of the one Leica MS50 Multistation mounted on a permanent reference pier (currently under test, see Figure 1) as well as an additional Leica MS50 Multistation to be installed on the roof of the Control room. Measurements are to be made to the prisms installed on the antennas and reference network first. The planned reference network is to consist of the on-site HRAO (IGS station), ESA, DLR and Russian GNSS to tie the measurement system in with GNSS observations to link it to the ITRF (see Figure 2).

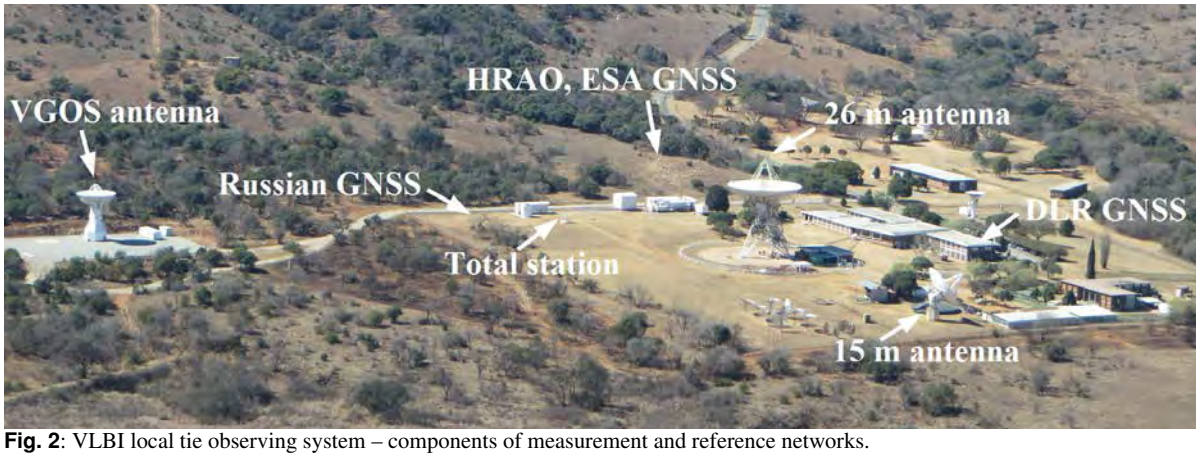

Fig. 2: VLBI local tie observing system – components of measurement and reference networks.

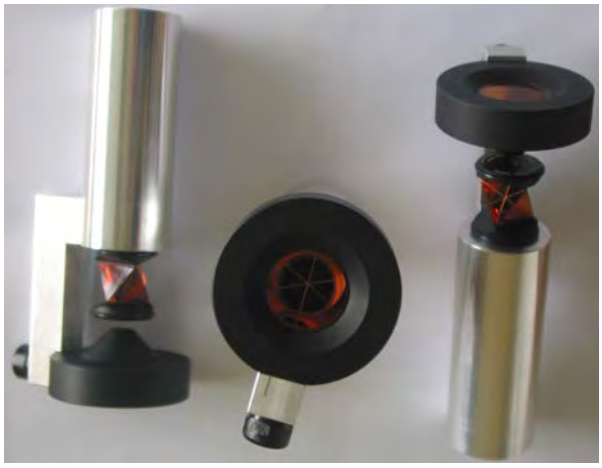

Fig. 3: Targets, consisting of a combination of Leica prisms and custom-made adapters.

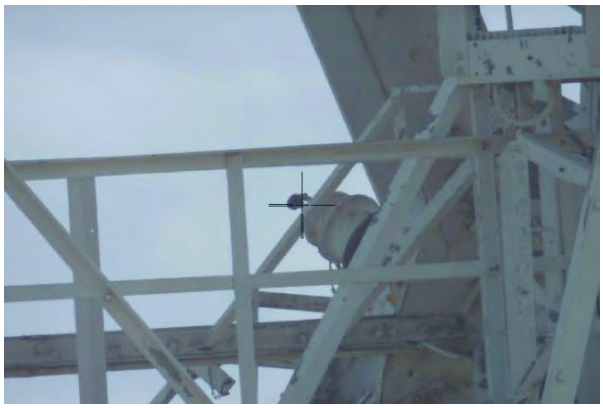

Fig. 4: Prism combination mounted at south end of 26 m polar shaft acquired by the Leica MS50 Multistation.

It is intended to mount the targets on both the 26 m and 15 m antennas on-axis where possible. Targets on the 26 m antenna are to consist of prisms mounted on each of the east and west ends of the declination shaft as well as at the south end of the polar shaft (see figures 3, 4, and 5). The north end of the polar shaft is obscured by the bearing housing, requiring the design of special adapters to mount prisms at this end. On the 15 m antenna, it is possible to mount a prism at the west end of the elevation shaft. The east end of the elevation shaft is obscured by the elevation cable wrap. Again, either special adapters will have to be designed to mount the prisms, or prisms will have to be mounted off-axis at this end (see Figure 6). Similarly for the 15 m's azimuth axis, which is not accessible for the placement of on-axis prisms. Any existing targets on the antenna's structure will also be employed. Targets will be measured by the two total stations, simultaneously, for various positions of the primary and secondary axes respectively.

For antennas with intersecting rotation axes, it is relatively straightforward to determine the VLBI reference point. However, the rotation axes of the HartRAO 26 m polar-mount and 15 m azimuth-elevation (az-el) mount do not intersect but an axis offset (AO) exists for each of the antennas. For the 26 m antenna, the VLBI reference point is represented by the intersection of the fixed Hour Angle (HA) axis with the perpendicular plane containing the moving Declination (DEC) axis. For the 15 m antenna, the VLBI reference point is represented by the intersection of the fixed azimuth axis with the perpendicular plane containing the moving elevation axis.

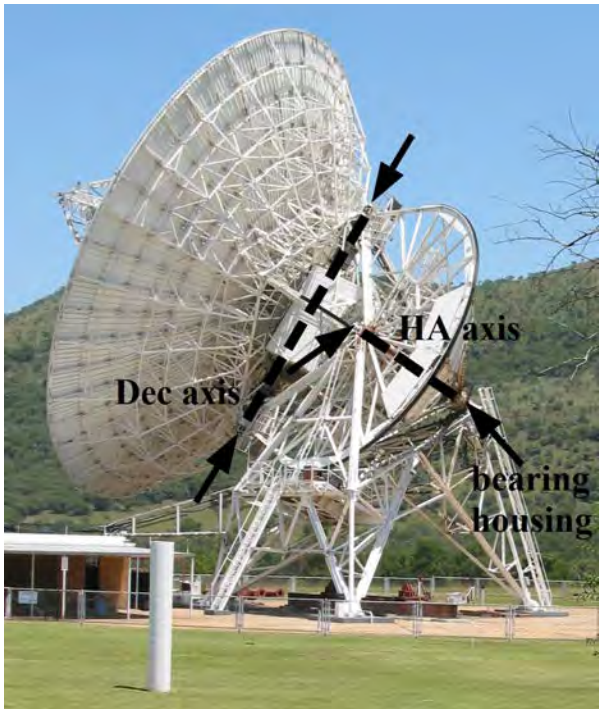

Fig. 5: HartRAO 26 m polar mount antenna – rotation axes and on-axis prism mounting points on Dec shaft (top and bottom arrows) and at south end of polar shaft (arrow in middle). The north end of the polar shaft is obscured by the bearing housing (arrow on right).

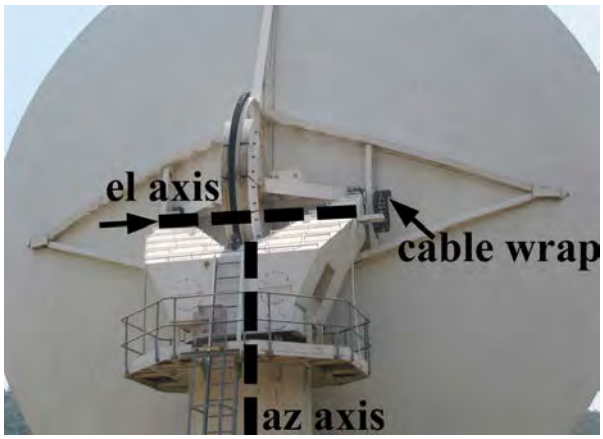

Fig. 6: HartRAO 15 m az-el mount – rotation axes and on-axis prism mounting point at west end of elevation shaft (arrow on left). The east end of the elevation shaft is obscured by the cable wrap (arrow on right).

For both the HartRAO 26 m and 15 m antennas, indirect measurement of the VLBI reference point is therefore required. In order to accomplish this indirect measurement, the intention is to, firstly, mount prisms with their optical reference points coincident with the rotation axis and then, secondly, mount prisms off-axis. The antenna is subsequently moved about one of the rotation axes with the other axis being held fixed in a specific position, for several different positions. Targets will then trace an arc in a circular plane normal to the axis being measured. The axis intersects the plane in the centre of the circle. The method suggested by Combrinck and Merry (1997) for finding the axis intersection and centre of the circle by making use of the intersection of co-planar lines, will be followed. Furthermore, comparing the results for on-axis and off-axis placement of prisms will allow for determining whether the on-axis prism is a valid and accurate measurement point for future use.

4 Outlook

A local tie survey, including all geodetic techniques on site, is currently in the planning stages. In addition to the daily measurement of various targets in the measurement and reference network by the automated total station, it is envisaged that the local tie and short baseline sessions will be conducted on a monthly basis. During the short baseline sessions, the 26 m and 15 m antennas will have to be run off the same clock. Possible variations of the baseline length will be investigated and an error budget will be drawn up for the short baseline ties. Once the VGOS telescope has been furnished with receivers, it will be included in the short baseline sessions.

Acknowledgements Copyright 2019. All rights reserved. HartRAO/SARAO is a facility of the National Research Foundation (NRF), South Africa. The portions of this research carried out at the Jet Propulsion Laboratory, California Institute of Technology were done under a contract with the National Aeronautics and Space Administration. The authors acknowledge the IVS and all its components for providing VLBI data (Nothnagel et al., 2017). The authors wish to thank Jonathan Quick (HartRAO) for his contribution to the first HartRAO short baseline session.

References

Beutler G, Pearlman M, Plag H-P, et al. (2009) Towards GGOS in 2020. In: H.-P. Plag, M. Pearlman (eds.) Global Geodetic Observing System - Meeting the Requirements of a Global Society on a Changing Planet in 2020. Chapter 10, 273–281, doi:10.1007/978-3-642-02687-4_10.

Böhm J, Böhm S, Boisits J, et al. (2018) Vienna VLBI and Satellite Software (VieVS) for Geodesy and Astrometry. *PASP*,130(986), doi:10.1088/1538-3873/aaa22b.

Combrinck W L, Merry C L (1997) Very long baseline interferometry antenna axis offset and intersection determination using GPS. *J Geophys Res*, 102(B11), 24741–24744, doi:10.1029/97JB02081.

Muller J M, Poyard J C (2015) Hartebeesthoek local tie survey. *IGN report*

Nothnagel A., Artz T., Behrend D., et al. (2017) International VLBI Service for Geodesy and Astrometry – Delivering high-quality products and embarking on observations of the next generation. *J Geod*, 91(7), 711–721, doi:10.1007/s00190-016-0950-5

Phogat A, Kronschnabl G, Plötz C, et al. (2018) Short Baseline Observations at Geodetic Observatory Wettzell. *Data*, 3(4), 64, doi:10.3390/data3040064.

In-depth Analysis of Schedules Optimized for Certain VLBI Experiments Using VieSched++

M. Schartner, J. Böhm, A. Müskens, A. Nothnagel, C. Plötz

Abstract Scheduling is an integral part of every VLBI experiment and, at this stage, already determines the geometric stability of the final solution. To increase the quality of the schedule, the TU Wien scheduling concept consists of two steps. The newly developed VLBI scheduling software VieSched++ offers the possibility to generate hundreds of different schedules for a single experiment automatically. Each of these schedules is then simulated hundreds of times using the VieVS VLBI module ending up with hundred thousands of simulations for a single experiment. The results are used to investigate the connection between scheduling optimization criteria and scheduling parameters with geodetic results gained during the analysis of simulations for the selection of the best suited schedule for the session at hand. In this work, we are providing an in-depth analysis of these correlations for the schedule of the T2129 session. We will show the importance of OHIGGINS for this network and highlight which optimization criteria play the biggest role in this session.

Keywords Scheduling · VieVS · VieSched++

Matthias Schartner · Johannes Böhm
TU Wien, Department of Geodesy and Geoinformation, Gußhausstraße 27–29, AT-1040 Vienna, Austria

Arno Müskens · Axel Nothnagel
Rheinische Friedrich-Wilhelms-Universität Bonn, Institut für Geodäsie und Geoinformation, Nußallee 17, DE-53113 Bonn, Germany

Christian Plötz
Geodetic Observatory Wettzell, Federal Agency for Cartography and Geodesy (BKG), Sackenrieder Straße 25, DE-93444 Bad Kötzting, Germany

(Correspondence: matthias.schartner@geo.tuwien.ac.at)

1 Introduction

The generation of a VLBI observing plan, the so-called schedule can be seen as an advanced optimization problem. So far, brute force algorithms are used to generate schedules on a scan by scan basis (Gipson, 2010; Sun, 2013; Schartner and Böhm, 2019a). At each step, all possible next scans are calculated, evaluated and compared to select the best one based on optimization criteria. Unfortunately, developing these optimization criteria is a serious challenge and some of the criteria are competing against each other like the need for a good sky-coverage and the need to maximize the number of observations as discussed in Gipson (2010) and Schartner and Böhm (2019a). Therefore, understanding VLBI scheduling is critical for improving VLBI in general, since the schedule directly determines which observations are available during the analysis of the session.

During the analysis, typically the least squares method is used where the correlations between estimated parameters can be derived directly (Nothnagel et al., 2002). With the recent development of a new VLBI scheduling software called VieSched++ (Schartner and Böhm, 2019a) and further developments in the Vienna VLBI and Satellite Software (Böhm et al., 2018) it is now possible to look at correlations between scheduling parameters and estimated geodetic parameters using Monte-Carlo simulations.

VieSched++ comes with a so-called multi-scheduling feature (Schartner and Böhm, 2019a,b), where multiple schedules for one VLBI session can be generated automatically. By simulating these sessions multiple times, the scheduling statistics are compared with repeatability values of estimated geodetic parameters as well as their formal errors.

This is demonstrated for a schedule of the official International VLBI Service for Geodesy and Astrometry (IVS) (Nothnagel et al., 2017), namely session T2129.

The goal of session T2129 is to provide high-quality station coordinates which can be used to derive terrestrial reference frames. In total, 15 VLBI stations are participating in this session. From a scheduling point of view, this session is especially interesting, since it has many challenges: The network geometry is far from optimal, with only two stations in the southern hemisphere, namely HART15M and OHIGGINS. Additionally, the sampling rate is very low with only 128 Mbit/s which is very problematic, since some antennas have poor sensitivity such as OHIGGINS with system equivalent flux densities (SEFD) of 10.000 Jansky (Jy) in X- and 18.000 Jy in S-band and VERAMZSW with an SEFD of 13.160 Jy in S-band. Together with the remote location of OHIGGINS in Antarctica, generating an optimal schedule, where OHIGGINS is properly included, is a serious challenge. This makes it a perfect candidate to investigate the correlations between scheduling statistics and estimated geodetic parameters to understand how this challenging session can be optimized from a scheduling point of view.

2 Method

Using the VieSched++ multi-scheduling feature, 500 schedules of session T2129 are generated. Each of these schedules follows a different scheduling logic specified through their weight factors and through allowing subnetting or not (Schartner and Böhm, 2019a). The weight factors directly determine the source selection and are therefore the most important factor one can vary in order to optimize the schedule (Schartner et al., 2017; Schartner and Böhm, 2019a,b). These sessions are then simulated 500 times each using VieVS. Together, this leads to a total of 250.000 simulations which can be analyzed. By combining the results of the 500 simulations per schedule, repeatability values can be calculated as well as mean formal errors. Therefore, a series of scheduling values such as number of observations, as well as a series of repeatability and mean formal error values are available and correlations can be calculated between those.

The simulation is calculated including tropospheric turbulences, clock drifts, and white noise (Pany et al., 2011), where the same simulation parameters are used for all stations. The troposphere is simulated using a turbulence simulator with C_n values of $1.8 \cdot 10^{-7}$ $m^{-1/3}$ (Nilsson et al., 2007) and scale height of 2 km, the clock is simulated using random walk and integrated random walk with an Allan standard deviation of $1 \cdot 10^{-14}$ after 50 minutes (Herring et al., 1990), and additionally 30 ps white noise is added to the observations.

3 Results

Figure 1 shows the correlation matrix between the scheduling parameters gained from 500 different schedules generated for session T2129. The first six rows and columns list general scheduling statistics, like the number of scans, the number of observations and the number of observed sources. The number of scans is further divided into scans scheduled with ("subnetting scans") and without ("single source scans") subnetting and scans scheduled during fillin-mode. Subnetting is a technique, where the software decides to split the network into two pieces and therefore is considering two scans simultaneously during the scheduling algorithm (Petrov et al., 2009). Fillin-mode is a concept which is used to reduce station idle time. During the wait time for slower slewing antennas, it is often possible to squeeze in another scan using a reduced antenna network, which is called fillin-mode (Gipson, 2010). VieSched++ uses a recursive scan selection to implement fillin-mode scans, see Schartner and Böhm (2019a,b).

Followed by the general scheduling statistics, the number of scans and observations are listed for each station. The last five rows and columns are the multi-scheduling parameters, which were varied to create the schedules. Among those are four weight factors and a boolean type parameter which shows whether subnetting was allowed during the creation of the schedule or not.

By focusing on the top left corner in Figure 1 where the correlations between the general scheduling statistics are visualized one can see that there is obviously a strong negative correlation between the number of scans scheduled with and without subnetting but also a negative correlation between the number of fillin-

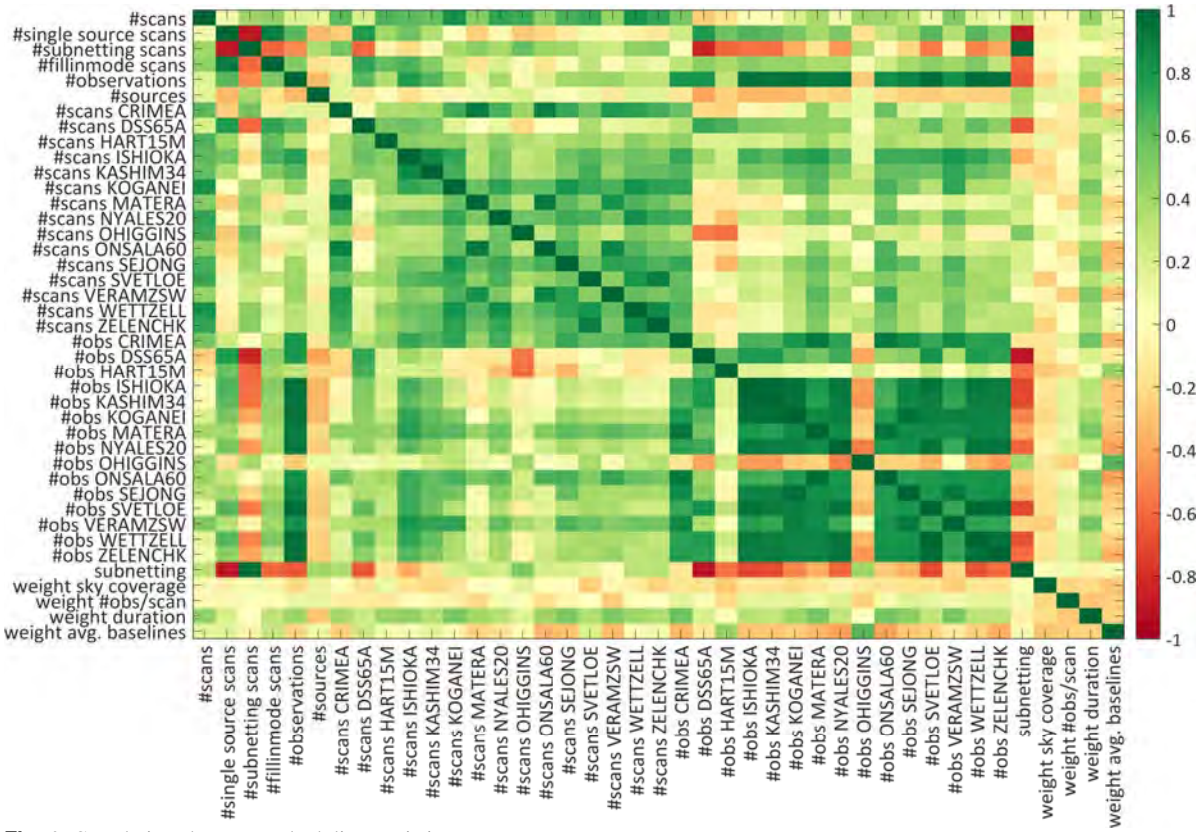

Fig. 1: Correlations between scheduling statistics.

mode scans and subnetting scans. While the first negative correlation can simply be explained by the definition that the sum of the scheduled subnetting scans and the scans scheduled without considering subnetting is the total number of scans. The second negative correlation is due to the better consideration of all stations when using subnetting which results in fewer fillin-mode scans. Interestingly, a high number of subnetting scans also results in a lower total number of observations, which also can be explained by the splitting of the full network into two smaller ones during subnetting. Additionally, there is a small negative correlation between the number of scheduled sources and the total number of observations.

When looking at the correlations between the general scheduling statistics and the number of observations per station, some interesting characteristics can be seen: All but two antennas show a strong positive correlation between the total number of observations and the number of observations per antenna. The only exception is HART15M, showing only a low positive correlation and OHIGGINS which is negatively correlated. This means, that a high number of observations with OHIGGINS results in a lower total number of observations in this schedule, which can be explained by the high cost of the inclusion of OHIGGINS into the schedule due to its remote location and very low sensitivity. Additionally, it can be seen that OHIGGINS gets the highest number of observations when subnetting is used extensively which can be explained through its remote location. This can further be confirmed when looking at the cross-correlations between the number of observations of individual stations. While the number of observations of almost all stations is strongly positively correlated, the number of observations of HART15M is almost not correlated with other stations, and the number of observations with OHIGGINS is negatively correlated with the number of observations with all other stations except HART15M.

While the previously discussed characteristics are necessary to understand VLBI scheduling, the most interesting question is how to generate a good schedule. This can be illustrated when looking at the correlations between the multi-scheduling parameters with

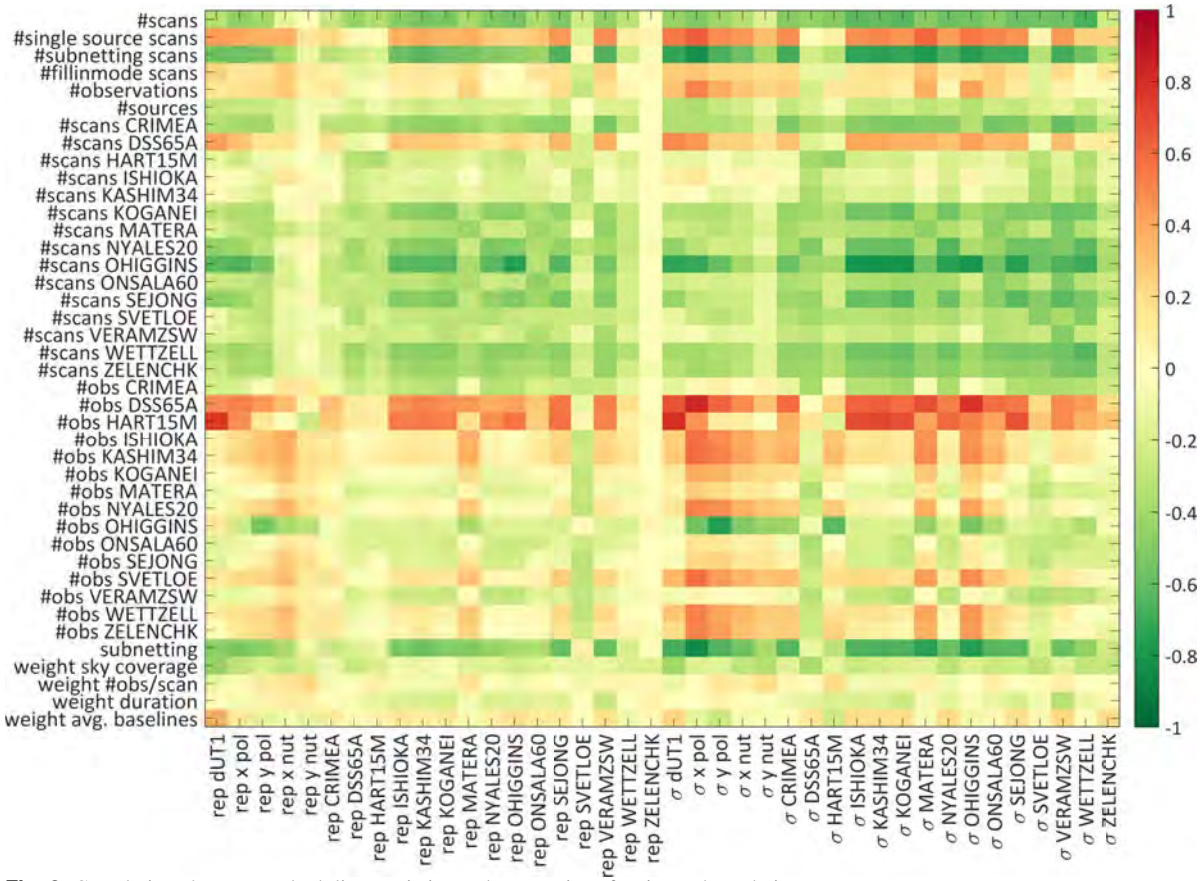

Fig. 2: Correlations between scheduling statistics and accuracies of estimated geodetic parameters.

the other quantities since the multi-scheduling parameters are the only input parameters which are changed to derive the different schedules. When looking at the multi-scheduling parameters, the enabling of subnetting clearly has the biggest effect on the result. It is strongly negatively correlated with the number of observations of all antennas except for OHIGGINS where it shows a positive correlation. Similar behavior can be seen for the weight factor which aims to average out the number of observations over each baseline ("weight avg. baselines"). This makes sense since OHIGGINS has the lowest number of observations thus leading to baselines with a low number of observations. The baselines then get a high weight during the scheduling logic resulting in an on average higher number of observations with OHIGGINS when the average baseline weight factor is given a high value, see Schartner and Böhm (2019a). It can also be verified that giving high weight to optimize the sky coverage, the number of observations is lowered due to the longer slew times. This effect can be countered by increasing the weight of the duration of a scan as well as the number of observations per scan, which results in more scans with more participating stations and, consequently, a higher number of total observations. As already discussed by Gipson (2010) and Schartner and Böhm (2019a) finding a sweet-spot between the optimization of the sky-coverage and the number of observations is one of the main challenges in geodetic VLBI scheduling.

Figure 2 depicts the correlation between scheduling statistics and geodetic parameters derived from simulations. The first half of the columns shows repeatability values derived from the 500 simulations per schedule, while the second half shows the mean formal error gained from the least squares adjustment. When looking at the correlations between the general scheduling statistics, in the first few rows with the geodetic parameters, it is evident that many subnetting scans significantly lower the formal errors and the repeatabili-

ties due to their negative correlation resulting in better results. Surprisingly, there is a positive correlation between the total number of observations and especially the formal errors, meaning that a higher number of observations results in poorer geodetic results. While this might seem wrong, it makes perfect sense in this case: First, a high total number of observations results in a poorer sky-coverage since the slew times are kept low and a good sky-coverage is necessary to estimate tropospheric time delays which are among the biggest error sources in geodetic VLBI (Schuh and Böhm, 2013). Additionally, it can be seen that especially observations with OHIGGINS show the biggest positive effect on the geodetic results and as already discussed previously, a high number of observations with OHIGGINS results in a low total number of observations. As already discussed: While a high number of observations is usually desirable, one has to find the sweet-spot between a high number of observations and a good sky-coverage.

Considering the multi-scheduling parameters shown in the last rows, it is evident that especially the allowance of subnetting has the most significant positive effect on the geodetic results, followed by a good sky coverage and a short duration of individual scans.

4 Conclusions and outlook

VieSched++ is using a multi-scheduling feature to create not only a single schedule for a session but multiple ones simultaneously. Based on Monte-Carlo simulations these schedules can be compared based on geodetic results to select the best schedule. As a by-product, correlations between scheduling statistics and estimated geodetic parameter accuracies can be calculated as shown here for session T2129. For these sessions, especially the proper inclusion of OHIGGINS plays an important role to optimize the schedule. The interaction between scheduling optimization criteria like improvement in the sky-coverage and maximizing the number of observations as well as scheduling features like subnetting are discussed.

While these results are only valid for session T2129 with its unique network geometry and challenges, the generation of the schedules and simulations, as well as the calculation of the correlation parameters, are fully automated in VieSched++ and VieVS to be able to replicate this study for all schedules generated with VieSched++.

References

Böhm J, Böhm S, Boisits J, et al. (2018) Vienna VLBI and Satellite Software (VieVS) for Geodesy and Astrometry. *PASP*, 130, 044503, doi:10.1088/1538-3873/aaa22b

Gipson J (2010) An Introduction to Sked. *IVS 2010 General Meeting Proceedings*, 77–84

Herring T, Davis J, Shapiro I (1990) Geodesy by radio interferometry: The application of Kalman Filtering to the analysis of very long baseline interferometry data. *J Geophys Res*, 95, 12561–12581, doi:10.1029/JB095iB08p12561

Nilsson T, Haas R, Elgered G (2007) Simulations of atmospheric path delays using turbulence models. *Proc. 18th EVGA Working Meeting*, 175–180

Nothnagel A, Vennebusch M, Campbell J (2002) On correlations between parameters in geodetic VLBI data analysis. *IVS 2002 General Meeting Proceedings*.

Nothnagel A, Artz T, Behrend D, et al. (2017) International VLBI Service for Geodesy and Astrometry. *J Geod*, 91, 711–721, doi:10.1007/s00190-016-0950-5

Pany A, Böhm J, MacMillan D, et al. (2011) Monte Carlo simulations of the impact of troposphere, clock and measurement errors on the repeatability of VLBI positions. *J Geod*, 85, 39–50, doi:10.1007/s00190-010-0415-1

Petrov L, Gordon D, Gipson J, et al. (2009) Precise geodesy with the Very Long Baseline Array. *J Geod*, 83, 859–876

Schartner M, Böhm J, Mayer D, et al. (2017) Recent Developments in Scheduling with VieVS. In: R. Haas, G. Elgered (eds.): *Proc. 23rd EVGA Working Meeting*, 113–116

Schartner M, Böhm J (2019a) VieSched++: A New VLBI Scheduling Software for Geodesy and Astrometry. *PASP*, 131, 084501, doi:10.1088/1538-3873/ab1820

Schartner M, Böhm J (2019b) VieSched++: A new Scheduling Tool in VieVS. In: K. L. Armstrong, K. D. Baver, D. Behrend (eds.): *IVS 2018 General Meeting Proceedings*, NASA/CP-2019-219039, 71–75

Schuh H, Böhm J (2013) Very Long Baseline Interferometry for Geodesy and Astrometry. *Berlin, Heidelberg: Springer*, 339–376, doi:10.1007/978-3-642-28000-9_7

Sun J (2013) VLBI scheduling strategies with respect to VLBI2010. *Geowissenschaftliche Mitteilungen*, 92

A Modified Approach for Process-Integrated Reference Point Determination

M. Lösler, C. Eschelbach, S. Riepl, T. Schüler

Abstract The Global Geodetic Observing System (GGOS) calls for continues and automated determination of the geometric reference points of space-geodetic techniques such as DORIS, GNSS, SLR and VLBI. Whereas the reference points of DORIS beacons and GNSS antennas can simply be measured by observing well-defined reference markers, the determination of SLR and VLBI reference points are a metrological challenge, because these reference points are inaccessible and non-materialized. Indirect methods are needed to estimate the reference points in a rigorous way, which fulfil the requirements on an automated and continues reference point determination of the Global Geodetic Observing System. In this investigation, a modified approach for reference point determination of SLR and VLBI telescopes is presented. The results of the new approach are compared to proven reference point models. The numerical deviations of the estimated reference point coordinates and the axis-offset are $\ll 50\,\mu$m and demonstrate the equivalence of the new approach.

Keywords Reference Point Determination · SLR · VLBI · Laser Tracker · Least-Squares Adjustment · In-Process Metrology · GGOS · VGOS

Michael Lösler · Cornelia Eschelbach
Frankfurt University of Applied Sciences, Laboratory for Industrial Metrology, Nibelungenplatz 1, DE-60318 Frankfurt am Main, Germany

Stefan Riepl · Torben Schüler
Federal Agency for Cartography and Geodesy, Geodetic Observatory Wettzell, Sackenrieder Str. 25, DE-93444 Bad Kötzting, Germany

(Correspondence: michael.loesler@fb1.fra-uas.de)

1 Reference point determination model

Reference point determination is a challenging metrological task in the framework of reverse engineering. Here, the telescope is analyzed and virtually deconstructed into its geometrical basic elements to reveal its desired design parameters, e.g. the reference point or the axis-offset. Such a model parametrizes the transformation of a telescope coordinate frame onto an Earth fixed global geodetic reference frame (e.g. Lösler and Hennes, 2008; Kallio and Poutanen, 2012).

Based on observed trajectories of mounted targets, telescope specific parameters are estimable by

$$\mathbf{P}_{j,k} = \mathbf{P}_{\mathrm{IRP}} + \ldots + \mathbf{R}_{\mathrm{x},\beta}\mathbf{R}_{\mathrm{y},\alpha}\mathbf{R}^{\mathrm{T}}_{\mathrm{Z},\kappa_k}\mathbf{R}_{\mathrm{y},\gamma}\left(\mathbf{E}_{\mathrm{AO}} + \mathbf{R}_{\mathrm{x},\omega_k}\mathbf{p}_j\right). \quad (1)$$

Here, matrix $\mathbf{R}$ denotes a basic rotation sequence that rotates around the axis and angle given in sub-index. The axis-offset is given by $\mathbf{E}_{\mathrm{AO}} = \begin{pmatrix} 0 & e_{\mathrm{AO}} & 0 \end{pmatrix}^{\mathrm{T}}$. The angle γ compensates for the non-orthogonality between the primary and the secondary axis. The tilt of the primary axis w.r.t. to the global frame is parameterised by the correction angles α and β. The position $\mathbf{p}_j$ referred to the telescope frame and rotated by κ_k and ω_k around the primary and secondary axis, respectively, corresponds to the position $\mathbf{P}_{j,k}$ in the global frame. The geometrical reference point of the telescope is $\mathbf{P}_{\mathrm{IRP}}$, which is often denoted as invariant reference point (IRP).

Figure 1 depicts the model parameters of the transformation model and the physical connection of the global geodetic reference frame (blue) and the telescope fixed coordinate system (green). The trajectory of the j-th marker $\mathbf{P}_j$ is pictured in several telescope orientations.

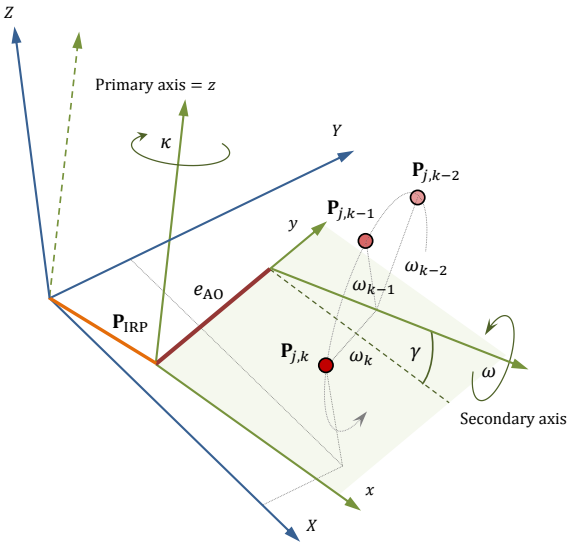

Fig. 1: Resulting trajectory of the mounted marker $\mathbf{P}_j$ observed in several telescope orientations w.r.t. the global geodetic frame and the telescope frame (Lösler et al., 2018a).

Eq. 1 is similar to the mathematical model, derived by Lösler (2008) and refined by Kallio and Poutanen (2012). Hereafter, the former approach is referred to as IRP I approach. The IRP I approach needs the observed angle encoder values of the telescope while the specific marker was registered by the terrestrial measurement system (e.g. Lösler and Hennes, 2008). Thus, a strict synchronisation of both, the measurement system and the telescope, is essential. As shown by Lösler et al. (2016), the uncertainty of the synchronisation corresponds to a position uncertainty of about $100\,\mu\mathrm{m\,m}^{-1}$ (worst-case) and, therefore, becomes a significant component of the total uncertainty. The synchronisation can be optimised by e.g. providing a stable trigger signal or a direct-reading of the telescope encoders. However, a better synchronisation only transfers the problem to a higher level of uncertainty but does not solve the original synchronisation problem.

2 IRP II approach

The goal of the new IRP II approach is to remove the dependence between the terrestrial measurement system and the telescope and, thus, to fully eliminate synchronisation errors. Hereafter, this new approach is referred to as IRP II approach. The inherent difference of the new IRP II approach (Eq. 1) is the exclusion of the datum definitions of the angle encoders. The IRP II approach defines κ_k and ω_k as additional unknown but fixed model parameters. The observations are only the observed marker positions $\mathbf{P}_{j,k}$. Each observed $\mathbf{P}_{j,k}$ provides three functional equations, which can be expressed as functions of the unknown parameters. Thus, ordinary least-squares techniques are sufficient to estimate the parameters (e.g. Mikhail, 1976, Ch. 5). However, the normal equation becomes singular because the parameters of the right hand side of Eq. 1 are unknowns, i.e., the positions $\mathbf{p}_j$ defined in the telescope frame as well as the parameters to transform $\mathbf{p}_j$ to the global geodetic frame are unknown. To solve the defect of the normal equation system, a modified observation and analysis strategy is needed.

1. At least two markers must be mounted at the telescope to be sensitive for changing in telescope rotations.
2. These two markers must be observed at the same time k in at least two different telescope orientations, e.g. κ_k, ω_k and κ_{k+m}, ω_{k+m}, with $m > 0$.
3. If more than two markers are mounted, subsets of at least two markers have to be selected and step 2 is repeated until the necessary topological information between all mounded markers is defined.
4. A no-net-rotation (NNR) constrain has to be introduced to solve the remaining datum defect of the secondary angle of the telescope.

The first three conditions are related to the observation process and can easily be done at the beginning or in the end of the normal operation procedures of the telescope or during maintenance intervals, if polar measurement instruments are used. A promising alternative to polar measurement instruments is the usage of mounted tracking GNSS antennas (e.g. Kallio and Poutanen, 2012; Ning et al., 2015). The forth condition concerns the adjustment process. Secondary angle based NNR constrains as well as coordinate based NNR constrains can be formulated, to solve the remaining rotation defect of the normal equations, and are discussed in detail by Lösler et al. (2018a, 2019). It should be noted that the NNR constrain does not affect the reference point position or the axis-offset but the estimated positions $\mathbf{p}_j$ as well as the angles κ_k and ω_k.

3 Model verification at SOS-W

The Geodetic Observatory Wettzell (GOW) is a core-station in the framework of the GGOS (cf. Plag and Pearlman, 2009, Ch. 2.8.1) and hosts instruments of four independent space-geodetic techniques at one site, i.e. eight GNSS antennas, one DORIS beacon, three VLBI radio telescopes and two SLR laser telescopes (e.g. Mähler et al., 2018). The observatory is cooperatively operated by the German Federal Agency for Cartography and Geodesy together with the Technical University of Munich.

For model verification that bases on real measurements, controlled environment and high-precision measurement instruments are needed, to achieve a better signal-noise-resolution, i.e., to separate model-related and measurement-related deviations. For that reason, the radome enclosed SLR laser telescope, the Satellite Observing System Wettzell (SOS-W), was chosen (Riepl et al., 2005). The protection radome offers a stable and controllable meteorological environment where e.g. the temperature will not falsify the measurements. The local terrestrial measurements were carried out by Hexagon's high-precision mobile Laser Tracker AT401. The measurement uncertainties of the instrument are specified by the manufacturer as $15\,\mu m + 6\,\mu m\,m^{-1}$. The protecting radome limits the measurement distance between the SOS-W and the laser tracker to <2.5 m. For that reason, the SLR telescope was equipped with four so-called Cat-Eye reflector (CER) at the turnable alidade. The CER provides a wide laser acceptance angle of ±60°.

For a single instrument station Figure 2 depicts the observable positions of a CER, which is mounted at the SOS-W. For comparison, the range of a common Corner-Cube reflector (CCR) and a Super Cat-Eye reflector (SCER) are also shown, that provide an accepting angle of ±30° and ±75°, respectively. For a complete hemispherical coverage, at least three instrument stations are needed, if CER or SCER are used. Furthermore, 14 CCR were used to combine the measurements of the instrument stations w.r.t. to the global geodetic reference frame.

In spring 2018, five fully automated reference point determinations were carried out at SOS-W, using different reflector configurations. The software package HEIMDALL was employed for controlling and scheduling the laser tracker. Thus, automated

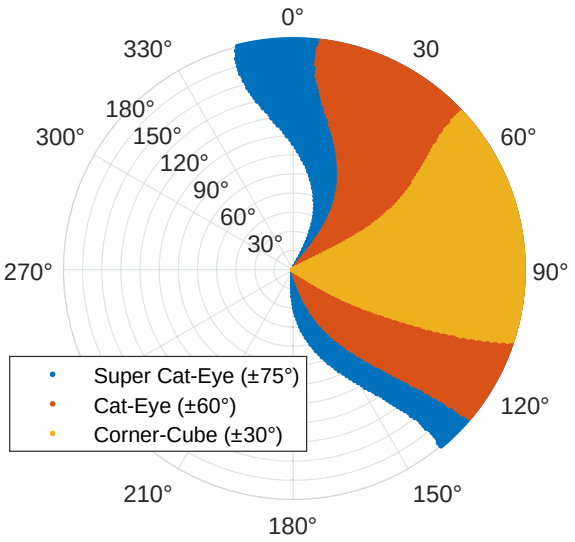

Fig. 2: Accepting range w.r.t. the telescope angles κ_k and ω_k for common Corner-Cube reflector (±30°) as well as for the two wide laser acceptance angle type reflectors: Cat-Eye (±60°) and Super Cat-Eye (±75°).

metrology was realised as suggested by GGOS (cf. Plag and Pearlman, 2009, Ch. 9.3.8).

For the first configuration the CER were aligned at right angles to the line of sight of the SOS-W, while for the second configuration the same reflectors were aligned in parallel to the line of sight. Figure 3 depicts the prepared telescope of the second configuration as well as the automated measuring AT401[1]. Five well distributed instrument stations around the SOS-W were

[1] https://youtu.be/Mdwt1VsWb68

Fig. 3: Automated ILRS reference point determination of the Satellite Observing System Wettzell, using the high-precision mobile laser tracker AT401.

selected, so that at least six CCR of the global geodetic reference system were observable from a single instrument station, cf. Fig 4.

The registered observations to more than 2.200 marker position of the five measurement campaigns were analysed together by a so-called *6-DOF* least-squares network adjustment, using Java·Applied·Geodesy·3D[2] software package (e.g. Lösler et al., 2018b). The adjusted coordinates as well as the fully populated dispersion matrix of the network adjustment process were introduced to the reference point determination model. Due to the lack of reference values for SOS-W, two approved models were used for deriving the reference point as well. The first approved model is the IRP I approach, which is applied for many years and not only at GOW (e.g. Kallio and Poutanen, 2012; Ning et al., 2015; Mähler et al., 2018). The second approved approach is the sphere fit that is usually used for reference point determinations of the ILRS laser telescopes at Wettzell (cf. Klügel et al., 2012; Riepl et al., 2019). The model of the sphere offers the smallest number of unknown parameters but presupposes an intersection of both telescope axes.

Table 1 summarises the obtained results of the reference point and the axis-offset derived by different approaches. The model deviations are negligible w.r.t. the uncertainties of 50 µm. In particular, the estimated axis-offset is insignificant and, thus, results in a high conformity of the estimated reference point between the sphere fit and the IRP I and IRP II approaches. Nevertheless, telescopes with axis-offsets exist and are incompatible to the sphere model. An existing but unknown axis-offset causes, when unaccounted for, systematic errors in Earth orientation parameters and biases the intra-technique derived topocentric vertical component of the reference point (e.g. Combrinck and Merry, 1997; Nilsson et al., 2015).

Table 1: Comparison of estimated reference point position $\mathbf{P}_{\mathrm{IRP}}$ derived by IRP I, IRP II and sphere approaches. The axis-offset e_{AO} is only parametrizable by IRP I and IRP II approaches. The variations of the estimated parameters are $\ll$50 µm for the coordinate components and the axis-offset.

Approach	X_{IRP} in m	Y_{IRP} in m	Z_{IRP} in m	e_{AO} in mm
IRP I	100.16246	197.69374	50.01237	−0.03
IRP II	**100.16246**	**197.69376**	**50.01234**	**−0.02**
Sphere	100.16247	197.69375	50.01234	–

[2] https://applied-geodesy.org

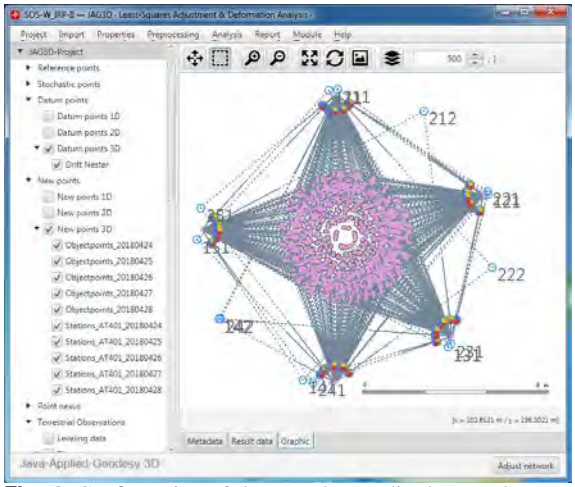

Fig. 4: Configuration of the complete realised network around the SOS-W. The more than 2.200 observed marker position at the SOS-W are symbolised by magenta dots as well as related confidence intervals (1σ, 1500:1). Points of the global geodetic reference frame are depicted as blue hexagons. Realised metrological observations from several instrument stations are plotted in grey coloured dashed lines. The *6-DOF* least-squares network adjustment was carried out using Java·Applied·Geodesy·3D software package.

4 Conclusions

A modified approach for ILRS as well as IVS reference point determination was presented. The new approach is similar to the former model derived by Lösler and Hennes (2008) and refined by Kallio and Poutanen (2012) but overcomes the necessary synchronisation between the terrestrial instrument and the telescope. The GGOS strives on an automated and continues reference point determination of space-geodetic techniques (cf. Plag and Pearlman, 2009, Ch. 9.3.8). The new approach allows for an in-process metrological determination of the reference point of such space-geodetic techniques and fulfils the GGOS requirements.

Using the high-precision mobile laser tracker AT401, more than 2.200 marker positions were observed at the Satellite Observing System Wettzell. Based on the adjusted marker positions and the related

fully populated dispersion matrix, the ILRS reference point was derived, applying the new IRP II approach. The parameter uncertainties are about 50 µm. Based on the same data set, the ILRS reference point is as well derived by two approved models. The variations of the estimated parameters between all evaluated approaches are $\ll$50 µm for the coordinate components and for the axis-offset. Thus, the IRP II approach yields comparable results. The estimated axis-offset of the SOS-W is insignificant w.r.t. to the derived uncertainties and, thus, the sphere model is applicable. Nevertheless, telescopes with axis-offsets exist and need a more specific model like the presented IRP approaches.

Acknowledgements We thank Swetlana Mähler for technical support and providing the adapters of the Cat-Eye reflectors, which enabled a free choice of positioning at the telescope structure. This research project is part of the JRP 18SIB01 "Large-scale dimensional measurements for geodesy" (GeoMetre) and has received funding from the EMPIR programme co-financed by the Participating States and from the European Union's Horizon 2020 research and innovation programme.

References

Combrinck W L, Merry C L (1997) Very Long Baseline Interferometry Antenna Axis Offset and Intersection Determination using GPS. *J Geophys Res*, 102(B11), 24741–24744, doi:10.1029/97JB02081

Kallio U, Poutanen M (2012) Can We Really Promise a mm-Accuracy for the Local Ties on a Geo-VLBI Antenna. In: Kenyon S, Pacino M, Marti U (eds.): *Geodesy for Planet Earth*, Springer, 136, 35–42, doi:10.1007/978-3-642-20338-1_5

Lösler M, Hennes M (2008) An Innovative Mathematical Solution for a Time-Efficient IVS Reference Point Determination. In: *Proc. joint Symposia: 13th FIG Symposium on Deformation Measurement and Analysis and 4th IAG Symposium on Geodesy for Geotechnical and Structural Engineering – Measuring the Changes*

Lösler M (2008) Reference Point Determination with a new Mathematical Model at the 20 m VLBI Radio Telescope in Wettzell. *JAG*, 2(4), 233–238, doi:10.1515/JAG.2008.026

Lösler M, Haas R, Eschelbach C (2016) Terrestrial Monitoring of a Radio Telescope Reference Point Using Comprehensive Uncertainty Budgeting – Investigations during CONT14 at the Onsala Space Observatory. *J Geod*, 90(5), 467–486, doi:10.1007/s00190-016-0887-8

Lösler M, Eschelbach C, Riepl S (2018) A Modified Approach for Automated Reference Point Determination of SLR and VLBI Telescopes. *tm – Technisches Messen*, 85(10), 616–626, doi:10.1515/teme-2018-0053

Lösler M, Eschelbach C, Jarecki F (2018) Auswerte- und Analysestrategie für automatisierte untertägige Überwachungsmessungen. In: J. Benndorf (ed.): 19. Geokinematischer Tag. TU Freiberg, 64–78

Lösler M, Eschelbach C, Riepl S, et al. (2019) Zur Bestimmung des ILRS-Referenzpunktes am Satellite Observing System Wettzell. In: Luhmann T, Schumacher C (eds.): Photogrammetrie - Laserscanning - Optische 3D-Messtechnik: Beiträge der 18. Oldenburger 3D-Tage 2019, Wichmann, 162–175

Klügel T, Mähler S, Schade C (2012) Ground Survey and Local Ties at the Geodetic Observatory. In: *Proc. 17th International Workshop on Laser Ranging*, Mitt. BKG, 48, Frankfurt, 127–131

Mähler S, Klügel T, Lösler M, et al. (2018) Permanent Reference Point Monitoring of the TWIN Radio Telescopes at the Geodetic Observatory Wettzell. *avn – Allgemeine Vermessungsnachrichten*, 125(7), 210–219

Mikhail EM (1976) Observations and Least Squares. Univerity Press of America, Lanham

Nilsson T, Mora-Diaz J A, Raposo-Pulido V, et al. (2015) Antenna Axis Offsets and their Impact on VLBI derived Reference Frames. In: T. van Dam (ed.): REFAG 2014 – Proceedings of the IAG Commission 1 Symposium, 146, Springer, 53–58, doi:10.1007/1345_2015_126

Ning T, Haas R, Elgered G (2015) Determination of the local tie vector between the VLBI and GNSS reference points at Onsala using GPS measurements. *J Geod*, 89(7), 711–723, doi:10.1007/s00190-015-0809-1

Plag H-P, Pearlman M (2009) Global Geodetic Observing System – Meeting the Requirements of a Global Society on a Changing Planet in 2020. Springer, Berlin, doi:10.1007/978-3-642-02687-4

Riepl S, Schlüter W, Dassing R, et al. (2005) The SOS-W – A two colour kilohertz SLR system. In: *Proc. 14th International Laser Ranging Workshop*, Ministerio De Defensa, Real Instituto y Observatorio de la Armada (ROA)

Riepl S, Müller H, Mähler S, et al. (2019) Operating two SLR systems at the Geodetic Observatory Wettzell: from local survey to space ties. *J Geod*, 1–9, doi:10.1007/s00190-019-01243-z

2018 IVS Network Performance

M. Bérubé, E. Himwich

Abstract In 2018, the IVS scheduled over 193 VLBI sessions for geodesy and astrometry. These 24-hour sessions involved more than 39 VLBI antennas operating in networks of 4 to 20 stations. As of today, 154 sessions have been correlated and analysed. These sessions required 1455 station-days and 494823 recorded scans. In 2018, over 85 % of data recorded at the VLBI stations made it through the correlators. Understanding the reasons for this data loss is critical for maintaining a high performance IVS network. This report will be presenting the main causes of missing data for the 2018 IVS Network with emphasis on stations having participated in 50 sessions or more. The results are also compared with previous years. The effect of RFI on stations will also be presented.

Keywords VLBI · IVS

1 Introduction

In 2018, the International VLBI Service for Geodesy and Astrometry (IVS) scheduled over 193 VLBI sessions for geodesy and astronomy. These 24-hour sessions involved 50 VLBI antenna operating in networks of 4 to 20 stations. As of today, 154 sessions have been correlated and analyzed. These sessions required 1455 stations-days and 494823 recorded scans. In 2018, over 85 % of data recorded at VLBI stations made it through the correlators and over 68 % were used by analysts. T his is consistent with previous years. Understanding the reasons for data loss is critical in maintaining a high performance IVS network.

Mario Bérubé · Ed Himwich
NVI, Inc., 7275D Hanover Parkway, Greenbelt, Maryland, 20770, USA

(Correspondence: mario.berube@nasa.gov)

2 2018 S/X observing network

The 2018 S/X observing network consists of 50 stations. This includes the 37 IVS Network Stations as official member components of the IVS as well as several cooperating sites that contribute to the IVS observing program, in particular the 10 stations of the VLBA and 3 NASA DSN stations as shown in Figure 1.

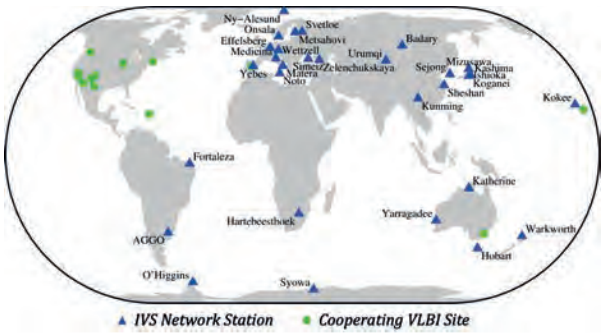

Fig. 1: Distribution plot of the VLBI stations that contributed to the 2018 IVS Master Schedule.

3 Network performance

The network performance is based on correlator and analysis reports from all 24-hours experiments corre-

lated as of February 28, 2019. Experiments correlated at VLBA were also included since available reports provided relevant information on reasons for data loss. The average number of stations per session is 9.4. Figure 2 shows the number of sessions that have been correlated for each station. Some stations have observed more than shown since 39 additional sessions are not correlated yet. In 2018, the 50 stations delivered an average of 85 % of their data. To better understand this global performance, the network has been analyzed by groups based on the station usage.

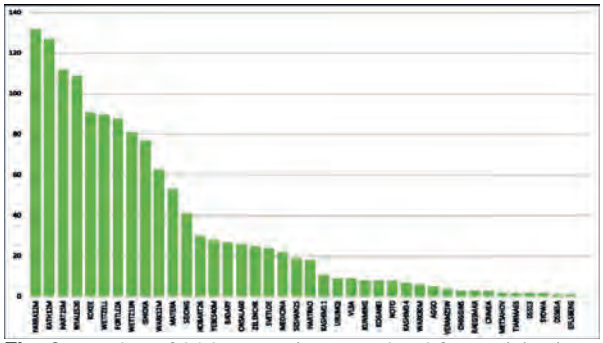

Fig. 2: Number of 24-hour sessions correlated for participating stations

The distinction between these groups was made on the assumption that results will be more meaningful for the stations with more sessions. The Large N group account for 88 % of the station-days and is dominant in determining the overall performance as shown in Table 1. The last two columns of the group analysis table indicate the number of stations that yield more than 90 % and less than 70 % of their data.

4 Historical performance

The 2018 performance is in line with historical data yield (85 % – 88 %) as shown in Figure 3.

Table 1: Group analysis of data yield

Category	Number stations	Station-days	Average	Median	>92 %	<70 %
Big Large N (>40)	12	1064	86.9 %	91.6 %	6	1
Large N (≥17)	21	1283	86.1 %	84.6 %	8	3
Small N (<17)	29	172	72.2 %	72.4 %	7	12
Full network	50	1455	84.9 %	79.4 %	15	15

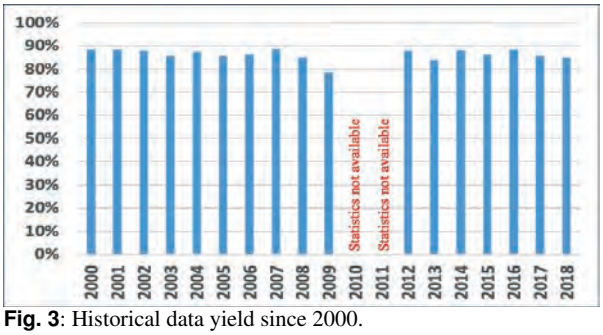

Fig. 3: Historical data yield since 2000.

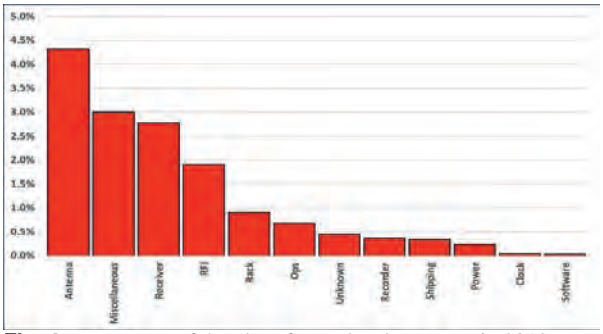

Fig. 4: Percentage of data loss for each sub-systems in 2018

5 Data loss

The data losses were also analyzed by sub-systems for each station but only network results are presented in Figure 4. Computing data loss is not always straightforward. In some cases, down time is used to compute data loss but for certain problems (warm receiver, pointing, RFI) the data loss is estimated from an approximate equivalent number of recorded bits lost.

The antenna problems have been the major cause of data lost for almost 10 years. This is probably due to aging antennas. The miscellaneous category includes problems that do not fit the other categories. These are mainly problems beyond the control of the station and is dominated by bad weather and scheduling conflicts. The receiver data losses were due to three stations that observed with warm receivers for a total of 67 stations-days.

Stations can receive their own results by contacting the authors.

6 RFI

This category includes all losses directly attributable to interference. RFI is mainly evaluated from dropped channels at correlation but there are some difficulties in distinguishing BBC and RFI problems. Some stations were contacted to confirm RFI presence at site. RFI due to commercial systems continues to be an important factor of data loss, mostly in S band. Table 2 provides a short list of dropped channels at the most affected stations in 2018.

Table 2: Most affected stations by RFI in 2018

Station	Data loss	Most affected channels (frequencies in MHz)
Sejong	18.0 %	SR4U (2295 MHz), SR5U (2345 MHz), SR6U (2365 MHz)
Kunming	13.9 %	SR5U (2345 MHz), SR6U (2365 MHz), SR1U (2225 MHz)
Zelenchukskaya	13.0 %	SR2U (2245 MHz), SR3U(2265 MHz), SR4U(2295 MHz)
Koganei11	12.5 %	No fringes in some sessions due to weak S band signal affected by RFI
Yebes 40 m	8.7 %	SR2U (2245 MHz), SR4U (2295 MHz)
Medicina	6.0 %	SR6U (2365 MHz)
Hobart26	5.1 %	SR5U (2272 MHz) SR6U (2288MHz) –AOV sessions SR5U (2281 MHz) SR6U (2297 MHz) –CRDS sessions SR5U (2345 MHz) SR6U (2365 MHz) –CRF, RD sessions
Matera	4.1 %	SR6U (2365 MHz)
Wark12m	3.8 %	SR5U (2345 MHz), SR6U (2365 MHz) –Intermittent
Fortaleza	3.1 %	SR4U (2295 MHz) –Mostly in September-December

Channels: SR1U = band|polarization|BBC#|sideband

7 Summary

Estimating station data losses could be subjective and some times approximative but is a useful tool for evaluating the health of the IVS network over the years. A station yielding over 80 % of data is considered very good and the statistics of the Large N group are showing that stations have been doing pretty well in 2018.

CONT17 From a VieVS Perspective

J. Böhm, M. Schartner

Abstract CONT17 is a special VLBI campaign of the International VLBI Service for Geodesy and Astrometry in November and December 2017 with three independent networks. Two legacy networks with 14 stations each are observing at S- and X-band for 15 days, while a network with six stations is observing in the new VGOS broadband mode. We investigate the CONT17 schedules with the new scheduling software VieSched++ to provide feedback on the legacy and VGOS schedules. Finally, we generate a schedule for mixed-mode observations which could be observed with the CONT17 stations.

Keywords Scheduling · VGOS · Mixed-mode

1 Introduction

Two legacy networks observed at S/X band from 28 November until 12 December 2017 and one VGOS network did broadband observing over five days from 4 to 8 December 2017. The plan for the CONT17 campaign was to *acquire state-of-the-art VLBI data to demonstrate the highest accuracy of which the legacy S/X VLBI system is capable, to investigate possible network biases, and to demonstrate some of the VGOS capabilities limited by the size and geometry of the available VGOS network and observation period.*

Johannes Böhm · Matthias Schartner
Technische Universität Wien, Department of Geodesy and Geoinformation, Gußhausstraße 27–29, AT-1040 Vienna, Austria

(Correspondence: johannes.boehm@geo.tuwien.ac.at)

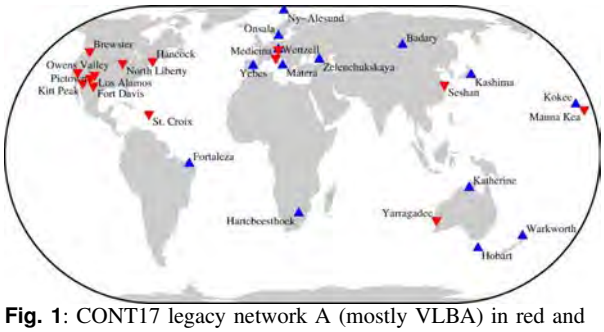

Fig. 1: CONT17 legacy network A (mostly VLBA) in red and network B in blue. The figure is taken from https://ivscc.gsfc.nasa.gov/program/cont17/ .

Fig. 2: VGOS station network during CONT17. ONSA13NE has been verifying the VGOS chain at the time of CONT17 and is not used here. The figure is taken from https://ivscc.gsfc.nasa.gov/program/cont17/ .

The legacy A network with 14 stations (mostly VLBA, correlated in Socorro) observed at a data rate of 256 Mbit/s and the legacy B network, also with 14 stations (correlated in Bonn), used a data rate of 512 Mbit/s (see Fig. 1). On the other hand, the VGOS network with six stations (see Fig. 2) observed at 8 Gbit/s and the baseband data were correlated at MIT Haystack Observatory.

In this report, we focus on the schedules of the CONT17 sessions which have been generated with *sked* (Gipson, 2010). Here, we use VieSched++ (Schartner and Böhm, 2019) to check whether there are improvements possible with those geodetic schedules. To assess both types of schedules, the simulation tool of the Vienna VLBI and Satellite Software (VieVS) (Pany et al., 2011; Böhm et al., 2018) has been applied with a refractive index structure constant of $1.8 \cdot 10^{-7} m^{-1/3}$ and a constant scale height of 2 km for all stations (Nilsson et al., 2007), a clock variation corresponding to an Allan Standard Deviation of 10^{-14} at 50 minutes (Herring et al., 1990), and a white noise per baseline observation of 30 picoseconds. The Monte-Carlo simulation is always based on 500 runs.

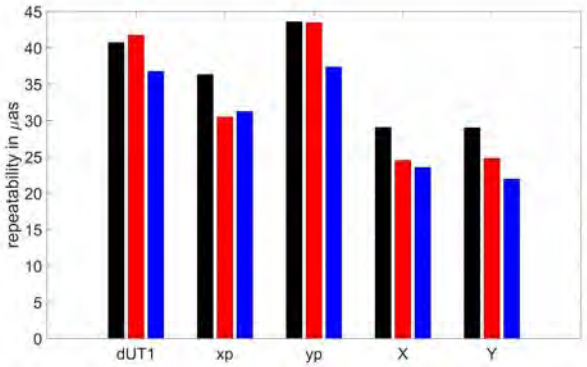

Fig. 3: Simulated repeatabilities in microarcseconds for the Earth orientation parameters for the schedules listed in Table 2. The black bars correspond to the actually observed schedules, the red and blue bars to the schedules generated with VieSched++ with the same and the extended source lists, respectively.

2 Schedules for the legacy B network

The multi-scheduling mode of VieSched++ is used to generate more than 1000 schedules with different weight factors, such as different weights for sky-coverage or the number of observations, for the first day of CONT17 and the legacy B network. Out of those schedules, 150 have been further tested with Monte-Carlo simulations as described in Section 1. Finally, we focus here on two schedules, namely v483 based on the same list of 100 sources as used by *sked* and v036 using an extended list of 300 good sources. Table 1 summarizes the number of observations and scans for the schedules.

Table 1: Characteristics of the schedules for the legacy B network. The first line corresponds to the actually observed schedule, the other two lines correspond to variants generated with VieSched++ with different source lists.

	# obs	# scans
C1701	13499	1499
v483	14921	1278
v036	15094	1478

Figure 3 depicts the repeatabilities of Earth orientation parameters as derived with Monte-Carlo simulations. In general, there is an improvement with the schedules generated with VieSched++, which is even more pronounced when using an extended source list for scheduling. In terms of station position repeatabilities, the improvement for the new schedules is not significant (not shown here).

3 Schedules for the VGOS network

We also scheduled one day of the VGOS network with the following stations participating as core stations: GGAO12M, WESTFORD, KOKEE12M, RAEGYEB. Other stations (ISHIOKA, ONSA13NE, ONSA13SW, WETTZ13S) were added in tag-along mode as was done for the actual schedule with *sked*. In accordance with the observed schedules, we used fixed values of 30 seconds for the scan times and the same down-times of the antennas. However, for the VGOS schedules generated with *sked*, a minimum slew time of 30 seconds was obviously set, too. While we understand the minimum scan lengths due to unknown fluxes at all frequencies, we do not follow the 30 seconds minimum slew times because the purpose is not clear and there is no possibility to apply that constraint in VieSched++.

Finally, two schedules are presented here: v066 with the same source list as used by *sked*, and v058 with an extended list of good sources (more than 250 mJy). The increase in number of observations and scans with about 60 % is substantial. This effect is mainly due to the minimum slew times applied with *sked* but other differences like the varied application of sub-netting plays an important role, too. Monte-

Table 2: Characteristics of the schedules for the VGOS network. The first line corresponds to the actually observed schedule with minimum slew times of 30 seconds, the other two lines correspond to variants with different source lists and without minimum slew times.

	# obs	# scans
17DEC03VS	12985	1180
v066	21041	1948
v058	21061	1985

Carlo simulations have not been carried out for these schedules.

4 Schedules for mixed-mode observations

We also generate schedules for mixed-mode observations for CONT17 as they could have been observed. In the following, we assume that the legacy A network is observing with data rates of 128 Mbit/s at X- and S-band and that the legacy B network is observing at 192 Mbit/s and 320 Mbit/s, respectively. Furthermore, we assume that the channels observed by the legacy B network comprise all channels observed by the legacy A network. Finally, we assume that the VGOS network is observing with a data rate of 2048 Mbit/s at S- and X-band, again including all channels observed by both legacy networks (cf. Fig. 3). Here, all integration times have been calculated based on the channels, and no special factor has been applied when observing with legacy S/X stations (circular polarized receivers) and VGOS stations (linear polarized) together.

Figure 4 depicts how many scans were observed with how many stations. It is evident that there is a high number of scans with many stations participating, i.e., the networks are very well connected. The schedule presented here includes 2016 scans and 126592 observations at an average idle time of 2.4 %.

Table 3: Number of baselines possible with a mixed-mode scenario.

band	data rate	# baselines	baselines
S	128 Mbit/s	399	A-A, A-B, A-V
S	192 Mbit/s	203	B-B, B-V
S	2048 Mbit/s	28	V-V
X	128 Mbit/s	399	A-A, A-B, A-V
X	320 Mbit/s	203	B-B, B-V
X	2048 Mbit/s	28	V-V

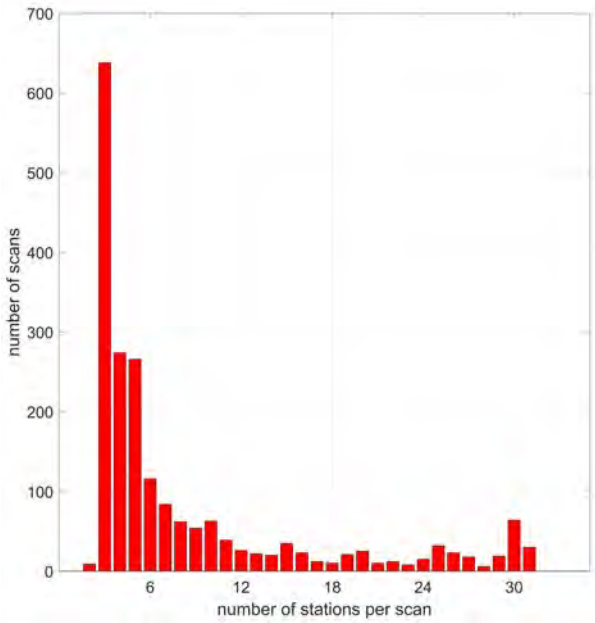

Fig. 4: Number of scans versus number of stations participating in the scans. For example, there are 638 scans with three stations and 64 scans with 30 stations.

5 Conclusions and outlook

We used the scheduling software VieSched++ (Schartner and Böhm, 2019) to assess the schedules generated with *sked* for CONT17. We could confirm that the schedules for the legacy networks are well optimized and only smaller improvements are possible with VieSched++.

The situation is different for the VGOS schedules, which could be greatly improved. It is not clear why the VGOS schedules do have constraints of minimum 30 seconds for scan and slew times. In particular, the slewing time can be well derived from the antenna specifications. Also a more sophisticated use of subnetting could improve the performance of the schedules.

It was also possible to generate a schedule in a mixed-mode scenario, which connects all networks, legacy and VGOS, in one schedule. This approach might be a useful scenario for a CONT2020 campaign.

Acknowledgements The authors would like to acknowledge the Austrian Science Fund (FWF) for supporting this work within project P31625.

References

Böhm J, Böhm S, Boisits J, et al. (2018) Vienna VLBI and Satellite Software (VieVS) for Geodesy and Astrometry. *PASP*, 130, 044503, doi:10.1088/1538-3873/aaa22b

Gipson J (2010) An Introduction to Sked. In: D. Behrend, K. D. Baver (eds.): *IVS 2010 General Meeting Proceedings*, NASA/CP-2010-215864, 77–84

Herring T, Davis J, Shapiro I (1990) Geodesy by radio interferometry: The application of Kalman Filtering to the analysis of very long baseline interferometry data. *J Geophys Res*, 95, 12561–12581, doi:10.1029/JB095iB08p12561

Nilsson T, Haas R, Elgered G (2007) Simulations of atmospheric path delays using turbulence models. *Proc. 18th EVGA Working Meeting*, 175–180

Nothnagel A, Artz T, Behrend D, et al. (2017) International VLBI Service for Geodesy and Astrometry. *J Geod*, 91, 711–721, doi:10.1007/s00190-016-0950-5

Pany A, Böhm J, MacMillan D, et al. (2011) Monte Carlo simulations of the impact of troposphere, clock and measurement errors on the repeatability of VLBI positions. *J Geod*, 85, 39–50, doi:10.1007/s00190-010-0415-1

Schartner M, Böhm J (2019) VieSched++: A New VLBI Scheduling Software for Geodesy and Astrometry. *PASP*, 131, 084501, doi:10.1088/1538-3873/ab1820

The IERS Rapid Service / Prediction Centre UT1−UTC Combined Solution: Present and Future Contributions

M. Davis, M.S. Carter, C. Dieck, N. Stamatakos

Abstract The IERS Rapid Service / Prediction Centre (RS/PC) is responsible for producing a daily combined-solution for Earth Orientation Parameters (EOP), including UT1−UTC. The daily RS/PC EOP solution is designed to produce the most accurate, precise, and robust EOP solution for a given day using the most up-to-date observations and models available. A high-quality 0-day UT1−UTC solution requires low-latency observations that can consistently produce accurate and precise UT1−UTC values. However, the IVS Intensives and UTGPS data series are the *only* two low-latency UT1 or UT1-like data sources, respectively, used in the RS/PC combined solution. Due to the importance of low-latency data in our Daily UT1−UTC Combination, we are investigating additional low-latency VLBI baselines that can robustly contribute to the UT1−UTC solution in circumstances where the standard IVS antennas become unavailable. To that end, we are in the process of characterizing a potential backup Intensive series using the VLBA Mauna Kea antenna together with the 20-meter Wettzell and new Wettzell North 13-meter antennas. If the characterization is successful, this will provide additional alternative baselines for operational use in the future, should they be necessary.

Maria Davis · Merri Sue Carter · Nick Stamatakos
U.S. Naval Observatory, IERS Rapid Service / Prediction Centre, 3450 Massachusetts Ave NW, Washington, D.C., 20392 U.S.A.

Christopher Dieck
U.S. Naval Observatory, USNO VLBI Analysis Center, 3450 Massachusetts Ave NW, Washington, D.C., 20392 U.S.A.

(Correspondence: maria.a.davis33.civ@mail.mil)

Keywords UT1−UTC · Combined-solution · Intensives · UTGPS

1 Introduction

The IERS Rapid Service / Prediction Centre (RS/PC) has been charged by the International Earth Rotation and Reference Systems Service (IERS) with producing a high-quality, daily Earth Orientation Parameters (EOP) solution available to the public (IERS Central Bureau, 2017). The RS/PC produces a daily and weekly EOP solution for Polar Motion x and y (*PM-x, PM-y*), UT1−UTC, Length of Day (*LOD*), and Celestial Pole Offsets ($d\psi$, $d\epsilon$ and *dX, dY*) (Table 1). *Finals.daily* is generated and verified 365 days a year by 17:30 UTC using the most recent EOP measurements

Table 1: IERS Rapid Service / Prediction Centre EOP Combination Products and Distribution Frequency

Product	Distribution Frequency	Description
Bulletin A (ser7.dat)	*weekly* (Thursdays by 19:00 UTC)	· 7 Combination days · 1 year of Predictions*
finals.all†		· Begins in 1973
finals2000A.all††		· EOPs re-calculated 1 year in past
finals.data†		· Begins in 1992
finals2000A.data††		· EOPs re-calculated 1 year in past
finals.daily†	*Daily* @ 17:30 UTC	· 90 Combination days
finals2000A.daily††		· 90 Prediction days

† Celestial Pole Offsets calculated in $d\psi$, $d\epsilon$
†† Celestial Pole Offsets calculated in dX, dY
* Excluding dX, dY and $d\psi$, $d\epsilon$

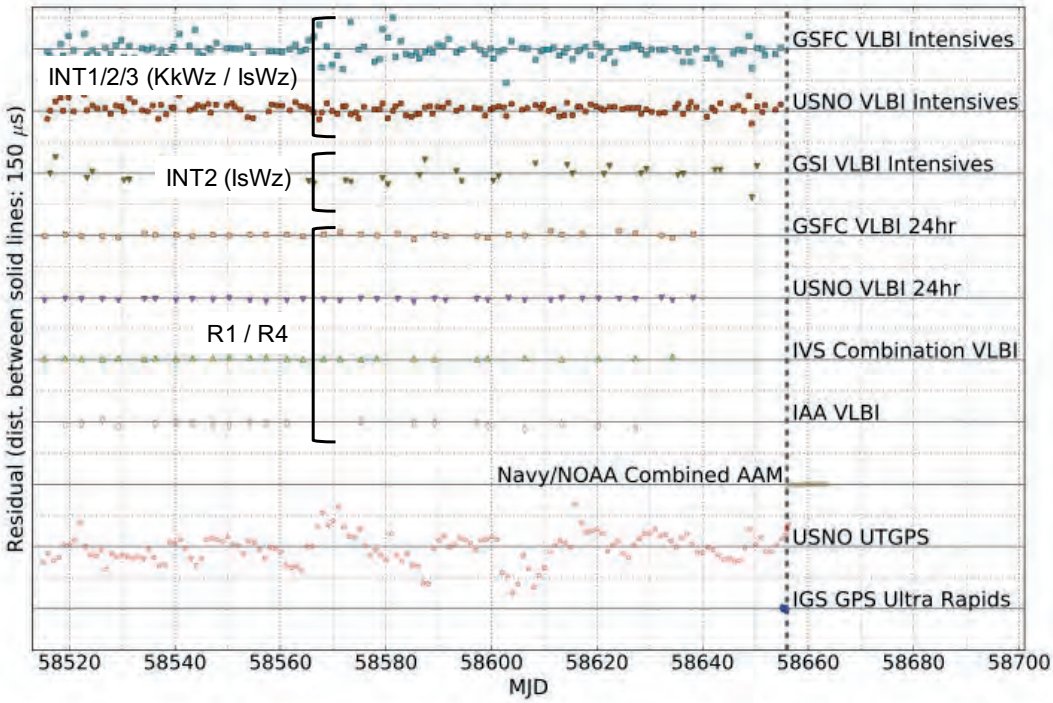

Fig. 1: Residuals of each Contributor after systematic corrections have been applied w.r.t. the Daily RS/PC UT1−UTC combined-solution (finals.daily). Analysis files from each Contributor are filtered to only include expected (or standard) baselines. The combined 0-day solution (indicated by the vertical dotted line) could be negatively impacted if the low-latency Intensives are not available and the solution is thus primarily dependent on the (currently) noisy UTGPS series. *Table 2 provides a description of shorthand used in this figure.*

and models from RS/PC Contributors. EOP solutions, whose accuracy are not verified prior to release, are also generated daily at 03:10, 09:10, and 21:10 UTC. While much of the discussion in this paper will also apply to the UT1−UTC values in our weekly products (Table 1), our focus will be on the unique requirements related to generating a quality daily UT1−UTC. The RS/PC produces and disseminates a number of other products that will not be discussed here; however, they can be found at https://maia.usno.navy.mil/ser7.

Each data series with a UT1−UTC value provided to the RS/PC by a Contributor has been assigned a weight indicating the influence the data series will have in the combined-solution, and systematic corrections to correct for any offsets from the reference series. The EOP contributions are combined using a weighted smoothing cubic spline (McCarthy and Luzum, 1991) to generate the daily combined-solution. Figure 1 shows an example of the residuals of each UT1−UTC Contributor with respect to (w.r.t.) the daily combined-solution (finals.daily); the vertical dotted line indicates the 0-day solution's epoch. The 0-day solution is considered to be the EOP combined-solution at the midnight epoch of the day the Combination is generated. Figure 1 also lists the baselines or series used from each IVS Analysis Center (Contributor) to generate the daily combined-solution. The RS/PC filters VLBI analysis files provided by Analysis Centers of the International VLBI Service for Geodesy and Astrometry (IVS) by baseline (for *.eopi files) or series (for *.eoxy files) and applies a single systematic correction to each Contributor prior to generating the Combination. Alternate baselines may be integrated into the combined-solution if the baseline has been characterized, and sufficient notice has been provided by the IVS Coordinating Center.

2 Generating a combined solution for UT1−UTC

Generating a consistent, high-quality daily UT1−UTC solution is non-trivial due to the challenge of obtain-

ing robust, low-latency contributions. Low-latency Contributors currently used by the RS/PC for the UT1−UTC combination are 1) the 12 UTC Ultra-rapid UTGPS series (*UTGPS* − a UT1-like value) generated by U.S. Naval Observatory (USNO) GPS Analysis Division, 2) the International GNSS Service (IGS) Ultra-rapid integrated LOD values, 3) combined Atmospheric Angular Momentum (*AAM*) predictions from the National Centers for Environmental Prediction (NCEP) and Navy Global Environmental Model (NAVGEM), and 4) the IVS VLBI INT1, INT2, and INT3 (Table 2) Intensives analyzed by Goddard Space Flight Center (GSFC), the Geospatial Information Authority of Japan (GSI), and the USNO. A timeline sketch in Figure 2 shows the regularly available low-latency Contributors utilized in the daily UT1−UTC solution. We will define low-latency contributions here to be processed and available observations or models that have a midpoint epoch within 24 hours of the Daily Combination, which begins at 17:00 UTC.

While the IGS Ultra-rapids, UTGPS, and AAM contributions are available daily, there are data delays and gaps in scheduled IVS Intensives due to station maintenance, local station national holidays, severe weather, or unforeseen station or internet outages. Hence, IVS Intensives cannot be included in the Combination when these events occur, leaving the remaining low-latency Contributors to determine the 0-day UT1−UTC solution. While the techniques utilized by these remaining Contributors are valuable in generating a high-quality 0-day solution, none of them are able to directly measure UT1−UTC as VLBI Intensives do. Therefore, any loss of IVS Intensives longer than 1−2 intermittent days can have significant and long-term impacts on the UT1−UTC time series, particularly if the lost Intensives are not in proximity to an IVS 24-hour R1 or R4 session, which would eventually compensate for the missing data (Stamatakos et al., 2015). In 2018, new Intensives were available prior to the beginning of the Daily Combination at 17:00 UTC 69 % of the year.

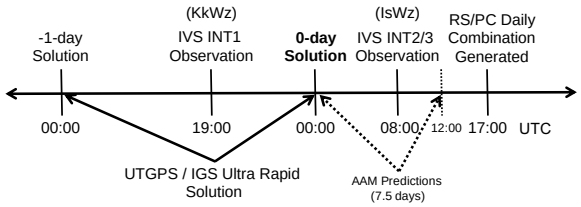

Fig. 2: Timeline of approximate midpoint epochs of UT1−UTC low-latency Contributors w.r.t. the 0-day UT1−UTC solution and the beginning of the Daily Combination. The RS/PC primarily utilizes the *KkWz* baseline for the INT1 series, and the *IsWz* baseline for the INT2/INT3 series (Table 2). The RS/PC Daily Combination begins every day at 17:00 UTC and is nearly always published by 17:30 UTC (Table 1). If the Intensive processing is delayed or unavailable for a given day, UTGPS, IGS Ultra-rapids, and AAM predictions determine the 0-day solution for UT1−UTC.

Table 2: A brief description of shorthand used to describe VLBI observations by session-type (*e.g.*, R1 or INT3) or baseline (*e.g.*, KkWz) as they are used in this paper. *(INT = Intensive; BL = Baseline)*

Baseline or Session	Description	Duration
Kk	· 20 m Kōke'e Park Radio Telescope	
Wz	· 20 m Wettzell Radio Telescope	
Wn	· 13 m Wettzell North Radio Telescope	
Is	· 13 m Ishioka Radio Telescope	
Mk	· 25 m VLBA Mauna Kea Radio Telescope	
Ny	· 20 m Ny-Ålesund Radio Telescope	
KkWz	· Kōke'e–Wettzell BL INT	1 hr
IsWz	· Ishioka–Wettzell BL INT	1 hr
MkWz	· Mauna Kea–Wettzell BL INT	1 hr
MkWn	· Mauna Kea–Wettzell North BL INT	1 hr
R1	· Multi-BL session; begins Monday	24 hr
R4	· Multi-BL session; begins Thursday	24 hr
INT1	· Single-BL session; Monday–Friday	1 hr
INT2	· Single-BL session; Saturday–Sunday	1 hr
INT3	· Single-BL session; Monday	1 hr

The effect of losing low-latency Intensives in the daily UT1−UTC combined-solution is observed in 2015 when the Kōke'e station (Kk) was unable to transmit their Intensives data electronically due to an internet outage from June 2014−January 2016, and was forced to mail their Intensives to the Washington Correlator. While the reference series, finals.data (Table 1), appears to not be significantly impacted by the increased Intensive latency w.r.t. the previous recent years, the 0-day daily solution was substantially influenced (Stamatakos et al., 2014, 2015, 2016). Increased noise in the UTGPS data series beginning mid-2015 (Davis and Stamatakos (2017)) also exacerbated the impact of the delayed INT1 Intensives. As we previously discussed, and can be visualized using Figures 1 and 2, consistent delays of 2−3 days in INT1 Intensives forces the 0-day UT1−UTC solution to become dependent on UTGPS, integrated IGS Ultra-rapid LOD, and AAM predictions. The mean

and standard deviation of the annual 0-day daily UT1−UTC solution residuals w.r.t. the C04 each show a 19 μs increase from 2013 (Stamatakos et al., 2014) to 2015 (Stamatakos et al., 2016). This corresponds to a 950 % and 51 % increase in the mean and standard deviation from 2013, respectively. However, the 2015 UT1−UTC 0-day solution would have likely been significantly less degraded if the UTGPS series had been less noisy or the INT1 Intensives maintained their expected latency of < 22 hours.

3 Creating a more robust UT1−UTC solution

There are several improvements in development to increase the robustness and general health of the daily UT1−UTC combined-solution. One modification that can be made to make the Combination more agile is to implement a more granular application of weights and systematic corrections (*i.e.*, minor adjustments used to remove any residual corrections not accounted for at the analysis level) to Contributor's VLBI data sets. Currently, our Daily Combination uses a whitelist filter on a given analysis file so that only desired session-types (*e.g.*, R1) or baselines (*e.g.*, KkWz) are included in the Combination process. Then, a single weighting and set of systematic corrections are applied to the whole series. *E.g.*, A GSFC Intensive analysis file is filtered to only include KkWz and IsWz (Table 2) baselines, and then a single weight and set of systematic corrections are applied to both baselines. Consequently, it is difficult to include non-standard baselines or series in the RS/PC Combination as they first need to be verified as having similar systematic corrections to the standard baselines. However, if we apply systematic corrections and assign weights by session-type and/or baseline, we will be able to more easily integrate new baselines into our Combination. The sketch in Figure 3 demonstrates the RS/PC's current and desired future method for utilizing multiple baselines and session-types.

Developing consistent, reliable backup baselines for the INT1 and INT2 Intensives that can be utilized when the standard baselines are unable to observe will also improve the robustness of the 0-day UT1−UTC solution. Ishioka and Kōke'e stations are currently able to substitute for one another, while Ny-Ålesund or Wettzell North stations can potentially substitute for

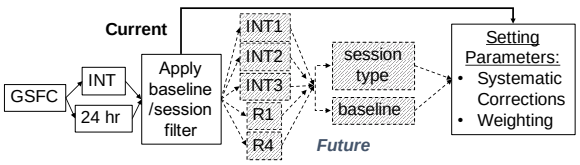

Fig. 3: Current and future flow of VLBI data in the RS/PC combined-solution, using GSFC as an example. Future additions are shown as shaded boxes. The RS/PC currently filters each data file provided by the Analysis Centers for specific baselines or session-types and then applies a *single* systematic correction and weight to the data series. In the future, we will be able to apply weights and systematic corrections to specific sets of data identified by session-type or characterized baseline.

Wettzell. However, the RS/PC needs to work with the IVS to determine *"official"* Intensive baseline backups, characterize those baselines, and be prepared to implement them in our Daily Combination with little notice.

3.1 Integrating a new VLBI Intensive baseline into the RS/PC combination

Prior to any new series or baseline being used in the RS/PC EOP Combination, we must "characterize" the session-type or baseline to determine 1) its systematic corrections w.r.t. the reference series and 2) if the new baseline or session-type significantly varies from the standard baseline or session-type already utilized from the given Analysis Center (*e.g.*, does the KkWn baseline vary significantly from the KkWz or IsWz baseline in the GSFC analysis file?). However, the RS/PC is currently developing software modifications, shown in Figure 3, to apply unique systematic corrections to a given session-type or baseline, eliminating the requirement for (2) above. An ideal data sample to characterize an Intensive baseline would include 100−200 observations over a 1−2 year period. However, the RS/PC only requires 60 observations over a minimum 4 month period, as an ideal sample size is impractical in many cases.

The USNO, IVS, and National Radio Astronomy Observatory (NRAO) are working together to characterize MkWz and MkWn (Table 2) baselines. These baselines are designed to quickly substitute for a Kōke'e or Ishioka station outage or scheduling conflict. We were particularly interested in utilizing the VLBA Mauna Kea antenna due to its geographic

location and proximity to Kōke'e station; Mauna Kea is on the Eastern side of Hawai'i at 4205 meters above sea level, and has often been able to continue observing when Kōke'e has had to shut down due to severe weather conditions. However, Mauna Kea's proximity to the Kilauea volcano has presented some challenges, as the station has moved due to Kilauea's volcanic activity in mid-2018. Dieck et al. (2019) discusses some of these challenges and describes the design of the MkWz / MkWn characterization sessions.

3.2 Improving UTGPS series

The UTGPS UT1-like data series (Kammeyer (2000)) is an invaluable contribution to producing a robust and reliable 0-day solution. As discussed in Section 2, UTGPS is the primary series used to determine the 0-day UT1−UTC value on days when a low-latency Intensive is unavailable. Data reliability is another advantage to using this data series, as there are only 2 days in 2018 when a solution was not available prior to the RS/PC Combination. UTGPS also generates 4 series each day, corresponding to the IGS Ultra-rapid production schedule. While the RS/PC only currently utilizes the 12 UTC UTGPS solution, we could potentially include the other three series calculated at the remaining quarter-day epochs.

However, the 12 UTC UTGPS UT1-like series has been very noisy since mid-2015, contributing to the decrease in the 0-day UT1−UTC solution quality (Davis and Stamatakos, 2017). The USNO GPS Analysis Division is currently investigating model-level modifications to improve the accuracy of the UTGPS data series, and the RS/PC is exploring revisions to the UTGPS pre-processing methodology used to account for the inherent time-series drift. While updates to the RS/PC preprocessing procedure may result in minor series improvements, our initial investigations with the GPS Analysis Division suggest that the UTGPS model requires updating to improve its accuracy.

4 Concluding thoughts

IVS Intensives are incredibly important to the health of the RS/PC UT1−UTC product. With improvements to integrating individual baselines into the RS/PC's Combination, and consistent and reliable low-latency backup Intensive baselines cultivated by the IVS, the 0-day UT1−UTC solution produced by the RS/PC should continue to improve in accuracy and precision. Although currently noisy, UTGPS generally provides an excellent low-latency check on the IVS Intensives and acts as a good backup when Intensives are unavailable.

As a final thought, the RS/PC would potentially be interested in a Southern Hemisphere Intensive observing simultaneously with the Northern Hemisphere INT1 series. The Southern Hemisphere Intensive could act as a corroboration and backup to the Northern Hemisphere Intensives.

Acknowledgements The authors would like to acknowledge the efforts of Nathan Shumate, Megan Johnson, Andrew Sargent, Jeffrey Tracey, Sharyl Byram, and NVI Inc who directly and indirectly contributed to the work presented in this paper.

References

Davis M, Stamatakos N (2017 September 25–27) Improving the IERS Rapid Service / Prediction Center UT1−UTC 0-Day Solution. Paper presented at *Journees 2017, des Systemes de Reference et de la Rotation Terrestre: Furthering our knowledge of Earth Rotation*, University of Alicante, Spain

Dieck C, Johnson M, Davis M, et al. (2019) Intensive sessions with the Mauna Kea VLBA Station. In: R. Haas, S. Garcia-Espada, J. A. López Fernández (eds.): *Proc. 24th EVGA Working Meeting*, 152–156

International Earth Rotation and Reference Systems Service (IERS), Central Bureau Appendix 1: IERS Terms of Reference. In: W. R. Dick, D. Thaller (eds.): *IERS Annual Report 2017*, 177–183

Kammeyer P (2000) A UT1-Like Quantity from Analysis of GPS Orbit Planes. *Celest. Mech. Dyn. Astr.*, 77, 241−272

McCarthy D D, Luzum B J (1991) Combination of precise observations of the orientation of the Earth. *Bulletin Gèodèsique* 65, 22−27 doi:https://doi.org/10.1007/BF00806339

Stamatakos N, Carter M S, Shumate N (2014) Rapid Service/Prediction Centre. In: W. R. Dick, D. Thaller (eds.) *IERS Annual Report 2013*, 65−82

Stamatakos N, Davis M, Shumate N, et al. (2015) Rapid Service/Prediction Centre. In: W. R. Dick, D. Thaller (eds.): *IERS Annual Report 2014*, 70−72

Stamatakos N, Davis M, Shumate N, et al. (2016) Rapid Service/Prediction Centre. In: W. R. Dick, D. Thaller (eds.): *IERS Annual Report 2015*, 79−81

Analysis of Intensive Sessions at BKG

A. Girdiuk, D. Thaller, D. Ullrich, G. Engelhardt, R. Wojdziak, C. Plötz

Abstract Currently hourly intensive sessions monitor Earth Rotation variations every day almost without breaks. Regular intensive sessions INT1, INT2 and INT3 collect data on various networks at different days of the week. The goal of the analysis of these intensive sessions is to monitor ongoing changes in dUT1. The Analysis Centers are obligated to provide estimates of dUT1 with very low latency which implies the product release on the same or next working day. These dUT1 variations are obtained by solving each intensive independently. Here we examine all intensive sessions and the corresponding parameterization.

Keywords Intensive sessions · Parametrization · dUT1

1 Introduction

The main purpose of intensive session analysis is to provide information on rapid changes in Earth Rotation. These special VLBI experiments are regular observations of about one hour duration. Recently, longer sessions INT1* (Dieck et al., 2019) started to observe over 1.5 h till 2 h. The first intensive experiments have been commenced in 1999. The session duration, network and final results were investigated on their basis, so that in 2002 the first regular intensives, now known as INT1, have been started. Intensives INT1 are run on weekdays at 18:30 UT. Shortly after the INT1 started the weekend gap was filled with intensives INT2. Their observations begin at 7:30 UT and are of the same one hour duration. The majority of these intensives employs 2 stations only. A small amount of INT1 experiments is observed in a 3-station network, mainly for test purposes only. In almost all intensives the core VLBI station at Wettzell participates and the second station is varied. The antenna in Wettzell is chosen because of the high stability governed by clock reliability, technical antenna specifications and high quality continuous maintenance. The first intensives were observed with NRAO20 or Kokee as the second station, and a few of them with Tsukub32. On the basis of these experiments only 1 baseline Wettzell – Kokee was selected for intensives INT1. Over the whole time span some other stations, Svetloe, Nyales20, Tsukub32 and Wettz13N, participated for a short time in INT1 during the maintenance periods of the main stations. The other intensives, INT2, were observed mostly on the baseline Wettzell – Tsukub32 in the beginning. Later, Wettzell and Ishioka participated in INT2 observations more frequently, so that Ishioka replaced Tsukub32. Occasionally Kokee takes part in these experiments as well. To improve the accuracy of dUT1 estimates a modification of intensives is required. The idea is to get more observations and a better network geometry. The majority of these INT3 sessions are observed in a 3-station network including Wettzell, Tsukub32 and Nyales20. The most recent experiments gather observations in more than 4-station networks, with Ishioka, Wettz13N and Svetloe. These efforts allow to achieve an unprecedented amount of observations (about 150 per session), compared to earlier intensives. However, most of the INT3 experiments collect about 70–80 observations.

Anastasiia Girdiuk · Daniela Thaller · Dieter Ullrich · Gerald Engelhardt · Reiner Wojdziak · Christian Plötz
Federal Agency for Cartography and Geodesy (BKG), Richard-Strauss-Allee 11, DE-60598 Frankfurt am Main, Germany

(Correspondence: Anastasiia.Girdiuk@bkg.bund.de)

Here, we investigate the characteristics of the intensives session, such as number of observations, participating antennas and observed sources. Besides this, the terrestrial and celestial reference frames are reviewed for the parametrization of intensive sessions.

2 Intensives time series

The BKG Analysis Center assembles time series of all intensives starting with the first experiments in 1999 (Table 1). Among all observed and correlated experiments this time series includes only intensives analyzed at BKG Analysis Center. All experiments are analyzed with the same approach in a uniform way. Thus, only a few unresolved sessions are excluded due to a smaller number of observations than unknowns. Also, because the routine analysis cannot incorporate INT3 sessions that are only provided in vgosDb format, 30 of these experiments are missing since 2018, and in total 470 intensives INT3 are analyzed. Besides this, the most recent INT* experiments are processed and included in the current BKG time series as a part of intensives INT1.

Based on the analysis of the intensives time series, the distributions of observations (time delays), sources, and stations per session are illustrated (Fig. 1). Relative numbers in percentage are expressed as parts of all sessions. In most of intensives INT1 the number of observations is about 18 delays per session obtained in 32 % of all intensive sessions. A large number of about 32 delays per session are collected in experiments INT2 which represent only 7 % of the complete data set. Even more observations per session, 70–80, are collected in experiments INT3 which represent only 2 % of all intensives.

This distribution indicates that a larger number of sources per session observed in INT2 may induce the increase in the number of time delays per session. A larger number of sources can be observed using a better scheduling algorithm, or faster antennas, or also more antennas. The number of sources observed in INT3 increased w.r.t. INT1 twice, and w.r.t. INT2 by 50 %. At the same time, observations in 3-station networks reveal approximately the same amount of 4 % of the INT1 and INT3 sessions. Intensives INT3 collect the majority of observations with 3 stations, while only 4 and 5 station networks allow to obtain 70 and more observations.

Table 1: Intensive sessions. Data amount includes all experiments at BKG Analysis Center until February 2019.

Mon	Tue	Wed	Thu	Fri	Sat	Sun	Amount of experiments
INT3							470
INT1*		INT1*	INT1*				10
INT1	INT1	INT1	INT1	INT1			3760
					INT2	INT2	1490
intensives before 2002							700

* new INT1 sessions.

Fig. 2 shows regular station attendance in each intensive experiment. Wettzell takes part in almost all experiments as expected. The second antenna in the first intensives is NRAO20 in more than half of cases and Kokee in the rest of them. Their successor INT1 shows an overwhelming majority of sessions on the Wettzell – Kokee baseline. Nyales20, Svetloe and Tsukub32 are used as 3rd station in 10 % of the INT1. INT2 was designed to employ a different network with the same core station at Wettzell. Tsukub32 is included mostly as the second station (75 %). Kokee and Ishioka participated in INT2 in approximately equal parts (10 %). It is seen that INT3 combines stations observed in INT1 and INT2. The core of the network is represented already by 3 stations: Wettzell, Nyales20 and Tsukub32, where Wettzell participates in most of experiments as well. Moreover, the new small 13 m antenna at Wettzell also successfully participates in 7 % of sessions INT3 together with the main dish and alone.

3 Parametrization

The parametrization applied in the routine analysis is defined by the currently valid set labeled as bkgint14 (Nothnagel, 2008). This set of parameters is utilized by the BKG Analysis Center to provide corresponding products for the IVS. A priori models are applied in agreement with the IERS Conventions (Petit and Luzum, 2010), with VTRF2008a (Böckmann et al., 2010) for station positions and velocities and ICRF2 (Fey et al., 2015) for source positions (Table 2). Since intensives have to be processed as soon as the correlation data is released the usage of predicted Earth Orientation Parameters (EOP) time series is required

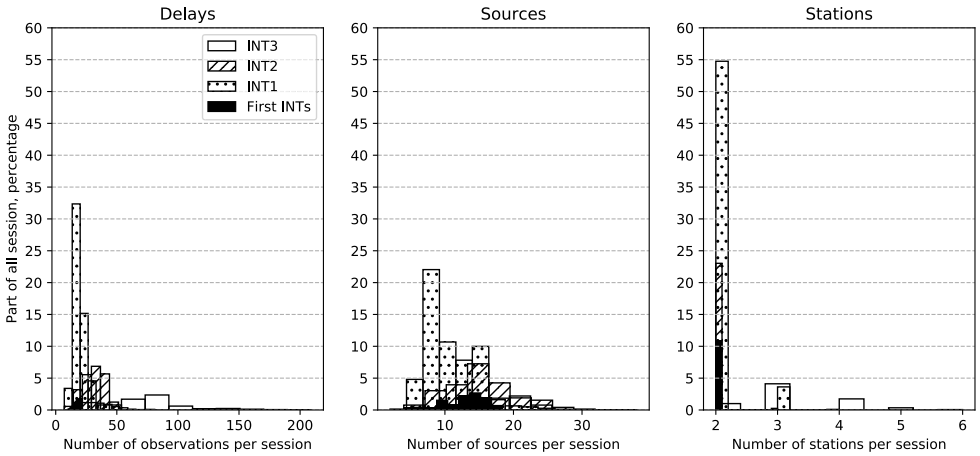

Fig. 1: Distribution of observations, sources and stations per session relatively to the number of all sessions in dependence on the intensives: first intensives INTs, INT1, INT2 and INT3.

as specified by Bulletin A (Dick and Thaller, 2017). This time series known as usno_finals.erp is adopted in this analysis as provided by the Goddard Space Flight Center (GSFC) group. The real meteorological data (if available) or the Vienna mapping functions (VMF1, Böhm et al., 2006) are applied for troposphere correction modelling in form of TRP files from GSFC (Thorandt et al., 2017).

Table 2: Parametrization of Intensive Sessions.

Parameter	Status	A priori corrections
Earth orientation dUT1	Yes	GSFC time series
Station clocks	Yes	No
Baseline clocks	No	No
Zenith troposphere	Yes	VMF1
Troposphere gradient	No	VMF1
Terrestrial frame	No	VTRF2008a
Celestial frame	No	ICRF2

Models employed in the current parametrization demand an update, in particular, alternatives for TRF and CRF are discussed here. The set of estimated parameters in the routine analysis includes clock polynomials up to 2nd degree, estimated per station except the clock reference station. In almost all cases we prefer to select Wettzell as the reference station. Additionally, one offset is estimated for atmospheric parameters and one for dUT1. This parametrization

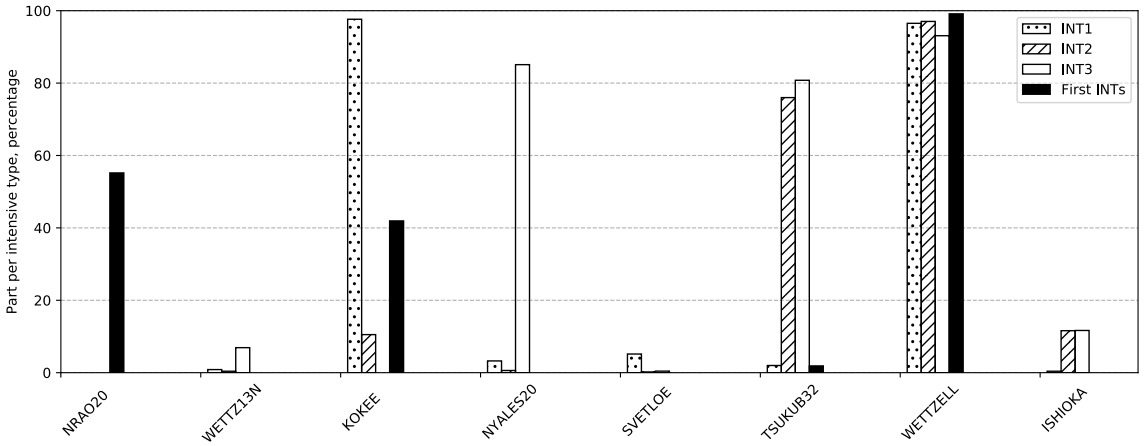

Fig. 2: Distribution of station attendance within intensive type.

gives feasible variations of the dUT1 estimates and their corresponding formal errors (Fig. 4). The majority of the dUT1 estimates are obtained within ±100 µas limit (Fig. 5, left). The formal errors are smaller for INT2 and even smaller for INT3. The numerous discrepancies of dUT1 estimates stem from the lack of reliable station positions. A priori corrections to the station positions as provided by VTRF2018 (Bachmann et al., 2016) and ITRF2014 (Altamini et al., 2016) are considered to influence the dUT1 estimates. The results are shown in Fig. 5 using the same time series of dUT1 estimates where the applied station positions are varied only in the parameter set. The dUT1 estimates are highlighted w.r.t. the station participated in the session. The current time series (Fig. 5, left) suffers from the lack of 24 hour experiments where Ishioka participates, because the applied internal method at BKG produces real time coordinates for Ishioka and Tsukub32 (Engelhardt et al., 2016) on the basis of the most recent 24 hour experiments. VTRF2018 reduces considerably dUT1 estimates as expected since it is the VLBI intra-technique combined TRF. ITRF2014 based on the other geodetic techniques besides VLBI reports additional numerous discrepancies for Wettzell. Lastly, an impact of source positions is calculated based on the newly released ICRF3 (Charlot et al., 2018). dUT1 estimates obtained in intensives with Ishioka and Tsukube32 are not plotted on Fig. 3. The resulting respective differences are assumed to be negligible because of their large formal errors.

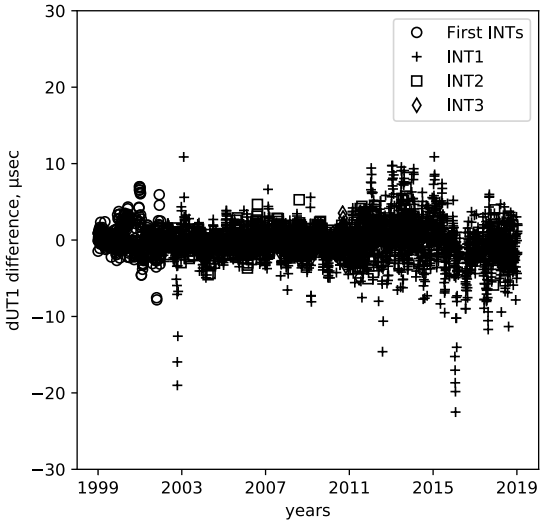

Fig. 3: Differences in dUT1 estimates. The estimates calculated using ICRF2 subtracted from estimates based on ICRF3. A priori ICRF is the only distinction in applied parametrization.

4 Conclusions and outlook

At this moment the time series of intensives reported by the BKG Analysis Center includes a decent set of observations notwithstanding a growing lack of sessions that are provided in vgosDb format only. The overview of intensive sessions INT1, INT2 and INT3 indicates the observation number growth, especially on 4 and more antenna networks. The dUT1 formal errors in larger networks show a smaller variations which require a more detailed investigation of the network configuration and scheduling.

The parametrization of the intensive sessions was examined with focus a on terrestrial and celestial reference frames. The VTRF2018 demonstrates better reduction, except special cases for Tsukuba coordinates which are best treated in a specially designed internal adjustment at BKG. Thus, for the time being VTRF2018 can be used as an intermediate solution to replace VTRF2008a while a better approach will be developed. The ICRF3 parametrization test illustrates no significant variations in terms of dUT1 differences (Fig. 3).

References

Altamini Z, Rebischung P, Métivier L, et al. (2016) ITRF2014: A new release of the International Terrestrial Reference Frame modeling nonlinear station motions. *J Geophys Res: Solid Earth*, 121, 6109–6131, doi:10.1002/2016JB013098

Bachmann S, Thaller D, Roggenbuck O, et al. (2016) IVS contribution to ITRF2014. Current intra-technique combination is available: https://ccivs.bkg.bund.de/index.php?uri=quarterly/vtrf *J Geod*, 90(7):631–654, doi:10.1007/s00190-016-0899-4

Böckmann S, Artz T, Nothnagel A (2010) VLBI terrestrial reference frame contributions to ITRF2008. *J Geod*, 84, 3, 201–219, doi:10.1007/s00190-009-0357-7

Böhm J, Werl B, Schuh H (2006) Troposphere mapping functions for GPS and VLBI from ECMWF operational analysis data. *J Geophys Res*, 111, B02406, doi:10.1029/2005JB003629

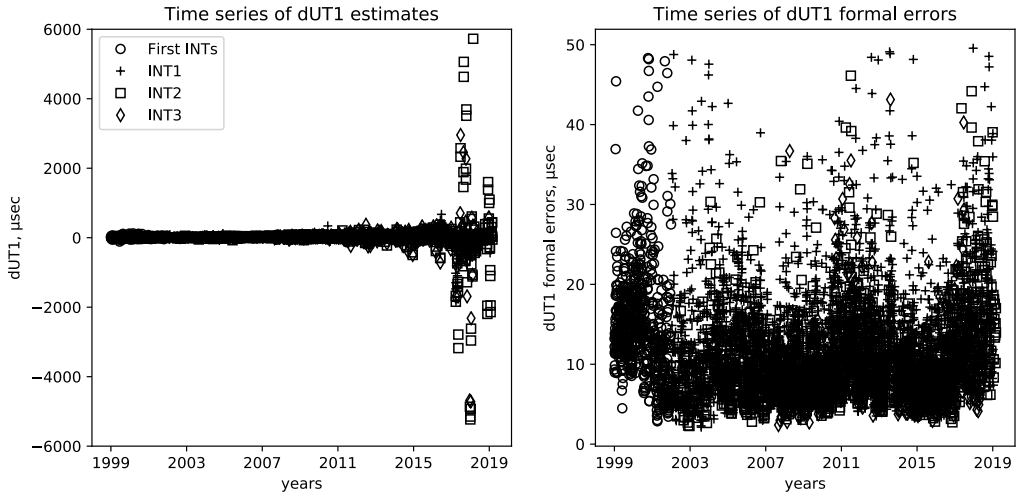

Fig. 4: Variations of dUT1 estimates on the left side and their formal errors on the right side.

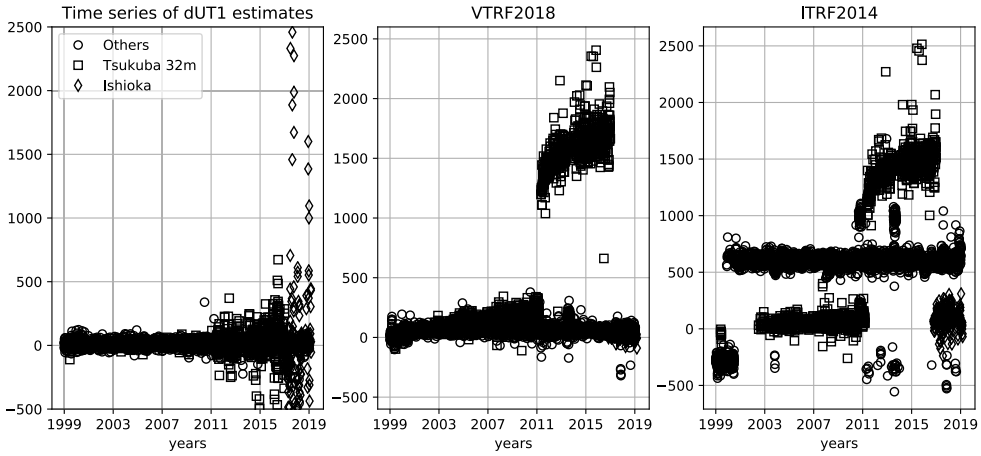

Fig. 5: Variations of dUT1 estimates: VTRF2008a, VTRF2018 and ITRF2014 (left to right).

Charlot et al. (2018) ICRF3 Documentation. in preparation for Astron. Astrophys, http://hpiers.obspm.fr/icrs-pc/newwww/icrf/index.php

Dick W, Thaller D (eds.) (2017) IERS Annual Report 2017. International Earth Rotation and Reference Systems Service, Central Bureau. Frankfurt am Main: Verlag des Bundesamts für Kartographie und Geodäsie

Dieck C, Davis M, Johnson M, et al. (2019) Intensive sessions with the Mauna Kea VLBA Station. In: R. Haas, S. Garcia-Espada, J. A. López Fernández (eds.): EVGA *Proc. 24th EVGA Working Meeting*, 152–156

Engelhardt G, Thorandt V, Ullrich D (2016) Refinement of the rapid UT1 estimation derived from Tsukuba VLBI measurements after the 2011 earthquake. In: D. Behrend, K. D. Baver, K. Armstrong (eds.): *IVS 2016 General Meeting Proceedings*, NASA/CP-2016-219016, 225–228

Fey A, Gordon D, Jacobs C, et al. (2015) The Second Realization of the International Celestial Reference Frame by Very Long Baseline Interferometry. *AJ*, 150, 58, doi:10.1088/0004-6256/150/2/58

Nothnagel A (2008) Short Note: Conventions on thermal expansion modelling of radio telescopes for geodetic and astrometric VLBI. *J Geod*, doi:10.1007/s00190-008-0284-z

Petit G, Luzum B (eds.) (2010) IERS Conventions (2010). IERS Technical Note, 36, Frankfurt am Main: Verlag des Bundesamts für Kartographie und Geodäsie.

Thorandt V, Engelhardt G, Ullrich D, et al. (2017) BKG/IGGB VLBI Analysis Center. In: K. D. Baver, D. Behrend, K. L. Armstrong (eds.): *IVS 2015+2016 Biennial Report*, NASA/TP-2017-219021

Scheduling of Twin Telescopes and the Impact on Troposphere and UT1 Estimation

A. Corbin, R.Haas

Abstract Recently, several VGOS twin telescopes in Europe were completed. We examine the use of VGOS twin telescopes by a new scheduling approach. This approach is based on integer linear programming and creates uniform distributed observations over time. Several VLBI intensive sessions are rescheduled involving the VGOS twin telescopes and the impact on the troposphere and UT1 estimation is investigated.

Keywords VLBI Intensive Sessions · VGOS Twin Telescopes · Scheduling · Simulation · Atmospheric Turbulence · Global Optimization

1 Introduction

VLBI intensive (INT) sessions (Schnell, 2006) are one hourly sessions that are used to provide information about the solar time UT1 on a regular basis and with low latency. From Monday to Friday the INT1 baseline from Wettzell to Kokee is observed and on the weekend the INT2 baseline from Wettzell to Ishioka. These baselines have large east-west components ensuring a high sensitivity to the solar time UT1. See Fig. 1 for the location of the telescopes. Currently, the legacy S/X setup is used for all INT sessions, however, at each of the stations involved in the INT1 and INT2 sessions a modern VGOS-compatible telescope is available. Thus, it is possible to observe broadband INT sessions. Moreover, there are VGOS twin telescopes at Wettzell enabling simultaneous observation of the INT1 and INT2 baselines. In total there are three twin telescopes on the globe, which are all located in Europe (Fig 1). Involving both the VGOS twin telescopes at Wettzell and Onsala, as well as the VGOS telescopes at Kokee and Ishioka, four baselines with large east-west component can be observed simultaneously.

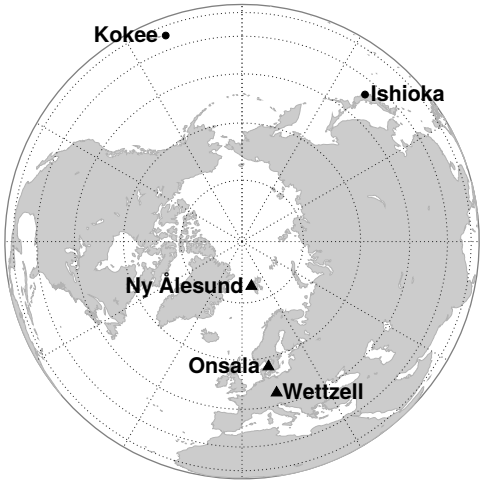

Fig. 1: Map of the northern hemisphere showing the position of all observatories with VGOS twin telescopes (triangles) and observatories with one only VGOS telescope used for the INT1 and INT2 sessions (circles).

We created new schedules for 187 INT sessions of the year 2018. For each of these sessions three different schedules were created. One without twin telescopes, one with the twin telescopes in Wettzell and another

Armin Corbin[1] · Rüdiger Haas
Chalmers University of Technology, Department of Space, Earth and Environment, Onsala Space Observatory, SE-439 92 Onsala, Sweden

(1) now at: Universität Bonn, Institut für Geodäsie und Geoinformation, Nußallee 17, DE-53115 Bonn, Germany

(Correspondence: corbin@geod.uni-bonn.de)

one with the twin telescopes in Wettzell and Onsala. We used a new scheduling approach capable of finding the schedule with the best sky coverage score (Sec. 2). In the next step, the observations of each schedule were simulated (Sec. 3). The simulator ensures that the atmosphere and the clocks for each session are independent of the schedule. Finally, the simulated observations were adjusted and the estimated parameters were compared (Sec. 3). All computations were done with the VLBI analysis toolbox ivg::Ascot (Halsig et al., 2017).

Table 1: Overview of the schedule setups. We use the IVS 2-letter code to identify the stations. A baseline or subnet is a group of 2-letter codes and different subnets are divided by white spaces.

scenario	scan sequence	#obs.	#scans	#stas.	#long bl.
ZT	`WnK2` (INT1) `WnIs` (INT2)	60	60	2	1
OT	3x `WnK2 WsIs` 3x `WnIs WsK2`	120	120	4	2
TT	3x `WnOeK2 WsOwIs` 1x `K2Is WsOw WnOe` 3x `WnOeIs WsOwK2` 1x `K2Is WsOw WnOe`	315	135	6	4

2 Scheduling

For each investigated INT session three different schedules were created. The main difference between them is the number of involved twin telescope stations. Thus, we call the scenarios *ZT (zero twin)*, *OT (one twin)*, and *TT (two twins)*.

In the *ZT* scenario the same observatories as in the original INT schedules are used, but with the VGOS instead of the S/X legacy telescopes.

In the *OT* scenario the INT1 and INT2 baseline are observed simultaneously with the VGOS telescopes in Kokee and Ishoika and the VGOS twin telescopes in Wettzell.

Finally, in the *TT* scenario the VGOS twin telescopes in Wettzell and Onsala as well as the VGOS telescopes in Ishioka and Kokee are used. In this scenario four baselines with large east-west component are observed simultaneously. To improve the sky coverage we also observe the short baselines between the twin telescopes in Onsala and Wettzell and the baseline between Ishioka and Kokee every fourth minute. The detailed scan sequence is presented in Tab. 1.

We created schedules with regular observations: In each minute each station is participating in one quasar observation. The first 30 s are reserved for the slewing of the telescope and the remaining 30 s are used for the observation. This is possible because VGOS telescope are very fast, i.e., they can slew to any source on the sky within 30 s. Only observations exceeding a signal to noise ratio (SNR) larger than 20 within the 30 s were scheduled. For the SNR computation (e.g. Gipson 2018) we assumed a VGOS broadband setup with 32 channels of 32 MHz bandwidth each and 2-bit sampling. However, we only used one polarization, leading to a pessimistic SNR compared with the VGOS setup. Moreover, the antennas of a twin telescope were never observing the same source together. In fact, the spherical distance between the simultaneously observed sources of a twin station had to be larger than 60°. At least 10 minutes had to past until the same source was observed again by the same station. Moreover, a source could not be observed more than 6 times by the same observatory (observations of a twin telescopes are not counted separately).

The optimization criterion for the scheduling is the local sky coverage. We used the sky coverage score described in Corbin et al. (2019): The hemisphere above each station is partitioned into cells of equal size and similar shape multiple times. If a cell includes an observation its surface area is added to the sky coverage score. The score is computed for a time period of 10 minutes which is shifted in 5 minutes steps. The partitions are computed following Beckers and Beckers (2012) and have 10, 18, 29 and 107 cells. Twin telescopes were treated as a single telescope for the computation of the sky coverage.

We used an integer linear program (ILP, Williams 2013) that incorporates all the constraints explained above to create the schedules. The ILP is described in detail in Corbin et al. (2019). However, the ILP we are using in this paper is extended with additional constraints to model the twin stations. Since the observation times and the subnets were predefined (see Tab. 1) the ILP's only task was to determine the source that was observed by each subnet. With these simplifications it is possible to find the schedule with the optimal sky coverage in a few minutes using a CPU with 2 cores at 2,7 GHz.

3 Simulations

To simulate an observation τ_{sim} we computed the geometric delay τ_g and distorted it with systematic and random errors:

$$\tau_{\text{sim}} = \tau_g + \text{clock}_2 - \text{clock}_1 + Mf(\epsilon_2)\cdot \text{ZWD}_2 - Mf(\epsilon_1)\cdot \text{ZWD}_1 + \text{wn} \quad (1)$$

For each station i we modeled the clock clock_i and the delay caused by the wet part of the troposphere in zenith direction ZWD_i, which was mapped to the elevation ϵ_i of the observation with a mapping function Mf. Here, we used the VMF1 mapping function (Böhm et al., 2006). To each observation, white noise with a standard deviation of 20 ps was added to simulate random errors.

The geometric delay τ_g was calculated according to the IERS conventions (Petit and Luzum, 2010). We used the ITRF2014 (Altamimi et al., 2016) for station coordinates and the ICRF2 (Fey et al., 2015) for source positions. The IERS C04 time series was used for nutation and polar motion. However, we used the BKG eopi time series for UT1, to reduce the interpolation error.

The geometric delay is the only deterministic term in Eq. 1. The other terms are stochastic and require a random generator for the computation. Each session was simulated three times, each time with a different schedule. To avoid different clocks for each simulation of the same session, the station clocks were precomputed and saved. We assumed an Allan standard deviation of 10 fs at 50 minutes. During the simulation the corresponding clock value was looked up and added to the delay. With this method, the station clocks are consistent for each run of the simulation and independent of the schedule.

To make sure that in each simulation of the same session and station the same troposphere was used, a reference troposphere was computed. To do so, the sky above each station was partitioned into 209 cells of equal size and similar shape using the method from Beckers and Beckers (2012). For each cell the equivalent zenith wet delay (EZWD) was computed with a temporal resolution of one minute. The EZWDs are calculated with the turbulence model from Nilsson and Haas (2010) using an initial delay of 450 ps. We used the turbulence parameters provided in Petrachenko et al. (2009), except for the station Onsala that is missing in the list.

During the simulation the EZWD from the cell containing the observation was mapped to the correct elevation and added to the simulated delay. For twin stations the same reference troposphere was used. See Fig.2 for an illustration of the reference troposphere.

To verify the simulator we simulated the observations of 114 INT sessions in the year 2018. Only sessions with more than 15 good[1] observations were used. Afterwards, the simulated as well as the observed sessions were analyzed using a least-squares adjustment with standard intensive parametrization[2]. For each session we computed the difference in UT1 between the solution using the simulated observations and the solution using the real observations. The WRMS of these differences is 14 µs which indicates that the simulated observations are reasonable.

4 Results

The simulated sessions were evaluated with a least-squares adjustment. Due to the large number of observations (Tab. 1), more parameters can be estimated than in regular INT sessions. Instead of one ZWD offset we approximated constant piece wise linear functions (CPWLF) with an interval length of 10 minutes (7 parameters per station). The station clocks were modeled with a CPWLF with 20 minutes interval length (4 parameters per station). The clock at WETTZ13N was fixed. The target parameter was UT1. We used two different parametrizations for the ZWD for the *OT* and *TT* scenario. In the first setup we estimated a CPWLF for each antenna. In the second setup we estimated common ZWD parameters for the twin stations. We call the solutions with combined ZWD parameters *OTc* and *TTc*.

We evaluated the different scenarios by comparing the estimated parameters with the true values. The differences between the estimated and the true value of UT1 and the ZWD are denoted with ϵ_{UT1} and ϵ_{ZWD}, respectively. For each scenario we calculated the error in UT1 ϵ_{UT1} in all sessions and computed its mean and the standard deviation. The results are summarized in Tab. 2. Using the broadband instead of the legacy S/X

[1] vgosDB quality code larger or equal to five

[2] The station clock in Wettzell was fixed, the other was estimated with a polynom of order two. We estimated one UT1 offset and for each station a ZWD offset.

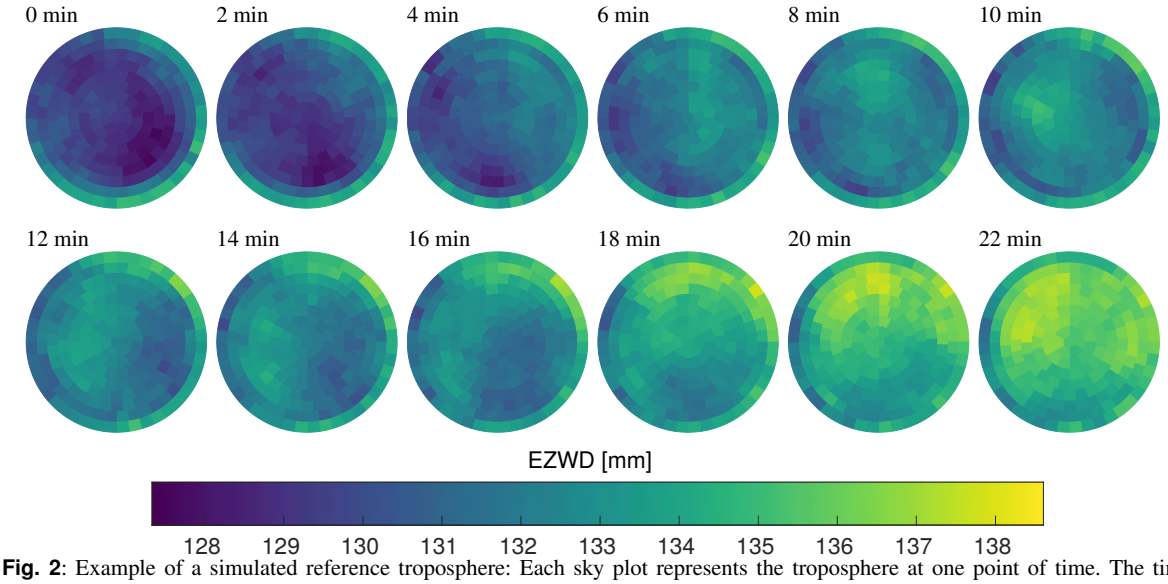

Fig. 2: Example of a simulated reference troposphere: Each sky plot represents the troposphere at one point of time. The time between two subsequent sky plots is two minutes, although the troposphere is computed with a temporal resolution of one minute. The sky plots are aligned to the north (top of this page) and the center cell corresponds to an elevation of 90 degrees. In this example, the wind is blowing from north-east direction.

Table 2: Mean and standard deviation of the error in UT1 w.r.t. all sessions. The *original* scenario is a simulation of the schedules that were used for the (observed) INT1 and INT2 sessions and analyzed with the standard intensive setup.

scenario	mean ϵ_{UT1} (µs)	std ϵ_{UT1} (µs)
original	−0.5	11.0
ZT	−0.2	8.3
OT	0.4	6.2
OTc	0.5	6.2
TT	0.1	4.2
TTc	0.1	4.2

Table 3: Mean and standard deviation of the error for the ZWDs of each station w.r.t. all sessions. The refractive index structure constants for the involved stations are give in the last row.

mean ϵ_{ZWD} (ps)

scenario	Wn	Ws	Kk	Is	On	Os
ZT	−0.06	-	−0.24	−0.60	-	-
OT	0.09	0.33	−0.44	−0.15	-	-
OTc	0.14		−0.53	−0.16	-	-
TT	−0.30	0.09	−0.53	0.22	−0.21	0.17
TTc	−0.10		−0.57	0.17	0.03	

std ϵ_{ZWD} (ps)

	Wn	Ws	Kk	Is	On	Os
ZT	9.3	-	17.0	11.9	-	-
OT	8.5	9.0	16.6	11.4	-	-
OTc	8.1		16.6	11.4	-	-
TT	8.6	8.7	15.0	10.3	7.0	6.9
TTc	8.0		15.0	10.4	6.1	
	structure constant C_n ($10^{-7}\mathrm{m}^{-\frac{1}{3}}$)					
	0.94		2.30	1.46	0.72	

setup (first row vs. second row) the standard deviation of the error in UT1 decreases by almost 3 µs.

With each additional twin telescope the scatter is further decreased. In the *TT* scenario the standard deviation of the error in UT1 is reduced to 4 µs. Combining ZWD parameters, however, has no significant effect on the estimation of UT1.

We computed the statistics of the error of the ZWDs in the same way. The estimated ZWDs were compared with the ZWDs in the center cell of the reference troposphere. The results are given in Tab. 3. The standard deviation of the error of the ZWDs decreases slightly by introducing one twin station (about a half picosecond). This applies also to the non-twin stations. By estimating common ZWDs parameters the standard deviation is roughly decreased by one picosecond. Furthermore, there is a strong correlation between the standard deviation of the error and the refractive index structure constant (see last row of Tab. 3).

In case of a rotational symmetric atmosphere the EZWD is independent of the elevation and the azimuth of the observations. This case is illustrated with a black dashed line in Fig. 3, which corresponds to the center cell of the reference troposphere. But when consid-

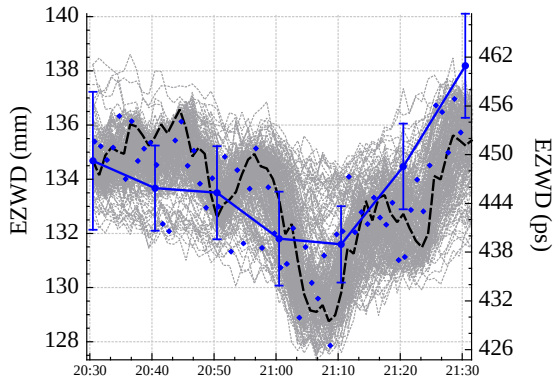

Fig. 3: Illustration of the reference troposphere at one station for one session (see Sec. 3 for a description).

ering turbulence, the EZWD depends on azimuth and elevation and cannot be illustrated with a single line only. Each gray dotted line in Fig. 3 corresponds to the EZWD in one of the reference troposphere's cells. The difference between the true EZWDs (blue diamonds) and the estimated ZWDs (solid blue line) can reach several millimeters. A more sophisticated troposphere model appears necessary to model the EZWDs more accurately.

5 Conclusions

Introducing VGOS twin stations into INT sessions leads to more observations with large east-west component, providing improved estimations of the solar time UT1. Our simulations show that the standard deviation of the error in UT1 decreases from 11 µs using the legacy S/X setup to 4 µs using two VGOS twin stations with a broadband setup. The ZWD estimation is only slightly improved (some picoseconds). To improve the estimation of the EZWD, a better troposphere model with more parameters appears necessary. Twin stations lead to more observations at the same observatory, and thus will allow in the future a more complex troposphere modeling.

References

Altamimi Z, Rebischung P, Métivier L, et al. (2016) ITRF2014: A new release of the International Terrestrial Reference Frame modeling nonlinear station motions. *J Geophys Research: Solid Earth*, 121(8), 6109–6131

Beckers B, Beckers P (2012) A general rule for disk and hemisphere partition into equal-area cells. *Computational Geometry*, 45(7), 275–283

Böhm J, Werl B, Schuh H (2006) Troposphere mapping functions for GPS and very long baseline interferometry from European Centre for Medium-range Weather Forecasts operational analysis data. *J Geophys Res*, 111, B02406

Corbin A, Niedermann B, Nothnagel A, et al. (2019) VLBI Scheduling with an Approach from Combinatorial Optimization. submitted to *J Geod*

Fey A L, Gordon D, Jacobs C S, et al. (2015) The second realization of the international celestial reference frame by very long baseline interferometry. *AJ*, 150(2), 1–16

Gipson J (2018) *Sked - VLBI Scheduling Software*. Technical report, NASA Goddard Spaceflight Center

Halsig S, Corbin A, Iddink A, et al. (2017) Current Development Progress in ivg::ASCOT. A new VLBI Analysis Software. In: R. Haas, G. Elgered (eds.): *Proc. 23rd EVGA Working Meeting*, 167–171

Nilsson T, Haas R (2010) Impact of atmospheric turbulence on geodetic very long baseline interferometry. *J Geophys Res: Solid Earth*, 115(B3)

Petit G, Luzum B (2010) *IERS Conventions (2010)* IERS Technical Note 36, International Earth Rotation and Reference Systems Service, Verlag des Bundesamtes für Kartographie und Geodäsie Frankfurt am Main

Petrachenko B, Niell A, Behrend D, et al. (2009) *Design Aspects of the VLBI2010 System-Progress Report of the IVS VLBI2010 Committee*. Technical report, NASA Goddard Space Flight Center

Schnell D (2006) *Quality aspects of short duration VLBI observations for UT1 determinations*. PhD thesis, Institut für Geodäsie und Geoinformation, University of Bonn

Williams H P (2013) *Model Building in Mathematical Programming*, volume 5. John Wiley & Sons.

Comparison of Troposphere Delays from GNSS and VLBI in R1 and R4 Sessions

V. Puente, Y. Gómez Espada, E. Azcue, S. Garcia-Espada

Abstract This contribution is devoted to the comparison of troposphere Zenith Total Delay (ZTD) derived from the processing of Very Long Baseline Interferometry (VLBI) and Global Navigation Satellite Systems (GNSS) data in co-located sites. On the one hand, global and subdaily differences between both techniques are analysed in R1 and R4 sessions for the period 2013–2018. On the other hand, we use GNSS-derived Zenith Wet Delays (ZWD) as a priori value in VLBI processing, by means of a modified version of VieVS 3.1. Long-term behaviour of troposphere ties needed to correct for the height difference between co-located instruments is also studied.

Keywords Troposphere · GNSS · VLBI

1 Introduction

The delay induced by the troposphere in the signal propagation is an important error source in the analysis of the observations of space geodetic techniques such as the Global Navigation Satellite Systems (GNSS) and Very Long Baseline Interferometry (VLBI). The magnitude of this delay depends on the atmospheric conditions (temperature, pressure, humidity), the elevation angle of the observation and also on the antenna location.

In this contribution, the differences in the troposphere Zenith Total Delay (ZTD) between both techniques are analysed in several stations in which GNSS and VLBI antennas are co-located. This analysis has been carried out using series of troposphere products from IVS (International VLBI Service for Geodesy and Astrometry, Nothnagel et al., 2017) and IGS (International GNSS Service, Dow et al., 2009). The dataset analysed corresponds to R1 and R4 sessions spanning from 2013 to 2018.

In addition, we have modified VieVS 3.1 to use GNSS-based ZTD as initial value in VLBI processing. Results in terms of baselines repeatability are also presented and compared to those obtained with the baseline version of VieVS 3.1. In addition, taking advantage of the computation of troposphere ties needed for this functionality, we analyse the long-term behaviour of the wet and hydrostatic troposphere ties.

To sum up, the aim of this work is to address the following questions based on the analysis of R1 and R4 sessions for the period 2013–2018:

- What are the differences of VLBI-based ZTD with respect to different solutions of GNSS-based ZTD in co-located sites?
- Is there any subdaily pattern in the differences between techniques?
- How GNSS-based ZTD used as a priori value impact VLBI estimation?
- What is the long-term behaviour of the wet and hydrostatic troposphere ties?

Víctor Puente · Yaiza Gómez Espada · Esther Azcue
Instituto Geográfico Nacional
C/General Ibañez de Ibero, Madrid, Spain

Susana Garcia-Espada,
Instituto Geográfico Nacional - RAEGE Santa Maria station, Azores, Portugal

(Correspondence: vpuente@fomento.es)

2 Resources

The analysis of ZTD is limited to those sites in which there are VLBI and GNSS antennas co-located. In particular, the ZTD corresponding to the following sites have been analysed:

- Bd (Badary)
- Hb (Hobart)
- Ke (Katherine)
- Kk (Kokee)
- Ma (Matera)
- Mc (Medicina)
- Ny (Ny-Alesund)
- On (Onsala)
- Ts (Tsukuba)
- Wz (Wettzell)
- Yg (Yarragadee)
- Zc (Zelenchukskaya)

VLBI-based ZTD were retrieved from IVS combination center (Heinkelmann, 2013). Three individual solutions from different software packages and the combined solution were analysed:

- CGS (Centro di Geodesia Spaziale), using Calc/Solve software package.
- IAA (Institute of Applied Astronomy), using QUASAR software package.
- VIE (TU Wien), using VieVS software package.
- IVS combined solution

Concerning, GNSS-based ZTD, two different solutions were used:

- CODE products (Dach et al., 2018): network solution and ZTD estimated at 2 hours sampling.
- IGS products: Precise Point Positioning (PPP, Zumberge et al., 1997) and ZTD estimated at 5 min sampling.

3 Results

3.1 GNSS-VLBI ZTD differences

The global differences between GNSS and VLBI derived ZTD are shown in Table 1 separately for each VLBI and GNSS solution in terms of mean value and standard deviation, having corrected the differences by the troposphere tie (ΔZTD) using the Brunner and Rüeger (1992) formulation. The differences are very similar between VLBI solutions and no apparent difference can be appreciated in using CODE (network solution technique) or IGS (PPP technique) derived ZTD.

Table 1: GNSS-VLBI ZTD differences (units: mm).

Solution	CGS	IAA	IVS	VIE
VLBI - GNSS CODE	0.7 ± 7.0	-1.2 ± 7.4	-0.7 ± 7.2	0.8 ± 7.9
VLBI - GNSS IGS	0.5 ± 7.7	-1.3 ± 8.3	-0.9 ± 8.0	0.8 ± 7.9

Nonetheless, a subdaily analysis of the differences has been carried out in order to find a potential bathtube effect in the differences between techniques, due to the fact that GNSS observation sessions start at 00:00 UTC and VLBI R1/R4 sessions start at 18:00 UTC. Figure 1 shows the histogram of the differences segmented by UTC hours for the period analysed (2013–2018) in Wettzell station when compared to CODE ZTD.

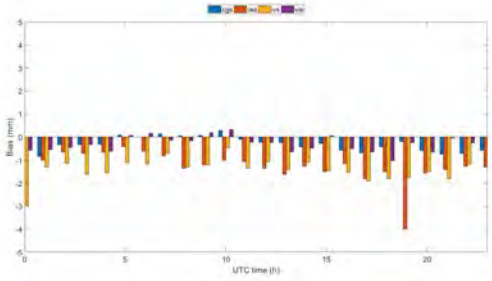

Fig. 1: GNSS CODE ZTD - VLBI ZTD at Wettzell.

Figure 2 provides the same histogram but using IGS ZTD.

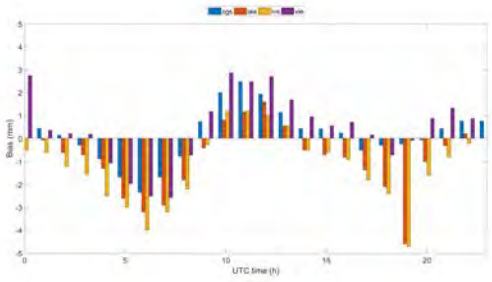

Fig. 2: GNSS IGS ZTD - VLBI ZTD at Wettzell.

It seems clear that IGS (PPP) solution has a subdiurnal pattern in the ZTD differences. Similar figures have been obtained for other stations. Only the ones

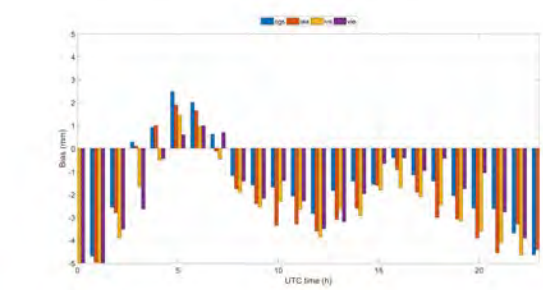

Fig. 3: GNSS CODE ZTD - VLBI ZTD at Badary.

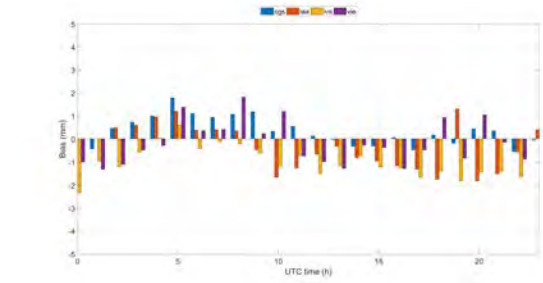

Fig. 4: GNSS IGS ZTD - VLBI ZTD at Badary.

corresponding to Badary site (figures 3 and 4) are included for the sake of brevity. We have tried to correlate this effect to several station displacement effects without any findings.

3.2 GNSS-based ZTD in VLBI processing

The other main topic dealt with in this work is the usage of GNSS-based ZTD as a priori value in VLBI processing. With this aim, VieVS 3.1 (Böhm et al., 2018) has been modified to automatically perform the following tasks:

- Read ZTD and gradients from CODE troposphere files (TRO SINEX) for the current and following day and store the data in an existing VieVS structure.
- Extract GNSS coordinates from SINEX file and add antenna eccentricity.
- For each observation:
  - Interpolate linearly GNSS ZTD and gradients to the VLBI observation epoch
  - Compute the zenith delay correction due to height difference ΔZTD (troposphere tie).
  - Compute a priori Zenit Wet Delay (ZWD) as follows:

$$ZWD = ZTD_{GNSS} - (ZHD_{VLBI} + \Delta ZTD) \quad (1)$$

  - Map ZHD and GNSS-derived ZWD to slant direction using VMF1 (Böhm et al., 2006) and add gradients contribution.

This rationale is only applied when GNSS data is available. We computed the trospophere ties (ΔZTD) using the Brunner and Rüeger (1992) formulation, taking atmosphere parameters from the VLBI observation files.

We processed R1 and R4 sessions using the baseline version of VieVS 3.1 and the modified version to use GNSS-derived ZTD as a priori value. In order to have consistent modelled delays and taking into consideration that not all VLBI sites have co-located GNSS antennas, it was needed to model a priori ZWD using VieVS capability of using the Askne and Nordius (1987) formulation. Figure 5 shows the repeatability for both solutions, where no significant difference is visible.

Nevertheless, we consider this analysis was not representative enough given that not all VLBI sites have co-located GNSS antennas. Due to this, we carried out the same analysis using CONT17 dataset and we only processed VLBI data for stations that have GNSS derived ZWD. Figure 6 shows the repeatability for CONT17 sessions, using nominal configuration, using ZWD and gradientes from GNSS to compute ZTD a priori value and fixing ZWD and gradientes from GNSS, i.e. not estimating the effect of the troposphere.

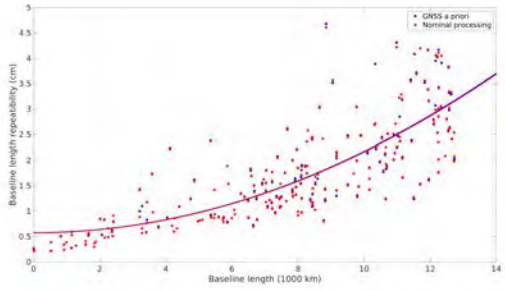

Fig. 5: R1 and R4 repeatability. Period 2013–2018.

Again, we found no improvement when using GNSS-derived ZTD as a priori value and the results worsen if we do not estimate troposphere effect.

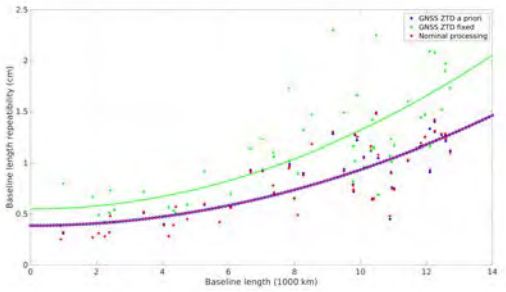

Fig. 6: CONT17 repeatability for the different configurations used.

Finally, we analysed the long-term behaviour of the wet and hydrostatic troposphere ties for the period 2013–2018. Table 2 shows the height difference between the GNSS antenna and the co-located VLBI antenna, and the mean and standard deviation of the wet (ΔZWD) and hydrostatic (ΔZHD) troposphere ties.

Hydrostatic troposphere ties have larger magnitude but small variation as they mainly depend on the height difference whereas the wet troposphere ties are almost negligible, with a mean value below one millimeter and standard deviation below 0.4 millimeters. These results are shown graphically in Figure 7.

Table 2: Behaviour of troposphere ties for the period 2013–2018.

Sites	ΔH (m)	ΔZWD (mm)	ΔZHD (mm)
Bd-BADG	10.2	-0.3 ± 0.2	-2.6 ± 0.2
Hb-HOB2	-0.1	0.0 ± 0.0	0.0 ± 0.0
Ke-KAT1	5.0	-0.3 ± 0.1	-1.3 ± 0.0
Kk-KOKE	9.2	-0.4 ± 0.0	-2.2 ± 0.0
Ma-MATE	7.6	-0.3 ± 0.1	-2.0 ± 0.1
Mc-MEDI	17.2	-0.8 ± 0.3	-4.7 ± 0.2
Ny-NYAL	3.7	-0.1 ± 0.0	-1.1 ± 0.0
Ts-TSKB	17.5	0.9 ± 0.4	-4.8 ± 0.2
On-ONSA	12.8	-0.5 ± 0.2	-3.6 ± 0.1
Wz-WTZR	3.1	-0.1 ± 0.0	-0.8 ± 0.0
Yg-YAR2	6.9	-0.3 ± 0.0	-1.8 ± 0.1
Zc-ZECK	8.8	-0.3 ± 0.1	-2.1 ± 0.1

4 Conclusions

The analysis of R1 and R4 sessions for the period 2013–2018 focused on troposphere delays led to the following conclusions:

- VLBI-based ZTD show similar level of agreement in terms of mean bias and standard deviation with CODE and IGS products.
- No subdaily pattern has been appreciated in the differences with respect to CODE ZTD but there is a subdaily pattern for IGS ZTD whose root cause has to be further analysed.
- GNSS-based ZTD used as a priori value in VLBI processing do not improve estimation in terms of repeatability.
- Long term analysis of troposphere ties shows stable behaviour of wet and hydrostatic ties, with standard deviation of wet tie below 0.4 mm for the set of stations analysed.

References

Askne J, Nordius H (1987) Estimation of tropospheric delay for microwaves from surface weather data. *Radio Sci.*, 22, 379–386

Böhm J, Werl B, Schuh H (2006) Troposphere mapping functions for GPS and Very Long Baseline Interferometry from european centre for medium-range weather forecasts operational analysis data. *J Geophys Res*, 111(B02):406, doi:10.1029/2005JB003629

Böhm J, Böhm S, Boisits J, et al. (2018) Vienna VLBI and Satellite Software (VieVS) for Geodesy and Astrometry. *PASP*, 130(986), 044503

Brunner F K, Rüeger J M (1992) Theory of the local scale parameter method for EDM. *Bull Géodésique* 66:355–364

Dach R, Schaer S, Arnold D, et al. (2018) CODE final product series for the IGS. Published by Astronomical Institute, University of Bern, http://www.aiub.unibe.ch/download/CODE, doi:10.7892/boris.75876.3

Dow J M, Neilan R E, Rizos C (2009) The International GNSS Service in a changing landscape of Global Navigation Satellite Systems. *J Geod*, 83:191–198, doi:10.1007/s00190-008-0300-3

Heinkelmann R (2013) IVS Rapid Troposphere Product – A Possible Extension Regarding the IGS TWG (C. Hackman). Presented at the 14th IVS Analysis Workshop, Espoo

Nothnagel A, Artz T, Behrend D, et al. (2017) International VLBI Service for Geodesy and Astrometry – Delivering high-quality products and embarking on observations of the next generation. *J Geod*, 91(7), 711–721

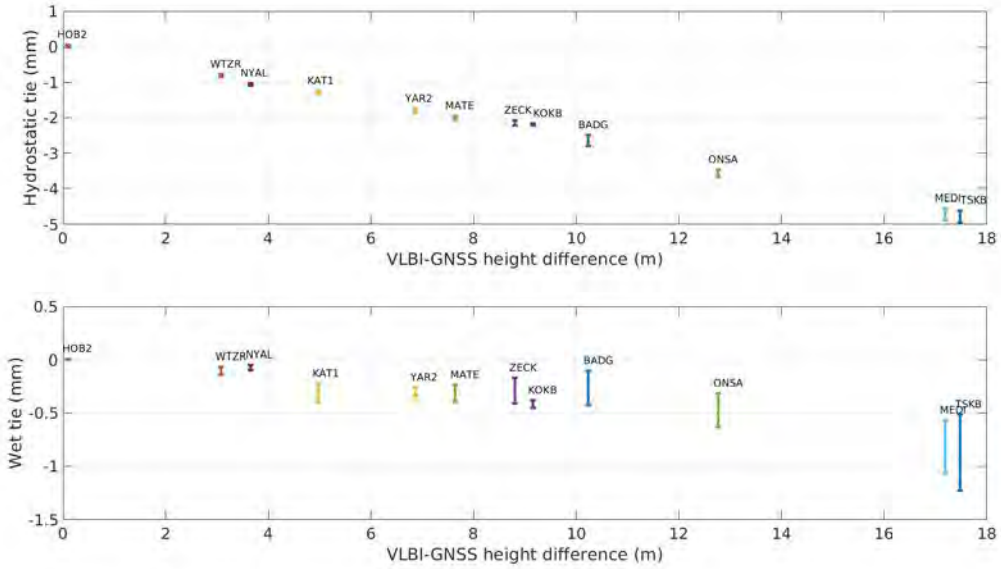

Fig. 7: Mean and standard deviation of wet and hydrostatic troposphere ties.

Teke K, Böhm J, Nilsson T, et al. (2011) Multi-technique comparison of troposphere zenith delays and gradients during CONT08. *J Geod*, 85(7):395–413, doi::10.1007/s00190-010-0434-y

Zumberge J F, Heflin M B, Jefferson D C, et al. (1997) Precise Point Positioning for the Efficient and Robust Analysis of GPS Data from Large Networks. *J Geophys Res*, 102 (B3): 5005-17

An Assessment of the Tropospheric Parameters Estimated From the CONT17 Campaign

T. Nilsson, K. Balidakis, T. Ning

Abstract We investigate the tropospheric parameters – the Zenith Total delays (ZTD) and horizontal gradients – estimated from the CONT17 VGOS sessions. These are compared to the results of the CONT17 legacy sessions, from GNSS, and from the ERA5 reanalysis. We find that the WRMS differences between the ZTD from the VGOS sessions and GNSS is on the level of 3–4 mm, which is similar or even slightly better than what is obtained from the legacy VLBI data. For the gradients the WRMS differences are about 0.3–0.4 mm, what is similar to the results from the legacy sessions.

Keywords VLBI · tropophere · GNSS · CONT17 · ERA5

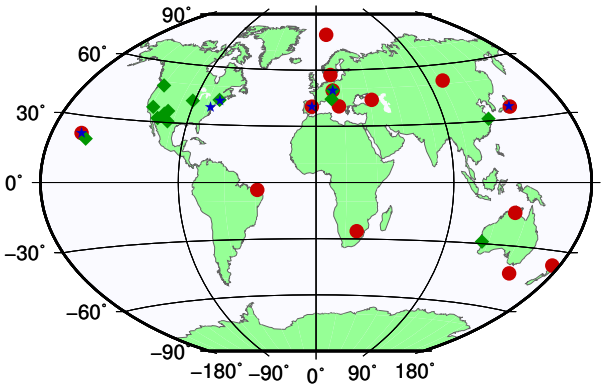

Fig. 1: Map of the locations of the stations participating in the CONT17 campaign. The red circles show the stations in the Legacy 1 network, the green diamonds the stations in the Legacy 2 network, and the blue stars the VGOS stations.

1 Introduction

The CONT campaigns are continuous 15-day VLBI campaigns performed approximately every third year to demonstrate the current state-of-the-art of geodetic VLBI. The data from the CONT campaigns are often used in studies to evaluate the performance of VLBI. For example, the tropospheric delays from VLBI during several CONT campaigns were compared to other techniques, such as GNSS, DORIS, water vapour radiometers, and numerical weather prediction models (NWM), in Teke et al. (2013).

The most recent CONT campaign was CONT17, which was performed from 28 November to 12 December, 2017 (Behrend et al., 2017). Different from the previous CONT campaigns, which only employed a single station network, there were three independent station networks observing in parallel in CONT17, see Fig. 1. There were two networks consisting of legacy VLBI antennas, called Legacy 1 (14 stations) and Legacy 2 (13 stations). In addition, there was a network of six new VGOS (VLBI Geodetic Observing System) stations observing for five days of the campaign, between December 3, 23:00 and December 9, 00:00. This is especially interesting since this is the first VGOS data set being publicly released, thus allowing for a first evaluation of the performance of the new VGOS concept and comparison with the legacy system.

Tobias Nilsson · Tong Ning
Lantmäteriet – The Swedish Mapping, Cadastral, and Land Registration Authority, Lantmäterigatan 2C, SE-801 82 Gävle, Sweden

Kyriakos Balidakis
GFZ German Research Centre for Geosciences, Telegrafenberg A17, DE-14473 Potsdam, Germany

(Correspondence: jan-tobias.nilsson@lm.se)

Table 1: A list of the VGOS antennas participating in the CONT17 VGOS test campaign, co-located legacy VLBI telescope participating in one of the legacy CONT17 networks, and the co-located GNSS antenna used in this work. For each GNSS antenna, the satellite systems used are also listed (G: GPS, R: GLONASS, E: Galileo).

VGOS	Legacy 1	Legacy 2	GNSS
WETTZ13S	WETTZELL	WETTZ13N	WTZZ (GRE)
WESTFORD	-	-	WES2 (GR)
GGAO12M	-	-	GODE (G)
ISHIOKA	-	-	ISHI (GRE)
KOKEE12M	KOKEE	-	KOKV (GRE)
RAEGYEB	YEBES40M	-	YEBE (G)

In this work we evaluated the tropospheric parameters – the Zenith Total Delays (ZTD) and horizontal gradients – estimated from the CONT17 VGOS sessions. This was done by comparing with the results from the legacy antennas at stations having telescopes participating in both the CONT17 VGOS network and a legacy network. In addition, we performed an external evaluation by comparing with the tropospheric parameters estimated from co-located GNSS receivers, as well as those calculated from the NWM fields from the fifth ECMWF reanalysis (ERA5, Copernicus Climate Change Service (C3S), 2017). The CONT17 VGOS antennas are listed in Table 1, along with the co-located legacy telescopes and the co-located GNSS station used in this work. It should be noted that the VGOS antenna in Yebes, Spain, RAEGYEB, experienced pointing problems during CONT17, and as a consequence only the data from the first day of the campaign were found usable.

2 Data analysis

2.1 VLBI

The VLBI data were analysed with the VieVS@GFZ software (Nilsson et al., 2015). The a priori modelling was done according to the IERS 2010 Conventions (Petit and Luzum, 2010) and the parameter estimation was done with the least squares module of the software. The Vienna Mapping Functions 1 (VMF1, Böhm et al., 2006) and the gradient mapping function of Chen and Herring (1997) were used. First, each one-day session was analysed individually, then for each network we combined all sessions in a global solution, estimating one set of station and radio source coordinates for the whole campaign. The ZTD and gradients were estimated with temporal resolution of 20 minutes and 2 h, respectively.

2.2 GNSS

The GNSS observations were analysed with the Bernese GNSS software version 5.2 (Dach et al., 2015). We applied the Precise Point Positioning (PPP) strategy, using the final orbits and clock products provided by CODE (Dach et al., 2018). The satellite systems used in the analysis are those listed in Table 1. We first analysed each day individually, then all days of CONT17 were combined with the `ADDNEQ2` module in order to obtain just one coordinate estimate per station for the whole period and continuous time series of the tropospheric parameter. The parametrisation of the tropospheric delays (temporal resolution and mapping function) was the same as was used in the VLBI analysis.

2.3 ERA5

Ray-tracing though the ERA5 fields (1 hour temporal resolution, 31 km spatail resolution) was performed at a number of predefined azimuth and elevation angles. To these ray-trace delays we then fitted 1st and 2nd order gradients. For more details, see Zus et al. (2014) and Balidakis et al. (2018).

3 Results

3.1 ZTD

In order to compare ZTD from different techniques, the ZTD estimates of all techniques must be reduced to a common height. This was done by applying tropospheric ties, following the procedure described in Teke et al. (2013). Given that the height differences between the co-located instruments were just a few meters at most, this method should be sufficient.

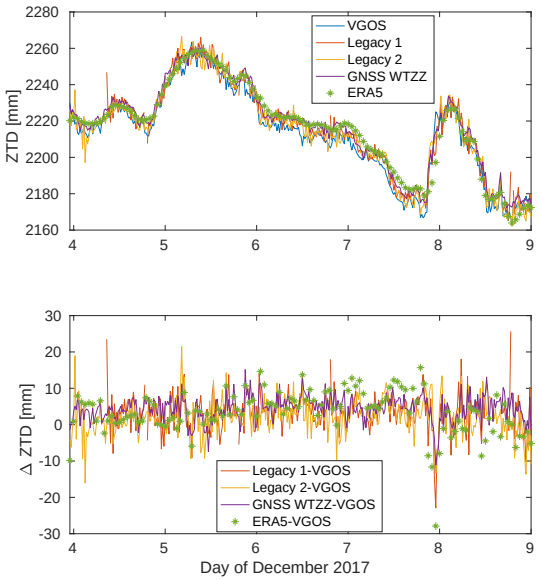

Fig. 2: Top plot shows time series of ZTD estimated at Wettzell during CONT17 from the VGOS VLBI telescope, the two legacy VLBI telescopes, the WTZZ GNSS antenna, and from ERA5. Bottom plot shows the difference between the VGOS time series and all others.

Figure 2 shows time series of ZTD from the Wettzell site in the time period 4-8 December, 2017. This station had telescopes in all three CONT17 networks: WETTZ13S (VGOS), WETTZELL (Legacy 1), and WETTZ13N (Legacy 2). The ZTD estimated from these three telescopes agree relatively on the level of 4–5 mm. The exception is in the beginning of December 8, where the WETTZ13S ZTD differs from the others by about 2 cm. Probably the sensitivity of WETTZ13S was lower during this period, resulting in the rapid increase in the ZTD not being captured as good as done by the other telescopes and the other techniques. The agreement with GNSS is actually slightly better than with legacy VLBI; the Weighted RMS (WRMS) difference between the ZTD from WETTZ13S and the GNSS antenna WTZZ is 3.2 mm. This is slightly better than for the legacy VLBI telescopes, where the WRMS difference to GNSS is 3.9 mm. The agreement with ZTD from ERA5 is worse, the WRMS difference is 5.3 mm for WETTZ13S, 5.2 mm for WETTZELL, and 5.4 mm for WETTZ13N.

Table 2 lists the Weighted Mean (WM) and WRMS of the differences between the ZTD estimated from the VGOS telescopes and from GNSS, from ERA5, and from legacy VLBI. For the case of REAGYEB (Yebes, Spain), it should be noted that the WM and WRMS values are only based on one day of data (compared to five days for the others), since there were only useful observations from this antenna for one day. We can note that the agreement with GNSS is similar or even slightly better than what is usually found between VLBI and GNSS, with a bias of a few mm and a WRMS difference of 3–4 mm. The exception is KOKEE12M, where the WRMS difference is 5.4 mm. This is larger than what is obtained for the legacy antenna KOKEE (legacy 1 network), where the WRMS difference to GNSS is 4.8 mm. One reason could be that KOKEE12M had fewer observations compared to the other VGOS telescopes, on average 350/1000 scans/observations per day. This is much lower than WETSFORD and GGAO12M, where there were more than 1000 scans resulting more than 2000 observations per day. However, for the other VGOS telescopes the number of scans/observations were not that different from KOKEE12M, for example ISHIOKA made about 410 scans and and 1200 observations per day. Hence the number of scans/observations is probably only part of the reason for the worse results at KOKEE12M. When comparing to ERA5 the WM and WRMS differences are slightly higher compared to when comparing to the GNSS. Notable is a bias of 1.3 cm at KOKEE12M. Most likely this is an issue with the finite spatial resolution of the ERA5 orography.

Table 2: Weighted mean and WRMS (in parenthesis) differences (in mm) between the ZTD estimated from the VGOS antennas and from co-located GNSS antennas, ERA5, and co-located legacy VLBI telescopes.

Antenna	GNSS	ERA5	Legacy 1	Legacy 2
WETTZ13S	−0.6 (3.2)	−1.9 (5.3)	−1.1 (4.5)	−2.2 (4.3)
WESTFORD	−3.8 (3.5)	−1.7 (4.6)	–	–
GGAO12M	3.3 (3.7)	−0.1 (3.9)	–	–
ISHIOKA	2.4 (3.7)	0.5 (6.9)	–	–
KOKEE12M	−3.9 (5.4)	13.1 (8.3)	−4.0 (5.9)	–
RAEGYEB	2.4 (3.1)	3.5 (3.8)	−0.1 (3.6)	–

3.2 Gradients

The comparison of the North gradients estimated using the different techniques at Wettzell is shown in Fig. 3. As usual when comparing gradients, the agreement be-

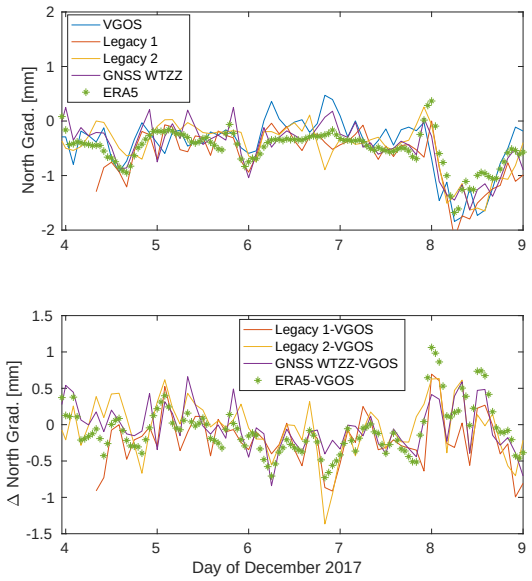

Fig. 3: Top plot shows time series of North gradients estimated at Wettzell during CONT17 from the VGOS VLBI telescope, the two legacy VLBI telescopes, the WTZZ GNSS antenna, and from ERA5. Bottom plot shows the difference between the VGOS time series and the other ones.

tween the techniques is not as good as in the case of ZTD. Nevertheless, we find a decent agreement. Especially, we can note that the all techniques see a decrease in the gradient on December 8.

Table 3: Weighted mean and WRMS (in parenthesis) differences (in mm) between the East gradients estimated from the VGOS antennas and from co-located GNSS antennas, ERA5, and co-located legacy VLBI telescopes.

Antenna	GNSS	ERA5	Legacy 1	Legacy 2
WETTZ13S	−0.2 (0.4)	−0.1 (0.3)	−0.2 (0.4)	−0.1 (0.3)
WESTFORD	−0.4 (0.3)	0.0 (0.3)	–	–
GGAO12M	0.1 (0.3)	0.0 (0.2)	–	–
ISHIOKA	0.0 (0.4)	−0.0 (0.4)	–	–
KOKEE12M	0.5 (0.5)	0.4 (0.5)	0.5 (0.4)	–
RAEGYEB	0.3 (0.3)	0.3 (0.3)	0.2 (0.3)	–

WM and WRMS differences between the gradients estimated from the VGOS antennas and the other techniques can be seen in Table 3 (East gradients) and Table 4 (North gradients). In general, the WRMS differences w.r.t. GNSS and ERA5 are on the level iof 0.3–0.4 mm, except for KOKEE12M where the WRMS differences are higher. As already discussed in Sec. 3.1, it

Table 4: Weighted mean and WRMS (in parenthesis) differences (in mm) between the North gradients estimated from the VGOS antennas and from co-located GNSS antennas, ERA5, and co-located legacy VLBI telescopes.

Antenna	GNSS	ERA5	Legacy 1	Legacy 2
WETTZ13S	0.0 (0.3)	0.1 (0.3)	0.2 (0.3)	0.0 (0.4)
WESTFORD	−0.2 (0.4)	0.1 (0.3)	–	–
GGAO12M	0.1 (0.4)	−0.1 (0.2)	–	–
ISHIOKA	−0.1 (0.4)	−0.2 (0.3)	–	–
KOKEE12M	1.0 (0.7)	0.7 (0.6)	0.6 (0.6)	–
RAEGYEB	0.1 (0.3)	0.0 (0.3)	0.1 (0.3)	–

seems that the results for this station is a not as good as for the other VGOS stations, the complete reason needs further investigations.

4 Conclusions and outlook

The results, especially for the ZTD, show that the performance of the VGOS telescopes, in terms of estimating the tropospheric delays, is at least as good as that of the legacy antennas. However, we could also identify some potential issues which need further investigations, like the performance of the KOKEE12M antenna. Furthermore, the goal of VGOS is to obtain results with a precision about one order of magnitude better than the legacy VLBI system, which was not achieved in the CONT17 VGOS campaign. Of course, this campaign was more designed towards showing that the new system works, rather than demonstrating its full potential, hence that level of precision cannot be expected. Thus, the fact that the VGOS telescopes give similar precision in the tropospheric delays to the legacy telescope is promising, however, there is still a lot of work to do in order to reach the full potential of VGOS.

Acknowledgements We are grateful to all parties that contributed to the success of the CONT17 campaign, in particular to the IVS Coordinating Center at NASA Goddard Space Flight Center (GSFC) for taking the bulk of the organizational load, to the GSFC VLBI group for preparing the legacy S/X observing schedules and MIT Haystack Observatory for the VGOS observing schedules, to the IVS observing stations at Badary and Zelenchukskaya (both Institute for Applied Astronomy, IAA, St. Petersburg, Russia), Fortaleza (Rádio Observatório Espacial do Nordeste, ROEN; Center of Radio Astronomy and Astrophysics, Engineering School, Mackenzie Presbyterian University, Sao Paulo and Brazilian Instituto

Nacional de Pesquisas Espaciais, INPE, Brazil), GGAO (MIT Haystack Observatory and NASA GSFC, USA), Hartebeesthoek (Hartebeesthoek Radio Astronomy Observatory, National Research Foundation, South Africa), the AuScope stations of Hobart, Katherine, and Yarragadee (Geoscience Australia, University of Tasmania), Ishioka (Geospatial Information Authority of Japan), Kashima (National Institute of Information and Communications Technology, Japan), Kokee Park (U.S. Naval Observatory and NASA GSFC, USA), Matera (Agencia Spatiale Italiana, Italy), Medicina (Istituto di Radioastronomia, Italy), Ny Ålesund (Kartverket, Norway), Onsala (Onsala Space Observatory, Chalmers University of Technology, Sweden), Seshan (Shanghai Astronomical Observatory, China), Warkworth (Auckland University of Technology, New Zealand), Westford (MIT Haystack Observatory), Wettzell (Bundesamt für Kartographie und Geodäsie and Technische Universität München, Germany), and Yebes (Instituto Geográfico Nacional, Spain) plus the Very Long Baseline Array (VLBA) stations of the Long Baseline Observatory (LBO) for carrying out the observations under the US Naval Observatory's time allocation, to the staff at the MPIfR/BKG correlator center, the VLBA correlator at Socorro, and the MIT Haystack Observatory correlator for performing the correlations and the fringe fitting of the data, and to the IVS Data Centers at BKG (Leipzig, Germany), Observatoire de Paris (France), and NASA CDDIS (Greenbelt, MD, USA) for the central data holds.Furthermore, we are grateful to the IGS (Dow et al., 2009) for providing the GNSS data and to ECMWF for the ERA5 data.

References

Balidakis K, Nilsson T, Zus F, *et al.* (2018) Estimating integrated water vapour trends from VLBI, GNSS and numerical weather models: sensitivity to tropospheric parameterization. *J Geophys Res*, 123(12):6356–6372, doi:10.1029/2017JD028049

Behrend D, Thomas C, Gipson J, *et al.* (2017) Planning of the continuous VLBI campaign 2017 (CONT17). In R. Haas, G. Elgered (eds.): *Proc. 23rd EVGA Working Meeting*, 132–135

Böhm J, Werl B, Schuh H (2006) Troposphere mapping functions for GPS and very long baseline interferometry from european centre for medium-range weather forecasts operational analysis data. *J Geophys Res*, 111:B02406, doi:10.1029/2005JB003629

Chen G, Herring T H (1997) Effects of atmospheric azimuthal asymmetry on the analysis of space geodetic data. *J Geophys Res*, 102(B9):20489–20502, doi:10.1029/97JB01739

Copernicus Climate Change Service (C3S) (2017) ERA5: Fifth generation of ECMWF atmospheric reanalyses of the global climate. Technical report, Copernicus Climate Change Service Climate Data Store (CDS), URL https://cds.climate.copernicus.eu/cdsapp{#}!/home. Accessed 14 June, 2019

Dach R, Lutz S, Walser P, *et al.* (eds.) (2015) *Bernese GPS Software Version 5.2 User Manual*. Astronomical Institute, University of Bern, Bern Open Publishing, doi:10.7892/boris.72297

Dach R, Schaer S, Arnold D, *et al.* (2018) CODE final product series for the IGS. Technical report, Astronomical Institute, University of Bern.

Dow J-M, Neilan R E, Rizos C (2009) The international GNSS service in a changing landscape of global navigation satellite systems. *J Geod*, 83:191–198, doi:10.1007/s00190-008-0300-3

Nilsson T, Soja B, Karbon M, et al. (2015) Application of Kalman filtering in VLBI data analysis. *Earth Planets Space*, 67(136):1–9, doi:10.1186/s40623-015-0307-y

G. Petit, B. Luzum (eds.) (2010) *IERS Conventions (2010)*. IERS Technical Note 36. Verlag des Bundesamts für Kartographie und Geodäsie, Frankfurt am Main, Germany

Teke K, Nilsson T, Böhm B, et al. (2013) Troposphere delays from space geodetic techniques, water vapor radiometers, and numerical weather models over a series of continuous VLBI campaigns. *J Geod*, 87(10-12):981–1001, doi:10.1007/s00190-013-0662-z

Zus F, Dick G, Douša J, et al. (2014) The rapid and precise computation of GPS slant total delays and mapping factors utilizing a numerical weather model. *Radio Sci*, 49(3):207–216, doi:10.1002/2013RS005280

Time Stability of the K-band Catalog Sources

K. Le Bail, A. de Witt, C. S. Jacobs, D. Gordon

Abstract The ICRF3 was adopted by the IAU in August 2018 and became effective January 1, 2019. It differs from ICRF and ICRF2 by the addition of two catalogs at higher frequencies, including a K-band (24 Ghz) catalog. The K-band data differs from the S/X data in different aspects that question if it may be possible to construct a more stable frame at K-band than at S/X band. We studied two source position time series solutions generated at GSFC using Calc/Solve: one obtained from K-band observations and one from S/X observations. Using the Allan variance, we determined their noise floor. Since the two source position time series solutions present very different sampling, we did three different comparisons: first we compared the two sets of time series using all the data as two independent solutions, then we limited the study to a common time period, and finally we compared the noise floor of the two catalogs on comparable sessions using the VLBA on a common period. The last comparison shows K-band has a comparable level of noise floor as S/X.

Keywords Celestial Reference Frame · ICRF · Quasar · K-band · Noise floor · Allan variance

Karine Le Bail · David Gordon
NVI, Inc., Greenbelt, MD, U.-S.

Aletha de Witt
SARAO/HartRAO, Krugersdorp, South Africa

Christopher S. Jacobs
Jet Propulsion Laboratory, California Inst. Technology/NASA, Pasadena, CA, U.-S.

(Correspondence: karine.lebail@nasa.gov)

1 Introduction

The ICRF3 is composed of catalogs at three frequencies. In this paper we examine the relative temporal stability of two of those, S/X and K bands.

The K-band data differs from the S/X data in that 1) the K-band in the north is VLBA-only; 2) the K-band data since 2015 are all at a high data rate of 2 Gbps; and 3) K-band is less affected by source structure. Thus it may be possible to construct a more stable frame at K-band than at S/X band (see de Witt et al. (2019) for more details on the K-band Celestial Reference Frame).

The two source position time series solutions we studied were generated at GSFC using Calc/Solve. These two solutions present very different sampling. The K-band observations cover the period May 2002 to November 2018 for a total of 65 sessions while the S/X observations cover the period August 1979 to January 2019 for a total of 6271 sessions (see Table 1).

Table 1: Statistics on GSFC K-band and S/X-band catalogs processed in January 2019.

	K solution Jan 2019	S/X solution Jan 2019
Source number	906	4775
Session number	65	6271
First epoch	May 2002	Aug. 1979
Last epoch	Nov. 2018	Jan. 2019
Source number (> 10 sessions)	354	788

In this paper, we compared the two source position time series solutions on three different configurations of common source sets depending on observation periods and session types (see summary in Table 2):

1. We consider the individual noise floor of the two independent solutions: we compute the source noise floor on the entire observation period for each of the 310 common sources observed in ten sessions or more of the two catalogs.
2. We focus on the same period of observation for the two solutions: we compute the source noise floor on the observation period November 2016 to November 2018 for each of the 87 common sources observed in ten sessions or more of the two catalogs.
3. We restrict the study to equivalent sessions: we compute the source noise floor for each of the 31 common sources observed in ten sessions or more in the 24-hour VLBA sessions (code UD for the K-band and codes UF/UG for the S/X bands) over the observation period November 2016 to November 2018.

Table 2: Three different configurations studied in this paper.

	Observation period	Session type	Source number
Config. 1	ALL avail.	ALL avail.	310
Config. 2	Nov. 2016 - Nov. 2018	ALL avail.	87
Config. 3	Nov. 2016 - Nov. 2018	VLBA	31

Figure 1 gives an example of right ascension position time series for the source 0552+398 for each of the configurations.

In the second section of this paper, we briefly describe the method we used. The third section presents the results for the three configurations. The last section concludes our study.

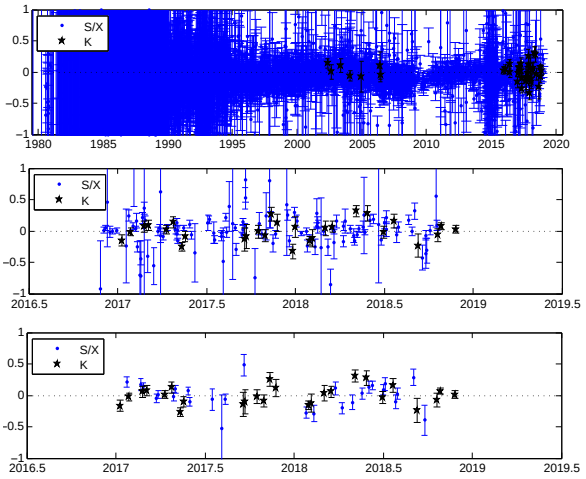

Fig. 1: Right Ascension time series for source 0552+398. The blue points correspond to the S/X solution, the black points to the K-band solution. Top plot: entire period (configuration 1). Middle plot: period November 2016 to November 2018 (configuration 2). Bottom plot: VLBA sessions between November 2016 and November 2018 (configuration 3).

2 Method

We could study these time series by using the standard deviation, but this quantity does not take into account the evolution of the position with time. So we choose to use the Allan variance instead and determine the noise floor using a method presented in Le Bail et al. (2017).

The Allan variance is a statistical tool that gives the level and type of noise of a time series. For more details, the reader can refer to previous work in Le Bail and Gordon (2010) or from Allan (1966). The major drawback of this statistical tool when applied to VLBI position time series is that it has to be applied to regularly spaced time series. As with any other statistical tool, the significance of the results depends greatly on the number of points of the time series.

The observed VLBI data presents challenges for this statistical tool: there may be some large gaps between observations, the sessions may be scarce and/or the number of observations is limited. For these reasons, we chose to perform monthly and yearly averaging of the time series. If the time series has a large gap or too many missing points, the time series is not considered in the study.

The different steps of the method are described hereafter:

1. Keep sources with ten or more observations to increase the significance of the statistics;
2. Monthly and yearly averages and interpolation to regularize our time series;
3. Allan variance processing for each source, each coordinate, each solution;
4. Noise floor determination for each source and each coordinate. If the noise type determined by the slope of the Allan variance curve (see Figure 2) is white or flicker, the noise floor is the lowest Allan variance. If the noise type is random walk, the noise floor is undefined.

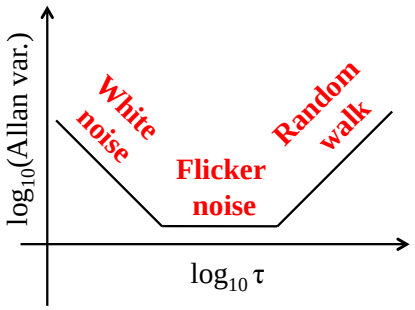

Fig. 2: Allan variance. Determination of noise scheme.

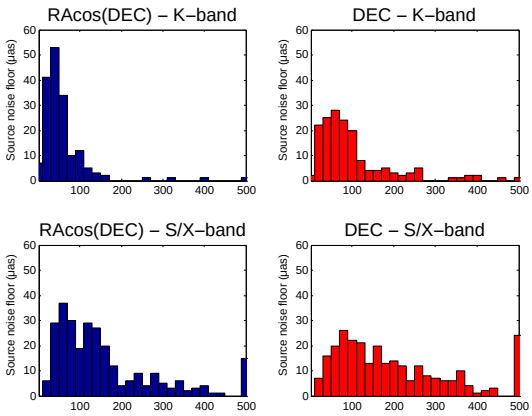

Fig. 3: Noise floor determined by the Allan variance. Configuration 1: entire observation period - 310 common sources. Top plots: K-band solution, bottom plots: S/X solution. Right plots: right ascension component, left plots: declination component.

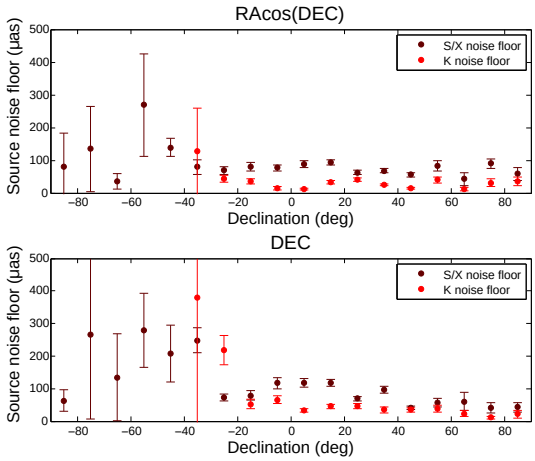

Fig. 4: Noise floor comparison in 10° declination bands. Configuration 1: entire observation period – 310 common sources. Top plot: right ascension component, bottom pot: declination component.

3 Results

3.1 Configuration 1: entire observation period – 310 common sources

The K solution contains 65 sessions over its entire period of observation (May 2002 to November 2019) and the S/X solution contains 6271 sessions (August 1979 to January 2019). There are 310 common sources that were observed in ten or more sessions.

We compute the noise floor for each of these 310 sources, for each component and each solution. The results are displayed in Figure 3 as individual source noise floor histograms and in Figure 4 as noise floor averages on 10° declination bands.

As seen in Figure 3, most of the sources in the K-band solution have a source noise floor lower than 80 μas for the right ascension component and 100 μas for the declination component. For the S/X solution, most of the sources have a noise floor lower than 200 μas for the right ascension component and it is more scattered for the declination component with a noise floor average around 200 μas.

Figure 4 presents the same results averaged over 10° declination bands. For declination bands higher than −20°, the noise floors for the S/X solution is visibly larger than for the K solution.

This seems to indicate that the K noise floor tends to be smaller than the S/X noise floor when we consider the two solutions on their entire period.

3.2 Configuration 2: Nov. 2016–Nov. 2018 observation period – 87 common sources

The VLBI technique has seen significant improvements and the quality of the data improved with time. The previous comparison is biased since the S/X solution contains all the data from the beginning of VLBI when the quality of the data was not as good as it is currently. In this section, the comparison is done on the common period of observation for the two solutions: November 2016 to November 2018, for a total of 44 sessions for the K solution and 391 sessions for the S/X solution. The common sources that were observed in ten or more sessions are 87 sources.

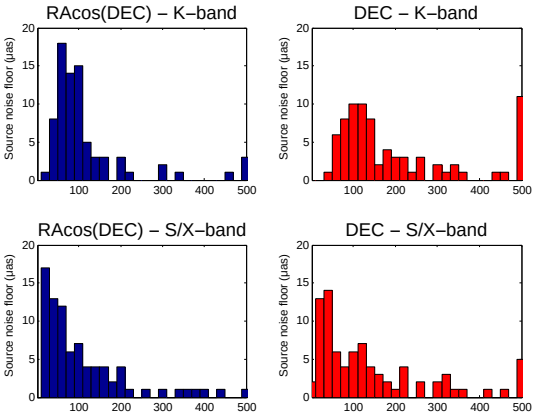

Fig. 5: Noise floor determined by the Allan variance. Configuration 2: Nov. 2016–Nov. 2018 – 87 common sources. Top plots: K-band solution, bottom plots: S/X solution. Right plots: right ascension component, left plots: declination component.

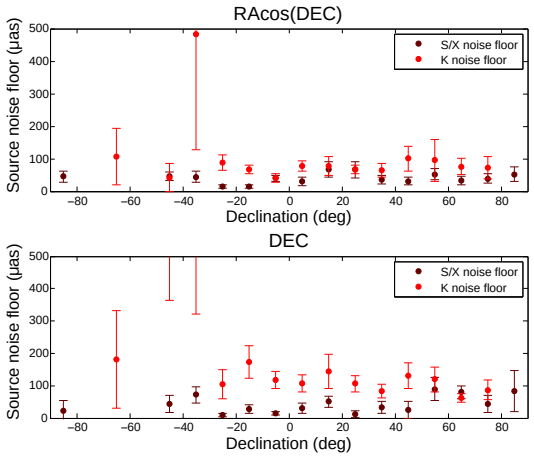

Fig. 6: Noise floor comparison in 10° declination bands. Configuration 2: Nov. 2016–Nov. 2018 – 87 common sources. Top plot: right ascension component, bottom pot: declination component.

The results are displayed in figures 5 and 6. Contrary to the previous configuration, the S/X noise floor tends to be smaller than the K noise floor in both figures.

3.3 Configuration 3: Nov. 2016–Nov. 2018 observation period of VLBA sessions – 31 common sources

The configuration 2 study could also be considered biased since we compared 44 sessions for the K solution to 391 for the S/X solution, all 391 sessions

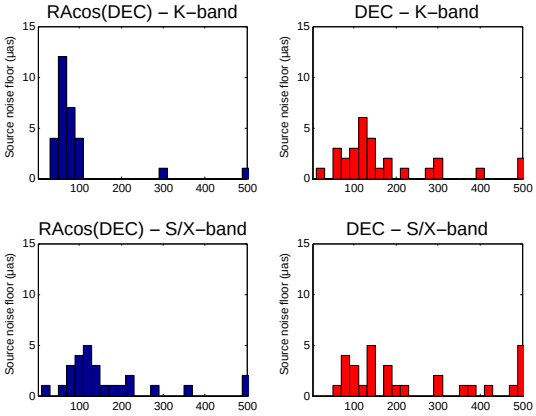

Fig. 7: Noise floor determined by the Allan variance. Configuration 3: Nov. 2016–Nov. 2018 and VLBA sessions – 31 common sources. Top plots: K-band solution, bottom plots: S/X solution. Right plots: right ascension component, left plots: declination component.

with different observation settings and quality. In this third part, we compared only on the common period (November 2016 to November 2018) for similar sessions. In this case, we consider the data from 40 24-hour VLBA sessions at S/X band, called UF001 and UG002 sessions, and 27 24-hour VLBA sessions at K-band, called UD sessions. The VLBA sessions at S/X band observed 4145 sources in a very small number of sessions while the VLBA sessions at K band observed 819 sources. The reason for the source number discrepancy is mostly explained by the goals of the VLBA sessions at S/X band. The goals were mostly to improve the precision of ICRF3, as well as for ICRF3 maintenance. So approximately 3300 of the weakest ICRF3 sources were re-observed during these sessions. There are 31 sources observed in ten or more observations that are common in the two subsets of the solutions.

The results are in figures 7 and 8. In Figure 7 for the right ascension component, most of the sources in the K band solution have a source noise floor lower than 100 μas while most of the sources in the S/X solution have a source noise floor lower than 150 μas. This is less significant for the declination component even though the distribution is more scattered for the S/X solution. When comparing on declination bands in Figure 8, the two solution noise floors are within the error bar for the declination bands higher than $-30°$.

In conclusion the K noise floor tends to be comparable to the S/X noise floor when considering similar sessions and a similar observing period.

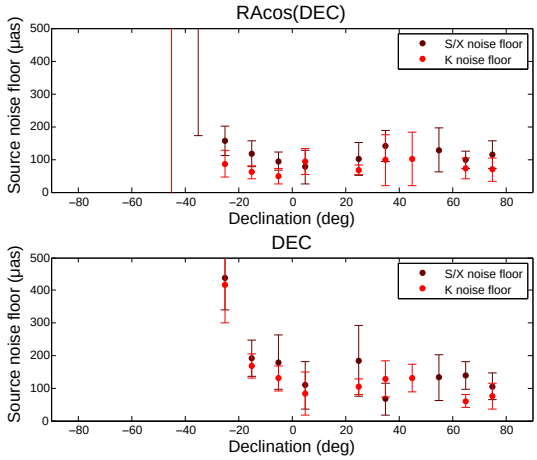

Fig. 8: Noise floor comparison in 10° declination bands. Configuration 3: Nov. 2016–Nov. 2018 and VLBA sessions – 31 common sources. Top plot: right ascension component, bottom pot: declination component.

4 Conclusions and outlook

The K-band observations have reached a level of stability equivalent to the level of current S/X observations. They benefited from the history of the S/X observations. The strength of the S/X data set is in its broad diversity of baselines and sessions. Comparing the VLBA sessions UD (K-band) and UF-UG (S/X), it seems to show that the K-band statistical stability is better than the S/X-band statistical stability. We need more K-band observations to continue monitoring and comparing the stability of the frame realized by the K-band observations.

Thanks to the VLBA, K-band observations have increased greatly in the past two years, prompting many studies as demonstrated by the four papers presented at the EVGA 2019.

Acknowledgements Copyright ©2019. All Rights Reserved. U.S. Government sponsorship acknowledged for work done at JPL-Caltech under a contract with NASA.
The VLBA is managed by NRAO, funded by the National Science Foundation, and operated under cooperative agreement by Associated Universities. The authors gratefully acknowledge use of the VLBA under the USNO's time allocation. This work supports USNO's ongoing research into the celestial reference frame and geodesy.
HartRAO is a facility of the National Research Foundation (NRF) of South Africa. The Hobart telescope is operated by the University of Tasmania and this research has been supported by AuScope Ltd., funded under the National Collaborative Research Infrastructure Strategy (NCRIS).

References

Allan D (1966) Statistics of Atomic Frequency Standards. *Proc IEEE*, 54(2):221–230

de Witt A, Gordon D, Jacobs C S, et al. (2019) The K-band (24 GHz) 2019a Celestial Reference Frame. Poster at the 24th EVGA Working Meeting, http://www.oan.es/evga2019/EVGA2019_PDF/P306_EVGA2019_deWitt.pdf

Krásná H, Gordon D, de Witt A, et al. (2019) Earth Orientation Parameters estimated from K-band VLBA measurements. In: R. Haas, S. Garcia-Espada, J. A. López Fernández (eds.), *Proc. 24th EVGA Working Meeting*, 238–242

Le Bail K, Gordon D (2010) Time-dependent Selection of an Optimal Set of Sources to Define a Stable Celestial Reference Frame. In: D. Behrend, K. Baver (eds.): *IVS 2010 General Meeting Proceedings*, NASA/CP-2010-215864, 280–284

Le Bail K, Gordon D, Gipson J M, et al. (2017) Investigating the noise floor of VLBI source positions. In: R. Haas, G. Elgered (eds.): *Proc. 23rd EVGA Working Meeting*, 186–189

Soja B, Jacobs C S, Runge T, et al. (2019) Ionospheric calibration for K-band celestial reference frames. Presentation at the 24th EVGA Working Meeting, http://www.oan.es/evga2019/EVGA2019_PDF/O316_EVGA2019_Soja.pdf

VLBA Imaging of ICRF 3 Sources

L. Hunt, M. Johnson, A. Fey, J. Spitzak, D. Gordon

Abstract We present results from a Very Long Baseline Array (VLBA) imaging campaign of sources included in the third realization of the International Celestial Reference Frame (ICRF). Imaging these sources allows us to determine spectral index, peak flux density, compactness and source structure index. This information is crucial to understanding source structure and variability which better allows us to determine if a source is suitable for inclusion in the ICRF and suitable as a phase reference calibrator. We also describe where the images and ancillary data will be publicly available in the future.

Keywords ICRF · Imaging · VLBA

1 Introduction

The International Celestial Reference Frame is comprised of positions of compact quasars calculated from Very Long Baseline Interferometry (VLBI) observations at 2.3 GHz and 8.4 GHz. It has now been through three full realizations (Hereafter ICRF1, ICRF2, and ICRF3) (Ma et al. (1998); Fey et al. (1998); Charlot et al. in progress). The third realization (ICRF3; Charlot et al. in progress) was recently adopted by the International Astronomical Union at the most recent general assembly as the standard reference frame.

ICRF1 (Ma et al., 1998) contained precise postions of 608 total sources from Very Long Baseline Interferometry observations between 1979 and 1995, with 212 of those sources being defining sources. The second realization of the ICRF (ICRF2, Fey et al., 1998) built on ICRF1 and included positions of 3,414 total sources with an updated list of 295 defining sources selected for their positional stability and to be as uniform as possible across the celestial sphere. ICRF3 includes positions of 4,536 sources calculated at multiple wavelengths, and an updated list of 303 defining sources.

Sources included in the ICRF are typically distant, compact radio loud quasars. It is important for an inertial reference frame that the sources used to make that reference frame are distant to minimize the corrections required for proper motion. It is also easier to get accurate positions from compact sources, and the brighter they appear at radio wavelengths, the easier it is to get an accurate position over a short integration. Bright sources are also easier to monitor for changes in structure which can affect the position measurement. Campaigns to monitor these changes have been carried out since 1995.

Many sources included in ICRF2 came from the Very Long Baseline Array (VLBA) Calibrator Survey (VCS, Beasley et al., 2002; Gordon et al., 2016) observations. The survey was designed to identify a large number of phase calibrators that can be used to calibrate future VLBA observations. Since the VCS was a source finding survey, most sources were observed a small number of times. The VCS added a large number of positions to the ICRF, but the small number of obser-

Lucas Hunt · Megan Johnson · Alan Fey
The United States Naval Observatory, 3450 Massachusetts Ave NW, Washington, D.C. 20392, United States

John Spitzak
Computational Physics, Inc. 8001 Braddock Road, Suite 210 Springfield, VA 22151-2110, United States

David Gordon
NVI Inc. 7257D Hanover Parkway Greenbelt, MD 20770, United States

(Correspondence: lucas.hunt@navy.mil)

vations made positional uncertainties relatively large compared to more frequently observed sources.

In 2016, the United States Naval Observatory (USNO) entered an agreement with the Long Baseline Observatory to contribute 50 % of the budget required to operate the VLBA in order to use 50 % of the time available for observation. With that time, USNO and the National Aeronautics and Space Administration Goddard Space Flight Center (NASA GSFC) have carried out a monitoring campaign of ICRF3 sources in order to get more accurate positions for many of the sources whose positions had only been measured once, and to image those sources to determine source structure and how that may impact the sources position. We also plan to make the calibrated data and the images publicly available for the astronomical and geodetic community to use. For example they could be used to correct source position, or find nearby calibrators for other astronomical studies.

This conference proceeding will discuss the imaging of the aforementioned monitoring campaign, and describe how the data will be accessible in the future.

2 Method

2.1 Observing setup

Data used for this report were obtained in 20 total observation sessions carried out at approximately twice a month between January 2017 to December 2017. Each observation session lasted 24 hours and observed approximately 280 sources with 3,628 total sources being observed over 12 months. The schedule was designed to do both astrometry and imaging, covering large portions of the sky and observing most sources multiple times in each session. This provided for a good map of the sky during each session and improved the UV coverage of the telescope to improve the imaging.

The observations were carried out at 2.3 GHz and 8.7 GHz simultaneously. These frequencies allow for accurate calibration of the Earth's ionosphere and allow for estimates of the spectral index of observed sources. The observations used 16 total sub-bands, four at 2.3 GHz and 12 at 8.7 GHz, with a 32 MHz bandwidth and 64 channels per sub-band. Observations were done with Right Circular Polarization only due to data transfer speed limits.

2.2 Calibration and Imaging

Calibration was done using the Astronomical Image Processing System (AIPS) (Wells, 1985) package. A basic calibration procedure was designed which makes corrections to digital correlator offsets, calibrates the amplitude, and corrects the phase. The full data set is then split into individual source files and written to disk.

The individual source files are then imported into the Difmap software package (Shepherd et al., 1994) to create the images. The images are created with an automated script that uses the clean algorithm (Högbom, 1974) and self-calibration to improve the quality of the image. At this point the images are inspected and any bad data points are removed. The imaging script is then run again to create a final image.

3 Results

We observed 3,628 sources over the 20 observations. Figure 1 shows nearly 3,000 sources were observed only once over the course of the year and only one source was included in every observation. Stronger sources with well-constrained positions were included in many observations to anchor the observations. The positions of these sources improved the overall accuracy of ICRF3 and the images will help us determine source structure corrections for the positions of all objects.

We were able to make images for ≈93 % of the sources at 8.7 GHz and ≈96 % of sources at 2.3 GHz. It is important to note that of the sources we created im-

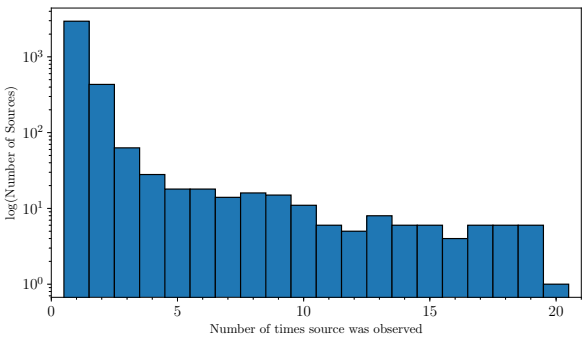

Fig. 1: This plot shows how often sources were visited over 20 observations

ages for, approximately 3 % of the images from each observation did not have enough data to create a high quality image. After the images are manually inspected and unreliable images are removed, the percentage of images created from each observation will likely be lower. Images of a selection of sources representing the variety in source shape and structure found in these observations can be seen in figures 2 and 3. There are also a number of observations that did not produce an image of the source likely due to very short observations that do not produce enough data to make an image. We have carried out longer observations of a small subset of sources that we were unable to image in this monitoring campaign in hopes of determining what caused the initial imaging failure. Calibration and imaging of data from these observations is currently underway.

USNO is responsible for preparing images of sources included in the ICRF. Traditionally we have made those images publicly available to the astronomical and geodetic communities through the Radio Reference Frame Image Database. We would like to announce that we are upgrading that website and changing the name to the Fundamental Reference Image Data Archive (FRIDA). The upgraded FRIDA website will include data from additional experiments including geodetic RDV experiments, and USNO VLBA survey experiments. The available images will go back to observations included in ICRF1 and include images of sources from S-band through Ka-band. The upgraded website will include data on each source including contour plots of the source, the calibrated data sets, and log files to show how the imaging was processed. The site will allow users to find sources based on specific search criteria, and download the data that might be useful to their research. We hope to make this available within the next year.

4 Conclusions and outlook

USNO has used time on the VLBA to monitor sources whose positions are included in ICRF3. The monitoring campaign has allowed us to make over 9,000 images of 3,628 sources and we will provide these to the astronomical and geodetic communities. We will make the images, calibrated data, and log files available on an updated, user friendly website to be known as FRIDA.

In the future, we plan to include the spectral index, the source structure index, and correction maps of each source in each observation within FRIDA. We also intend to update our calibration and imaging process to improve the reliability of our images while reducing the amount of manual input required to create a large number of images. We are also working towards implementing newer software that is more likely to be maintained in the future and add tools as needed to make calibration and imaging easier. Finally, we also plan to continue imaging the USNO monitoring experiments and to make that data publicly available as close to the observations as possible.

References

Beasley A J, Gordon D, Peck A B, et al. (2002) The VLBA Calibrator Survey – VCS1. *ApJS*, 141, 13–21, doi:10.1086/339806

Fey A L, Gordon D, Jacobs C S, et al. (2015) The second realization of the international celestial reference frame by very long baseline interferometry. *AJ*, 150(2), doi:10.1088/0004-6256/150/2/58

Gordon D, Jacobs C, Beasley A, et al. (2016) Second epoch VLBA calibrator survey observations: VCS-II. *AJ*, 151(6), 154, doi:10.3847/0004-6256/151/6/154

Ma C, Arias E F, Eubanks T M, et al. (1998) The International Celestial Reference Frame as Realized by Very Long Baseline Interferometry. *AJ*, 1, 516–546, doi:10.1086/300408

Högbom J A (1974) Aperture Synthesis with a Non-Regular Distribution of Interferometer Baselines. *A&A*, 15, 417

Shepherd M C, Pearson T J, Taylor G B (1994) DIFMAP: an interactive program for synthesis imaging. *Bull. Am. Astron. Soc.*, 26(2), 987–989

Wells D C (1985) NRAO'S Astronomical Image Processing System (AIPS). In: V. Di Gesù, L. Scarsi, P. Crane, J. H. Friedman, S. Levialdi (eds.) *Data Analysis in Astronomy*, Ettore Majorana International Science Series, vol 24. Springer, Boston, MA, 195–209, doi:10.1007/978-1-4615-9433-8_18

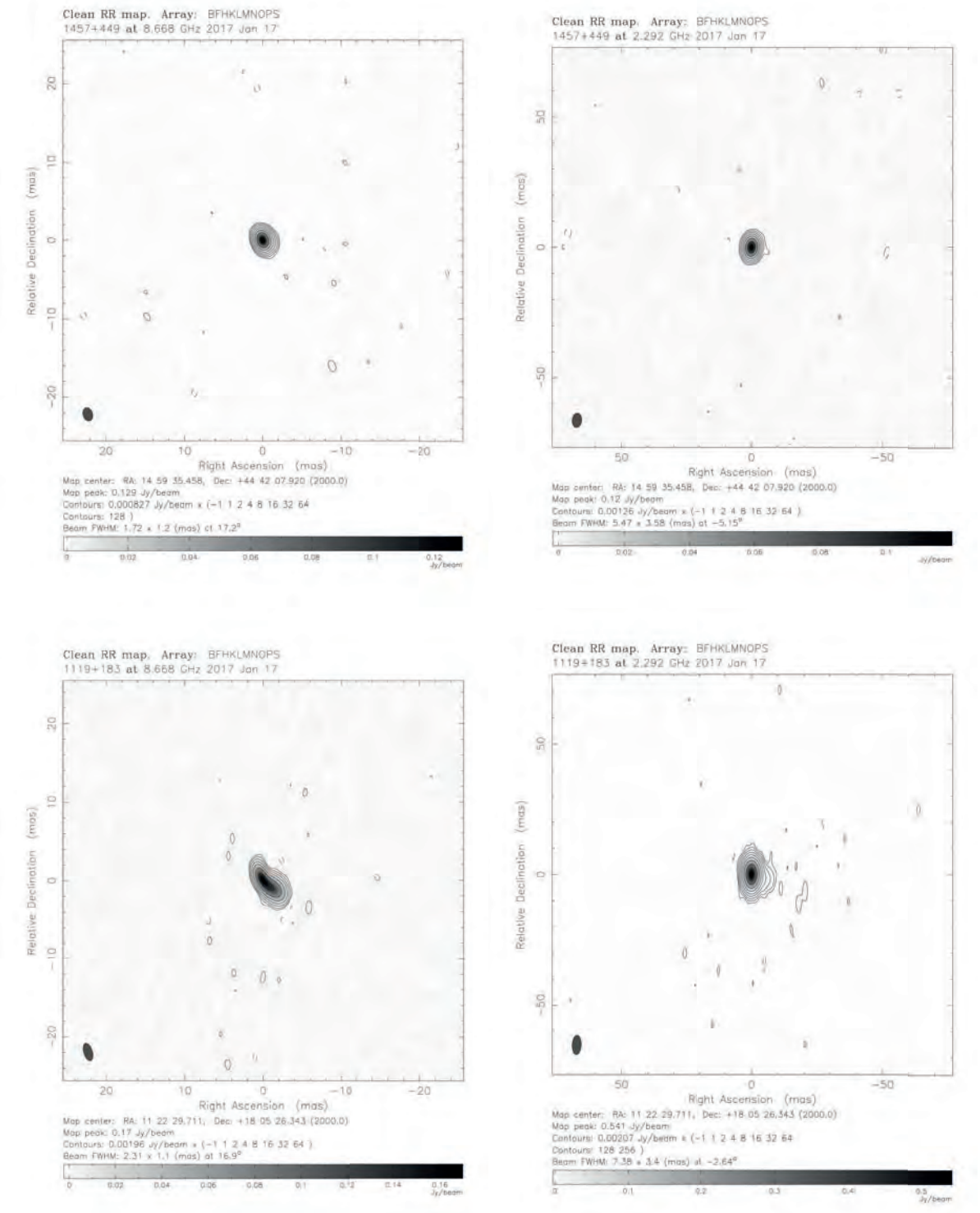

Fig. 2: Examples of images created from our observations displaying the variety in source structure. Images are of the same source at both 8.6 GHz and 2.3 GHz

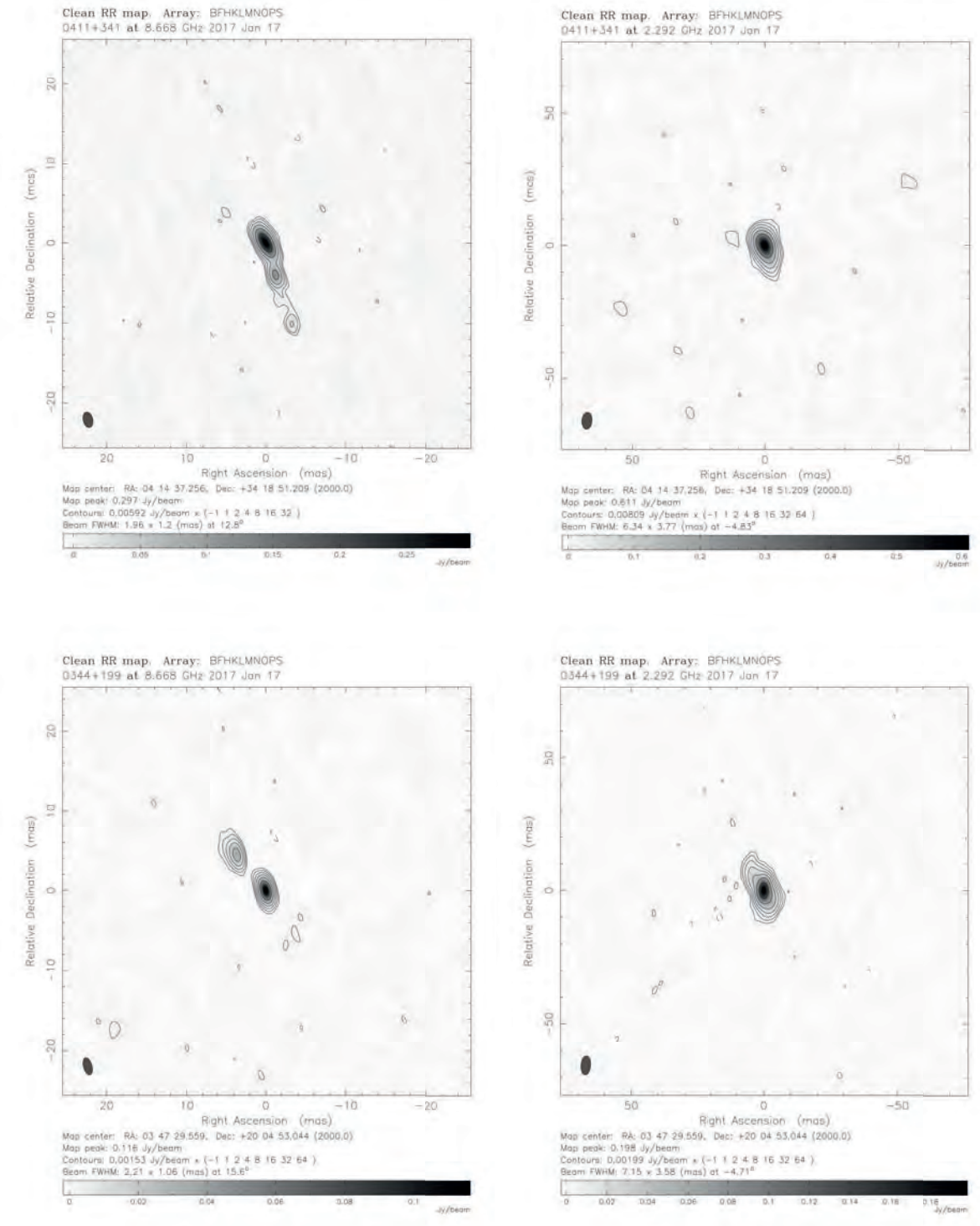

Fig. 3: Examples of images created from our observations displaying the variety in source structure. Images are of the same source at both 8.6 GHz and 2.3 GHz

The Second Version of the Bordeaux VLBI Image Database (BVID)

A. Collioud, P. Charlot

Abstract A new version of the Bordeaux VLBI Image Database (BVID) is now available online at the following address: **http://bvid.astrophy.u-bordeaux.fr**. This second version, with more than 6000 VLBI images and associated data (especially those that qualify the source structure, i.e. compactness and structure index information) has an enhanced clean and modern interface. New tools and functionalities are available to explore the database. Using these, we discuss the flux density and structure index distributions for the approximately 1300 ICRF3 sources comprised in the BVID.

Keywords Radiosource · Image · Database · Source structure · Reference frame

1 Context

The current Celestial Reference Frame, i.e. the ICRF3, is based on the VLBI positions of 4536 extragalactic radio sources, including 303 defining sources. The source position accuracy depends on a certain extent on the compactness of the sources: sources with point-like structure are more suited for building such reference frame. Unfortunately, most of the sources exhibit non point-like structures on VLBI scales (Fey and Charlot, 1997). In addition, those structures are frequency dependent and can also fluctuate over time. Assessing the source compactness and its evolution over time thus requires to monitor and image the sources on a regular basis. The International VLBI Service for Geodesy and Astrometry (IVS) organizes observing sessions adapted to such purpose: these are the bi-monthly "Research and Development with the VLBA" (RDV) sessions conducted since 1997 using a global VLBI network with the 10 VLBA stations and up to 10 other IVS stations.

The Laboratoire d'Astrophysique de Bordeaux, as an IVS Analysis Center, processes RDV sessions to produce images of the reference frame sources, in order to assess their structure. Such images, along with additional products (structure correction maps, visibility maps, flux density values, etc.), are provided to the community through the Bordeaux VLBI Image Database (BVID). Besides astrometric applications, the BVID images are also useful for astrophysical studies, i.e. for investigating source morphology and superluminal motions in those extragalactic radio sources. The BVID is complementary to the Radio Reference Frame Image Database (RRFID)[1] maintained at the United States Naval Observatory (USNO).

Section 2 presents details about the new version of the BVID: a description of the user interface and new tools, the products available and some general statistics. A brief study of the ICRF3 sources included in the BVID data is available in Section 3.

Arnaud Collioud · Patrick Charlot
Laboratoire d'Astrophysique de Bordeaux, Univ. Bordeaux, CNRS, B18N, allée Geoffroy Saint-Hilaire, FR-33615 Pessac, France

(Correspondence: arnaud.collioud@u-bordeaux.fr)

[1] Available at the address https://rorf.usno.navy.mil/RRFID/.

2 The new version of BVID

The BVID was initially developed in 2008 and officially presented during the 19^{th} EVGA Working Meeting held in Bordeaux in 2009 (Collioud and Charlot, 2009). In 2018, we decided to modernize the BVID and we started the development of the second version of the database, which is detailed in this section. The BVID may be found at the following address: **http://bvid.astrophy.u-bordeaux.fr**.

2.1 Interface

The new version of the BVID has an enhanced clean and modern interface (Figure 1), which is based on the currently available web technologies. The user interface is now more dynamic, and its design is adaptive to different devices, from mobile phones to computers with large screens. In addition to the public website, one can create a user account on the BVID in order to access additional functionalities and data, manage downloading information and check favourite sources or sessions.

2.2 Tools

The BVID database can be queried in several ways:

- source name: the name to search may be the IERS name (e.g. *0202+149*), the ICRF name (*ICRF J020450.4+151411*), any other popular name (*4C15.05*, *NRAO91*, etc.). It is also possible to specify partial names (*0202* or *4C1*). This form allows one to narrow down the search to a single source and then to display the corresponding page (Figure 2).
- session name or date, using the dedicated forms or the timeline of all available sessions.
- source coordinates, by specifying the Right Ascension/Declination and a search radius. Various coordinates formats are allowed (see the help next to the form).
- multi-criteria: one can specify one or several criteria on the source, the session or the data (flux density, structure index, etc.). The result is a list of individual records (i.e. the observation of one source during one session) that comply with all criteria, and which can be organized by data, source name or session name. This is a new functionality of the BVID version 2.

The new design of the interface is focused on improving the user experience: the search forms are simpler, the query results are as interactive as possible, all the plots are responsive, data tables can be filtered and exported easily, etc. In particular, we developed a tool called the "Skymap" which allows one to display the sky distribution of the BVID sources at a given frequency band (Figure 3). Each point is colour-coded based on the selected parameter (for example the flux density) and the size of each point represents the number of sessions available for the source. Two distributions are also available below the skymap: one for the number of sessions, and the other for the selected parameter. These distributions can be used to filter the sources. Finally, a list of the displayed sources is available at the bottom of the page.

2.3 Products

The BVID provides VLBI images (in graphical form and FITS format), the underlying source models (CLEAN components files) and the flux density values. From the source model, we calculate structure correction delays for all possible baseline lengths and orientations on Earth. These delays are then plotted in the structure correction maps, from which we derive the structure index. This index characterizes the magnitude of the structure corrections for the source (Fey and Charlot, 1997, 2000).
In the same way, we build visibility maps which display the values of the visibility amplitude (normalized to 1 using the total integrated flux density in the image) for all possible baseline lengths and orientations on Earth. Visibility maps are used to estimate the source compactness (Charlot, 2008). In addition, ancillary plots like the uv-plots or plots of the amplitude vs. uv-radius are available.
To access some products (e.g. the FITS files), it is mandatory to be logged in through a user account.

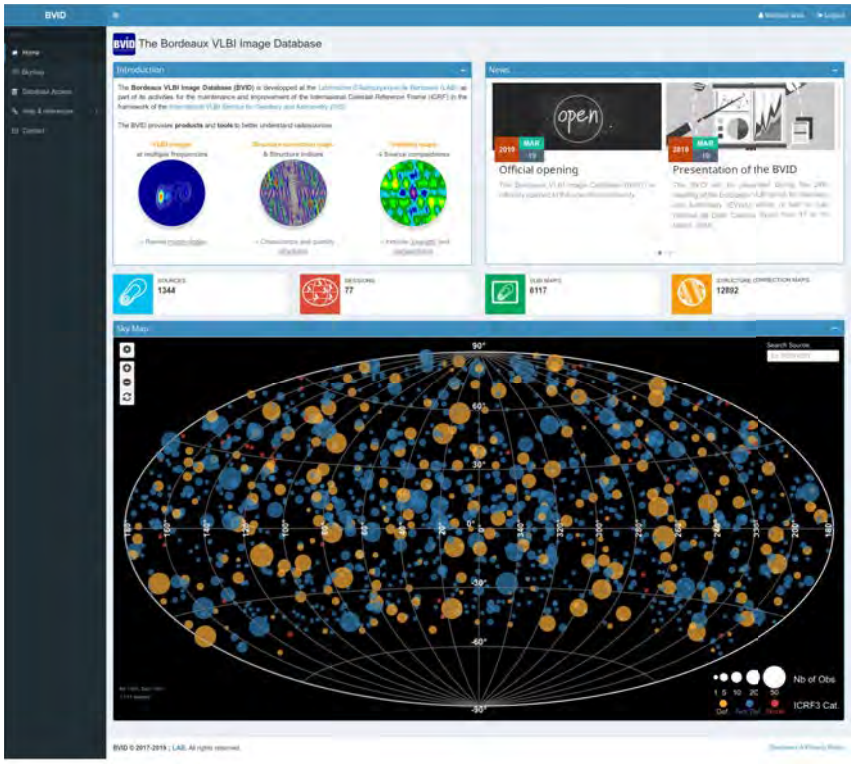

Fig. 1: The homepage of the BVID interface presents the latest news, some statistics related to the BVID content and the sky distribution of all the sources included in the BVID, colour-coded according to their ICRF3 category.

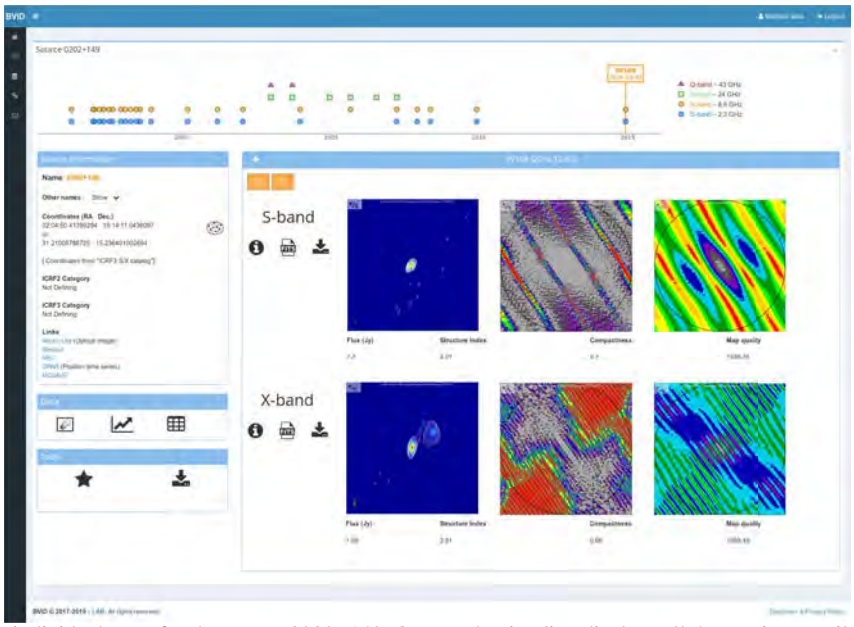

Fig. 2: View of the individual page for the source 0202+149. On top, the timeline displays all the sessions available for that source (here at four different frequencies). On the left-hand side, one can find general information about the source, the tools to visualize the corresponding data (images, time series, tables) and some general functionalities like the “Add to favourite” tool or the “Source Download Manager” tool which allows one to easily export and download the data and images available.

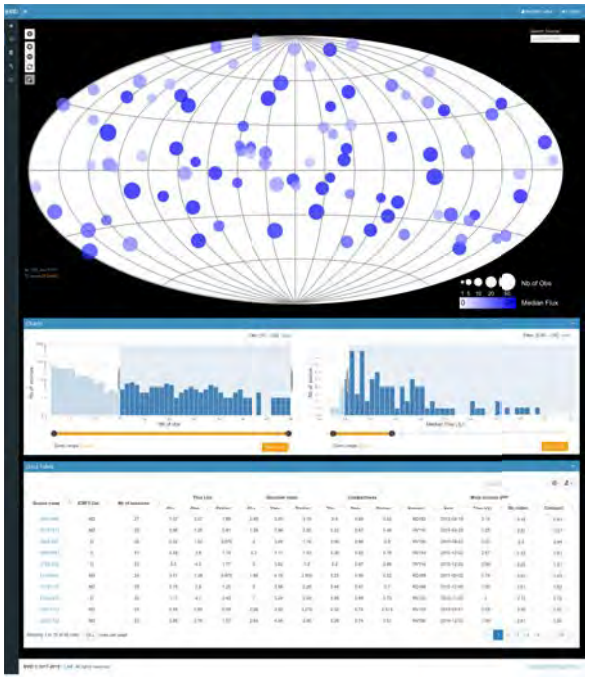

Fig. 3: View of the "Skymap" tool which allows one to display and filter sources based on the value of a given parameter (here the flux density at X-band). In this case, we selected the sources with a median flux density value larger or equal to 0.5 Jy and with a number of sessions larger than 15. This leads to a selection of 92 sources, which can be individually inspected on the sky distribution or in the source list.

2.4 Statistics

The BVID currently comprises 6117 VLBI maps produced in Bordeaux, along with 6775 links to images from the RRFID, for 1344 different sources.
A total of 77 sessions are online (59 RDV sessions, among which 34 were analysed in Bordeaux) at four frequency bands: S- (2.3 GHz), X- (8.6 GHz), K- (24 GHz) and Q-band (43 GHz). On average, there are 4 to 5 sessions available for each source at X/S band, with a minimum number of 1 and a maximum number of 49. The first session took place in 1994 and the last one available at present in 2016. The BVID thus covers a substantial time span of 22 years. Additionally, there are also 12892 structure correction maps available, along with the same number of structure indices, visibility maps and compactness values.

3 BVID and ICRF3

Among the 1344 sources comprised in the database, 1299 (97 %) are part of ICRF3. In other words, 29 % of the 4536 ICRF3 sources have an image available in the BVID. More precisely, the BVID comprises 246 of the 303 defining sources (81 %) and 1053 of the 4233 non-defining sources (25 %). Finally, 45 sources which originated from other VLBI projects are not part of ICRF3. Using the large amount of data in the BVID, we can derive and examine the distributions of the median flux density and structure index (SI) at S- and X-band for the defining and non-defining ICRF3 sources.

From the median flux distribution (Figure 4), we conclude that the defining sources are, on average, twice as strong as the non-defining sources at both bands, and that the flux density distributions are very similar for each ICRF3 category. By looking at the median SI distribution (Figure 5), we notice that the median SI for the defining sources is clearly lower than that for the non-defining sources. For example, at X-band, the median SI is 2.65 for the defining sources and 3.21 for the non-defining sources. This is consistent with the fact that the ICRF3 defining sources were chosen to be as compact as possible.

4 Conclusions

The Bordeaux VLBI Image Database (BVID) delivers images and information about the structure of the reference frame sources (i.e. structure index) through a refurbished clean and modern interface. It also provides dynamic tools to query and display the data. The BVID data may be used for astrometric applications, but is also useful for astrophysics, e.g. to study jet evolution. Finally, the BVID is available to host and disseminate images produced by other groups in the VLBI community with full credits to the author(s). If you are interested, please contact us.

Acknowledgements The authors are indebted to the *Observatoire Aquitain des Sciences de l'Univers (OASU)* for supporting the development of the second version of BVID. Arnaud Collioud is also grateful to the Programme National GRAM of CNRS/INSU with INP and IN2P3 co-funded by CNES for travel support to attend this conference.

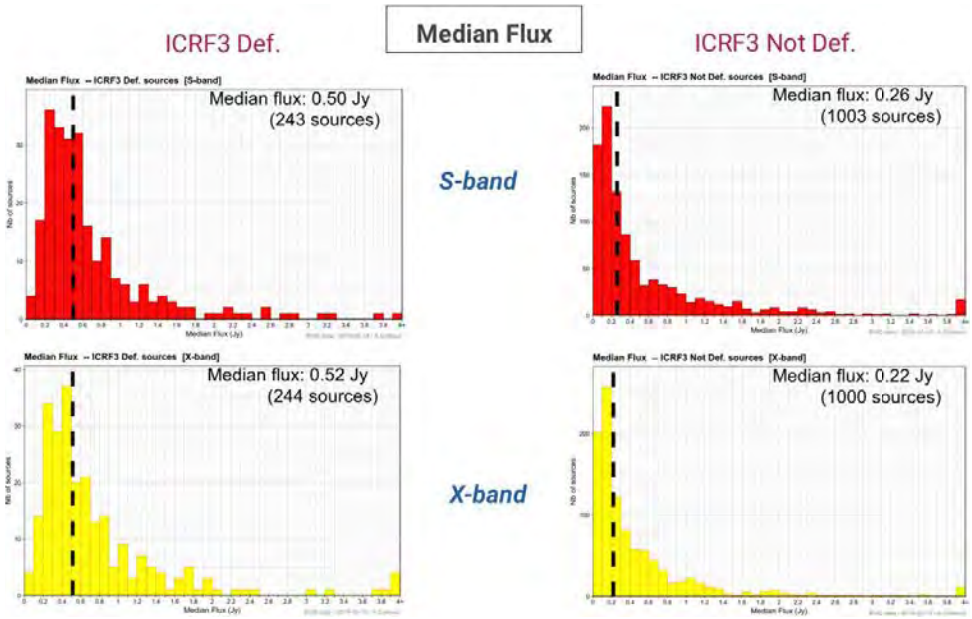

Fig. 4: Distribution of the median flux density for the ICRF3 defining (left-hand side) and non-defining (right-hand side) sources included in the BVID. The upper and lower panels are for S- and X-band, respectively. The dashed line in each histogram represents the median value of the distribution.

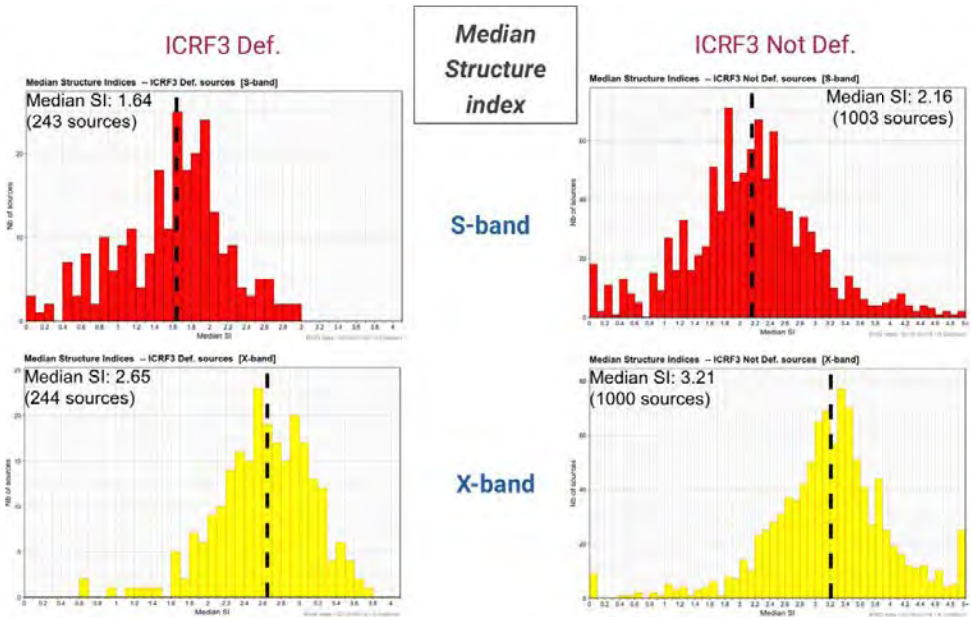

Fig. 5: Same as Figure 4 for the median structure index.

References

Charlot P (2008) Astrophysical Stability of Radio Sources and Implication for the Realization of the Next ICRF. In: A. Finkelstein, D. Behrend (eds.): *IVS 2008 General Meeting Proceedings*, 345–354

Collioud A, Charlot P (2009) The Bordeaux VLBI Image Database. *19th EVGA Working Meeting*, 19C

Fey A, Charlot P (1997) VLBA Observations of Radio Reference Frame Sources. II. Astrometric Suitability Based on Observed Structure. *ApJS*, 111, 95, doi:10.1086/313017

Fey A, Charlot P (2000) VLBA Observations of Radio Reference Frame Sources. III. Astrometric Suitability of an Additional 225 Sources. *ApJS*, 128, 17, doi:10.1086/313382

The Source Structure Effect in Broadband Observations

S. Bolotin, K. Baver, O. Bolotina, J. Gipson, D. Gordon, K. Le Bail, D. MacMillan

Abstract Analysis of the VGOS CONT17 observations showed that the broadband delays are sensitive to brightness distributions of radio sources. In this presentation we discuss the impact of source structures on the broadband observations and the application of source structure models (two points model, multiple points model, etc.) in data analysis.

Keywords VGOS · Broadband · Source structure

1 Introduction

The new VLBI Global Observing System (VGOS) made a great improvement in recent years and reached a level of maturity. The first publicly available VGOS observations were made at the end of 2017.

Starting from 1994, VLBI stations participated in specially designed continuous observation sessions. Such campaigns of VLBI observations, usually designated as CONT, are conducted roughly every three years.

The last CONT VLBI campaign, CONT17, was carried out with three independent networks of VLBI stations: the legacy, the VLBA and the VGOS networks. While the first two networks observed in the two standard S/X bands, the VGOS network used broad band (2 to 14 GHz) to acquire signals from radio sources. Also, to optimize the resources, the VGOS network observed only five continuous days recording only half of the possible channels to give a data rate of 8 Gbps instead of the possible 16 Gbps.

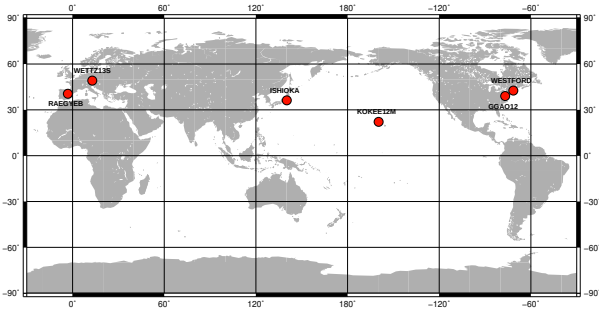

Fig. 1: VGOS stations participated in the CONT17 VLBI campaign.

As shown in Fig. 1, there were six VGOS stations that participated in CONT17 campaign: GGAO12M (Goddard, Maryland), ISHIOKA (Ishioka, Japan), KOKEE12M (Kokee Park, Hawaii), RAEGYEB (Yebes, Spain), WESTFORD (Westford, Massachusetts) and WETTZ13S (Wettzell, Germany). They started to observe on December 3 and finished on December 8, 2017.

The VGOS observations were correlated at the MIT Haystack Correlator. Preliminary data analysis was performed at Goddard Space Flight Center, NASA and the observations now are available for public access at the IVS data centers. Unfortunately, one of the VGOS stations, RAEGYEB, had a problem with

Sergei Bolotin · Karen D. Baver · John M. Gipson · David Gordon · K. le Bail · Daniel S. MacMillan
NVI, Inc., NASA GSFC Code 61A, 8800 Greenbelt Road, Greenbelt, Maryland 20771, USA

Olga Bolotina
5818 Pecking Stone St, New Market, Maryland 21774, USA

(Correspondence: sergei.bolotin@nasa.gov)

hardware during all but first sessions, so it was not included in the further analysis.

2 Data analysis

The observations were processed by vSolve software (Bolotin et al., 2016) using the embedded ECMAScript to treat data uniformly.

Baseline vectors, source positions and angles of nutation were estimated as local parameters (i.e., one estimate for each session). Station clock offsets, wet zenith delays, and atmospheric gradients were estimated as stochastic parameters using a random walk model.

The number of total (correlated), good (with the quality code greater than 4) and used (in data analysis) observations as well as weighted post-fit residuals are shown in the Tab. 1. In general, the WRMS of VGOS sessions are much better than for the legacy S/X sessions with the same parameterization, that are typically about 8ps.

Table 1: Numbers of total, good and used observations and post-fit residuals of the VGOS CONT17 sessions.

Session	N_{tot}	N_{good}	N_{used}	WRMS, ps
17DEC03VG	5999	3800	3533	1.8
17DEC04VG	5037	3775	3519	2.0
17DEC05VG	5833	3987	3765	2.1
17DEC06VG	5166	3461	3224	1.9
17DEC07VG	6043	4168	3937	2.1

During data analysis abnormal distributions of post-fit residuals for the radio source 0552+398 were noticed. In Fig. 2, an example of such a distribution in the session 17DEC04VG is shown for baselines of three stations, GGAO, ISHIOKA and KOKEE12M. The weighted post-fit residuals of the observations of this radio source are 12ps which is several times greater than the overall residuals of the session.

The residuals of the source 0552+398 have a similar pattern for all five broadband sessions. The "standard" data editing procedure would consider these residuals as outliers and they would be removed from the data analysis. However, the behavior of the residuals suggests that there is a systematic effect which was not taken into account during data analysis.

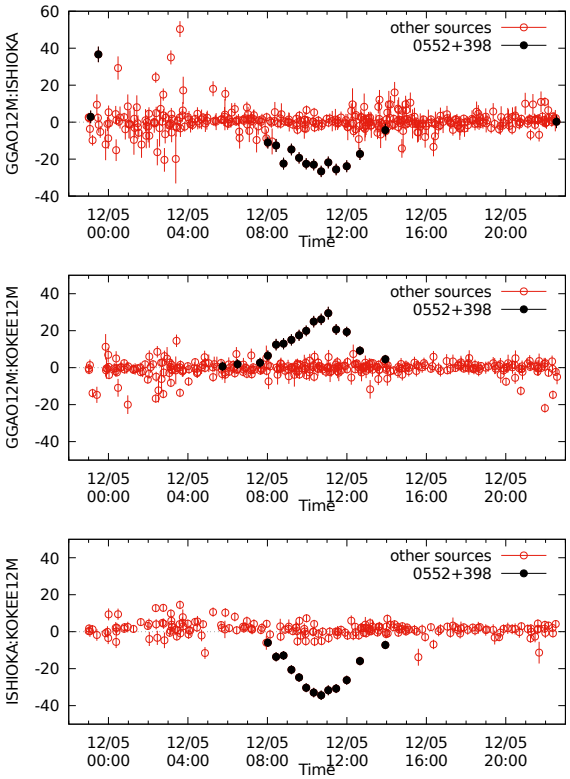

Fig. 2: Group delay residuals (ps) for the baselines of GGAO, ISHIOKA and KOKEE12M. Residuals of the radio source 0552+398 are plotted with filled circles, open circles represent all other radio sources.

3 Modeling the source structure

The first assumption of the nature of the systematic effect was influence of source structure on the observed group delays. Previous work on the source structure effect in geodetic VLBI observations, Thomas (1980) and Charlot (1990), discussed point like models of source structure and how the models affect group delays and delay rates.

In general, the group delay contribution due to a brightness distribution $I(\mathbf{P},\omega,t)$ of a radio source as a function of coordinates $\mathbf{P}$, circular frequency $\omega = 2\pi f$ and time t can be expressed as

$$\tau_s = \frac{Z_s \frac{\partial Z_c}{\partial \omega} - Z_c \frac{\partial Z_s}{\partial \omega}}{{Z_s}^2 + {Z_c}^2}$$

where

$$Z_c = \iint I(\mathbf{P},\omega,t)\cos(\omega\frac{\mathbf{b}\cdot\mathbf{P}}{c})d\Omega$$

$$Z_s = \iint I(\mathbf{P},\omega,t)\sin(\omega\frac{\mathbf{b}\cdot\mathbf{P}}{c})d\Omega$$

and $\mathbf{b}$ is a baseline vector.

First, we investigated a two-point source structure model. This model consists of two close points, where the brightness distribution on the sky is (assuming there is no frequency and time dependence):

$$I(\mathbf{P}) = g_1\delta(\mathbf{P}-\mathbf{P_1}) + g_2\delta(\mathbf{P}-\mathbf{P_2})$$

If we choose the origin of structure coordinates at the brightest point, $\mathbf{P_1} = \mathbf{0}$, and introduce a ratio of amplitudes of the components $K = g_2/g_1$, then the correction to the group delay will be

$$\tau_s = -\frac{R}{f}\frac{K(K+\cos(2\pi R))}{1+K^2+2K\cos(2\pi R)}$$

where the scalar product

$$R = \frac{\mathbf{b}}{\lambda}\cdot\mathbf{P_2}$$

and λ is the wave length.

The expression for τ_s is simple and can be used in least squares estimation. The model has two parameters, the scalar K, a ratio of amplitudes of the components and a vector $\mathbf{P_2}$, a distance of the second component from the brightest one. However, the model is highly non-linear and before using the least squares estimation we need to find appropriate *a priori* values for K and $\mathbf{P_2}$. To do this we ran a set of estimations of the ratio K for a fixed position $\mathbf{P_2}$ and searched for minimal post-fit residuals for the source 0552+398 as a function of $\mathbf{P_2}$. The estimations were done in the same way as described in the Sect. 2, except that K was added to the estimated parameters.

Fig. 3 displays changes of the weighted post-fit residuals of the source 0552+398 for each estimation. The lighter areas in the figure correspond to smaller residuals. There are several areas that could possibly be used as *a priori* parameters. Only one of them yields parameter estimates that are physically meaningful, i.e., the value of ratio of components is $0 < K < 1$ and the process of iterative estimation (when estimates are used as *a priori* values for the next iteration) converges.

After the initial *a priori* values of the parameters were found, the data analysis of all five VGOS CONT17 sessions were performed and the parameters

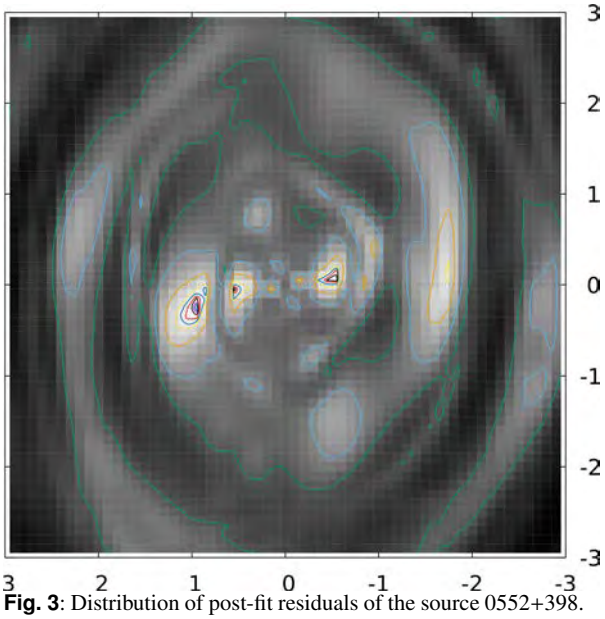

Fig. 3: Distribution of post-fit residuals of the source 0552+398. The darker color corresponds the bigger value of the residuals. The x-coordinate (in direction of the right ascension) and y-coordinate (in direction of the declination) correspond to the fixed position of the second component.

Table 2: Results of estimation the double-point source structure model parameters for the source 0552+398 from the VGOS CONT17 sessions.

Session	Model parameters					
	K		x, μas		y, μas	
	value	σ	value	σ	value	σ
17DEC03VG	0.385	0.006	900	5	−128	8
17DEC04VG	0.352	0.012	930	10	−223	20
17DEC05VG	0.390	0.007	900	5	−105	10
17DEC06VG	0.384	0.007	905	5	−98	10
17DEC07VG	0.378	0.007	911	5	−155	9

of the model were estimated along with the other parameters. Tab. 2 shows values and uncertainties of the estimated ratio of the amplitudes and relative position of the second component for each session.

Tab. 3 is a statistical summary of the solutions: number of observations (potentially usable and used in a solution) and WRMS for the source 0552+398. The WRMS are shown for two cases, when the model was not applied ("Model:off") and when the model parameters were estimated ("Model:on").

As one can see, the results of estimation of the double-point source structure model for the source 0552+398 are nearly the same for all five VGOS sessions. Applying the model reduces the residuals of this source to the level of the overall post-fit residuals of a

Table 3: Statistical information on estimation of the parameters of the double-point source structure model from the VGOS CONT17 sessions: the numbers of potentially usable and used in data analysis observations of the source 0552+398 and the weighted post-fit residuals of the source without and with the model.

Session	Number of obs.		0552+398 WRMS, ps	
	Usable	Used	Model:off	Model:on
17DEC03VG	134	132	13.6	2.8
17DEC04VG	118	118	13.5	2.3
17DEC05VG	138	137	13.8	2.6
17DEC06VG	90	90	15.2	3.2
17DEC07VG	149	149	13.3	2.8

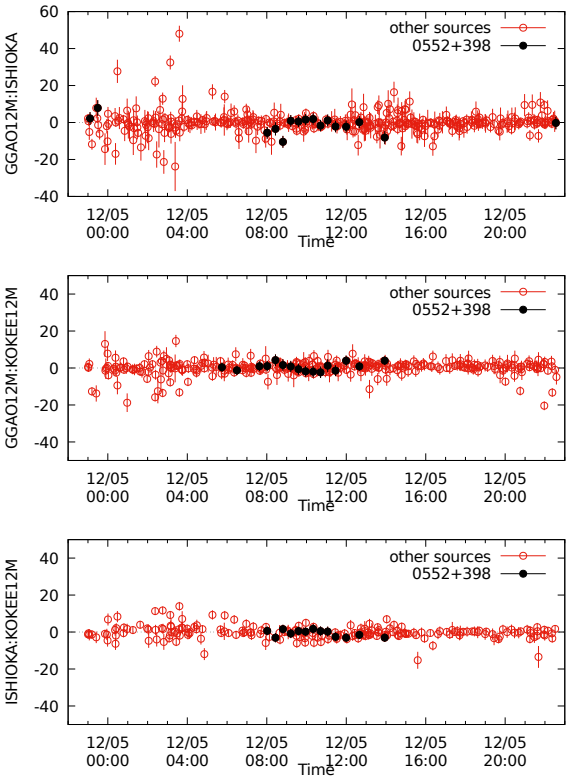

Fig. 4: Group delay residuals (ps) for the baselines of GGAO, ISHIOKA and KOKEE12M. Residuals of the radio source 0552+398 are plotted with filled circles, open circles represent all other radio sources. The double-point source structure model has been applied.

session. In Fig. 4, the post-fit residuals of the baselines of stations GGAO, ISHIOKA and KOKEE12M are plotted for the case when the source structure model has been applied. In contrast to Fig. 2, the systematic effect in the source residuals is gone.

Further investigation of VGOS CONT17 observations shows that many sources reveal source structure effects, although the changes of post-fit residuals for them are much smaller than for the source 0552+398. All radio sources with few exceptions that have relatively big declination and were frequently observed show improvement of the residuals after applying the source structure model.

The point-like model of source structure can be extended to an arbitrary number of points, N. In this case the brightness distribution can be written as

$$I(\mathbf{P}) = g_0\delta(\mathbf{P}-\mathbf{P_0}) + \sum_{i=1}^{N} g_i\delta(\mathbf{P}-\mathbf{P_i})$$

We assume that the coordinate system of source structure is centered at the position of the brightest component, $\mathbf{P_0}$. Also, we express the brightness of each component by the ratio to the brightness of the central component, $k_i = \frac{g_i}{g_0}$, where $g_i < g_0$, and use a scalar product $R_i = \frac{\mathbf{b}}{\lambda}\mathbf{P_i}$. Then, the source structure effect in group delay will be

$$\tau_s = -\frac{1}{f}\frac{A+B}{Z^2}$$

where

$$A = \sum_{i=1}^{N} k_i R_i (k_i + \cos(2\pi R_i))$$

$$B = \sum_{i=1}^{N-1}\sum_{j=i+1}^{N} k_i k_j (R_i + R_j)\cos(2\pi(R_i - R_j))$$

$$Z^2 = 1 + \sum_{i=1}^{N} k_i{}^2 + 2[\sum_{i=1}^{N} k_i \cos(2\pi R_i) + \sum_{i=1}^{N-1}\sum_{j=i+1}^{N} k_i k_j \cos(2\pi(R_i - R_j))]$$

The procedure of searching the initial values for the multi point source structure model is similar to the two-point model. First, we search for the second component; if it is found, we estimate model parameters from data analysis. After that we fix the obtained parameters for the second component and search for a third one. If searching for the *a priori* reveals physically meaningful values, we can use them in data analysis and estimate

Table 4: Results of estimation of a three-point source structure model for the source 2229+695 in session 17DEC03VG.

Idx	Model parameters					
	K		x, μas		y, μas	
	value	σ	value	σ	value	σ
1	0.357	0.02	−750	20	−120	20
2	0.157	0.03	550	80	−160	60

the model parameters of the second and third component.

As an example, Tab. 4 shows the result of estimation of the multiple point source structure model in the case of $N = 3$ for radio source 2229+695. As one can see, the standard deviations are significantly bigger than for the two-point model. By increasing the number of VGOS stations, we expect that components of multiple point models will be better resolved.

Fig. 5 illustrates variations of the post-fit residuals found in searching for the second and third components of the multiple point model.

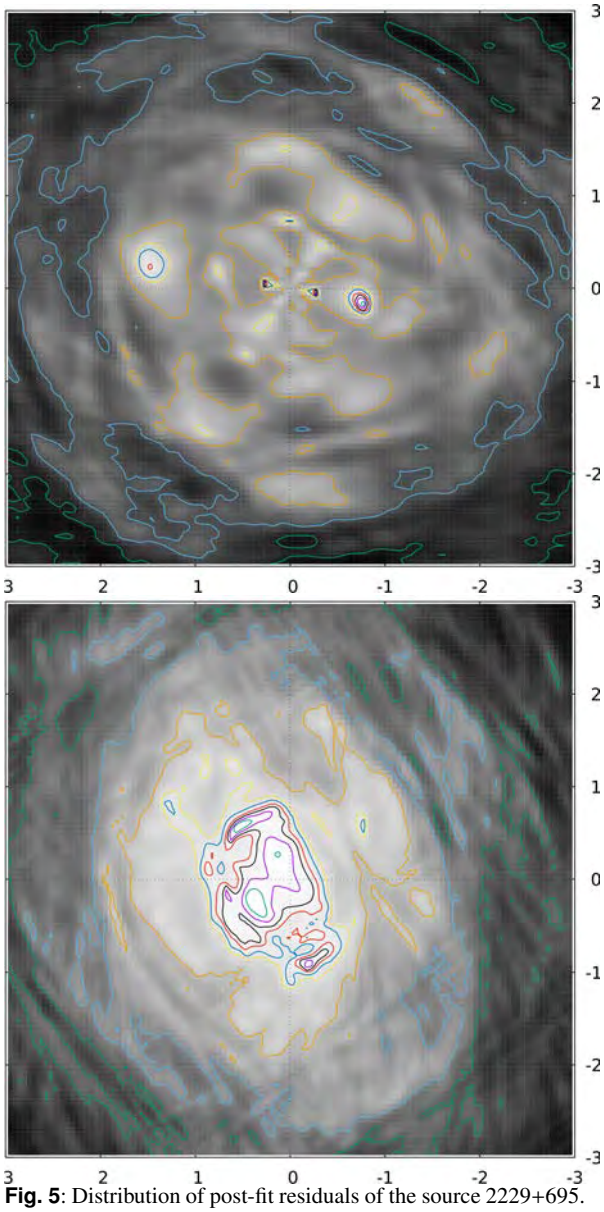

Fig. 5: Distribution of post-fit residuals of the source 2229+695. On the top: searching for the *a priori* values of the second component of the model. On the bottom: searching the third component.

4 Conclusions

Data analysis of the VGOS CONT17 sessions shows a significant increase of the accuracy of VLBI observations compared with legacy S/X. One consequence of this is the detection of source structure in the group delays. This effect degrades determination of source positions and EOP; however, it can be taken into account with the simple point-like source structure models.

References

Bolotin S, Baver K, Gipson J, *et al.* (2016) Transition to the vgosDb format. In: D. Behrend, K. D. Baver, K. L. Armstrong (eds.): *IVS 2016 General Meeting Proceedings*, NASA/CP-2016-219016, 222–224

Charlot P (1990) Radio-source structure in astrometric and geodetic very long baseline interferometry. *AJ*, 99, 1309–1326, doi:10.1086/115419

Niell A., Barrett J, Burns A, *et al.* (2018) Demonstration of a Broadband Very Long Baseline Interferometer System: A New Instrument for High-Precision Space Geodesy. *Radio Sci*, 63, 1263-1291, doi:10.1029/2018rs006617

Thomas J B (1980) An Analysis of Source Structure Effects in Radio Interferometry Measurements. *NASA-JPL Publ.* 80–84

Source Structure Effects in Next-generation VLBI Observations

S. Salarpour, S. Shabala, L. McCallum, J. McCallum, L. Chin Chuan

Abstract Next-generation VLBI (VGOS) may struggle with the source structure issue to determine accurate celestial and terrestrial reference frames. Observations over a wide bandwidth of 2 – 14 GHz will be influenced by source structure which is highly frequency dependent. Moreover, the structure of a quasar often evolves on timescales of months. To calculate visibility phase changes over the broadband frequency range, the source structure module of the Vienna VLBI Software (VieVS) is extended. So far, we have focused on a single source (J0136+4751) to obtain these effects as a function of frequency and time for varying geometries. By using this approach and simulated VGOS networks, we can estimate the number of observations within a session that may be affected by source structure on the dependence of the source's evolution over time, as well as baseline length and observing geometry.

Keywords Quasar · VLBI · Source Structure · VGOS

1 Introduction

Very Long Baseline Interferometry (VLBI) is a space geodetic technique used to define terrestrial and celestial reference frames by measuring the stations and quasars positions respectively. VLBI geodesy requires to observe bright and compact (ideally point-like) sources, which are stable both in time and frequency. These requirements are challenging. Quasars have often extended structure on milliarcsecond scales e.g. Charlot (1990); Fey et al. (1996). The structure dependency on time and frequency put restrictions on source positions and consequently on VLBI observations (Plank et al., 2016; Shabala et al., 2014; Tornatore & Charlot, 2007). Although the source structure effects are usually considered as systematic errors in legacy VLBI at the millimetre level (Shabala et al., 2015), these effects could be a hurdle for the next generation VLBI system.

The VLBI Global Observing System (VGOS) is based on finding broadband delay. In this system, quasars are observed with 12-m radio telescopes in four frequency bands between 2–14 GHz range (Niell et al. , 2007). The broadband delay calculation will be difficult in the presence of quasar structure that prevents phase connectivity through four VGOS bands (Petrachenko et al., 2016). So far, some work has been done to address and determine the source structure effects in broadband frequency e.g. Niell (2006a,b).

In this research, we investigate the time evolution of a source by looking at the time series of total flux density and structure index. By developing Niell's idea (Niell, 2006a,b), we construct a frequency-dependent source model using real images at different frequencies. The current source structure module of VieVS (Böhm et al., 2018; Shabala et al., 2015) is used to simulate real observations in the presence of source structure. We also estimate the source structure effects in future VGOS network observations. This research will help to improve the scheduling of observations, based on the combination of broadband source structure and geometry.

Simin Salarpour · Stanislav Shabala · Lucia McCallum · Jamie McCallum · Lim Chin Chuan
University of Tasmania, School of Natural Sciences, Private Bag 37, Hobart, AU-7001 Australia

(Correspondence: simin.salarpour@utas.edu.au)

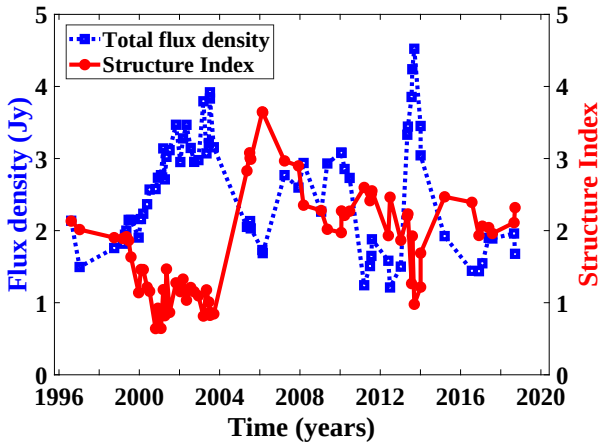

Fig. 1: Total flux density and structure index time series at 8.6 GHz, source J0136+4751.

2 Method

2.1 Image processing

After a search among well-observed ICRF2 sources and the Astrogeo (*http://astrogeo.org/*) image database, J0136+4751(0133+476) was chosen. J0136+4751 is a variable source which is frequently observed and often has structure. For this source, there were 59, 71, and 39 images in S (2.3 GHz), X (8.6 GHz), and U (15.4 GHz) bands respectively available. We took advantage of automated scripts to find a functional source model based on Gaussian fitting at each epoch and frequency. The automated scripts provide flux density, size, and position parameters for each component of a source, which are required to construct the source model and evolution over time at different frequencies. Figure 1 shows source structure and total flux density evolution over time which have been obtained from automated scripts. We note that the total flux densities obtained from the fitted code are in good agreement with the total flux densities extracted from the image header. In this case, an average of 89 % of integrated flux density is recovered.

2.1.1 Time evolution

Figure 1 shows the time variability of the source. There are two main reasons to see fluctuations in total flux density: changes in beaming (Lister et al., 2009), and intrinsic changes in jet power (Cao, 2003). The unresolved part of the jet (core component) is the innermost and optically thick region. When the source ejects new components and the jet becomes optically thin, it is known as a flaring event. This event can be recognized from the peak in time series of total flux density (Blandford et al., 1979). The core component is getting brighter and at its most compact during flare in the total flux density. Changes in the source structure can be seen from variations of the measured structure index which is anti-correlated with the fluctuations of total flux density (Shabala et al., 2017). In Figure 1, between 2002 and 2004 we expect a flare and as a result, a compact source compared to 2006 when probably the source is more extended. In the next section, these structure changes will show their impact on multi-frequency simulations of VGOS observations.

2.2 Source model

The Gaussian fitting is applied to the images to find source components and their positions using automated scripts. Our frequency dependent source model is suggested by Niell (2006a,b). This model is defined by flux density, size, and position parameter of each source component as well as spectral indices below and above the turnover frequency. The spectral indices have been obtained based on the flux densities at different frequencies and they are time-dependent parameters. The turnover frequency of the core component occurs at higher frequency whereas for other extended components, it can be observed at lower frequencies. Left plot in Figure 2 is an example of our source model for one time epoch. We have used X-band images as proxy for the whole VGOS frequency range (Salarpour et al., 2018). The measured visibility phase based on this model is highly dependent on time and frequency. Along with this time and frequency dependency, geometric variations also have a significant impact (Figure 2, right plot).

The visibility phase is a function of baseline length and projected jet direction. The structure effect of an extended source on visibility phase is different for various baseline angles (Figure 2 (right), solid line). There is no structure contribution to the visibility phase when the baseline is perpendicular to the jet direction (Charlot, 1990; Shabala et al., 2015). For other jet angles,

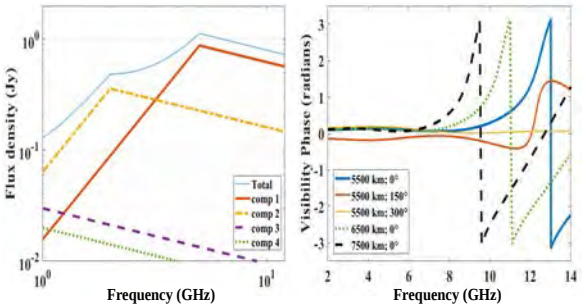

Fig. 2: Left: source model with four jet components. Right: visibility phase changes with respect to different geometry over a broad bandwidth. Solid lines (yellow, red, and blue) are the same baseline length in different angles; dot lines (green and black) are different baseline lengths with the same angle as blue solid line.

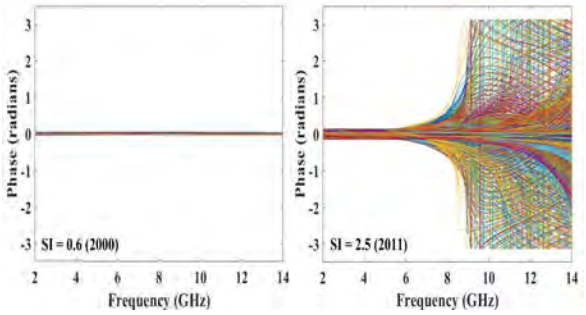

Fig. 3: Visibility phase obtained from the source model over a broad bandwidth (2 to 14 GHz). Right: J0136+4751 with SI = 2.5 in 2011; Left: the source with SI = 0.6 in 2000. Each line represents one observation of the schedule.

we expect to see quasar structure effect. Figure 2 (right plot, dotted line) also shows that rapid phase changes related to source structure effect are detectable at lower frequencies for longer baselines.

2.3 VieVS simulation

For more realistic results and predicting future experiments, simulation tools are used. The schedule is simulated as a 24-hour session using the VieSched++ (Vienna VLBI Scheduling Centre) (Schartner and Böhm, 2019), an improved standalone scheduling tool derived as part of the VieVS. Standard catalog files from the SKED website are used. The source 0133-476 (J0136+4751) is selected from the VieSched++ graphical user interface to be observed with 10 stations which are, or expected to be involved in the VGOS experiments. The selected stations are GGAO12M, HART15M, ISHIOKA, KATH12M, KOKEE, NYALES20, ONSA13SW, RAEGYEB, WETTZ13N, and YARRA12M, where each station is scheduled to observe the source once every 10 minutes. Since only one source is selected in the schedule, fill-in mode and subnetting do not influence the schedule output. For this test network, we found 144 scans and 2460 observations to this single source. The visibility phase for each observation and baseline are calculated by using the source structure module of VieVS (Shabala et al., 2015).

3 Results

There are two questions here: 1. How does the source structure affect a 24-hour observation session for variable structure over time? 2. What is the baseline geometry role in source structure effect detection? In the following, we will examine these two issues.

3.1 Effects of changing source structure

The visibility phase derived from the model indicates sudden changes over broad bandwidth at those epochs in which the source tends to show more structure. By contrast, the phase changes are well-behaved when the source is more compact. As an example, Figure 3 demonstrates phase changes from 2 GHz to 14 GHz for two different epochs that J0136+4751 has different structure indices: an SI of 0.6 corresponds to a compact source, while SI = 2.5 is a source with extended structure. In this figure, each colour line stands for one observation in a 24-hour session. While in compact source times no rapid changes were detected (3, left plot), visibility phase was varied quick by the extended structure (3, right plot). We assume a flat spectrum source, i.e. the source structure appears the same at all frequencies. Charlot (1990) showed that the source structure will have a contribution to the group delay when the observed phase varies with frequency. Such rapid phase changes (phase wraps) are a challenge for VGOS that aims to observe sources in four frequency bands spread over 2 to 14 GHz. This problem is exacer-

bated when attempting to connect phases across VGOS bands. Phase wraps can even prevent phase connectivity.

3.2 Baseline effects

According to the results for SI = 2.5 (2011), in 24-hour session observations with the selected VGOS network, baselines with the length shorter than 8000 km are not affected by adopted source structure. Figure 4 shows the affected observations percentage (Red diamonds) and phase wraps distribution in each baseline (Blue boxes). In each blue box, which represents the phase wraps distribution, the central mark is the median value while the bottom and top edges are 25th and 75th percentiles. As an example, the phase wrap distribution for baseline 9500 Km (KOKEE-YARRA) is from 12 to 13 GHz and the affected observations fraction is 20 %. In this Figure, one sees, the fraction of affected observations is increasing with baseline length. This is due to a better resolution of longer baselines (Middelberg & Bach, 2008). At the same time, it is shown that the point of phase wrap occurrence moves towards lower frequencies. The distribution of these frequencies, as shown in Figure 4, is broader for longer baselines. This would make predicting the VGOS frequency band most affected by source structure very challenging- for example, it will highly depend on knowing the source structure to high precision. The percentage of troublesome observations sometimes exceeds 50 percent in some baselines which is not good at all for VGOS. It should be kept in mind that due to the Earth rotation, the projected jet angle is changed for a specific baseline (Plank et al., 2015). This causes all observations of a source by that baseline not to be equally affected by the source structure.

4 Conclusions and outlook

We used source images to study the flux density variability of ICRF2 quasars. Most sources have milliarcsecond level of structure, and this structure often evolves with time. Besides the time variability, the quasar structure is highly dependent on frequency. This is a challenge for VGOS observations which aim to observe in wide range frequency. We made a frequency dependent source model of J0136+4751 to study source structure effects on broad bandwidth observations. We show that source structure can cause rapid changes in visibility phase, creating a problem for phase connectivity through four VGOS bands and making it challenging to find a group delay. Using

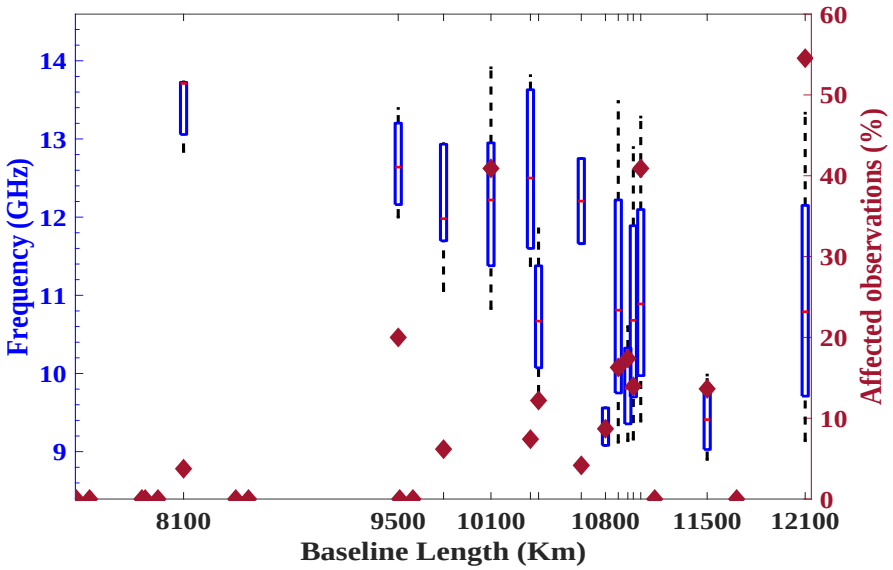

Fig. 4: Phase wraps distribution and percentage per baseline for a 24-hour session observing J0136+4751 in 2011 (SI = 2.5).

the VieVS structure module helps us to find quasar structure effects on visibility phase for a selected VGOS network. The observed effects of an extended source in various baselines at broad bandwidth are different due to the baselines' geometry. In a fictitious VGOS schedule of a global network observing a single source over 24 hours, a significant fraction (up to 50 %) of longer baselines can be affected due to better source structure resolution.

Applying our approach to more well-observed sources as well as improving the fitting routines will provide more precise frequency-dependent models to investigate source structure effects. While up to now our broadband structure investigations mostly rely on images at X band, we would like to add-in also information from other frequencies if available. We hope to connect our theoretical findings with future UTAS VGOS observations. We also hope that the contribution of this work and more studies concerning careful source selection, network geometry and observing time may help to avoid source structure effects in the next generation geodetic VLBI observations.

References

Blandford R, Königl A (1979) Relativistic jets as compact radio sources. *ApJ*, 232

Böhm J, Böhm S, Boisits J, et al. (2018) Vienna VLBI and satellite software (VieVS) for geodesy and astrometry. *PASP*, 130(986), 044503

Cao X (2003) Jet formation in BL Lacertae objects with different accretion modes. *ApJ*, 599(1), 147

Charlot P (1990) Radio-source structure in astrometric and geodetic very long baseline interferometry. *AJ*, 99, 1309

Fey A L, Clegg A W, Fomalont E B (1996) VLBA Observations of Radio Reference Frame Sources. I. *ApJS*, 105, 299

Kovalev Y Y, Ros E, Savolainen T et al. (2009) MOJAVE: Monitoring of jets in active galactic nuclei with VLBA experiments. V. multiepoch VLBA images. *AJ*, 137(3), 3718

Middelberg E, Bach U (2008) High resolution radio astronomy using very long baseline interferometry. *Rep. Prog. Phys.*, 71(6), 066901

Niell A (2006a) Source Structure Simulation. *IVS Memorandum 2006-017v01*, ivscc.gsfc.nasa.gov/publications/memos/ivs-2006-017v01.pdf

Niell A (2006b) Source Structure Examples. *IVS Memorandum 2006-018v01*, ivscc.gsfc.nasa.gov/publications/memos/ivs-2006-018v01.pdf

Niell A, Whitney A, Petrachenko W, et al. (2007) VLBI2010: A Vision for future geodetic VLBI. *Dynamic Planet*, 757–759

Plank L, Lovell J, Shabala S, et al. (2015) Challenges for geodetic VLBI in the southern hemisphere. *ASR*, 56, 304

Plank L, Shabala S, McCallum J, et al. (2016) On the estimation of a celestial reference frame in the presence of source structure. *MNRAS*, 455, 343

Petrachenko B, Charlot P, Collioud A, et al. (2016) VGOS Source Selection Criteria. In: D. Behrend, K. D. Baver, K. L. Armstrong (eds.): *IVS 2016 General Meeting Proceedings*, NASA/CP-2016-219016, 82–86

Salarpour S, McCallum L, Shabala S, et al. (2018) Investigating quasar structure in VGOS with simulations. In: K. L. Armstrong, K. D. Baver, D. Behrend (eds.): *IVS 2018 General Meeting Proceedings*, NASA/CP-2019-219039, 88–92

Schartner M, Böhm J (2019) VieSched++: A New VLBI Scheduling Software for Geodesy and Astrometry. *PASP*, 131(1002), 084501

Shabala S, Rogers J, McCallum J, et al. (2014) The effects of frequency-dependent quasar variability on the celestial reference frame. *J Geod*, 88(6), 575

Shabala S, McCallum J, Plank L, et al. (2015) Simulating the effects of quasar structure on parameters from geodetic VLBI. *J Geod* , 89(9), 873

Shabala S, Plank L, Schaap R, et al. (2017) The effects of simulated and observed quasar structure on the VLBI reference frame. *IAG Symposia*, 146, 191–199

Tornatore V, Charlot P (2007) The impact of radio source structure on European geodetic VLBI measurements. *J Geod*, 81, 469

VLBI Analyses at the National Geographic Institute of Spain (IGN)

E. Azcue, V. Puente, S. Garcia-Espada, Y. Gómez Espada, M. Valdés

Abstract Beyond taking part over the last decades through the participation of the Astronomical Center of Yebes on VLBI observations and the development of the RAEGE project for an Atlantic Network of Geodynamical and Space Stations, the National Geographic Institute of Spain (IGN) is committed to expand its contribution to geodetic VLBI in terms of data analysis. An analysis team has been working on the data analysis with different software packages for the last two years. In this work, the results of the last processing campaigns using different software packages are presented, as well as several comparisons in order to test the solution.

Keywords Analysis · VieVS Software · VLBI · Where Software

1 Introduction

Over the last years, the National Geographic Institute of Spain (IGN) has been strongly involved in technical aspects of geodetic VLBI. In this sense, it should be highlighted its participation on observation campaigns through the Astronomical Center of Yebes (with the 14-m radio telescope -Yb- in Yebes from 1995 to 2003 and the 40-m radio telescope -Yg- from 2008 to present) or the development of the RAEGE project for an Atlantic Network of Geodynamical and Space Station, setting up a Spanish-Portuguese network of four Geodetic Fundamental Stations (two of them, Yebes -Yj- and Santa Maria -Sa- VGOS antennas, are already operational). At present, the National Geographic Institute of Spain (IGN) is committed to expand its contribution to geodetic VLBI. For this reason an analysis team has been established. For the last two years several test with different software packages has been performed.

In Azcue et al. (2019) first results of VLBI processing carried out at IGN were shown. Two VLBI software packages were used for experimentation activities in order to compare and validate the solution beyond the software used. These tools were VieVS 3.0 (Böhm et al., 2018) and Where v0.8.1 Kirvirk$_2$017.

Currently, The IGN analysis team continues with several VLBI processing activities such as the routinary processing of R1 and R4 sessions using Where (and contrasted with VieVS processing) or diverse research activities using both softwares.

In this work, the estimated Earth Orientation Parameters (EOP) for the period spanning from to 2002 to 2018 obtained using Where v0.16.3 are presented. These outputs are compared to the those from Analysis Centers which are consistent in terms of configuration, specifically concerning terrestrial and celestial frames and IERS models (Petit and Luzum, 2010).

Esther Azcue · Yaiza Gómez Espada · Víctor Puente · Marcelino Valdés
Instituto Geográfico Nacional
C/General Ibañez de Ibero, Madrid, Spain

Susana Garcia-Espada
Instituto Geográfico Nacional - RAEGE Santa Maria station, Azores, Portugal

(Correspondence: eazcue@fomento.es)

2 Processing strategy

Where v0.16.3 software package has been used to process R1 and R4 VLBI sessions for the period spanning from 2002 to September 2018. The summary of the configuration used is shown in Table 1. The set of estimated parameters is the following:

- Station and source coodinates.
- EOP (polar motion and rates, UT1, LOD and celestial pole offsets).
- Station clock (1 h interval).
- Zenith troposphere delay (1 h interval) and gradients (6 h interval) per station.

Table 1: Summary of the configuration

Frames	ICRF2 and ITRF14
IERS Conventions	2010
EOP a priori	C04 series
Precession/nutation model	IAU 2006/ IAU 2000A
Troposphere	VMF1 model
Geophysical models	solid tide tidal ocean loading (TPXO.7.2) solid and ocean pole tides atmosphere tides thermal antenna deformation
Estimation model	Kalman Filter

3 Results

EOP differences for the period analysed with Where v0.16.3 have been compared to EOP 14 C04 series (Bizouard et al., 2019). The same comparison has been carried out using EOP estimated by other Analysis Centers such as BKG, GSF, OPA and USN, as well as with the IVS combined solution. These solutions were retrieved from IVS ftp (Nothnagel et al., 2017). Differences shown in Figure 1 are shifted in y axis for each Analysis Center for the sake of clarity. Mean value and percentile 95th of the differences for each solution are shown in Table 2. Percentile 95th is used instead of standard deviation to avoid the influence of some outliers present in the series.

4 Conclusions and future plans

The results presented in this work lead to conclude that the accuracy of IGN solution is, in general, within the same order of magnitude than other VLBI Analysis Centers.

An odd behaviour has been detected regarding Celestial Pole Offsets. For the period processed, it would be expected to get a sinusoidal pattern due to Free Core Nutation but this is not the case.

In the light of these results, IGN team is driven to contribute as much as possible to IVS analysis activities. In this respect, in January 2019 a bid to become potential analysis center was submitted to the IVS Combination Center.

References

Azcue E, Gómez Espada Y, Puente V, etal. (2019) Initial VLBI Data Analyses at the National Geographic Institute of Spain. In: K. L. Armstrong, K. D. Baver, D. Behrend (eds.): *IVS 2018 General Meeting Proceedings*, NASA/CP-2019-219039, 233–236

Bizouard C, Lambert S, Gattano C, et al. (2019) The IERS EOP 14C04 solution for Earth orientation parameters consistent with ITRF 2014. *J Geod* 93(5), 621–633, doi:10.1007/s00190-018-1186-3

Böhm J, Böhm S, Boisits J, et al. (2018) Vienna VLBI and Satellite Software (VieVS) for Geodesy and Astrometry. *PASP*, 130, 986, doi:10.1088/1538-3873/aaa22b

Kirvirk A-S, Hjelle G A, Dahnn M, et al. (2018) WHERE — A New Software for Geodetic Analysis. In: R. Haas, G. Elgered (eds.): *Proc. 23rd EVGA Working Meeting*, 248–252

Nothnagel A, Artz T, Behrend D, et al. (2017) International VLBI Service for Geodesy and Astrometry – Delivering high-quality products and embarking on observations of the next generation. *J Geod*, 91(7),711–721, doi:10.1007/s00190-016-0950-5

Petit G, Luzum B (2010) IERS Conventions. *IERS Technical Note*, 36, Frankfurt am Main: Verlag des Bundesamts für Kartographie und Geodäsie

Fig. 1: EOP differences with respect to EOP 14 C04 series.

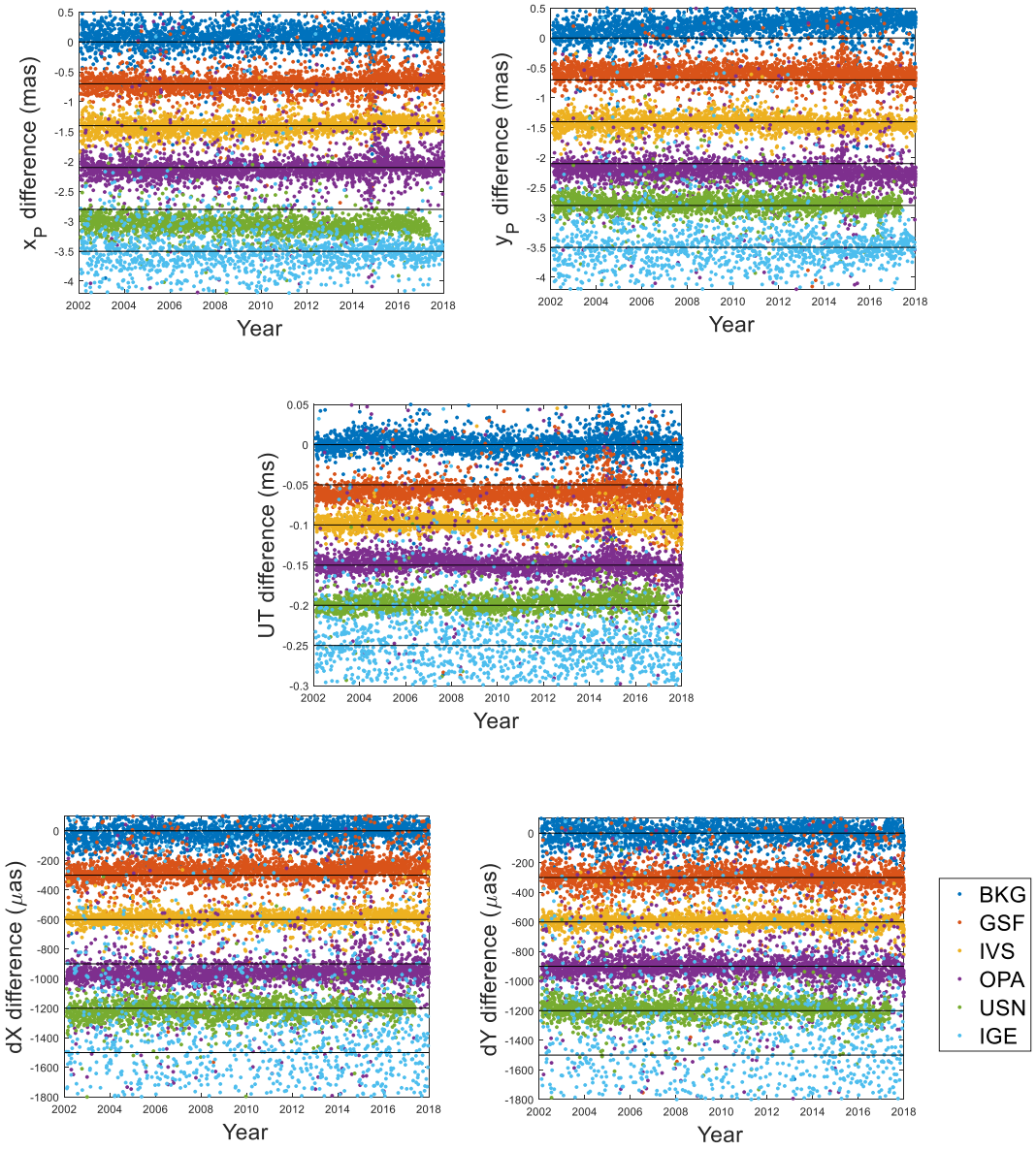

Table 2: Statistical summary of the EOP differences for each solution with respect to EOP 14 C04 series (2002-2018).

EOP	Parameter	BKG	GSF	IVS	OPA	USN	IGN
Samples		2710	2889	2226	3048	2078	1595
xp (mas)	Mean	0.18	−0.03	−0.01	0.05	−0.25	−0.20
	P95	0.56	0.39	0.20	0.88	−0.02	0.89
yp (mas)	Mean	0.24	−3.57	−0.02	−0.01	0.02	−0.09
	P95	0.89	0.60	0.41	0.19	0.49	0.24
UT (ms)	Mean	−0.13	2.54	−0.10	−0.11	−0.15	−0.13
	P95	0.03	0.04	0.02	0.07	0.02	0.12
dX (μas)	Mean	−1.94	23.29	12.62	57.75	−9.66	2.41
	P95	176.99	207.66	79.69	186.99	89.62	1599.62
dY (μas)	Mean	8.87	−10.15	−1.21	110.65	8.59	−26.62
	P95	180.74	174.90	71.92	230.80	111.09	1622.31

Earth Orientation Parameters Estimated From K-band VLBA Measurements

H. Krásná, D. Gordon, A. de Witt, C. S. Jacobs, B. Soja

Abstract The Earth Orientation Parameters (EOP), which connect the Terrestrial and Celestial Reference Frame, are regularly estimated by Very Long Baseline Interferometry (VLBI). The UT1-UTC and nutation components of EOP can only be measured using the VLBI technique. Until recently, published VLBI estimates of EOP were based solely on observations from the S/X frequency band.
We present VLBI estimates of EOP from an observing frequency independent of the traditional SX-band using Very Long Baseline Array (VLBA) measurements at K-band (24 GHz, 1.2 cm). We have over two years of regular VLBA experiments conducted with telescopes located in U.S. territory. We investigate the potential of K-band VLBI to produce more accurate EOP because of its reduced source structure effects relative to S/X-band. We compare our K-band EOP computed with two analyses software packages (Calc/Solve and VieVS) to the IERS C04 data.

Keywords K-band · EOP · VLBA · VLBI

Hana Krásná
Technische Universität Wien, Vienna, Austria
Astronomical Institute, Czech Academy of Sciences, Prague, Czech Republic

David Gordon
NVI, NASA Goddard Space Flight Center, USA

Aletha de Witt
SARAO/HartRAO, South Africa

Christopher S. Jacobs · Benedikt Soja
Jet Propulsion Laboratory, California Institute of Technology, USA

(Correspondence: hana.krasna@geo.tuwien.ac.at)

1 Introduction and data

In this paper we present solutions containing 69 K-band VLBI observing sessions with the first one in May 2002 and the last one in January 2019. From that amount, 52 sessions were observed with the VLBA network on the U.S. territory (15 sessions before 2015). The remaining 17 experiments are the single baseline sessions between HartRAO and Hobart26 which makes less that 1 % of the total number of K-band observations. In these single baseline sessions the Earth Orientation Parameters (EOP) were fixed in the analysis to their a priori values and the sessions are used mainly to strengthen the Celestial Reference Frames (CRF) estimation.
The data rates increased significantly from 128 to 256 Mbps before 2015 to 2048 Mbps after the year 2015. After the Mark6 recorder upgrade a data rate of 4096 Mbps is anticipated. For further information about the K-band project we refer to de Witt et al. (2019); Le Bail et al. (2019); Soja et al. (2019).

2 Parametrization

We show two independent solutions of the EOP. The GSFC-k-190207 was computed at the Goddard Space Flight Center with the software package Calc/Solve and the TUW-k-190223 was processed at the Technische Universität Wien with the VieVS software package (Böhm et al., 2018) using the NGS cards as input. Some of the differences between the TUW and GSFC solution are, e.g., that GSFC includes delay rates to the analysis, and that the Galactic aberration was modeled and applied in the GSFC solution to give source posi-

tions at the 2015.0 epoch.
In both solutions the same global parameters were estimated. The Terrestrial Reference Frame (TRF) was realized with the VLBA station positions and linear velocities for epoch 2010 with applying the No Net Translation (NNT) and No Net Rotation (NNR) condition w.r.t. ITRF2014. The celestial reference frame was estimated with source positions where the TUW solution used an unweighted NNR w.r.t. ICRF2 defining sources, whereas the GSFC solution applied an unweighted NNR constraint on 193 ICRF3 defining sources.
For the session-wise estimated parameters we used a similar parametrization in both solutions:

- TRF — station position of HartRAO, Hobart26, Tianma65, Tidbinbilla70
- Clock parameters — 60 min estimation intervals
- Zenith wet delay — continuous piece-wise linear offsets in 30 min intervals with 1.5 cm relative constraints
- Troposphere gradients -– continuous piece-wise linear offsets in 360 min intervals with 0.05 cm relative constraints
- EOP — 1 offset per session from VLBA
- EOP from single baseline sessions were fixed to IERS 14 C04 combined series (Bizouard et al., 2019).

Table 1: Median formal error of the estimated EOP.

		median formal error
x pole	GSFC-k-190207	71
[µas]	(pre-2015 / post-2015)	109 / 58
	TUW-k-190223	80
	(pre-2015 / post-2015)	168 / 72
y pole	GSFC-k-190207	89
[µas]	(pre-2015 / post-2015)	184 / 78
	TUW-k-190223	108
	(pre-2015 / post-2015)	288 / 97
dUT1	GSFC-k-190207	6
[µs]	(pre-2015 / post-2015)	9 / 5
	TUW-k-190223	7
	(pre-2015 / post-2015)	17 / 6
nutation dX	GSFC-k-190207	42
[µas]	(pre-2015 / post-2015)	54 / 38
	TUW-k-190223	50
	(pre-2015 / post-2015)	78 / 45
nutation dY	GSFC-k-190207	41
[µas]	(pre-2015 / post-2015)	58 / 34
	TUW-k-190223	49
	(pre-2015 / post-2015)	72 / 40

Ionosphere corrections were estimated from 2 hour average JPL GPS ionosphere maps by David Gordon and applied in both solutions.

3 Results

Plots in the left-hand side column in Fig. 1 show the session-wise estimated offsets w.r.t. the IERS 14 C04 EOP from the VLBA sessions, and in the right-hand side column the respective formal errors are depicted. The black colour represents the GSFC-k-190207 solution, the light red colour the TUW-k-190223 solution, and the formal errors of the IERS 14 C04 EOP are depicted with blue plus signs. In the Table 1 the median of the formal errors of the two EOP solutions is summarized. In addition we distinguish between the data sets before the year 2015 and after 2015. We see a decrease of the median formal error in all five EOP after 2015 of about a factor of two. Table 2 shows statistics for the EOP estimates w.r.t. IERS 14 C04 time series, such as the weighted mean, median, wRMS, χ^2 and normalized deviation from unity $(\chi^2-1)/\sigma(\chi^2)$. Post-2015 wRMS scatter is noticeably improved for the polar motion. However, nutation do not improve much except for Vienna dX nutations. Offset in the y-pole component is related to the VLBA telescope distribution. Future investigations will be devoted to understand why the offset in the y-pole component is so prominent in the TUW-k-190223 solution.

4 Conclusions and outlook

Reasonable EOP series can be produced from the K-band VLBA measurements. Comparison of two independent global adjustments computed with two software analysis packages (VieVS and Calc/Solve) is shown. Future plans: We anticipate a factor of 1.4 increase in sensitivity from doubling the data rates to 4096 Mbps. Testing of the new rate will start this year. Operations may begin in 2019/20. Both the Celestial and Terrestrial Frames should improve with time thereby improving EOP.

Table 2: Statistics of the difference between estimated EOP and IERS 14 C04.

		weighted mean [µas, µs]	median [µas, µs]	wRMS [µas, µs]	χ^2 [–]	$(\chi^2-1)/\sigma(\chi^2)$ [–]
x pole	GSFC-k-190207 (pre-2015 / post-2015)	−49 / 272	−30 / 299	249 / 143	3.69 ± 0.38 / 3.29 ± 0.24	7.11 / 9.71
	TUW-k-190223 (pre-2015 / post-2015)	−102 / 185	−164 / 218	270 / 165	1.92 ± 0.38 / 3.34 ± 0.24	2.42 / 9.94
y pole	GSFC-k-190207 (pre-2015 / post-2015)	−160 / 189	−287 / 232	504 / 203	7.20 ± 0.38 / 5.42 ± 0.24	16.41 / 18.76
	TUW-k-190223 (pre-2015 / post-2015)	−1228 / −72	−1119 / −89	344 / 201	1.28 ± 0.38 / 3.56 ± 0.24	0.74 / 10.85
dUT1	GSFC-k-190207 (pre-2015 / post-2015)	15 / −14	15 / −14	37 / 52	10.48 ± 0.38 / 11.52 ± 0.24	25.08 / 44.63
	TUW-k-190223 (pre-2015 / post-2015)	16 / −18	4 / −18	38 / 52	3.88 ± 0.38 / 10.57 ± 0.24	7.61 / 40.62
nutation dX	GSFC-k-190207 (pre-2015 / post-2015)	−120 / −18	−106 / −45	137 / 129	4.10 ± 0.38 / 3.66 ± 0.24	8.21 / 11.29
	TUW-k-190223 (pre-2015 / post-2015)	−66 / 58	−97 / 20	133 / 105	12.98 ± 0.38 / 4.41 ± 0.24	31.69 / 14.48
nutation dY	GSFC-k-190207 (pre-2015 / post-2015)	−32 / −67	−62 / −58	105 / 109	2.44 ± 0.38 / 2.98 ± 0.24	3.80 / 8.42
	TUW-k-190223 (pre-2015 / post-2015)	−39 / −62	−51 / −53	98 / 104	7.25 ± 0.38 / 5.59 ± 0.24	16.53 / 19.46

Acknowledgements We acknowledge our respective sponsors: HK acknowledges the Austrian Science Fund (FWF, Project T697-N29). SARAO/HartRAO is a facility of the National Research Foundation (NRF) of South Africa. Portions of this work done at Jet Propulsion Laboratory, California Institute of Technology under contract with NASA. We gratefully acknowledge the grant of observing time on the VLBA under the USNO time allocation.

References

Bizouard C, Lambert S, Gattano C, et al. (2019) The IERS EOP 14C04 solution for Earth orientation parameters consistent with ITRF 2014. *J Geod*, 93, 621–633, doi:10.1007/s00190-018-1186-3

Böhm J, Böhm S, Boisits J, et al. (2018) Vienna VLBI and Satellite Software (VieVS) for Geodesy and Astrometry. *PASP*, 130/986, 1–6, doi:10.1088/1538-3873/aaa22b

de Witt A, Gordon D, Jacobs C S, et al. (2019) The K-band (24 GHz) Celestial Reference Frame. Poster at the 24th EVGA Working Meeting, http://www.oan.es/evga2019/EVGA2019_PDF/P306_EVGA2019_deWitt.pdf

Le Bail K, de Witt A, Jacobs C S, et al. (2019) Time stability of the K-band catalog sources. In: R. Haas, S. Garcia-Espada, J. A. López Fernández (eds.): *Proc. 24th EVGA Working Meeting*, 209–213

Soja B, Jacobs C S, Runge T, et al. (2019) Ionospheric calibration for K-band celestial reference frames. Presentation at the 24th EVGA Working Meeting, http://www.oan.es/evga2019/EVGA2019_PDF/O316_EVGA2019_Soja.pdf, doi:10.13140/RG.2.2.34409.95840

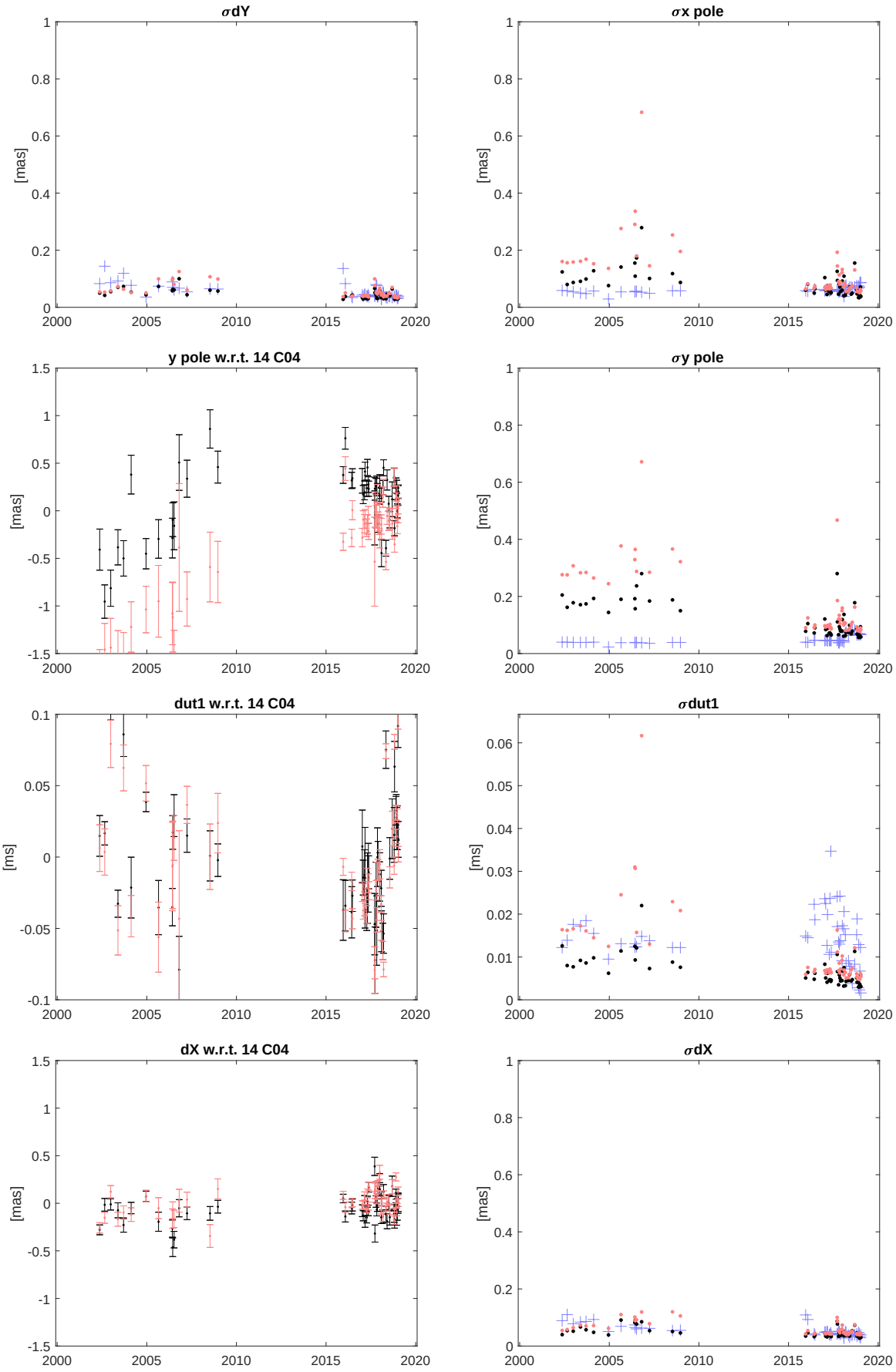

Fig. 1: Caption next page.

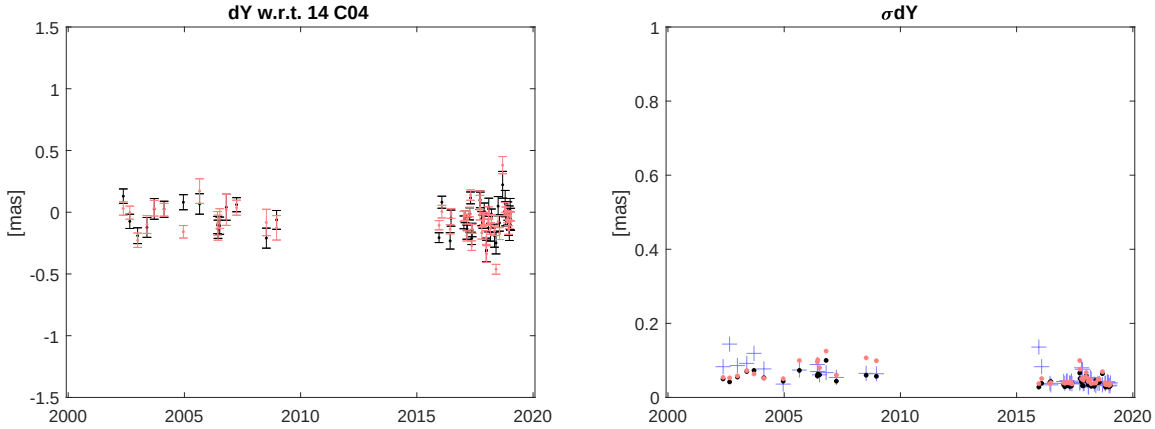

Fig. 1: On the left-hand side EOP offsets w.r.t. the IERS 14 C04 values are shown and on the right-hand side the respective formal errors. The GSFC-k-190207 solution is plotted in black, the TUW-k-190223 solution in light red, and the formal errors of the IERS 14 C04 EOP are depicted with blue plus signs.

AUA047: Students at TU Wien Organize Their own VLBI Session

H. Wolf, M. Schartner, J. Gruber, J. Böhm, L. McCallum, J. McCallum, W. Hankey

Abstract At Technische Universität Wien (TU Wien) students had the chance to fully organize the official IVS session AUA047. We will give an overview of the individual parts of this course, including, scheduling, large-scale Monte Carlo simulations, an correlation exercise and analysis. The workflow of carrying out the AUA047 VLBI session using the Vienna VLBI and Satellite Software (VieVS) and the new scheduling tool VieSched++ is described. We provide, as well, the scheduling statistics achieved with VieSched++ and the results of the analysis.

Keywords IVS, scheduling · Large-scale Monte Carlo simulations · Correlation · Analysis · VieSched++ · VieVS

1 Introduction

As part of the lecture "Space Geodetic Techniques" at TU Wien, students organized an official VLBI session of the International VLBI Service for Geodesy and Astrometry (IVS) (Nothnagel et al., 2017). The experiment is part of the AUSTRAL VLBI program (Plank et al., 2017) with the session code AUA047. Observation start was the 4th of December 2018. More than 30 students participated in this course and worked independently in groups to perform all necessary steps, including large-scale Monte-Carlo simulations, scheduling, correlation and analysis. As a result of a cooperation with the University of Tasmania, it was possible to observe the VLBI session successfully with Australian telescopes. The participating stations were Hobart (26 m), Katherine and Yarragadee, shown in Figure 1.

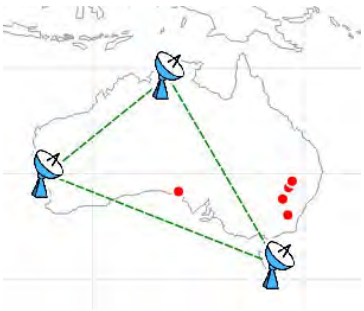

Fig. 1: The network of the AUA047 session consisting of Hobart (26m), Katherine and Yarragadee.

2 Scheduling

Schedules were created by each group independently using the software VieSched++ (Schartner and Böhm, 2019). The students could decide if they want to optimize the schedule for a geodetic, astrometric or intensive-like purpose. For this optimization the VieSched++ multi-scheduling tool was used. The students investigated the impact on the schedule of using different optimization criteria such as, number of observations, sky coverage, scan duration, maximum allowed idle time and minimum number of stations per scan. Additionally, the individual weights of the

Helene Wolf · Matthias Schartner · Jakob Gruber · Johannes Böhm
TU Wien, Department of Geodesy and Geoinformation, Gußhausstraße 27-29, AT-1040 Wien, Austria

Lucia McCallum · Jamie McCallum · Warren Hankey
University of Tasmania, Private Bag 37, 7001 Hobart, Australia

(Correspondence: helene.wolf@geo.tuwien.ac.at)

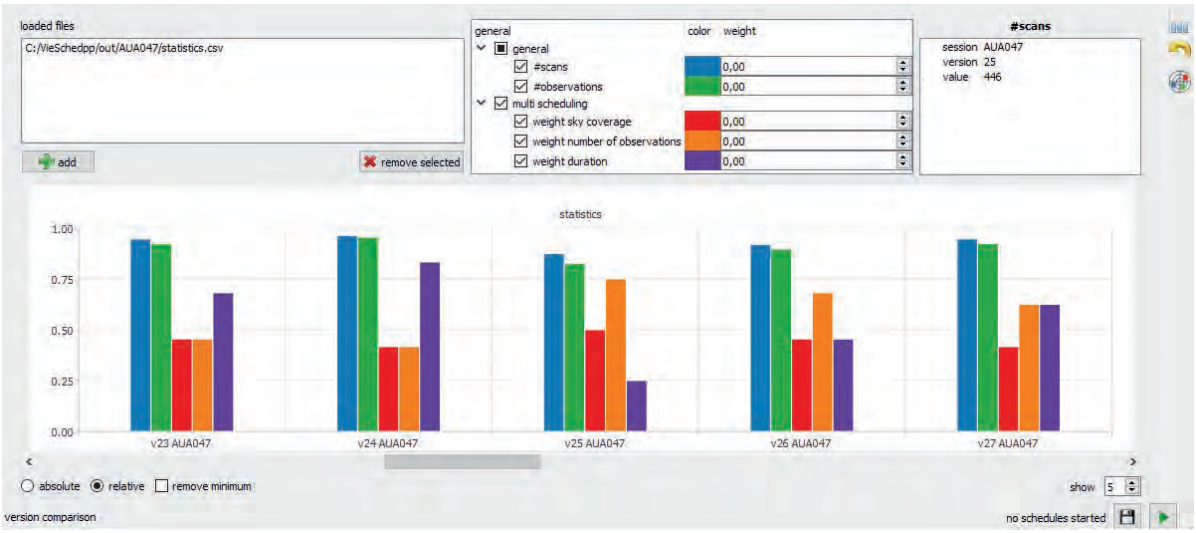

Fig. 2: VieSched++ statistics tool for comparing created schedules using the multi-scheduling tool. The bars symbolise the relative value of parameters such as, number of scans (blue), number of observations (green) and weight factors (red, orange, purple).

Fig. 3: VieSched++ Analyzer displaying the sky coverage of the in the session included stations, with dots representing observed sources, color-coded by the different cable wraps, counterclockwise (red), neutral (green) and clockwise (blue). The smaller grey dots represent the sources which are not observed in the selected time span.

stations were investigated with focus on the station Hobart, as this is the slowest but most sensitive station.

Figure 2 shows the VieSched++ statistics tool which was used for comparing the statistics of the created schedules. This tool allows the ranking of the schedules according to different properties, like for example, number of scans or number of observations.

The evaluation of a schedule was also done using the VieSched++ Analyzer, shown in Figure 3. This tool displays the sky coverage of the involved stations. Therefore it allows a comparison of the created schedules based on the distribution of observed sources.

In total, several hundred schedules were created and further simulated and analysed using the Vienna VLBI and Satellite Software (VieVS) (Böhm et al., 2018). The schedule from one group was selected based on simulated repeatability values and successfully observed with the Australian telescopes.

Table 1 shows the achieved scheduling statistics of the observed schedule. It is worth mentioning that the students optimized the schedule, so that the antennas in

Table 1: Scheduling statistics of the observed schedule created using VieSched++

	AUA047
number of scans	513
number of observations	1358
number of scheduled sources	66
average observing time	58.65 %
average slew time	30.11 %
average idle time	1.77 %

average idle just for 1.77 % and observe for 58.65 % of the time.

3 Simulation

Simulations of the produced schedules were carried out for assessing the accuracy of the earth orientation parameters (EOP) and station coordinates. These large-scale Monte Carlo simulations were performed using VieVS (Pany et al., 2011). The clock accuracy was set to an Allan standard deviation (ASD) of 1×10^{-14} at 50 min (Herring et al., 1990), and a white noise of 30 ps was used. The refractive index structure constant of the troposphere C_n was set to $1.8 \times 10^{-7} m^{-1/3}$ with a scale height of 2 km (Nilsson et al., 2007). In total, several tens of thousands of simulations were generated and analyzed.

4 Correlation

After the session was observed, the students got an introduction of the correlation of VLBI sessions with the Distributed FX-style correlator (DiFX) (Deller et al., 2007) and a presentation of the correlation on the Vienna Scientific Cluster (VSC-3).

During this course the students had to work on exercises to calculate the expected data size, transfer time and correlation time for AUA047. In order to enable the students to get a brief insight into the procedure of correlation, the students had to develop a FX- and a XF-style correlator in MATLAB and to compare the processing times.

5 Analysis

The analysis was done with VieVS using the vgosDB format. The students found and removed four clock breaks at the station Yarragadee. Further, outlier detection was performed, shown in Figure 4.

The optimising analysis was done by each group independently based on their scientific goal. The students varied for example, zenith wet delay intervals, constraints and the mapping functions. Finally, a session fit of 38.6 ps was achieved.

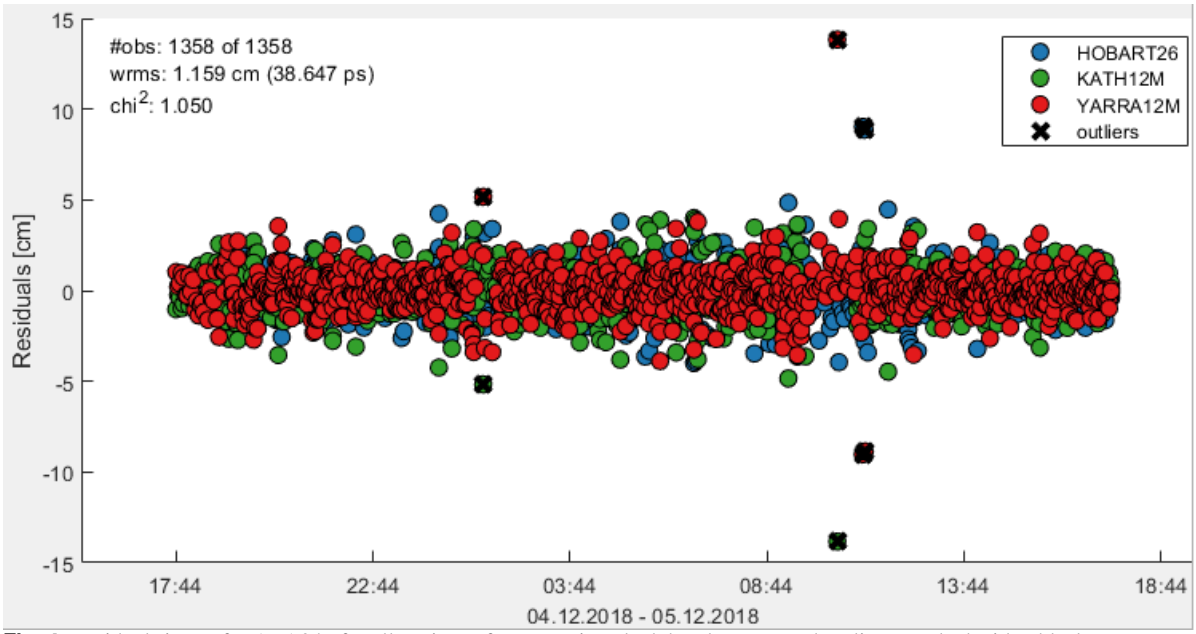

Fig. 4: Residuals in cm for AUA047 for all stations after removing clock breaks. Detected outliers, marked with a black cross, were removed in a next step.

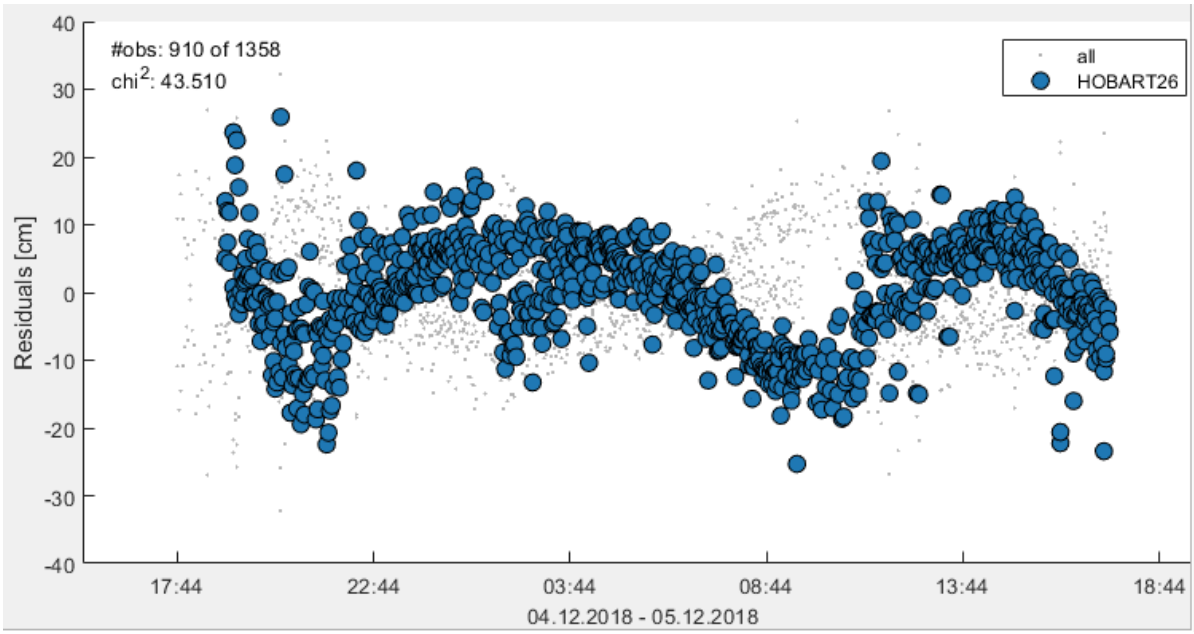

Fig. 5: Residuals in cm for AUA047 at station Hobart showing the effect of not considering the a priori model of solid earth tides.

To demonstrate the effect of a priori models like solid earth tides, tidal atmospheric loading and tidal ocean loading, the students investigated the residuals of the analysis without including these models separately and compared their results with the results obtained by applying the models. Figure 5 shows the effect of solid earth tides at station Hobart.

6 Conclusion

The official IVS session AUA047 was fully organized by students at TU Wien. All necessary steps, including scheduling, large-scale Monte Carlo simulations, correlation and analysis were done by each group independently. This shows that both software packages, VieSched++ and VieVS, are understandable and easy to use. The students got an insight into VLBI through the practical tasks and exercises. Next to the success in university teaching this course delivered scientific results as any other VLBI session does, like station coordinates and earth orientation parameters.

References

Böhm J, Böhm S, Boisits J, et al. (2018) Vienna VLBI and Satellite Software (VieVS) for Geodesy and Astrometry. *PASP*, 130, 044503, doi:10.1088/1538-3873/aaa22b

Deller A T, Tingay S J, Bailes M, et al. (2007) DiFX: A software correlator for very long baseline interferometry using multiprocessor computing environments. *PASP*, 119, 318–336, doi:10.1086/513572

Herring T, Davis J, Shapiro I (1990) Geodesy by radio interferometry: The application of Kalman Filtering to the analysis of very long baseline interferometry data. *J Geophys Res*, 95, 12561–12581, doi:10.1029/JB095iB08p12561.

Nilsson T, Haas R, Elgered G (2007) Simulations of atmospheric path delays using turbulence models. *Proc. 18th EVGA Working Meeting*, 175–180

Nothnagel A, Artz T, Behrend D, et al. (2017) International VLBI Service for Geodesy and Astrometry. *J Geod*, 91, 711–721, doi:10.1007/s00190-016-0950-5

Pany A, Böhm J, MacMillan D, et al. (2011) Monte Carlo simulations of the impact of troposphere, clock and measurement errors on the repeatability of VLBI positions. *J Geod*, 85, 39–50, doi:10.1007/s00190-010-0415-1

Plank L, Lovell J, McCallum J, et al. (2017) The AUSTRAL VLBI observing program *J Geod*, 91, 803–817, doi:10.1007/s00190-016-0949-y

Schartner M, Böhm J (2019) VieSched++: A New VLBI Scheduling Software for Geodesy and Astrometry. *PASP*, 131, 084501, doi:10.1088/1538-3873/ab1820

Comparison of Integrated GNSS LOD to dUT1

M. Mikschi, J. Böhm, S. Böhm, D. Horozovic

Abstract The problem of estimating the bias of Length of Day (LOD) data from Global Navigation Satellite Systems (GNSS) is discussed. A method for estimating the bias is described and ideal parameters of the method for the used data are given. The time correction dUT1 is estimated using four different GNSS data sets and the achieved results are presented and discussed. For the best data set the root mean square error (RMSE) of the dUT1 estimate is 40 μs after 7 days and 60 μs after 14 days.

Keywords dUT1 · LOD · GNSS

1 Introduction

The time correction dUT1 is an important Earth orientation parameter that is regularly determined with Very-Long-Baseline Interferometry (VLBI) intensive sessions. While VLBI is the only technique that is capable of estimating dUT1 directly, its (negative) time derivative, Length of Day (LOD), can be measured with, among other techniques, a global GNSS network. Therefore, it is possible to estimate dUT1 by integrating GNSS LOD values and adding the known dUT1 value at t_0.

Markus Mikschi · Johannes Böhm · Sigrid Böhm · Dzana Horozovic
Technische Universität Wien, TU Wien, Karlsplatz 13, AT-1040 Vienna, Austria

(Correspondence: markus.mikschi@geo.tuwien.ac.at)

$$dUT1(T) = \int_{t_0}^{T} -LOD(t)dt + dUT1(t_0) \qquad (1)$$

However, GNSS LOD values contain a bias which has to be accounted for in order to achieve good dUT1 estimates. This bias mainly stems from perturbations of the GNSS orbits which cannot be differentiated from changes in the LOD estimates. Especially the effects of solar radiation pressure on the right ascension of the ascending node are problematic.

2 Methods

Four different GNSS LOD data sets from Horozovic and Weber (2018) are used for estimating dUT1. Two of which consist solely of GPS data and two are calculated based on a combination of GPS and Galileo. For both of these variants one and three day solutions with one hour resolution are used. All of the data sets encompass the time frame from 1-JUL-2017 to 1-NOV-2017, use the ECOM model and are referred to as 1D GPS, 3D GPS, 1D GPSGAL and 3D GPSGAL in this paper. The data was processed with Bernese 5.2 (Dach et al., 2015) using data from over 190 IGS stations. For both the calibration of the offset in the GNSS LOD data, as well as the integration constant the IERS 14C04 data set (Bizouard et al., 2018), hereafter referred to as C04, is used. Furthermore, it is also used for the assessment of the estimated dUT1 values.

For the integration of the discrete LOD values the cumtrapz function in Matlab (R2016b) is used, which approximates the integral with trapezoids. A better approximation with integrating a cubic spline interpolation yields no significant improvements. In order to as-

sess the quality of the dUT1 estimates, the LOD values are integrated over a specific integration period and the differences to the C04 dUT1 is calculated. Subsequently the integration window is shifted by one day and the process is repeated as long as there is data available. Thereafter the computed differences to C04 are stacked as a function of t-t_0 and the mean error as well as the RMSE are calculated. In Figure 1 an example of this stacking can be seen. Each of the faint lines is the difference between the estimated dUT1 for a specific integration period and the C04 dUT1. Due to the shifting by one day, each LOD value contributes to multiple integration periods and as a consequence some repeating patterns in the difference to C04 can be seen.

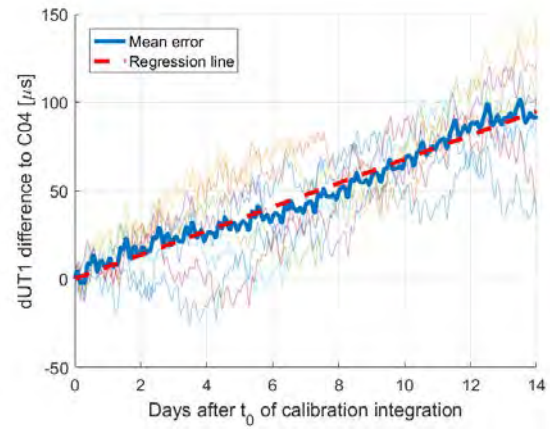

Fig. 1: Illustration of the stacking of integration periods and the bias estimation method.

The GNSS LOD data possesses an offset as is normal with this kind of data. Since dUT1 has to be known at t_0 it is sensible to assume that LOD is also known at that time. Therefore the bias can be estimated as the difference between the GNSS LOD and that known LOD at t_0. However, the calculated LOD difference at t_0 does not represent the offset over the integration period due to the noisy nature of the LOD data. Applying the same technique to smoothed GNSS LOD does not deliver satisfying results either.

In order to overcome this problem, a period with certain length prior to the integration start t_0 is chosen as a calibration period. During this period the LOD is integrated in a moving integration window and the resulting difference to C04 gets stacked as described above. Because the offset in the LOD data is approximately constant during an integration period, the calculated mean error of the dUT1 estimate drifts linearly. Thus the offset can be estimated by fitting a linear function to the mean error and taking the slope as is illustrated in Figure 1.

For comparison, the IGS corrects for the LOD bias by averaging the differences of the daily LOD values from every analysis center of the past weeks from the actual LOD value determined by the IERS Rapid Service. This produces an analysis center specific LOD bias which is used in the estimation (Kammeyer, 2000).

3 Results

Different parameters for the used calibration method were tested in order to get the best dUT1 estimates. Among them were weighted averaging of the different integration periods when calculating the mean error and different lengths for both the overall calibration window and the integration period within that window. The rational behind a weighted average of the different integration periods is that more recent periods may be more indicative of the current LOD offset. However, it is found that the more equally the different periods are weighted the better the calibration performs and a normal averaging yields the best results. It is important to note that the used calibration method introduces a weighting of the LOD values by itself. This is because the integration window is always completely contained in the calibration period and gets shifted by one day each time. As a consequence the first and the last LOD value contribute to one integration period, the second and second last to two and so on.

For the calibration length 7, 14, 21, 28 and 35 day periods were tested. Since the used calibration method acts similar to a moving mean, the resulting LOD bias signal gets smoother with a prolonged calibration period as can be seen in Figure 2. In order to achieve a good end result in terms of the RMSE as well as to preserve some of the bias variation a compromise of 21 days was chosen.

Concerning the length of the integration window within the calibration period 3, 5, 7, 10 and 14 days were tested, with 14 days resulting in the best calibration. For the following results a calibration with normal averaging, 21 day calibration period and 14 day integration window was used.

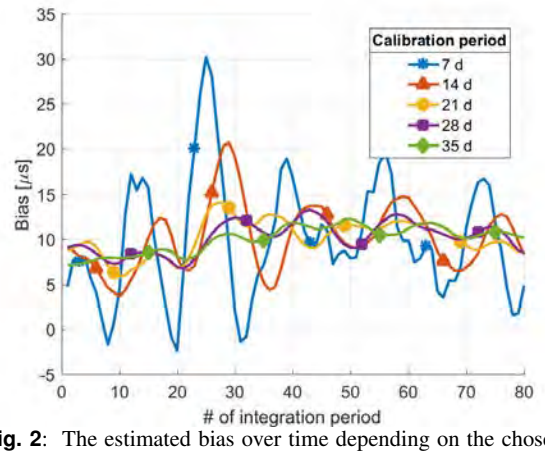

Fig. 2: The estimated bias over time depending on the chosen length of the calibration period.

Using this configuration good dUT1 estimates can be achieved. Figure 3 depicts the mean error and the RMSE of the dUT1 estimates when compared to the C04 as is described above. The calibration of the LOD bias was successful to a certain degree, as the mean errors of all four data sets are approximately zero. The three day solutions outperform the one day solutions by a large margin. The addition of Galileo to GPS for 1D yields a much bigger improvement than for 3D, for which the improvement is almost negligible. The RMSE for the best data set, 3D GPSGAL, after seven days is approximately 40 μs.

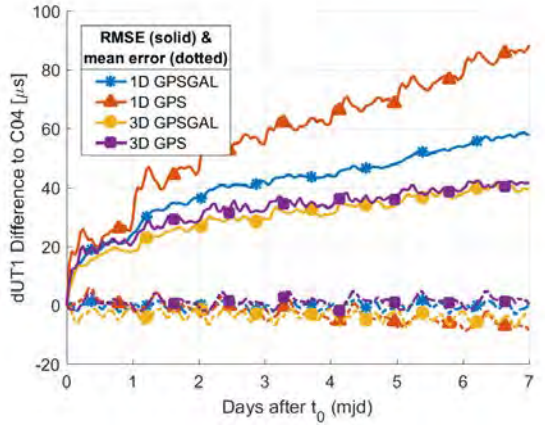

Fig. 3: The mean error and RMSE for the four data sets as a function of t-t_0.

Part of the reason that the calibration fails for the 1D GPS dataset is that the offset is assumed to be constant over the integration period. However, this assumption particularly does not hold true for this data set. Figure 4 shows the estimated biases for the different GNSS data sets over time. The bias for 1D GPS has the biggest amplitude and very steep slopes, which makes it hard to estimate with the employed method.

Both the mean error and RMSE of all solutions exhibit some periodic behavior. This is partly due to the fact that the C04 dUT1 values have a temporal resolution of one day while the GNSS LOD data has a temporal resolution of one hour. In order to compare the estimated dUT1 with the C04 data the latter is linearly interpolated. In addition, the LOD data contains some residual components of the ocean tides which were not removed by the model used in Bernese 5.2 (Dach et al., 2015).

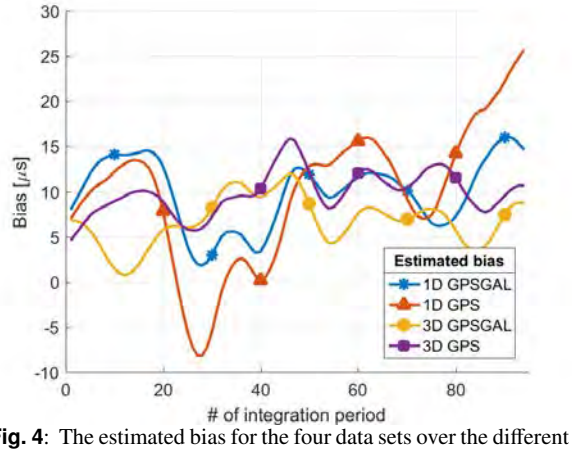

Fig. 4: The estimated bias for the four data sets over the different integration periods.

Assuming the distribution of the differences between GNSS LOD and C04 LOD is symmetrical and has an expectation value of zero, the RMSE follows a true random walk error and is proportional to the square root of time:

$$RMSE \propto \sqrt{t - t_0} \tag{2}$$

Figure 7 shows the RMSE of the dUT1 estimates over 7 days at the time-stamps of the C04 data. In addition the results of a curve fit of

$$RMSE \approx a * \sqrt{t - t_0} + d \tag{3}$$

to these points is shown. The estimated parameters as well as the goodness of fit (*gof*) values are listed

in Table 1. The offset parameter d would be zero in an ideal case and the exhibited deviations from that theoretical value are due to remaining biases in the corrected GNSS LOD. These most likely stem from orbital perturbations, mainly due to radiation pressure, which were not completely modeled by the used ECOM model in Bernese 5.2 (Dach et al., 2015).

3D GPS and 3D GPSGAL follow the fitted function quite well although their *gof* parameters are not particularly good. On the other hand 1D GPS has the best *gof* parameters but exhibits a positive curvature after day 3 which means that the RMSE does not truly follow a square root function. This is explored further in the next section with a 14 day integration period.

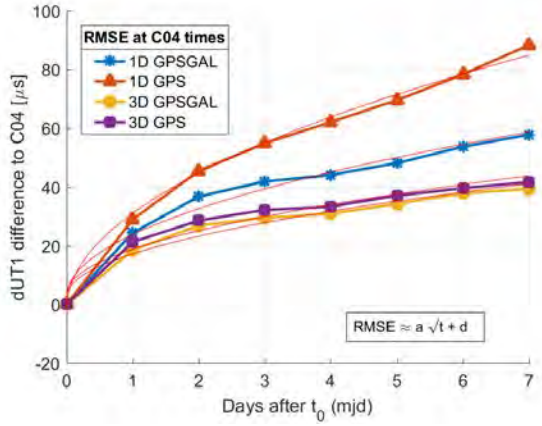

Fig. 5: Result of fitting a square root function with an offset term to the RMSE at the C04 sampling points.

Table 1: Fitting parameters and goodness of fit for 7 days

Data set	a	d	R^2	RMS
GPS 1D	32.71	-1.70	0.995	2.120
GPSGAL 1D	21.22	2.56	0.985	2.466
GPS 3D	15.20	3.56	0.966	2.662
GPSGAL 3D	14.51	2.68	0.974	2.220

Figure 6 shows the progression of the mean error and RMSE for an integration period of 14 days. The 1D GPS estimate is by far the worst and its RMSE increases linearly with time instead of the square root of time. This means that the conditions of a pure random walk error are not met, which is apparent when looking at the trend of the respective mean error which is quite significant. The already small advantage of 3D GPSGAL over 3D GPS pretty much vanishes after approximately 9 days. However, when looking at the trend of their respective mean errors, it becomes clear that 3D GPS profits of a much better bias estimation than 3D GPSGAL. Since their RMSE are so similar it can be inferred that GPSGAL 3D has a lower scattering but the bias is either not as constant as for the other data sets, harder to be estimated or both. It is interesting to note that bias estimation for GPS improves when going from the 1D to the 3D solution but for GPSGAL it is the other way around. The reasons for this have to be investigated.

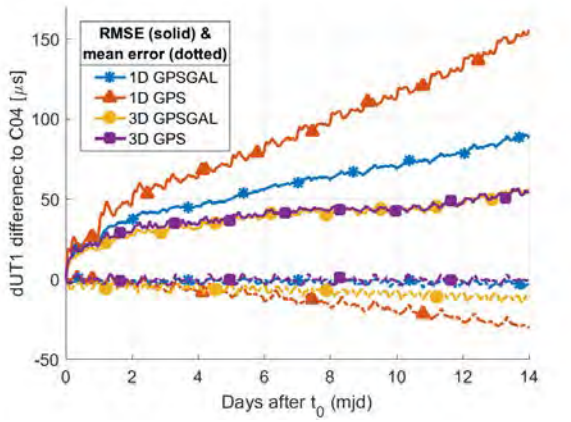

Fig. 6: The mean error and RMSE for the four data sets as a function of t-t_0 for a longer integration window of 14 days.

Figure 7 depicts the RMSE of the dUT1 estimates over 14 days at the sampling points of the C04 data set and the results of a curve fit according to Equation 3. The parameters resulting from this fit are listed alongside the *gof* measurements in Table 2. In addition the figure also shows a RMSE reference, which was taken from a paper about estimation of a dUT1-like quantitiy based on GPS orbit planes (Kammeyer, 2000). Within that paper the RMS change over time was investigated over longer periods and the resulting RMS approximation is given with 30μ s $\sqrt{w}$ wherein w is the elapsed time in weeks.

Table 2: Fitting parameters and goodness of fit for 14 days

Data set	a	d	R^2	RMS
GPS 1D	40.58	-12.04	0.972	7.590
GPSGAL 1D	21.61	2.70	0.989	2.516
GPS 3D	12.33	7.77	0.943	3.346
GPSGAL 3D	12.70	5.30	0.957	2.835

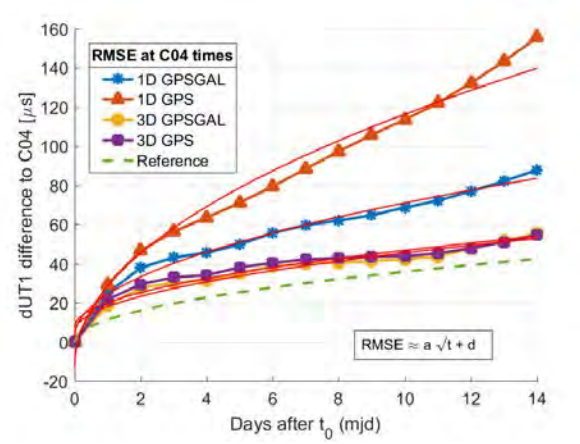

Fig. 7: RMSE over 14 days at C04 times and the curve fitting results. Additionally a reference curve is shown.

Interestingly the estimate for the *a* parameter decreases quite drastically between the 7 and 14 day fits for the two 3D solutions. The *d* parameter on the other hand gets bigger. This points to disturbances of the pure random walk error that get absorbed in the *a* parameter in case of the 7 day fit, but move to the *d* term in the 14 day fit. The 1D GPS dUT1 estimate performs even worse, has bad *gof* parameters and exhibits a positive curvature that is even more visible in Figure 7 than it was in the previous ones.

Both 3D solutions perform similar, although a bit worse than the reference data. However, this is due to the sharp increase at the beginning of the integration period. The actual course of the RMSE as described by the *a* term is very similar with 12.33 and 12.70 compared to 11.34. The *a* term for the reference data results from a scaling of the weekly coefficient by $\frac{1}{\sqrt{7}}$. The reasons for the steep increase in the RMSE at the very beginning of the integration period need to be investigated further.

4 Conclusions

The presented bias estimation method yields good results and enables to obtain usable dUT1 estimates. It works best for the used 1D GPSGAL and 3D GPS data sets while struggling with GPS 1D. Both 3D data sets yield good dUT1 estimates with the 3D GPSGAL doing so despite a slightly worse bias estimation based on the mean error. 1D GPS results in the worst bias estimation and the worst RMSE by a big margin. This is most likely due to a higher variability of the bias during a single integration period.

The best case RMSE after 7 days with the used data is 40 μs with the 3D GPSGAL data set. After 14 days the estimates based on 3D GPSGAL and 3D GPS are nearly identical and exhibit an RMSE of almost 60 μs. All those accuracy measures do not include the uncertainty of the initial dUT1 value at t_0. The attainable accuracy of dUT1 from VLBI intensive sessions is 20 μs for the best global intensives (Schuh and Böhm, 2013) and about 40 μs for European intensives (Schartner et al., 2018).

When comparing the obtained dUT1 RMSE to the aforementioned reference data set the former falls behind a bit. While the best GNSS data sets, 3D GPS and 3D GPSGAL exhibit a similar *a* parameter for the curve fit, the steep incline of the RMSE at the beginning and the accompanying high *d* value lead to a worse overall performance.

References

Kammeyer P (2000) A UT1-Like Quantity from Analysis of GPS Orbit Planes. *Celestial Mechanics and Dynamical Astronomy*, 77, 241–272

Horozovic D, Weber R (2018) Bestimmung von hochfrequenten Erdrorationsparametern unter Verwendung von GPS und Galileo Beobachtungsdaten. In: *Abstract Book Geodätische Woche 2018*

Dach R, Lutz S, Walser P, et al. (2015) Bernese GNSS Software Version 5.2. Astronomical Institute, University of Bern doi:10.7892/boris.72297 http://www.bernese.unibe.ch

Matlab, version R2016b (9.1.0.441655) The MathWorks Inc.

Schuh H, Böhm J (2013) Very long Baseline Interferometry for Geodesy and Astrometry In: Guochang Xu (ed.): *Sciences of Geodesy II, Innovations and Future Developments*, Springer Verlag, ISBN 978-3-642-27999-7, doi:10.1007978-3-642-28000-9, 339–376

Schartner M, Böhm J, Bolaño R, et al. (2018) VLBI Intensive sessions on a European baseline for the estimation of dUT1; *GRA*, 20, EGU2018-14986, EGU General Assembly 2018

Bizouard C, Lambert S, Gattano C, *et al.* (2019) The IERS EOP 14C04 solution for Earth orientation parameters consistent with ITRF 2014. *J Geod*, 93, 621–633, doi10.1007/s00190-018-1186-3

Combination of IVS Intensive Sessions – Approach, Benefit, and Operability

S. Bachmann, D. Thaller, A. Girdiuk

Abstract In this contribution we present the status of the intra-technique combination of VLBI intensive sessions for dUT1 estimation. So far, only 24h sessions are routinely combined using the contributions of various IVS Analysis Centers. We present our approach and first results to establish a combined IVS product for intensive sessions based on datum-free normal equations. We applied a so called σ^2-approach to estimate the individual weighting factor for each AC reflecting the inner accuracy of the constituent and, consequently, its contribution to the combined solution. The individual and the combined solutions are compared to dUT1 from IERS 14C04 series, where we found a WRMS of 26.6 µs for the combined solution and 32.8, 33.9, 34.6, and 24.2 for the individual AC solution. An offset of 7.9 µs for the combined solution has been estimated. Additionally, we compared the combined solution to dUT1 as reported in the GSFC *Intensives* series and to the IVS Quarterly 24h combined EOP series. We found an offset of −4.0 µs, a WRMS of 35.2 µs, and a RMS of 79.8 µs w.r.t. the GSFC series, and an offset of 2.8 µs, a WRMS of 34.9 µs, and a RMS of 40.7 µs compared to IVS Quarterly 24h series. Both comparisons show baseline-dependent statistics for the different INT networks (INT1, INT2, and INT3). Eventually, we discuss the benefit of such a combined product as well as the possibilities and challenges to install an operational IVS product.

Keywords Combination · Earth orientation parameters (EOP) · Intensives · UT1 · VLBI

Sabine Bachmann · Daniela Thaller · Anastasiia Girdiuk
Federal Agency for Cartography and Geodesy (BKG), Richard-Strauss-Allee 11, DE-60598 Frankfurt am Main, Germany

(Correspondence: sabine.bachmann@bkg.bund.de)

1 Motivation and objective

Combined VLBI products are well established in the International VLBI Service for Geodesy and Astrometry (IVS, Nothnagel et al., 2017) for station coordinates and Earth orientation parameter (EOP), given that a combined product shows improved statistics in comparison to a single individual solution (c.f. Böckmann et al., 2010; Bachmann et al., 2016). Improving and expanding the range of combined products is one of the tasks of the IVS Combination Center. So far, only daily 24h sessions have been used to generate IVS combined products. The aim of this study is to evaluate whether IVS intensive 1h sessions (also called *Intensives*) benefit from a combination on a comparable level as 24h sessions do, to carve out a combination approach and to evaluate the feasibility to establish an operational product.

2 Input contributions and combination approach

In analogy to the combination approach for 24h sessions (see Bachmann et al., 2016), the *Intensives* combination is based on datum free normal equations provided in SINEX format. The contributions of various IVS Analysis Centers (AC) are stacked to generate a combined solution, as shown in Fig. 1.

The input SINEX files contain station coordinates, pole coordinates and their rates, dUT1 and LOD. In the first step, the parameters of all input contributions are transformed to mid-session epochs. Additionally, the station coordinates are transformed to equal a priori station coordinates. The a priori station coordinates are extracted from the most recent VLBI combined long-

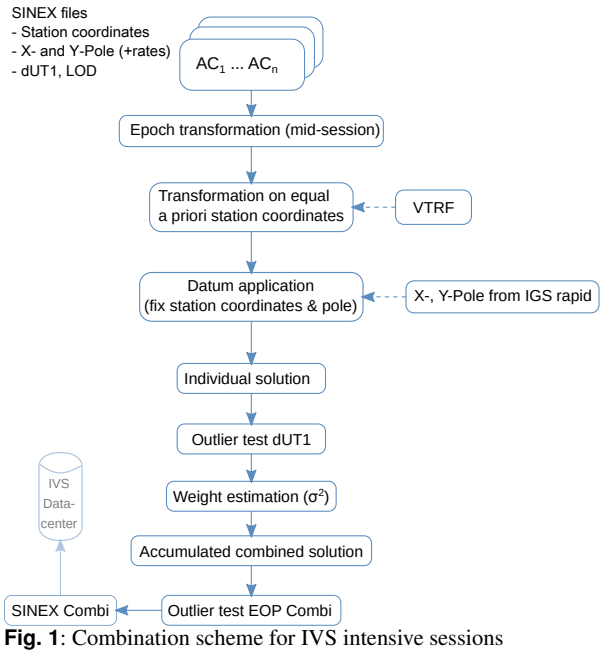

Fig. 1: Combination scheme for IVS intensive sessions

term solution VTRF, which is updated four times a year to ensure up-to-date coordinates (see https://ccivs.bkg.bund.de/index.php?uri=quarterly/vtrf for additional information). IVS *Intensives* are dedicated to provide dUT1 values on a daily basis, which requires an extended east-west baseline. Due to this single baseline configuration the estimable parameters of IVS *Intensives* are limited to dUT1. Errors in other EOPs, especially polar motion and nutation, propagate directly into dUT1 as has been evaluated by, e.g., Nothnagel and Schnell (2008). It is thus crucial to introduce these parameters with high accuracy. Therefore X-, Y-pole, and LOD a priori values are introduced using IGS rapid solutions for higher accuracy. Rapid IGS products have a 17-41 hours latency, which is generally sufficient for IVS *Intensives*. In the next step, individual solutions for each AC are generated to be used for an outlier test for dUT1 and for the estimation of the weighting factors for individual solutions. In contrast to a variance component estimation (VCE), which is applied for 24h sessions (see Bachmann et al. (2016) for further details), a σ^2-approach is applied to determine the individual weighting factor w:

$$w = \frac{1}{\sigma_i^2} \quad \text{with i = 1 ... n} \tag{1}$$

This factor is then used in the combination of IVS *Intensives*, where n is the number of contributing ACs and σ_i^2 is the a posteriori variance factor of the individual AC solution determined in the preceding step.

The last step is the accumulation of the datum free normal equations using the individual weighting factors for each AC and to produce the combined solution, and a SINEX file containing the combined datum free normal equation, the appropriate variance-covariance matrix, and the estimates. The datum is applied likewise as for the individual solutions. The final step would be to provide the combined SINEX file operationally to the IVS data center. Since too few ACs provide *Intensives* on operational basis to have a sufficient amount of SINEX files (>3), this step cannot be established at this time. For this study we included SINEX files available at the IVS data center, namely from AC BKG and USNO. Given the necessity to transform all contributions to the same a priori station coordinates and EOP, SINEX files containing solely dUT1 are therefore not suitable for our purposes. Additionally, SINEX contributions from AC SHA and VIE provided on request are used. Altogether we included four contributions using two different software packages. The input contributions comprise each type of *Intensives* from 2017. Overall 258 equal sessions for all ACs are used in this study.

3 Results of combination

In the following section we evaluate the results of the combined dUT1 solution over a one year time span in 2017. We are interested to see if our weighting approach is appropriate, i.e. it reflects the inner quality of the contributing solutions, and if the combination can deliver an improved dUT1 product.

3.1 Weighting factor estimation

For IVS *Intensives* a VCE, using station coordinates and EOP, cannot be applied as for 24h sessions, because of the the baseline configuration. Commonly, a VCE is applied to define the accuracy relations between the constituents by distinguishing the individual variance components from the total variance. To reproduce a relationship of the inner accuracy within

the *Intensives* combination, the σ_2-approach has been chosen (see Sect. 2). First, external effects are minimized by introducing equal a priori values for station coordinates and EOP, as well as transforming to equal epochs (see Fig. 1). Individual solutions are calculated and the resulting weighting factors are estimated eventually. The estimated weighting factors vary between one and two with some peaks for two ACs. The mean values are 2.4 for BKG, 1.4 for SHA, 1.5 for USNO, and 1.0 VIE, with some larger peaks reaching 19 at the maximum. Subsequently, the reason for the peaks is not yet clear and needs to be identified. Nevertheless, the individual weighting factors estimated using the σ^2-approach provides reliable results reflecting the inner accuracy between the constituents appropriately.

3.2 dUT1 results

We are interested to see if IVS *Intensives* do have a benefit from a combination as 24h sessions do (see Bachmann et al., 2016). Since VLBI is the only space geodetic technique having direct access to dUT1, finding appropriate external comparisons is challenging. Hence, we compare our estimated dUT1 time-series on a session-wise basis to the IERS 14C04 series, to the IVS 24h Quarterly combined series, and to the EOP series provided by Goddard Space Flight Center (GSFC), which is derived solely from *Intensives*. This series is independent, because no SINEX files of this AC are included in the combined solution.

Comparison to IERS 14C04

Figure 2 shows the dUT1 residuals from each of the contributing ACs and the combined solution w.r.rt. the IERS 14C04 series (c.f. Bizouard et al., 2018). Slight offsets are present for two ACs (see also Table 1), and slight irregularities between 2017.9 and 2018.0 are visible. Table 1 lists the WRMS, RMS, and the offset of the dUT1 time-series w.r.t. IERS 14C04 series. The variability tends to attenuate for the combined solution.

Comparison to GSFC *Intensives* time series

The comparison to the GSFC *Intensives* series in Fig. 3 shows a scatter of the residuals of ±30 µs, with an offset of −4.0 µs, a WRMS of 6.5 µs and a RMS of 46 µs. The small scatter is due to the fact that both dUT1 values are estimated from IVS *Intensive* series. When looking into sessions details, we see separation between the *Intensive* observations: INT1 sessions shown as black dots in Fig. 4, and INT2 sessions shown as red triangles in the same figure. INT1 sessions are observed regularly Monday to Friday at 18:30h UTC between stations Kokee Park (Hawaii, USA) and Wettzell (Germany). INT2 sessions are observed regularly on Saturday and Sunday at 7:30h UTC between stations Ishioka (Japan) and Wettzell (Germany), and INT3 sessions are observed regularly on Monday at 7:00h UTC between stations Ishioka (Japan), Ny-Ålesund (Svalbard, Norway), and Wettzell (Germany). The latter is shown as blue squares in Fig. 3. Table 2 shows the offset, WRMS, and RMS for each of the INT observations. INT1 and INT2 show a comparable offset, but differences in the (W)RMS values due to the different variability of the residuals. The influence of the baseline configuration on dUT1 estimation can be found in Nothnagel and Schnell (2008). INT3 sessions show the largest variations and offset due to its sparse observation, which results from few input contributions.

Table 1: RMS and Offset for dUT1 w.r.t. IERS 14C04 series (258 equal sessions for each AC)

AC	RMS [µs]	WRMS [µs]	Offset [µs]
BKG	36.5	32.8	5.3
SHAO	37.1	33.9	8.1
USNO	38.2	34.6	11.0
VIE	33.4	24.2	2.1
COMBI	28.2	26.6	7.9

Table 2: Offset, WRMS, and RMS for dUT1 combined solution w.r.t. GSFC *Intensives* series

INT series	Offset [µs]	WRMS [µs]	RMS [µs]	Nb. sessions
INT1	−6.2	27.0	79.8	208
INT2	−8.2	7.4	39.0	95
INT3	40.5	102.5	211.4	11
all	−4.0	35.2	79.8	314

Comparison to IVS Quarterly combined solution

The IVS Quarterly solution is a combined EOP series using all IVS 24h sessions suitable for EOP determination, and is thus independent from IVS *Intensives*. Also the nutation parameters are estimated, while for *Intensives* the nutation parameters need to be fixed to the a priori precession/nutation model (see Malkin (2011)

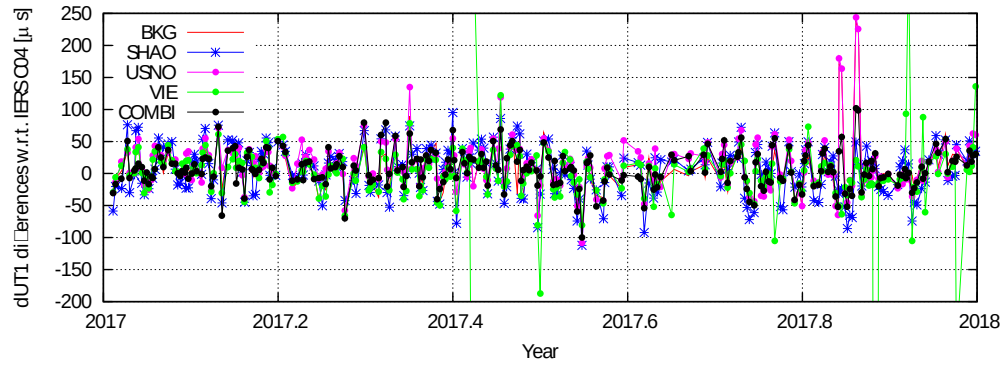

Fig. 2: dUT1 residuals w.r.t. IERS 14C04

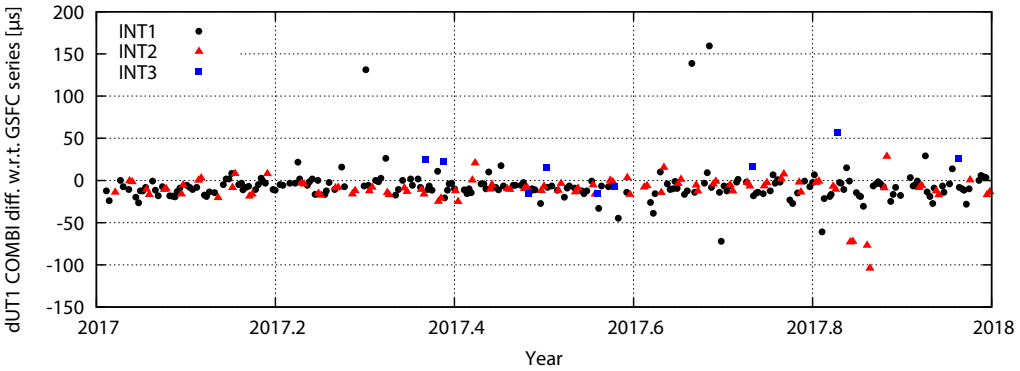

Fig. 3: dUT1 residuals w.r.t. GSFC eopi series. INT1 sessions are shown as black points, INT2 sessions as red triangles, and INT3 sessions as blue squares

for details on the impact of the nutation on dUT1 estimation). IVS 24h dUT1 values are cubic spline interpolated to the *Intensives* session epochs using regularization functions (cf. Ch. 8 of IERS Conventions 2010).

Figure 4 shows the results of the differences to the interpolated IVS 24h sessions. We observe a scatter of the residuals of about ±75 µs which is – as expected – larger than *Intensives*-only comparisons. The residuals show an overall offset of 2.8 µs, a WRMS of 34.9 µs, and a RMS of 40.7 µs, while the variations are smaller w.r.t. each other, but larger compared to the GSFC series. Considering interpolation biases, introduced by sparse sampling points with gabs of up to 3.5 days, the comparison to the IVS Quarterly solution shows good results in the expected range. Comparable to the GSFC comparison, we see clear differences in the offset for the different INT sessions (see Table 3). Additionally, we notice a session-dependent larger scatter after 2017.8 for INT2, that can be explained by a baseline change for those sessions (Seshan-Wettzell in replacement for Ishioka-Wettzell due to IVS CONT17 activities). The influence of the baseline geometry on dUT1 estimation is explained in Nothnagel and Schnell (2008).

Table 3: Offset, WRMS, and RMS for dUT1 combined solution w.r.t. IVS Quarterly solution

INT series	Offset [µs]	WRMS [µs]	RMS [µs]	Nb. sessions
INT1	−0.4	25.7	28.3	208
INT2	6.1	50.2	58.0	95
INT3	24.4	31.6	45.6	11
all	2.8	34.9	40.7	314

4 Conclusions

These first results show that combining individual IVS *Intensives* is a considerable way to introduce an improved dUT1 product in terms of statistics. In comparison to the well-established IVS 24h rapid combined solution, we introduced an adapted combination method-

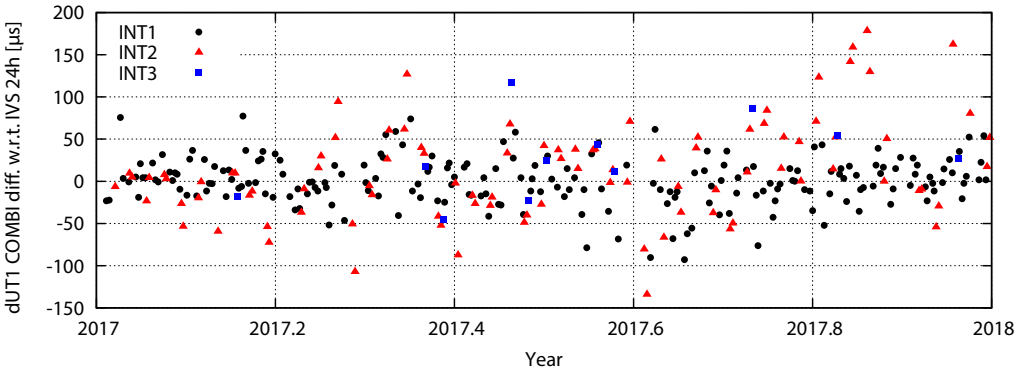

Fig. 4: dUT1 residuals w.r.t. IVS Quarterly 24h solution. INT1 sessions are shown as black points, INT2 sessions as red triangles, and INT3 sessions as blue squares

ology for IVS *Intensives* with an appropriate weighting strategy and datum application. The combined dUT1 results show an offset of 7.9 µs, an RMS of 28.2 µs, and a WRMS of 26.6 µs w.r.t. the IERS 14C04 series. Comparing to the GSFC *Intensives* series, the overall offset is −4.0 µs, and the WRMS and RMS are 35.2 µs and 79.8 µs, respectively. The comparison to the IVS 24h Quarterly series show an overall offset of 2.8 µs, a WRMS and a RMS of 34.9 µs and 40.7 µs, respectively. But there is a clear dependency on the specific INT (INT1, INT2, and INT3) sessions visible. So far, only a small number of IVS ACs are currently analyzing and submitting *Intensive* SINEX files operationally. Including more AC contributions (esp. from divers software packages) is thus highly desired in the near future. Then, adjusting a weighting strategy considering different software packages can be envisaged, comparably to the process used in the 24h combination (see Bachmann et al. (2016) for details). The objective is to establish an operational combined IVS *Intensive* product (depending on availability of individual AC contributions and achievable latency).

We thank our colleagues from Shanghai Observatory, US Naval Observatory, and Vienna University of Technology for providing SINEX files, which allowed us to set up the combination process and to carry out these first investigations.

References

Bachmann S, Thaller D, Roggenbuck O, et al. (2016) IVS contribution to ITRF2014. *J Geod*, 90(7):631–654, doi:10.1007/s00190-016-0899-4

Bizouard C, Lambert S, Gattano C, et al. (2018) The IERS EOP 14C04 solution for earth orientation parameters consistent with ITRF2014. *J Geod*, 93:621–633, doi:10.1007/s00190-018-1186-3

Böckmann S, Artz T, Nothnagel A, et al. (2010) International VLBI service for geodesy and astrometry: Earth orientation parameter combination methodology and quality of the combined products. *J Geophys Res*, 115(B04404), doi:10.1029/2009JB006465

Malkin Z (2011) The impact of celestial pole offset modelling on VLBI UT1 intensive results. *J Geod*, 85(9):617–622, doi:10.1007/s00190-011-0468-9

Nothnagel A, Schnell D (2008) The impact of errors in polar motion and nutation on UT1 determinations from VLBI Intensive observations. *J Geod*, 82(12):863–869, doi:10.1007/s00190-008-0212-2

Nothnagel A, Artz T, Behrend D, et al. (2017) International VLBI Service for Geodesy and Astrometry - Delivering high-quality products and embarking on observations of the next generation. *J Geod*, 91(7):711–721, doi:10.1007/s00190-016-0950-5

Comparison of VLBI-based Luni-solar Nutation Terms

V. Puente, J. Y. Richard, M. Folgueira, N. Capitaine, C. Bizouard

Abstract In this work, nutation time series determined by several International VLBI Service for Geodesy and Astrometry (IVS) analysis centers are compared in terms of corrections to luni-solar nutation terms. Different VLBI-based series of celestial pole offsets are used as input for a least-square harmonic fitting of corrections to nutation terms.

Keywords Earth rotation · Nutation · VLBI

1 Introduction

Very Long Baseline Interferometry (VLBI) is the only space geodesy technique that can directly observe the celestial pole offsets. These values are time-dependent corrections to the IAU200A/2006 nutation and precession model that are estimated by different VLBI analysis centres. The celestial pole offsets, together with the rest of Earth Orientation Parameters (EOP) are combined by the IERS and disseminated in official series.

Víctor Puente
National Geographic Institute of Spain, General Ibañez de Ibero 3, ES-28003, Madrid, Spain

Marta Folgueira
Department Section of Astronomy and Geodesy, Faculty of Mathematics, University Complutense of Madrid, ES-28040 Madrid, Spain

Jean-Yves Richard · Nicole Capitaine · Christian Biozuard
SYRTE, Observatoire de Paris, PSL Research University, CNRS, Sorbonne Universités, UPMC Univ. Paris 06, 61 avenue de l'Observatoire, FR-75014, Paris, France

(Correspondence: vpuente@fomento.es)

The purpose of this contribution is to compare the differences between the celestial pole offsets from different VLBI-based series consistent in terms of software configuration. Series provided by the International VLBI Service for Geodesy and Astrometry (IVS, Nothnagel et al., 2017) and combined solutions are analysed. The celestial pole offsets series from each source are used as pseudo-observations for a least-square harmonic fitting to obtain different corrections to nutation terms.

2 Theoretical background

The Earth Orientation Parameters constitute the key input for the coordinate transformation between the Geocentric Celestial Reference System (GCRS) and International Terrestrial Reference System (ITRS). These parameters are the components of the polar motion (x_P, y_P), the difference UT1-UTC and the celestial pole offsets (dX, dY) with respect to IAU200A/2006 nutation and precession model.

From VLBI-based series of celestial pole offsets (dX, dY), it is possible to perform a least-square harmonic fit of the main luni-solar nutation terms of the IAU2000A model:

$$\begin{aligned} dX &= \sum_{i=1}^{42} a_{real,i}\cos(ARG_i) + a_{imag,i}\sin(ARG_i), \\ dY &= \sum_{i=1}^{42} a_{real,i}\sin(ARG_i) + a_{imag,i}\cos(ARG_i), \end{aligned} \tag{1}$$

where ARG_i are linear combinations (multipliers factor k_i in Table 2) of the fundamental arguments (F_i) of the luni-solar nutation theory IERS Conventions (2010):

$$ARG_i = k_{i,1}F_1 + k_{i,2}F_2 + k_{i,3}F_3 + k_{i,4}F_4 + k_{i,5}F_5$$

$$\begin{aligned} F_1 &= 134.96340251^\circ + 1717915923.2178"t \\ &+31.8792"t^2 + 0.051635"t^3 - 0.00024470"t^4, \\ F_2 &= 357.52910918^\circ + 129596581.0481"t \\ &-0.532"t^2 + 0.000136"t^3 - 0.00001149"t^4, \\ F_3 &= 93.27209062^\circ + 1739527262.8478"t \\ &-12.512"t^2 - 0.001037"t^3 + 0.00000417"t4, \\ F_4 &= 297.85019547^\circ + 1602961601.2090"t \\ &-6.706"t^2 + 0.006593"t^3 - 0.00003169"t^4, \\ F_5 &= 125.04455501^\circ - 6962890.5431"t \\ &+7.4722"t^2 + 0.007702"t^3 - 0.00005939"t^4, \end{aligned} \quad (2)$$

where t is measured in Julian centuries of TDB.

Table 1 includes the list of the 42 nutation harmonic terms to be fitted. Columns k_i correspond to the multiplier factor of Delaunay arguments shown in Equation 2.

3 Software analysis

Table 2 presents a summary of the estimation strategies of the IVS analysis centers whose products are used in this work. This information is available at IVS servers. Solutions not using ICRF2 as celestial frame or not using IAU200A/2006 nutation and precession model have been excluded of the analysis.

4 Results

The corrections to IAU 2000A model were computed by means of a least-square harmonic fitting after having removing Free Core Nutation (FCN) effect using B16 model Belda et al. (2016).

This FCN model is based on the following equations:

$$\begin{aligned} X_{FCN} &= A_C \cos(\sigma_{FCN} t) - A_S \sin(\sigma_{FCN} t) + X_0, \\ Y_{FCN} &= A_S \cos(\sigma_{FCN} t) + A_C \sin(\sigma_{FCN} t) + Y_0, \end{aligned} \quad (3)$$

where A is the amplitude, t is the time since J2000.0 expressed in days, P is the period (=430.0027 solar days), $\sigma_{FCN} = 2\pi/P$ is the frequency of FCN and X_0 and Y_0 are constant offsets. A sliding window of 400 days and a step of one day was used to fit a FCN model for each solution analysed, i.e. the set of VLBI-based solutions aforementioned and also two series of combined solutions: IVS and EOP 14 C04 Bizouard et al. (2019).

Analysed time span was restricted to 1993-2019, since data before 1993 has poorer precision and temporal resolution Belda et al. (2016). Median amplitudes of the corrections to IAU 2000A model and the range between the values are shown in Figure 1 and compared to the results reported by Yao (2013) and Gattano et al. (2017). It should be noted that in Gattano et al. (2017) all IVS solutions were used regardless their configuration, using data starting from 1984. For Yao (2013), the fitted amplitudes correspond to an individual solution, so there is no figure for the range.

Table 3 includes a statistical summary of the differences between the amplitudes obtained in this work and the ones obtained by Yao (2013) and Gattano et al. (2017). These differences are computed removing the FCN signal — column w/o FCN — and without removing the FCN model — w/ FCN—. The results show a better agreement between the different solutions for a_{real} amplitudes than for a_{imag}; and removing the FCN signal (median differences below 0.4 μas). These results were also confirmed by an ANOVA analysis.

5 Conclusions and outlook

A comparison of the differences between corrections to the principal nutations of the IAU 2000A model have been computed based on celestial pole offsets from different VLBI-based series. The results show in general a good agreement with similar studies on this topic. Disagreement with Gattano's results for the longest nutation periods are probably due to the different set-up of the analysis: different set and time span of IVS solutions and different model to remove the FCN signal.

In the future, it is expected to enrich this analysis with GNSS-based estimation of celestial pole offsets Puente et al. (2018). This would be a valuable contribution to the study of short-period nutation terms.

References

Belda S, Ferrándiz J M, Heinkelmann R, et al. (2016) Testing a new Free Core Nutation empirical model. *J Geodyn*, 94-95, 59–67

Bizouard C, Lambert S, Gattano C et al. (2019) The IERS EOP 14C04 solution for Earth orientation parameters consistent with ITRF 2014. *J Geod*, 93(5),621–633, doi:10.1007/s00190-018-1186-3

Gattano C, Lambert S B, Bizouard C (2017) Observation of the Earth's nutation by the VLBI: how accurate is the geophysical signal. *J Geod*, 91(7), 849–856, doi:10.1007/s00190-016-0940-7

IERS Conventions (2010) In: G. Petit, B. Luzum (eds.) *IERS Technical Note* 36, Frankfurt am Main: Verlag des Bundesamts für Kartographie und Geodäsie,

Nothnagel A, Artz T, Behrend D, et al. (2019) International VLBI Service for Geodesy and Astrometry - Delivering high-quality products and embarking on observations of the next generation. *J Geod*, 91(7), 711–721

Puente V, Capitaine N, Richard J Y, et al. (2018) Nutation determination by means of GNSS: status and prospects. 20th EGU General Assembly

Yao K (2013) Estimation de la nutation de la Terre par les techniques VLBI et GPS. Thesis at University Pierre and Marie Curie.

Table 1: Harmonic terms and corresponding periods of luni-solar nutation.

i	$k_{i,1}$	$k_{i,2}$	$k_{i,3}$	$k_{i,4}$	$k_{i,5}$	Period (days)
1	0	0	0	0	1	−6798.38
2	0	0	0	0	−1	6798.38
3	0	0	0	0	2	−3399.19
4	0	0	0	0	−2	3399.19
5	2	0	−2	0	−2	−1615.75
6	−2	0	2	0	2	1615.75
7	2	0	−2	0	−1	−1305.48
8	−2	0	2	0	1	1305.48
9	2	0	−2	0	0	−1095.18
10	−2	0	2	0	0	1095.18
11	0	−1	0	0	−1	−386.00
12	0	1	0	0	1	386.00
13	0	−1	0	0	0	−365.26
14	0	1	0	0	0	365.26
15	0	−1	0	0	1	−346.64
16	0	1	0	0	−1	346.64
17	0	0	−2	2	−2	−182.62
18	0	0	2	−2	2	182.62
19	0	−1	−2	2	−2	−121.75
20	0	1	2	−2	2	121.75
21	1	0	0	−2	0	−31.81
22	−1	0	0	2	0	31.81
23	−1	0	0	0	0	−27.55
24	1	0	0	0	0	27.55
25	−1	0	−2	2	−2	−23.94
26	1	0	2	−2	2	23.94
27	0	0	0	−2	0	−14.77
28	0	0	0	2	0	14.77
29	−2	0	0	0	0	−13.78
30	2	0	0	0	0	13.78
31	0	0	−2	0	−2	−13.66
32	0	0	2	0	2	13.66
33	1	0	−2	−2	−2	−9.56
34	−1	0	2	2	2	9.56
35	−1	0	−2	0	−2	−9.13
36	1	0	2	0	2	9.13
37	−1	0	−2	0	−1	−9.12
38	1	0	2	0	1	9.12
39	0	0	−2	−2	−2	−7.10
40	0	0	2	2	2	7.10
41	−2	0	−2	0	−2	−6.86
42	2	0	2	0	2	6.86

Table 2: Estimation strategies of different IVS solutions analysed.

Analysis center	BKG	GSF	IAA	OPA	USN
Software package	Calc 10.0/Solve	Calc 11.0/Solve	OCCAM/GROSS	Calc 11.0/Solve	Calc 11.0/Solve
Celestial frame	ICRF2	ICRF2	ICRF2	ICRF2	ICRF2
Terrestrial frame	ITRF08	ITRF14	ITRF14	ITRF14	ITRF14
IERS Conventions	2010	2010	2006	2010	2010
Nutation/precession model	IAU200A/2006	IAU200A/2006	IAU200A/2006	IAU200A/2006	IAU200A/2006
Estimation model	Least squares	Least squares	Kalman filter	Least-squares	Least-squares
Troposphere	VMF1	VMF1	VMF1	VMF1	VMF1

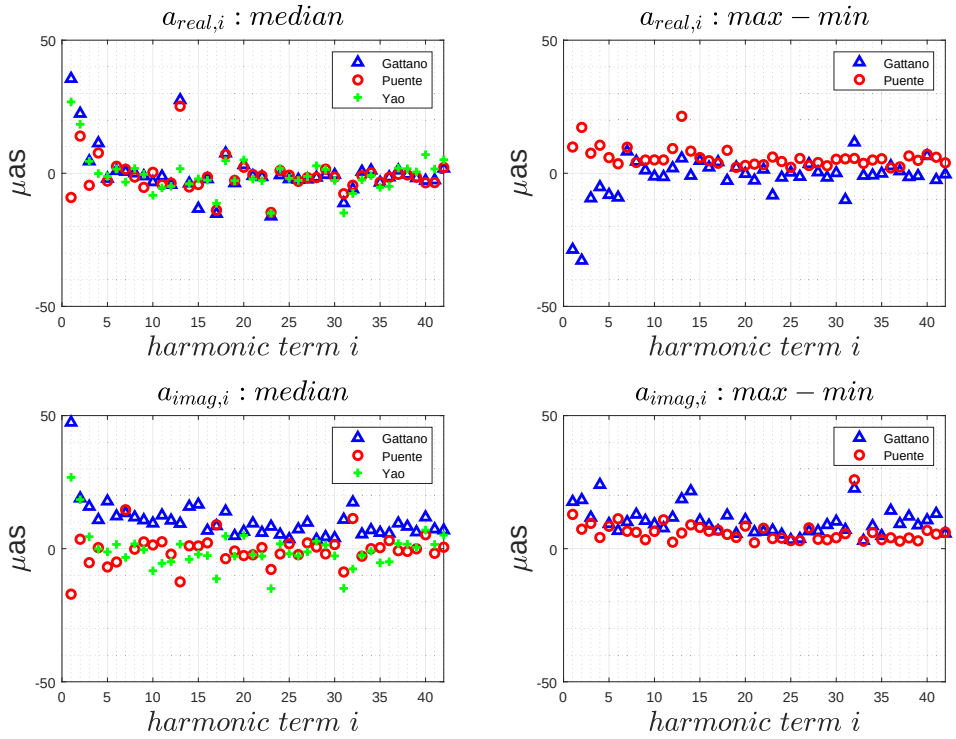

Fig. 1: Comparison of the median and range of the amplitudes with respect to Yao (2013) and Gattano et al. (2017).

Table 3: Statistical summary of the differences in the computed corrections to IAU 2000A.

Period (days)	Puente vs. Yao				Puente vs. Gattano			
	a_{real}		a_{imag}		a_{real}		a_{imag}	
	w/o FCN	w/ FCN	w/o FCN	w/ FCN	w/o FCN	w/ FCN	w/o FCN	w/ FCN
−6798.38	−35.9	14.0	−2.7	19.2	−44.6	11.6	−11.4	16.8
6798.38	−4.4	38.3	−14.7	15.8	−8.4	36.3	−18.7	13.8
−3399.19	−9.0	0.0	1.9	−2.8	−9.0	4.1	1.9	1.3
3399.19	7.7	5.6	16.2	−10.2	−3.7	5.6	4.8	−10.2
−1615.75	−1.8	2.6	1.1	5.7	−1.0	1.2	1.9	4.3
1615.75	1.0	3.6	−6.1	4.4	1.7	4.1	−5.4	4.9
−1305.48	4.8	3.9	5.4	2.3	0.9	6.4	1.5	4.8
1305.48	−3.2	−0.5	−0.1	−1.3	−1.4	−4.6	1.7	−5.4
−1095.18	−4.9	−2.5	−8.3	−7.5	−4.2	1.5	−7.6	−3.5
1095.18	8.7	3.4	11.6	5.6	3.7	2.6	6.6	4.8
−386.00	1.2	−1.1	10.2	−3.1	−3.1	4.0	5.9	2.0
386.00	1.2	−3.4	2.5	−3.2	0.6	−4.0	1.9	−3.8
−365.26	23.5	−16.7	14.7	−5.4	−2.3	−18.1	−11.1	−6.8
365.26	−1.1	8.1	−0.9	8.3	−1.3	2.0	−1.1	2.2
−346.64	−2.1	8.5	−5.6	5.4	9.1	−3.7	5.6	−6.8
346.64	1.2	−4.7	3.7	−2.6	0.8	0.0	3.3	2.1
−182.62	−2.6	3.5	−3.2	3.9	1.3	4.8	0.7	5.2
182.62	2.4	−4.2	2.3	−5.8	−0.4	−1.0	−0.5	−2.6
−121.75	0.1	−1.3	−1.0	1.0	1.0	−3.1	−0.1	−0.8
121.75	−2.7	−1.9	−2.7	−2.3	−0.8	−2.4	−0.8	−2.8
−31.81	1.7	−1.0	2.7	−0.	0.5	0.4	1.5	1.3
31.81	1.8	2.9	1.5	1.7	0.4	−1.0	0.1	−2.2
−27.55	0.3	−4.4	1.6	−4.7	1.5	0.5	2.8	0.2
27.55	−0.8	−4.4	−0.7	−4.4	1.7	−0.4	1.8	−0.4
−23.94	1.2	−2.5	1.3	−2.1	1.5	1.6	1.6	2.0
23.94	−0.3	0.1	0.3	1.2	−0.6	−1.0	0.0	0.1
−14.77	−0.4	−1.0	−0.2	−0.5	0.7	−1.3	0.9	−0.8
14.77	−4.4	1.8	−4.7	1.4	0.0	0.2	−0.3	−0.2
−13.78	0.1	−1.5	−1.3	−3.2	2.1	−0.4	0.7	−2.1
13.78	1.3	−2.3	2.0	−1.3	−0.8	1.5	−0.1	2.5
−13.66	7.2	3.5	7.0	0.6	3.5	1.2	3.3	−1.7
13.66	3.1	−0.2	4.8	−0.4	1.5	−0.3	3.2	−0.5
−9.56	1.6	−1.0	0.1	−1.0	−1.5	−1.9	−3.0	−1.9
9.56	1.1	1.2	1.7	−1.7	−0.9	0.8	−0.3	−2.1
−9.13	2.0	−2.4	3.7	−3.4	0.2	0.5	1.9	−0.5
9.13	3.3	0.6	1.9	0.5	−0.1	0.4	−1.5	0.3
−9.12	−2.3	−0.8	−1.5	−1.0	−1.5	−1.6	−0.7	−1.8
9.12	−2.3	−4.0	−2.7	−2.0	−0.1	0.4	−0.5	2.4
−7.10	−2.0	−2.8	−5.3	−1.0	0.3	1.0	−3.0	2.8
7.10	−10.6	5.4	−7.5	7.4	−0.8	−1.3	2.3	0.7
−6.86	−5.1	2.5	−7.0	0.7	−0.9	0.8	−2.8	−1.0
6.86	−2.9	1.8	−3.5	−0.4	0.4	1.0	−0.2	−1.2
Median	0.1	−0.3	0.2	−0.7	−0.0	0.4	0.4	−0.3
Unit in μas								

Index of authors

This page is intentionally left blank.

Program of the EVGA 2019

Sunday, March 17

	Icebreaker reception	Register, get your badge, meet your friends, have fun!	19:00-21:00

Monday, March 18

	Rafael Robaina Romero (Rector of Las Palmas University); José Antonio López-Fernández (Astronomy, Geophysics and Space Applications Subdirector at IGN); Rüdiger Haas (EVGA Chair)	Opening ceremony of the EVGA 2019	09:00-09:30

	Session 1.1	09:30-10:30, chair: Gino Tuccari	
O101	José Antonio López-Fernández	The current status of RAEGE	09:30-09:45
O102	Rüdiger Haas	Status of the Onsala twin telescopes	09:45-10:00
O103	Leif Morten Tangen	Status for the establishment of a new fundamental site in Ny-Ålesund	10:00-10:15
O104	Jinling Li	The Sheshan 13-m radio telescope	10:15-10:30

	coffee break	10:30-11:00

	Session 1.2	11:00-12:00 chair: Evgeny Nosov	
O105	Michael Lösler	Measuring focal-length variations of VGOS-telescopes using unmanned aerial systems	11:00-11:15
O106	Pablo de Vicente	Instrumentation developed for VGOS at IGN Yebes Observatory	11:15-11:30
O107	Gino Tuccari	DBBC3 towards the BRAND EVN receiver	11:30-11:45
O108	Walter Alef	BRAND - A wideband receiver for astronomy and geodesy	11:45-12:00

	”stretch your legs” break	12:00-12:15

	Session 1.3	12:15-13:15 chair: Pablo de Vicente	
O109	Evgeny Nosov	The stability of delay in VLBI digital backends	12:15-12:30
O110	Jakob Gruber	A simulator to generate VLBI baseband data in Matlab	12:30-12:45
O111	Roberto Ricci	Optical fiber links used in VLBI networks and remote clock comparisons: the LIFT/MetGesp project	12:45-13:00
O112	Mamoru Sekido	Italy-Japan broadband VLBI experiment for optical clock comparison	13:00-13:15
		lunch break	13:15-14:15
	Session 1.4	14:15-15:15 chair: Walter Alef	
O113	Xin Zheng	Researching and application of VLBI differential phase delay in lunar exploration	14:15-14:30
O114	Walter Brisken	Status and development plans of the VLBA	14:30-14:45
O115	Aard Keimpema	Recent technical developments at JIVE	14:45-15:00
O116	Tetsuro Kondo	Comparison of results between CVN and K5 software correlators	15:00-15:15
		”stretch your legs” break	15:15-15:30
	Session 2.1	15:30-16:30 chair: Aletha de Witt	
O201	Laura La Porta	The Bonn Correlation Center and VGOS	15:30-15:45
O202	Walter Alef	The EU-VGOS project	15:45-16:00
O203	Maria Eugenia Gomez	Implementation of a geodetic path at the JIVE correlator	16:00-16:15
O204	Takahiro Wakasugi	Activity report on the Asia-Oceania VLBI Group (AOV)	16:15-16:30
		coffee break	16:30-17:00
	Session 2.2	17:00-18:00 chair: Laura La Porta	
O205	Aletha de Witt	The Southern VLBI Operations Centre	17:00-17:15

O206	Matthias Schartner	Results with the scheduling software VieSched++	17:15-17:30
O207	Christian Plötz	INT9 - dUT1 determination between the geodetic observatories AGGO and Wettzell	17:30-17:45
O208	Torben Schüler	LCONT18 - The local continuous measurement campaign at Wettzell of 2018	17:45-18:00

Poster session	**Look at all the nice posters!**	18:00-19:30

Tuesday March 19

	Session 2.3	09:00-9:45 chair: Torben Schüler	
O209	Jing Sun	Preliminary work on promoting radar astronomical study	09:00-09:15
O210	Oleg Titov	Observations of radio sources near the Sun	09:15-09:30
O211	Alexander Neidhardt	Autonomous observations of VLBI radio telescopes	09:30-09:45

”stretch your legs” break		09:45-10:00

	Session 3.1	10:00-10:45 chair: Arthur Niell	
O301	Dan MacMillan	Analysis of EOP and scale from the simultaneous CONT17 networks	10:00-10:15
O302	Johannes Böhm	CONT17 from a VieVS perspective	10:15-10:30
O303	Maria Davis	The IERS Rapid Service / Prediction Center UT1-UTC combined solution: Present and future Contributions	10:30-10:45

coffee break		10:45-11:15

	Session 3.2	11:15-12:00 chair: Dan MacMillan	
O304	Anastasiia Girdiuk	Analysis of regular and specific intensive sessions	11:15-11:30
O305	Armin Corbin	Scheduling of twin telescopes and the impact on troposphere and UT1 estimation	11:30-11:45

O306	Arthur Niell	VLBI tie between the KOKEE12M and KOKEE20M antennas	11:45-12:00

	”stretch your legs” break	12:00-12:15

	Session 3.3	12:15-13:15 chair: Johannes Böhm	
O307	Axel Nothnagel	Gravitational deformation investigations and their impact on global telescope coordinates: The Onsala 20 m radio telescope case	12:15-12:30
O308	John Gipson	Gravitational deformation of VLBI antennas and the impact on the TRF	12:30-12:45
O309	Matthias Glomsda	Impact of non-tidal loading in VLBI analysis	12:45-13:00
O310	Kyriakos Balidakis	How does geophysical loading affect Earth rotation? Simulations and reality	13:00-13:15

	lunch break	13:15-14:15

	Session 3.4	14:15-15:15 chair: Axel Nothnagel	
O311	Víctor Puente	Comparison of troposphere delays from GNSS and VLBI in R1 and R4 sessions	14:15-14:30
O312	Periklis-Konstantinos Diamantidis	Comparison of tropospheric delay estimation using VLBI CONT14 data and WVR for the Onsala station	14:30-14:45
O313	Tobias Nilsson	An assessment of the tropospheric parameters estimated from the CONT17 campaign	14:45-15:00
O314	Frédéric Jaron	An analytical VLBI delay formula for Earth satellites	15:00-15:15

	”stretch your legs” break	15:15-15:30

	Session 3.5	15:30-16:15 chair: John Gipson	
O315	Grzegorz Klopotek	Geodetic VLBI observations of lunar radio sources – Current status and recommendations for future research	15:30-15:45
O316	Benedikt Soja	Ionospheric calibration for K-band celestial reference frames	15:45-16:00
O317	Karine Le Bail	Time stability of the K-band catalog sources	16:00-16:15

		coffe break	16:15-16:45
	Session 3.6	16:45-17:45 chair: Karine Le Bail	
O318	Patrick Charlot	ICRF3, the new realization of the International Celestial Reference Frame	16:45-17:00
O319	James M. Anderson	Toward imaging 3000+ ICRF sources from closure quantities from 1979–present	17:00-17:15
O320	Lucas Hunt	VLBA Imaging of ICRF 3 sources	17:15-17:30
O321	Arnaud Collioud	The Bordeaux VLBI Image Database (BVID)	17:30-17:45
		"stretch your legs" break	17:45-18:00
	Session 3.7	18:00-19:00 chair: Patrick Charlot	
O322	Ming Hui Xu	Structure effects in broadband VGOS data	18:00-18:15
O323	Sergei Bolotin	The source structure effect in broadband observations	18:15-18:30
O324	Simin Salarpour	Source structure effects in the next-generation of VLBI observations	18:30-18:45
O325	Leonid Petrov	Remaining problems in geodesy / astrometry VLBI and approaches to their solutions	18:45-19:00
	Rüdiger Haas	Closing remarks	19:00-19:15
		EVGA dinner	19:15-23:59

Posters

	Session 1	
P101	David Cordobés	Status of the future RAEGE radio telescope at Gran Canaria
P102	Andrea Prudencio	First steps in gravitational deformation modeling of the VLBI Yebes radio telescopes
P103	Gunnar Elgered	The Onsala Tide Gauge Station: Experiences from the first three years of operation
P104	Hiroshi Munekane	VLBI-GNSS collocation survey at the Ishioka VLBI station
P105	Nataliya Zubko	Progress and current status on VGOS project at the Metsähovi Geodetic Research Station
P106	Alexander Neidhardt	Centralized monitoring of VLBI antennas for seamless auxiliary data
P107	Alexander Neidhardt	Remote access to the NASA Field System via Web browser
P108	Weimin Zheng	Space low-frequency radio observatory and the Earth-moon VLBI experiment
P109	Ahmad Jaradat	An artificial radio signal for VLBI satellite tracking
	Session 2	
P201	Xuan He	Mixed-mode VLBI observations with Chinese stations in APSG40
P202	Christopher Dieck	Intensive sessions with the Mauna Kea VLBA Station
P203	Dirk Behrend	Roll-out status of the VGOS network
P204	Hayo Hase	Argentinean-German Geodetic Observatory (AGGO)
P205	Karen Baver	The effect of source flux catalog latency on IVS-INT01 scheduling
P206	Marisa Nickola	HartRAO local tie measurements: VLBI and ground survey
P207	Matthias Schartner	Impact of different observing rates on geodetic results
P208	Matthias Schartner	In-depth analysis of schedules optimized for certain VLBI experiments using VieSched++
P209	Michael Lösler	A modified approach for process-integrated reference point determination
P210	Fengchun Shu	High sensitivity astrometry with the AOV

P211	Jakob Gruber	Vienna correlation activities
P212	Ed Himwich	2018 IVS Network Performance
P213	Dhanya G. Nair	GMVA image database at 86 GHz now online
P214	Juan Zhang	The progress of CVN Software correlator and its applications
	Session 3	
P301	Andreas Hellerschmied	Vienna VLBI Analysis Center (VIE)
P302	Christopher S. Jacobs	The X/Ka-band 2019a celestial frame:
P303	Esther Azcue	VLBI analyses at the National Geographic Institute of Spain
P304	Hana Krásná	Earth orientation parameters estimated from K-band VLBA measurements
P305	Helene Wolf	AUA047: Students at TU Wien organize their own VLBI session
P306	Aletha de Witt	The K-band (24 GHz) Celestial Reference Frame
P307	Markus Mikschi	Comparison of integrated LOD values from GNSS and AAM to dUT1 from VLBI
P308	Niko Kareinen	Simulated combined effect of extended source structure and baseline geometry to geodetic parameters estimated with VLBI
P309	Sabine Bachmann	Combination of IVS intensive sessions ' approach, benefit, and operability
P310	Susanne Lunz	Radio source position offsets among various radio frames and Gaia
P311	Suxia Gong	Comparison of ionospheric delays between VLBI and GNSS
P312	Tuomas Savolainen	NT-VGOS - Mitigating the source structure errors in the VGOS era
P313	Simona Di Tomaso	Inter-comparison of GNSS and VLBI tropospheric parameters at co-located sites in Italy
P314	Víctor Puente	Comparison of VLBI-based series of celestial pole offsets
P315	Ming Hui Xu	Comparison between time series of closure analysis and source positions since 1980
P316	Svetlana Mironova	Diurnal and sub-diurnal EOP variations from VLBI global solution

List of participants EVGA 2019

Name	Affiliation and Email address
Alef, Walter	Max Planck Institute for Radio Astronomy, MPIfR, Germany walef@mpifr-bonn.mpg.de
Anderson, James M.	Technische Universität Berlin, TU Berlin/German Research Centre for Geosciences, GFZ, Germany anderson@tu-berlin.de
Araña Pulido, Victor	Las Palmas de Gran Canaria University, ULPGC, Spain varana@dsc.ulpgc.es
Azcue, Esther	Instituto Geográfico Nacional, IGN, Spain eazcue@fomento.es
Bachmann, Sabine	Bundesamt für Kartographie und Geodäsie, BKG, Germany sabine.bachmann@bkg.bund.de
Balidakis, Kyriakos	German Research Centre for Geosciences, GFZ, Germany kyriakos.balidakis@gfz-potsdam.de
Behrend, Dirk	NVI, Inc., USA dirk.behrend@nviinc.com
Belov, Konstantin	NASA/Jet Propulsion Laboratory, JPL, California Institute of Technology, USA Konstantin.V.Belov@jpl.nasa.gov
Benito, María Ángeles	Instituto Geográfico Nacional, IGN, Spain mabenito@fomento.es
Böhm, Johannes	Technische Universität Wien , TU Wien, Austria johannes.boehm@tuwien.ac.at
Bolotin, Sergei	NVI, Inc., USA sergei.bolotin@nasa.gov
Bourda, Geraldine	Laboratoire d'Astrophysique de Bordeaux, France geraldine.bourda@u-bordeaux.fr
Brisken, Walter	National Radio Astronomy Observatory, NRAO, USA wbrisken@nrao.edu
Charlot, Patrick	Laboratoire d'Astrophysique de Bordeaux, France patrick.charlot@u-bordeaux.fr
Chen, Wen	Yunnan Observatories, Chinese Academy of Science, China chenwen@ynao.ac.cn
Collioud, Arnaud	Laboratoire d'Astrophysique de Bordeaux, France arnaud.collioud@u-bordeaux.fr
Colomer, Francisco	Joint Institute for VLBI ERIC, JIVE, The Netherlands colomer@jive.eu
Corbin, Armin	Chalmers University of Technology, Sweden armin.corbin@chalmers.se
Cordobés Gallo, David	Instituto Geográfico Nacional, IGN, Spain d.cordobes@oan.es
Davis, Maria	U.S. Naval Observatory, USNO, USA maria.a.davis33.civ@mail.mil
de Vicente, Pablo	Yebes Observatory/Instituto Geográfico Nacional, IGN, Spain p.devicente@oan.es

de Witt, Aletha	South African Radio Astronomy Observatory, SARAO, South Africa alet@hartrao.ac.za
Di Tomaso, Simona	E-GEOS ASI, Italy simona.ditomaso@e-geos.it
Diamantidis, Periklis-K.	Chalmers University of Technology, Sweden periklis.diamantidis@chalmers.se
Dieck, Christopher	U.S. Naval Observatory, USNO, USA christopher.dieck@navy.mil
Domínguez Cerdeña, Itahiza	Instituto Geográfico Nacional, IGN-Canarias, Spain ifdominguez@fomento.es
Dutka, Michael	U.S. Naval Observatory, USNO, USA mdutka@cpi.com
Elgered, Gunnar	Chalmers University of Technology, Sweden gunnar.elgered@chalmers.se
Eschelbach, Cornelia	Frankfurt University of Applied Sciences/Laboratory for Industrial Metrology, Germany cornelia.eschelbach@fb1.fra-uas.de
Eskelinen, Joona	Finnish Geospatial Research Institute, FGI, Finland joona.eskelinen@nls.fi
García Castellano, Abel	Instituto Geográfico Nacional, IGN, Spain abel.garcia@oan.es
Garcia-Espada, Susana	RAEGE Santa Maria-Azores/Instituto Geográfico Nacional, IGN, Spain sgespada@fomento.es
Gipson, John	NVI, Inc., USA john.gipson@nviinc.com
Girdiuk, Anastasiia	Bundesamt für Kartographie und Geodäsie, BKG, Germany anastasiia.girdiuk@bkg.bund.de
Glomsda, Matthias	Deutsches Geodätisches Forschungsinstitut, Technische Universität München, DGFI-TUM, Germany matthias.glomsda@tum.de
Gómez, Maria Eugenia	Laboratoire d'Astrophysique de Bordeaux, France maria.gomez@u-bordeaux.fr
Gómez Espada, Yaiza	Instituto Geográfico Nacional, IGN, Spain becario.yge@fomento.es
Gómez González, Jesus	Instituto Geográfico Nacional, IGN, Spain jggonzalez@fomento.es
Gong, Suxia	German Research Centre for Geosciences, GFZ, Germany susia201507@gmail.com
González Matesanz, Javier	Instituto Geográfico Nacional, IGN, Spain fjgmatesanz@fomento.es
Gruber, Jakob	Technische Universität Wien , TU Wien, Austria jakob.franz.gruber@geo.tuwien.ac.at
Haas, Rüdiger	Chalmers University of Technology, Sweden rudiger.haas@chalmers.se
Haftings, Phillip	U.S. Naval Observatory, USNO, USA phillip.haftings@navy.mil
Hall, David	U.S. Naval Observatory, USNO, USA daveh922@verizon.net

Hao, Longfei	Yunnan Observatories, Chinese Academy of Science, China haolongfei@ynao.ac.cn
Hardin, Matthew	Universities Space Research Association, USRA/U.S. Naval Observatory, USNO, USA mhardin42@gmail.com
Hase, Hayo	Bundesamt für Kartographie und Geodäsie, BKG, Germany - Argentina hayo.hase@bkg.bund.de
He, Xuan	Shanghai Astronomical Observatory, SHAO, Chinese Academy of Science, China hexuan@shao.ac.cn
Hellerschmied, Andreas	Federal Office of Metrology and Surveying, Austria andreas.hellerschmied@bev.gv.at
Himwich, Ed	NVI, Inc., USA ed.himwich@nviinc.com
Huang, Yidan	Shanghai Astronomical Observatory, SHAO, Chinese Academy of Science, China hyd@shao.ac.cn
Hunt, Lucas	U.S. Naval Observatory, USNO, USA lucas.hunt@navy.mil
Jaradat, Ahmad	Institute of Geodesy and Geoinformation, Bonn University, Germany s7ahjara@uni-bonn.de
Jaroenjittichai, Phrudth	National Astronomical Research Institute, Thailand phrudth@gmail.com
Jaron, Frédéric	Institute of Geodesy and Geoinformation, Bonn University, Germany jaron@igg.uni-bonn.de
Johnson, Megan	U.S. Naval Observatory, USNO, USA megan.johnson@navy.mil
Kareinen, Niko	Finnish Geospatial Research Institute FGI, Finland niko.kareinen@nls.fi
Keimpema, Aard	Joint Institute for VLBI ERIC, JIVE, The Netherlands keimpema@jive.nl
Kirkvik, Ann-Silje	Norwegian Mapping Authority, NMA, Norway ann-silje.kirkvik@kartverket.no
Klopotek, Grzegorz	Chalmers University of Technology, Sweden grzegorz.klopotek@chalmers.se
Kondo, Tetsuro	Shanghai Astronomical Observatory, SHAO, Chinese Academy of Science, China kondo@shao.ac.cn
Kotary, Nancy	MIT Haystack Observatory, USA nwk@mit.edu
La Porta, Laura	Reichert GmbH/ Bundesamt für Kartographie und Geodäsie, BKG, Germany laporta@mpifr-bonn.mpg.de
Lanotte, Roberto	E-GEOS ASI/Space Geodesy Center, CGS, Italy roberto.lanotte@e-geos.it
Le Bail, Karine	NVI, Inc., USA karine.lebail@nasa.gov
Li, Jinling	Shanghai Astronomical Observatory, SHAO, Chinese Academy of Science, China jll@shao.ac.nc
Lösler, Michael	Frankfurt University of Applied Sciences/Laboratory for Industrial Metrology, Germany michael.loesler@fb1.fra-uas.de

López Fernández, Jose	Instituto Geográfico Nacional, IGN, Spain jalfernandez@fomento.es
L'Orange, Simon	Norwegian Mapping Authority, NMA, Norway simon.lorange@kartverket.no
Lunz, Susanne	German Research Centre for Geosciences, GFZ, Germany susanne.lunz@gfz-potsdam.de
Ma, Langming	National Time Service Center, Chinese Academy of Sciences, China malm@ntsc.ac.cn
MacMillan, Dan	NVI, Inc., USA dan.macmillan@nviinc.com
Merkowitz, Stephen	NASA/Goddard Space Flight Center, USA stephen.m.merkowitz@nasa.gov
Mikschi, Markus	Technische Universität Wien , TU Wien, Austria markus.mikschi@geo.tuwien.ac.at
Munekane, Hiroshi	Geospatial Information Authority of Japan, Japan munekane-h96nu@mlit.go.jp
Negusini, Monia	National Institute of Astrophysics, INAF-IRA, Italy negusini@ira.inaf.it
Neidhardt, Alexander	Technische Universität München, TUM, Forschungseinrichtung Satellitengeodaesie, Germany neidhardt@fs.wettzell.de
Nickola, Marisa	South African Radio Astronomy Observatory, SARAO, South Africa marisa@hartrao.ac.za
Niell, Arthur	MIT Haystack Observatory, USA aniell@mit.edu
Nilsson, Tobias	Lantmäteriet, Sweden jan-tobias.nilsson@lm.se
Nosov, Evgeny	Institute of Applied Astronomy, Russian Academy of Sciences, IAA RAS, Russia nosov@iaaras.ru
Nothnagel, Axel	Institute of Geodesy and Geoinformation, Bonn University, Germany nothnagel@uni-bonn.de
Petrov, Leonid	NASA/Goddard Space Flight Center, USA Leonid.Petrov@nasa.gov
Plötz, Christian	Bundesamt für Kartographie und Geodäsie, BKG, Germany christian.ploetz@bkg.bund.de
Porcas, Richard	Max Planck Institute for Radio Astronomy, MPIfR, Germany porcas@mpifr-bonn.mpg.de
Puente, Víctor	Instituto Geográfico Nacional, IGN, Spain vpuente@fomento.es
Raut, Shrishail	Technische Universität Berlin, TU Berlin, Germany shrishail.raut@campus.tu-berlin.de
Ricci, Roberto	National Institute of Astrophysics, INAF-IRA, Italy ricci@ira.inaf.it
Salarpour, Simin	University of Tasmania, Australia simin.salarpour@utas.edu.au
Sandmo, Trond	Norwegian Mapping Authority, NMA, Norway trond.sandmo@kartverket.no
Sargent, Andrew	U.S. Naval Observatory, USNO, USA andrew.j.sargent@navy.mil

Savolainen, Tuomas	Aalto University Metsahovi Radio Observatory, Finland tuomas.k.savolainen@aalto.fi
Schartner, Matthias	Technische Universität Wien , TU Wien, Austria matthias.schartner@geo.tuwien.ac.at
Schott Guilmault, Vladimir	Centre National d'Estudes Spatiales, CNES, France schottguilmault@ipgp.fr
Schuh, Harald	German Research Centre for Geosciences, GFZ, Germany schuh@gfz-potsdam.de
Schüler, Torben	Geodetic Observatory Wettzell, Germany gow@mailbox.org
Sekido, Mamoru	National Institute of Information and Communications Technology, NICT, Japan sekido@nict.go.jp
Shu, Fengchun	Shanghai Astronomical Observatory, SHAO, Chinese Academy of Science, China sfc@shao.ac.cn
Soja, Benedikt	Jet Propulsion Laboratory, JPL, California Institute of Technology, USA bsoja@jpl.nasa.gov
Sun, Jing	National Astronomical Observatory, China sunjing@bao.ac.cn
Sust, Eberhard	MT Mechatronics, Germany eberhard.sust@mt-mechatronics.de
Tangen, Leif Morgen	Norwegian Mapping Authority, NMA, Norway leif.morten.tangen@kartverket.no
Titov, Oleg	Geoscience Australia, Australia oleg.titov@ga.gov.au
Tuccari, Gino	National Institute of Astrophysics, INAF-IRA/Max Planck Institute for Radio Astronomy, MPIfR, Italy tuccari@mpifr-bonn.mpg.de
Valdés, Marcelino	Instituto Geográfico Nacional, IGN, Spain mvaldes@fomento.es
Verkouter, Harro	Joint Institute for VLBI ERIC, JIVE, The Netherlands verkouter@jive.eu
Wakasugi, Takahiro	Geospatial Information Authority of Japan, Japan wakasugi-t96kg@mlit.go.jp
Wolf, Helene	Technische Universität Wien , TU Wien, Austria helene.wolf@geo.tuwien.ac.at
Xu, Ming Hui	Huazhong University of Scinece and Technology, China mhxu@shao.ac.cn
Yang, Ying	National Time Service Center, Chinese Academy of Sciences, China xiyinghe1@163.com
Zhang, Juan	Shanghai Astronomical Observatory, SHAO, Chinese Academy of Science, China zhangjuan@shao.ac.cn
Zheng, Weimin	Shanghai Astronomical Observatory, SHAO, Chinese Academy of Science, China zhwm@shao.ac.cn
Zheng, Xin	Shanghai Astronomical Observatory, SHAO, Chinese Academy of Science, China zhengxin@shao.ac.cn
Zubko, Nataliya	Finnish Geospatial Research Institute, FGI, Finland nataliya.zubko@nls.fi

3rd IVS Training School on VLBI for Geodesy and Astrometry

The participants of the 3rd IVS Training School on VLBI for Geodesy and Astrometry, held at the University of Las Palmas de Gran Canaria, 14–16 March 2019

The 3rd IVS Training School on VLBI for Geodesy and Astrometry, held at the University of Las Palmas de Gran Canaria, 14–16 March 2019. There were 54 registered participants, out of 23 were ”real students”, i.e. participants who are still in educational programs (Bachelor, Master, or PhD), and 31 ” senior students”, i.e. senior scientists and post-docs. The participants came from institutions worldwide, see Tab. 1.

Table 1: Number of participants and country codes of their home institutions.

ES	US	CN	DE	AT	NO	SE	AU	FI	FR	SA	TH	NL
12	11	8	7	4	4	2	1	1	1	1	1	1

The school was meant to cover the complete ”VLBI chain”, from scheduling, observations, correlation and fringe fitting to data analysis. Twelve teachers were active in the school, see Tab. 2, giving one lecture each. The lectures were complemented with 4 exercises that aimed at using the acquired knowledge somehow in practical application. Also real observations with the two VGOS antennas RAEGYEB and ONSA13NE were performed as part of the VLBI school.

The complete program of the VLBI school is given in Table 3. The teaching material is available on the evga webpage under www.evga.org. All lectures were filmed, too, and the films can be made available on request.

The LOC took very good care of the participants and the teachers. There were regular coffee breaks, and lunches. At the last day, the school ended with the VLBI school dinner in a nice restaurant on the country side, including music and dance.

Table 2: Teachers and lecture topics.

Axel Nothnagel (AN)	Intro Geodesy
Alet de Witt (AdW)	Intro Astrometry
Patrick Charlot (PC)	Radio Sources
Gunnar Elgered (GE)	Telescopes/Feeds/Receivers
Harro Verkoputer (HV)	Data acquisition and transport
Gino Tuccari (GT)	Digital Backends
John Gipson (JG)	Scheduling
Walter Brisken (WB)	Correlation and fringe fitting
Rüdiger Haas (RH)	Fringe fitting/Fourfit
Dan MacMillan (DMM)	Geophysical modelling
Johannes Böhm (JB)	Signal propagation
Sergei Bolotin (SB)	Data analysis

Table 3: Program of the 3rd IVS school on VLBI.

Day-1, Thursday, 14 March 2019

08:50-09:00 Welcome and practical information (Susana Garcia-Espada + Rüdiger Haas)
09:00-09:45 L01: Why do we do it? A motivation for VLBI for Geodesy and Geosciences (AN)
09:45-10:00 – *Stretch your legs break* –
10:00-10:45 L01: – continued (AN)
10:45-11:15 – *Coffee break* –
11:15-12:00 L02: Why do we do it? A motivation for VLBI for Astrometry (AdW)
12:00-12:15 – *Stretch your legs break* –
12:15-13:00 L02: – continued (AdW)
13:00-14:00 – *Lunch break* –
14:00-14:45 L03: What do we observe? Radio sources (PC)
14:45-15:00 – *Stretch your legs break* –
15:00-15:45 L03: – continued (PC)
15:45-16:00 – *Coffee break* –
16:00-16:45 L04: What do we use to observe? VLBI stations, radio telescopes, receivers (GE)
16:45-17:00 – *Stretch your legs break* –
17:00-17:45 L04: – continued (GE)
17:45-18:00 – *Stretch your legs break* –
18:00-19:00 EX-1: Exercises on technical aspects (GE)

Day-2, Friday, 15 March 2019
09:00-09:45 L05: How do we store and transport the data? Data acquisition and transport (HV)
09:45-10:00 – *Stretch your legs break* –
10:00-10:45 L05: continued (HV)
10:45-11:15 – *Coffee break* –
11:15-12:00 L06: How do we sample data? Digital backends (GT)
12:00-12:15 – *Stretch your legs break* –
12:15-13:00 L06: continued (GT)
13:00-14:00 – *Lunch break* –
14:00-14:45 L07: How do we plan observations? Scheduling (JG)
14:45-15:00 – *Stretch your legs break* –
15:00-15:45 L07: continued (JG)
15:45-16:15 – *Coffee break* –
16:15-17:00 EX-2: Exercises on scheduling (JG)
17:00-17:15 – *Stretch your legs break* –
17:15-18:00 L08: How do we determine delays? Correlation and fringe-fitting (WB)
18:00-18:15 – *Stretch your legs break* –
18:15-19:00 L08: continued (WB)
19:00-19:15 – *Stretch your legs break* –

19:15-20:00 L09: How do we determine group delays? Fringe-fitting with FourFit (RH)

Day-3, Saturday, 16 March 2019
09:00-09:45 EX-3: Exercise on correlation with DiFX and fringe-fitting with Fourfit (WB + RH)
09:45-10:00 – *Stretch your legs break* –
10:00-10:45 EX-3: continued (WB + RH))
10:45-11:15 – *Coffee break* –
11:15-12:00 L10: How do we model observations? Geophysical modeling (DMM)
12:00-12:15 – *Stretch your legs break* –
12:15-13:00 L11: How do we model observations? Signal Propagation (JB)
13:00-14:00 – *Lunch break* –
14:00-14:45 L12: How do we analyze the data? Data analysis for geodesy (SB)
14:45-15:00 – *Stretch your legs break* –
15:00-15:45 L12: continued (SB)
15:45-16:00 – *Coffee break* –
16:00-16:45 EX-4: Exercise on data analysis (SB)
16:45-17:15 – *Stretch your legs break* –
17:15-18:00 EX-4: continued (SB)
20:00-23:59 – *VLBI school dinner* –

After the IVS training school on VLBI, the participants were asked to evaluate the event. About 50 % of the participants gave their feedback. Detailed results and answers from the evaluation are given in the next Section. In short, the probably five most important lessons from this evaluation can be summarized as:

- In general, the participants increased their knowledge in VLBI, i.e. they learnt something.
- The 'hands on' exercises were appreciated, and should be intensified in future schools.
- There is a strong interest to participate in future IVS VLBI schools.
- The IVS VLBI school should be held more often than every 3rd year.
- The IVS VLBI school should be longer than 3 days.

Evaluation of the 3rd VLBI school

To evaluate the 3rd IVS training school on VLBI for Geodesy and Astrometry, a questionnaire was sent to all participants. This questionnaire was split into two parts of 10 questions each. Part-I was closely related to the actual lectures and exercises and tried to measure whether there was a learning experience. We received answers to the questions of Part-I by 25 of the participants. Part-II was also giving the opportunity to give feedback in text form, and here 29 participants answered.

The 20 questions were:

1. How much of a general overview about VLBI for Geodesy and Astrometry did/do you have before/after the VLBI school?
2. What was/is your knowledge about radio sources before/after the VLBI school?
3. What was/is your knowledge about technical equipment at VLBI stations?
4. What was/is your knowledge about data sampling and data transport before/after the VLBI school?
5. What was/is your knowledge about scheduling VLBI experiments before/after the VLBI school?
6. What was/is your knowledge about correlation and fringe fitting before/after the VLBI school?
7. What was/is your knowledge about geophysical modeling, including signal propagation before/after the VLBI school?
8. What was/is your knowledge about VLBI data analysis before/after the VLBI school?
9. The lectures: What is your impression on the lectures that we had during the VLBI school?
10. The exercises: What is your impression on the exercises that we did during the VLBI school?
11. What was BEST with the VLBI Training school? What did you like most?
12. What was WORST with the VLBI Training school? What did you dislike most ?
13. Are there any topics that you were missing? If so, which?
14. Would you be interested in attending another VLBI school in the future?
15. In case you wanted to attend another VLBI school in the future, would you be willing to pay a special participation fee?
16. What is your opinion on how often the IVS should organise VLBI trainings schools?
17. Do you have suggestions on how to improve the VLBI school? If so, please indicate how?
18. What is your educational background?
19. If relevant, how many years have you been active in VLBI?
20. Any more feedback from your side?

Q1: How much of a general overview about VLBI for Geodesy and Astrometry did/do you have?

	VERY GOOD (5 points)	GOOD (4 points)	OK (3 points)	BAD (2 points)	VERY BAD (1 point)	∑ points
BEFORE the school	2	4	14	4	1	77
AFTER the school	5	17	3	0	0	102

Q2: What was/is your knowledge about radio sources?

	VERY GOOD (5 points)	GOOD (4 points)	OK (3 points)	BAD (2 points)	VERY BAD (1 point)	∑ points
BEFORE the school	4	4	8	6	3	75
AFTER the school	9	5	10	1	0	97

Q3: What was/is your knowledge about technical equipment at VLBI stations?

	VERY GOOD (5 points)	GOOD (4 points)	OK (3 points)	BAD (2 points)	VERY BAD (1 point)	∑ points
BEFORE the school	0	4	7	10	4	61
AFTER the school	6	7	11	0	1	92

Q4: What was/is your knowledge about data sampling and data transport?

	VERY GOOD (5 points)	GOOD (4 points)	OK (3 points)	BAD (2 points)	VERY BAD (1 point)	∑ points
BEFORE the school	1	3	10	5	6	63
AFTER the school	5	9	6	3	1	86

Q5: What was/is your knowledge about scheduling VLBI experiments before/after the VLBI school?

	VERY GOOD (5 points)	GOOD (4 points)	OK (3 points)	BAD (2 points)	VERY BAD (1 point)	$\sum$ points
BEFORE the school	2	4	8	8	3	69
AFTER the school	3	12	9	1	0	92

Q6: What was/is your knowledge about correlation and fringe fitting?

	VERY GOOD (5 points)	GOOD (4 points)	OK (3 points)	BAD (2 points)	VERY BAD (1 point)	$\sum$ points
BEFORE the school	0	3	7	7	8	55
AFTER the school	2	9	9	2	3	80

Q7: What was/is your knowledge about geophysical modeling, including signal propagation?

	VERY GOOD (5 points)	GOOD (4 points)	OK (3 points)	BAD (2 points)	VERY BAD (1 point)	$\sum$ points
BEFORE the school	2	8	9	5	1	80
AFTER the school	5	12	7	1	0	96

Q8: What was/is your knowledge about VLBI data analysis?

	VERY GOOD (5 points)	GOOD (4 points)	OK (3 points)	BAD (2 points)	VERY BAD (1 point)	$\sum$ points
BEFORE the school	4	10	4	5	2	84
AFTER the school	5	15	2	2	1	96

Q9: The lectures: What is your impression on the lectures that we had during the VLBI school?

	VERY GOOD (5 points)	GOOD (4 points)	OK (3 points)	BAD (2 points)	VERY BAD (1 point)	$\sum$ points
L01	12	12	1	0	0	111
L02	8	15	2	0	0	106
L03	8	12	5	0	0	103
L04	11	11	2	1	0	107
L05	10	13	1	1	0	107
L06	5	14	5	1	0	98
L07	8	13	4	0	0	104
L08	6	15	3	0	1	100
L09	7	10	6	0	1	94
L10	8	13	4	0	0	104
L11	8	11	6	0	0	102
L12	0	9	7	5	4	71

Q10: The exercises: What is your impression on the exercises that we did during the VLBI school?

	VERY GOOD (5 points)	GOOD (4 points)	OK (3 points)	BAD (2 points)	VERY BAD (1 point)	$\sum$ points
EX-1	3	9	10	3	0	87
EX-2	4	11	9	1	0	93
EX-3	6	9	9	0	1	94
EX-4	2	6	9	3	5	72

Q11: What was BEST with the VLBI Training school? What did you like most?

- Meet lots of people who are experts in this field and learn from them. Also meet people from any place in the world who is starting to work in this field.
- Practical exercises.
- The corresponding exercises were BEST, and I like most them.
- Data analysis and exercise.
- Exercises - I liked the fact we were 3-4 in a group and could work TOGETHER.
- Meeting very interesting people.
- Interaction, exercise part.
- Technical knowledge of the speakers.
- Learning the complete overview of the field.

- Exercise sessions.
- The exercises.
- Data acquisition and transport and Digital backends.
- The opportunity to learn and review all VLBI topics.
- The complete coverage from the observation to the analysis.
- Talking with other people during coffee breaks.
- Meeting the right people. Those who have lot of VLBI experience along all the steps of VLBI.
- A summary of the most important aspects of VLBI in ”only” 3 days, given by the top international experts. Hands-on experience with REAL data employing state-of-the-art software. Feedback from VLBI specialists. Mentimeter was very nice!
- The hands on parts were probably the most useful.
- The people, they were very nice and interesting.
- Practical Tasks.
- Meeting people, L01, L02.
- The location and people.
- Understanding which are the problems and how to resolve them, and see what is the VLBI state of the art.
- The order of the talks, good introduction talks, a clear simplification of some of the specific talks.
- Exercise.
- Organization of lectures, interaction with experts on fundamental level.
- Introduction by Prof. Nothnagel.
- Exercises.
- The practicality of teaching in particular areas.

Q12: What was WORST with the VLBI Training school? What did you dislike most?

- It should be at least 1 day more, it was too good but too short!
- Some days were just too long. Hard to stay concentrated.
- Unfamiliar content, such as radio , etc., I have very little harvest because the teacher taught too fast.
- I think the worst part is the nusolve part. he did not explain nusolve clearly
- Some of the presentations had too much theory and no application
- Some speeches were a little bit rough
- Not really
- The analysis session was quite messy
- Hands-on sessions where the number of server accounts are limited to 10, so, 3 or 4 students have to share
- Stretch legs breaks without coffee!
- Nothing
- Data analysis for geodesy

- Too long days.
- The time was too short to understand everything - may be a personal problem ;-)
- Analysis exercise and talk and too many many lectures during one day
- The schedule was too tight. I would prefer not to have lecture exercises after 5 pm if possible.
- The days were too long. 8 or 9 hours a day is the most one can generally handle it was to short, i would prefer more time to improve my skills
- EX-3, L12, EX-4
- VLBI data analysis part was bad
- Students hadn't slides beforehand to look figure details closer. You could put them at a local server just at the beginning of the lesson
- Exercises, practice part
- It was a bit too much intensive for 3 days.
- Analysis
- NA
- Maybe it could be done over more days

Q13: Are there any topics that you were missing? If so, which?

- Radio emission
- Yes? more information or progress about Spacecraft Geodetic VLBI
- No
- Not really
- No
- No
- CRF, TRF
- The topic I was more interested was data analysis and I couldn't understand anything
- Topics related to station operations.
- –
- I would love to see more analysis and analysis background and a bit less technical details.Ê
- I would like something more about analysis and vlbi processing.
- Global solution and multi-technique combination, a summary of what are the most important issues that impede progress in VLBI - perhaps one slide from every lecturer
- None
- More detailed explanations of the basics
- Field system, pre-check routines
- In my opinion, all the relevant aspects were covered there.Ê
- Analysis methods, step between fringe fitting and group delays analysis
- AIPS or Difmap or CASA data processingÊ
- NO
- no
- NA

Q14: Would you be interested in attending another VLBI school in the future?

yes	27
no	2

Q15: In case you wanted to attend another VLBI school in the future, would you be willing to pay a special participation fee?

yes	22
no	7

Q16: What is your opinion on how often the IVS should organise VLBI trainings schools?

every year	every 2nd year	every 3rd year	every 4th year	never
4	15	11	0	0

Q17: Do you have suggestions on how to improve the VLBI school? If so, please indicate how?

- Keep doing it in Canary Islands.
- I would suggest shortening some talks to 45 min or less.
- Whether to share the course ppt with everyone before training.
- Holding time can be extended, preferably 4-5 days.
- The days were too long. I would have preferred one more day and more exercises.
- More days to have so much information or special time for the most up-to-date one.
- End-to-end scheduling, correlation and analysis of the same session throughout all the practical sessions.
- Again, the number of hands-on server accounts. It would be nice if there are more, e.g 2 or less students per account.
- I think 3 days are not sufficient time to learn that amount of information. Maybe 4 or 5 days school is better.
- No.
- In general, I think it is really well organized.
- Maybe one extra day.
- More time to explain more stuff in detail (derivations of formulas etc.)
- Change some lecturers, distribute software better, more hands on exercises using state of the art software (no calculations by hand).

- In some ”cases” of lecture exercises, it would be better if we follow the lecturer and he/she explain every necessary step. Specially those related to correlation and data analysis. It will allow us to ask questions at the same time we make the exercise.
- More fancy presentation tools (e.g., gifs+animations), more interaction with audience (questions + 60 sec tasks), 10-point multiple choice quiz after every lecture (5 min) -¿ lecturers get feedback on how well the job was done.
- Shorter days. Make activity groups 3 people or less (hard to get 4 people around a screen). Perhaps having a mentor or experienced user for each group if possible (ex. Fourfit tutorial). Try to make lecture slides available before the school (easier to follow along/take notes on things if you have everything right in front of you).
- To give the presentation notes or slides before the school.
- More time for solving the practical tasks and a handout for using the software which is used.
- Better explanation of the basics.
- Distribute the amount of info on e.g. 4 days instead of 3.
- Generally is a very good event with top professionals. Maybe there were many lessons in a short time (2 days and a half) and I would extend lunch time a bit (1.5 hours) for the people to chat and relax a bit.
- Look for university lectors, create school lectures on-line
- The duration of school could be extended to 4 days, more time for exercises.
- More explanation on fundamentals in antenna theory.
- NA

Q18: What is your educational background?

Geodesy	9
Physics/Astrophysics/Astronomy	7
Communication / Electrical / Space Engineering	4
Mathematics	1
Meteorology	1
various	6

Q19: If relevant, how many years have you been active in VLBI?

≤ 1 year	$1 \leq 2$ years	$2 \leq 5$ years	> 5 years
10	7	7	4

Q20: Any more feedback from your side?

- Keep doing it, it was awesome and very useful!

- Thank you very much for the organization!
- NO?Thanks?
- No
- Thank your for giving us this kind of opportunity !
- I was satisfied with the school. Thank you!
- The school is VERY helpful! Thanks a lot for organizing!
- Thanks for very interesting lessons!
- Altogether, it was great to get the overview. I was hoping to understand more details, but that cannot happen in three days, at least not with me. The reason why I would not pay for another school is simply because I have been there now, and any next time (in a few years) would be hard to justify. In fact, I think it is worth paying for!
- Please add one extra day and spread out the lectures over 4 days. Or shorten/remove some talks. You can shorten: What do we use to observe? How do we store and transport data? and Digital backends (bring less details, focus more on general idea)
- It was a very nice experience and very well organized.
- No
- Thank you for let me be part of this school
- No
- Well, I'm starting in VLBI. Maybe you could send an email with some weblinks to 'must read' paper, articles, webs, etc. before the school for the students to get familiar with them.
- NA

Selected photos from the VLBI school

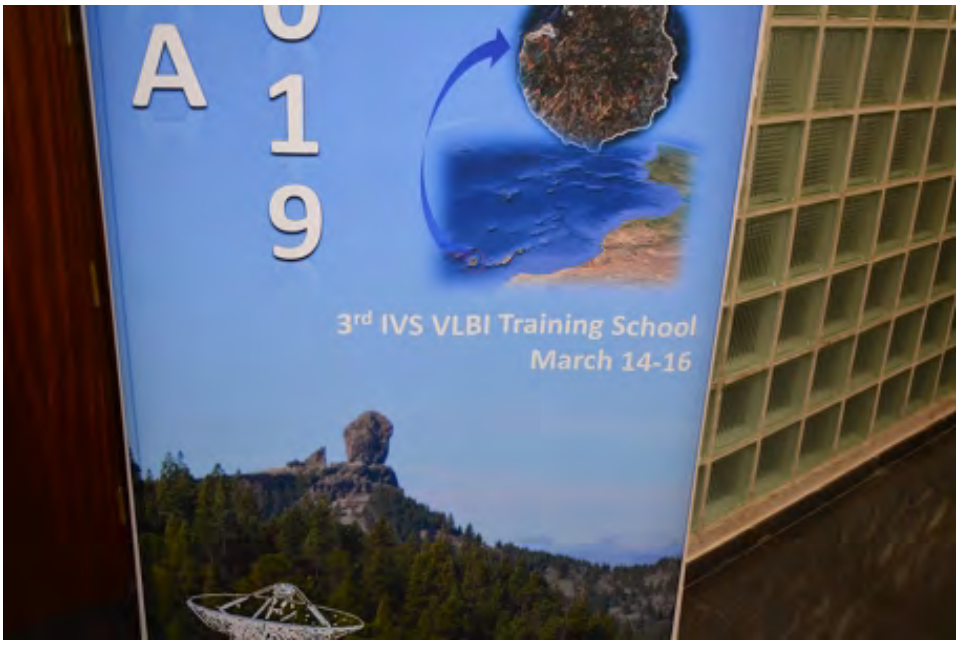

Fig. 2: The VLBI school banner.


Fig. 3: The lecture hall for the VLBI school.

Fig. 4: The lecture hall for the VLBI school.

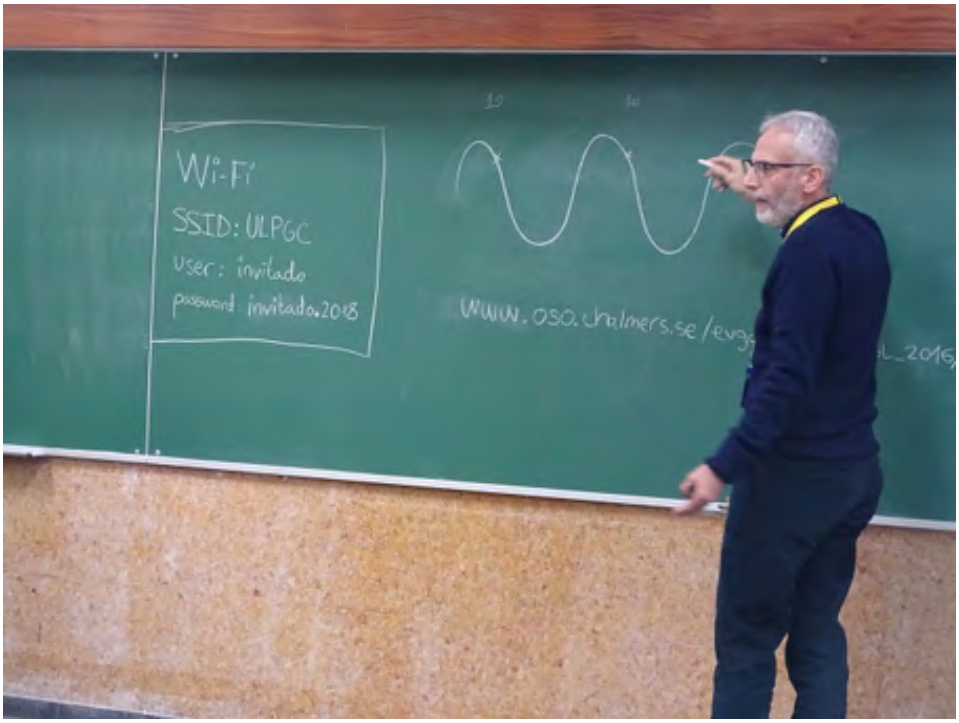

Fig. 5: Gino Tuccari explaining Nyquist sampling.

Fig. 6: Coffee break with intense discussions.

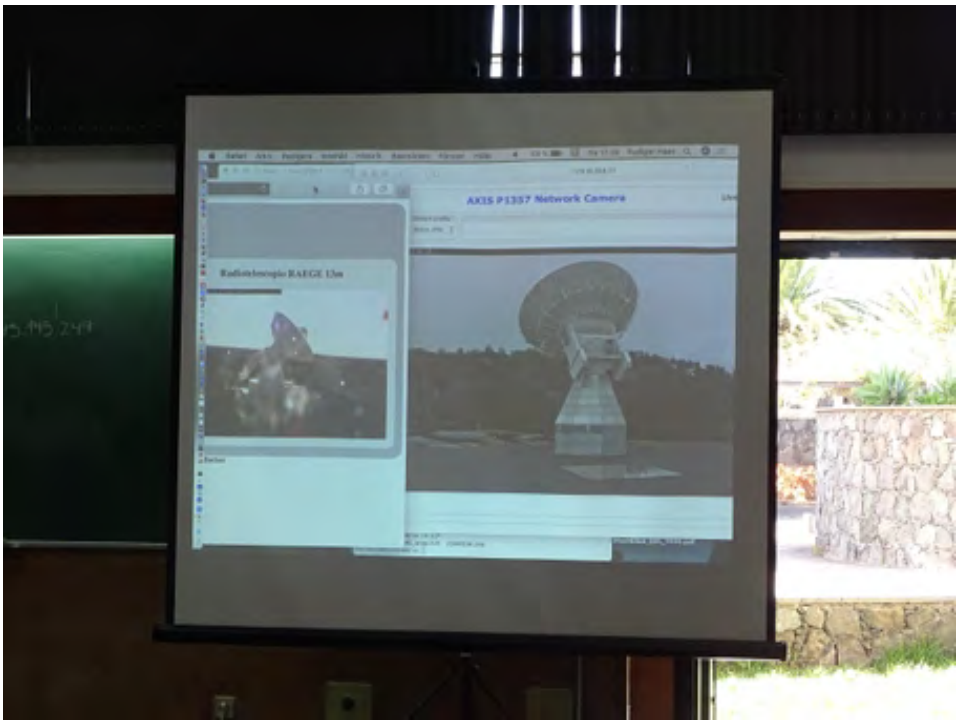

Fig. 7: Real observations during the VLBI school.

Fig. 8: Axel Nothnagel helping during the exercises.

Fig. 9: VLBI school lunch.

Fig. 10: Members of the LOC for the VLBI school.


Fig. 11: The VLBI school dinner.

EVGA 2019 Organization

The National Geographic Institute (IGN) of Spain is a General Directorate depending on the Ministry of Public Works of Spain (Ministerio de Fomento). It performs, among others, the functions of planning, scientific exploitation, technological development and operational management of its own astronomical, space geodesy and geodynamical instrumentation and infrastructures, and the planning and management of national passive and active geodetic networks. To this end, it has a network of geodetic stations distributed through the country and an Observatory in Yebes (Guadalajara, Spain) with two radio telescopes of 40 meters and 13.2 meters in diameter respectively and laboratories for the development of radio astronomical instrumentation. It is currently deploying a network called RAEGE ("Atlantic Network of Geodynamical and Space Stations"), in collaboration with the Regional Government of Azores, which will consist of four geodynamical stations in Yebes (Guadalajara, Spain), Artenara (Gran Canaria, Spain), Santa Maria and Flores (Azores, Portugal).

The National Center of Geographic Information (CNIG) is an autonomous entity assigned to the National Geographic Institute (IGN) that aims to produce, develop and distribute the works and publications of geographical nature that the society demands, including the commercialization of those performed by the IGN in execution of the functions that are legally attributed to it, the elaboration of derived and thematic products and their national and international distribution, without prejudice to the possible competences conferred to other entities of the Administration in the production and maintenance of various cartographic products, with special dedication to the realization of projects based on advanced technologies, research and development programs and provision of technical assistance in the field of geographic sciences and techniques.

UNIVERSIDAD DE LAS PALMAS
DE GRAN CANARIA

The ULPGC, established in 1989, has more than 25,000 students and 1,500 lecturers. It has modern facilities and equipment, with Wi-Fi area in all its centres.
The ULPGC offers the university community a wide range of cultural and sports activities to complement academic learning, promoting values such as solidarity, social justice, gender equality, and respect for diversity and the environment among members of the community.
The ULPGC is a leading university in e-learning. Degrees and Master programmes as well as a wide range of courses at all learning levels are offered online. The ULPGC has signed agreements with universities from the five continents, to facilitate the mobility of teachers, researchers, students, and administrative staff.
In 2007, the ULPGC won the Quality Award for Public Service and Special Mention for Best Management Practices, both from the Government of the Canary Islands. In 2010, the ULPGC was evaluated by an International Committee and earned the qualification of Campus of International Excellence, from the Ministry of Education of the Government of Spain.
It also develops an intense work in the field of development cooperation. It is worth noting the achievement of several UNESCO Chairs at the ULPGC.

EVGA 2019 Sponsors

The local government of Gran Canaria Island is ruled by the Cabildo. This institution with more than 100 years of history is in charge of many infrastructures, nature protected areas, tourism, culture, etc. The Cabildo of Gran Canaria is not only supporting the EVGA meeting but also the deployment of the future radio telescope for VLBI purposes on the island.

Established as a non-profit making Foundation, it is born thanks to the joint efforts of local public institutions and private companies of the tourist sector. It is actually composed of the following members: Tourist Board of Gran Canaria, The Town Hall of Las Palmas de Gran Canaria, Foundation Las Palmas de Gran Canaria Auditorium, The Canarian Institution of Trade Fairs, Expomeloneras, The Hotel, Restaurant and Cafe Business Employers Federation of Las Palmas and Chamber of Commerce, Industry and Navigation Services Gran Canaria.

MT Mechatronics GmbH, located in Mainz, Germany, provides global services as prime contractor for design, development, system integration, commissioning, training, maintenance and operations for communication and deep space antennas, radio and optical telescopes, mechatronic equipment for research institutions, launching facilities for the European space program and large medical systems for the next generation of particle cancer therapies. With over fifty years of experience in the telescope and antenna business MT Mechatronics has assembled a highly qualified team of engineers and experts with all relevant capabilities and experience to provide the best value and highest quality for your Mechatronic product.

This page is intentionally left blank.

EVGA 2019

Centro Nacional de Información Geográfica
Instituto Geográfico Nacional (Ministerio de Fomento)
Calle General Ibáñez de Ibero, 3
28003 Madrid
www.ign.es - consulta@cnig.es